NOAA Technical Memorandum NWS WR-218

NWS WINTER WEATHER WORKSHOP
PORTLAND, OREGON

National Weather Service
Weather Service Forecast Office
Portland, Oregon

December 1992

NOAA TECHNICAL MEMORANDA
National Weather Service, Western Region Subseries

The National Weather Service (NWS) Western Region (WR) Subseries provides an informal medium for the documentation and quick dissemination of results not appropriate, or not yet ready, for formal publication. The series is used to report on work in progress, to describe technical procedures and practices, or to relate progress to a limited audience. These Technical Memoranda will report on investigations devoted primarily to regional and local problems of interest mainly to personnel, and hence will not be widely distributed.

Papers 1 to 25 are in the former series, ESSA Technical Memoranda, Western Region Technical Memoranda (WRTM); papers 24 to 59 are in the former series, ESSA Technical Memoranda, Weather Bureau Technical Memoranda (WBTM). Beginning with 60, the papers are part of the series, NOAA Technical Memoranda NWS. Out-of-print memoranda are not listed.

Papers 2 to 22, except for 5 (revised edition), are available from the National Weather Service Western Region, Scientific Services Division, P.O. Box 11188, Federal Building, 125 South State Street, Salt Lake City, Utah 84147. Paper 5 (revised edition), and all others beginning with 25 are available from the National Technical Information Service, U.S. Department of Commerce, Sills Building, 5285 Port Royal Road, Springfield, Virginia 22161. Prices vary for all paper copies; microfiche are $3.50. Order by accession number shown in parentheses at end of each entry.

ESSA Technical Memoranda (WRTM)

2   Climatological Precipitation Probabilities. Compiled by Lucianne Miller, December 1965.
3   Western Region Pre- and Post-FP-3 Program, December 1, 1965, to February 20, 1966. Edward D. Diemer, March 1966.
5   Station Descriptions of Local Effects on Synoptic Weather Patterns. Philip Williams, Jr., April 1966 (Revised November 1967, October 1969). (PB-17800)
8   Interpreting the RAREP. Herbert P. Benner, May 1966 (Revised January 1967).
11   Some Electrical Processes in the Atmosphere. J. Latham, June 1966.
17   A Digitalized Summary of Radar Echoes within 100 Miles of Sacramento, California. J. A. Youngberg and L. B. Overaas, December 1966.
21   An Objective Aid for Forecasting the End of East Winds in the Columbia Gorge, July through October. D. John Coparanis, April 1967.
22   Derivation of Radar Horizons in Mountainous Terrain. Roger G. Pappas, April 1967.

ESSA Technical Memoranda, Weather Bureau Technical Memoranda (WBTM)

25   Verification of Operation Probability of Precipitation Forecasts, April 1966-March 1967. W. W. Dickey, October 1967. (PB-176240)
26   A Study of Winds in the Lake Mead Recreation Area. R. P. Augulis, January 1968. (PB-177830)
28   Weather Extremes. R. J. Schmidli, April 1968 (Revised March 1986). (PB86 177672/AS). (Revised October 1991 - PB92-115062/AS)
29   Small-Scale Analysis and Prediction. Philip Williams, Jr., May 1968. (PB178425)
30   Numerical Weather Prediction and Synoptic Meteorology. CPT Thomas D. Murphy, USAF, May 1968. (AD 673365)
31   Precipitation Detection Probabilities by Salt Lake ARTC Radars. Robert K. Belesky, July 1968. (PB 179084)
32   Probability Forecasting--A Problem Analysis with Reference to the Portland Fire Weather District. Harold S. Ayer, July 1968. (PB 179289)
36   Temperature Trends in Sacramento--Another Heat Island. Anthony D. Lentini, February 1969. (PB 183055)
37   Disposal of Logging Residues Without Damage to Air Quality. Owen P. Cramer, March 1969. (PB 183057)
39   Upper-Air Lows Over Northwestern United States. A.L. Jacobson, April 1969. PB 184296)
40   The Man-Machine Mix in Applied Weather Forecasting in the 1970s. L.W. Snellman, August 1969. (PB 185068)
43   Forecasting Maximum Temperatures at Helena, Montana. David E. Olsen, October 1969. (PB 185762)
44   Estimated Return Periods for Short-Duration Precipitation in Arizona. Paul C. Kangieser, October 1969. (PB 187763)
46   Applications of the Net Radiometer to Short-Range Fog and Stratus Forecasting at Eugene, Oregon. L. Yee and E. Bates, December 1969. (PB 190476)
47   Statistical Analysis as a Flood Routing Tool. Robert J.C. Burnash, December 1969. (PB 188744)
48   Tsunami. Richard P. Augulis, February 1970. (PB 190157)
49   Predicting Precipitation Type. Robert J.C. Burnash and Floyd E. Hug, March 1970. (PB 190962)
50   Statistical Report on Aeroallergens (Pollens and Molds) Fort Huachuca, Arizona, 1969. Wayne S. Johnson, April 1970. (PB 191743)
51   Western Region Sea State and Surf Forecaster's Manual. Gordon C. Shields and Gerald B. Burdwell, July 1970. (PB 193102)
52   Sacramento Weather Radar Climatology. R.G. Pappas and C. M. Veliquette, July 1970. (PB 193347)
54   A Refinement of the Vorticity Field to Delineate Areas of Significant Precipitation. Barry B. Aronovitch, August 1970.
55   Application of the SSARR Model to a Basin without Discharge Record. Vail Schermerhorn and Donal W. Kuehl, August 1970. (PB 194394)
56   Areal Coverage of Precipitation in Northwestern Utah. Philip Williams, Jr., and Werner J. Heck, September 1970. (PB 194389)
57   Preliminary Report on Agricultural Field Burning vs. Atmospheric Visibility in the Willamette Valley of Oregon. Earl M. Bates and David O. Chilcote, September 1970. (PB 194710)
58   Air Pollution by Jet Aircraft at Seattle-Tacoma Airport. Wallace R. Donaldson, October 1970. (COM 71 00017)
59   Application of PE Model Forecast Parameters to Local-Area Forecasting. Leonard W. Snellman, October 1970. (COM 71 00016)
60   An Aid for Forecasting the Minimum Temperature at Medford, Oregon, Arthur W. Fritz, October 1970. (COM 71 00120)
63   700-mb Warm Air Advection as a Forecasting Tool for Montana and Northern Idaho. Norris E. Woerner, February 1971. (COM 71 00349)
64   Wind and Weather Regimes at Great Falls, Montana. Warren B. Price, March 1971.
65   Climate of Sacramento, California. Tony Martini, April 1990. (Fifth Revision) (PB89 207781/AS)
66   A Preliminary Report on Correlation of ARTCC Radar Echoes and Precipitation. Wilbur K. Hall, June 1971. (COM 71 00829)
69   National Weather Service Support to Soaring Activities. Ellis Burton, August 1971. (COM 71 00956)
71   Western Region Synoptic Analysis-Problems and Methods. Philip Williams, Jr., February 1972. (COM 72 10433)
74   Thunderstorms and Hail Days Probabilities in Nevada. Clarence M. Sakamoto, April 1972. (COM 72 10554)

75   A Study of the Low Level Jet Stream of the San Joaquin Valley. Ronald A. Willis and Philip Williams, Jr., May 1972. (COM 72 10707)
76   Monthly Climatological Charts of the Behavior of Fog and Low Stratus at Los Angeles International Airport. Donald M. Gales, July 1972. (COM 72 11140)
77   A Study of Radar Echo Distribution in Arizona During July and August. John E. Hales, Jr., July 1972. (COM 72 11136)
78   Forecasting Precipitation at Bakersfield, California, Using Pressure Gradient Vectors. Earl T. Riddiough, July 1972. (COM 72 11146)
79   Climate of Stockton, California. Robert C. Nelson, July 1972. (COM 72 10920)
80   Estimation of Number of Days Above or Below Selected Temperatures. Clarence M. Sakamoto, October 1972. (COM 72 10021)
81   An Aid for Forecasting Summer Maximum Temperatures at Seattle, Washington. Edgar G. Johnson, November 1972. (COM 73 10150)
82   Flash Flood Forecasting and Warning Program in the Western Region. Philip Williams, Jr., Chester L. Glenn, and Roland L. Raetz, December 1972, (Revised March 1978). (COM 73 10251)
83   A comparison of Manual and Semiautomatic Methods of Digitizing Analog Wind Records. Glenn E. Rasch, March 1973. (COM 73 10669)
86   Conditional Probabilities for Sequences of Wet Days at Phoenix, Arizona. Paul C. Kangieser, June 1973. (COM 73 11264)
87   A Refinement of the Use of K-Values in Forecasting Thunderstorms in Washington and Oregon. Robert Y.G. Lee, June 1973. (COM 73 11276)
89   Objective Forecast Precipitation Over the Western Region of the United States. Julia N. Paegle and Larry P. Kierulff, September 1973. (COM 73 11946/3AS)
91   Arizona "Eddy" Tornadoes. Robert S. Ingram, October 1973. (COM 73 10465)
92   Smoke Management in the Willamette Valley. Earl M. Bates, May 1974. (COM 74 11277/AS)
93   An Operational Evaluation of 500-mb Type Regression Equations. Alexander E. MacDonald, June 1974. (COM 74 11407/AS)
94   Conditional Probability of Visibility Less than One-Half Mile in Radiation Fog at Fresno, California. John D. Thomas, August 1974. (COM 74 11555/AS)
95   Climate of Flagstaff, Arizona. Paul W. Sorenson, and updated by Reginald W. Preston, January 1987. (PB87 143160/AS)
96   Map type Precipitation Probabilities for the Western Region. Glenn E. Rasch and Alexander E. MacDonald, February 1975. (COM 75 10428/AS)
97   Eastern Pacific Cut-Off Low of April 21-28, 1974. William J. Alder and George R. Miller, January 1976. (PB 250 711/AS)
98   Study on a Significant Precipitation Episode in Western United States. Ira S. Brenner, April 1976. (COM 75 10719/AS)
99   A Study of Flash Flood Susceptibility-A Basin in Southern Arizona. Gerald Williams, August 1975. (COM 75 11360/AS)
102 A Set of Rules for Forecasting Temperatures in Napa and Sonoma Counties. Wesley L. Tuft, October 1975. (PB 246 902/AS)
103 Application of the National Weather Service Flash-Flood Program in the Western Region. Gerald Williams, January 1976. (PB 253 053/AS)
104 Objective Aids for Forecasting Minimum Temperatures at Reno, Nevada, During the Summer Months. Christopher D. Hill, January 1976. (PB 252 866/AS)
105 Forecasting the Mono Wind. Charles P. Ruscha, Jr., February 1976. (PB 254 650)
106 Use of MOS Forecast Parameters in Temperature Forecasting. John C. Plankinton, Jr., March 1976. (PB 254 649)
107 Map Types as Aids in Using MOS PoPs in Western United States. Ira S. Brenner, August 1976. (PB 259 594)
108 Other Kinds of Wind Shear. Christopher D. Hill, August 1976. (PB 260 437/AS)
109 Forecasting North Winds in the Upper Sacramento Valley and Adjoining Forests. Christopher E. Fontana, September 1976. (PB 273 677/AS)
110 Cool Inflow as a Weakening Influence on Eastern Pacific Tropical Cyclones. William J. Denney, November 1976. (PB 264 655/AS)
112 The MAN/MOS Program. Alexander E. MacDonald, February 1977. (PB 265 941/AS)
113 Winter Season Minimum Temperature Formula for Bakersfield, California, Using Multiple Regression. Michael J. Oard, February 1977. (PB 273 694/AS)
114 Tropical Cyclone Kathleen. James R. Fors, February 1977. (PB 273 676/AS)
116 A Study of Wind Gusts on Lake Mead. Bradley Colman, April 1977. (PB 268 847)
117 The Relative Frequency of Cumulonimbus Clouds at the Nevada Test Site as a Function of K-Value. R.F. Quiring, April 1977. (PB 272 831)
118 Moisture Distribution Modification by Upward Vertical Motion. Ira S. Brenner, April 1977. (PB 268 740)
119 Relative Frequency of Occurrence of Warm Season Echo Activity as a Function of Stability Indices Computed from the Yucca Flat, Nevada, Rawinsonde. Darryl Randerson, June 1977. (PB 271 290/AS)
121 Climatological Prediction of Cumulonimbus Clouds in the Vicinity of the Yucca Flat Weather Station. R.F. Quiring, June 1977. (PB 271 704/AS)
122 A Method for Transforming Temperature Distribution to Normality. Morris S. Webb, Jr., June 1977. (PB 271 742/AS)
124 Statistical Guidance for Prediction of Eastern North Pacific Tropical Cyclone Motion - Part I. Charles J. Neumann and Preston W. Leftwich, August 1977. (PB 272 661)
125 Statistical Guidance on the Prediction of Eastern North Pacific Tropical Cyclone Motion - Part II. Preston W. Leftwich and Charles J. Neumann, August 1977. (PB 273 155/AS)
126 Climate of San Francisco. E. Jan Null, February 1978. Revised by George T. Pericht, April 1988. (PB88 208624/AS)
127 Development of a Probability Equation for Winter-Type Precipitation Patterns in Great Falls, Montana. Kenneth B. Mielke, February 1978. (PB 281 387/AS)
128 Hand Calculator Program to Compute Parcel Thermal Dynamics. Dan Gudgel, April 1978. (PB 283 080/AS)
129 Fire whirls. David W. Goens, May 1978. (PB 283 866/AS)
130 Flash-Flood Procedure. Ralph C. Hatch and Gerald Williams, May 1978. (PB 286 014/AS)
131 Automated Fire-Weather Forecasts. Mark A. Mollner and David E. Olsen, September 1978. (PB 289 916/AS)
132 Estimates of the Effects of Terrain Blocking on the Los Angeles WSR-74C Weather Radar. R.G. Pappas, R.Y. Lee, B.W. Finke, October 1978. (PB 289767/AS)
133 Spectral Techniques in Ocean Wave Forecasting. John A. Jannuzzi, October 1978. (PB291317/AS)
134 Solar Radiation. John A. Jannuzzi, November 1978. (PB291195/AS)
135 Application of a Spectrum Analyzer in Forecasting Ocean Swell in Southern California Coastal Waters. Lawrence P. Kierulff, January 1979. (PB292716/AS)
136 Basic Hydrologic Principles. Thomas L. Dietrich, January 1979. (PB292247/AS)
137 LFM 24-Hour Prediction of Eastern Pacific Cyclones Refined by Satellite Images. John R. Zimmerman and Charles P. Ruscha, Jr., January 1979. (PB294324/AS)
138 A Simple Analysis/Diagnosis System for Real Time Evaluation of Vertical Motion. Scott Heflick and James R. Fors, February 1979. (PB294324/AS)
139 Aids for Forecasting Minimum Temperature in the Wenatchee Frost District. Robert S. Robinson, April 1979. (PB298339/AS)
140 Influence of Cloudiness on Summertime Temperatures in the Eastern Washington Fire Weather district. James Holcomb, April 1979. (PB298674/AS)
141 Comparison of LFM and MFM Precipitation Guidance for Nevada During Doreen. Christopher Hill, April 1979. (PB298613/AS)

NOAA Technical Memorandum NWS WR-218

NWS WINTER WEATHER WORKSHOP
PORTLAND, OREGON

National Weather Service
Weather Service Forecast Office
Portland, Oregon

December 1992

This publication has been reviewed
and is approved for publication by
Scientific Services Division,
Western Region

Ken Mielke

Kenneth B. Mielke, Chief
Scientific Services Division
Salt Lake City, Utah

National Weather Service

-
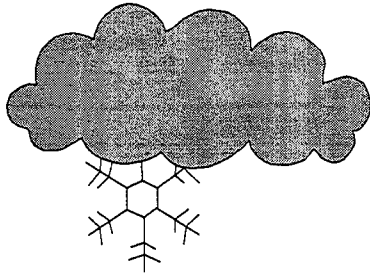
Winter Weather Workshop

Portland, Oregon

September 15 - 18, 1992

NATIONAL WEATHER SERVICE

WINTER WEATHER WORKSHOP

SEPTEMBER 15th - 18th

JANTZEN BEACH RED LION

PORTLAND, OREGON

SPONSOR: National Weather Service

HOSTS: National Weather Service
                                              Western Region
                                              Thomas D. Potter, Director

                                              Weather Service Forecast Office
                                              Portland, Oregon
                                              George Miller, Area Manager

PROGRAM
CHAIRMAN: John A. Jannuzzi, Area Manager
                                              National Weather Service
                                              Boise, Idaho

LOGISTICS SUPPORT: Steve Todd
                                              Deputy Meteorologist In Charge

ACKNOWLEDGEMENTS:

Kenneth B. Mielke, Chief, Scientific Services Division
Elaine J. Robinson, Scientific Services Division
Susan Butner, Boise WSFO

Winter Weather Workshop Agenda
September 15 - 18, 1992

	Tue	Wed	Thu	Fri
8:00	Welcome	Labs II.	Abstracts	Abstracts
8:30	NESDIS lab	"	"	"
9:00	(part I)	"	"	"
9:30	"	"	"	"
10:00	map disc/brk	map disc/brk	map disk/brk	map disk/brk
10:30	NESDIS lab	Labs II.	Abstracts	Abstracts
11:00	(part II)	(cont'd)	"	wrapup
11:30	"	Lunch	Lunch	"
12:00	Lunch/	"	"	Dismiss
12:30	Speaker	"	"	
13:00	"	Abstracts	Abstracts	
13:30	Abstract	"	"	
14:00	Labs I.	Labs III.	"	
14:30	"	"	"	
15:00	"	"	Break	
15:30	"	"	Abstracts	
16:00	"	"	"	
16:30	"	"	"	
17:00	Dismiss	Dismiss	Dismiss	
17:30	Ice Breaker			
18:00		Ice Breaker		
19:00		Banquet/		
		Speaker		

note An afternoon break on Tuesday and Wednesday (15 minutes)
will be accommodated at a time determined by lab
instructors.

Labs
Winter Weather Workshop

Mike Mogil and   Use of Satellite Information for Improved
Frank Smigielski   Surface Analysis in the North Atlantic Ocean.

Eric Thaler   Quasigeostrophic Theory and it's Application
                        in Evaluating Vertical Motion.

Larry Ruthy   Refining Precipitation Forecasts using the
                        WSR-88D.

Bruce Terry   Synoptic and Climatological Patterns
                        Associated with Heavy Snows, also,
                        NMC Model Performance Characteristics.

Dennis Rogers   Mini-labs using the PROFs workstation to
                        evaluate the 15 November 1987 Denver Snow
                        storm.

Post-Prints
NWS Winter Weather Workshop
Portland, Oregon
September 15 - 18, 1992

Tuesday, September 15

1:30   River Flood Forecasting in the Northeast During Ice Jam
        Situations, by Tom Hawley, BOS WSFO

Wednesday, September 16

1:00   Using Rawinsonde Data to Forecast Frontal (and Rainband)
        Motion, by James Fenner, Oregon Institute of Technology

1:30   Low-Level Jet Formation and Prediction Using the Nested
        Grid Model, by Paul Janish, EFF/NSSL/CIMMS

Thursday, September 17
Morning

8:00   NDBC Automated Observation Systems and Characteristics,
        by Eric Meindl, National Data Buoy Center

8:30   Diagnosing Cyclogenesis Using Unconventional Methods, by
        Eric Thaler, DEN WSFO

9:00   The Front Range/Palmer Divide Blizzard of 7 January 1992,
        by Ray Wolf, DEN WSFO

9:30   Observing and Forecasting a Mesoscale Snow Event using
        MAPS, by Robert Glancy, DEN WSFO

10:30   Operational Use of an Orographic Snow Model, by Chris
        Scott, CYS WSFO

11:00   Operational Use of an Orographic Precipitation Model, by
        Pam Speers Hayes, U.S. Forest Service, Seattle

Thursday, September 17
Afternoon

1:00   An Analysis of the Record-Breaking Northern Plains Snowstorm of October 27-29, by William Abeling, BIS WSFO

1:30   Snowstorms in the Puget Sound Lowlands, by Garth Ferber, SEA WSFO

2:00   The Use of High Resolution Data from the NGM for The Prediction of Lake Effect Snow, by Thomas Niziol, BUF WSFO

2:30   Lake Effect Snow Prediction Techniques, by Warren Snyder, ALB WSFO

3:30   Characteristics of Surface Cyclone Forecasts in the Aviation Run of the Global Circulation Model, by Richard Grumm, NMC

4:00   Rapidly Deepening Cyclones in NMC's Nested Grid Model, by Robert Oravec, NMC   -
       [paper not included - submitted for publication to the A.M.S. journal, *Weather and Forecasting*]

4:30   Forecaster and Model Biases in a Stagnant Pattern of Low Clouds and Fog, by Timothy McClung, SLC WSFO

Friday, September 18

8:00   An Overview of the Alaska Region Operations Network, by Paul Shannon, NWS ARH

8:30   Forecast Application and Imagery System, by Glen Sampson, SSD WRH

9:00   NGM Model Output Error and the Effect on Forecasting a Great Basin Cyclogenic Event, by Michael Conger, SLC WSFO

9:30   A Winter Severity Index for Pittsburgh, Pennsylvania, by Victor Nouhan, PIT WSFO

10:30 Polar Travelogue - High Latitude Activity, by Dennis Stossel, Atmospheric Environment Service, Canada
       [paper not included - only available in a slide presentation]

River Flood Forecasting in the Northeast During Ice Jam Situations

A. Austin-Smith, T. Hawley, B. Kilpatrick, P. Gabrielsen
Hydrologists, Eastern Region, National Weather Service

Abstract

The Northeast River Forecast Center (NERFC) is one of thirteen National Weather Service River Forecast Centers in the United States. NERFCs area of responsibility includes most rivers in New York and all rivers in New England. Service hydrologists at Weather Service Forecast Offices (WSFOs) in Albany and Buffalo New York, and Portland Maine, support NERFC river forecasting operations.

Rainfall and river gage data are collected, quality controlled and processed to drive an interactive antecedent precipitation index (API) river forecasting model. This model calculates river stage forecasts a six hour intervals. When specified criteria are met river flood watches and warnings are issued.

Normally during the winter, river flows in the northeast are low and along with cold temperatures, encourage the formation and growth of river ice. During the start of the spring runoff river flow volumes increase, causing river ice to break up and jam, usually at constricted river channel locations. Ice jams historically form, but are not limited to the same river locations. When ice jams form they cause a combination of backwater and down stream flooding.

Forecasting ice jam flooding presents unique challenges to the hydrologist. API models do not adequately forecast ice jam flooding because, it is more hydraulic than hydrometeorologic in nature. Hydraulic models such as the NWS Dambreak and Army Corps of Engineers HEC2 back water model have shown limited success in real time ice jam flood forecasting. NERFC and supporting WSFOs use specialized operational procedures to monitor river ice, forecast flood levels, and coordinate flood watches and warnings during ice jam flooding. Knowledge of ice jam prone areas in the WSFOs area also assist in monitoring and forecasting ice jam flooding. Annually, ice jam areas are reviewed and methods of ice jam control are monitored. Ice jams flooding locations in the northeast are reviewed and ice jam flooding that occurred in Portland's HSA during the spring of 1991 and 1992 are presented as operational experiences.

River Forecast Operations

The Northeast River Forecast Center (NERFC) is one of thirteen National Weather Service (NWS) River Forecast Centers (RFCs) in the United States. NERFCs area of responsibility includes Lake Erie, Lake Ontario and the Hudson River drainage in New York; Lake Champlain drainage in New York and Vermont; and all other rivers in New England. Operations are supported by service hydrologists at Weather Service Forecast Offices (WSFOs) in Portland, Maine; Albany, New York; and Buffalo, New York.

NERFC and the three WSFOs are responsible for specific Hydrologic Service Areas (HSAs) in the northeast defined by major watershed boundaries. Hydrometeorologic parameters including; precipitation, river stage, and daily temperatures are collected by a data collection network of cooperative weather observers and automated river and rainfall gages.

NERFC collects hydrometeorological data at specified times during normal river forecasting operations from HSA offices in Standard Hydrologic Exchange Format (SHEF) over the AFOS regional distribution circuit. This hydrometeorological data in combination with NERFCs local HSAs data are quality controlled and processed. Precipitation and temperature data are distributed spatially in time series to represent the climatological state of the river basin. River and reservoir data are processed into observed time series for specified forecast locations. The data are used to compute river stage forecasts at six hour intervals using an interactive API model.

API is an index that reflects soil moisture conditions of a watershed above a river forecast point. NERFCs interactive forecast model recognizes that runoff is related to numerous factors, API being a very essential one. Along with API, precipitation amount, intensity and duration are also important when computing storm runoff.

Hydrologists at NERFC have the ability to interactively adjust each hydrograph for forecast locations by adjusting the watersheds; API, storm precipitation totals and/or distribution, and by blending the observed data river data and modelled data. The final adjusted hydrographs are converted to six hourly river stage forecasts and distributed through AFOS to the appropriate WSFO.

River Ice Formation

River ice begins to form when air temperature stay below freezing and discharge velocities remain low for prolonged periods of time.

These conditions promote river ice sheet formation. As the winter progresses, ice grows downward and thickens. This process is aided by snow cover which prevents heat loss, and as it accumulates thickens into a frozen mass of slush, referred to as snow ice.

Ice also forms when supercooled water is passed under an insulated ice layer. The supercooled water will freeze to the underside of the ice layer. Frazil ice which is formed at severe surface turbulence and cold air temperatures (< 20 degrees F) also accumulates to the bottom of the existing ice sheet. Both of these under growth ice formation have the tendency to form hanging dams. Hanging dams usually produce very serious backwater flooding during high discharge volumes.

Ice Jam Formation

Ice jams, for the most part, form as the weather gradually warms during the spring months. Flows initially increase as the snowpack and ice cover begin to melt and along with rainfall usually set the stage for most ice jams. The severity of an ice jam primarily depends on ice strength and river discharge velocities. Ice strength deteriorates as flow rates increase resulting in an ice break up. The more competent the ice and the higher the flow, the more severe the jam. The tendency for winter ice jams to be more severe than spring jams can be related to ice thickness. Winter ice jams usually occur during periods of unseasonably warm weather, heavy rainfall and rapid snowmelt. When rivers respond very quickly with a dramatic increase in river discharge and very strong winter ice is still on the river, a solid ice jam can occur. A rapid ice breakup coupled with a heavy rainfall event can prove to be disastrous to an ice jam prone area.

Ice jam prone areas are for the most part historical in that they do not change from year to year. These areas are usually where the river makes a sharp bend, narrows or there is some form of constriction, hydraulic jump or reduced slope. The constriction can be in either natural or man-made such as bridges, dams or small islands. It is at these constrictions, bends or areas of decreased flow where the ice flowing downstream becomes trapped and jams. Once the jam occurs the ice continues to stack. This acts like a dam rapidly increasing the water level upstream from the ice jam, sometimes resulting in a flood situation. It is very difficult to forecast the exact time or duration of an ice jam although when the key ingredients are present, the areas of greatest potential are readily apparent.

Flooding due to ice jams can be quite severe. Ice jams destroy bridges by lifting them off their piers. Houses can be completely destroyed by blocks of ice as they move downstream. It is not uncommon for the water level behind a jam to rise 3 to 4 feet in a few minutes during ice jam events. When the ice jam finally breaks, water levels downstream increase rapidly usually resulting in a flash flood situation.

Ice Jam Areas in the Northeast

Many rivers in the northeast experience recurrent ice jam problems. In Albany's HSA river ice and jamming are normally, but not always, more severe in northern areas and often of little or no consequence in areas south of the Mohawk River.

Ice jamming occurs regularly on all the major rivers in Vermont including the upper Connecticut River Basin along the eastern border. In some years their effects have been devastating, such as the Montpelier ice jam flood of March 1992. Many of the rivers in northern Vermont have long sections of flat, relatively still water, which favor thick ice accumulation.

Southern Vermont is not as severely affected by ice jam flooding as northern Vermont. Prolonged cold is not as common, and rain events also tend to keep the river ice thinner. Also most of the rivers are swifter flowing and have less still water to form thick ice. The Connecticut River is an exception and due to river regulation has had a history of significant ice jam problems. The Army Corps of Engineers has taken advantage of this regulation by trying to break up the ice dynamically at Windsor, Vermont (Ferrick et al., 1988) using controlled releases from flood control and hydroelectric dams.

Ice jamming is both common and severe in the Adirondack Region of New York due to the winter's intensity and the type of residential, recreational and commercial development. Because of the rural nature of the area most roads, homes and businesses, follow the rivers and streams. While this area is lightly populated, there is a great deal of vacation and recreational development along the rivers that are effected by ice jams flooding. Ice jamming is also quite common in the major rivers in the St. Lawrence Valley in north central New York due to long flat river sections.

In Buffalo's HSA a few of the creeks are known for having annual ice jam problems. This is due primarily to the small watershed sizes and the low discharges accompanied with significant lake effect snow fall which sets up the ideal ice formation scenario.

The Black River has a unique problem in that it flows northward. The headwaters are therefore geographically south. As the ice breaks up and the snow thaws the increased flow moves downstream into regions that are colder. This sets the stage for potentially serious ice jams problems each season on the Black River.

Many of rivers in Maine have ice jam problems as do most rivers in northern and central New Hampshire. The two rivers Portland's HSA that are the most susceptible to ice jams are the Aroostook and St. John Rivers in Northern Maine. Like the Black River, these rivers also flow from south to north. Their headwaters are located in North Central Maine. In the spring and even in the winter

during a warm spell there can be a tremendous difference in temperature along the length of both rivers. This leads to the break up of ice and increased river flows far upstream. This ice then travels downstream, where it jams on stationary ice simply because downstream locations are much colder and the ice has not yet begun to melt.

Ice Jams in Maine

This is the exact scenario that occurred during the devastating ice jams of April 1991 on the St. John River. Temperatures in the headwaters of the St. John for the two days preceding the event were close to 70 degrees F, while downstream at Dickey and Allagash temperatures remained near 40 degrees F. During this time 1 to 2 inches of rain fell rapidly, increasing flows. Ice began breaking up and moving downstream where it eventually jammed on a solid sheet of ice in a relatively flat and shallow reach of the river.

Average temperatures for the three winter months combined ranged from 1 to 2 degrees below normal in Maine east of the Kennebec River. New Hampshire and Western-Maine were 1 to 2 degrees above normal. Snowfall was below normal in most of Maine and New Hampshire, and as much as 60 percent below normal in some areas of Southern New Hampshire. Water equivalent of snow on the ground was also below normal, with the exception of northern Maine and portions of Coos county New Hampshire. Water equivalents of 5 to 7 inches were common in Northern Maine and Northern New Hampshire. River ice was 3 to 4 feet thick on portions of the St.John River, probably due to the below normal winter temperatures and the below normal snowfall. Elsewhere, river ice was not thicker than normally expected.

Even with the thicker than normal ice, no ice jams occurred on Northern Maine Rivers in 1992. Warm weather moved in and softened the ice but rainfall was not particularly heavy. The ice became very soft and flowed downstream without incident. In Central Maine however, the situation was much different. During the last week of March, 4 inches of rain fell in some locations of Central Maine. Temperatures were not very warm, ranging from the upper 30's to mid 40's. However, the tremendous amount of runoff caused by the rainfall and melting snow increased flows rapidly resulting in the break up of the ice on the central Maine rivers. The ice jams were confined to smaller river basins where the ice had not yet melted. The ice in the large rivers had gone out earlier in the spring. The Sandy, Carrabassett, and Piscataquis Rivers were still choked with ice. Several evacuations were necessary along all three of these rivers. Damage was not extensive as only small areas along these rivers were affected. In New Hampshire, minor flooding due to ice jams occurred during the middle of March from ice jams that had formed on the Pemigewasset, Connecticut, and Sugar Rivers. Little or no damage was reported from these jams.

Ice Jam Operational Concerns

In an attempt to decrease the impact of ice jam flooding there are numerous techniques that are implemented in the northeast by federal agencies and private concerns to reduce ice jam flooding. These techniques include both structural and operational solutions as well as observing programs. These methods not only decrease the potential of an ice jam at a given location, but also decrease the effect of increased flow downstream once a jam breaks. Knowledge of these techniques can greatly enhance the ability of the hydrologist to effectively monitor and forecast ice jam situations

An ice boom installed on the Lamoille River in Hardwick, Vermont is an example of a structural solution to an ice jam problem. Ice booms are constructed from material such as timber, steel or tires and are placed across the surface of the river channel. The ice booms purpose is to contain and stabilize large ice sheets in the channel above a known ice jam location. The ice boom serves as a sieve allowing smaller less dangerous chunks of ice downstream. This method proved successful in reducing the severity of an ice jam event in Hardwick, Vermont in March 1992. This method is used when ice jams historically reoccur at a given location. The narrower the channel the greater the effectiveness of the ice boom technique.

Discharge on the Connecticut River near Windsor, Vermont area is controlled by Wilder Dam upstream and Bellows Falls Dam downstream. The Army Corps of Engineers (Ferrick et al. 1988) studied using controlled releases from upstream dams to break up river ice at a known jam location. By studying the ice thickness and temperature, the program focused on breaking up ice with a controlled dynamic wave of water before the natural ice breakup occurred. This program requires a detailed knowledge of current river ice conditions and river morphology. This annual program is an example of operational control of ice jams.

These structural and operational techniques cannot be haphazardly implemented. Consideration must be given to river channel size, ice type, ice thickness, and local considerations before they can be used.

River sections prone to ice jams can be monitored in a number of ways. Ice problem locations are identified by type, location and severity. Cooperative weather observers provide information on point source ice problems, there are also a number of ice observing networks.

In Vermont, a program is now in place where the Vermont Agency of Transportation (VAOT) has a network that provides information on ice packs and their characteristics in the state. NERFC tries to get this information in a timely fashion. Annually research is done to uncover these local networks and set up communications to get their data.

Another agency that assists the NWS monitor ice jams is the Maine Emergency Management Agency. They work with the Maine Air National Guard to fly over certain river basins if the NWS requests it. The Guard is supplied with maps outlining the ice jam locations, see Figure 1 . Their mission is to detail ice conditions encountered at each location and relay that information back to the NWS in a log, see Figure 2.

Existing hydraulic models and studies also provide a basis for reviewing annual ice jam prone areas. Flood insurance studies, working hydraulic models, navigation models, and backwater studies can be reviewed to identify possible ice jams and associated flooding. These methods have little real time application because of the extensive data required, but allow the hydrologist to review "what if" scenarios when time is available.

NERFC Ice Jam Operations Plan

Once an ice jam potential is identified, a flood potential outlook statement is issued by the local NWS office. River Ice Statements are issued when available information warrants such action. When done correctly, these statements precede any detection of an ice jam. Once an ice jam situation is verified it may result in a flash flood situation. With this possibility, ice jam flood situations are usually issued under the Flash Flood categories over AFOS, this is the responsibility of the HSA. When the NERFC becomes involved, the products are issued as a Flood Watches, Flood Warnings or Flood Statements depending on the extent of the ice jam problem.

It is critical that the roles of the NWS, the State, local government and the observers change during an ice jam flood event. Instead of the RFC being the provider of key information to the WSO, WSFOs and state and local offices, these offices now provide the RFCs with most of the information that these hydrologic products are based on. Without up to date information from local officials and observers the RFCs and HSAs hands are unable to provide accurate hydrologic watches and warnings. Currently, hydrologic models are unable to accurately model ice jams. Information on snow, ice characteristics, and river conditions provide the basis for accurate and timely RFC support. Coordination and cooperation between the observers, state and local agencies and the NWS is the driving element for accurate and timely hydrologic product issuance during an ice jam flood.
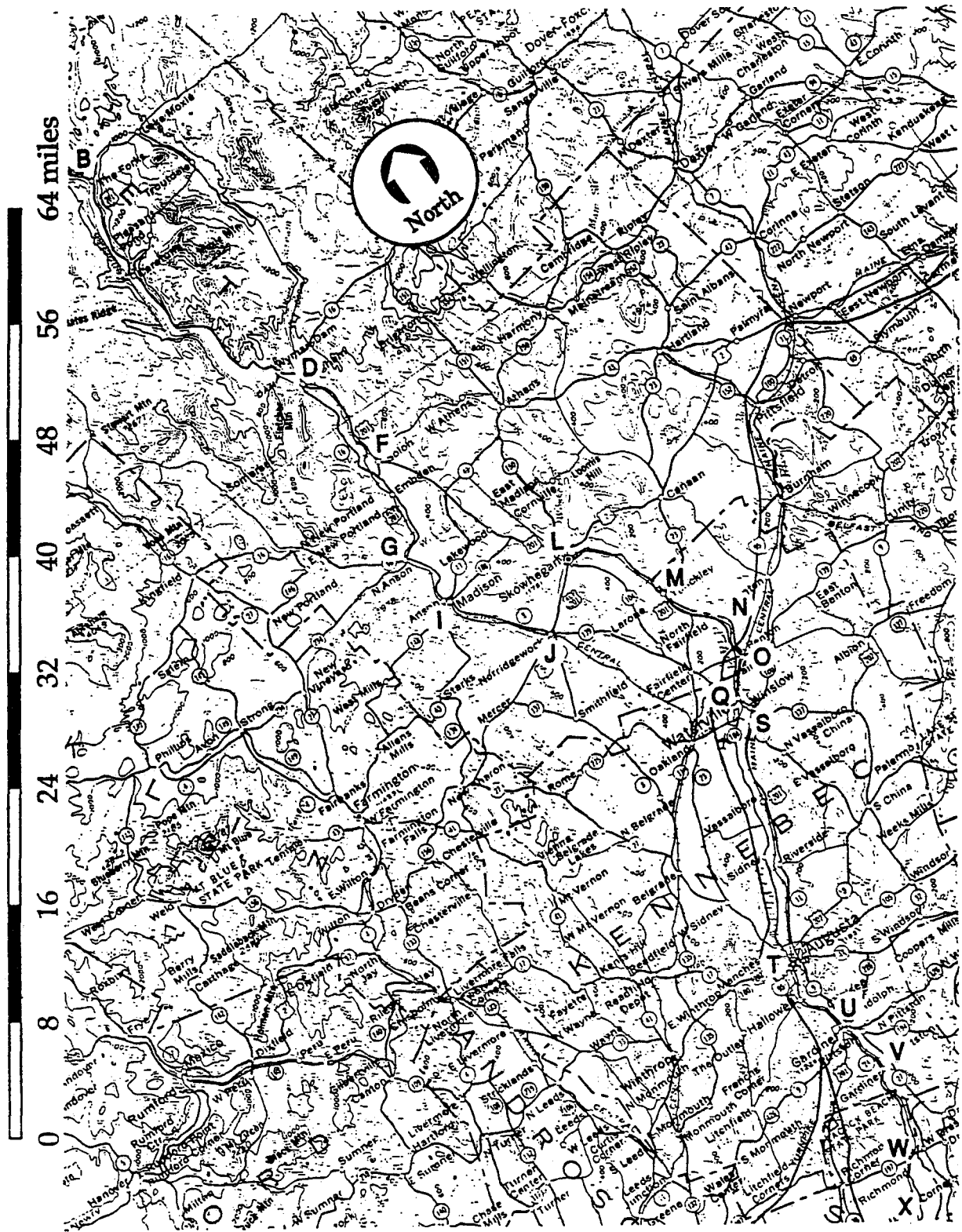
Maine Geological Survey/Hydrogeology Division

Figure 1

KENNEBEC RIVER

RIVER RECONNAISSANCE

DATE [   ]   A/C TYPE [   ]

PILOT [   ]   A/C # [   ]

OBSERVER [   ]   MISSION # [   ]

WEATHER CONDITIONS [   ]

TAKE OFF TIME [   ]   LANDING TIME [   ]

LOCATION	AREA FLOODING		ICE JAM		DAM CONDITION		BRIDGE CONDITION			BUILDINGS	
Observed	Y	N	Potent	Act	End Erosion	Flood Over	Abutment Problem	Ice Against	Water Over	Water Around	Ice Around
MOOSEHEAD BRIDGE											
THE FORKS BRIDGE											
LONG FALLS DAM											
BINGHAM BRIDGE											
WILLIAMS DAM											
SOLON BRIDGE											
NORTH ANSON BRIDGE											
MADISON BRIDGE											
MADISON DAM											
NORRIDGEWOCK BRIDGE											
SKOWHEGAN BRIDGES											
SKOWHEGAN DAM											
HINKLEY BRIDGE											
SHAWMUT DAM											
FAIRFIELD BRIDGES											
WATERVILLE BRIDGES											
WATERVILLE DAM											
WINSLOW BRIDGES											
WINSLOW DAM											
AUGUSTA DAM & BRIDGES											
HALLOWELL											
GARDINER											
RICHMOND BRIDGE											
SWANS ISLAND											

Figure 2

References

Ferrick, M., Lemieux, G..E. Weyrick, P.B., and Demont, W., 1988; Options for Management of Dynamic Ice Breakup Control for the Connecticut River near Windsor, Vermont, CRREL Report 88-1, U.S. Army Cold Regions Research and Engineering Laboratory, Hanover NH.

Interagency Hazard Mitigation Team Report, March 1985; Response to FEMA-938-DR-VT.

New Brunswick Subcommittee on River Ice, August 1989; New Brunswick Department of the Environment, New Brunswick River Ice Manual., Smith, C.A., Hunter C.S., 1985; Flood Forecasting Services for the Northeast.

U.S. Army (1982) "Ice Engineering," EM 1110-2-1612, 15 October 1982; Corps of Engineers, Washington D.C.

U.S. Army (1990) "Winter Navigation on Inland Waterways," EM 1110-8-1(FR), 31 December 1990; Corps of Engineers, Washington D.C.

Using Soundings to Forecast Frontal and Rainband Motion

J H Fenner

Oregon Institute of Technology, Klamath Falls, Oregon 97601

Summary

Forecasting speed and direction of frontal or rainband motion may be one of the least known and least practiced forecasting techniques. Yet, to make an accurate short-period forecast of the onset or ending of frontal-related weather (such as precipitation, strong wind gusts, or the time of a significant temperature drop), the forecaster *should* rely on the rate of frontal and/or rainband movement. Numerical guidance and extrapolation may help the forecaster, but a more precise estimate of frontal or rainband motion requires upper-level wind and temperature information, i.e. soundings. Moreover, small features identifiable on soundings correlate well with mesoscale features recognizable on satellite imagery or on weather maps. One method for estimating frontal and/or rainband motion, mainly for time periods up to about 18 hours, relies on identifying fronts and rainbands, often with the help of soundings, and knowing or estimating the average speed and direction of the wind through the active depth of the respective system. Sounding help in the latter situation, too. The paper gives four case studies, one of rainbands and three of fronts. The method estimates speed of motion somewhat better than direction. More case studies are needed to improve the method.

1. Introduction

Forecasting speed and direction of frontal or rainband motion may be one of the least known and least practiced forecasting techniques. Very few articles address the topic. Very few operational forecasters know how to estimate frontal movement, and fewer still has any idea how to predict the motion of rainbands associated with fronts. Yet, to make an accurate short-period forecast of the onset or ending of frontal-related weather (such as precipitation, strong wind gusts, or the onset of a temperature drop), the forecaster *should* rely on the rate of frontal and/or rainband movement.

Numerical guidance and simple extrapolation of previous movement may help the forecaster. However, for a more precise estimate of frontal or rainband motion, including an estimate of the exact time of passage at any station, the forecaster can and should use upper-level wind and temperature information, i.e. soundings. This paper summarizes one method for improving the timing and accuracy of such forecasts, mainly for time periods up to about 18 hours.

In addition to supplying the weather forecaster with the *only* source of meteorological information which gives *only* significant data points (the significant levels), the radio-wind sounding (rawinsonde), when plotted, provides the weather forecaster with a tool for identifying fronts, rain bands, regions of potential thunderstorm activity, and many other weather phenomena. In particular, many small features identifiable on plotted soundings often correlate well with smaller-scale (i.e. mesoscale) features recognizable on satellite imagery or weather maps. Publications by the United States Air Force's Air Weather Service (AWS), the National Weather Service (NWS), the World Meteorological Organization (WMO), and other national weather services, tell forecasters how to use soundings to improve their forecasts.

Observations of frontal systems during the past decade or two (e.g. Hobbs, 1978; Carbone, 1982) indicated that frontal systems typically exhibit organized mesoscale precipitation bands in the vicinity of the surface front. Numerous investigators have proposed a variety of physical mechanisms to explain the banded nature of frontal systems. These theories do not form part of this paper; however, one proposed mechanism (Moncrieff and Green, 1972) provides the basis for the forecasting method described here; this theory will be summarized in the next section. For those wishing to read more on our understanding of frontal bands, refer to Parsons and Hobbs (1983), who reviewed the present state of knowledge.

Whatever the mechanism for the generating and sustaining bands of precipitation near frontal zones, one thing appears clear: The geostrophic potential vorticity plays an important role in frontal dynamics. Other observations generally regarded as typical for fronts and their associated rainbands include significant ageostrophic components of the wind and a sounding exhibiting a temperature trace closely

following pseudo-moist adiabats, i.e. an environment nearly neutral for moist slantwise convection (Emanuel, 1985).

Bjerknes (1919) described empirically how frontogenetic forcing and the ascent of warm, moist air over cooler air gave rise to precipitation. Later work described physically how this ascent occurs. The present case appears to follow this pattern. Cold air moving south increased the horizontal temperature gradient in the lower few kilometers of the atmosphere without simultaneously increasing the vertical wind shear. This condition upsets the thermal wind balance, producing a thermally direct transverse circulation trying to restore that balance. Greene (1971, unpublished lecture notes) and Emanuel (1985) showed that the rising air is often restricted horizontally, but the compensating downward motion occurs on a broad scale, resulting in the possibility for the rising air to form banded precipitation with dimensions on the mesoscale. The present paper uses this knowledge to arrive at an empirical method to estimate both speed and direction of motion of fronts and rainbands.

2. Conceptual Models

Throughout the years, numerous investigators have developed and promulgated a myriad of conceptual models of meteorological phenomena, such as Byers and Braham's well known thunderstorm model (Byers and Braham, 1949). Conceptual models of fronts have an even longer history, beginning when Margules (1906) offered a model of a stationary front, and continuing with, e.g. Jeffreys (1919), Sutcliff (1938), Brunt (1939), and Sawyer (1952). All these later investigators also attempted to explain frontal translation. However, none of the models they introduced attempted to explain how to forecast the rate of frontal movement.

In 1972, Moncrieff and Greene (1972) introduced a two-dimensional theoretical model of a steady thunderstorm as the basis for estimating the speed of motion. Fenner (1974) showed that this model produced accurate speed forecasts for many types of thunderstorms, and that it could be modified and extended to predict the velocity of fronts and rainbands as well. Moncrieff and Green's conceptual model, as modified, provides the basis for the method of prediction in this paper. As a quick refresher, Moncrieff and Greene's model assumed an unmixed updraft and compensating unmixed downdraft in the cloud. Given this condition, the authors found a "steering level" where the relative wind was zero, hence found the speed of motion of the system. Although very few, if any, real weather systems--even severe thunderstorms--come close to meeting this stringent requirement for an unmixed updraft fully compensated by an unmixed downdraft, squall-lines and some large thunderstorms closest to meeting the requirement. Fronts and rainbands do not meet this assumption. (To extend the model to other meteorological systems, the author relaxed the requirement for the unmixed updraft and downdraft in the upper half of the cloud, leaving only unmixed up- and downdrafts in the lower half of the cloud. Many thunderstorms, fronts, and rainbands appear to come close to satisfying this more lenient requirement. The predicted motion for fronts and rainbands also agrees better with actual motion when using the author's modified method.)

Figures 1, 2, and 3 show schematic models of fronts. **Figure 1** shows a conceptual model of a front associated with an upper-tropospheric wind maximum (a "jet stream"), a model sometimes referred to as a "dynamic front" because of its association with a dynamical process in the atmosphere. **Figure 2** shows a "classical" conceptual model of a front, that is, a moving mass of cold air displacing warmer air at the surface of the earth. This model is devoid of dynamic atmospheric processes which might cause it to persist for long periods of time and move over extended distances. **Figure 3** shows another dynamic front, but one without associated rainbands.

In **Figs. 1, 2, and 3**, the tropopause is denoted "TROP" and the upper-level wind maximum by "Jet." The depth of the active region of the front is denoted "H," generally the depth of the cloud layer, and the depth of the rainbands by "H'." "LLJ" denotes the wind maximum in the lower troposphere, often called the "low-level jet."
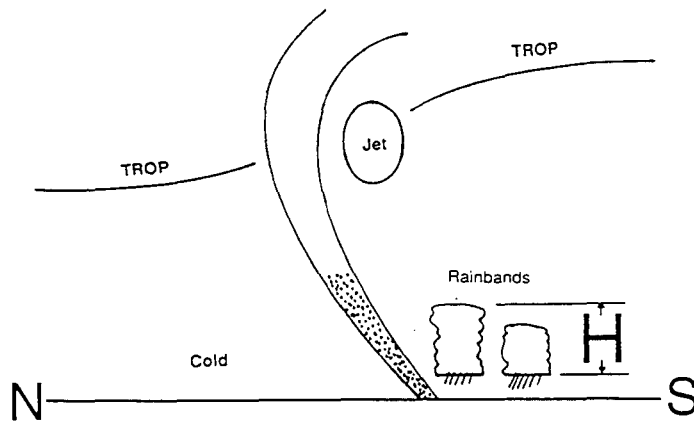
Figure 1: A schematic model of a dynamic front and its associated rainbands. A dynamic front is the name given to an active frontal system, one always associated with a region of maximum wind in the middle to upper troposphere (a "jet", marked "J"). A dynamic front generally extends into the lower stratosphere, as indicated by the solid curve in the figure. Rainbands are denoted by "R" and their active depth by "H" in the figure. The active depth of the front is indicated by the stippled area. "Trop" indicates the tropopause.
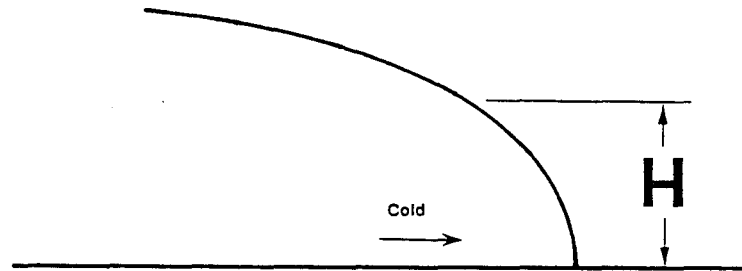
Figure 2: A schematic representation of a "classical" cold front, that is, one which demarcates the boundary between a cold pool of air and a warmer region. The arrow indicates the direction of motion of the cold front; the curve denotes the frontal boundary, and "H" indicates the active depth of the front.
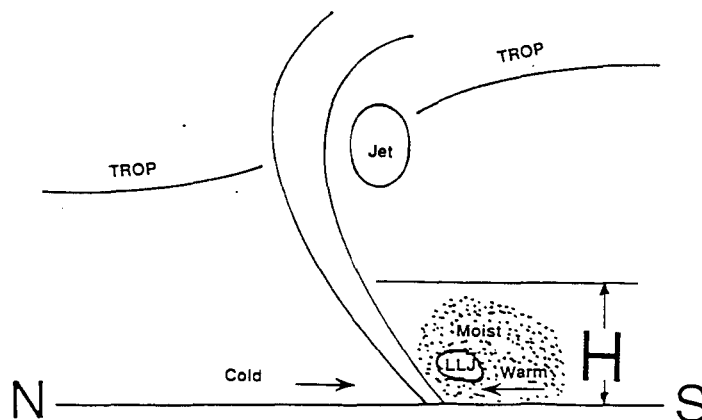
Figure 3: A schematic model of a "dynamic" front (as in Fig. 1), but without rainbands. Dashed arrows indicate the direction of the thermodynamically direct circulation transverse to the front (see text), while solid arrows denote the direction of motion of cold and warm air relative to the moving front. Many dynamic fronts exhibit a low-level wind maximum (the "low-level jet, LLJ") within or near the moist, warm air (stippled area). The upper-tropospheric wind maximum is marked "Jet," while "H" is the active depth of the front. The active depth is often about equal to the depth of the moist layer ahead of and/or above the surface position of the front.

3. Forecasting Speed and Direction of Frontal Motion

To forecast the velocity of any meteorological phenomena, one must first find and identify it. Methods of finding fronts using soundings should be well known to operational weather forecaster; thus, this paper will not detail them. These methods have been explained in numerous texts, articles, and pamphlets. One such readily available reference is Air Weather Service Manual 105-124 (1975).

Estimating speed and direction of frontal motion accurately, however, requires quite a bit more thought and effort than the relatively simple "rules of thumb" given in most texts and manuals would indicate. (Many texts, for example, mention that fronts tend to move at, for example, about half the wind speed at 500 hPa (mbar); or at about 70% of the speed of the wind at 700 hPa (mbar); or give some similar rules of thumb. None, however, indicate *why* fronts tend to move at these speeds.)

In general, fronts move along with the atmospheric depression with which they are associated. Since disturbances embedded in the flow tend to move at the speed and in the direction of the average wind through their depth (or, more specifically, the average wind through their dynamically active depth), fronts tend to move with the average wind. As a result, Moncrieff and Green's two-dimensional model, as modified, gives a good estimate of general frontal and rainband movement. The method is as follows:

1. Select, or, if time permits, construct, a representative sounding for the location and time of interest. **Figure 4** shows a sounding for one recent case.

2. Construct and plot the equivalent potential temperature curve (Θ_e) on the sounding. (You may plot wetbulb potential temperature, Θ_w, instead of Θ_e; it makes virtually no difference.) For simplicity, this is not shown; rather, Θ_e is plotted by itself in **Figure 5**.

3. Find the level of free convection (LFC), if any, and draw the pseudo-moist adiabatic curve through the LFC. **Figure 4** shows this for a recent case. The depth of the layer between the LFC and where the pseudo-moist adiabatic curve again intersects the temperature trace of the sounding is, of course, the expected depth of the convection. (Many soundings near fronts and rainbands will not show any LFC; many will exhibit a temperature trace nearly coincident with the pseudo-moist adiabatic curve, a condition sometimes referred to as "moist-neutral" stability. A "moist-neutral" sounding somewhat complicates the forecasting method, but does not render it invalid.)

4. Locate the region of the atmosphere represented on the sounding by the *lowest* equivalent potential temperature. In **Figures 4 and 5**, this is the region between about 800 hPa and 670 hPa. From the author's studies of the past twenty years, this region correlates well with the "steering level" of thunderstorms, fronts, and rainbands. As a first estimate of frontal or rainband motion, use the average wind speed and direction though this layer of the atmosphere. For a more accurate estimate, continue through the following steps.

5. If you have time, plot the winds in polar coordinates. This results in a representation of the wind known as a hodogram. **Figure 6** shows the hodogram for a recent case. The mean wind speed and direction through the depth of the convection (from step 3) gives a reasonably accurate estimate of the motion of rainbands, not as good results of frontal motion.

6. The mean wind through the *active* depth of the front or rainband ("H" or "H'") gives the best estimate of frontal or rainband motion, respectively. The depth of the cloud, estimated from sounding or satellite imagery, corresponds well with the active depth of fronts and rainbands. In very few cases does the active depth of a front or rainband extend upwards beyond seven kilometers, and it averages about five. Rainbands often extend higher than the front with which they are associated.

When applying this step, look for the *general* depth of the cloud, not the highest cloud top. Individual cells often extend well above the average cloud top; use the average value in estimating the over-all movement. The larger, embedded cells will move faster than the average, as Fenner (1974) noted. (Squall-lines tend to move faster than fronts, because their active depth is greater, thus the average wind speed higher. Rainbands may move either slower or faster than the front, depending on their depth relative to the active depth of the front.)
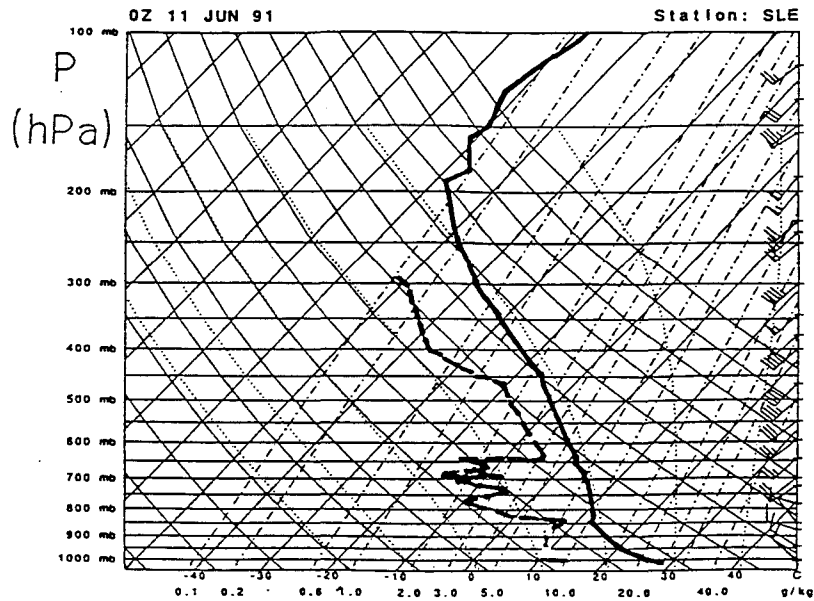
Figure 4: Sounding for Salem, Oregon, from 0000 Universal Time (UT), 11 June 1991. The solid curve is the temperature trace plotted against pressure as a vertical coordinate, while the dew point temperature is the dashed curve. "H" denotes the active depth of the front. Dotted curves are pseudo-moist adiabats. Winds are plotted on the right as wind barbs; one long barb equals ten knots and a short barb five.
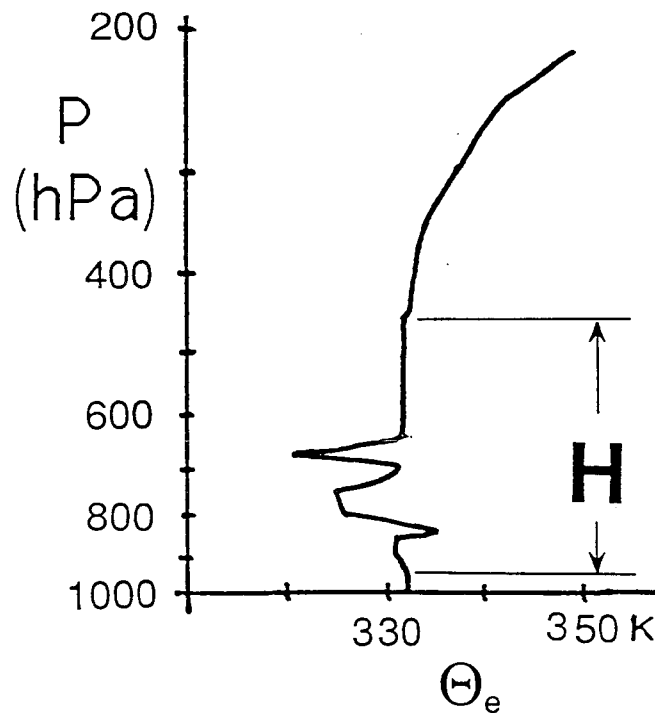

Figure 5: A smoothed plot of equivalent potential temperature (Θ_e) against pressure as a vertical coordinate for Salem, Oregon, from 0000 Universal Time (UT), 11 June 1991. "H" denotes the active depth of the front. The mean wind through depth H was from approximately 240 degrees at 30 knots.
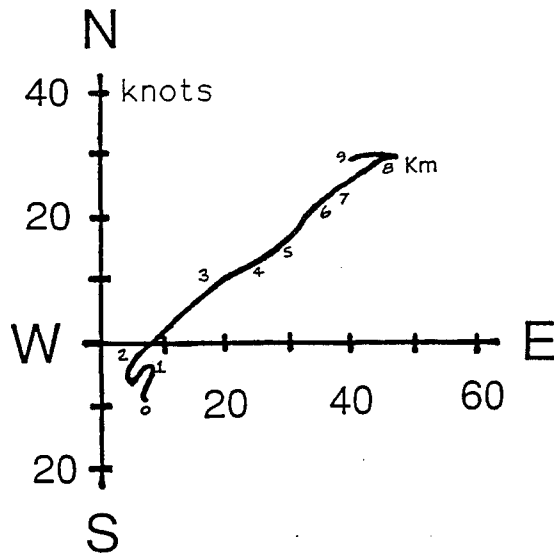
Figure 6: Winds plotted in polar coordinates (a hodogram) for Salem, Oregon, 0000 UT, 11 June 1991. The curve represents the locus of the tip of the vector wind when plotted with the tail of the vector at the origin. Eastward and northward components of the wind are taken as positive. The height of the wind in kilometers is indicated by numbers along the curve.
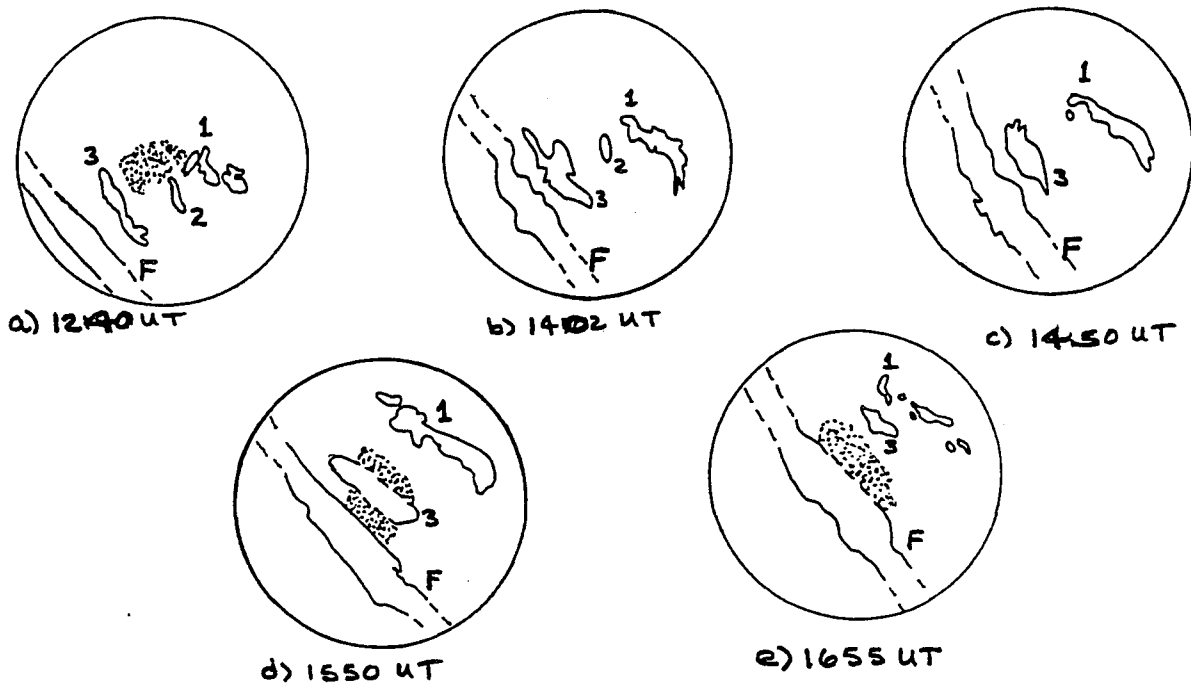
Figure 7: Radar returns from the radar at the Institute for Meteorology, Free University of Berlin, from 12:40 UT to 16:55 UT (13:40 to 17:55 local time) 20 May 1976. The outer circle is the 150 kilometer range ring. Rainbands are numbered 1, 2, and 3, while the front is marked "F." The stippled area indicates ground clutter. Radar antenna elevation remained at 0.5 degrees during this period.

If the hodogram shows significant directional change with height, the larger and stronger embedded cells will often deviate from the direction of the mean wind. Fenner (1974) noted this and attempted to explain it. Fronts and rainbands in middle latitudes do not generally exhibit this deviate motion, but many thunderstorm and squall-lines do.

4. Examples of Estimating Frontal and Rainband Motion

A. The front and three rainbands from 20 May 1976 in Germany.

Figure 7 shows the outline of several rainbands as taken from a radar display. Figure 8 shows the corresponding sounding for the same time and location. Table I at the end of this paper gives the actual motion of these rainbands, as deduced from radar.

Figures 8, 9, and 10 show the position of fronts as analyzed by operational forecasters together with the corresponding sounding. Table I lists time and date of the front and/or rainband, along with estimated motion (front the method given here) and actual frontal motion as deduced from the operational maps shown. Note that *actual* frontal motion is not in the direction perpendicular to the front, as often mistakenly assumed. Most forecasters (and the public) generally think of the component of motion normal to the front; however, the front actually moves in quite a different direction.

The next three examples come from the Pacific Northwest from the spring of 1991. Those people living in the area will remember the unusually cool, wet season. However, even though amply rainfall fell during the early part of the year, surface maps from April, May, and June show only a relatively small number of very well defined fronts passing through the Pacific Northwest.

B. The front from 9 April 1991 in the western United States.

Figure 8 shows portions of two National Weather Service weather maps, for 12UT and 18UT, 9 April 1991, respectively, along with the sounding from Salem, Oregon, for 12UT on the same date. Washington (WA), Oregon (OR), and California (CA) are indicated for geographic reference. The portion of the front lying over southern Washington and the northern half of Oregon appears to be moving very nearly from west to east; however, the analyzed juncture between the northern portion of the front (with occluded frontal character) and the remaining portion (with cold frontal character) has moved from near Portland, OR, at 12UT, 9 April, to just west of Spokane, WA, at 18UT. The juncture, denoted by two short lines across the front, has thus moved from a direction of about 240 degrees, considerably different the apparent motion of the front as an entity.

The sounding for Salem, OR, (Fig. 8c) was taken just prior to frontal passage on the surface. It shows a nearly "moist-neutral" lapse rate up to a height of about six kilometers, with most of the moisture confined to the lower three kilometers of the atmosphere. After frontal passage (not shown), the moisture extended only up to about five kilometers. The average wind through the depth of the active front (about five kilometers) was 250 degrees at 28 knots.

This weather system produced 0.20 inches of rainfall at Salem, and 1.03 inches at the Corvallis water bureau's measuring site. Stations along the Oregon coast generally reported more than one inch of precipitation, with a maximum of 2.10 inches recorded at near Nehalem (Taylor, 1991).

Table I summarizes the prediced and actual motion for this case.

C. The front from 24 April 1991 in the Western United States.

Figure 9 shows portions of three National Weather Service weather maps, for 00UT, 12UT, and 18UT, 24 April 1991, respectively, along with the sounding from Salem, Oregon, for 12UT on the same date. Washington (WA), Oregon (OR), and California (CA) are indicated for geographic reference. The portion of the front approaching Washington and Oregon at 00UT appears to be moving from the west-southwest. In this case, unlike the previous one, the analyzed juncture between the northern portion of the front (with occluded frontal character) and the remaining portion (with cold frontal character) also appears to be moving in the same direction. For the period 00 to 18UT, both the front and the juncture point appear to be moving from about 235 degrees at 24 knots.

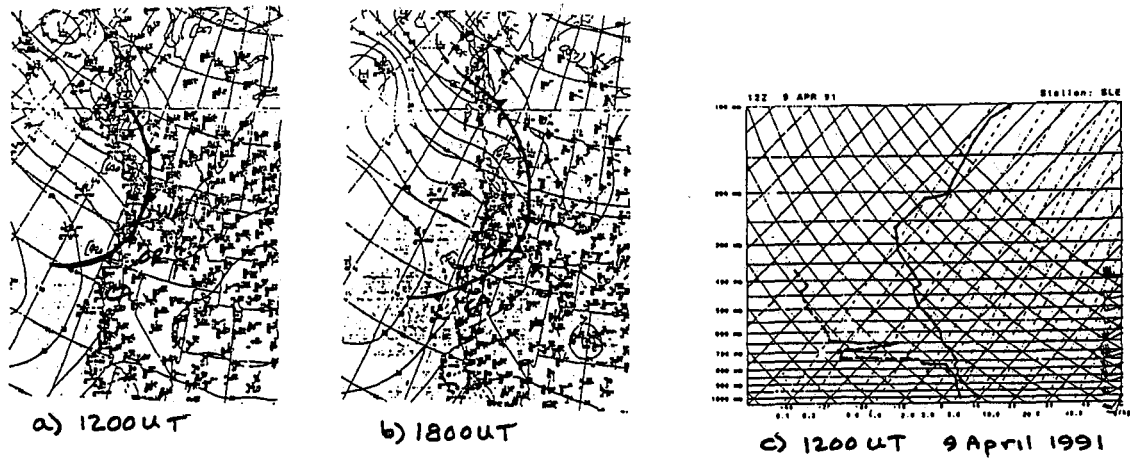a) 1200 UT   b) 1800UT   c) 1200 UT   9 April 1991

Figure 8: (A) and (B) are National Weather Service surface weather maps for the western portion of the United States and Canada for 12UT and 18UT, 9 April 1991, respectively. Washington ("WA"), Oregon ("OR"), and California ("CA") are marked for geographic reference. (C) The sounding for Salem, Oregon for 12 UT, 9 April 1991.
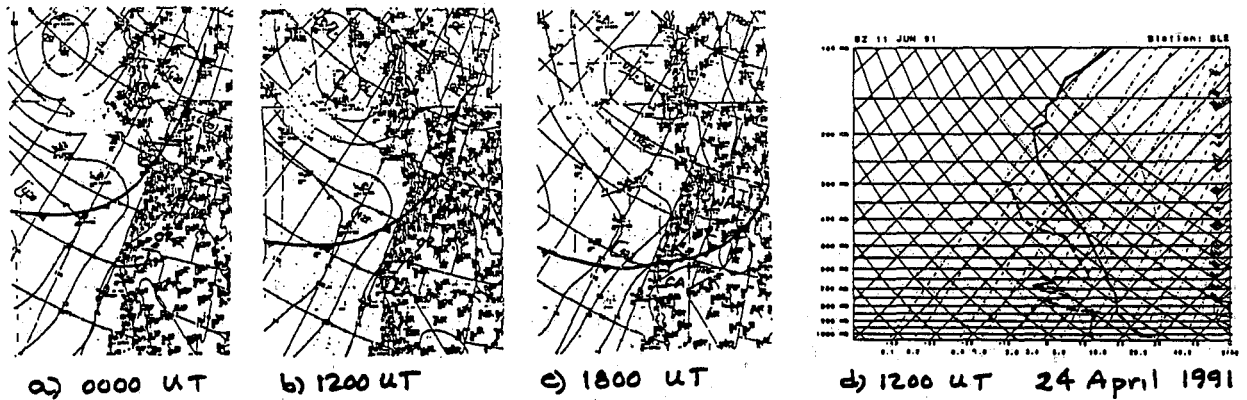

a) 0000 UT   b) 1200 UT   c) 1800 UT   d) 1200 UT   24 April 1991

Figure 9: Similar to figure 8, except (A), (B), and (C) are surface maps for 00, 12, and 18UT, 24 April 1991. (D) is the sounding for Salem, Oregon, for 12UT, 24 April 1991.

a) 1800 UT 10 June 91   b) 0000 UT   c) 1200 UT 11 June 91   d) 0000 UT 11 June 91
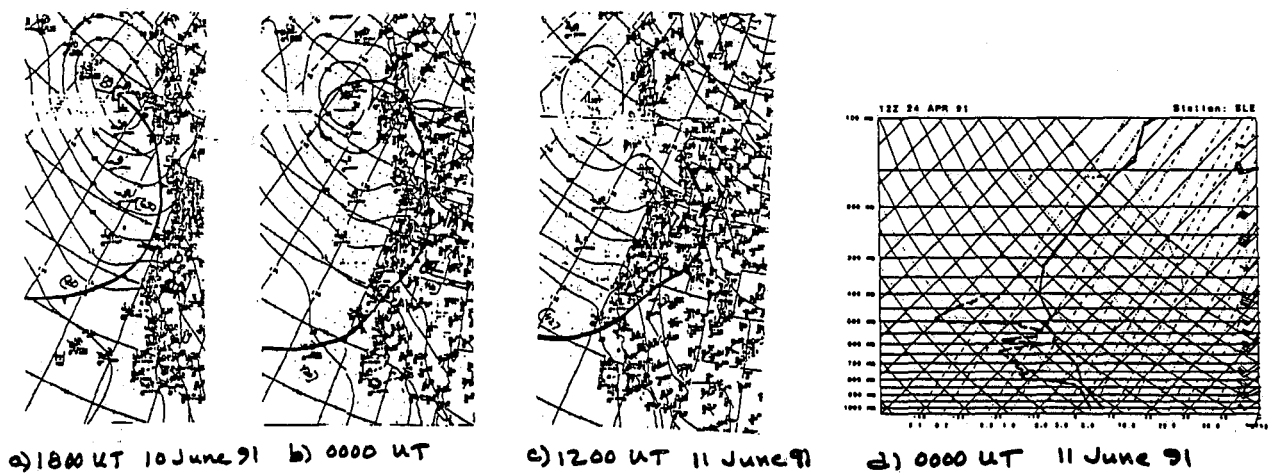
Figure 10: As figure 9, except surface maps are for 18UT, 10 June 1991, and 00 and 12UT, 11 June 1991, and the sounding is for 00UT, 11 June 1991. (The sounding is also shown in figure 4.)

The sounding for Salem, OR, (Fig. 9d), taken after frontal passage on the surface, shows a nearly "moist-neutral" lapse rate up to a height of about four kilometers. Prior to frontal passage (not shown), the moisture extended no higher. The average wind through the depth of the active front (about 4 1/2 kilometers) was 235 degrees at 28 knots.

This weather system produced 0.28 inches of preciptation on the 23rd and another 0.18 inches of rainfall at Salem on the 24th. Stations along the coast averaged about one inch of rainfall on the 24th (Taylor, 1991).

Table I includes the prediced and actual motion for this case, too.

D. The front from 10-11 June 1991 in the Western United States.

Figure 10 shows portions of three National Weather Service weather maps, for 18UT 10 June 1991, and 00UT and 12UT 11 June 1991, along with the sounding from Salem, Oregon, for 00UT 11 June. As with the previous two cases, Washington (WA), Oregon (OR), and California (CA) are indicated for geographic reference. The portion of the front approaching Washington and Oregon at 18UT appears to be moving from the west. As with the prior example, the analyzed juncture between the portion of the front with occluded frontal character and the portion with cold frontal character also appears to be moving in the same direction. Both the front and the juncture point appear to be moving from about 270 degrees at 22 knots.

The sounding for Salem, OR, (Fig. 10d) was taken just prior to frontal passage on the surface. As with the previous two examples, it shows a nearly "moist-neutral" lapse rate—in this case up to a height of about six kilometers. The moisture also extends to about that height. The average wind through the depth of the active front (about six kilometers) was 250 degrees at 20 knots.

This weather system produced less rainfall than the previous two, with many of Oregon's reporting stations, including Salem, receiving no measurable rainfall at all. On the other hand, a number of stations (17) recorded maximum temperatures more than seven Kelvin degrees above normal on the 10th and 11th, and another five stations recorded minimum temperatures more than five Kelvin degrees above normal. Salem reported an eleven Kelvin degree drop in maximum temperature from the 10th to the 12th, and a seven Kelvin degree drop in average temperature over the same period (Taylor, 1991).

Table I summarizes the prediced and actual motion for this case, too.

5. Conclusions

Forecasting speed and direction of frontal and rainband motion does not require a great expenditure of time. The results can, however, improve the timing of forecasts of frontal phenomena, such as beginning and ending of precipitation, onset of post-frontal freezing temperatures, etc.

Although the case studies presented here do not indicate the directional estimates are very good, please note that these cases were not selected because the predictions turned out to be accurate; rather, we selected the cases based on their having a sounding near the time of frontal passage.

Table I: Actual and Estimated Frontal and Rainband Motion Compared

Date / Time (UT)	Actual Motion	Predicted Motion
760520, 13:40 to 17:55 UT:		
Front	240 at 12 knots	
Rainband #1	210 at 15	
Rainband #3	200 at 10	
910409 12 UT	226 at 31	250 at 28 knots
910424 12 UT	235 at 24	235 at 28
910611 00 UT	270 at 22	250 at 20

Table I: Actual and Estimated Frontal and Rainband Motion Compared

6. References

Air Weather Service, 1975: Air Weather Service Manual 105-124 (Rev)

Bjerknes, J. 1919: On the structure of moving cyclones. *Geofys. Publikajoner*, Norske Videnskaps-Akad. Oslo, *1*, pp.1-8.

Brunt, D. 1939: *Physical and Dynamical Meteorology*. Cambridge University Press.

Byers, H.R. and R.R. Braham 1949: *The Thunderstorm*. United States Government Printing Office, 287pp.

Carbone, R.E. 1982: A severe frontal rainband, Part I: Stormwide hydrodynamic structure. *J. Atmos. Sci. 39*, pp.258-279.

Emanuel, K.A. 1985: Frontal circulations in the presence of small moist symmetric stability. *J. Atmos. Sci. 42*, pp.1062-1071.

Fenner, J.H. 1974: The Organization and Movement of Convective Cells. Doctoral thesis, Imperial College of Science and Technology, London University, London, England. 86pp.

Green, J.S.A. 1960: A problem in baroclinic stability. *Quart. J. Roy. Meteorol. S. 86*, pp.237-251.

Green, J.S.A. 1971: Lecture notes on dynamic meteorology. Unpublished. Imperial College of Science and Technology, London University, London, England.

Hobbs, P.V. 1978: Organization and structure of clouds and precipitation on the mesoscale and microscale in cyclonic storms. *Rev. Geophys. Space Phys. 16*, pp.741-755.

Jeffreys, H. 1919: On travelling atmospheric disturbances. *Phil. Mag. 37*, pp.1-8.

Margules, M. 1906: Über Temperatureschichtung in stationär bewegter und in ruhrender Luft. *Meteorol. Z*, pp.243-254.

Moncrieff, M.W. and J.S.A. Green, 1972: The propagation and transfer properties of stead convective overturning in shear. *Quart. J. Roy. Meteor. Soc. 98*, pp.336-352.

Parsons, D.B. and P.V. Hobbs 1983: The mesoscale and microscale structure and organization of clouds and precipitation in midlatitude cyclones, XI: Comparisons between observational and theoretical aspects of rainbands. *J. Atmos. Sci. 40*, pp.2377-2397.

Sawyer, J.S. 1952: Dynamical aspects of some simple frontal models. *Quart. J. Roy. Meteor. Soc. 78*, pp.170-178.

Sutcliff, R.C. 1938: On development in the field of barometric pressure. *Quart. J. Roy. Meteor. Soc. 64*, pp.495-504.

Taylor, G.H. 1991: Oregon Weather Summary for April and June, 1991. Issued by the State Climatologist, Oregon Climate Service, Oregon State University, Corvallis, OR.

Low-Level Jet Formation and Prediction
using the Nested Grid Model

Paul R. Janish
EFF/NSSL/CIMMS
1313 Halley Circle
Norman, OK 73069

and

Steven W. Lyons
NOAA/NWS/SRH
819 Taylor St. Room 10A26
Ft. Worth, TX 76102

ABSTRACT

Seven return flow events and associated low-level jets (LLJs) over the Gulf of Mexico and southern U.S. were observed between 26 January and 27 March 1988 coincident with the GUFMEX (Lewis et al., 1989) extensive observing period. The ability of the National Meteorological Center's Nested Grid Model (NGM) to develop and predict the LLJ is examined. Individual cases and case composites utilizing NGM analyses and forecasts are compared and contrasted with one another and with special GUFMEX observations. Model strengths and weaknesses are illustrated.

Low-level jets associated with return flow events developed first in the southern High Plains near southeastern Colorado, eastern New Mexico, and the Texas Panhandle, then forming southward and eastward toward the Gulf of Mexico. All cases of strong return flow were associated with LLJ formation and cyclogenesis in the lee of the Rockies. The jet developed in response to three primary mechanisms: (1) anticyclonic southwesterly flow at the surface and aloft over the southern High Plains, (2) lee mountain troughing which locally enhanced the geostrophic flow and, (3) ageostrophic isallobaric flow. The isallobaric wind accelerated the flow into the developing cyclone and dominated the LLJ formation process in model analyses.

Over the southern Plains, jets formed near 850 mb. They advanced eastward with developing cyclones and were maintained by strong pressure gradients. As they developed south and east, they did so in response to the same mechanisms which formed them farther north, yet did so at a lower height. LLJ maxima in the western Gulf of Mexico are typically observed near 950 mb. This suggests an upward slope in height of the jet as it advances inland coincident with the inversion structure capping the moist layer.

NGM forecasts tend to underestimate the degree of lee troughing and ageostrophic acceleration in developing the jet initially and later in time farther south. Part of this error appears to be due to a model bias, namely, the development of cyclones too far north in the lee of the Rockies. As cyclones move into the central Plains, the NGM tends to deepen them too much, thus creating a stronger pressure gradient than is observed. This enhanced gradient results in a representative wind speed forecast, however, there is a significant westerly bias to the flow over the region. LLJ wind speeds were consistently too low over the western Gulf of Mexico and also displayed a westerly bias. In addition, the NGM appears to have difficulty in forecasting the thermodynamic structure of the lower troposphere, especially the evolution of inversion layers which cap the moist layer and are coupled with the LLJ. Consequently, the upward sloping character of the LLJ as it advances northward from the Gulf of Mexico is absent in NGM forecasts.

1. Introduction

During the cool season, transient synoptic systems frequently impact the southern U.S. Cold-air outbreaks push across the Gulf coast and into the Gulf of Mexico where the air is modified before returning to the continent. The cycle of cold-air outbreak and return flow has been defined by Crisp and Lewis (1992), as the *return flow cycle* and is comprised of two distinct phases. The first phase involves the movement of cold dry air from the continent to the ocean and is called the *offshore-flow phase*. The second is defined as movement of warm, more moist air from the ocean to the continent and is called the *onshore-flow phase*. Forecasts of precipitation, cloud, temperature, humidity, and wind during this cycle are particularly challenging for operational forecasters due to the complexity of modification processes over the Gulf and an incomplete understanding of the transport mechanisms associated with various phases of the cycle. Numerical weather prediction models such as the Nested Grid Model (NGM) (Phillips, 1979) simulate these processes however, they experience difficulties with particular aspects. Evaluations of model performance regarding air mass modification and subsequent forecasts have been conducted by Sanders (1987), Petersen (1988), Junker and Hoke (1990), Jensenius (1990), Janish and Lyons (1992) and Junker et al. (1992). Additional studies regarding cyclone and anticyclone position/intensity forecasts have been presented by Alexander and Young (1990), Grumm and Seibers (1989a, 1989b), Mullen and Smith (1990), Smith and Mullen (1991), and Grumm et al. (1991).

Results from this study will examine the formation and prediction of the low-level jet (LLJ). It's purpose is to illustrate model strengths and weaknesses in predicting the jet's temporal and spatial evolution, it's vertical structure, and role in moisture transport during periods of onshore flow.

2. The Low-Level Jet

The LLJ (Bonner, 1968) is a layer of maximum wind which must equal or exceed 12 ms^{-1} (25 kts) and must decrease by at least 6 ms^{-1} (12 kts) to the next higher minimum or to the 3-km level, whichever is lower. Climatology of the southerly LLJ shows a maxima in frequency over the south central Plains of the U.S. with secondary maxima over south Texas and off the North Carolina coast (Bonner, 1968). Over the central Plains, the jet has been found to be the primary mechanism for moisture transport during the return flow cycle (Engel, 1991).

Several types of LLJ's have been documented. Formation processes of nocturnal jets have been examined by Blackadar (1957), Wexler (1961), Lettau (1967), McNider and Pielke (1981), Paegel et al. (1984), Parrish et al. (1988), Fast and McCorcle (1990), and Frisch et al. (1992). These theories are based on the evolution of boundary layer processes over a diurnal cycle. Jets associated with this type of development are primarily a summertime, meso-alpha scale phenomena and account for a large percentage of the frequency in Bonner's climatology over the central Plains.

The synoptic scale LLJ associated with return flow appears to be synoptically forced resulting from pressure gradient responses to lee side cyclogenesis to the east of the Rockies (Fig. 1, Newton, 1967). The synoptic scale LLJ is primarily a cool season phenomena as described by Djuric and Dimiani (1980) and Djuric and Ladwig (1983). They have shown that the LLJ associated with return flow first appears over the High Plains between west Texas and eastern Colorado and expands southward and eastward rapidly in time until it taps the warm, humid air over the Gulf and transports it northward. This jet is maximum near or below 850 mb and is capped by a subsidence inversion. These jets are typically stronger than the summertime phenomena with most vigorous LLJ's associated with most rapidly developing baroclinic waves and degree of lee Rocky mountain cyclogenesis (Walters, 1988). Jets of this type may or may not display a nocturnal maximum. Uccellini (1980) and Uccellini et al. (1987) have recently related the evolution of the synoptic scale LLJ to interactions between upper-level jet streaks and diabatic processes associated with cyclogenesis. They showed that changes in the pressure gradient force related to leeside cyclogenesis, leeside troughing and the isallobaric wind response to these changes seem to be an integral part of the processes that leads to the development of the LLJ's observed in the Great Plains. In all cases, the presence of a boundary layer inversion was critical to the development and maintenance of the jet.

3. Data acquisition and analysis technique

Data used in this study consist of NMC's Regional Analysis and Forecast System's (RAFS) gridded analyses and 24- through 48-h forecasts over a 41 X 38 gridded array defined on a Northern Hemispheric polar stereographic map projection oriented at 60 N, 105 W. Grid spacing is 190.5 km at this location. The gridded data, which were obtained from an NMC archive at NCAR, are not the original NGM C-grid data (91.45 km grid at 60 N), but rather are a subset of the coarser resolution LFM grid, to which the NGM C-grid fields are interpolated for archiving. The period of study encompasses a two month period from 26 January to 27 March 1988, coincident GUFMEX 1988 special observing period.

An evaluation of NGM performance was facilitated through a comparison of NGM 24- and 48-h forecasts with subsequent NGM analyses (used for verification). Results illustrated model strengths and weaknesses in developing and predicting the LLJ. Features observed between 48-h forecasts and NGM analyses were observed in 24-h comparisons as well, however, 48-h comparisons best illustrated model performance. A comprehensive discussion of the NGM and validity of using NGM analyses as "ground truth" is given in Janish and Lyons (1992).

In order to apply the definition of return flow cycle to the NGM grid point data, specific grid points were chosen relative to the south central U.S. Upon evaluating temperature, moisture, and wind field evolution over several individual and groups of grid points, at various levels, the meridional wind v at 950 mb along the Texas coast was determined to best represent the cycle. It was most sensitive to changes in the synoptic

regime influencing the Gulf. An example of this time series is given in Fig. 2. The cycles (once defined) were then evaluated in a composite study as well as individually.

3.1 Composite Study

From the v-wind depiction of the return flow cycle (Fig. 2), seven (7) events were associated with large meridional wind oscillations and cycles of offshore and onshore flow. Each cycle displayed two (2) phases, as defined by Crisp and Lewis (1992), which can clearly be identified. They include an offshore flow, characterized by a negative v-wind component, and an onshore or "return" flow, characterized by a positive v-wind component. Sub-classification is given in the form of five (5) specific verification periods:

VERIFICATION PERIOD 1: (T-1)	Approximate start time of offshore flow. V-wind component is approximately zero (point of change from +v to -v).
VERIFICATION PERIOD 2: (T-2)	Approximate time of maximum cold/dry air advection into the Gulf. This period coincides with the maximum negative v-wind component.
VERIFICATION PERIOD 3: (T-3)	Approximate start time of return flow. V-wind component is approximately zero (point of change from -v to +v).
VERIFICATION PERIOD 4: (T-4)	Approximate time of maximum return flow of moisture back to the continent. This period coincides with the maximum positive v-wind component.
VERIFICATION PERIOD 5: (T-5)	Approximate end time of the return flow. The V-wind component is approximately zero (point of change from +v to -v).

Hereafter, the above verification periods will be called T-1, T-2, T-3, T-4, and T-5, respectively. The purpose of defining verification periods was to identify key periods within the return flow cycle for analysis. The first step in the compositing technique was to apply the definition of each of the five verification periods to each of the seven return flow cycles. These sub-phases are highlighted in Fig. 2 with T-1 through T-5 labeled for the second cycle. Meteorological variables including; u- and v-wind components, mixing ratio, relative humidity, temperature, and equivalent potential temperature, were composited relative to each verification period over each of the seven cycles. Respective fields were summed, then divided by the total number of fields used. Hence, if a spatial distribution of mixing ratio relative to T-4 was desired over the entire 33 X 24 gridded array, all of the T-4 periods for all seven cycles would be averaged at each of the 1558 grid points over the NGM data archive domain. Results represent mean synoptic patterns for a particular verification period of the return flow cycle.

4

Because of the 12-h data resolution and the fact that only the v-wind component was used to define the periods, the exact timing of onset for each period may be in slight error. Nonetheless, this technique clearly defines sub-phases of the return flow cycle which can be analyzed on synoptic scales.

3.2 Extreme Case

An examination of individual return flow cycles was made in order to see how particular cases compared with the composite. Of these, the most extreme cold air outbreak and return flow event occurred during a 5-day period from 10-14 February 1988. Particular attention was paid to this event to determine whether or not observed features in a single case were similar to those illustrated in the composite over seven events. It also allowed for analysis of the temporal evolution of a cycle. Comparison between this extreme event, other events, and the seven event composite indicated that the composite was a good representation of the overall scenario, while the extreme event had a similar although stronger signature than the composite.

4. Evaluation of NGM Performance

An evaluation of NGM performance during the return flow cycle was conducted with emphasis on wind field evolution. Comparisons of NGM 24- and 48-h forecasts with subsequent NGM analyses (used for verification) illustrated model strengths and weaknesses.

The synoptic scale LLJ first develops over the High Plains near southeastern Colorado, eastern New Mexico, and the Texas Panhandle. NGM analyses indicate that the LLJ begins to develop at T-3 over this region and forms in response to three features (Figs 3, 4). *First*, the polar anticyclone at 850 mb (typically associate with the previous cold air outbreak) must move over south Texas or the western Gulf of Mexico to enable a southwesterly synoptic flow over the region (Fig. 3a). *Secondly*, a lee Rocky mountain trough must be present to enhance the southwesterly geostrophic wind over the same area

(Fig. 3a). *Finally, and most importantly*, the jet accelerates in response to a strong isallobaric, ageostrophic wind from the south directed toward rapid pressure falls in the lee of the Rockies associated with cyclogenesis (Fig 4a). The lee trough is always present in cases of LLJ formation; however, its presence alone does not initiate LLJ development. Only after synoptic scale winds become southwesterly, and deepening of the lee trough initiates a strong isallobaric, ageostrophic wind from the south, will a jet begin to develop. These processes are observed near the base of the synoptic scale boundary layer inversion during T-3.

NGM forecasts of LLJ formation are hindered by difficulties in developing these three features adequately (Figs. 3b, 4b). One primary reason for this deficiency appears to be the NGM's bias in developing cyclones over the central Plains. Initially, the NGM develops weaker lee troughing and synoptic southwesterly flow over the region than is observed (Fig. 4). In addition, 850 mb and surface height/pressure falls are displaced significantly farther north than are observed. Misplaced cyclogenesis is corroborated by Grumm and Siebers (1989a) and Mullen and Smith (1990). As a result, initial development of the LLJ is poorly forecast by the NGM.

Development of the LLJ eastward is tied to cyclone development and motion. Over the southern Plains, the jet moves east and is maintained by an increasingly strong pressure gradient. To the south, the LLJ forms in response to those features which developed it further north but does so at a lower height. The LLJ reaches the Gulf of Mexico some 18-36 h after initial formation over eastern New Mexico. Maximum onshore flow over the western Gulf and inland (T-4) typically occurs 36-48 h after T-3. Upon reaching the western Gulf, the LLJ is characterized by an upward slope. Namely, maximum winds occur at 950 mb over the western Gulf (Fig. 5c) and at 850 mb over the south central Plains (coincident with the slope of the inversion) during T-4 (Fig. 5a). The reason the LLJ is strongest at 950 mb in the western Gulf is because the ageostrophic cross-height flow is largest there (Fig. 6), the reason the LLJ is strongest at 850 mb over the south central U.S. is because the ageostrophic cross-height flow was largest there and is maintained by a strong pressure gradient in the central Plains (Figs. 4, 5). While this jet does display somewhat of a diurnal maximum (typically strongest at night when the boundary layer inversion is typically strongest) it usually persists throughout the day unlike the summertime/nocturnal LLJ as discussed by Blackadar (1957), Bonner (1968), and Wexler (1961). Formation processes of these two jets show significant dissimilarities and should be thought of separately when making forecasts.

Typically, as the LLJ continues eastward, it becomes supergeostrophic and begins to weaken. Cyclones which continue to develop are likely to maintain the jet farther east, however strong southerly flow along the Gulf coast is diminished as the most significant height falls are displaced increasingly further north as the parent cyclone moves northeast. This is apparently one reason for the relative minima in LLJ frequency over the eastern and central Gulf coast as compared to the western Gulf.

5. Operational implications

While the NGM provides detailed guidance to operational forecasters during the return flow cycle, its use can be enhanced by noting model biases, model deficiencies, pattern evolution, and applying conceptual models to forecasts. Comparisons of NGM forecasts with verifying analyses illustrated model strengths and weaknesses which impact operational forecast decisions.

Figure 3a shows the LLJ first developing in the Texas Panhandle some 18-36 h prior to reaching the western Gulf of Mexico. Studies of moisture field evolution have shown that the LLJ is the primary conveyor belt of water vapor during periods of return flow (Engel, 1991; Janish and Lyons, 1992). As a result, a dual channel return flow is set up across Texas. Low-level moisture typically returns along the LLJ axis over central Texas into west-central Oklahoma near 850 mb first, before the onset of deeper moisture return is observed region wide. Even if southerly winds are observed along the Texas coast, it isn't until the jet reaches the western Gulf that deep moisture return is observed. Examination of NGM gridded moisture fields (particularly specific humidity) near the LLJ level (near 850 mb over the central Plains) should aid forecasters in determining whether or not the model has a good handle on moisture return.

NGM analyses showed that the LLJ typically forms at the top of the boundary layer near the base of the synoptic scale inversion. Figure 7 shows the analysis and forecast inversion base using theta-e analysis for T-4. The upward slope with height inland (NGM analysis) corresponds to the upward sloping character of the LLJ typically observed during periods of return flow. NGM forecasts of the thermodynamic profile show a significant discrepancy and does not adequately predict the sloping structure of

the inversion or LLJ. Since forecasts of moisture return during return flow are critical, isentropic analysis will help depict and track features better than constant pressure field analysis.

During periods of strong southerly flow, the NGM tends to overdevelop and displace surface cyclone centers in relation to their analyzed positions. The NGM which initially is too weak in developing the lee Rocky mountain trough (T-3, Fig. 3) overdeepens and displaces the cyclone center significantly north of verifying analyses by T-4 (Fig. 5). As a result, initialization and subsequent LLJ formation including both magnitude and direction over the southern U.S. are in error. Winds in NGM forecasts appear representative of actual magnitudes over the central Plains (Figs. 5a, b) however display a westerly bias and appear to be more strongly geostrophically forced than are the analyses. The low level pressure gradient developed by the model is clearly stronger in NGM forecasts than are analyzed. Along the Gulf coast, NGM winds are weaker than analyzed and also display a westerly bias. The weak/westerly bias of model forecasts (during T-4) over the western Gulf of Mexico likely impacts moisture return by inhibiting the advance of rich moist air northward and perhaps by entraining dry air from the Mexican plateau over south and central Texas compounding the problem. This possibility has yet to be investigated. Although NGM wind forecasts are generally weaker and more westerly than observed (especially over Oklahoma and Texas), the timing of return flow (winds only) is generally good (Fig. 5). Forecasters should note that while timing may be good, moisture forecasts are usually significantly deficient which will impact many other parameters.

These biases likely impact the type and distribution of significant weather associated with developing cyclones during their intensification and movement over the central Plains. Pattern recognition and incorporation of conceptual models is necessary to enhance forecasts during these events.

Final upgrades to the NGM physics package were implemented 7 November 1990 and 7 August 1991. These changes included improvements to the soil moisture profile along coastal zones, enhanced orography, inclusion of stability dependent surface fluxes over water, enhanced resolution by expanding the B- and C-grids and eliminating the A-grid, a fourth order difference scheme to improve the model spatial resolution and the inclusion of a new regional data assimilation which incorporates a new first guess for the model (Petersen et al., 1991; DiMego et al., 1992). Model performance following these changes needs to be examined to determine their influence on the NGM's ability to

forecast the return flow cycle. Nonetheless, preliminary studies of moisture field evolution during the spring of 1992 indicate that the impact of model changes was minimal and that deficiencies found in 1988 persist today. The NGM is now frozen (no model changes will occur) in order to develop a stable set of model output statistics (MOS). Thus, the strengths and weaknesses illustrated here will likely persist in future model runs.

REFERENCES

Alexander, G. D. and G. S. Young, 1990: The use of quantitative surface cyclone characteristics to determine systematic departures from mean nested grid model forecast errors. *Nat. Wea. Dig.*, **15**, 6-12.

Blackadar, A. K., 1957: Boundary layer wind maxima and their significance for the growth of nocturnal inversions. *Bull. Amer. Meteor. Soc.*, **38**, 283-290.

Bonner, W. D., 1968: Climatology of the low-level jet. *Mon. Wea. Rev.*, **96**, 833-850.

Crisp, C. A. and J. M. Lewis, 1992: Return flow in the Gulf of Mexico, Part I: A classificatory approach with a global historical perspective. *J. Appl. Meteor.* 31, 868-881.

DiMego, G. J., D. E. Mitchell, R. A. Petersen, J. E. Hoke, J. P. Gerrity, J. J. Tuccillo, R. L. Wobus, and H-M. H. Juang, 1992: Changes to NMC's regional analysis and forecast system. *Wea. Forecasting*, **7**, 185-198.

Djuric, D., and M. S. Damiani, Jr., 1980: On the formation of the low-level jet over Texas. *Mon. Wea. Rev.*, **108**, 1854-1865.

Djuric, D., and D. S. Ladwig, 1983: Southerly low-level jet in the winter cyclones of the Southwestern Great Plains. *Mon. Wea. Rev.*, **111**, 2275-2281.

Engel, G. T., 1991: Low-level wind maxima over the western Gulf of Mexico and their role in water vapor advection. M.S. Thesis, Department of Meteorology, Texas A&M University, *CIAMS Report No. 9109-2*, 122 pp.

Fast, J. D, and M. D. McCorcle, 1990: A two-dimensional numerical sensitivity study of the Great Plains low-level jet. *Mon. Wea. Rev.*, **118**, 151-163.

Frisch, A. S., B. W. Orr, and B. E. Martner, 1992: Doppler radar observations of the development of a boundary-layer nocturnal jet. *Mon. Wea. Rev.*, **120**, 3-16.

Grumm, R. H. and A. L. Siebers, 1989a: Systematic surface cyclone errors in NMC's nested grid model November 1988 - January 1989. *Wea. Forecasting*, **4**, 246-252.

Grumm, R. H. and A. L. Siebers, 1989b: Systematic surface anticyclone errors in NMC's nested grid model December 1988 - August 1989. *Wea. Forecasting*, **4**, 555-561

Grumm, R. H., R. J. Oravec, and A. L. Siebers, 1991: A comparison of cyclone forecast errors in NMC's AVN and NGM September 1990 through May 1991. Ninth AMS Conference on Numerical Weather Prediction 14-18 October 1991, Denver, Colorado, 726-729.

Janish, P. R. and S. W. Lyons, 1992: NGM performance during cold air outbreaks and periods of return flow over the Gulf of Mexico with emphasis on moisture field evolution. *J. Appl. Meteor.*, 31, 995-1017.

Jensenius, J. S. Jr., 1990: A statistical comparison of the forecasts produced by the NGM and LFM for the 1987/88 cool season. *Wea. Forecasting*, 5, 116-127.

Junker, N. W. and J. E. Hoke, 1990: An examination of nested grid model precipitation forecasts in the presence of moderate-to-strong low-level southerly inflow. *Wea. Forecasting*, 5, 333-344.

Junker, N. W., J. E. Hoke, B. E. Sullivan, K. E. Brill, and F. J. Hughes, 1992: Seasonal and geographic variations in quantitative precipitation prediction by NMC's Nested-Grid Model and medium-range forecast model. Wea. Forecasting, 7, 410-429.

Lettau, H. H., 1967: Small to large scale features of boundary structures over mountain slopes. *Proc. Symp. Mountain Meteorology*. Colorado State University, 74pp.

Lewis, J. M., C. M. Hayden, R. T. Merrill, and J. M. Schneider, 1989: GUFMEX: A study of return flow in the Gulf of Mexico. *Bull. Amer. Meteor. Soc.*, **70**, 24-29.

McNider, R. T., and R. A. Pielke, 1981: Diurnal boundary layer development over sloping terrain. *J. Atmos. Sci.*, **38**, 2198-2122.

Mullen, S. L., and B. B. Smith, 1990: An analysis of sea level cyclone errors in NMC's Nested Grid Model (NGM) during the 1987-1988 winter season. *Wea. Forecasting*, **5**, 433-447.

Newton, C. W., 1967: Severe convective storms. *Advances in Geophysics*, Vol. 12, Academic Press, 257-303.

Paegle, J. N., M. McCorcle, and E. Miller, 1984: Diagnoses and numerical simulation of a low-level jet during ALPEX. *Beitr. Phys. Atmos.*, **57**, 419-430.

Parish, T. R., A. R. Rodi, and R. D. Clark, 1988: A case study of the summertime Great Plains low-level jet. *Mon. Wea. Rev.*, **116**, 94-105.

Petersen, R. A., 1988: Evaluating systematic performance characteristics of RAFS mid- and low-level forecast fields. *Preprints, Eighth Conf. on Numerical Weather Prediction.* Baltimore, Amer. Meteor. Soc., 839-843.

Petersen, R. A., G. J. DiMego, J. E. Hoke, K. E. Mitchell, J. P. Gerrity, R. L. Wobus, H-M. H. Juang, and M. J. Pecnick, 1991: Changes to NMC's regional analysis and forecast system. *Wea. Forecasting*, **6**, 133-141.

Phillips, N. A., 1979: The Nested Grid Model. *NOAA Tech. Report NWS 22*, U. S. Department of Commerce, Washington, D. C., 80 pp.

Sanders, F., 1987: Skill of NMC operational dynamical models in prediction of explosive cyclogenesis. *Wea. Forecasting*, **2**, 322-336.

Smith, B. B. and S. L. Mullen, 1991: Sea-level cyclone errors in NMC's Nested Grid and Global Spectral Model: The impact of model averaging and flow regime dependendce. *Ninth AMS Conference on Numerical Weather Prediction 14-18 October 1991*, Denver, Colarado, 730-733.

Uccellini, L. W., 1980: On the role of upper tropospheric jet streaks and leeside cyclogenesis in the development of low-level jets in the Great Plains. *Mon. Wea. Rev.*, **108**, 1689-1696.

Uccellini, L. W., R. A. Petersen, K. F. Brill, P. J. Kocin, and J. J. Tuccillo, 1987: Synergistic interactions between an upper-level jet streak and diabatic processes that influence the development of a low-level jet and a secondary coastal cyclone. *Mon. Wea. Rev.*, **115**, 2227-2261.

Walters, M. K., 1988: *Synoptic-Scale Forcing of the Low-Level Jet in Developing Baroclinic Waves*. Ph. D. Dissertation, Department of Meteorology, Texas A&M University, 131 pp.

Wexler, H., 1961: A boundary layer interpretation of the low-level jet. *Tellus*, **13**, 368-378
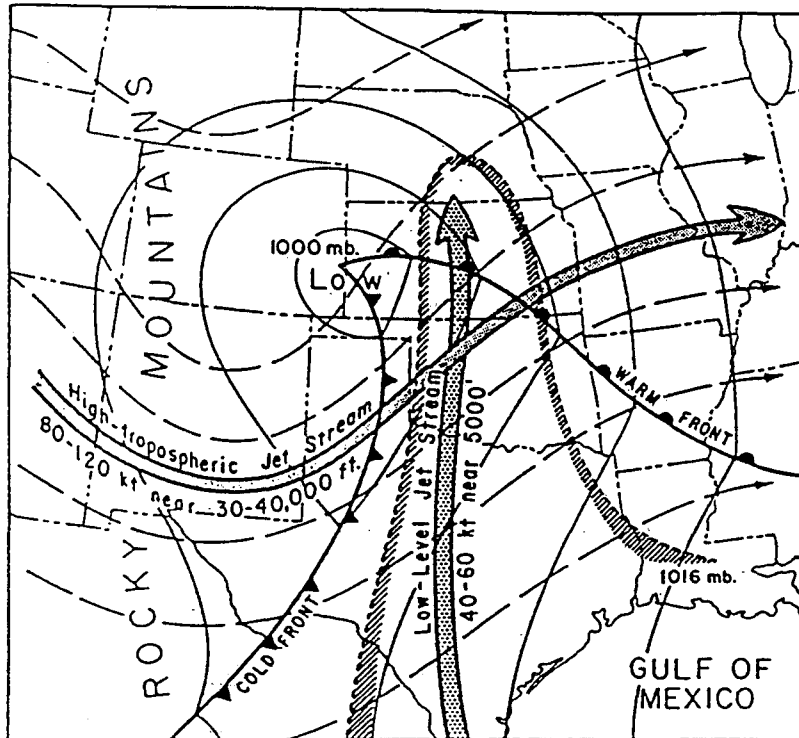
Fig. 1. Schematic model of synoptic features associated with lee-side Rocky Mountain cyclogenesis over the south-central United States. Sea level isobars are solid, upper-tropospheric geopotential is dashed, and moist, potentially unstable air mass originating from the Gulf of Mexico is outlined by hatching (from Newton, 1967).
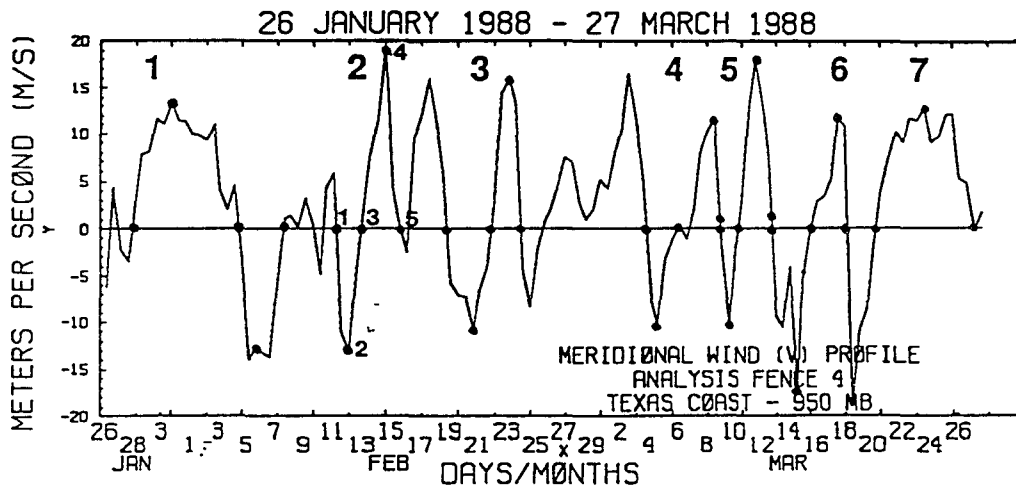
Fig. 2. A time series of the meridional wind component (v) at 950 mb along the Texas coast. Seven cycles are indicated. The approximate verification periods for cycle 2 are given.

Composite Geopotential Height and Wind Field Analysis
850 mb Level
Valid for Verification Period 3
Height Contours Expressed in Geopotential Meters

a
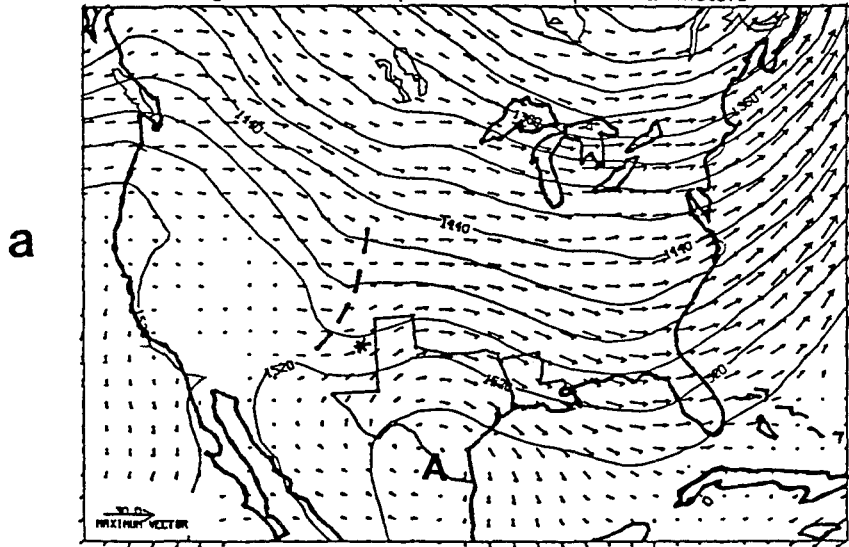
Composite Geopotential Height and Wind Field Analysis
850 mb Level
48 h FX Valid for Verification Period 3
Height Contours Expressed in Geopotential Meters

b
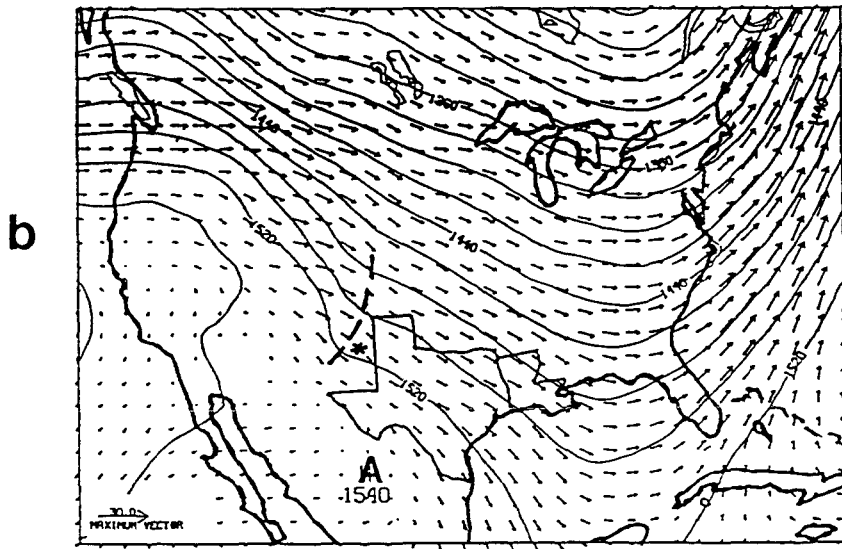
Fig. 3. Geopotential height and wind composites at 850 mb for NGM analyses and 48 h forecasts at T-3. NGM analysis and 48 h forecast are given in Figs. 3a and 3b respectively. Cyclone and anticyclone positions are marked with a "C" and an "A" respectively. The 850 mb trough axis is indicated by the dashed line with the contour interval being 20 gpm, and the maximum wind vector given in m s⁻¹ at the lower left. Asterisks are given for points of reference.

COMPOSITE STUDY GEOPOTENTIAL TENDENCY AND AGEOSTROPHIC WIND FIELD ANALYSIS
850 MB LEVEL (INITIAL FIELD DATA)
VALID FOR VERIFICATION PERIODS 3-2

a
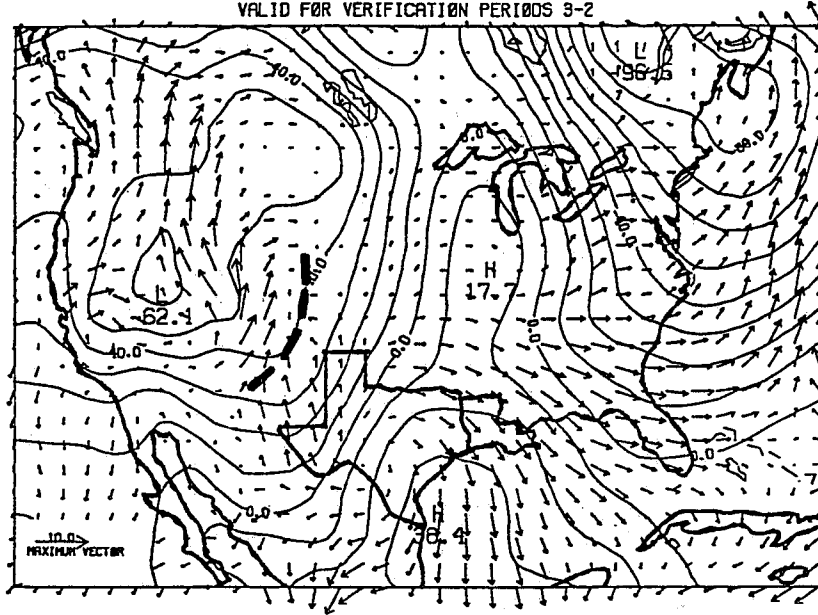
COMPOSITE STUDY GEOPOTENTIAL TENDENCY AND AGEOSTROPHIC WIND FIELD ANALYSIS
850 MB LEVEL (48 H FX FIELD DATA)
VALID FOR VERIFICATION PERIODS 3-2

b
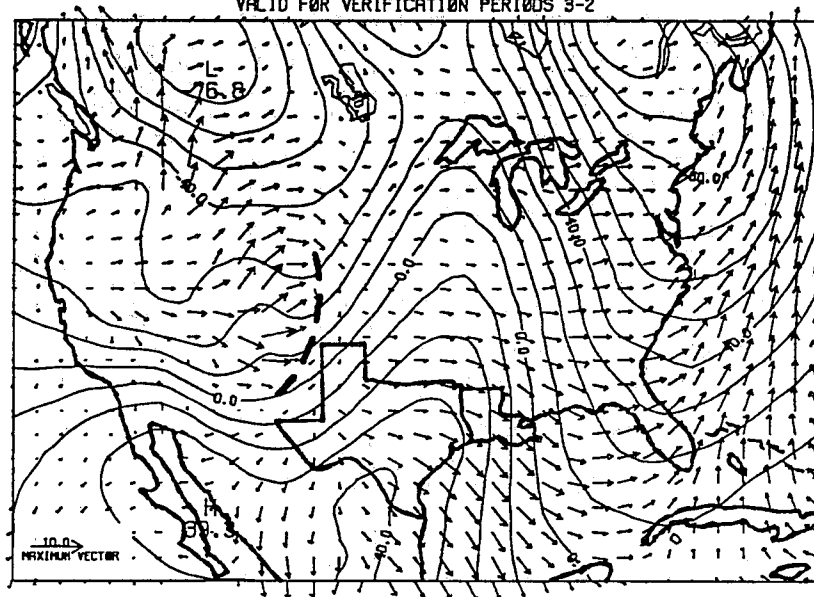
Fig. 4. Composite geopotential height tendency between T-2 and T-3 at 850 mb for the (a) NGM analysis and (b) 48 h forecast. Tendencies are computed for the geopotential height at T-3 minus the geopotential height at T-2. Charts include the ageostrophic wind field for T-3. The contour interval is 10 gpm with the maximum ageostrophic wind vector given in $m\ s^{-1}$ at lower left.

Fig. 5. Geopotential height and wind composites for NGM analyses and 48 h forecasts at T-4. Figs. 5a and 5b give the analysis and forecast at 850 mb while Figs. 5c and 5d give the analysis and forecast at 950 mb. Cyclone and anticyclone positions are marked with a "C" and an "A" respectively. Trough axes are indicated by a dashed line. The contour interval is 20 gpm with.. the maximum wind vector given in m s⁻¹ at lower left.

Fig. 6. Composite geopotential height tendency between T-3 and T-4 at 950 mb for the (a) NGM analysis and (b) 48 h forecast. Tendencies are computed for the geopotential height at T-4 minus the geopotential height at T-3. Charts include the ageostrophic wind field for T-4. The contour interval is 10 gpm with the maximum ageostrophic wind vector given in m s^{-1} at lower left. The grid values highlighted in Fig. 6b indicate the axis of the vertical cross section (discussed later.

**Vertical Cross Section of the 1000–700 mb Layer
Analysis of Theta–E
Initial Field Data Valid for Verification Period 4
Contours are Expressed in Degrees Kelvin**
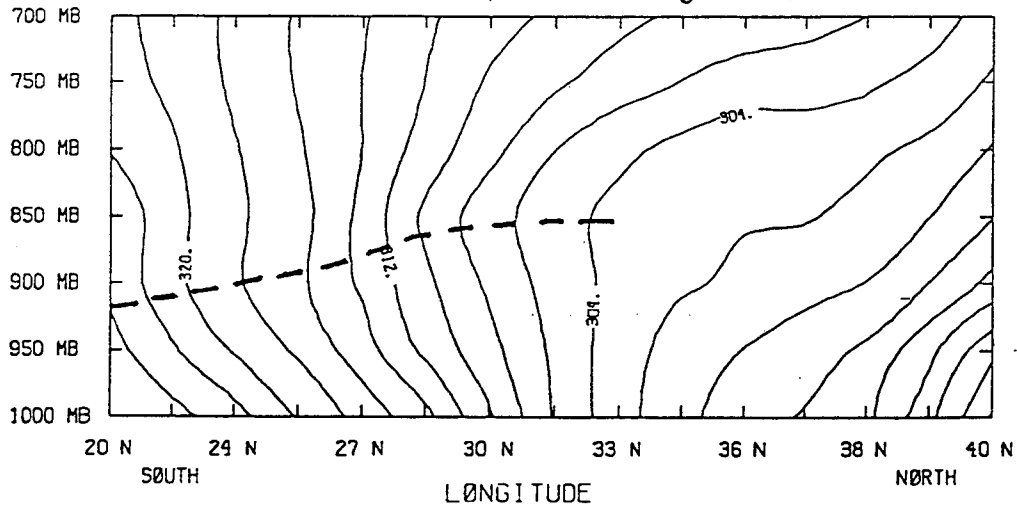
a

**Vertical Cross Section of the 1000–700 mb Layer
Analysis of Theta–E
NGM 48 H FX   Valid for Verification Period 4
Contours are Expressed in Degrees Kelvin**
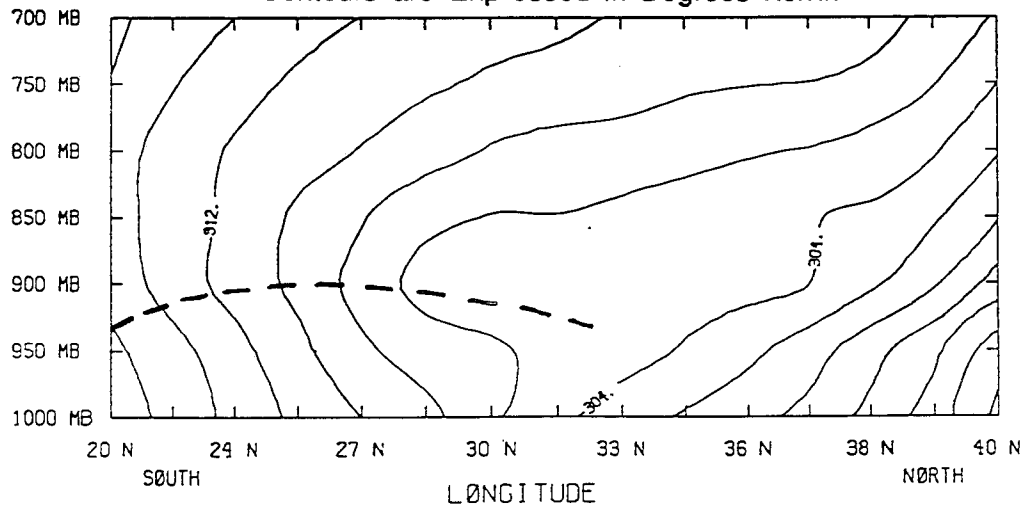
b

Fig. 7. Vertical sections of theta-e (K) in the 1000-700 mb layer for (a) NGM analysis and (b) NGM 48 h forecast at T-4. The meridional axis of the vertical section is displayed in Fig. 6b. Primary inversion layers are marked with dashed lines. The contour interval is 2 K.

CHAPTER 1: MARINE OBSERVATIONS

Eric Meindl (Section 1.1)
National Data Buoy Center
National Weather Service
Stennis Space Center, MS 39529-6000

and

Stephen K. Rinard (Sections 1.2 and 1.3)
Meteorological Services Division
Southern Region Headquarters
National Weather Service
Fort Worth, TX 76102-6154

Observations, whether taken on land or water, are the basis of scientific initiation and verification. The science of meteorology is certainly no exception. However, observations taken and used by the forecaster in the marine environment are unique when compared to those over land. It is therefore fitting that we begin this manual discussing the different types of marine observations.

1.1   NATIONAL DATA BUOY CENTER

1.1.1   Introduction

The National Data Buoy Center (NDBC) is a major center of the National Weather Service headquartered at the Stennis Space Center, Mississippi. NDBC is responsible for the deployment and maintenance of moored buoys and some fixed coastal stations, and for the quality control of data from those sources.

The NDBC station network of December 1991 consists of 115 stations, most of which are located in the oceans and coastal areas surrounding the continental United States. The network includes 61 moored buoy stations, and 54 fixed stations of the Coastal-Marine Automated Network (C-MAN). All stations report hourly via the GOES system. A fully operational station reports barometric pressure, wind speed and direction, peak wind, and air temperature. In addition, all moored buoys and some C-MAN stations report sea surface temperature and sea state.

NDBC also monitors data from approximately 35 expendable drifting buoys whose reports are disseminated on an irregular schedule through NOAA polar-orbiting satellites.

This section presents information on types of buoys, types of moorings, electronic payloads, measurement methods, sampling frequencies, averaging periods, communications, data quality control, and service philosophy of NDBC and provides suggested references for more information.

1.1.2   Station types

NDBC operates automated monitoring systems aboard moored buoys, fixed platforms, and drifting buoys. Many of the moored buoys and most of the C-MAN stations are supported by NWS base funding. Required locations of the base-funded stations are specified by the Office of Meteorology, Marine and Applied Services Branch.

In addition, several buoy and C-MAN stations are supported by non-NWS groups or agencies via reimbursable funds. Such stations have specific environmental monitoring requirements and should be considered temporary. The station is discontinued when data requirements are satisfied and funding by the funding agency is withdrawn. All such stations are identified in the weekly *Data Platform Status Report* available through NDBC.

1.1.2.1   Moored buoy hull types

The table below lists some characteristics and sensor height (MSL) of the different moored buoy hull types.

BUOY HULLS

TYPE	SENSOR HEIGHT (Relative To Sea Level)			
	WINDS	PRESSURE	AIR TEMP.	SEA TEMP.
12M Discus	10m	0m	10m	-1m
10M Discus	10m	0m	10m	-1m
6M NOMAD	5m	0m	5m	-1m
3M Discus	5m	0m	4m	-.5m
2.3M Discus	3m	0m	3m	-.5m
12M LNB	13.8m	0m	11.4m	-1.1m

An important feature to note relative to operational forecasting is the different heights of anemometers aboard different buoy types. Details on averaging periods are contained in Section 1.1.6.

Moored station locations are shown in Figs. 1.1.2.1-1 and 1.1.2.1-2. The 12-m (Fig.1.1.2.1-3) buoys are normally reserved for the harshest environmental areas such as the Bering Sea and the North Pacific, while the 10-m buoys are placed in less severe climates such as the central Gulf of Mexico. The 6¥3 m boat-shaped NOMAD buoy (Fig. 1.1.2.1-4) is used in many deep ocean areas. The 3-m buoy (Fig. 1.1.2.1-5) is commonly found in coastal areas, the Great Lakes, and occasionally in the tropics. A 2.3-m coastal buoy is undergoing testing and is expected to become operational in early 1992.

1.1.2.2   C-MAN stations

At the end of 1991, the C-MAN network consisted of 54 automated meteorological stations installed on fixed sites in data-sparse, coastal areas of the U.S. and its territories. The location of current C-MAN stations in the continental U.S. is shown in Fig. 1.1.2.2-1.

Basic parameters measured by the C-MAN are wind speed and direction, wind gust, air temperature, and barometric pressure. Dewpoint, precipitation, water temperature, water level (tide), wave parameters, and visibility are identified expansion parameters for selected sites. Due to the wide variability of C-MAN locations and platforms, forecasters should consult Fig. 1.1.2.2-2 for specific site information.

C-MAN stations are either fixed (physically attached to a platform, lighthouse, or other permanent coastal structure) or are aboard U.S. Coast Guard (USCG) navigational buoys. Although administratively part of the C-MAN program, data from the USCG navigational buoys appear to the field forecaster the same as data from the NDBC moored buoys. NDBC monitoring equipment has been placed on six USCG Large Navigational Buoys (LNB) and two Exposed Location Buoys (ELB). Shown below are some characteristics and sensor heights (MSL) of USCG Navigational Buoys which are equipped as NDBC automated stations.
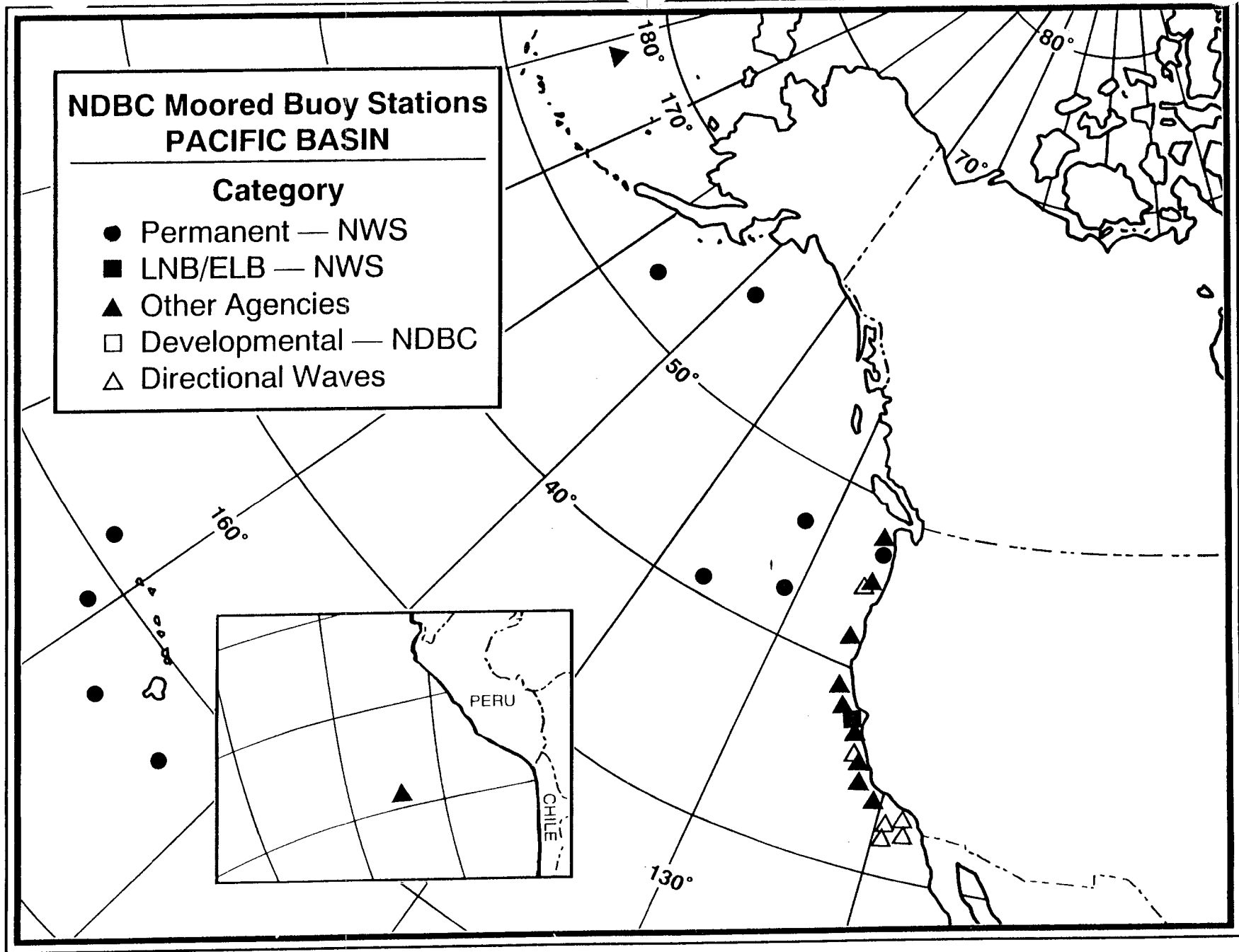
NDBC Moored Buoy Stations
ATLANTIC BASIN

Category
- ● Permanent — NWS
- ■ LNB/ELB — NWS
- ▲ Other Agencies
- □ Developmental — NDBC
- △ Directional Waves

NDBC Moored Buoy Stations
PACIFIC BASIN

Category
● Permanent — NWS
■ LNB/ELB — NWS
▲ Other Agencies
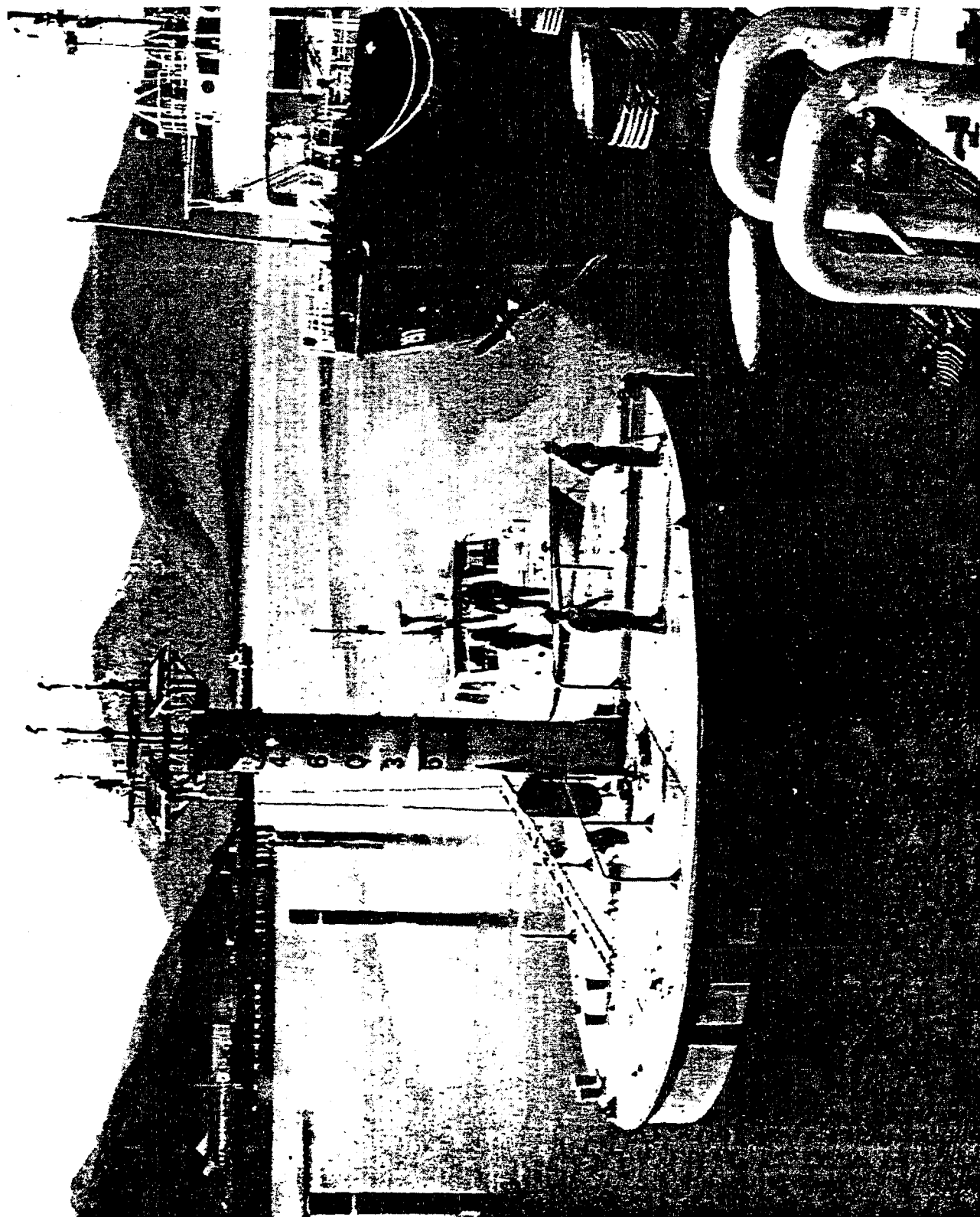□ Developmental — NDBC
△ Directional Waves
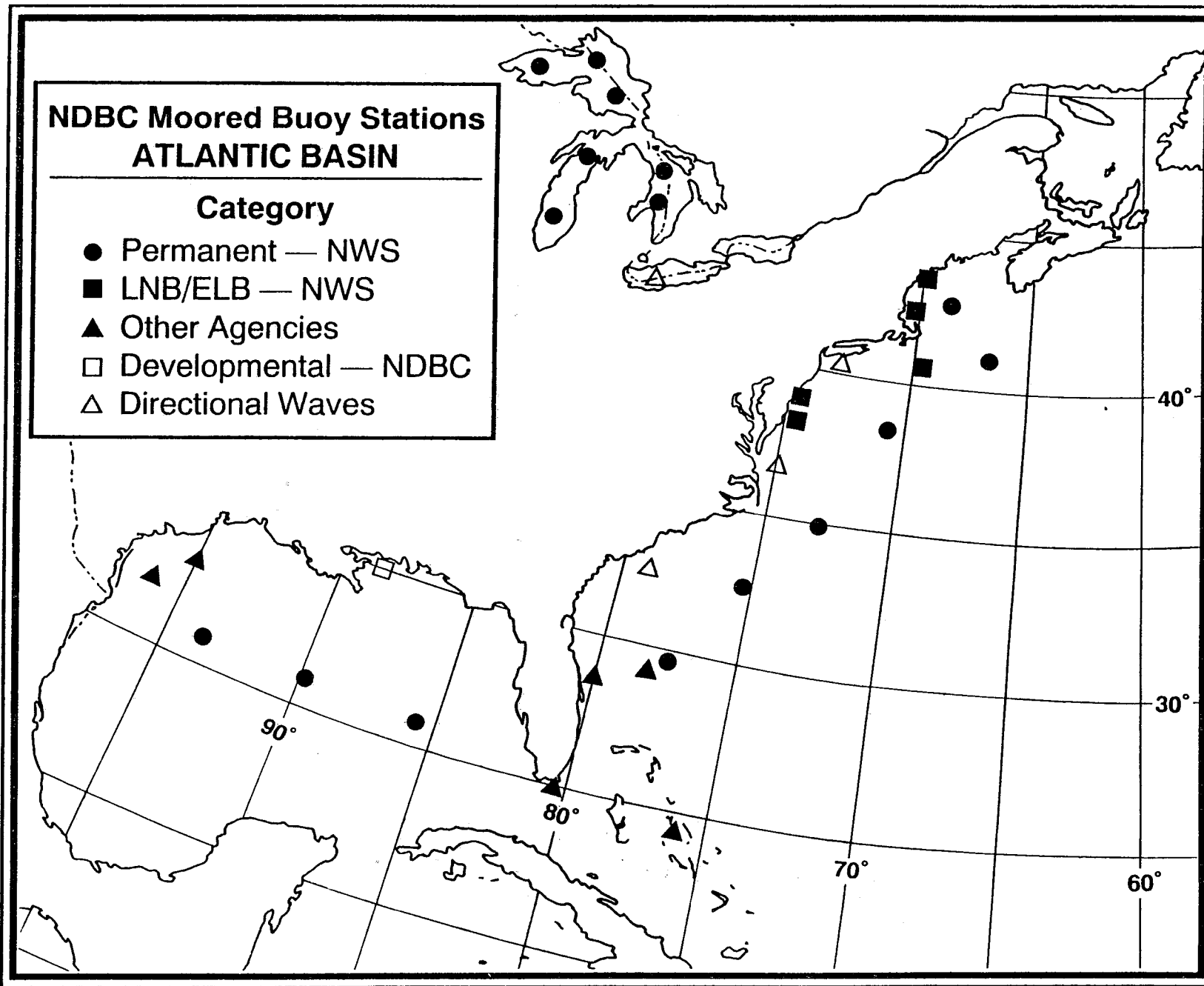
Fig. 1.1.2.1-3   NDBC 12-N   Discus Buoy
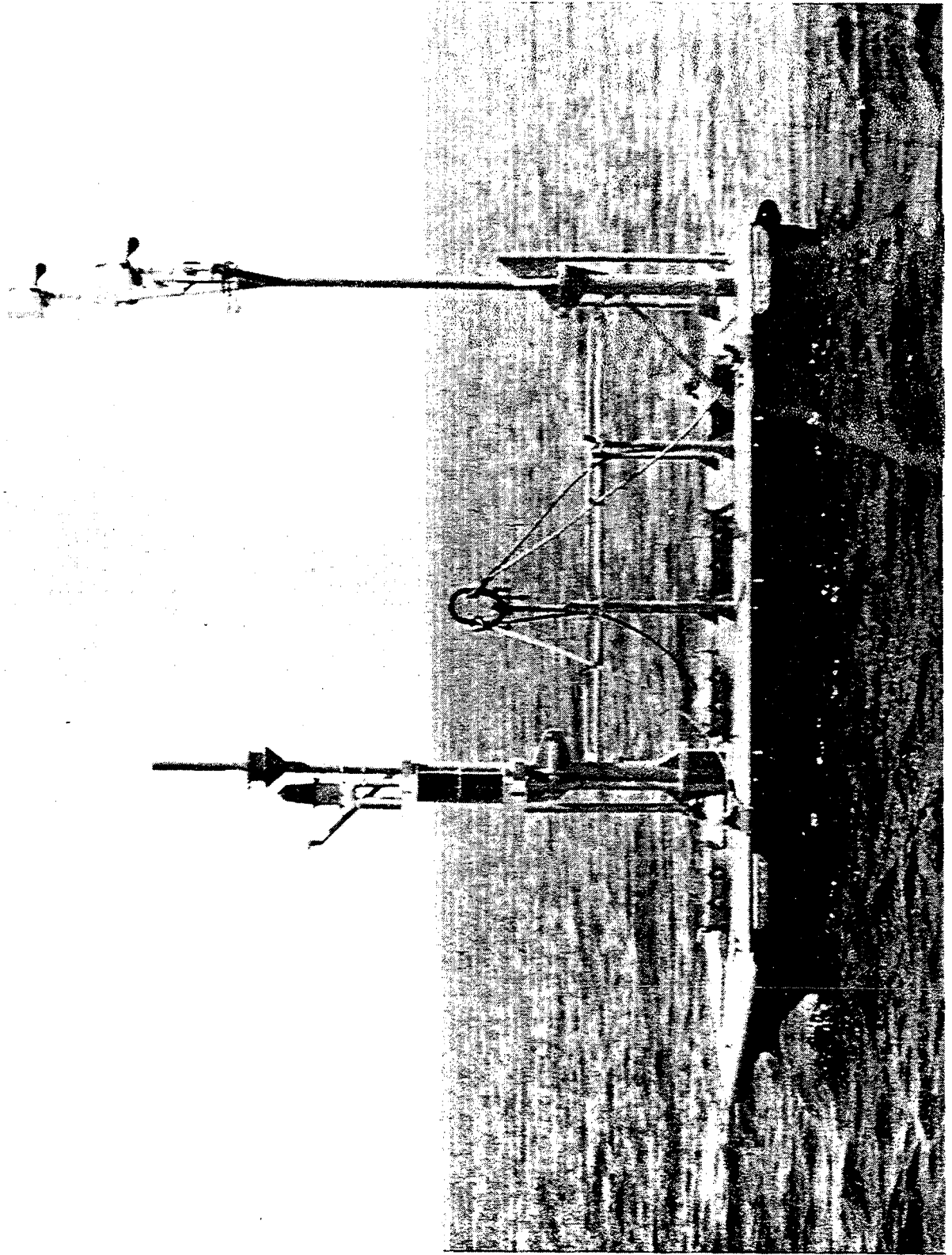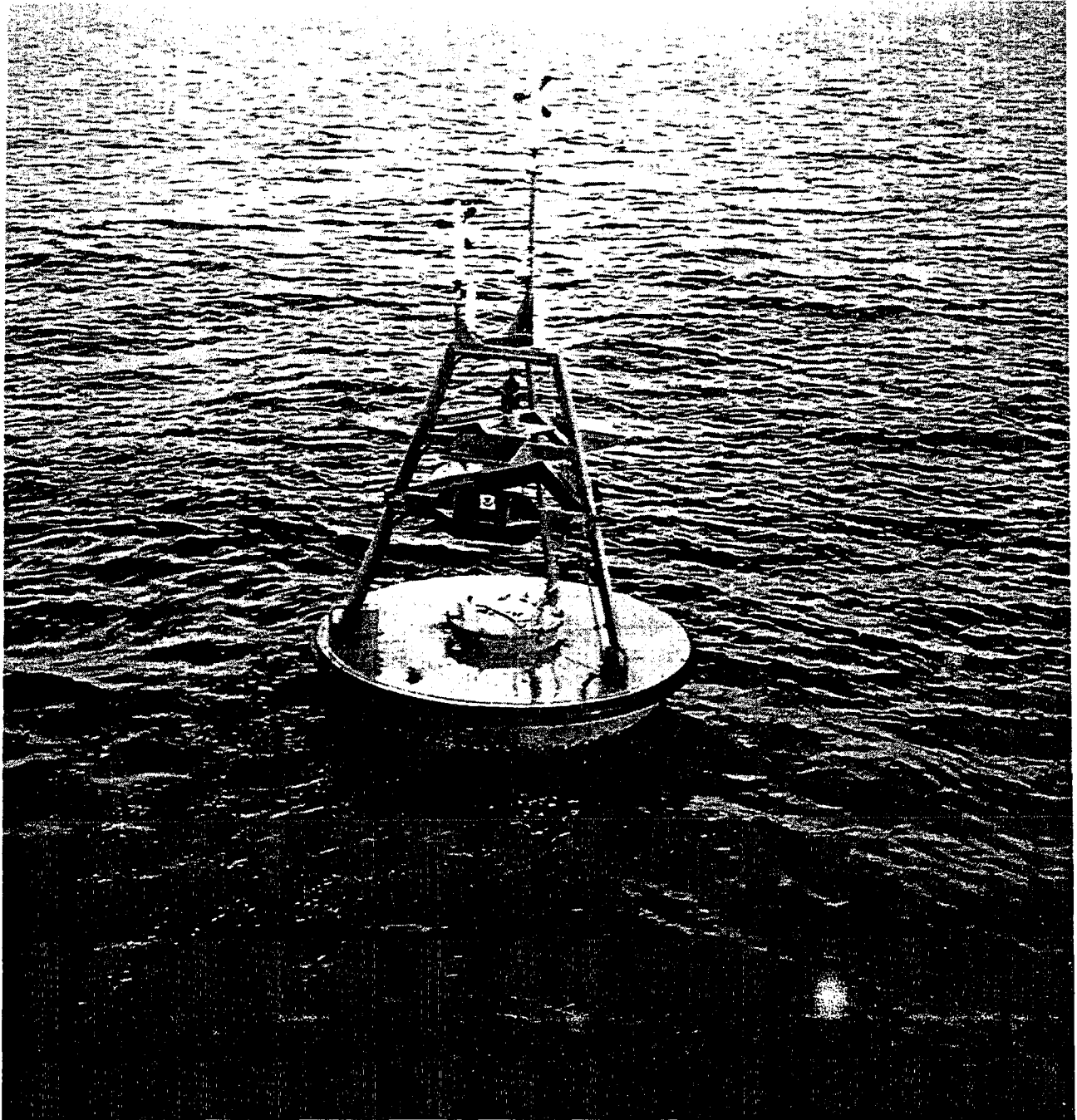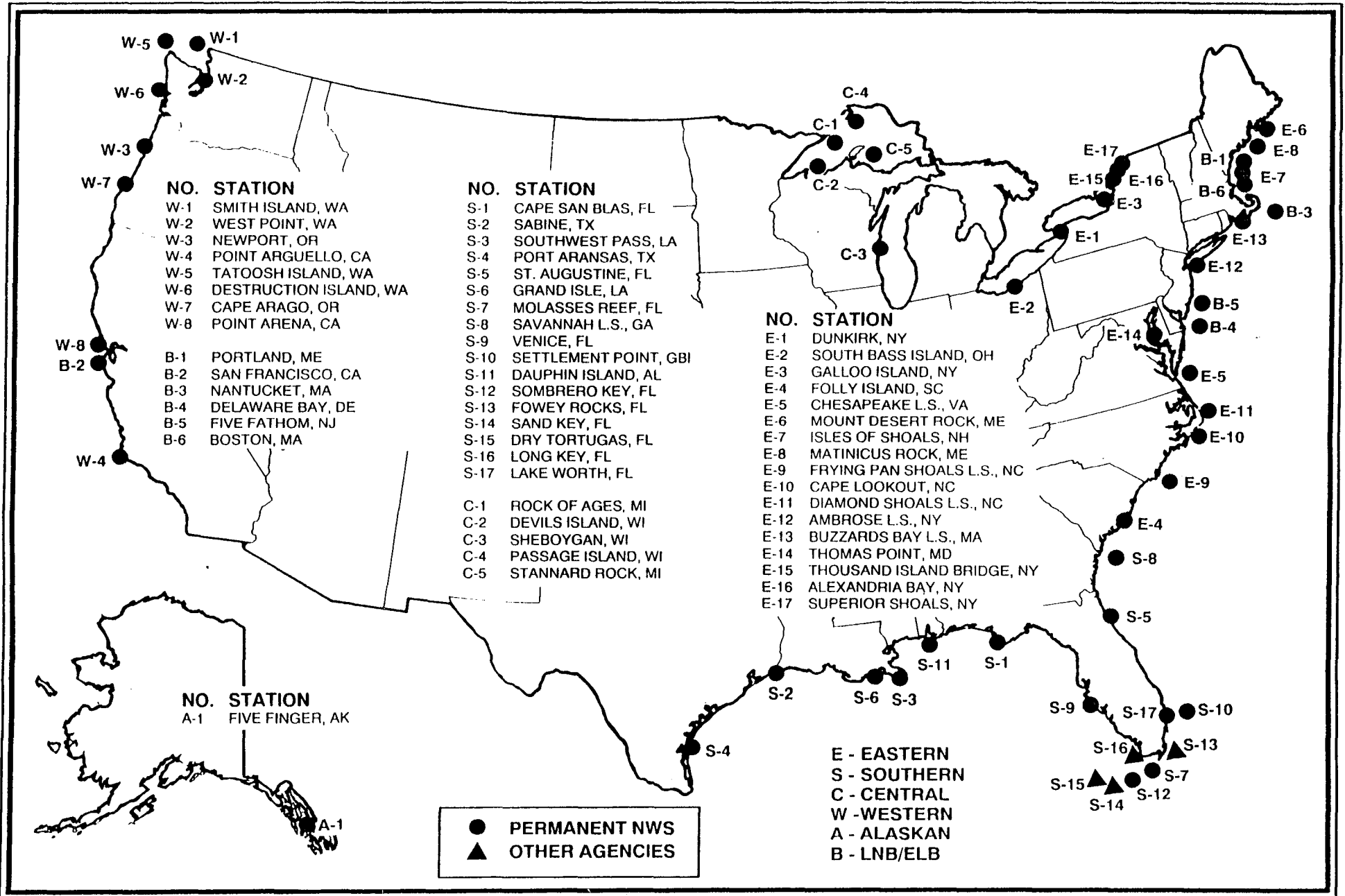
Fig. 1.1.2.1-4   NDBC 6-Meter NOMAD Buoy

Fig. 1.1.2.1-5   NDBC 3-Meter Discus Buoy

C-MAN SITES

NO.	STATION
W-1	SMITH ISLAND, WA
W-2	WEST POINT, WA
W-3	NEWPORT, OR
W-4	POINT ARGUELLO, CA
W-5	TATOOSH ISLAND, WA
W-6	DESTRUCTION ISLAND, WA
W-7	CAPE ARAGO, OR
W-8	POINT ARENA, CA
B-1	PORTLAND, ME
B-2	SAN FRANCISCO, CA
B-3	NANTUCKET, MA
B-4	DELAWARE BAY, DE
B-5	FIVE FATHOM, NJ
B-6	BOSTON, MA

NO.	STATION
S-1	CAPE SAN BLAS, FL
S-2	SABINE, TX
S-3	SOUTHWEST PASS, LA
S-4	PORT ARANSAS, TX
S-5	ST. AUGUSTINE, FL
S-6	GRAND ISLE, LA
S-7	MOLASSES REEF, FL
S-8	SAVANNAH L.S., GA
S-9	VENICE, FL
S-10	SETTLEMENT POINT, GBI
S-11	DAUPHIN ISLAND, AL
S-12	SOMBRERO KEY, FL
S-13	FOWEY ROCKS, FL
S-14	SAND KEY, FL
S-15	DRY TORTUGAS, FL
S-16	LONG KEY, FL
S-17	LAKE WORTH, FL
C-1	ROCK OF AGES, MI
C-2	DEVILS ISLAND, WI
C-3	SHEBOYGAN, WI
C-4	PASSAGE ISLAND, WI
C-5	STANNARD ROCK, MI

NO.	STATION
E-1	DUNKIRK, NY
E-2	SOUTH BASS ISLAND, OH
E-3	GALLOO ISLAND, NY
E-4	FOLLY ISLAND, SC
E-5	CHESAPEAKE L.S., VA
E-6	MOUNT DESERT ROCK, ME
E-7	ISLES OF SHOALS, NH
E-8	MATINICUS ROCK, ME
E-9	FRYING PAN SHOALS L.S., NC
E-10	CAPE LOOKOUT, NC
E-11	DIAMOND SHOALS L.S., NC
E-12	AMBROSE L.S., NY
E-13	BUZZARDS BAY L.S., MA
E-14	THOMAS POINT, MD
E-15	THOUSAND ISLAND BRIDGE, NY
E-16	ALEXANDRIA BAY, NY
E-17	SUPERIOR SHOALS, NY

NO.	STATION
A-1	FIVE FINGER, AK

● PERMANENT NWS
▲ OTHER AGENCIES

E - EASTERN
S - SOUTHERN
C - CENTRAL
W - WESTERN
A - ALASKAN
B - LNB/ELB

6-1

SITE	WIND SENSOR MOUNTING	ELECTRONICS EQUIPMENT ENCLOSURE	PRIMARY POWER	TELE	SITE*	BARO*	WIND SENSOR**	AIR TEMP**	INST DATE
DEVILS ISLAND, WI	LADDER	WATCH ROOM	BAT/SOLAR	NO	629	711	83	13	10/83
ROCK OF AGES, MI	LADDER	WATCH ROOM	BAT/SOLAR	NO	602	733	134	29	10/83
PASSAGE ISLAND, MI	LADDER	WATCH ROOM	BAT/SOLAR	NO	641	688	51	32	05/84
SHEBOYGAN, WI	TILT MAST	WATCH ROOM	AC	YES	577	638	63	51	10/83
STANNARD ROCK, MI	LADDER	WATCH ROOM	BAT/SOLAR	NO	600	715	118	32	07/84
SOUTH BASS ISLAND, OH	TILT MAST	BASE OF TOWER	AC	YES	580	602	69	22	09/83
DUNKIRK, NY	TILT MAST	WATCH ROOM	AC	YES	600	649	67	42	03/83
GALLOO ISLAND, NY	17.5 TROLLEY	GROUND LEVEL	BAT/SOLAR	NO	248	253	68	19	09/83
MOUNT DESERT ROCK, ME	22-FT TROLLEY	FIRST TOWER LEVEL	AC	NO	30	54	74	50	08/84
MATINICUS ROCK, ME	22-FT TROLLEY	WATCH ROOM	AC	NO	53	87	54	30	09/84
ISLES OF SHOALS, NH	22-FT TROLLEY	WATCH ROOM	AC	NO	43	62	63	39	09/84
BUZZARDS BAY, MA	17.5-FT TROLLEY	TOWER BUILDING	AC	NO	0	24	142	72	07/85
AMBROSE LS, NY	17.5-FT TROLLEY	TOWER BUILDING	AC	NO	0	13	161	93	11/84
THOMAS POINT, MD	17.5-FT TROLLEY	FOG SIGNAL ROOM	AC	NO	0	30	59	57	10/85
CHESAPEAKE LS, VA	17.5-FT TROLLEY	FIRST TOWER LEVEL	AC	NO	0	37	142	73	08/84
DIAMOND SHOALS LS, NC	17.5-FT TROLLEY	FIRST TOWER LEVEL	AC	NO	0	135	153	93	11/84
CAPE LOOKOUT, NC	30-FT TOWER	ON TOWER	SOLAR	NO	15	36	32	21	11/84
FRYING PAN SHOALS LS, NC	17.5-FT TROLLEY	FIRST TOWER LEVEL	AC	NO	0	127	14	76	11/84
FOLLY ISLAND, SC	30-FT TOWER	ON TOWER	SOLAR	YES	14	32	1	22	05/84
SAVANNAH LS, GA	17.5-FT TROLLEY	FIRST TOWER LEVEL	SOLAR	NO	0	80	90	66	05/85
ST. AUGUSTINE, FL	25-FT TROLLEY	BASE OF MAST	AC	YES	27	29	27	25	09/86
SETTLEMENT POINT, GBI	30-FT T-MAST	TIDE HOUSE	SOLAR	NO	9	9	32	30	10/85
LAKE WORTH, FL	22-FT TROLLEY	TIDE HOUSE	AC/SOLAR	YES	11	19	25	23	07/84
***FOWEY ROCKS, FL	TROLLEY	PARAPET	SOLAR	YES	0				
MOLASSES REEF, FL	17.5-FT TROLLEY	DAY MARKER SHACK	SOLAR	NO	0	37	52	51	12/87
SOMBRERO KEY, FL	30-FT TROLLEY	PARAPET	SOLAR	NO	0	130	159	33	02/88
***SAND KEY, FL		TOWER	SOLAR	YES	0				
VENICE, FL	22-FT TROLLEY	ON MAST	AC	YES	12	16	26	24	03/86
CAPE SAN BLAS, FL	30-FT TOWER	ON TOWER	AC/SOLAR	YES	6	27	32	20	11/82
DAUPHIN ISLAND, AL	30-FT TROLLEY	TIDE HOUSE	SOLAR	YES	25	28	32	30	11/86
SOUTHWEST PASS, LA	SLIDE MAST	WATCH ROOM	SOLAR	NO	0	109	111	45	02/84
MAIN PASS BLOCK, MP133C, LA	20-FT WINCH MAST	COMMUNICATIONS SHACK	AC	YES	0	108	132	132	02/88
GRAND ISLE, LA	30-FT TROLLEY	BARRACKS BUILDING	AC	YES	6	30	52	50	12/84
GARDEN BANKS, LA	SLIDE MAST	COMMUNICATIONS SHACK	AC	YES	0	163	189	188	08/89
SABINE, TX	SLIDE MAST	PARK HQ SECOND LEVEL	SOLAR	YES	3	42	41	39	02/84
PORT ARANSAS, TX	TILT MAST	ON MAST	AC	YES	17	21	32	30	03/84
***EXXON LENA, LA									
***SHELL BULLWINKLE, LA									
POINT ARGUELLO, CA	30-FT TOWER	ON TOWER	AC	NO	40	61	31	21	04/84
POINT ARENA, CA	42-FT TROLLEY	ON MAST	AC	YES	57	62	41	20	10/84
CAPE ARAGO, OR	SLIDE MAST	WATCH ROOM	AC	YES	59	106	49	33	08/84
NEWPORT, OR	30-FT TOWER	ON TOWER	AC	YES	30	51	31	21	04/84
WEST POINT, WA	30-FT TOWER	ON TOWER	BAT/SOLAR	YES	10	29	32	18	01/84
DESTRUCTION ISLAND, WA	SLIDE MAST	WATCH ROOM	AC	NO	70	168	103	32	08/84
SMITH ISLAND, WA	TILT MAST	BASE OF TOWER	BAT/SOLAR	NO	50	65	56	15	01/84
TATOOSH ISLAND, WA	30-FT TROLLEY	WATCH ROOM	AC	NO	101	156	83	51	08/84
FIVE FINGER, AK	17.5-FT TROLLEY	THIRD LANDING	AC	NO	22	95	75	14	07/84
FARAULEP ISLAND, CAROLINE IS	30-FT TOWER	ON TOWER	SOLAR	NO	5	9	35	35	10/88
ENIWETOK, MARSHALL IS	30-FT TOWER	ON TOWER	SOLAR	NO	5	9	35	35	11/89
UJAE, MARSHALL IS	30-FT TOWER	ON TOWER	SOLAR	NO	5	9	35	35	11/89
***PAGAN, N. MARIANAS									
***MILI, MARSHALL IS									
***KUSAIE, MICRONESIA									
***ULITHI, MICRONESIA									
***EPON, MARSHALL IS									

*ELEVATION IN FEET ABOVE MEAN SEA LEVEL
**HEIGHT IN FEET ABOVE SITE
***PLANNED IN 1990-1991

RHC 6/90

Fig. 1.1.2.2-2   Characteristics of NDBC C-MAN Stations

Type	Wind	Air Temp	Press	Waves	Sea Temp
LNB 12 m	13.8 m	11.4 m	0 m	0 m	- 1.1 m

Detailed C-MAN information can be found in the *Coastal-Marine Automated Network (C-MAN) User's Guide.*

1.1.2.3 Drifting buoys

Drifting buoys are expendable devices launched by ships or aircraft into the oceans and allowed to float freely with ocean currents. Only rarely is a drifting buoy recovered and refurbished. While usually deployed on the high seas, there have been a few instances when drifters have been launched in coastal areas. For example, four drifting buoys were launched in the Atlantic Ocean ahead of hurricane Josephine in 1984 and three were used in the Gulf of Alaska in conjunction with tracking the *Exxon Valdez* oil spill in 1989.

The typical role of NDBC with regard to drifting buoys is to procure the buoys for other groups or agencies, arrange logistical and launch support, and perform data quality checks. The drifters are normally FGGE type[1] spar buoys, approximately 3 m long and less than 1 m across at the widest point. Buoy position is tracked via satellite and can be used to roughly approximate ocean currents even when atmospheric measurements are no longer available.

The FGGE drifter measures barometric pressure and air temperature 1 m above the water surface. Sea temperature is measured through the hull approximately 0.5 m below water level. If so equipped, wind speed and direction are measured at 1 m above the water surface.

1.1.3   Buoy moorings

Mooring a buoy in the ocean is a unique engineering problem. Each mooring must be designed for a specific application, taking into account water depth, size and type of buoy, mission, and

---

[1]FGGE refers to the First GARP Global Experiment. GARP refers to the Global Atmospheric Research Project. The FGGE drifter was developed in the mid 1970s.

environmental application. NDBC buoys are moored in water depths from less than 15 m to approximately 5000 m.

The three basic types of moorings used by NDBC are all-chain, semi-taut, and inverse catenary (Fig.1.1.3-1). The all-chain and semi-taut types are shallow water moorings. Inverse catenary moorings, which are a combination of chain and buoyant rope, are used as deep ocean moorings because: 1) the weight of an all chain mooring could sink the buoy, and 2) the curves in the inverse catenary moorings serve to dissipate wave energy which would cause excessive wear and failure of the lower mooring which lies along the bottom attached to the anchor.

The design life of most of the major mooring components is six years. Premature mooring failures occasionally occur, usually due to fishbite or longline fishing activity.

1.1.4   Sea state measurement

Sea state is measured by all NDBC moored buoys and at some C-MAN stations. Such measurements have not yet been perfected on drifting buoys. Wave data are released in real time in two ways. Basic sea state information, specifically significant wave height and peak wave period, is included in the hourly meteorological message. A more detailed message containing wave energy spectra is released every three hours. The energy spectra allows the forecaster to more thoroughly analyze sea conditions. This topic is covered in detail in the *NDBC Real Time Directional Wave Information User's Guide* available to all NWS coastal offices, and in Chapter 3 of this manual.

1.1.4.1   Types of wave data

All NDBC moored buoys and some C-MAN stations measure nondirectional wave data. Several moored buoys provide directional wave data in real time. While nondirectional systems provide the wave energy spectra, directional wave systems tell from which direction wave energy is propagating at different wave periods. This information can be very useful to the marine forecaster, such as when forecasting the onset of heavy surf on the Pacific coast. NDBC uses only discus buoys for directional wave measurements since the hulls are axisymmetric. Directional wave measurements are not made with the NOMAD hull type.

NYLON

NYLON

NYLON

ALL CHAIN
SCOPE 3:1 TO 5:1
SHALLOW DEPTHS
(UP TO 200 FT)

POLY-NYLON
SPLICE

GLASS
FLOATS

20-80 FT

SEMITAUT
SCOPE: VARIOUS
INTERMEDIATE DEPTHS
(200 TO 2000 FT)

POLYPRO

20 FT

20 FT

FLOAT INVERSE CATENARY
SCOPE: ≅ 1.25:1
DEEP OCEAN (2000 TO > 20000 FT)
AND GREAT LAKES

POLY-NYLON INVERSE CATENARY
SCOPE: ≅ 1.25:1
DEEP OCEAN (200 TO > 20000 FT)
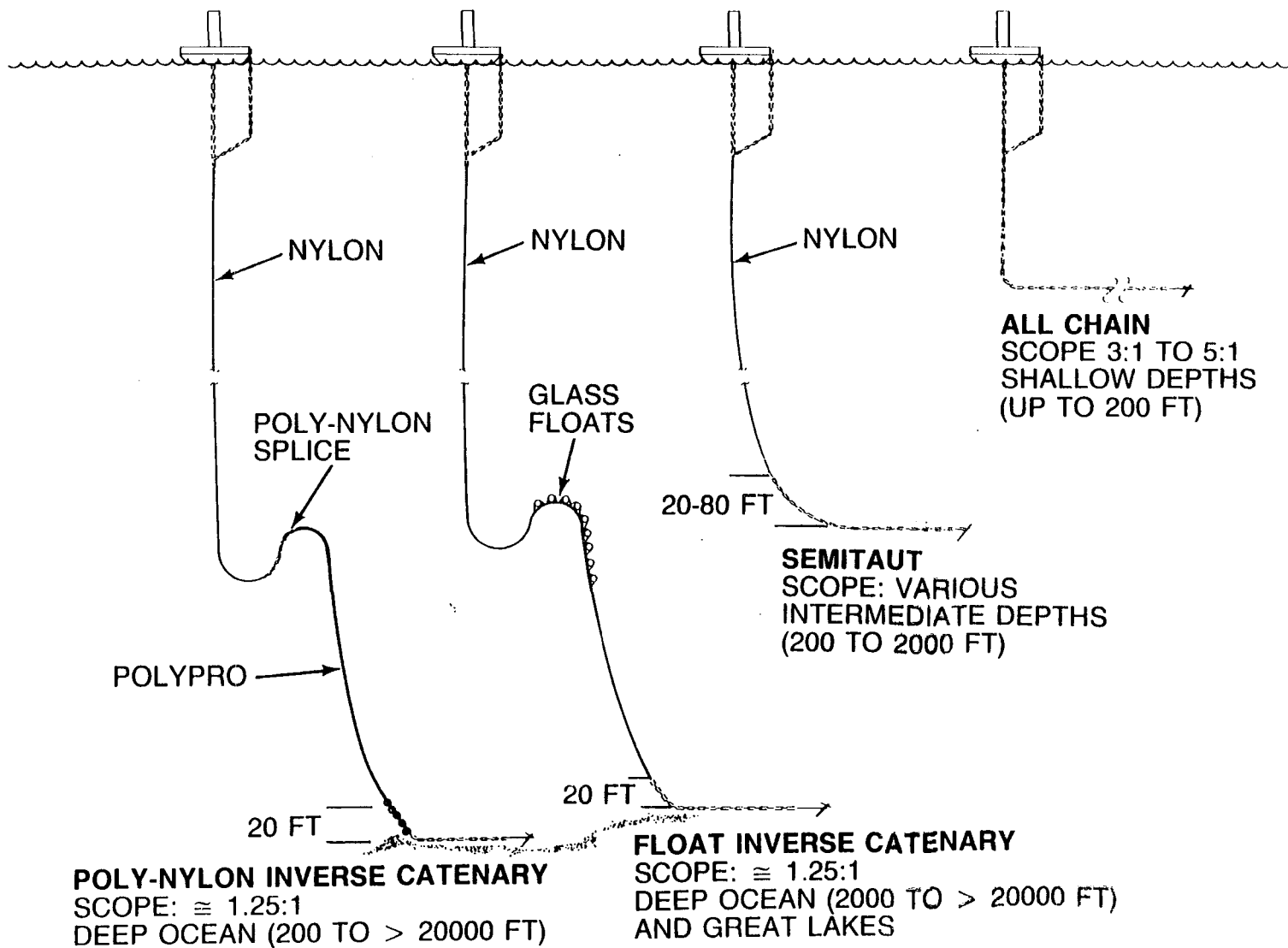
Fig. 1.1.3-1   NDBC Mooring Designs

1.1.4.2   Wave measurement systems

Wave measurements from each nondirectional moored buoy are derived from a fixed, single-axis, vertical accelerometer mounted near the waterline in the center of the hull compartment.   Hull motion is sampled for 20 minutes each hour and processed on board to derive hull acceleration or displacement values.   Data are then sent to shore via GOES for further processing.   While the system is simple, it does have the disadvantage of only sampling data for 20 minutes per hour and is not able to determine values of maximum wave height with enough accuracy for operational use.

After the wave data are received from GOES into the NWS Telecommunications Gateway (NWSTG), empirically derived coefficients are applied to compensate for the varying responses of different hull types and moorings to determine significant wave height and period.   Nondirectional sea state is then disseminated in wave energy spectra and the basic hourly meteorological message formats familiar to forecasters.

Directional wave systems use a magnetometer to measure compass angles of hull pitch, roll, and compass headings, and compute wave directions for the dominant waves.   These directional wave data are reported with a resolution of 10 degrees in spectral messages over AFOS.

C-MAN stations that measure nondirectional waves use electronic wave staffs or infrared lasers to measure wave heights. The wave staff is normally mounted on a support piling, while the laser wave sensor is mounted above the water surface looking downward.

1.1.5   NDBC station power sources

1.1.5.1   Moored buoys

NDBC moored buoys are typically powered by strings of secondary batteries recharged by solar panels and primary batteries. The primary batteries are a backup power source in the event that the solar recharging system malfunctions.   In addition to DC sensor output, power is used for the on-board processor and clock.

1.1.5.2   C-MAN stations

When available, local AC power is used at C-MAN stations; however, most of the time power is supplied in a manner similar to that described for moored buoys.

1.1.5.3   Drifting buoys

Drifting buoys are powered by pucks of 1.5-volt, D-size, alkaline batteries identical to those used in flashlights. Each puck contains 24 batteries hooked into two strings of 12 batteries each. Five to seven pucks power each buoy.

1.1.6   NDBC data stream

1.1.6.1   Data acquisition

Measurements at most NDBC stations are taken during acquisition periods that end approximately 10 minutes before the hour. Aboard moored buoys, barometric pressure, wind, air and sea surface temperatures are sampled over an 8-min period and averaged. The 8-min sampling period represents the shortest time period possible to measure representative winds from the buoy platform. However, this relatively long averaging period tends to produce a lower wind speed average than forecasters are accustomed to seeing from other marine data sources, such as ship reports, which often provide wind speeds averaged over 1 or 2 minutes. This is discussed more completely in Section 1.1.7.1. The peak wind can be the highest 5-sec average within the sampling period or the highest 5-sec average during the past hour. The peak 5-sec wind for the entire hour, if available, is encoded in Section 5 of the data message in the form 3GGgg 4ddfff, where GGgg is the hour and minute (Z) when the peak wind occurred.

Measurements of barometric pressure, wind, and air and sea temperatures from fixed C-MAN stations are averaged over a 2-min period. If sea state is observed, it is measured over the same length of time as with moored buoys.

The wind direction on most moored buoys and on all C-MAN stations is a vector average. Wind speed is usually a scalar average.

Some moored buoy and C-MAN stations record wind continuously by computing and storing six 10-min averages which are transmitted to shore each hour. A peak 5-sec gust for the entire hour can thus be obtained. However, *only the 8-min average mentioned above is sent in the real time message available to the forecaster.* Presently, "continuous winds" are only available from the archives; however, efforts are proceeding to include these data in the real-time message.

Measurements from the drifting buoys are taken over varying sampling periods depending upon the program for which the buoy was deployed. Each of these samples is then averaged and stored for up to 4 hours until it can be relayed to shore via polar orbiting satellites.

Older models of drifting buoys continuously took measurements and reported each sample to the satellite. The data were available at random times only if received by the overflight of the satellite. Sampling length and rates were variable.

1.1.6.2 Data transmission

1.1.6.2.1 Moored buoys and C-MAN stations

The data transmission path from station to user is depicted in Fig. 1.1.6.2.1-1. Data from moored buoys and fixed C-MAN stations are sent hourly via GOES to the National Environmental Satellite, Data, and Information Service (NESDIS) ground receiving station at Wallops Island, VA. Data are transmitted from moored buoys using a 40-watt transmitter and omnidirectional antenna. Fixed C-MAN stations send data to the satellite using a 10-watt transmitter and a directional antenna. (Although imagery capability aboard a GOES may have failed, the GOES can still serve as a satellite communications platform). From Wallops Island, data are forwarded via landline to the NWSTG at Suitland.

At the NWSTG, buoy and C-MAN data are subjected to automated quality checks and are then routed to communications circuits such as AFOS, NWS Domestic Data Service, and the Global Telecommunications System (GTS). Data are also routed to the National Meteorological Center (NMC) for computer model ingestion. The time between the end of data acquisition and routing through the NWSTG is normally less than 20 minutes.

DATA FLOW

WEST GOES

EAST GOES

ARGOS

NESDIS CDA → STATION DATA → NWSTG → REAL-TIME REPORTS → COMMS NETWORK

- PLATFORM CONTROL
- BACKUP DATA

- DATA BASE MANAGEMENT
- STATION DATA
- PROCESSED DATA
- DRIFTING BUOY DATA

NDBC → NCDC

NODC

MONTHLY ARCHIVAL

- DATA PROCESSING
- QUALITY CONTROL
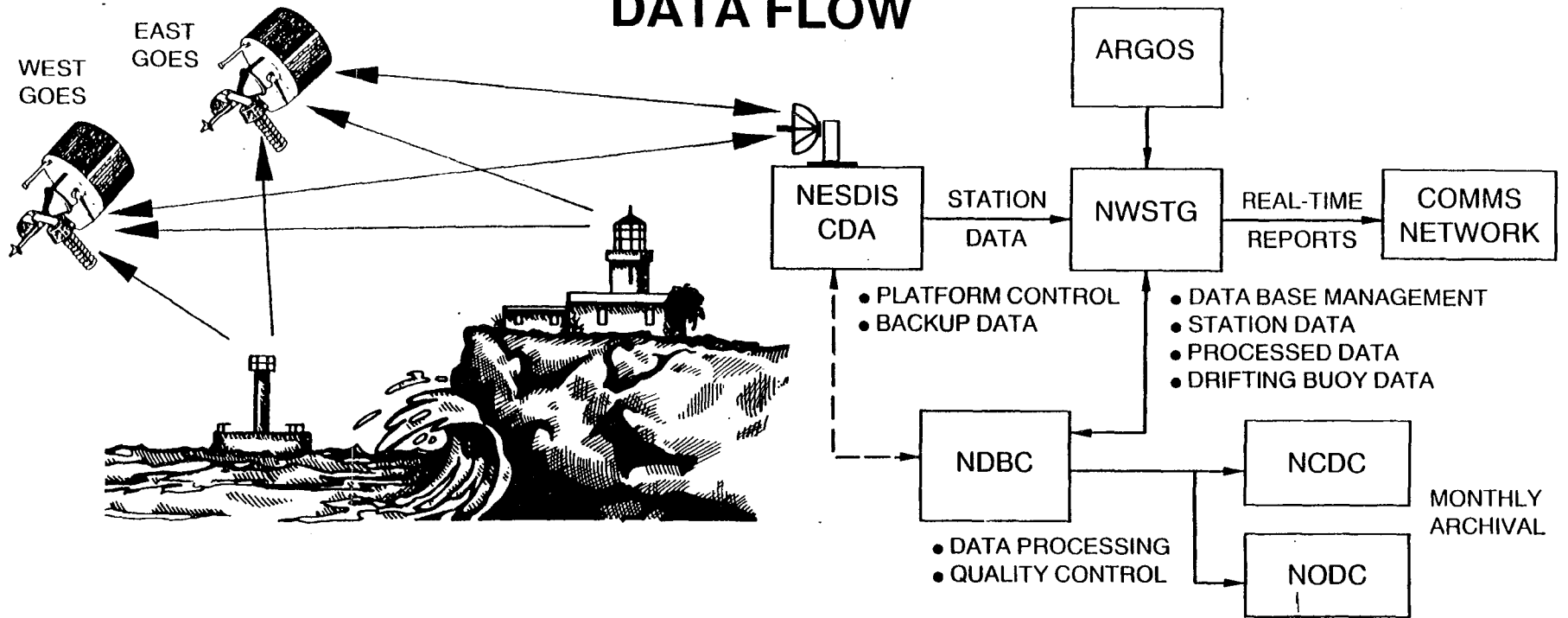
TYPICAL HOURLY DATA TIME SEQUENCE
OBSERVATION TIME

TIME (MIN)	-30	-20	-10	0	+10	+20	+30	+40

DATA ACQUISITION

DATA TRANSMISSION

NWSTG REPORT GENERATION

REPORT DISSEMINATION
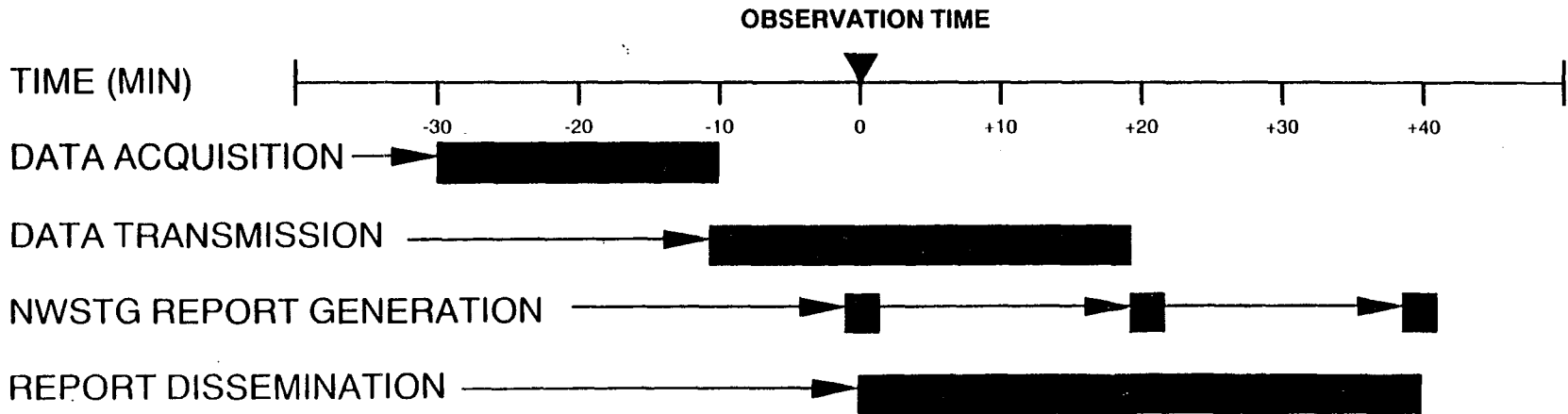
Fig. 1.1.6.1.1-1 Data Flow from NDBC Moored Buoys and C-MAN Stations

NESDIS allocates to NDBC specific minutes and channels over which data may be transmitted. The time each station samples data is usually tied to the minute in each hour the measurements are transmitted to the satellite. Because of a limited number of "ideal" time slots near the beginning of the hour, the stations in the network do not all acquire data at the -same time. The minute the observation was taken is included in all C-MAN messages in the "9" group at the end of Section 1 of the coded observation. This time slot limitation is the reason that reports from C-MAN stations in some areas do not reach the field until 40 minutes after the hour. The transmission time for stations on the Pacific and Gulf of Mexico coasts are between 25 and 39 minutes past the hour. Since the NWSTG generates the station collectives every 20 minutes starting at minute zero of each hour, the earliest that data from stations in those areas can be disseminated to the field is at 40 minutes past the hour. Improvements are planned to NESDIS ground equipment by 1993 which will allow for greater availability of "ideal" time slots.

1.1.6.2.2 Drifting buoy data transmission

Data from drifting buoys are transmitted to NOAA polar orbiting satellites (Fig. 1.1.6.2.2-1) and are immediately relayed to the ground. Thus, when a drifting buoy and the ground station are simultaneously within line-of-sight of the satellite, the station can receive transmissions in real time. More importantly, the data received from the buoys when the ground receiving station is outside the satellite footprint are also stored by the satellite until within range of a ground station capable of receiving the rebroadcast of stored data.

Upon receipt, the data are sent to the Service Argos U.S. Global Processing Center in Landover, MD where messages are constructed in drifting buoy code (FM 18 DRIFTER) and distributed through NWSTG.

1.1.7   Data quality control

All NDBC data are subjected to two phases of quality control. Automated checks are applied to the data at NWSTG in real time, while checks incorporating a man-machine mix are performed at NDBC within 24 hours. Details of the NDBC quality control philosophy and methods are described by Gilhousen (1988).

POLAR-ORBITING
SATELLITE

GROUND STATIONS | RAW DATA → ARGOS USGPC | DRIBU DATA → NWSTG | REAL-TIME REPORTS → GTS AND OTHER COMMS NETWORKS

- DISPOSE FILE DATA
- PLATFORM CONTROL

- DATA BASE MANAGEMENT
- ANALYSIS FIELDS
- DRIBU DATA

NDBC PROCESSING/ QUALITY CONTROL

NCDC

NODC

MONTHLY ARCHIVAL
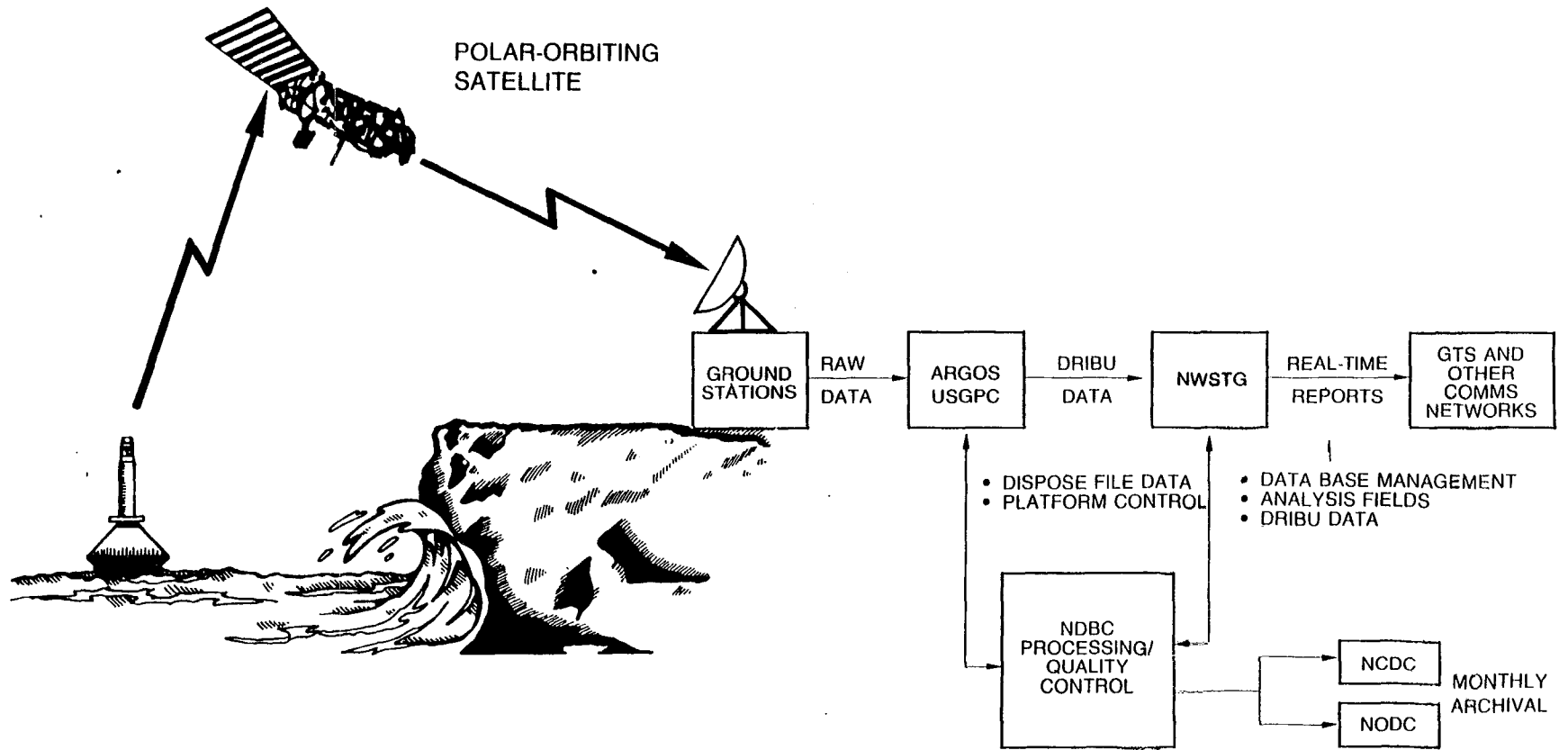
DBG 10/89

Fig. 1.1.6.2.2-1   Data Flow from Drifting Buoys

Automated checks will detect the majority of data problems and are most effective for situations when a sensor suddenly fails. Gross error checks and time continuity algorithms are used to delete or flag data that fall outside predetermined climatological limits, or that change from one hour to the next by an excessive amount. The automated checks are removed in special circumstances so that extreme but valid measurements will not be deleted from real time distribution. This situation could occur, for example, near a hurricane or during explosive marine cyclogenesis.

The man-machine data quality control methods are more effective in detecting more problems such as the calibration drift of a sensor. These checks are performed at NDBC within 24 hours using time series plots, surface weather maps, and other printed and graphic tools.

1.1.7.1 Moored buoy winds

Numerous discussions have centered around the quality of wind measurements from moored buoys. Forecasters have sometimes commented that wind speeds measured by moored buoys are too low. Casual comparison with ship reports might tend to confirm this observation. However, NDBC feels strongly that most of this perceived discrepancy can be explained by keeping in mind three important points. First, measured buoy winds are averaged over 8 to 10 minutes to remove errors that might be induced by hull motion. A subjective ship observation is taken by a human observer whose level of skill and busy shipboard duties might adversely affect the quality of the observation. Second, ship observations are usually taken with the ship underway which can introduce significant errors when the ship's movement is removed from the observed apparent wind. Third, the anemometer aboard the buoy is at 5 to 10 m above the water (depending on the hull type), while a ship's anemometer, if one is available, is usually much higher (most ships do not have an anemometer, resulting in estimated winds). The question of ship versus buoy winds is analyzed in great detail by Pierson, *et al.* (1990) and Gilhousen (1987).

In an effort to provide marine forecasters with a standard reference, NDBC extrapolates wind speeds taken at "non-standard" levels. The extrapolated winds appear in Section 5 (555 11XXX 22YYY) of the moored buoy and C-MAN real time messages. The extrapolation technique incorporates the air-sea temperature

difference to determine atmospheric stability and computes a theoretical wind speed for 10-m (11XXX) and 20-m (22YYY) heights. In the case of some C-MAN stations located more than 20 m above the water, the extrapolation technique computes downward to these same levels. In cases where either air or sea temperature are unavailable, neutral stability is ¬assumed. Details on the extrapolation technique can be obtained from the NDBC Data Systems Division.

1.1.7.2 Data availability

At NWS field offices, the typical method of acquiring real time data from NDBC stations is over AFOS. Data are also available to outside users from the NWS Family of Services. The various communications headers carrying meteorological data from moored buoys and C-MAN stations are shown in Fig. 1.1.7.2-1. Spectral wave data communications headers are shown in Fig. 1.1.7.2-2. Data from drifting buoys that are quality checked by NDBC are found under the AFOS header NMCBOYDB1 (WMO headers SSVX08 KWBC or SSVX02 KWBC).

Moored buoy meteorological data are disseminated in FM 13-IX SHIP code. Data from C-MAN fixed stations are sent in C-MAN code, a U.S. national code that is a slightly modified version of FM 12-IX SYNOP. Drifting buoy observations are encoded into FM 18 DRIFTER code.

Wave energy spectra are encoded and disseminated every 3 hours over AFOS under the Spectral Wave Code, a U.S. national code form. Non-AFOS communications systems disseminate wave data every hour under FM 65-IX WAVEOB, an international code.

SYNOP, SHIP, DRIFTER, and WAVEOB code formats are described in the WMO Manual on Codes, No. 306. The significant differences between the C-MAN code and the SYNOP code are explained in the C-MAN User's Guide. The format for the Spectral Wave Code can be obtained from the NDBC Data Systems Division.

1.1.7.3 Archived data

NDBC prepares monthly "clean" data sets on magnetic tape for moored buoys, C-MAN Stations, and drifting buoys within 21 days after the end of the month during which the measurements were

Bulletin Headers				Content
Hourly AFOS	Hourly WMO	3-Hourly (03Z,09Z, etc.) WMO	6-Hourly (00Z,06Z, etc.) WMO	Area/ Description
NMCBOYOC5	SNVD15 KWBC	SIVD15 KWBC	SMVD15 KWBC	Atlantic offshore and Gulf of Mexico buoys
NMCBOYOC7	SNVD17 KWBC	SIVD17 KWBC	SMVD17 KWBC	Pacific offshore buoys
(Not available)	SNVE15 KWBC	SIVE15 KWBC	SMVE15 KWBC	Hawaiian buoys
NMCBOYGL5	SNVD45 KWBC	SIVD45 KWBC	SMVD45 KWBC	Great Lakes buoys
NMCBOYCM5	SNVD20 KWBC	SIVD20 KWBC	SMVD20 KWBC	Atlantic Coastal buoys
NMCBOYCM7	SNVD22 KWBC	SIVD22 KWBC	SMVD22 KWBC	Pacific Coastal buoys
NMCBOYBS1	SNVS19 KWBC	SIVD19 KWBC	SMVD19 KWBC	Alaska buoys
NMCBOYOC9	SNVC15 KWBC	SIVC15 KWBC	SMVC15 KWBC	TOGA buoys
NMCBOYCM1	SXUS20 KWBC	SIUS20 KWBC	SMUS20 KWBC	Eastern C-MAN headland
NMCBOYCM2	SXUS21 KWBC	SIUS21 KWBC	SMUS21 KWBC	Southern C-MAN headland
NMCBOYCM3	SXUS22 KWBC	SIUS22 KWBC	SMUS22 KWBC	Great Lakes C-MAN headland
NMCBOYCM4	SXUS23 KWBC	SIUS23 KWBC	SMUS23 KWBC	Pacific C-MAN headland
(Not available)	SXPN20 KWBC	SXPN20 KWBC	SXPN20 KWBC	Western Pacific headland

Fig. 1.1.7.2-1   Communication Headers from NDBC Moored Buoys and C-MAN Stations

Bulletin Headers			Content	
Hourly	3-Hourly			
WMO	WMO	AFOS	Area/Description	
SXVX40 KWBC	SXVX60 KWBC	NMCBSOP0	Southeast	Nondirectional
SXVX41 KWBC	SXVX61 KWBC	NMCBSOP1	Gulf of Mexico	Nondirectional
SXVX42 KWBC	SXVX62 KWBC	NMCBSOP2	Northeast	Nondirectional
SXVX43 KWBC	SXVX63 KWBC	NMCBSOP3	Great Lakes	Nondirectional
SXVX44 KWBC	SXVX64 KWBC	NMCBSOP6	Mid-Atlantic	Nondirectional
SXVX45 KWBC	SXVX65 KWBC	NMCBSOP8	Atlantic/Gulf of Mexico	Directional
SXVX46 KWBC	SXVX66 KWBC	NMCBSOP4	Pacific	Nondirectional
SXVX47 KWBC	SXVX67 KWBC	NMCBSOP5	Pacific	Nondirectional (overflow)
SXVX48 KWBC	SXVX68 KWBC	NMCBSOP4A	Pacific	Nondirectional (overflow)
SXVX49 KWBC	SXVX69 KWBC	NMCBSOP7	Pacific	Directional

Fig. 1.1.7.2-2   Communication Headers from NDBC Moored Buoy Spectral Wave Data

taken. These data sets are examined extensively by NDBC to ensure the most accurate and highest quality data. The tapes are sent for archival at the National Climatic Data Center (NCDC) and the National Oceanographic Data Center (NODC). The archive centers transfer the data to established formats available for users.

The *NDBC Data Availability Summary* lists data that are available from NDBC stations since the early 1970's. It is updated every August. Additionally, NDBC periodically publishes the *Climatic Summaries for NDBC Buoys and Stations* which contain climatologies for all NDBC moored buoy stations that have a data record of 3 years or more.

1.1.8   Station repair and maintenance

1.1.8.1   Responsibility for station maintenance and repair

The NDBC Operations Division is responsible for installation, repair, and routine maintenance of moored buoys and C-MAN stations. Teams of technicians employed by the Data Buoy Support Contractor are assigned to visit stations. Generally, drifting buoys are not recovered or repaired.

Field offices are encouraged to report data from NDBC systems that appear to be bad. Station problems noted by field offices should be reported to NDBC Data Systems Division [FTS 494-2836 or (601) 688-2836].

1.1.8.2   Transportation

The U.S. Coast Guard (USCG) is a critical component of NDBC. In addition to the 15 personnel assigned to NDBC, including the Center's Deputy Director, nearly all transportation and operational support for deployment and servicing operations are provided by the USCG. General oversight of on-scene operations is provided by USCG Warrant Officers.

Service and deployment of buoys and C-MAN stations varies with the individual station. Moored buoys require buoy tenders or other large ships. C-MAN stations can be reached by ground transportation, ship, or helicopter.

1.1.8.3   NDBC repair philosophy

In addition to transportation scheduling, the timeliness of NDBC station repairs depends on many factors. These include seasonal priorities, predicted weather and sea conditions, station density in the area, time until the next scheduled station maintenance or buoy exchange, whether there has been a total system failure or only a sensor failure, and which sensor has failed. For example, NDBC typically plans to service all moored buoys in the central Gulf of Mexico in mid to late spring in order to have all systems operating for the hurricane season. For any buoy failure, NDBC initially considers whether a buoy swapout (hull exchange) is scheduled within the near term. If so, then repairs would likely be postponed since data would be restored at that time. Also, a buoy with failed air temperature sensors would not be specially scheduled for repair; however, a buoy whose anemometers or barometers had failed probably would be specifically scheduled for service.

1.2   SHIP OBSERVATIONS

1.2.1   Beaufort Scale

To the mariner, wind speeds over the ocean are usually grouped in accordance w.. ...: Beaufort Scale devised in 1806 by Admiral Sir Francis Beaufort. A.. adopted in 1838, Beaufort numbers range from 0 (calm) to 12 (hurricane) (Fig.1.2.1-1) and describe the sea surface as it appears under the influence of different wind speeds. This scale is useful in predicting sea conditions from forecasted winds and, conversely, by observing the state of the sea to obtain an estimate of the speed of the wind.

The majority of ships that observe weather on the high seas do not have wind-measuring equipment. Thus, the observer must estimate the wind speed. In practice, the crew member observes the sea surface, noting the size of the waves and finds the Beaufort Force that describes the sea surface and thus determines the corresponding wind speed. An advantage of this simple system, besides the lack of instruments, is that the motion of the ship and associated wind across the deck does not have to be considered in determining the estimated wind speed across the sea surface.

The Beaufort Wind Scale implies a steady state wind and a fully arisen sea. The wind of a given Beaufort value will produce a characteristic appearance of a sea surface provided that the wind has been blowing for a sufficient length of time and over a sufficiently long fetch. From Figure 1.2.1-2, one can note that waves would reach 90% of a maximum height of 8 ft at the end of a 60 mile fetch after the wind blows for 12 hours at Beaufort Force 5.

1.2.2   Voluntary Observing Ship Program (VOS)

The Voluntary Observing Ship Program is discussed in detail in Chapter 12.1 of this manual and WSOM B-30. At this stage, forecasters should become familiar with the ship observation code as discussed in the referenced NWS Observing Handbook No. 1 - *Marine Surface Weather Observations.*

BEAUFORT WIND SCALE
WITH CORRESPONDING SEA STATE CODES

Beau-fort number or force	Wind speed				World Meteoro-logical Organi-zation (1964)	Estimating wind speed			Sea State	
	knots	mph	meters per second	km per hour		Effects observed far from land	Effects observed near coast	Effects observed on land	Term and height of waves, in meters	Code
0	under 1	under 1	0.0-0.2	under 1	Calm	Sea like mirror.	Calm.	Calm; smoke rises vertically.	Calm, glassy, 0	0
1	1-3	1-3	0.3-1.5	1-5	Light air	Ripples with appearance of scales; no foam crests.	Fishing smack just has steerage way.	Smoke drift indicates wind direction; vanes do not move.		
2	4-6	4-7	1.6-3.3	6-11	Light breeze	Small wavelets; crests of glassy appearance, not breaking.	Wind fills the sails of smacks which then travel at about 1-2 miles per hour.	Wind felt on face; leaves rustle; vanes begin to move.	Calm, rip-pled, 0-0.1	1
3	7-10	8-12	3.4-5.4	12-19	Gentle breeze	Large wavelets; crests begin to break; scattered whitecaps.	Smacks begin to careen and travel about 3-4 miles per hour.	Leaves, small twigs in constant motion; light flags extended.	Smooth, wave-lets, 0.1-0.5	2
4	11-16	13-18	5.5-7.9	20-28	Moderate breeze	Small waves, becoming longer; numerous whitecaps.	Good working breeze, smacks carry all canvas with good list.	Dust, leaves, and loose paper raised up; small branches move.	Slight, 0.5-1.25	3
5	17-21	19-24	8.0-10.7	29-38	Fresh breeze	Moderate waves, taking longer form; many whitecaps; some spray.	Smacks shorten sail.	Small trees in leaf begin to sway.	Moderate, 1.25-2.5	4
6	22-27	25-31	10.8-13.8	39-49	Strong breeze	Larger waves forming; whitecaps everywhere; more spray.	Smacks have doubled reef in mainsail; care required when fishing.	Larger branches of trees in motion; whistling heard in wires.	Rough, 2.5-4	5
7	28-33	32-38	13.9-17.1	50-61	Near gale	Sea heaps up; white foam from breaking waves begins to be blown in streaks.	Smacks remain in harbor and those at sea lie-to.	Whole trees in motion; resistance felt in walking against wind.		
8	34-40	39-46	17.2-20.7	62-74	Gale	Moderately high waves of greater length; edges of crests begin to break into spindrift; foam is blown in well-marked streaks.	All smacks make for harbor, if near.	Twigs and small branches broken off trees; progress generally impeded.	Very rough, 4-6	6
9	41-47	47-54	20.8-24.4	75-88	Strong gale	High waves; sea begins to roll; dense streaks of foam; spray may reduce visibility.		Slight structural damage occurs; slate blown from roofs.		
10	48-55	55-63	24.5-28.4	89-102	Storm	Very high waves with overhanging crests; sea takes white appearance as foam is blown in very dense streaks; rolling is heavy and visibility reduced.		Seldom experienced on land; trees broken or uprooted; considerable structural damage occurs.	High, 6-9	7
11	56-63	64-72	28.5-32.6	103-117	Violent storm	Exceptionally high waves; sea covered with white foam patches; visibility still more reduced.			Very high, 9-14	8
12	64 and over	73 and over	32.7 and over	118 and over	Hurricane	Air filled with foam; sea completely white with driving spray; visibility greatly reduced.		Very rarely experienced on land; usually accompanied by widespread damage.	Phenomenal, over 14	9

Note: Since January 1, 1955, weather map symbols have been based upon wind speed in knots, at five-knot intervals, rather than upon Beaufort number.

Fig. 1.2.1-1 Beaufort Wind Scale with Corresponding Sea State Codes (from *American Practical Navigator*)

Beaufort force of wind.	Theoretical maximum wave height (ft) unlimited duration and fetch.	Duration of winds, (hours), with unlimited fetch, to produce percent of maximum wave height indicated.			Fetch (nautical miles), with unlimited duration of blow, to produce percent of maximum wave height indicated.		
		50%	75%	—90%	50%	75%	90%
3	2	1.5	5	8	3	13	25
5	8	3.5	8	12	10	30	60
7	20	5.5	12	21	22	75	150
9	40	7	16	25	55	150	280
11	70	9	19	32	85	200	450

Fig. 1.2.1-2. Beaufort Wind Scale related to Fetch and Duration of Winds (from *American Practical Navigator*).

As a general discussion of the ship observation program:

- Ship observations are often the only observation available in the marine data-sparse environment. This is especially true beyond the coastal regions. Such high seas observations are likely to be early indicators of explosive marine cyclogenesis or large swell moving towards coastal areas.

- Ship observations are taken by "ships of opportunity." The observation is normally made during transit and is therefore seldom made at the same place. Many oceanic areas that are not on normal shipping lanes are therefore even more sparsely observed than frequently traveled tracks.

- Wind and sea observations are normally subjective estimates and are not normally based on instruments. During times of reduced visibility such as fog and darkness, such observations are often based on persistence.

- Ship observations are a primary source of data input into marine climatic atlases.

- Ship observations are sent to shore-based receivers in four major ways:

    1. CW (Morse Code) - CW requires a radio operator to contact a radio station ashore such as the Coast Guard or a commercial marine station. Such transmissions are normally limited to the duty hours of the ship's radio operator. This method of sending marine observations is decreasing in popularity to more efficient methods.

    2. INMARSAT - A commercial marine satellite communications system through which marine observations are sent directly to NMC. This is presently the most popular means to send marine observations.

    3. SITOR - radioteletype transmission

    4. SEAS - The Shipboard Environmental Data Acquisition System is a NOAA-sponsored program to facilitate the transmission of ship observations into NMC. Through an onboard PC, menu-driven software prompts the crew for all data needed for the observation. The observation is transmitted automatically to a satellite and on to a NOAA receiving station. In late 1991, about 110 ships reporting about 15% of the available marine meteorological data transmitted their observations through SEAS. The program continues to expand as more ships are equipped with SEAS.

1.2.3   MAriner REPort - MAREP

The MAREP program supplements the coastal, buoy, and high seas marine observation program with plain language observations sent by radio to a land station which, in turn, are relayed to NWS.

The MAREPs are taken by all types of mariners from weekend sailors to commercial fishermen to tug operators. Land stations include contract radio operators, commercial marine radio stations, HAM radio operators, Sea Grant agents, marina operators, and commercial marine transportation companies.

MAREP networks across the country are as diverse as the ocean. MAREPs are normally distributed over AFOS header PLS - Plain Language Ship.

1.3   EXERCISES

1. Print a ship observation from AFOS. Discuss the code. What are the advantages/disadvantages of observations from the VOS program.

2. Print a buoy and C-MAN observation from AFOS. Discuss the code. What are the advantages/disadvantages of the observation. Over what period of time are the wind and wave observations averaged? How is this significant? What is the elevation of the wind observations? What is the elevation of the extrapolated wind observation?

3. Where is the nearest MAREP observer to your station? What are the advantages/disadvantages of the MAREP program?

4. What applications do estimates from the Beaufort Scale have in the NWS marine program?

1.4. REFERENCES

Bowditch, N., 1984: *American Practical Navigator.* Defense Mapping Agency Hydrographic/Topographic Center, Washington, D.C.

Earl, M. D., 1990: *NDBC Real-Time Directional Wave Information User's Guide.* National Data Buoy Center, Stennis Space Center, Mississippi, 24 p.

Gilhousen, D. B., 1987: A field evaluation of NDBC moored buoy winds. *J. of Atmospheric and Oceanic Technology,* **4,** 94-104.

_____, 1988: *Quality control of meteorological data from automated marine stations.* Proceedings, Fourth International Conference on Interactive Information and Processing Systems for Meteorology, Oceanography and Hydrology, Anaheim, CA, 248-252.

Hamilton, G. D., 1986: National Data Buoy Center programs. *Bull. Amer. Meteor. Soc.,* **67 (4),** 411-415.

National Data Buoy Center, 1990: *Climatic Summaries for NDBC Buoys and StationsæUpdate 1.* Stennis Space Center, MS, 454 p.

_____, 1990: *Coastal-Marine Automated Network (C-MAN) User's Guide.* Stennis Space Center, MS, 45p.

_____, 1990: *NDBC Data Availability Summary.* Stennis Space Center, MS, 88 pp.

_____: *NDBC Data Platform Status Report* (weekly). Stennis Space Center, MS.

Pierson, W. J., 1990: Examples of, reasons for, and consequences of the poor quality of wind data from ships for the marine boundary layer: Implications for remote sensing. *J. Geophys. Res.,* **95,** 13313-13340.

U.S. Dept of Commerce, 1991: *Marine Surface Weather Observations.* National Weather Service Observing Handbook No. 1, July.

Wilkerson, J. C. and M. D. Earle, 1990: A study of differences between environmental reports by ships in the voluntary observing ship program and measurements from NOAA buoys. *J. Geophys. Res.*, **95,** 3373-3385.

World Meteorological Organization, 1988: *Manual on Codes.* WMO No. 306, Vol. I & II.

EXTREMES MEASURED BY NDBC SYSTEMS

PARAMETER	VALUE	STATION	PLATFORM	DATE
SIGNIFICANT WAVE HEIGHT	16.9 M	46003	6N	01-19-91
WIND SPEED	122.6 kn	FWYF1	C-MAN	8-24-92
WIND GUST	146.7 kn	FWYF1	C-MAN	8-24-92
BAROMETRIC PRESSURE (MAX)	1054.9 hPa	46001	6N	02-04-89
BAROMETRIC PRESSURE (MIN)	940.3 hPa	FBIS1	LAND	09-22-89
AIR TEMPERATURE (MAX)	38.7°C	SJLF1	C-MAN	07-19-86
AIR TEMPERATURE (MIN)	-31.1°C	46016	LAND	02-19-87
WATER TEMPERATURE (MAX)	34.3°C	42002	10D	08-19-85
WATER TEMPERATURE (MIN)	-1.9°C	TPLM2	C-MAN	12-27-89

EAM 9/92

PROBLEMS WITH NDBC?

DATA QUALITY
    FRED ABELL
    ED SMITH   }   601-688-3134
    PHIL NEWKIRK

DEPLOYMENT STATUS / MISSING DATA
    MIKE BURDETTE
    DAVE GILHOUSEN   }   601-688-2836
    ERIC MEINDL

NEVER SEND A MAN TO DO A BUOY'S WORK!

92-134

DIAGNOSING CYCLOGENESIS USING NONTRADITIONAL METHODS

Eric R. Thaler
National Weather Service Forecast Office
Denver, Colorado 80239

1. Introduction

The plains of eastern Colorado are one of the most active cyclogenesis regions on the North American continent (Whittaker and Horn 1981). Consequently, many times each year meteorologists in Denver and surrounding areas are faced with predicting when and where cyclogenesis will occur. Due to the extreme topographical variations in Colorado, the location of cyclogenesis (and its resulting cyclone) is extremely critical. A deviation in cyclone position of as little as 100-200 km can mean the difference between a high wind event and an all out blizzard along the Front Range of the Rockies and over the adjacent plains regions. Needless to say, forecasting eastern Colorado cyclogenesis is one of the most important problems forecasters in the central Rockies and nearby locations face.

Until recently, meteorologists in Denver have had to treat cyclogenesis events using a small set of data available mainly on the Automation of Field Operations and Services (AFOS) system. This data set made it straightforward to apply the Petterssen-Sutcliffe development theory (Petterssen 1956), which, in its simplest form, is based on vorticity advection at the level of nondivergence and the Laplacian of thickness advection in the layer from the surface (1000 mb) to the level of nondivergence. Unfortunately, applying this theory with the available data sets has proven to be less than adequate in many situations.

Within the last several years, different approaches to the cyclogenesis problem have come into vogue. These include Q-vectors (Hoskins and Pedder 1980), isentropic potential vorticity (IPV) (Hoskins et al. 1985), and most recently tropopause undulations (Hirschberg and Fritsch 1991a,b).

Applying these techniques using only data available on AFOS is not possible. With the arrival of the Denver Advanced Weather Information and Processing System (AWIPS) Risk Reduction and Requirements Evaluation (DARE) workstation in the late 1980's, Denver forecasters have had the opportunity to apply these new ideas in real time in an operational setting. This has been made possible through the availability of gridpoint numerical model output and application programs that readily and efficiently manipulate these data. Furthermore, the workstation provides the ability to easily integrate these new data sets with information from Doppler radar, satellites, wind profilers, and mesoscale (in both a temporal and spatial sense) objective surface and upper air analyses and numerical forecasts.

Rather than providing a detailed case study, this paper is structured to simulate an operational forecast shift. First, some of the data available on AFOS will be presented, allowing the reader to apply "current" thinking to the forecast problem. Next, the reader will be presented with some new data sets and shown how these can be used to apply some "future" thinking about the same problem. The problem is to determine if and when cyclogenesis will occur somewhere over the central Rocky Mountain region and if it does, where the cyclone will be located.

Due to space limitations, only a minuscule number of products can be shown. However, it is hoped that this will allow the reader to see some of the opportunities that forecasters in the modernized National Weather Service will have to better apply their science to operational forecasting.

2. Forecasting the Event Using Traditional Data

At 0000 UTC 7 January 1992, a 500 mb low was located over west central Utah with its associated cold pool south and southwest of the low center (not shown). Twelve-hour geopotential height falls of 100 gpm were observed in western Colorado ahead of the low. The jetstream at 300 mb (not shown) flowed from southern California eastward across southern Arizona and then east into Texas with evidence of a jetstreak over southern Arizona. The surface chart at 0000 UTC (not shown) indicated a broad trough in

the mean sea level isobars extending from a low in northeast Wyoming to another low over south central New Mexico. Moderate south to southeast flow existed over western Kansas which was advecting moisture northwestward from the Gulf of Mexico. The isallobaric field was rather disorganized with no extraordinary maxima or minima being noted.

Figure 1 shows the 0-, 6-, 12-, and 18-hour NGM forecasts of 500 mb heights and vorticity initialized at 0000 UTC 7 January 1992. The initial 500 mb panel corresponded reasonably well with the actual rawinsonde observations and satellite data (not shown). As seen in Fig. 1 the NGM forecasts the low to move basically due east during this 18-hour period, deepens it 30 gpm, and increases its intensity considerably as it arrives in east central Colorado at 1800 UTC. The positive vorticity advection (PVA) ahead of the system over eastern Colorado is virtually nonexistent at 0000 and 0600 UTC with moderate PVA at 1200 and 1800 UTC. Much stronger PVA is forecast over southwest Kansas at 1200 UTC which moves into Nebraska by 1800 UTC.

The mean sea level pressure and 1000-500 mb thickness forecasts corresponding to the times in Fig. 1 are shown in Fig. 2. As was the case at 500 mb, the initial surface panel corresponded reasonably well with the actual data observed at 0000 UTC. By 0600 UTC the low over New Mexico is forecast to fill with the Wyoming low moving to east of Cheyenne while deepening about 7 mb. Judging from the thickness pattern, the cold air associated with this system is supposed to be crossing the Continental Divide at this time. By 1200 UTC the NGM forecasts the Wyoming low center to move just a bit to the northeast while the pressure gradient increases and the cold air continues pushing eastward into Kansas. At 1800 UTC the model moves the low center about 250 km to the southeast and continues to intensify it.

This rather bizarre movement of the sea level pressure low center should make the forecaster a bit uneasy. Why would the low move to the southeast and deepen considerably during one 6-hour period, then move northeastward and not deepen during the next six hours, and then move rapidly southeast and deepen slightly again? This is especially disturbing in light of the fact that between 0600 and 1200 UTC some of the best PVA is over eastern Colorado which should favor development there rather than in southeast Wyoming.

This type of problem is not uncommon in Colorado (and for that matter in most high elevations) and is probably due (at least in part) to the difficulties in reducing pressures to mean sea level. Note from the 1000-500 mb thickness charts in Fig. 2 that throughout the 18-hour period the cold air associated with the Great Basin upper low penetrates across nearly all of Colorado except the northeast, where a ridge in the thickness pattern exists and extends into southeast Wyoming. Furthermore, note that in each panel the mean sea level pressure low center resides in this "warm" air. (This warm anomaly over southeast Wyoming and northeast Colorado is even more pronounced in the 850 mb isotherms). Recalling that reducing pressure to sea level involves multiplying the station pressure by an exponential factor whose argument contains the temperature in the denominator (Wallace and Hobbs 1977), in warm air the reduced pressure is often times too low. Consequently, it is likely that this sea level low is not representative of the surface cyclone, but rather is a result of the fictitious pressure reduction to sea level. (The poor resolution of the terrain in the model is also a possible factor in this pressure reduction problem.)

By 0900 UTC developments are still not terribly clear. The mean sea level pressure analysis (not shown) places a low just to the south of Denver. The temperature at Denver is still relatively warm so that we are still faced with the pressure reduction problem discussed earlier and the low center in the sea level pressure pattern may indeed not represent the center of the cyclonic circulation at the surface. The isallobaric analysis (not shown) indicates a large area of pressure falls extending from southeast Wyoming and western Nebraska into Texas and Oklahoma with weak minima in northwest Kansas and in east central Colorado. Unfortunately the last three (0300, 0600, 0900 UTC) isallobaric analyses have been discouraging as they have failed to reveal any clear trend in the position of the isallobaric minima.

Satellite data show that the upper low is moving about as forecast, having reached southeast Utah by 0900 UTC. However, abundant cold topped cloudiness exists over eastern Colorado where little PVA was indicated on the 6-hour NGM forecast. Light freezing drizzle was occurring in parts of northeast Colorado under this cloud mass.

The zone forecasts are due at 1100 UTC. What is the forecast going to be? If we follow the NGM guidance without modification, we forecast strong winds over most of northeast Colorado along with

some snow showers as a result of the PVA. The most likely areas for the precipitation would be near the Kansas and Nebraska borders closer to the surface low.

The pressure falls seem to suggest that the low may develop south of the NGM forecast position in which case we may need to forecast more precipitation than just snow showers due to the resulting upslope flow into the Front Range. That the NGM has a known northerly bias in developing surface lows also lends credence to this latter solution. But how far south do we want to adjust the model's solution? The final position we decide upon for the cyclone will then determine what mesoscale affects we will need to consider in the forecast. All in all, with the data we have at our disposal, we are faced with a very difficult forecast situation.

3. Forecasting the Event Using Nontraditional Data

Prior to demonstrating how nontraditional data sets can be used to aid in forecasting this event it will be beneficial to review some concepts that seem to have "vanished" from operational forecasting.

First, cyclogenesis is defined in the Glossary of Meteorology (Huschke 1980) as "Any development or strengthening of cyclonic circulation in the atmosphere..." It goes on to say that "While cyclogenesis usually occurs together with deepening (a decrease in atmospheric pressure), the two terms should not be used synonymously". More often than not forecasters are interested in where the "L" is going to show up on the sea level pressure analysis, rather than in the circulation around that "L". Consequently, more emphasis is placed on the actual value of the central pressure of the low (the minimum in the pressure field) and its changes rather than on the low's intensity, defined as the Laplacian of the pressure field (Bluestein 1992), and its trends. An intense low need not have an extremely low value for its central pressure.

Interestingly, the intensity of a low is, under geostrophic conditions, directly proportional to the vorticity of the (geostrophic) wind, which in turn is a measure of the cyclonic circulation around the low. Hence, it is much more useful to monitor trends in the vorticity (Laplacian of the pressure field, intensity of the low) rather than the actual values of pressure. Note that these ideas can be applied equally to either mean sea level pressure, geopotential heights or Montgomery streamfunction. (The AFOS product NMCGPH9AV depicts geostrophic vorticity at the surface).

The other "new" item of interest deals with tropopause undulations and their relationship to cyclogenesis (Hirschberg and Fritsch 1991a,b). Their conceptual model shows that pressure and geopotential height changes (and consequently changes in geostrophic relative vorticity) are a result of temperature changes in the lower stratosphere which result from undulations in the tropopause.

With this bit of background information, we are now ready to start taking a look at some of the data sets available on the DARE workstation to try to diagnose where cyclogenesis is going to occur.

We begin by examining several fields generated by the Local Analysis and Prediction System (LAPS) (McGinley 1989; McGinley et al. 1991). Although these analyses are available hourly, here we only show those from 0600 and 0900 UTC 7 January 1992 in Fig. 3. Shown are the potential temperature (Θ), equivalent potential temperature (Θ_e), and winds (every 20 km), all valid at the surface.

Several items are worth noting in these analyses. First, note the strong gradient in both the Θ and Θ_e fields between Limon (LIC) and Akron (AKO) in east central Colorado. This tight Θ gradient indicates the existence of a baroclinic zone. The tight Θ_e gradient shows a rapid change in static stability with a relative minimum in the region of the Θ_e maximum. Although the gradients weaken somewhat during the 3-hour period, they remain relatively intact and in roughly the same location. These regions should catch the forecaster's eye as being potential locations for development. (Note that the strong gradients to the northwest of Denver (DEN) are not real but are due to terrain problems in the vicinity of the maximum analyzed just to the west.)

In the wind analysis at 0600 UTC notice the strong convergence and cyclonic relative vorticity north of LIC and west of AKO. From this chart alone the forecaster should be on the lookout for rather substantial increases in the relative vorticity in this general area in the immediate future. (An increase of relative vorticity of course means an increase in cyclonic circulation). The 0900 UTC chart confirms these ideas as the cyclonic circulation has indeed increased with its center shifting slightly to the southeast. With the increased circulation (vorticity)

the convergence has intensified as well. This convergence/vorticity synergism is likely to continue for the next couple of hours, especially considering the developments aloft.

To determine the situation aloft, we turn to the gridpoint data from the NGM. Figure 4 shows the initial analysis and 6-, 12-, and 18-hour forecasts of 250 mb temperature and temperature advection. Note from these charts that the warm anomaly (tropopause undulation) over central Arizona at 0000 UTC is forecast to move to the east northeast during the first 6 hours of the forecast then make a sharp turn to the northeast and eventually arrive over east central Colorado by 1800 UTC. Increasingly strong warm air advection at 250 mb associated with this anomaly is forecast to be over the surface baroclinic zone, the Θ_e maximum and the relative vorticity maximum discussed in the previous paragraph from 0000 UTC through roughly 1200 UTC. Thereafter, the warm air advection decreases as the center of the warm anomaly reaches east central Colorado. Applying the Hirschberg and Fritsch (1991a,b) conceptual model to these charts, we would expect cyclogenesis to occur on the baroclinic zone between LIC and AKO, with the most rapid development sometime around 1200 UTC, the time when the 250 mb warm advection is the strongest. The development should end sometime around 1800 UTC when the warm anomaly arrives over east central Colorado.

To get a more concise picture of what we expect Fig. 5 shows time/height cross sections generated from the NGM gridpoint data. Figure 5a depicts the actual forecast temperature advection while Fig. 5b and 5c show the difference in height and temperatures from the initial time. Note that geopotential heights are falling throughout the troposphere through about 1800 UTC, after which time they begin to rise. Temperatures throughout the troposphere are cooling during the period of the cross section while they are warming significantly in the lower stratosphere as the tropopause undulation moves over the area. The temperature advection is maximized near 250 mb at 1200 UTC. It is clear from this figure that the warmest stratospheric air will be over the "suspect" area of east central Colorado between 1800 UTC and 0000 UTC, during which time development should cease.

Once again the zone forecasts are due at 1100 UTC. With the information we now have available, we should feel fairly confident that the 12-hour NGM surface forecast is bogus, and instead we should

forecast the cyclone to be well south of the model position. The location of the cyclone at 1200 UTC will likely be along the tight Θ or Θ_e gradient in the vicinity of the surface relative vorticity maximum in east central Colorado. Furthermore, we should expect the trends we are seeing in the surface vorticity and divergence fields to continue for the next 3-6 hours, probably resulting in a more intense cyclone than the NGM predicts even at 1800 UTC. The rapid development that the model forecasts is good and development should cease shortly after 1800 UTC. There is really nothing to make the forecaster believe that the surface cyclone will be in southeast Wyoming at 1200 UTC.

4. What Actually Happened

The trends we expected in the surface vorticity and divergence fields did occur as shown in the LAPS wind analysis at 1200 UTC (Fig. 6a). Note the strong convergence north of LIC as well as the continued increase in cyclonic circulation over east central Colorado. The surface cyclone continued to intensify through about 1800 UTC after which it maintained its strength while very slowly moving to the east.

Strong cyclogenesis also occurred aloft over east central Colorado. Figures 6b, 6c, 6d show the 700 mb geopotential height analyses at 1200, 1500, and 1800 UTC 7 January 1992 generated by the Meso-scale Analysis and Prediction System (MAPS) (Benjamin et al. 1991). This is where we expected it to occur based on the passage of the tropopause undulation (the warm pool at 250 mb). Cyclogenesis ceased after 1800 UTC and the cyclone weakened after 0000 UTC 8 January 1992 as the warm pool moved out ahead of it to the northeast.

5. Concluding Remarks

Forecasting cyclogenesis in eastern Colorado is one of the most formidable problems facing forecasters in Denver and adjacent areas. Applying the Petterssen-Sutcliffe development theory using only the limited data sets available on AFOS has been less than satisfactory. However, the arrival of gridpoint data from local mesoscale and NMC numerical models, high temporal and spatial resolution objective analyses, and the availability of an advanced workstation to easily and efficiently manipulate these data is beginning to change the way this problem is approached.

This paper has shown how a "new" (the ideas have been around for a long time but not used much in operational forecasting!) conceptual model of cyclogenesis was applied using these advanced data sets to better evaluate the NMC model data and make some significant deviations from the model guidance in preparing the forecast.

This is the first case where this conceptual model has been applied. It is based on sound theory and worked very well here. It will continue to be utilized during the 1992-93 cool season to determine if it is an effective tool in more cases of eastern Colorado cyclogenesis.

6. References

Benjamin, S.G., K.A. Brewster, R. Brümmer, B.F. Jewett, T.W. Schlatter, T.L. Smith, P.A. Stamus, 1991: An isentropic three-hourly data assimilation system using ACARS aircraft observations. *Mon. Wea. Rev.*, 119, 888-906.

Bluestein, H.B., 1992: *Synoptic-Dynamic Meteorology in Midlatitudes, Vol 1.* Oxford University Press, 431 pp.

Hirschberg, P.A. and J.M. Fritsch, 1991a: Tropopause undulations and the development of extratropical cyclones. Part I: Overview and observations from a cyclone event. *Mon. Wea. Rev.*, 119, 496-517.

Hirschberg, P.A. and J.M. Fritsch, 1991b: Tropopause undulations and the development of extratropical cyclones. Part II: Diagnostic analysis and conceptual model. *Mon. Wea. Rev.*, 119, 518-550.

Hoskins, B.J. and M.A. Pedder, 1980: The diagnosis of middle latitude synoptic development. *Quart. J. Roy. Meteor. Soc.*, 106, 707-719.

Hoskins, B.J., M.E. McIntyre, and A.W. Robertson, 1985: On the use and significance of isentropic potential vorticity maps. *Quart. J. Roy. Meteor. Soc.*, 111, 877-946.

Huschke, R.E., 1980: *Glossary of Meteorology.* Amer. Meteor. Soc. 638 pp.

McGinley, J.A., 1989: The local analysis and prediction system. Preprints: *12th Conf. Weather Analysis and Forecasting.* Monterey, Amer. Meteor. Soc. 15-19.

McGinley, J.A., S.C. Albers, P.A. Stamus, 1991: Validation of a composite convective index as defined by a real-time local analysis system. *Wea. Forecasting,* 6, 337-356.

Petterssen, S., 1956: *Weather Analysis and Forecasting, Vol 1.* McGraw-Hill, 428 pp.

Wallace, J.M. and P.V. Hobbs, 1977: *Atmospheric Science: An Introductory Survey.* Academic Press, 467 pp.

Whittaker, L.M. and L.H.Horn, 1981: Geographical and seasonal distribution of North American cyclogenesis, 1958-1977. *Mon. Wea. Rev.*, 109, 2312-2322.
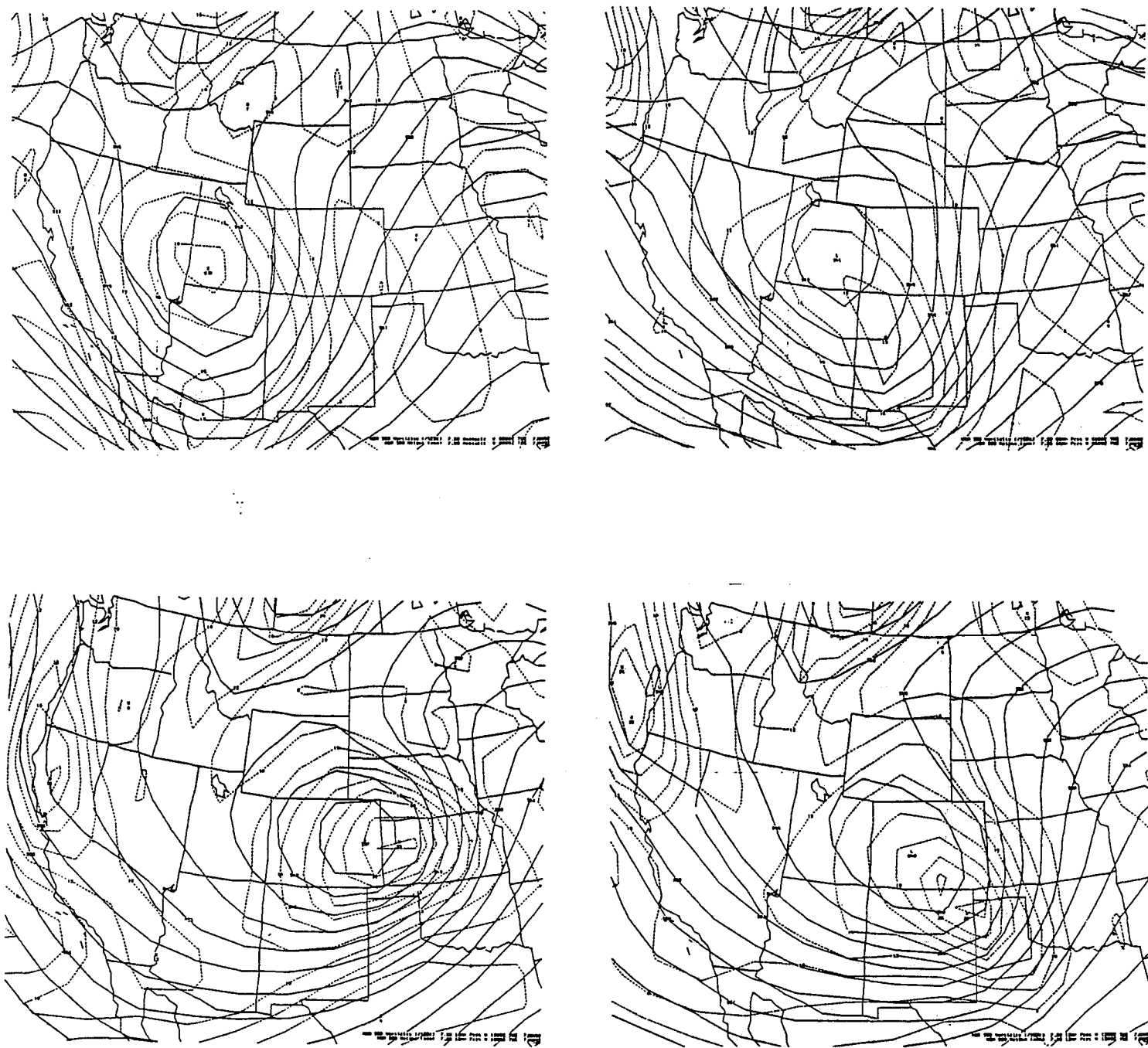
Figure 1.   500 mb heights (gpm, solid) and vorticity ($\times 10^5$ sec^{-1}, dashed) from the NGM initialized at 0000 UTC 7 January 1992. Clockwise from top left, 0-, 6-, 12-, and 18-hour forecasts.
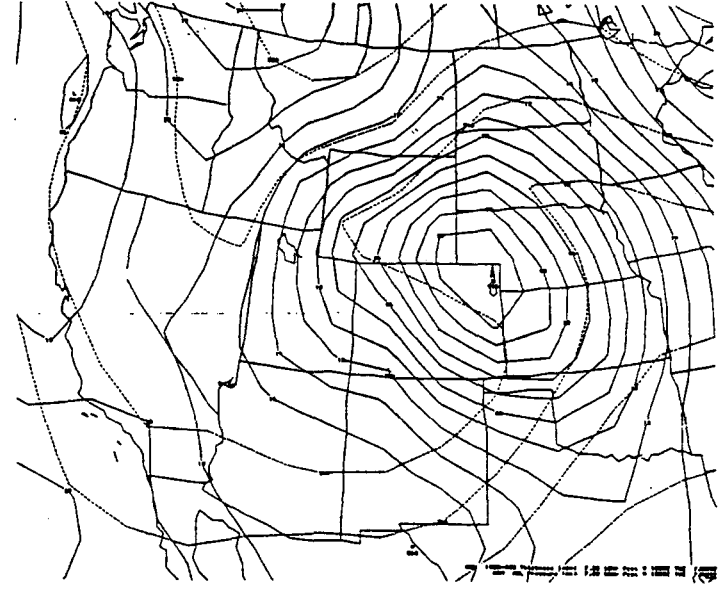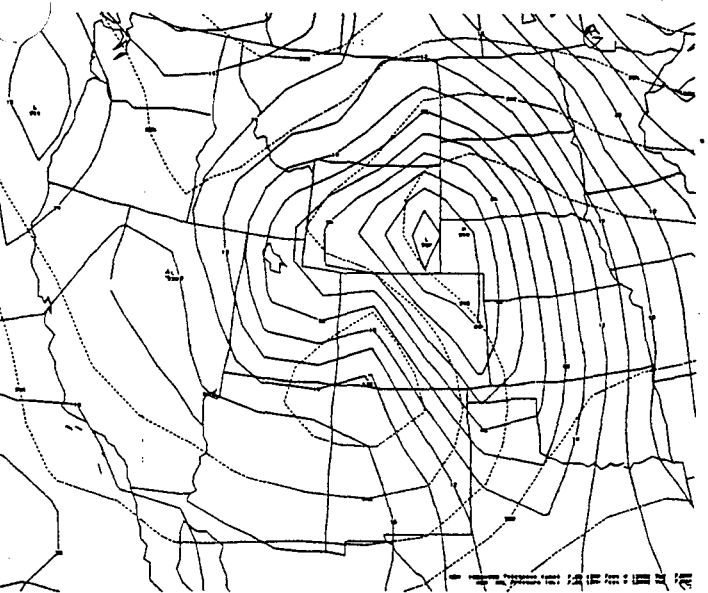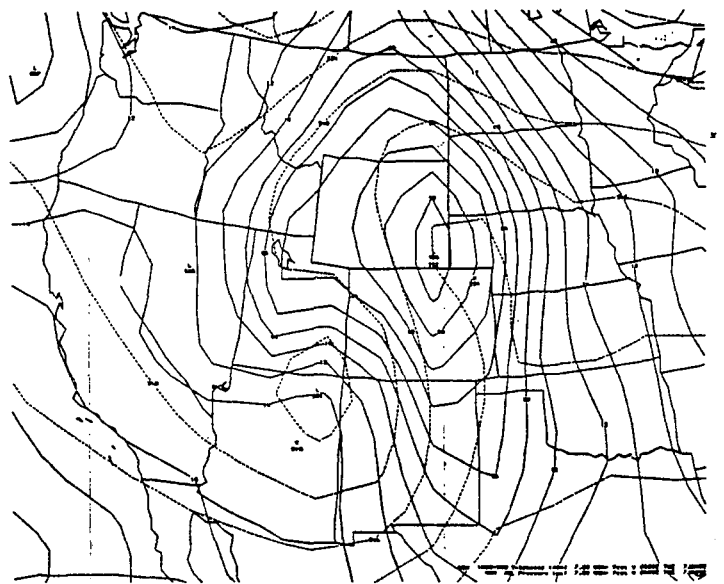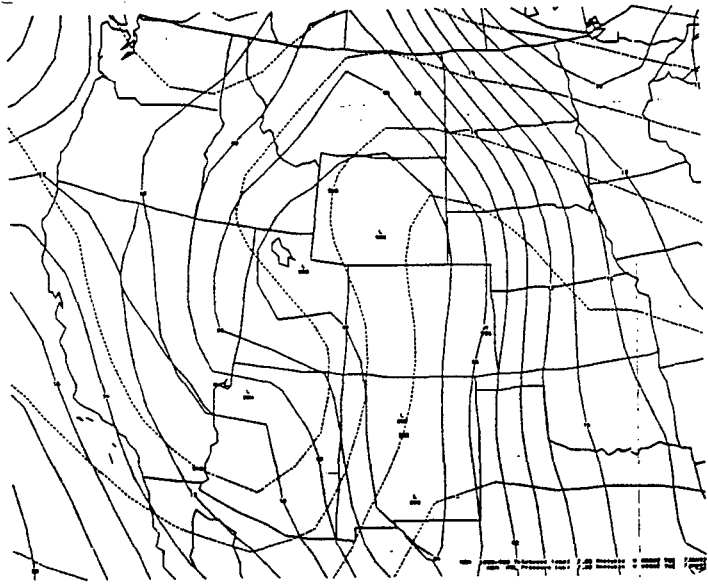
Figure 2. Mean sea level pressure isobars (mb, solid) and 1000-500 mb thickness (gpm, dashed) from the NGM initialized at 0000 UTC 7 January 1992. Clockwise from top left, 0-, 6-, 12-, and 18-hour forecasts.
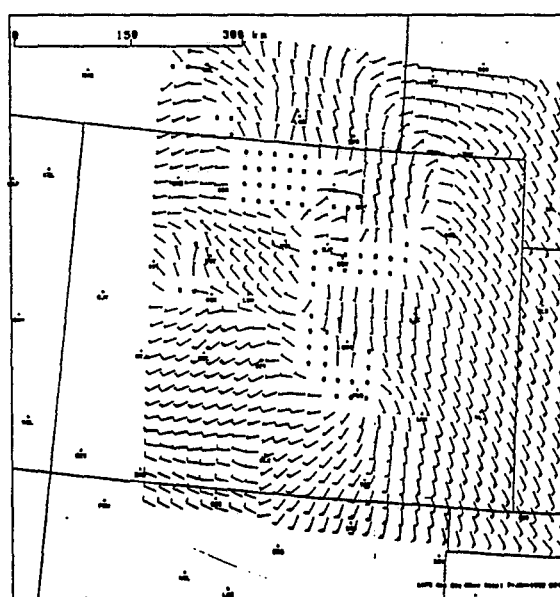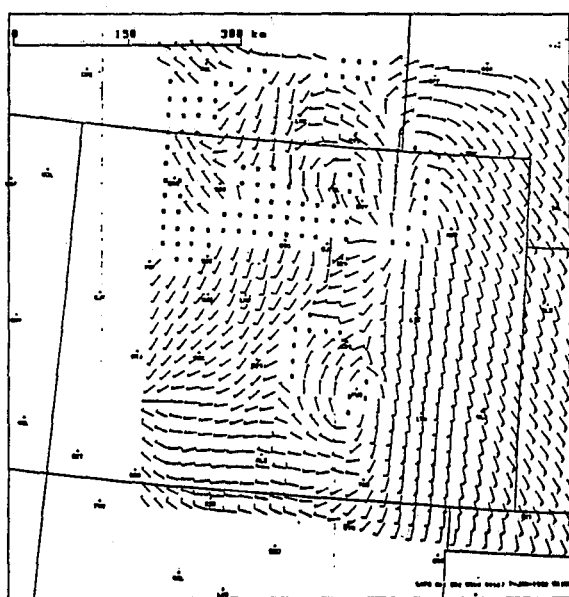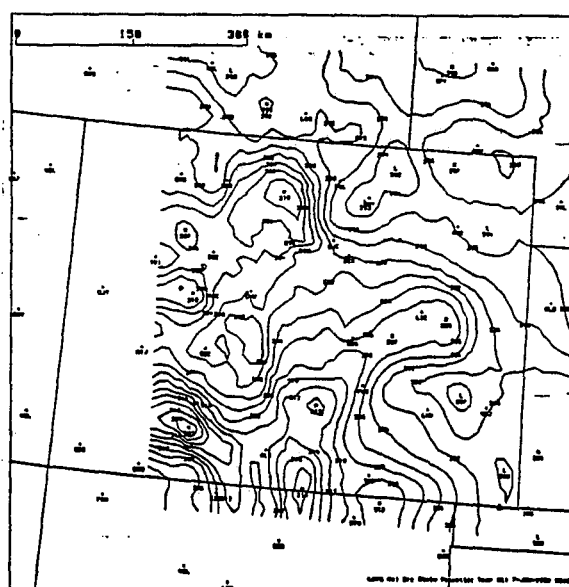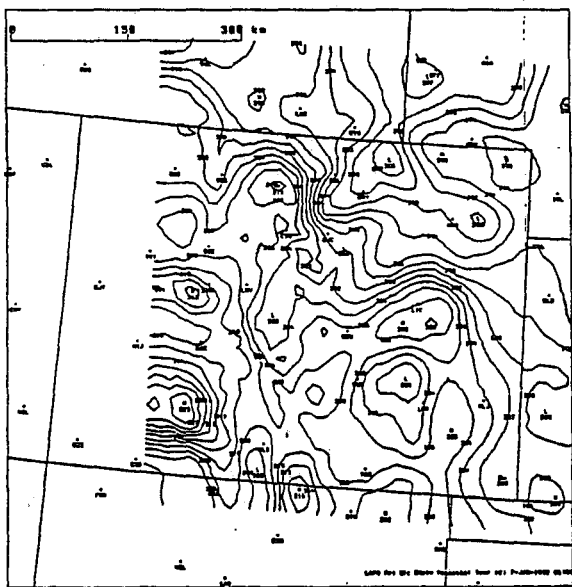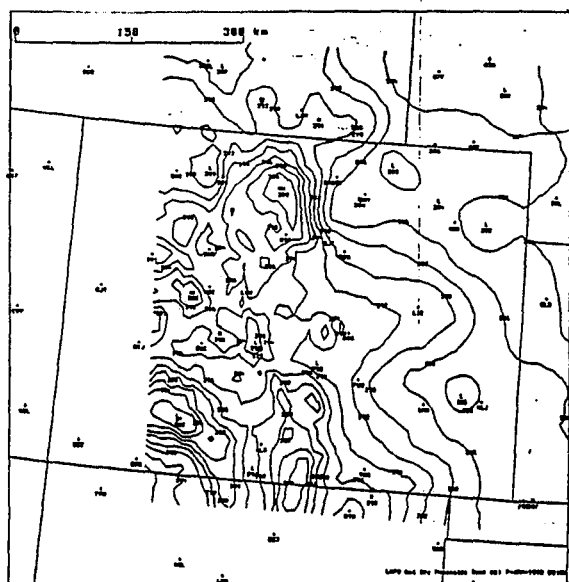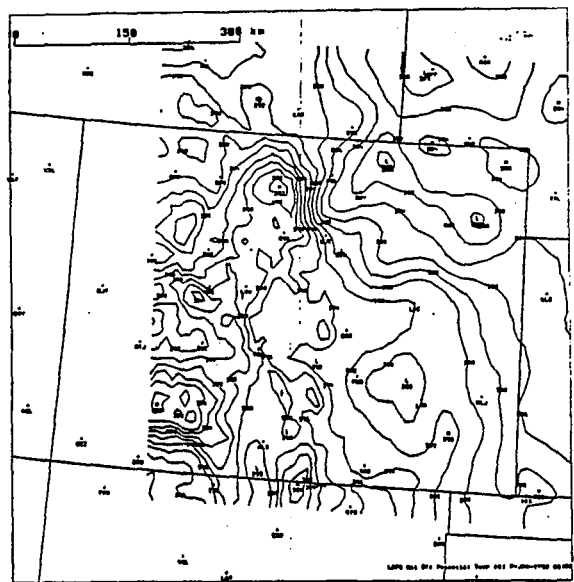
Figure 3.   LAPS analyses of surface potential temperature (top) (θ,K), surface equivalent potential temperature (middle) (θ_e, K) and surface winds (bottom) (kts) for 0600 UTC 7 January 1992 (left column) and 0900 UTC 7 January 1992 (right column).
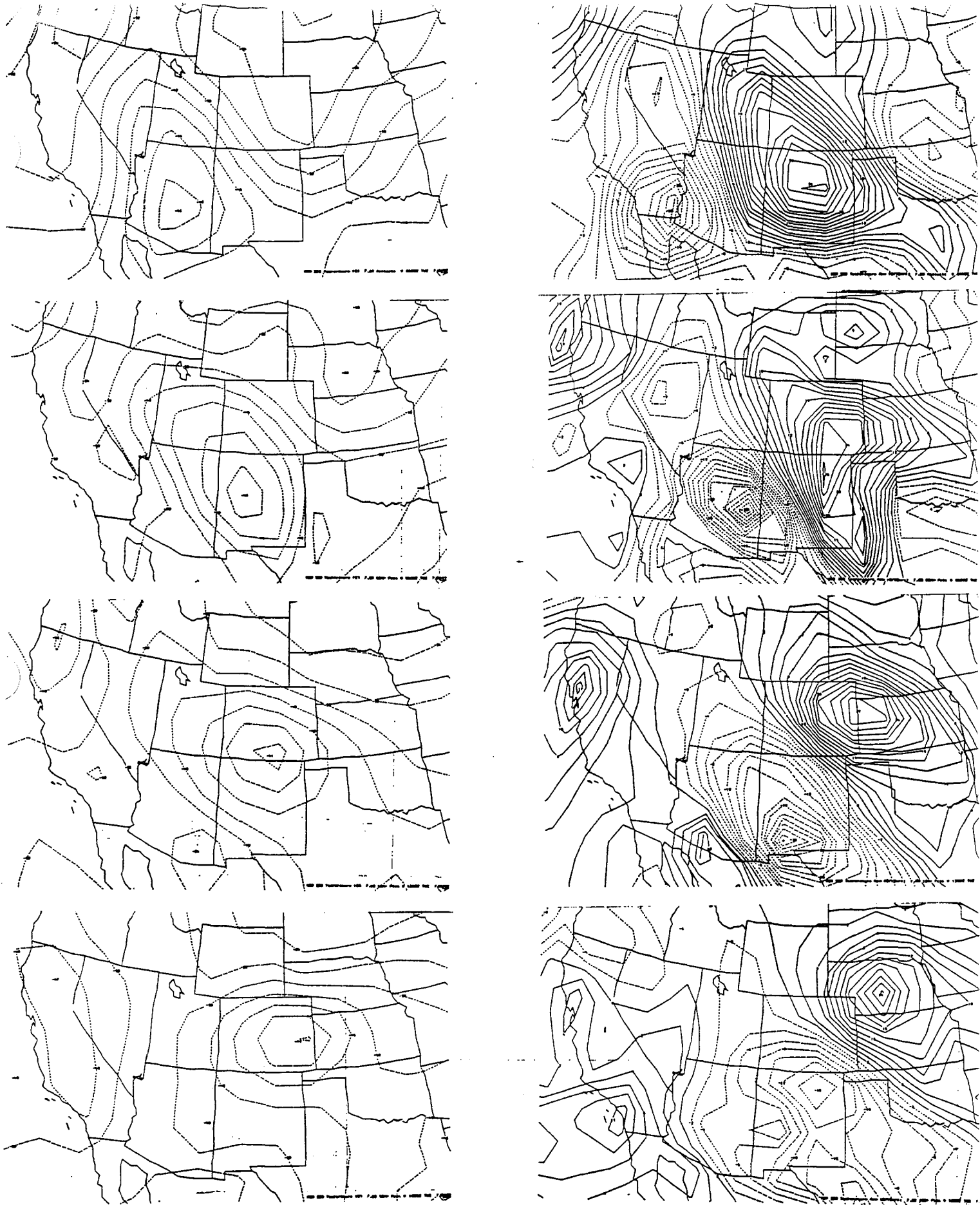
Figure 4.   250 mb temperatures (°C, left column) and 250 mb temperature advection (°C/12 hr, right column) from the NGM initialized at 0000 UTC 7 January 1992. Top row 0-hour forecast, second row 12-hour forecast, third row 12-hour forecast, bottom row 18-hour forecast.
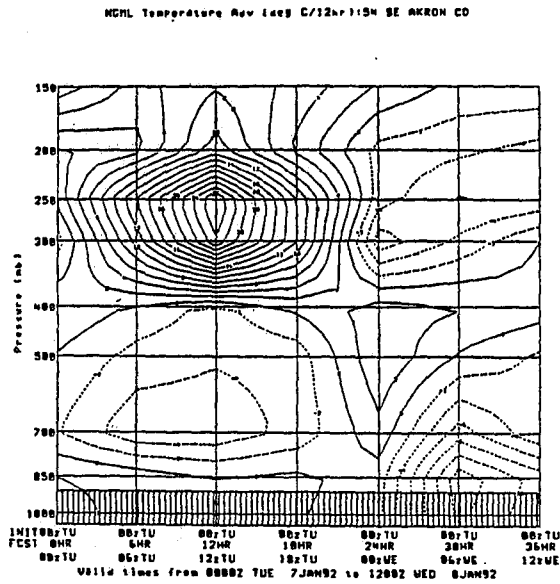
(a)
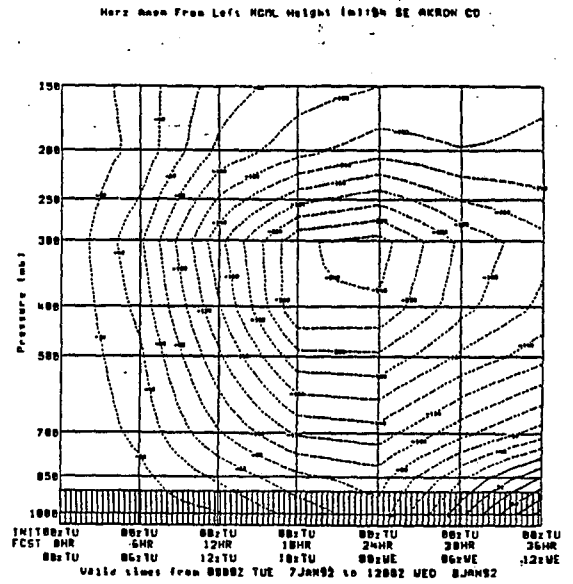
(b)
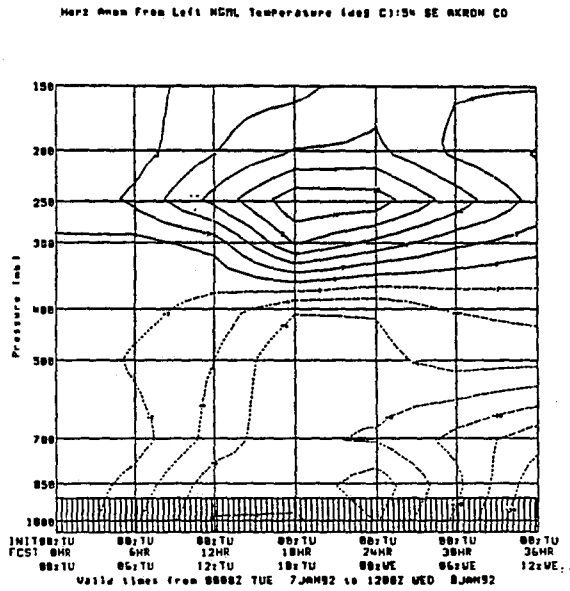
(c)

Figure 5.   Vertical time sections of NGM forecast data. Initial time on left with 36-hour forecast on right. (a) temperature advection (°C/12hr); (b) height changes (gpm) from initial time; (c) temperature changes (°C) from initial time.
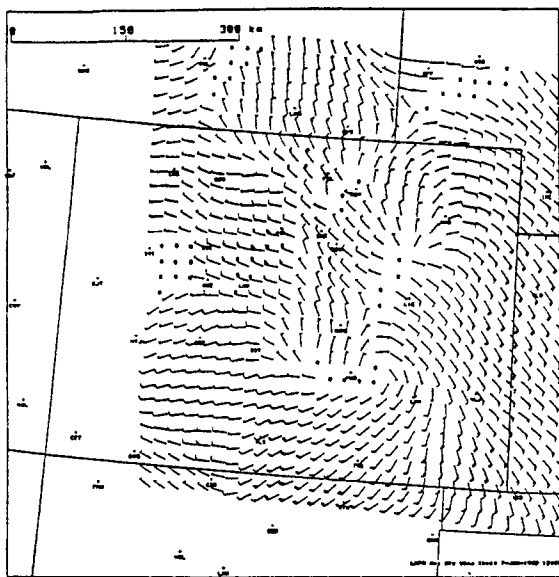
(a)
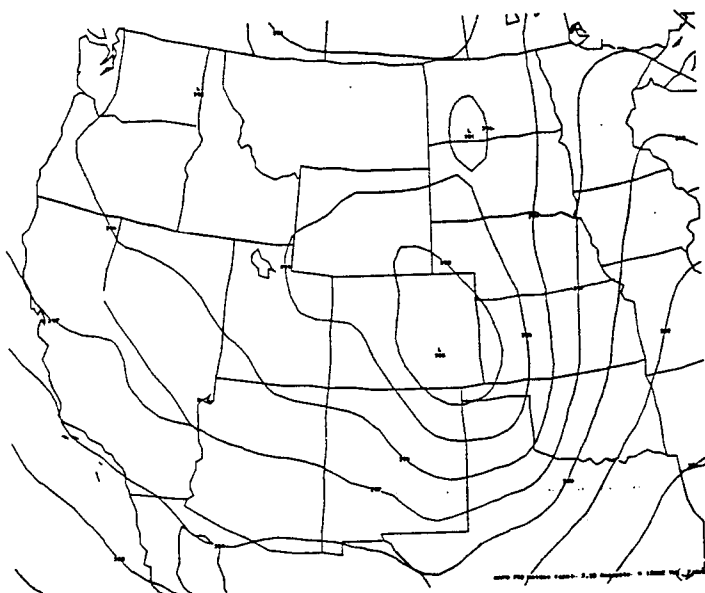
(b)
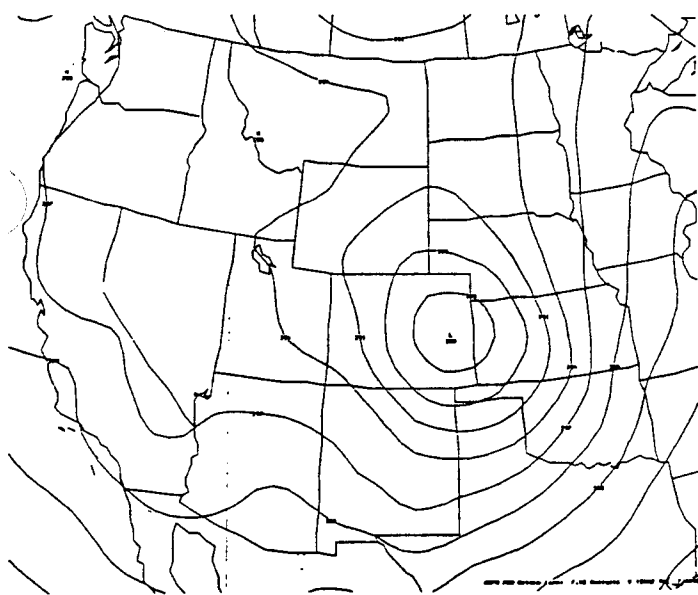
(c)
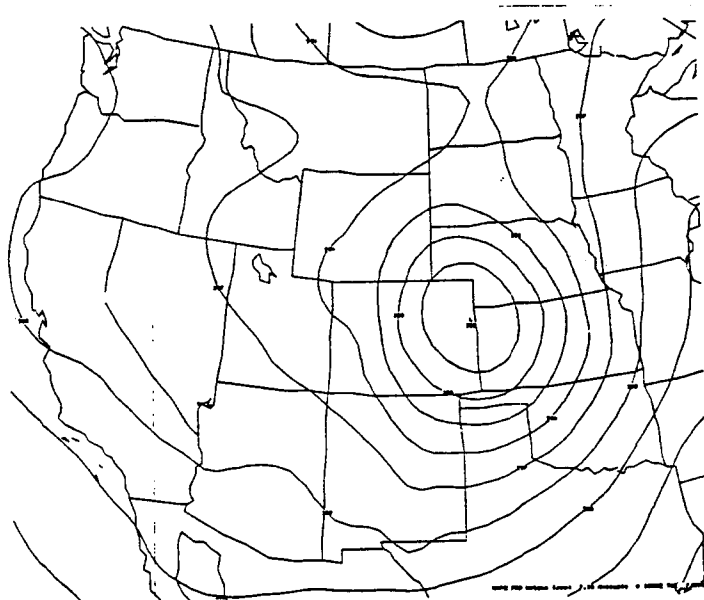
(d)

Figure 6.   (a) LAPS surface wind (kts) analysis 1200 UTC 7 January 1992. MAPS 700 mb
height (gpm) analyses at (b) 1200 UTC, (c) 1500 UTC, (d) 1800 UTC 7 January
1992.

THE FRONT RANGE/PALMER DIVIDE BLIZZARD OF 7 JAN 1992

RAY WOLF and RON McQUEEN

INTRODUCTION

A moderate intensity blizzard struck the eastern edge of the Colorado Front Range and northeast Palmer Divide on 7 January 1992. The storm produced up to 22 inches of snow with 3 to 6 foot drifts (including 14 inches of snow in twenty-four hours at the Weather Service Forecast Office in Denver (WSFO DEN), a record for January). This was a result of a rapidly intensifying eastward moving cyclone. Blizzard conditions were most pronounced in a 30 to 40 mile wide band mainly east of Interstate-25 from the Wyoming border south to the Palmer Divide (Fig. 1).

This storm also caused heavy snow in the Four Corners area on the 6th and the Colorado mountains on the 6th and 7th. Widespread heavy snow on the 6th amounted to between 3 and 8 inches in the Four Corners. Two day snowfall totals for the mountains ranged from 12 to 18 inches in the Southwest Mountains and between 8 and 25 inches in the Northern and Central Mountains.

This storm provided an excellent opportunity for forecasters at WSFO DEN to use the Denver AWIPS Risk Reduction and Requirements Evaluation (DARE) workstation to its fullest diagnostic and forecasting capacities. The DARE workstation is the functional prototype AWIPS workstation. Forecasters at Denver have been using this system exclusively in the routine preparation of forecasts and warnings for nearly three years.

Interestingly, with the new ease of higher resolution diagnosis, there has also begun a revival, of sorts, of the science of meteorology. For example, no longer is 500 mb height and vorticity acceptable to determine atmospheric vertical motion. Rather, a more complete application of quasi-geostrophic theory has taken its place. In the same way, mean relative humidity fields are being used less now than fields such as specific humidity and condensation pressure deficit at specific isobaric and isentropic levels. Stability indices are no longer as revered as are detailed analyses and forecasts of lapse rates.

The addition of a tremendous number of varied and complex forecast and analysis products has also brought a search for simplicity. Foremost, the forecasters at Denver have come to focus on the question "Will there be upward vertical motion?". This then leads to a search for the intensity, location and timing of the lift, and furthermore a determination of the moisture and thermal structure of the atmosphere. With the help of the DARE system, we will analyze the 7 January 1992 blizzard as pertains to these elements.

METEOROLOGY

Circulation and Stability: A closed circulation center, and associated cold pool south of the center, moved into northwest California on Sunday evening 5 January 1992. The circulation remained nearly closed as it moved across the Great Basin on the 6th. Heavy mountain snows over the Sierras and parts of the Great Basin spread into western Colorado by

late afternoon on the 6th associated with strong negative Q-vector divergence (or Q-vector convergence). This upward forcing was a result of geostrophic frontogenesis. The Grand Junction, CO (GJT) sounding from 12 UTC 6 January 1992 indicated a 700-500 mb lapse rate near 8 degrees C/km (approximately psuedo adiabatic) and a 700-500 mb temperature difference around 20 degrees C (Fig. 2).

As specific humidity increased, a number of thundersnow-storms occurred that afternoon and evening in the Four Corners area and adjacent Southwest Mountains. The 12 UTC 6 January 1992 DEN sounding indicated stability similar to GJT with a 700-500 mb lapse rate near 8 degrees C/km. This moist adiabatic air over northeast Colorado remained in place through the night of the 6th even as specific humidity rapidly increased with the help of a 40 to 50 kt southerly jet apparent from the Granada, CO (GDA) profiler.

Pressure Falls: As the cyclone center crossed into central Colorado on the 7th, surface pressure falls on the order of 8 to 10 mb were measured at both Pueblo, CO (PUB) and DEN in a 12 to 15 hour period. The cyclone center rapidly intensified over east-central Colorado and became vertically stacked by 19 UTC on the 7th with the surface low of 993.5 mb centered between Limon, CO (LIC) and Goodland, KS (GLD). The development of deep north to northeast wind over northeastern Colorado resulted in strong isentropic upglide by 12 UTC as well. This upglide, as forecast by the Mesoscale Analysis and Prediction System (MAPS) (Benjamin et al. 1991), was to last the entire day.

Confluence and convergence: The MAPS 00 UTC model run on the 7th indicated moderate 700 mb deformation (implying confluence) over west-central and southwest Colorado associated with the main dynamic forcing. This area shifted steadily to the Front Range and strengthened significantly by 15 UTC of the 7th (Fig. 3). This deformation field was frontogenetic. A MAPS analyses valid at 15 UTC of the 7th showed massive 700 mb convergence of 7 to 10×10^{-5} s^{-1} centered over the northern Front Range. Thus, both confluence and convergence occurred simultaneously in this instance. Meanwhile, a 70 kt plus jet core at 400-500 mb rotated out of New Mexico and across the Texas panhandle placing northeast Colorado in the cyclonic exit region aloft, which indeed corresponded with a divergence lobe at 400 mb, according to MAPS. In addition, NGM Q-vector divergence fields implied an area of deep synoptic-scale forcing for upward vertical motion over northeast Colorado.

Front Range Heavy Snow Band: The question arose in our minds whether the 30 to 40 mile wide heavy snow band was a result of cold air damming and, consequently, a barrier jet along the Front Range. After later analyses, we think more likely the focused heavy snow was due to strong convergence in a baroclinic zone caused by the storm systems tilt with height early on the 7th and resulting frontogenetically forced ageostrophic circulation. By late on the 7th the system became vertically stacked, easing the convergence, and hence the heavy snow.

Development of the strong surface low in east-central Colorado early on the 7th caused strong north to northwest (apparent downslope) winds to develop. Most of the area immediately adjacent to the foothills, with the exception of the Fort Collins, CO (FCL) area, did not receive heavy snowfall because of this flow. The system's tilt to the south southwest with height was such that easterly winds increased above the low level

flow, or from about 550 mb to 250 mb (Fig. 4). This appeared to cause strong deep convergence mostly from 20 to 50 miles east of the Front Range as well as a strong 40 kt plus low level jet oriented north-northwest to south-southeast through the heavy snow band. The verticality of the system after 19 UTC is implied by the deep northerly winds, reaching the surface at 30 to 45 kts as the lower level pressure gradient increased. Blizzard conditions became most pronounced after this time, even though the heaviest snow had ended. The blizzard ended by 04 UTC 8 January as the cyclone moved far enough into Nebraska to lessen gradient winds over eastern Colorado.

The Platteville profiler seemed to suggest a barrier jet, but the strong easterly flow was never indicated below 550 mb. The Front Range peaks are near 600 mb. This is not to say a bubble of cold air did not dam aloft (mesonet data never showed surface damming) and add convergence to some extent. The low level jet considerations may also help explain the lack of snow to the west (right exit region divergence) and abundance to the east (left exit region convergence). But if so, we were not able to diagnose either feature from the MAPS 60 km gridded data.

Models: The 120 hour MRF valid 00 UTC Tuesday 7 January 1992 indicated a closed surface low over eastern Colorado. Successive runs thereafter, however, including the early short range model runs, trended away from this scenario with a weaker, more open wave passing mainly north of Colorado. The location of leeside cyclogenesis is critical for forecasts of eastern Colorado weather. Typically, upslope precipitation occurs to the north of the low while westerly winds to the south and west of the low are downslope, occasionally at speeds requiring high wind warnings, and usually precipitation-free. Thus the dilemma faced by the forecasters was to choose between dry downslope winds or heavy snow in the northeast. The 30 hour NGM forecast valid 18 UTC on the 7th started to show a reversal of the "open wave to the north" scenario but still indicated an open 700 mb trough with the center west of North Platte, NE (LBF).

As it turned out, the actual 700 mb low was 50 to 60 meters lower and 175 miles to the south-southwest within a LIC-GLD-LHX triangle. Interestingly, the NGM 500-300 mb layer Q-vector divergence forecast valid from 12 UTC Tuesday to 06 UTC Wednesday indicated massive Q-vector convergence (implying forcing for upward vertical motion) across northeast Colorado (in spite of the height forecast problems) with strongest values centered at 18 UTC Tuesday (Fig. 6). The point here is, that despite the new fields used in diagnosing and forecasting an event, the models still retain their flaws and biases, and these need to be evaluated as in the past.

CONCLUSION

Even though significant improvements to specifics of the forecast were made using various elements of the DARE system, especially the gridded fields of the NGM and MAPS, this complex storm illustrates the tremendous difficulty in trying to think in the four dimensions (three spatial plus time). We are learning a great deal from evaluations, such as this, which have led to better application of the science of meteorology. We expect, with time and experience, to see more dramatic improvements in forecasts.

REFERENCE

Benjamin, S.G., K.A. Brewster, R. Brummer, B.F. Jewett, T.W. Schlatter,
    T.L. Smith, and P.A. Stamus, 1989, "An Isentropic Three-Hourly Data
    Assimilation System Using ACARS Aircraft Observations", MWR,
    119:888-906.

Fig. 1 48hr SNOWFALL ENDING WED AM 8 JAN 1992
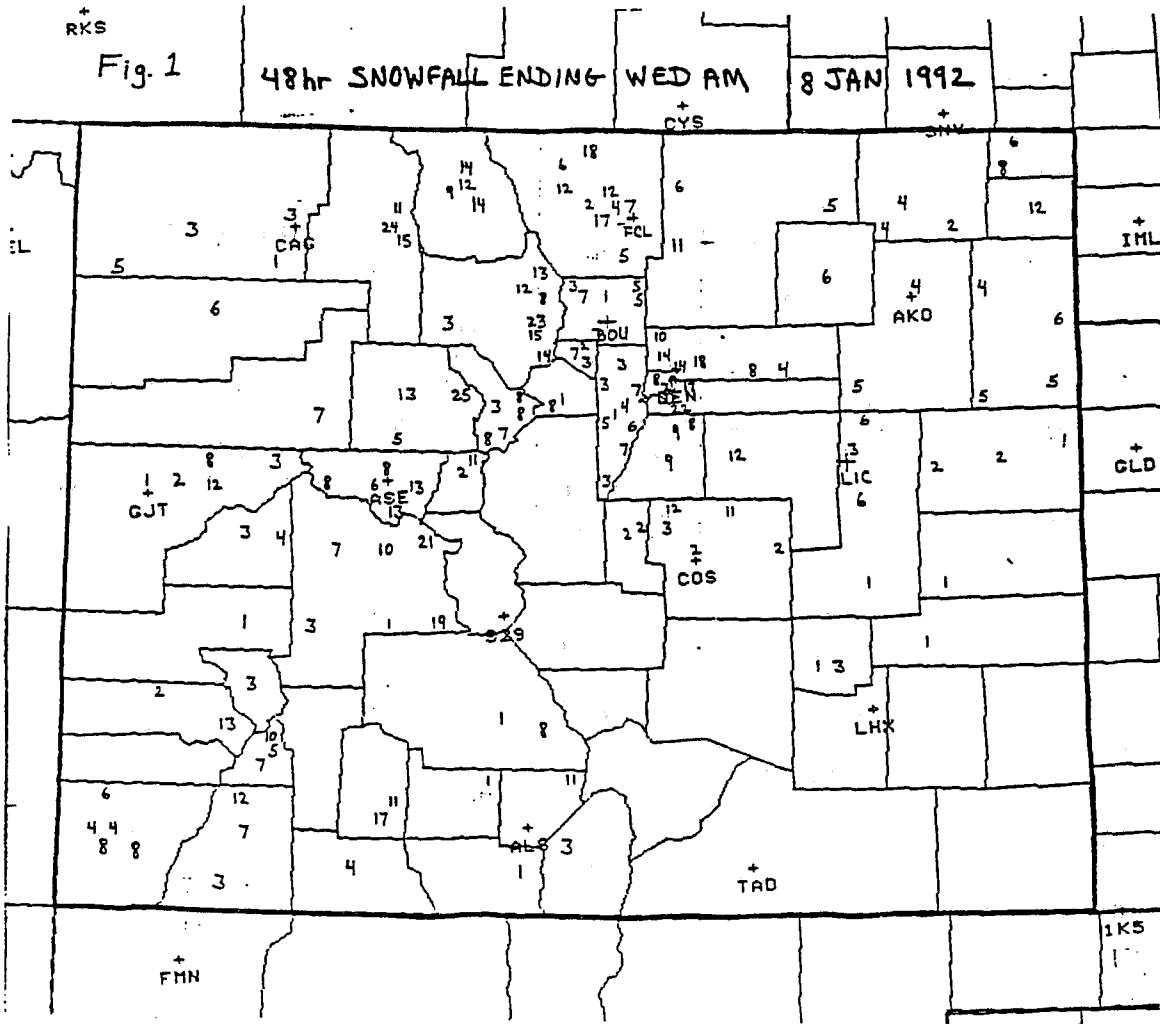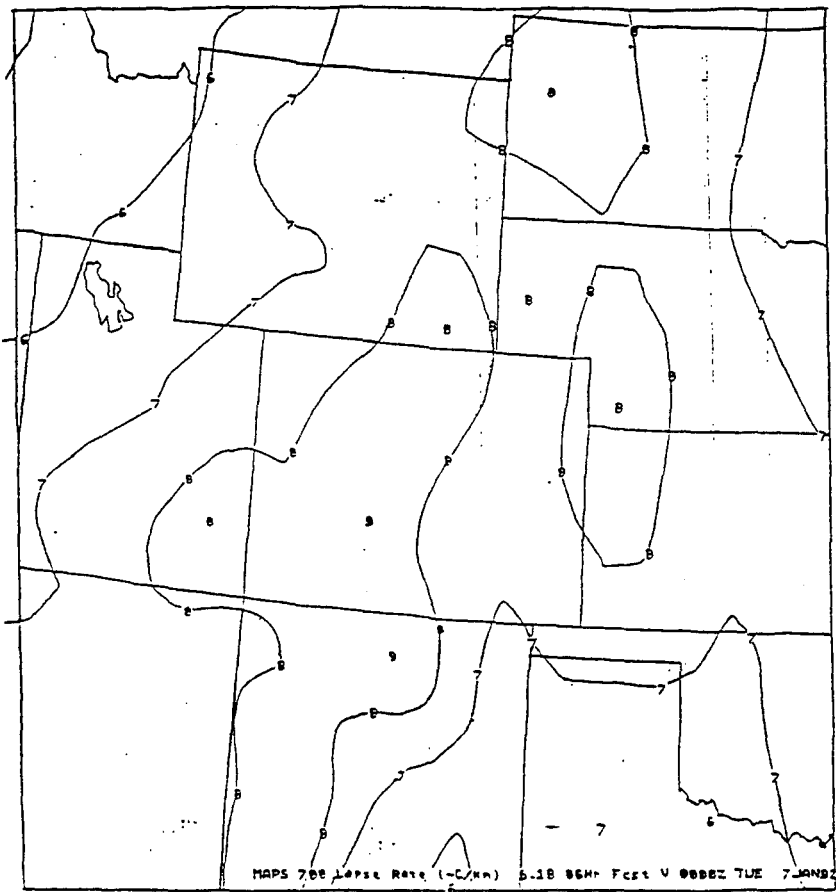
Figure 2.   MAPS 700 mb lapse rates,
            06 hr forecast valid 00 UTC 7 Jan 1992.
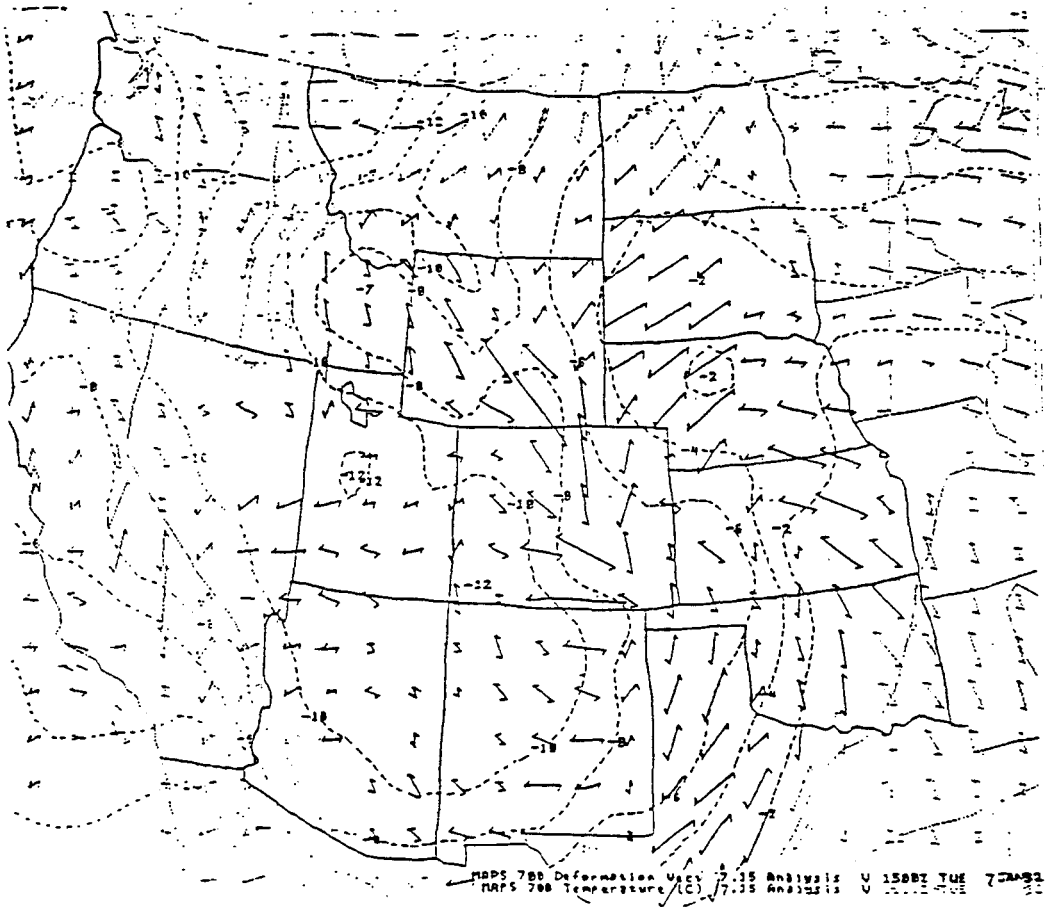
Figure 3.   MAPS 700 mb deformation vectors and temperature,
            analysis 15 UTC 7 Jan 1992.
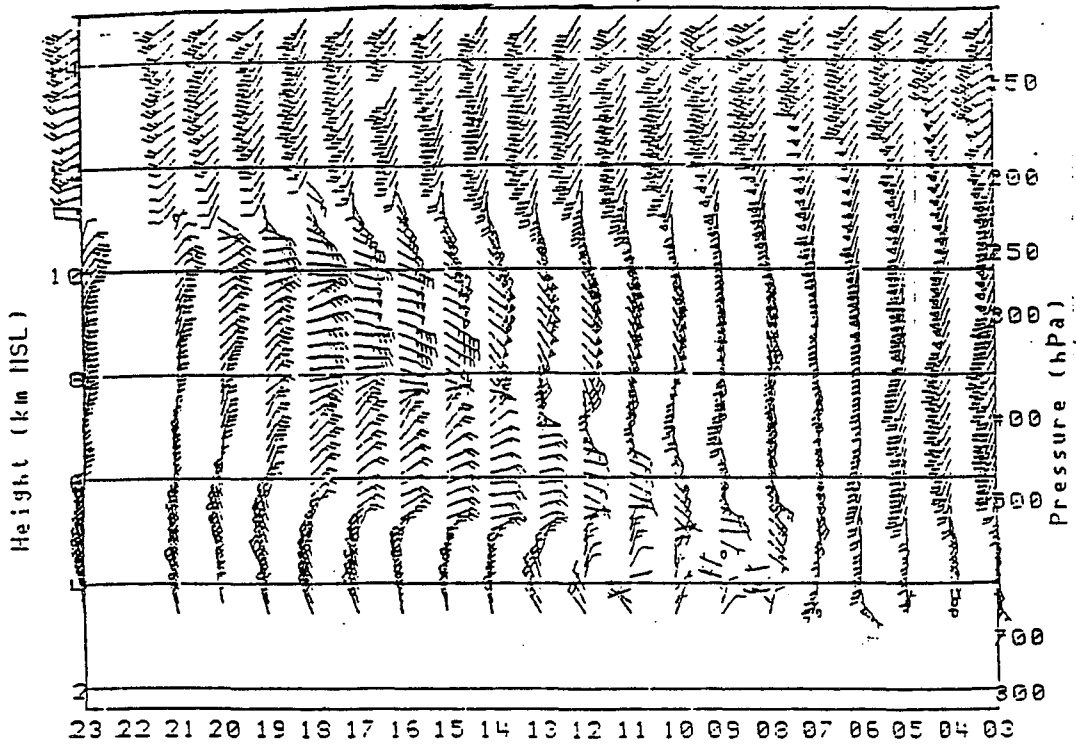
Figure 4. Platteville, CO profiler, 03 UTC to 23 UTC 7 Jan 1992.
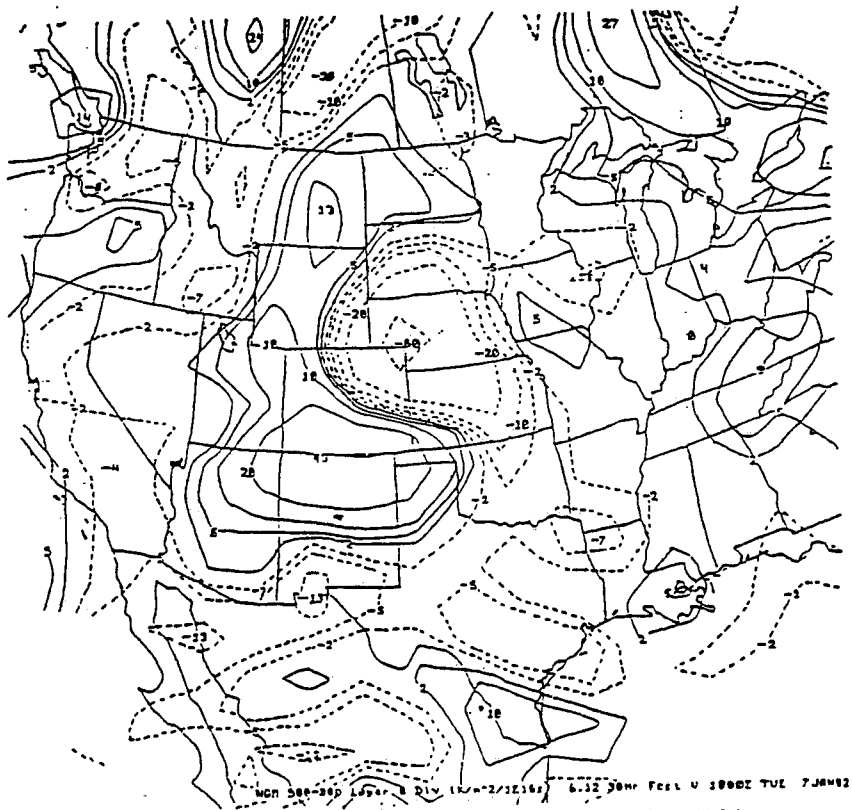
Figure 5. NGM 500-300 mb layer Q-vector divergence,
30 hr forecast valid 18 UTC 7 Jan 1992.

OBSERVING AND FORECASTING A MESOSCALE SNOW EVENT USING MAPS

Robert T. Glancy, Ray A. Wolf, Eric R. Thaler
National Weather Service Forecast Office
Denver, Colorado

1. INTRODUCTION

On 22 December 1991 a closed upper level low began to lift northeast into the Southern Plains. The Nested Grid (NGM) and Aviation (AVN) models forecast the 500 mb low to move from western New Mexico at 1200 UTC to southwest Kansas at 0000 UTC 23 December (Fig. 1a,b). Positive vorticity advection (PVA) was forecast to move across southeast Colorado during the day. At the surface, a low was forecast to intensify and move from southeast Colorado at 1200 UTC 22 December to the northern Texas Panhandle at 0000 UTC 23 December, with high pressure building into northeast Colorado from Wyoming (Fig. 2a,b). This pattern is well known as a precipitation producer for eastern Colorado. Forecasts reflected high probabilities of precipitation for most of eastern Colorado during the day, but because of the southern location of the upper low and quick movement of the 500 mb PVA into Kansas, no heavy precipitation was forecast.

The 12-hour forecast from the NGM model verified well with both the track and intensification of the 500 mb low. However, the 700 mb low at 0000 UTC was a little deeper than forecast by the NGM, elongated further to the north, and there was a tighter 700 mb temperature gradient in northeast Colorado (Fig. 3a,b). The grid spacing of the NGM likely hampered its ability to delineate this temperature gradient and the subsequent mesoscale snow event that occurred during the afternoon of 22 December. During a 7-hour period from 1800 UTC 22 December to 0100 UTC 23 December, 6 to 16 inches of snow fell in a narrow band to the east and south of Akron, Colorado (AKO) (Fig. 4).

This heavy snow was not forecast by the WSFO Denver forecasters. A detailed post analysis revealed that the Mesoscale Analysis and Prediction System (MAPS) data provided many clues to the general location and duration of this mesoscale snow event.

2. OVERVIEW OF MAPS

The first isentropic version of MAPS became available to forecasters at WSFO Denver with the arrival of the second generation prototype AWIPS workstation (DARE-II) in December 1989. The version of MAPS in use in December 1991 consisted of a complete surface and upper air analysis available every 3 hours. Data from RAOBS, profilers, satellite, surface observations and automated aircraft reports are used by MAPS, with boundary conditions provided by the NGM. The data is analyzed on a 60 km horizontal resolution grid with 25 vertical levels (5 terrain following sigma layers and 19 isentropic levels). Forecasts are made using a primitive equation model formulated in isentropic coordinates. Forecasts for 3 and 6 hours are available every 3 hours and at 0000 and 1200 UTC 3-, 6-, 9-, and 12-hour forecasts are produced.

MAPS data arrives in the workstation in gridded form on both isentropic and isobaric surfaces, as well as on the sigma layers. This information is then accessed in real time using application programs which display the output in either plan view or cross section form. Forecast soundings can also be created. MAPS data can be fully integrated with the numerous other data sets available on the workstation. Further details on the inner workings of the MAPS model can be found in Benjamin (1989) and Benjamin et al. (1991a and b).

Utilizing the isobaric data from MAPS at the WSFO has been relatively straightforward. However, using the isentropic data has been a bit more complex. Isentropic analysis is only now beginning to make a comeback to the popularity it enjoyed several decades ago. Few operational forecasters have had the opportunity to use this type of information in day-to-day forecasting so that training and experience are necessary to become adept at exploiting them.
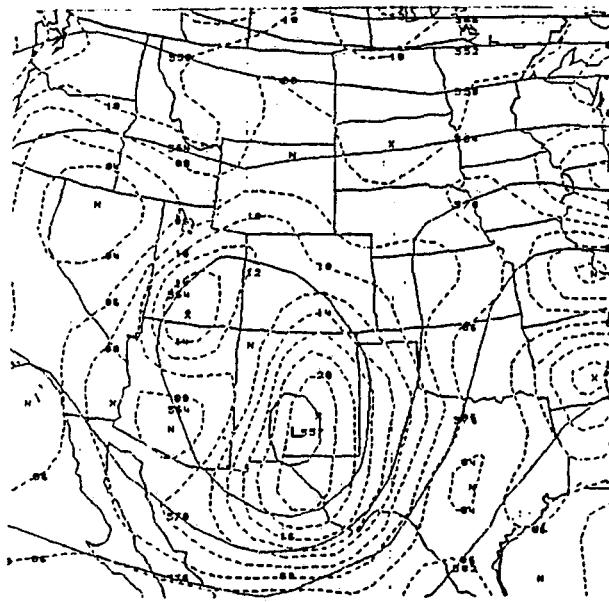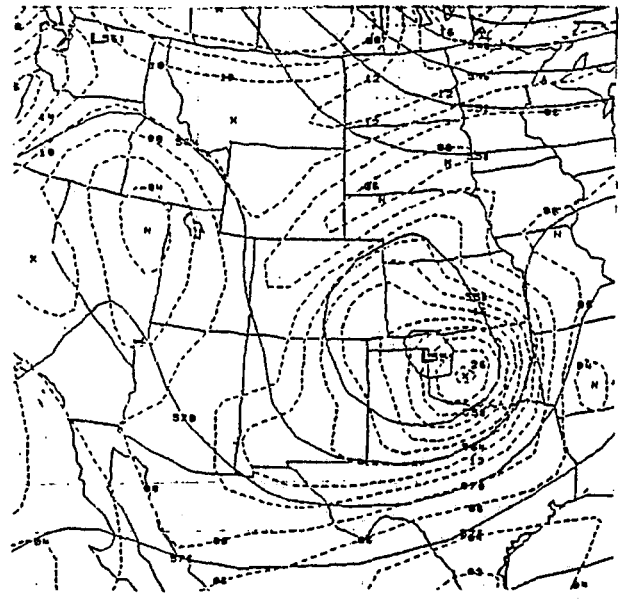
Fig. 1 NGM 500 mb heights and vorticity; 1a) analysis 1200 UTC 22 December
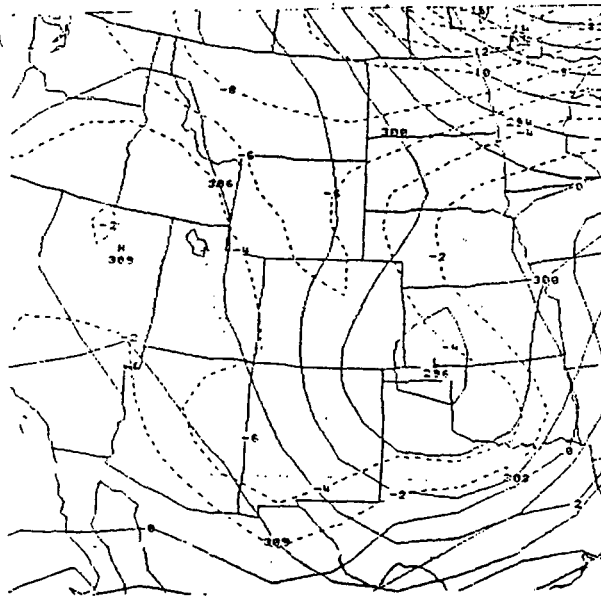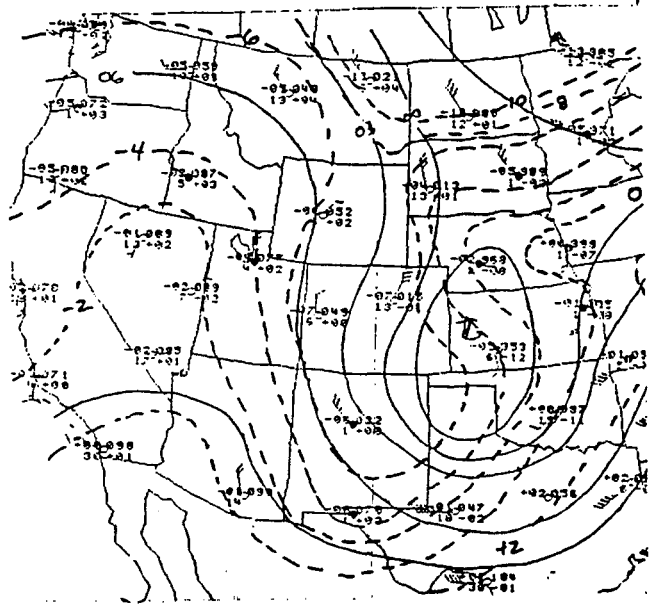1991 and 1b) 12 hour forecast valid 0000 UTC 23 December, 1991.
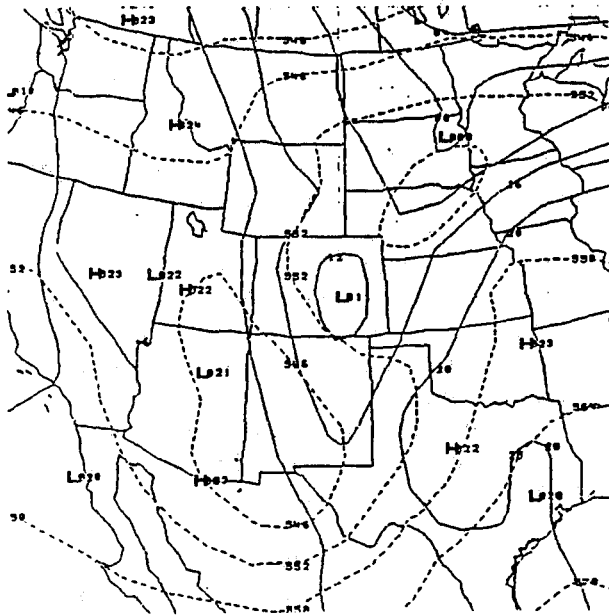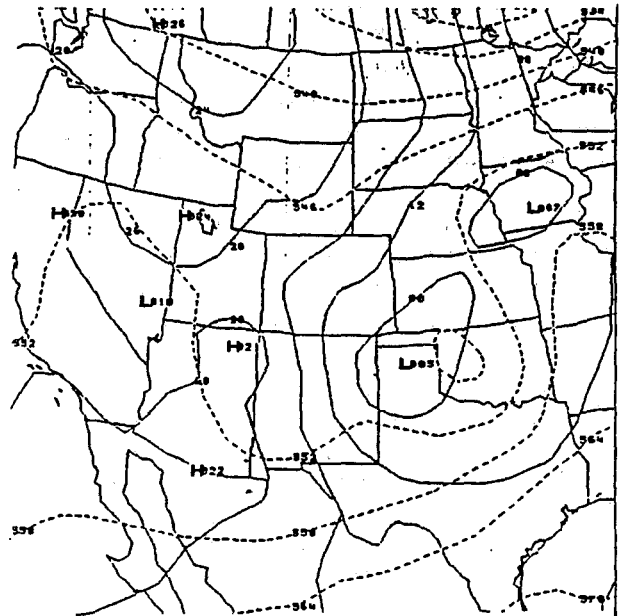
Fig. 2 NGM surface pressure and surface to 500 mb thicknesses; 2a) analysis
1200 UTC 22 December 1991, and 2b) 12 hour forecast valid 0000 UTC
23 December, 1991.

3a.

3b.

Fig. 3 Comparison between: 3a) NGM 12 hour forecast of 700 mb heights
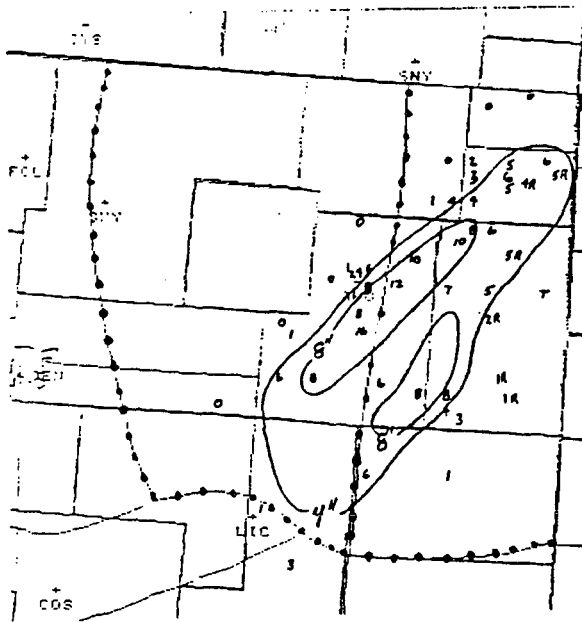and temperatures, valid 0000 UTC 23 December 1991, and 3b) a 0000 UTC
analysis at the same time.

Fig. 4 Snowfall map, 1800 UTC 22 December
1991 to 0100 UTC 23 December 1991.
Snowfall contoured at 4 inches and 8
inches. Light solid lines indicate
county and state borders, dotted lines
are zone boundaries. R indicates rain
mixed with snow.
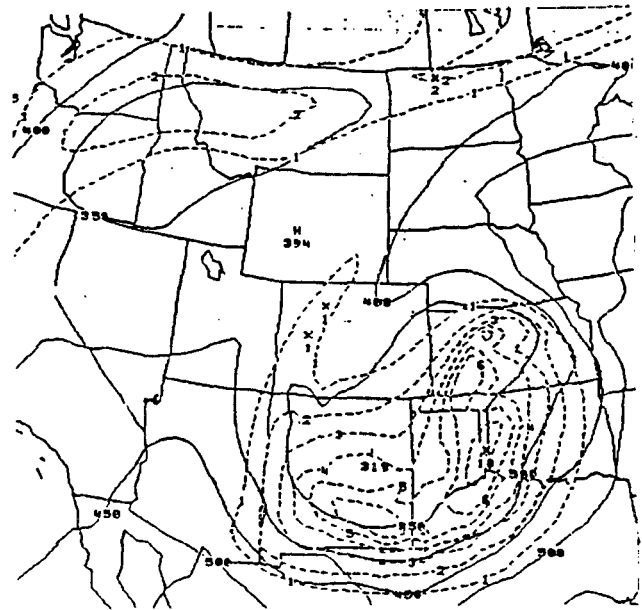
Fig. 6 MAPS 12 hour forecast of 316K
pressure and potential vorticity
valid 0000 UTC 23 December, 1991.
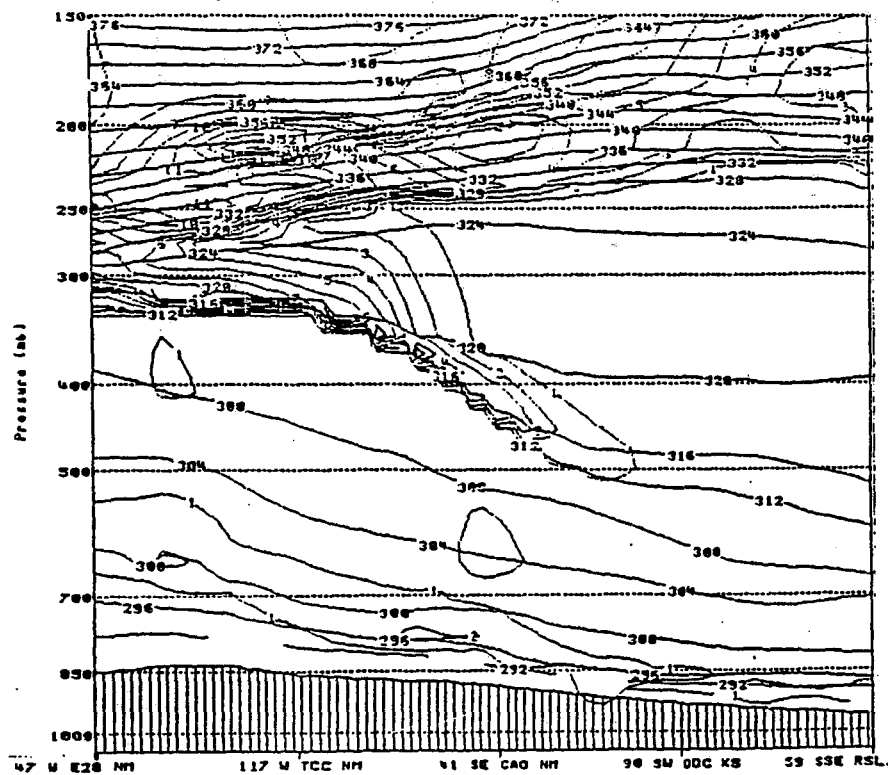
Fig. 5 Cross-section of MAPS theta and
potential vorticity from northeast
New Mexico to southwest Kansas,
1200 UTC 22 December 1991.
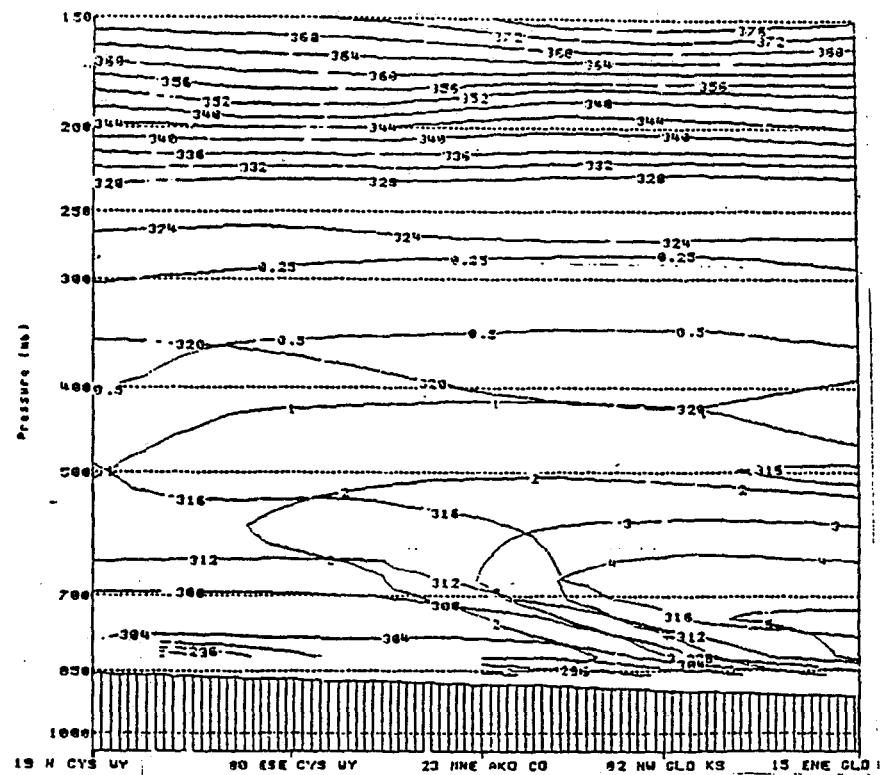
Fig. 7 MAPS forecast Cross-section from southeast
Wyoming to northwest Kansas of theta-E and mixing
ratio, valid 1800 UTC 22 December, 1991.

Although there are some problems associated with isentropic analysis, the many advantages far outweigh any difficulties iproblems that may be encountered. Several of the advantages of isentropic analyses have been cited by Moore (1987). These include better resolution of frontal zones, more coherent patterns of moisture transport, more direct indications of areas of ascent and descent, and with the use of cross sections, a quick indication of locations of fronts, and static stability.

3. SYNOPTIC AND MESOSCALE DISCUSSION

At 1200 UTC 22 December 1992, the 700 and 500 mb lows were located near Albuquerque, New Mexico (ABQ). MAPS cross sections indicated a well defined stratospheric extrusion of high potential vorticity (PV) air to 500 mb over southeast Colorado (Fig. 5). The PV bullseye on the 316K isentropic surface associated with this extrusion was forecast to advect into southwest Kansas during the afternoon (Fig. 6).

It has been shown (Hoskins et al. 1985, Smith and Benjamin 1989) that on isentropic surfaces, PV is a good conservative tracer to follow the motion of upper troughs in the atmosphere. It maintains its continuity until altered by some diabatic process or friction. On a constant theta surface, the advection of PV from the base of a cold trough to the northeast would bring the PV lower into the troposphere, and from an area of relatively high static stability to relatively low stability. As the column of air is stretched in the area of lower static stability, the relative vorticity increases, and the trough intensifies (Holton 1972). On 22 December, the high PV air over southeast Colorado was descending into air with very high 500-850 mb lapse rates (32 °C) and so further intensification was expected.

As the system lifted northeast and intensified, the lows at 700 and 500 mb became more elongated than indicated on either the NGM or MAPS forecasts. This was one element helpful to the development of the mesoscale snowstorm, as the circulation around the 700 and 500 mb lows was brought closer to northeast Colorado. Although MAPS height fields did not indicate this elongation, MAPS temperature, moisture, and wind fields on isentropic surfaces, and at 700 mb and 850 mb, provided strong indications of the developing snowstorm.

A well defined sloping frontal boundary was forecast by MAPS in northeast Colorado that afternoon. A forecast cross section valid at 1800 UTC 22 December from near Cheyenne, Wyoming (CYS) to near Goodland, Kansas (GLD) showed the frontal boundary in the theta-e isentropes, with abundant moisture riding up over the boundary (Fig. 7).

MAPS 700 mb forecasts valid at 2100 and 0000 UTC showed a tight temperature gradient between Denver and Akron (Fig. 8a, b). Deformation vectors at 2100 UTC were parallel to the isotherms indicating maintainence of the temperature gradient. By 0000 UTC, the magnitude of the deformation vectors were smaller, while cross isotherm vectors to the west suggested a weakening of the temperature gradient. This was an early clue to the duration of the event.

MAPS forecasts at 700 mb valid at 1800 UTC showed an axis of confluence to the east of the temperature gradient. This axis extended from southwest Nebraska into Colorado near Limon. A moisture gradient was indicated, with a large area of condensation pressure deficits (the amount of lifting in millibars necessary to reach saturation) less than 20 mb to the southeast of the confluent axis (Fig. 9). A divergence chart at 850 mb indicated convergence oriented along the axis (Fig. 10). A cross section of divergence from near CYS to near GLD displayed this area of low level convergence below 600 mb, with mid level divergence of equal magnitude centered at 500 mb (Fig. 11).

In the warmer moist air, 850-700 lapse rates forecast the least stable air (6°C/km) to be located in extreme southwest Nebraska and northwest Kansas (Fig. 12). By 2100 UTC, the least stable air from 700 to 500 mb, with a lapse rate of 7 °C/km was located along and just west of the 700 mb confluent axis (Fig. 13).

Isentropic forecasts at several levels valid at 1800 UTC provided a three dimensional look at the flow above the frontal zone, showing the advection and condensation of moisture over the boundary. Figure 14 shows the limited moisture available at the 296 K level (about 800 mb), but strong southeast winds in Kansas would be advecting moisture into northeast Colorado during the afternoon. Figure 15 shows a larger area of nearly saturated air to the southeast of the confluent boundary at the 300K isentropic surface. Condensation pressure deficits were 10 mb

at Goodland, and 150 mb at Akron, which was located in the very dry low level air to the west of the boundary. This chart indicates that the southeast winds in Kansas were lifting the moist air to saturation over the sloping frontal boundary.

At the 308K and 312K isentropic surfaces (about 550 mb and 450 mb), respectively, the confluent axis was located further west, consistent with a sloping frontal boundary. Moderate east to southeast winds were blowing across northeast Colorado. Saturation of the airmass was evident, with condensation pressure deficits of 10 mb or less over a larger area, and much further west than at lower isentropic levels (Fig. 16, 17).

Note that the winds were northeast at 300K backing to east southeast at 308K. Wind forecasts valid three hours later, at 2100 UTC, showed winds becoming northerly below 700 mb, with deepening east to northeast winds above 700 mb.

The development of convection requires moisture, instability and some lifting mechanism. The MAPS forecast charts indicated that each of these elements was available over northeast Colorado during the afternoon of 22 December. The next section suggests how a forecaster might have monitored the development of the heavy snow.

4. REAL TIME EVALUATION OF THE EVENT

Profiler data through the day was very informative in evaluating the developing system. The Granada profiler (GDA, located in southeast Colorado) depicted the passage of a closed circulation between 500 and 600 mb at 2200 to 2300 UTC (Fig 18). Prior to the passage of the low, strong southeast winds were noted at 700 mb. The Platteville (PLT) profiler, located 30 miles north northeast of Denver, showed strong east component winds between 500 and 250 mb at 1700 UTC. These winds backed to more northeast during the day, finally turning northerly at 0200 UTC (Fig 19). Although not available to the forecaster during the afternoon, the McCook profiler in southwest Nebraska depicted the passage of a circulation at about 600 mb during the early evening (not shown).

Infrared and visible satellite imagery indicated a band of convection which began in extreme northwest Kansas at 1800 UTC. As discussed earlier, this was the area over which MAPS forecasted the strongest

850 convergence, and lowest 850-700 lapse rates at 1800 UTC. Along the strong southeast steering winds, the band of convection rotated northwest and moved over the sloping frontal boundary. The boundary provided a focus for the continuation of the convective process in a relatively narrow band. Conditional instability was also required to produce the locally heavy snow. Convection continued only in the areas of sustained condensation of moisture by lifting over the frontal boundary.

While this event was not easily detected in surface pressure patterns, the sequence of surface weather observations at AKO is consistent with this postulation (Table 1). Until 1900 UTC, Akron was post frontal, with northwest winds and low dewpoints. The sloping frontal boundary extended aloft over Akron, and the first indication of the event at Akron was the northeast winds beginning at 1946 UTC. Snow began at 2004 UTC, and continued heavy at times until 2343 UTC, dropping 2 inches of snow at the airport. As indicated in the MAPS 0000 UTC 700 mb divergence analysis, the convergence over northeastern Colorado had weakened significantly (Fig. 20). The winds at Akron turned northwest once again, and the dewpoint dropped.

The network radar at Limon, Colorado indicated light precipitation (VIP 1) in the area of heavy snow for the duration of the event. Although Doppler data from the Mile High radar was not available during the afternoon, but based on previous experience, it would have detected the band of heavy snow.

5. CONCLUDING REMARKS

The MAPS model will in time become available to forecasters at WFO's across the country. We at WSFO Denver have incorporated it into our daily analyses and forecasts and this is but one example of its utility in producing a better mesoscale forecast. Our experience has shown that the ability to incorporate new forecast tools takes time, and depends on an individual's initiative and interest. Also, for the short term forecast, a weather watch must be ongoing. In this case, MAPS indicated the potential for significant precipitation. However it was the formation of convection outside the area of concern that advected into northeast Colorado that caused the heavy snow. There may be as many cases in which the potential for locally heavy snow is indicated, but not realized. We are convinced that a forecaster dedicated to mesoscale analysis would

have identified this event. Even with the missing Doppler radar data, MAPS forecasts would have heightened awareness, and through close contact with spotters, a better mesoscale forecast would have been produced.

There is a large volume of data available on MAPS, and an additional challenge to forecasters will be to learn to focus on the most useful data fields. Of course this will vary with the season and with the event. Identifying those forecast fields useful to mesoscale forcing is a major goal of an ongoing mesoscale risk reduction at WSFO Denver. (Maddox, 1992).

6. REFERENCES

Benjamin, S. G., 1989: An Isentropic Meso-Scale Analysis System and Its Sensitivity to Aircraft and Surface Observations. Mon. Wea. Rev., 117, 1586-1603.

Benjamin, S.G., K.A. Brewster, R. Brummer, B.F. Jewett, T.W. Schlatter, T.L.Smith, and P.A. Stamus, 1991: An Isentropic Three Hourly Data Assimilation System Using ACARS Aircraft Observations. Mon. Wea. Rev., 119, 888-906.

Benjamin, S.G., T.L. Smith, P.A. Miller, D. Kim, and T.W. Schlatter, R. Bleck, 1991: Recent Improvements in the MAPS Isentropic-Sigma Data Assimilation System. Preprints, Ninth Conference on Numerical Weather Prediction, Denver, AMS, 118-121.

Holton, J.R., 1972, An Introduction to Dynamic Meteorlogy, Academic Press, 319 pp.

Hoskins, B.J., M.E. McIntyre, and A.W. Robinson, 1985: On the Use and Significance of Isentropic Potential Vorticity Maps. Quart. J. Roy. Met. Soc., 111. 877-946.

Maddox, M.R. 1992: Mesoscale Forecasting Project at WSFO Denver. National Weather Association Newsletter, 92-7.

Moore, James T., 1989: Isentropic Analysis and Interpretation, Operational Applications to Synoptic and Mesoscale Forecast Problems. AWS/TN-87/002, Air Weather Service, Scott Air Force Base, Il, 62225

Smith, T.L. and S.G. Benjamin, 1989, Weather Forecasting Applications of Potential Vorticity Analyses on Isentropic Surfaces. Preprints, 12th Conference on Weather Analysis and Forecasting, Monterey, AMS, 260-265.
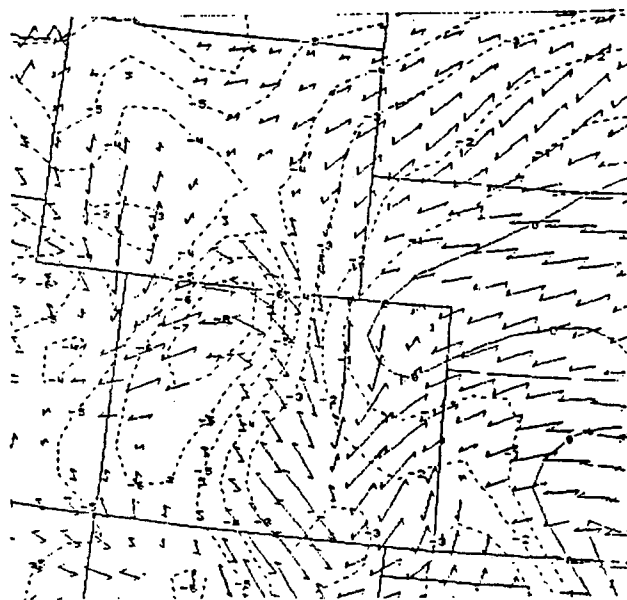
8a.
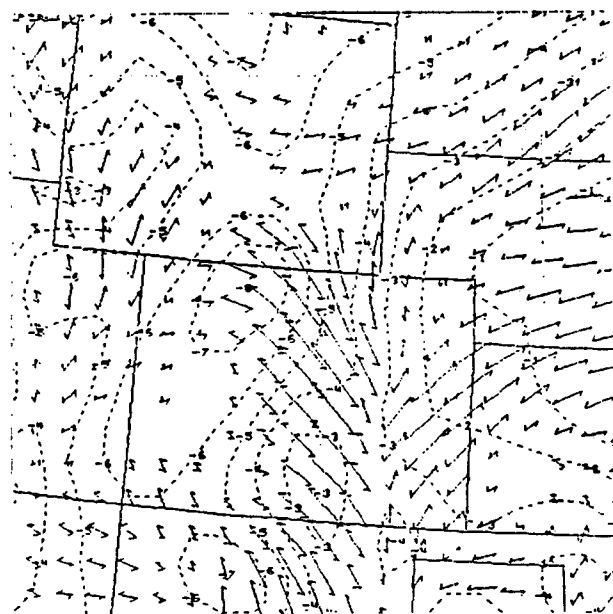
8b.

Fig. 8 MAPS forecasts of 700 mb temperature and deformation valid: 8a) 2100 UTC 22 December 1991, and 8b) 0000 UTC 23 December 1991.
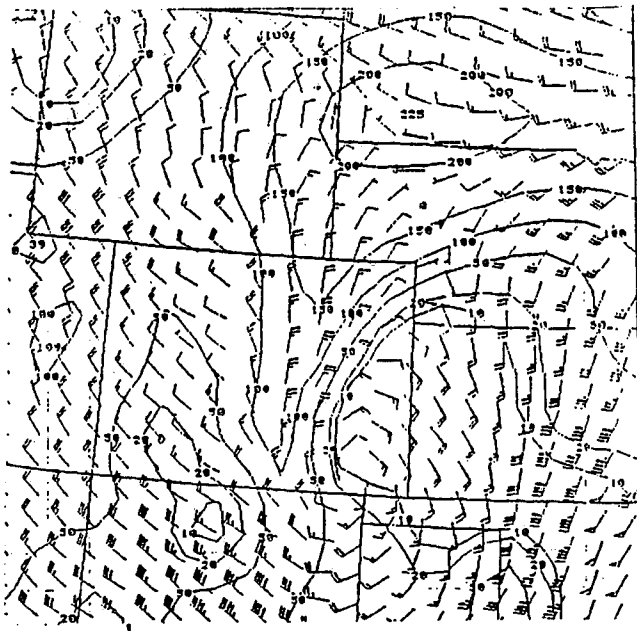
Fig. 9 MAPS forecast of 700 mb wind and
   condensation pressure deficit, valid
   1800 UTC 22 December, 1991.
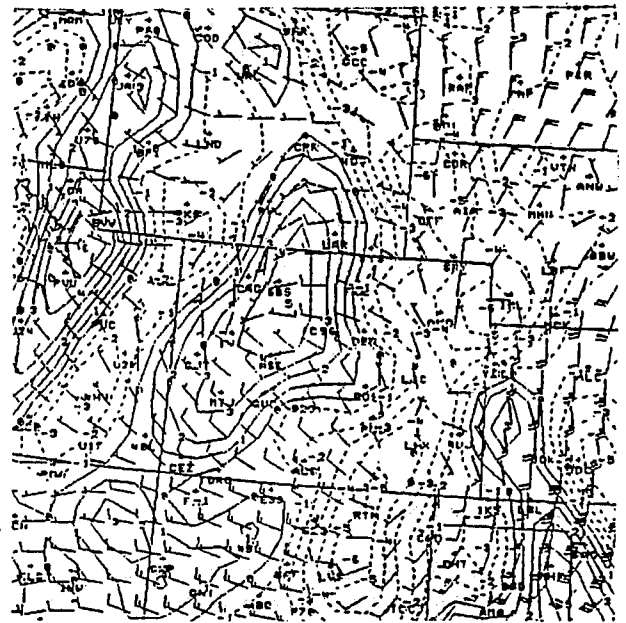
Fig. 10 MAPS forecast of 850 mb
   divergence and wind, valid
   1800 UTC 22 December, 1991.
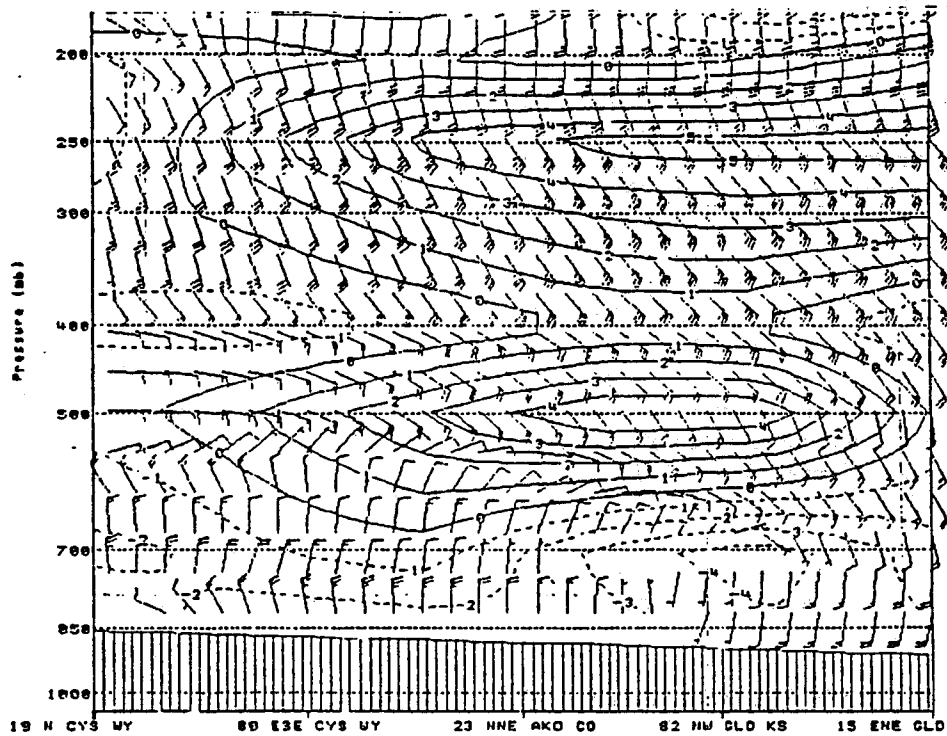
Fig. 11 MAPS forecast Cross-section from southeast Wyoming
   to northwest Kansas of wind and divergence, valid 1800 UTC
   22 December 1991.
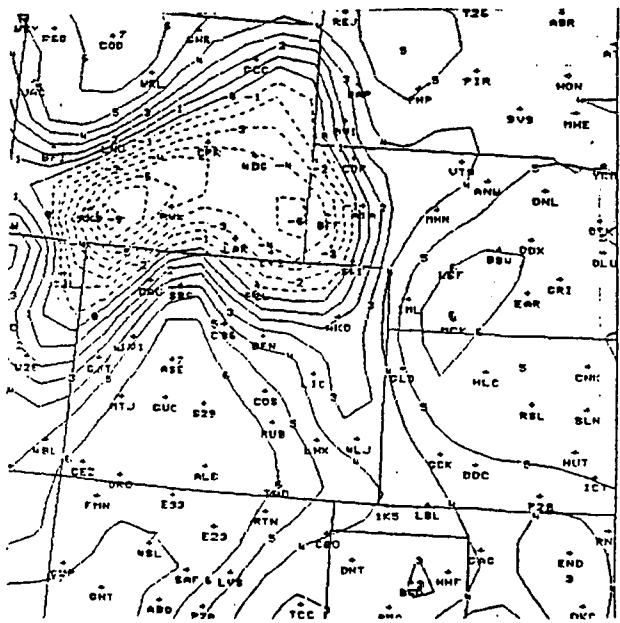
Fig. 12 MAPS forecast 850 mb
   lapse rate, valid 1800 UTC
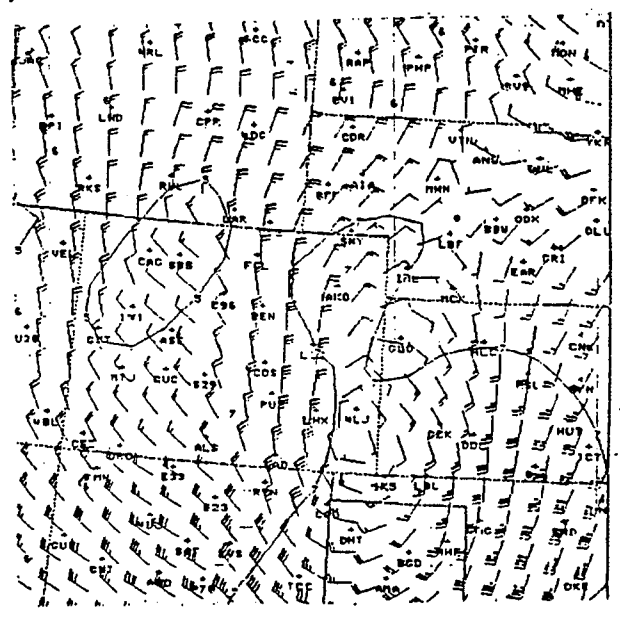   22 December, 1991.

Fig. 13 MAPS forecast of 700 mb
   wind and lapse rate, valid
   2100 UTC 22 December, 1991.
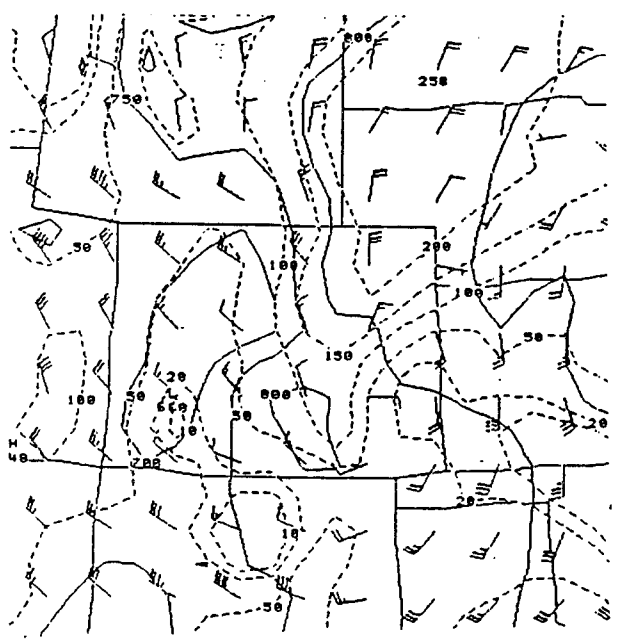
Fig. 14 MAPS forecast, 296K isentropic
   surface of pressure, wind and
   condensation pressure deficit,
   valid 1800 UTC 22 December 1991.
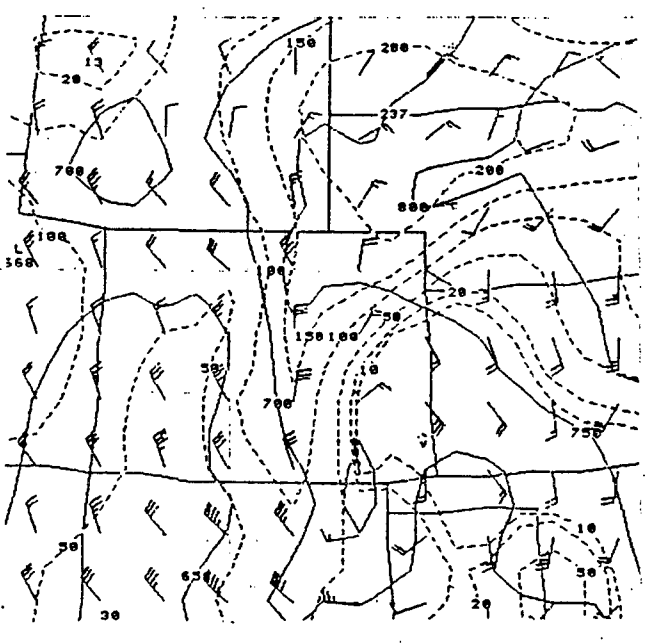
Fig. 15 MAPS forecast, 300K isentropic
   surface of pressure, wind, and
   condensation pressure deficit,
   valid 1800 UTC 22 December, 1991.
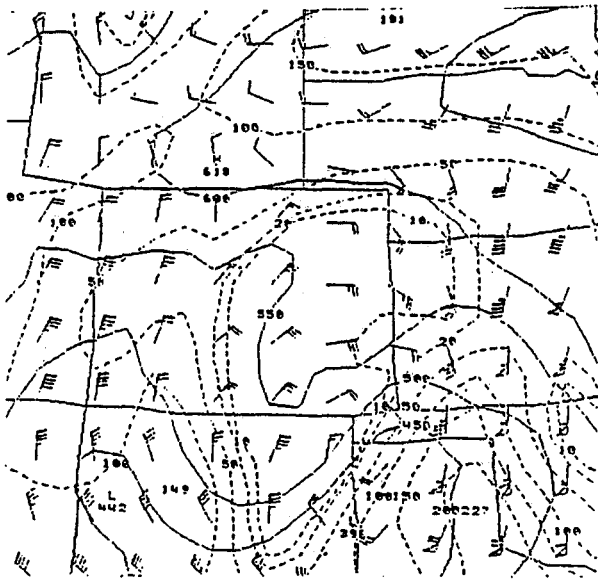
Fig. 16 MAPS forecast, 308K isentropic surface of pressure, wind, and condensation pressure deficit, valid 1800 UTC 22 December, 1991.
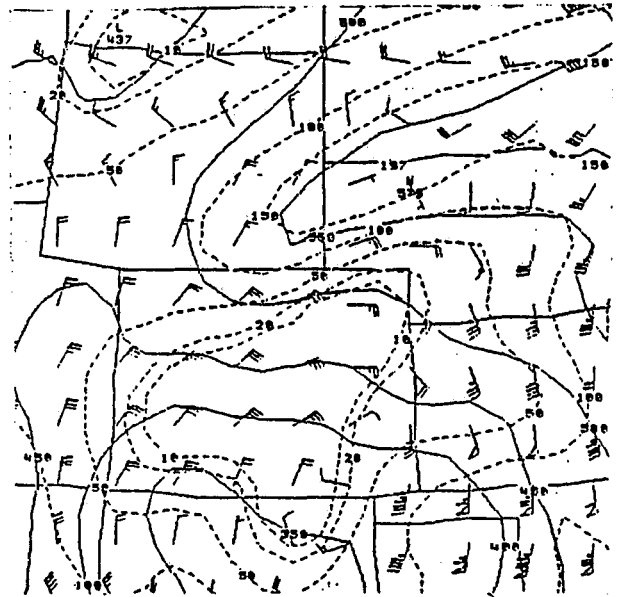
Fig. 17 MAPS forecast, 312K isentropic surface of pressure, wind, and condensation pressure deficit, valid 1800 UTC 22 December, 1991.
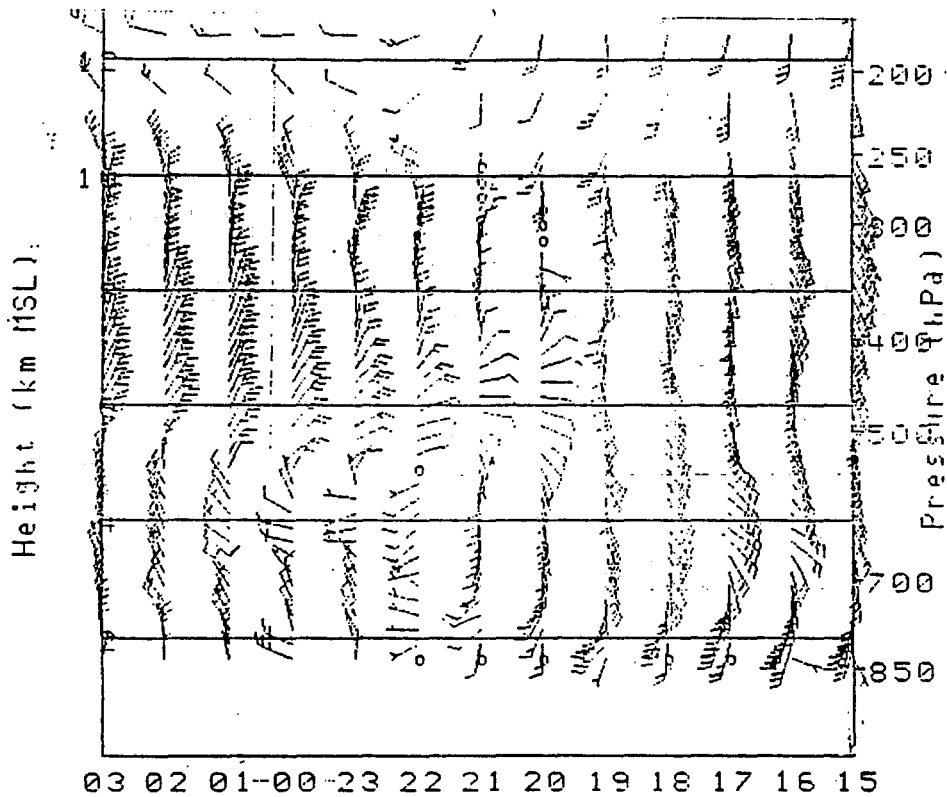
Fig. 18 Time-series, Granada Wind Profiler, 1500 UTC 22 December to 0300 UTC 23 December 1991.
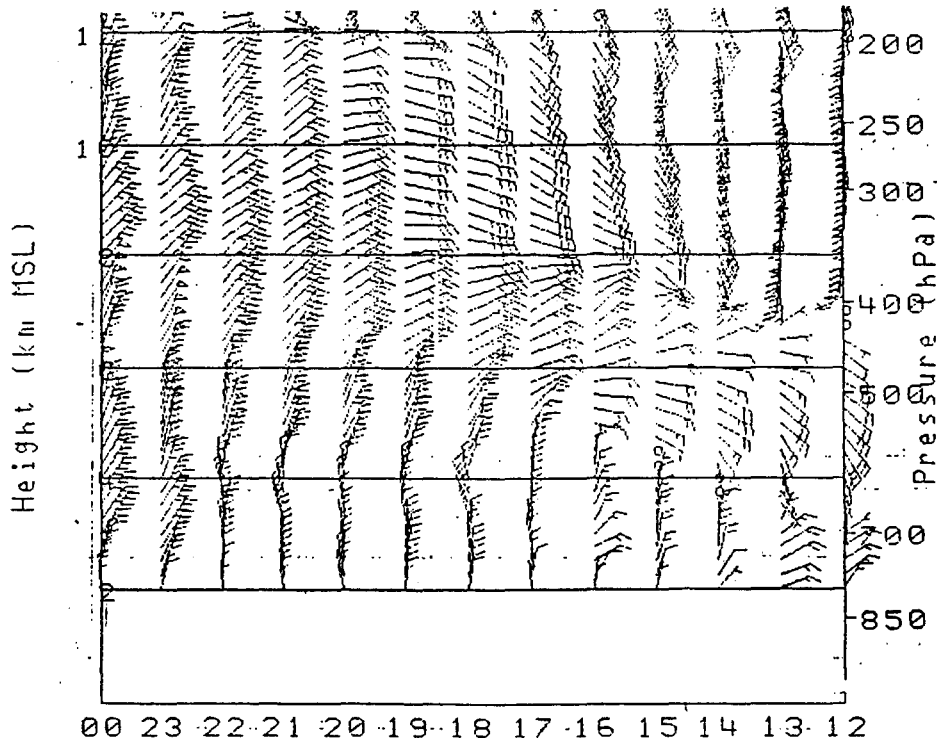
Fig. 19 Time series, Platteville Wind Profiler, 1200 UTC
22 December to 0000 UTC 23 December 1991.


```
AKO SA 0148 E35 BKN 80 OVC 20 168/32/22/3107/995
AKO SP 0128 E35 BKN 80 OVC 15 2910/994
AKO SA 0047 E25 BKN 60 OVC 15 157/30/26/2911/992
AKO SP 0030 E25 BKN 50 OVC 10 2911/991
AKO RS 2353 E10 OVC 3F 111/30/24/3610/989/SE43/ 31515 90402
AKO SP 2328 W4 X 1S-F 0215/989
AKO SA 2250 W2 X 1/4S+F 139/28/28/0414/986
AKO SA 2146 W4 X 1/2SF 117/32/27/0214/981
AKO SP 2105 W4 X 1/2SF 0414/981
AKO SA 2048 E9 OVC 1S-F 114/34/17/0510/981/SB04/ 500
AKO SP 2032 E9 OVC 1S-F 0314/981/SB04
AKO SP 2017 E15 OVC 2S-F 0412/980/SB04
AKO SP 2004 E25 OVC 10S- 0310/980/ SB04
AKO SA 1946 E50 BKN 100 OVC 20 101/36/17/0206/980
AKO SA 1849 E60 BKN 100 OVC 30 099/34/17/3507/979
AKO SA 1748 E80 BKN 120 OVC 30 105/35/18/3309/981/ 805 28
```

Table 1. Surface Observations at Akron,
Colorado (AKO) 1748 UTC 22 December 1991
through 0148 23 December 1991.
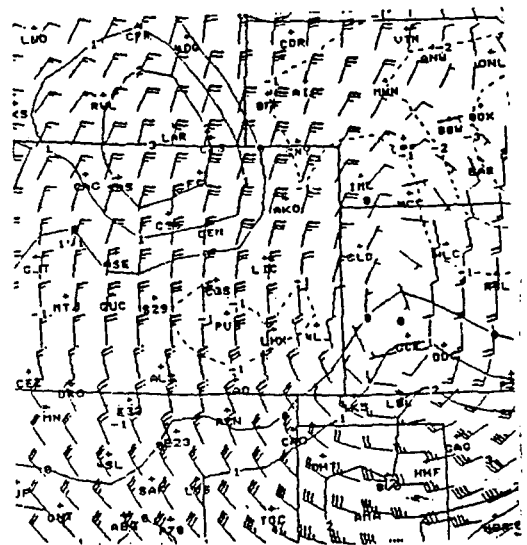
Fig. 20 MAPS analysis of 700 mb
divergence and wind, 0000 UTC
23 December, 1991.

OPERATIONAL USE OF AN OROGRAPHIC SNOW MODEL

Christopher Scott
National Weather Service
Cheyenne, Wyoming

1. Introduction

An orographic snow model has been used at the National Weather Service Forecast Office in Cheyenne, Wyoming since 1989. The model was designed by Mentzer and Berry (unpublished manuscript) to forecast snowfall amounts for the mountains of Wyoming. The model is uniquely adapted to the operational environment of the Cheyenne forecast office and uses the available weather service "AFOS" mini-computer and a personal computer for processing the model input.

2. Theoretical basis

Much of the theoretical basis of the model was derived from Harley (1965). Orographic forcing is expressed in the terrain dependent form of the "omega" equation as follows:

$$\omega_T = -g\rho_0 V \nabla_h \left(\frac{700}{p_0}\right)^{2.5} \qquad (1)$$

where:

ω_T = vertical motion in isobaric coordinates
g = acceleration due to gravity
ρ_0 = density at the surface (850 mb)
V = velocity vector
∇_h = gradient of the terrain slope
p_0 = pressure at the surface (850 mb)

The precipitation rate is a function of vertical motion and saturated ascent as follows:

$$P_r = K \sum \frac{T_v}{g L_v} \overline{\omega} (\Delta S_a)_{\theta \omega} \qquad (2)$$

where

P_r = the rate of precipitation
K = constant for unit conversion
T_v = virtual temperature
L_v = latent heat of vaporization
$(\Delta S)_{\theta \omega}$ = entropy decrease along a pseudo-adiabatic surface of virtual temperature T_v

other symbols as equation (1)

For simplicity of calculations precipitable water is calculated from the following regression equation:

$$W_p = .70(a_1 D_m + a_2 HH + a_3) \qquad (3)$$

where

W_p = precipitable water
D_m = moisture depth in feet
HH = thickness in geo-potential meters
a_n = regression constants
.70 = empirical adjustment for heights above 4500 feet

Then the rate of precipitation is calculated from another regression equation of the form:

$$P_r = b_1 \omega_T + b_2 W_p + b_3 \qquad (4)$$

where

b_n = regression constants and other symbols are as before

In summary the model input required includes the u and v components of the horizontal wind, the terrain's elevation, the surface moisture depth (i. e. above 850 mb), 1000-500 mb thickness, and relative humidity in the troposphere as a test of saturation.

2

3. Operational Use of the model

To use the model operationally, the forecaster is first required to run an application on AFOS which creates a matrix based on National Meteorological Center (NMC) numerical guidance. The output is shown in figure 1. Locations correspond to the NMC Winds Aloft forecast points for Wyoming and surrounding states (FDUW01, FDUW03, FDUW05, FDUM01, FDUM03, and FDUM05). Numerical output is interpolated as necessary. Columns represent 6, 18 and 30 hour forecasts of each element. A key feature of the matrix is that input elements may be manipulated by the forecaster before the model is run. Once the matrix has been created and modified, it sent to a personal computer and included as input for the actual model processing.

DATA FOR SNOWFALL INPUT

	WINDS		WINDS		WINDS		UVV	UVV	UVV	RH	RH	RH	HH	HH	HH
PIH	2720	-02	2924	-01	3127	-10	0.7	0.2	-0.7	29	38	28	551	543	542
BIL	2617	-08	2822	-06	3126	-12	0.5	0.8	-0.3	49	87	85	540	530	525
DLN	2722	-07	2828	-06	3323	-13	2.1	0.9	-0.3	66	92	54	533	527	530
SLC	2717	03	3020	05	3122	-03	0.8	0.5	-0.4	41	32	16	560	554	551
CZI	2618	-04	2822	-02	2931	-10	0.0	0.2	0.2	42	71	74	550	542	534
LND	2721	-01	2825	01	2929	-09	0.4	0.1	-0.2	33	41	33	555	548	544
MBW	2724	03	2821	04	2931	-02	-0.5	-0.4	0.8	35	56	63	560	554	544
RKS	2720	03	2825	05	2927	-03	0.2	0.1	0.2	38	44	39	560	554	547
BFF	2625	03	2618	04	2830	-02	0.1	0.0	-0.5	39	54	64	557	551	539
RAP	2419	-04	2621	-04	2724	-06	0.6	1.4	-1.1	53	66	80	546	541	529

Figure 1. Output matrix from AFOS compilation program. UVV is calculated upward vertical velocity (cms^{-2}) at 700 mb. RH is mean tropospheric relative humidity. HH is 1000-500 mb thickness in geo-potential meters. (see text for further description).

At the personal computer the model has been gridded for Wyoming terrain. Further forecaster input includes an estimate of the moisture depth above the 850 mb "surface" and the duration of the conditions. During processing synoptic and orographic upward vertical motion are added together, a snowfall/precipitation ratio of 10:1 is assumed, and no snowfall is predicted if grid temperature is greater than 4 degrees Celsius or mean relative humidity is less than 70 percent. Saturation is assumed to be 85 percent with linear interpolation of intermediate values.

The output is in both gridded and graphical form. Due to limitations of available equipment, a data file is sent to AFOS where a contour map of predicted snowfall is created.

Limitations of the model which need to be taken into account when subjectively analyzing the output include the following:

1. Input is fixed during the entire 12 hour forecast period.
2. Parameterization of precipitation rate is statistical.
3. Interpolation is grid to grid with no objective scheme.
4. Due to linear assumptions of input equations the model over-forecasts snowfall for steep slopes and under-forecasts for very gentle slopes.
5. A 10:1 snowfall/precipitation ratio is always assumed.
6. Any forcing besides orographic is either not accounted for or is indirectly implied from upward vertical velocity calculations from NMC numerical output.

4. Comparison of Model Output to an Actual Case

The example used for verification of the model is from November 5, 1990. Figure 2a is a contour map of the forecast model output between 05 Nov 1990 0000-1200 UCT. Figure 2b represents actual measured snowfall for the same period or estimates of snowfall from United States Soil Conservation snow course water equivalent measurements. Figures 3a, 3b, are constant pressure analyses for 500 and 700 mb levels at 05 November 1990 00 UCT. The snow model predicted the snowfall for mountains in far west Wyoming fairly well. It under-forecast the snowfall in Jackson Hole (12 inch maximum figure 2b) and did not forecast the snowfall as far east as actually occurred. The under-forecast was possibly related to the gentle terrain of Jackson Hole, while grid interpolation problems may have accounted for the eastward limit of the model forecast.

5. Summary and Conclusions

The orographic snow model presented here has proven to be a good first guess of predicted snowfall. The operational forecaster has been able to focus on locations where significant snowfall may occur and to provide a better delimitation for issuing heavy snow forecasts. One subjective observation has been the sensitivity to relative humidity in situations of strong westerly flow. An all or nothing scenario is created both in the model and in reality, depending on the forecast or observed relative humidity. Anyone interested in obtaining the model on floppy disk may contact the author at 307-772-2468. Instructions will also be provided for gridding terrain.

3. Operational Use of the model

To use the model operationally, the forecaster is first required to run an application on AFOS which creates a matrix based on National Meteorological Center (NMC) numerical guidance. The output is shown in figure 1. Locations correspond to the NMC Winds Aloft forecast points for Wyoming and surrounding states (FDUW01, FDUW03, FDUW05, FDUM01, FDUM03, and FDUM05). Numerical output is interpolated as necessary. Columns represent 6, 18 and 30 hour forecasts of each element. A key feature of the matrix is that input elements may be manipulated by the forecaster before the model is run. Once the matrix has been created and modified, it sent to a personal computer and included as input for the actual model processing.

```
DATA FOR SNOWFALL INPUT
      WINDS      WINDS      WINDS      UVV  UVV  UVV  RH  RH  RH  HH  HH  HH
PIH  2720 -02  2924 -01  3127 -10    0.7  0.2 -0.7  29  38  28 551 543 542
BIL  2617 -08  2822 -06  3126 -12    0.5  0.8 -0.3  49  87  85 540 530 525
DLN  2722 -07  2828 -06  3323 -13    2.1  0.9 -0.3  66  92  54 533 527 530
SLC  2717  03  3020  05  3122 -03    0.8  0.5 -0.4  41  32  16 560 554 551
CZI  2618 -04  2822 -02  2931 -10    0.0  0.2  0.2  42  71  74 550 542 534
LND  2721 -01  2825  01  2929 -09    0.4  0.1 -0.2  33  41  33 555 548 544
MBW  2724  03  2821  04  2931 -02   -0.5 -0.4  0.8  35  56  63 560 554 544
RKS  2720  03  2825  05  2927 -03    0.2  0.1  0.2  38  44  39 560 554 547
BFF  2625  03  2618  04  2830 -02    0.1  0.0 -0.5  39  54  64 557 551 539
RAP  2419 -04  2621 -04  2724 -06    0.6  1.4 -1.1  53  66  80 546 541 529
```

Figure 1. Output matrix from AFOS compilation program. UVV is calculated upward vertical velocity (cms^{-2}) at 700 mb. RH is mean tropospheric relative humidity. HH is 1000-500 mb thickness in geo-potential meters. (see text for further description).

At the personal computer the model has been gridded for Wyoming terrain. Further forecaster input includes an estimate of the moisture depth above the 850 mb "surface" and the duration of the conditions. During processing synoptic and orographic upward vertical motion are added together, a snowfall/ precipitation ratio of 10:1 is assumed, and no snowfall is predicted if grid temperature is greater than 4 degrees Celsius or mean relative humidity is less than 70 percent. Saturation is assumed to be 85 percent with linear interpolation of inter- mediate values.

The output is in both gridded and graphical form. Due to limitations of available equipment, a data file is sent to AFOS where a contour map of predicted snowfall is created.

3

Limitations of the model which need to be taken into account when subjectively analyzing the output include the following:

1. Input is fixed during the entire 12 hour forecast period.
2. Parameterization of precipitation rate is statistical.
3. Interpolation is grid to grid with no objective scheme.
4. Due to linear assumptions of input equations the model over-forecasts snowfall for steep slopes and under-forecasts for very gentle slopes.
5. A 10:1 snowfall/precipitation ratio is always assumed.
6. Any forcing besides orographic is either not accounted for or is indirectly implied from upward vertical velocity calculations from NMC numerical output.

4. Comparison of Model Output to an Actual Case

The example used for verification of the model is from November 5, 1990. Figure 2a is a contour map of the forecast model output between 05 Nov 1990 0000-1200 UCT. Figure 2b represents actual measured snowfall for the same period or estimates of snowfall from United States Soil Conservation snow course water equivalent measurements. Figures 3a, 3b, are constant pressure analyses for 500 and 700 mb levels at 05 November 1990 00 UCT. The snow model predicted the snowfall for mountains in far west Wyoming fairly well. It under-forecast the snowfall in Jackson Hole (12 inch maximum figure 2b) and did not forecast the snowfall as far east as actually occurred. The under-forecast was possibly related to the gentle terrain of Jackson Hole, while grid interpolation problems may have accounted for the eastward limit of the model forecast.

5. Summary and Conclusions

The orographic snow model presented here has proven to be a good first guess of predicted snowfall. The operational forecaster has been able to focus on locations where significant snowfall may occur and to provide a better delimitation for issuing heavy snow forecasts. One subjective observation has been the sensitivity to relative humidity in situations of strong westerly flow. An all or nothing scenario is created both in the model and in reality, depending on the forecast or observed relative humidity. Anyone interested in obtaining the model on floppy disk may contact the author at 307-772-2468. Instructions will also be provided for gridding terrain.
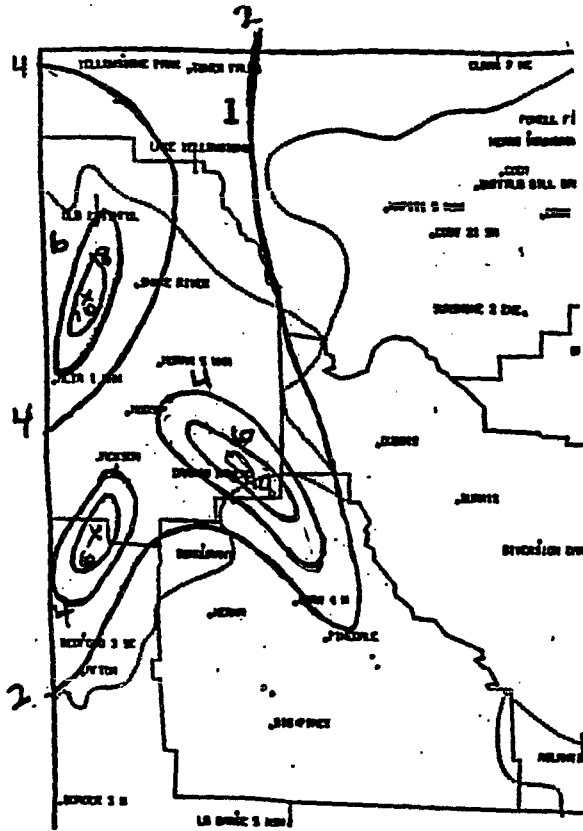
Figure 2a. Model forecast snow amounts for 05 Nov 90 00 UCT - 12 UCT.
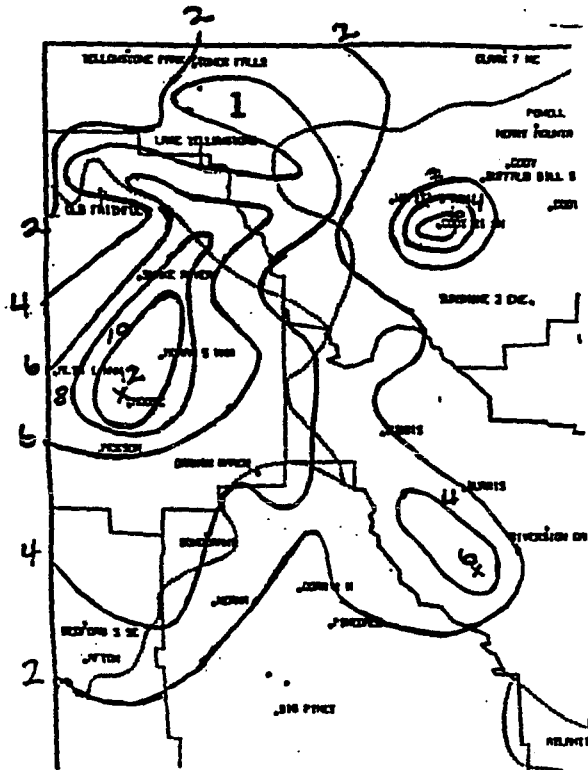(Isohytes in two inch intervals).

Figure 2b. Actual snowfall amounts (analysis as figure 2a).

Figure 3a. 500 mb (50Kpa) constant pressure analysis for 05 Nov 1990, 00 UCT. Solid lines are intervals of 60 geo-potential meters. Dashed lines are intervals of 5 deg. C. Shading indicates areas of dew point depression 5 deg. C. or less.

Figure 3b. 700 mb (70Kpa) constant pressure chart. Solid lines are intervals of 30 geo-potential meters. The remainder of the analysis is as 3a.

6

Acknowledgements:

References:

Harley, W. S., 1965: An Operational Method for Quantitative Precipitation Forecasting. J. of Appl Meteor, 4, 305-319.

Mentzer, S. and Berry, E.: An Operational Snowfall Model for Wyoming. (Unpublished Manuscript, copy available from The National Weather Service Forecast Office, 4000 Morrie Avenue, Cheyenne, Wyoming, 82001.)

Operational Use of an Orographic Precipitation Model

Pamela Speers Hayes

Abstract

A simple orographic precipitation model designed for the Pacific Northwest is presented. The model assumes that precipitation is proportional to vertical velocity. Vertical velocities are calculated from the surface windfield generated by the Mass and Dempsey (1985) windflow model and from an imposed geostrophic windfield. The model uses simple parameterizations to account for areal moisture differences that result from the trajectory of weather systems or from the Cascade Mountains acting as a west to east moisture barrier. Output from the NGM model runs is used to initialize the windflow and precipitation models. The precipitation model was used operationally at the Northwest Avalanche Center during the second half of the 1990-91 and 91-92 forecast seasons. Although model output generally produced good results, there are two principle limitations to the accuracy of model forecast precipitation. The precipitation calculations are very dependent on terrain and on the surface wind. The use of more realistic terrain data and a three-dimensional wind model might significantly improve the precipitation model results.

1. INTRODUCTION

An orographic precipitation model was developed to provide forecasters' at the Northwest Avalanche Center in Seattle, Washington with an objective aid for quantitative precipitation forecasts. The Washington State Department of Transportation and the United States Forest Service granted funding for model development.

The Mass and Dempsey windflow model provides the surface windfield for the orographic precipitation model. Precipitation is assumed to be proportional to vertical velocity. A vertical velocity field is calculated from the Mass and Dempsey surface windfield and from an imposed large scale windfield. A relatively simple precipitation parameterization is employed.

The topography for model runs is based on terrain data from the National Center for Atmospheric Research. The original point data, recorded at 30 second intervals, was averaged to produce a 7.5 km by 7.4 km grid that extends from 45-50 N latitude and 119-126.4 W longitude.

850 mb and 700 mb level height and temperature gridded data from the National Weather Service Nested Grid Model (NGM) are automatically transferred twice daily from the University of Washington Department of Atmospheric Sciences. Mandatory level data from the 00 Z and 12 Z Quillayute, WA and Salem, OR soundings as well as forecast relative humidity data for Salem, OR, Seattle, WA and Vancouver, B.C. from the NGM model are transferred from the National Weather Service AFOS system. To run the precipitation model, a forecaster simply types one command and then answers a series of questions. This process takes about 1 minute to complete. The model requires approximately 20 minutes to run on a

386 computer equiped with a Weitek math coprocessor. Model results
for 28 stations, including precipitation quantities and wind
direction and speed are automatically printed out for each model
run.

2. MODEL DESCRIPTION

The orographic precipitation model uses surface winds from the
Mass-Dempsey wind model and upper level winds from an imposed
geostrphic windfield to calculate vertical velocities, which are
proportional to precipitation.

Mass and Dempsey Wind Model

The Mass and Dempsey wind model calculates surface wind and
temperature by integrating the horizontal momentum equation and
surface temperature tendency equation in sigma coordinates using a
second-order Adam's Bashforth scheme. The horizontal momentum
equation includes terms for advection, Coriolis acceleration, the
pressure gradient force, frictional drag and horizontal diffusion.
Changes in surface temperature occur by temperature advection,
adiabatic heating and cooling in response to changes in surface
pressure, diabatic heating and cooling, and horizontal diffusion.
Surface pressure, an unknown in both equations, is calculated by
integrating the hydrostatic equation between the surface and
reference pressure level (850 mb).
Model initialization requires the geopotential height and
temperature taken from a reference level (850 mb), and the free
atmosphere lapse rate between 850 and 700 mb taken from a sounding
near the inflow boundary. Gridded data from the National
Meteorological Center Nested Grid Model (NGM) provides geopotential
height and temperature input data. The model currently runs on
analysis data or on the 6, 12, 18, or 24 hour prognoses. The free
atmosphere lapse rate is taken from the Quillayute, WA sounding or
from gridded data at 47.5 N latitude and 125 W longitude.
The model equations are integrated to steady state using a
time step of 180 seconds, requiring approximately 240 time steps.
The model is run on a 75 by 74 point grid with a 7.5 km resolution.
Although a higher resolution would be preferable for the
precipitation model, the hydrostatic balance assumed for the wind
model by Mass and Dempsey limits the possible grid length
reduction. Model initialization and integration requires
approximately 20 minutes on a 25 or 33 mHz 386 personal computer
equiped with a Weitek math coprocessor if the average tendencies of
the wind components are required to fall below .00003 m/s.
The wind model is initially run with 25 geopotential heights
and temperatures as input. If the average tendencies of the wind
components do not converge, the wind model is rerun with the
average geopotential height and temperature gradient along a north-
south line at 125 W longitude from 45-50 N latitude. If a front
exists diagonally across this line, the average tendencies of the
wind components will again not converge, and the model run is
aborted.

Precipitation Model Description

The orographic precipitation model addition to the Mass-Dempsey wind model assumes that precipitation is proportional to vertical velocity.

Vertical Velocity Calculation

The model vertical velocity can be decomposed into three individual vertical velocity components; 1) the slope induced vertical velocity, which is the vertical component of the wind vectors from the Mass-Dempsey wind model, 2) convergence vertical velocity, again from the wind model, and 3) an imposed wind field vertical velocity, which is the vertical component of a separate geostrophic windfield imposed on the model terrain.

1) The Mass-Dempsey sigma coordinate model produces a slope parallel surface wind field. The vertical components of the wind vectors are calculated at each grid point in the domain using a method similar to Danard's.

2) The vertical velocity from convergence is calculated using the velocity divergence form of the continuity equation.

$$\frac{1}{\rho} \frac{d\rho}{dt} + \nabla \cdot U = 0 \qquad (1)$$

Expanding $\nabla \cdot U$ and assuming incompressibility gives

$$\frac{\partial w}{\partial z} = -\left(\frac{\partial u}{\partial x} + \frac{\partial v}{\partial y}\right) \qquad (2)$$

where $\partial w / \partial z$ is the vertical velocity at the surface from convergence. $\partial u / \partial x + \partial v / \partial y$ are calculated from the u and v wind components generated by the Mass-Dempsey model. Surface wind convergence is assumed to decrease linearly with height (H), becoming zero when H is 2000 meters above the topography. This figure was chosen because it is consistent with the 2000 meter topographic influence assumption in the Mass-Dempsey wind model. The component of the vertical velocity from convergence is found by integrating $\partial w / \partial z$ from the surface upward 2000 meters.

3) The winds produced by the Mass-Dempsey model result from the interaction of the surface flow with complex terrain. In high elevation terrain, momentum from higher levels in the atmosphere is also felt; therefore, a separate wind field representing the large scale flow is imposed on the model terrain.

The large scale wind field has a constant wind direction with height calculated by averaging the direction of the 850 and 700 mb level winds either from the Quillayute sounding or from the gridded data centered at 47.5 N latitude and 125 W longitude.

The variation of wind speed with height, which is case dependent, fits the vertical wind profile measured by the radiosonde ascent for analysis runs and calculated from the gridded data for prognosis runs. In order to eliminate the effect of the surface flow from the large scale windfield, the surface wind speed is subtracted at all levels from the vertical wind speed profile. At each grid point, a wind speed that depends on grid point elevation is assigned. The vertical components of the wind vector are then calculated.

The imposed windfield vertical velocity calculation is performed on a 15 x 15 km terrain grid with the wind vector

3

normally 3.75 km inside the upwind terrain boundary; however, when significant convection is expected, the model is run with the wind vector centered in the 15 x 15 km terrain grid.

Downward motion on the lee side of a barrier is typically less than the vertical velocities on the windward side, especially when the airmass involved is neutral or slightly stable. A strong inversion often exists east of the Washington Cascades during the winter. The associated very stable cold air inhibits downward motion. To account for these factors and to compensate for the lack of three-dimensionality in the model, negative components of vertical velocity are divided by 4 before the total vertical velocity in each grid point is summed. The value 4 was selected based on statistical analyses of model results. This factor would be expected to produce the best results during relatively two-dimensional flow patterns involving slightly stable airmasses. It does less well when; 1) a deep layer of cold air exists east of the Cascades, in which case air moving eastward across the Cascades experiences little or no downward motion, or 2) the airmass is unstable.

Precipitation Parameterization

In the model, precipitation is assumed to be directly proportional to vertical velocity. A simple precipitation parameterization scheme is employed.

Condensation, ie, the amount of water (in meters) condensed out in lifting an air parcel from the surface upward 1500 m, is given by:

$$c = W_{total} \cdot \frac{dq_s}{dz} \cdot D \cdot t \qquad (3)$$

where W_{total} is the total vertical velocity, dq_s/dz is the change in saturated mixing ratio with height, D (1500 m) is the depth of the lifted airmass and t is the length of time that the airmass is lifted. Hill et al concluded that 80% of the orographic enhancement of precipitation occurs within 1500 meters above the terrain. Although D equals 1500 meters in the model, the actual value of D is not critical because it is a constant. t varies from case to case depending on the expected duration of precipitation. dq_s/dz is calculated using:

$$\frac{dq_s}{dz} = \left(\Gamma_m - \Gamma_d \right) \frac{c_p}{L} \qquad (4)$$

where c_p is the specific heat of dry air at constant pressure, L is the latent heat of vaporization, and Γ_m and Γ_d are the moist and dry lapse rates, respectively.

. The saturated mixing ratio often varies significantly from north to south depending on many factors, including the trajectory of weather systems. To allow for north-south moisture differences, dq_s/dz is varied linearly south to north based on gridded data at 45 N, 47.5 N and 50 N latitude.

The airmass is lifted dry adiabatically until saturation is reached. For analysis runs, the 850 mb temperatures and dew point depressions for Salem and Quillayute are used to calculate the amount of lifting necessary to reach saturation. Based on the

values for these two stations, the amount of lifting required to reach saturation is altered north-south through the model's domain. A similar approach is used for the prognosis runs; however, since specific dew point depression data is not available, NGM generated relative humidity forecasts corresponding to the time of the model run provide equivalent information.

If all of the precipitation that forms falls in the same grid where it is generated, precipitation (P) equals:

$$P_T = C \times E_1 + P_s \qquad (5)$$

assuming a constant condensation to precipitation efficiency (E_1). E_1 equals .5. P_s is the synoptic precipitation term, ie, the amount of precipitation that would be expected if the terrain were flat or if precipitation were measured over the ocean.

Under strong wind conditions, or in winter when precipitation may fall as snow, it is unrealistic to assume that all precipitation falls vertically to the ground. In addition, small ice crystals or water droplets may be carried considerable distances downwind before they precipitate or evaporate. To account for particle fall trajectories and non-precipitating cloud droplets, a constant percentage of the condensation (R) in each grid is carried to the next grid downwind where it is combined with the condensation generated at that grid point. R is calculated as follows:

$$R = (C - C \times E_1) \times E_2 \qquad (6)$$

E_2 is the condensation carrying efficiency, defined as the percentage of remaining condensate that is carried by the wind to the next grid downwind. E_2 is given a value of .75. Although the actual downwind transport of condensation is dependent on the wind speed and temperature, suggesting that E_2 should be varied from case to case, the total precipitation calculation is not very sensitive to the value of E_2. Taking account of R, precipitation equals:

$$P_T = E_1(C + R) + P_s \qquad (7)$$

The precipitation calculation starts at the upwind border of the domain and progresses in the direction of the large scale flow.

Thus far, the precipitation calculation assumes that the amount of moisture available for precipitation is constant west to east across the domain. For SSW to NNW wind directions, the Cascades act as an efficient moisture barrier, with the saturated mixing ratio decreasing as an airmass moves eastward. To compensate for decreasing moisture availability, F, a moisture depletion factor, is included in the precipitation calculation.

100% of generated condensation is carried from the model's western domain boundary to the foothills of the Cascades. Condensation decreases by 67% between the western and eastern Cascade foothills, and then remains at 33% of its original value to the eastern domain boundary.

Although the rain shadow in the lee of the Olympic Mountains shifts with wind direction, the Olympics were not included in the moisture depletion factor for two reasons. 1) There are relatively few stations recording precipitation around the Olympic Mountains.

making it difficult to determine an empirical factor. 2) Negative
vertical velocities from the imposed large scale wind field
effectively account for the rain shadow.

3. MODEL SIMULATIONS

The period from March 7th through March 24th 1991 produced a
wide variation in synoptic weather, with the upper level flow
ranging from northerly counterclockwise through southeasterly. Two
case studies, March 7 and March 12, are presented. The
precipitation model was additionally run at 12 hour intervals for
the entire period with total observed precipitation for 19 stations
compared to model precipitation.

CASE 1: 00 GMT MARCH 7, 1991, NORTH-NORTHWESTERLY LARGE-
        SCALE FLOW

At 00 GMT on March 7th, an upper-level ridge of high pressure
existed over southeast Alaska and northern British Columbia with a
north-northwesterly flow aloft over Washington and Oregon. The
corresponding 850 mb level analysis is presented in Figure 1.

The sounding for 00 GMT March 7th at Quillayute is shown in
Figure 2. The sounding is nearly saturated at 900 mb, but is
relatively dry above that.

The observed precipitation for the 24 hour period ending at 12
GMT March 7th and the corresponding model generated precipitation
are given in Table 1. The model was run for 5 hours with no
synoptic precipitation. The model reproduced the nearly 1 inch of
precipitation that fell at Paradise on Mt. Rainier while most other
stations received .1 inches or less. The model did less well for
Mt Hood Meadows and Government Camp, both in the Mt. Hood area.
Observed precipitation for these stations measured .20 and .34
inches whereas the model generated less than .1 inches. At Mt.
Hood Meadows, the model's surface winds, which did not match the
observed winds, account for the error. The model winds diverged
and were downslope, which produced a negative vertical velocity.
Although an upslope surface wind at Government Camp dominated the
vertical velocity calculation, it was too weak to produce
precipitation to match the observation.

CASE 2: 00 GMT MARCH 12, 1991, MOIST SOUTHWESTERLY FLOW

At 00 GMT March 12th, the upper level flow was characterized
by a trof of low pressure centered off the west coast along 135 W
longitude with a moist southwesterly flow moving through Oregon and
Washington. A weak upper level ridge existed along 120 W longitude
primarily in Oregon and California. The 850 mb analysis (Fig. 3)
shows a closed low over and west of Vancouver Island with a trof
extending south from the low along 130 W longitude. The Quillayute
sounding had a nearly saturated adiabatic lapse rate from the
surface to 600 mb (Figure 4).

The imposed large scale wind field taken from the Quillayute
sounding is shown in Figure 5. 25 kt or greater winds occurred at
all levels above the surface, with the winds at the 850 mb level
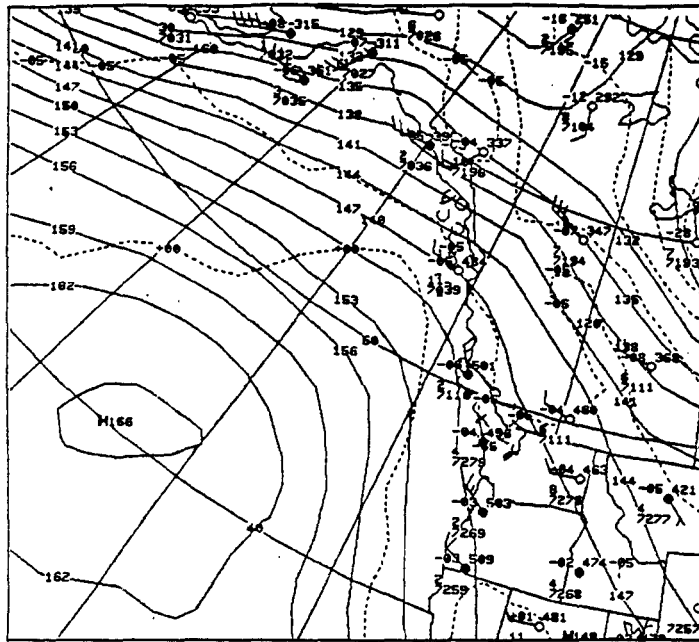stronger than those at 700 mbs.

6

Figure 1. NMC 850 mb height and temperature analysis for
00 GMT March 7, 1991. Height contours (solid
lines) are drawn at 30 m intervals and are
labeled in tens of meters: temperature contours
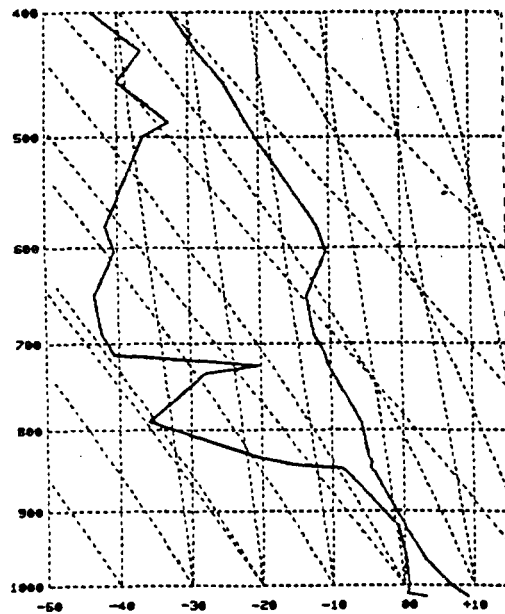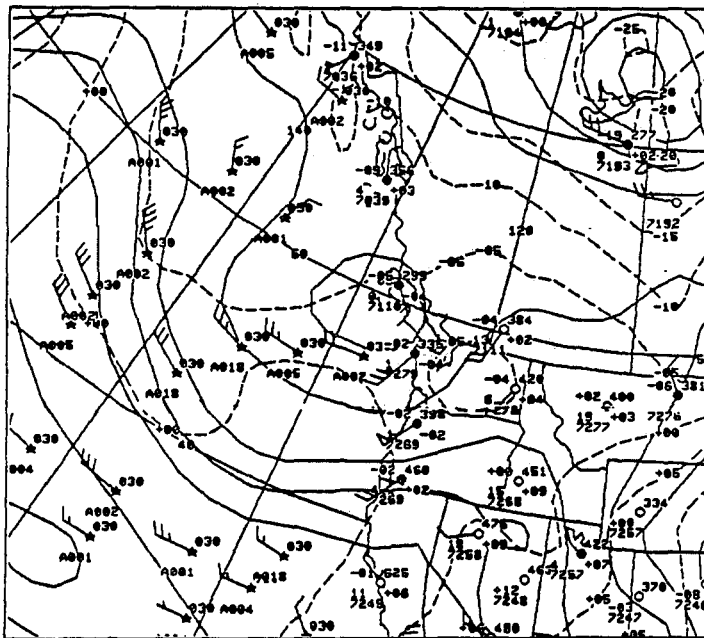(dashed lines) are labeled in degrees Celsius.

Figure 2. Quillayute, Washington radiosonde sounding for 00
GMT March 7, 1991.

7

TABLE 1 Observed (OBS) and model (MODEL) predicted
        precipitation for 19 sites in western Washington
        and Oregon for 00 GMT March 7, 1991.

STATION NAME	OBS PRECIP	MODEL PRECIP
Mt Baker	0.00"	0.00"
Stevens Pass	0.00"	0.06"
Mission Ridge	0.00"	0.12"
Snoqualmie Pass	0.00"	0.00"
Crystal Mountain	0.01"	0.08"
Paradise/Mt. Rainier	0.95"	0.98"
White Pass	0.00"	0.07"
Mt. Hood Meadows	0.20"	0.00"
Government Camp	0.34"	0.09"
Stampede Pass	0.10"	0.01"
Quillayute	0.04"	0.03"
Astoria	0.13"	0.02"
Bellingham	0.00"	0.02"
Seattle	0.00"	0.00"
Tacoma	0.01"	0.04"
Olympia	0.03"	0.09"
Portland	0.09"	0.05"
Wenatchee	0.00"	0.00"
Yakima	0.00"	0.00"

Figure 3. NMC 850 mb height and temperature analysis for
           00 GMT March 12, 1991. Height contours (solid
           lines) are drawn at 30 m intervals and are
           labeled in tens of meters; temperature contours
           (dashed lines) are labeled in degrees Celsius.

8
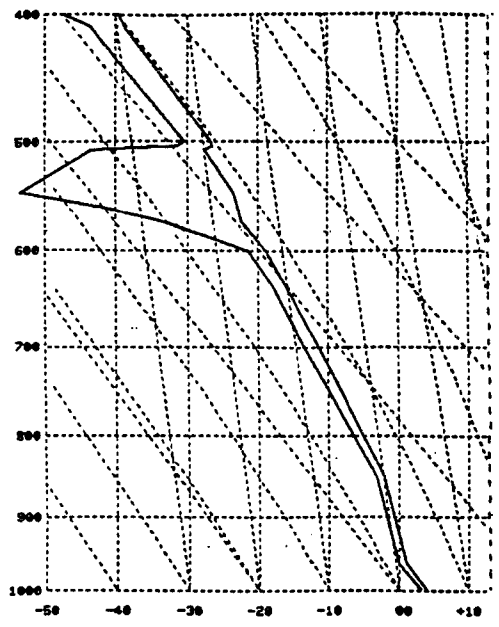
Figure 4. Quillayute, Washington radiosonde sounding for
00 GMT March 12, 1991.
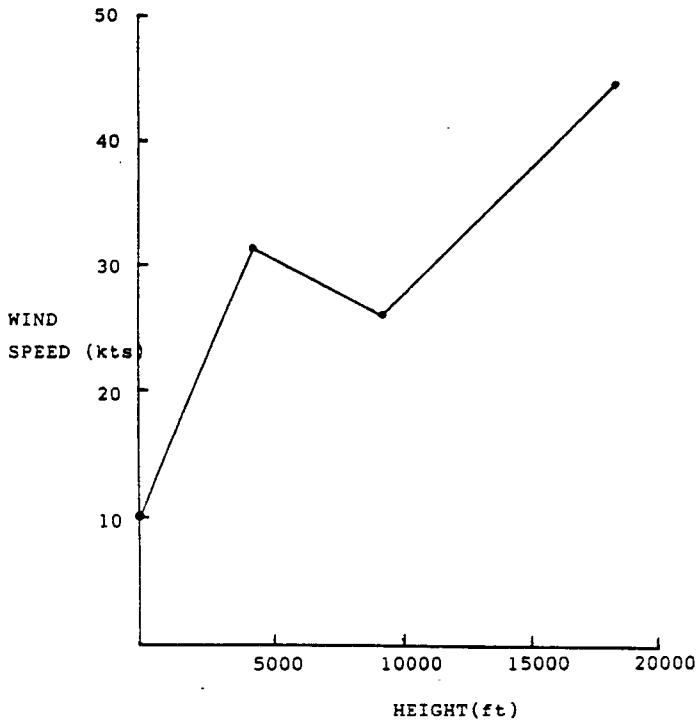
Figure 5. Wind speed as a function of height for the
Quillayute, WA radiosonde sounding for 00 GMT
March 12, 1991.

9

Model generated and observed precipitation for the 24 hour period ending at 12 GMT March 12th are compared in Table 2. The precipitation model was run for 6 hours with a .04"/hr synoptic precipitation rate. For most stations, model and observed precipitation compare favorably, with the model essentially duplicating the precipitation that fell at the following stations: 1.58" at Paradise, .52" at Snoqualmie Pass, .33" at Mt Baker Ski Area and .28" at Olympia.

Significant differences occur in the Mt. Hood area where Mt. Hood Meadows and Government Camp measured .98 and .87 inches of precipitation respectively, whereas the model only generated .18 and .53 inches. Two factors may explain this discrepancy. First, the imposed wind field is derived from the Quillayute sounding; however, in this case, the 850 mb level winds from the Salem sounding were significantly stronger than Quillayute's 850 mb winds (55 kts/32 kts). Had Salem's winds been used for the imposed wind field in the south, the Mt. Hood area would have received substantially more precipitation. Second, the model surface winds at Mt. Hood Meadows were southeast 17 kts. For this wind direction, the terrain produced a strongly negative vertical velocity which factored significantly in the total vertical velocity calculation. The observed winds at Mt Hood Meadows measured southwest 22 kts. Southwest winds would have produced strong positive vertical velocities which would have resulted in a more accurate precipitation forecast.

The model also underpredicted precipitation along the Pacific coast, especially at Astoria where measured precipitation was 1.17 inches compared with the model's .29 inches. This is a consistent problem with the precipitation model where little slope induced vertical velocity results from either the Mass-Dempsey surface windfield or from the imposed windfield. The Mass-Dempsey wind model produces frictional convergence along the coast as the airflow moves from water onto land. At Astoria, the total vertical velocity for this case results almost exclusively from convergence (97%); however, the magnitude is insufficient to account for the relatively heavy precipitation.

The model overestimated precipitation at Yakima and Wenatchee in spite of decreasing the moisture available for condensation by 67%. Although Yakima's surface winds were only 9 kts from the southeast, the terrain configuration produced upslope winds for both the southeast surface winds and the southwest imposed wind field winds, as well as converging surface winds in the Yakima River valley, thus, all three vertical velocity components were positive for this case. The imposed wind field wind (SW 20 kts) accounted for 42% of the total vertical velocity. It may be unrealistic to use the Quillayute sounding to imply large scale winds this far from the coast. Including Spokane's sounding to determine the imposed large scale wind field may improve model results.

CLIMATOLOGY SIMULATION: MARCH 7 - MARCH 24 1991

The model was run for 00 GMT and 12 GMT analyses for the period from March 7th through March 24th. The days from March 7th through March 24th demonstrated a relatively wide range of weather conditions. Precipitation amounts from March 7th and 8th were highly variable and resulted from a moderate northwesterly flow.

TABLE 2 Observed (OBS) and model (MODEL) predicted
         precipitation for 18 sites in western Washington
         and Oregon for 00 GMT March 12, 1991.

STATION NAME	OBS PRECIP	MODEL PRECIP
Mt Baker	0.33"	0.31"
Stevens Pass	0.43"	0.54"
Snoqualmie Pass	0.52"	0.56"
Crystal Mountain	0.67"	0.49"
Paradise/Mt. Rainier	1.58"	1.58"
White Pass	0.41"	0.30"
Mt. Hood Meadows	0.98"	0.18"
Government Camp	0.87"	0.53"
Stampede Pass	0.73"	0.42"
Quillayute	0.44"	0.27"
Astoria	1.17"	0.29"
Bellingham	0.32"	0.24"
Seattle	0.45"	0.28"
Tacoma	0.43"	0.29"
Olympia	0.28"	0.36"
Portland	0.19"	0.46"
Wenatchee	0.00"	0.21"
Yakima	0.00"	0.18"

TABLE 3 Total observed and model predicted precipitation
         for 19 sites in western Washington and Oregon for
         the period from March 7 through March 24 1991

STATION NAME	TOTAL OBSERVED PRECIPITATION	TOTAL PREDICTED PRECIPITATION
Mt Baker	2.29"	1.60"
Stevens Pass	1.11"	1.67"
Mission Ridge	0.55"	0.78"
Snoqualmie Pass	2.30"	1.48"
Stampede Pass	2.78"	1.46"
Crystal Mountain	2.70"	0.81"
Paradise/Mt. Rainier	6.83"	7.01"
White Pass	1.42"	1.38"
Mt. Hood Meadows	2.21"	3.97"
Government Camp	3.01"	3.81"
Quillayute	2.59"	1.55"
Astoria	2.65"	1.27"
Bellingham	1.19"	0.97"
Seattle	1.35"	0.90"
Tacoma	1.64"	1.10"
Olympia	1.46"	1.41"
Portland	2.41"	1.45"
Wenatchee	0.20"	0.75"
Yakima	0.25"	0.60"

11

March 9th was dry. A moist southwesterly flow aloft characterized
the 10th through 13th when most stations received moderate amounts
of precipitation each day. The jet stream, which moved inland over
British Columbia on the 10th sagged southward through the 13th.
This trend is characterized by decreasing daily precipitation
amounts at Mt. Baker and increasing amounts in the Mt. Hood area.
A strong split in the upper level flow off the west coast resulted
in little or no precipitation in the Pacific northwest from the
14th to the 18th. The only exception occurred at Paradise on Mt
Rainier which received .24" of water equivalent ending on the
morning of the 15th. Precipitation increased again from the 19th
through the 24th when the main storm track moved through California
and the Pacific Northwest was under a southeast to southwest upper
level flow.

Model generated precipitation for the period March 7 through
March 24 is compared to observed precipitation totals in Table 3.
22 model runs produced precipitation.   The model did very well
for a number of stations, including Paradise on Mt. Rainier, White
Pass and Olympia. As occurred in Case 2, the model underestimated
precipitation along the Pacific coast (Quillayute and Astoria) and
overestimated precipitation at stations east of the Cascade crest
(Yakima, Wenatchee and Mission Ridge).

Low elevation coastal stations have little if any slope
induced vertical velocity contribution from either the Mass-Dempsey
surface wind field or from the imposed geostrophic wind field.
Forecasters should expect the model to underestimate coastal
precipitation, especially during moist south to southwest upper
level flows. This is especially true for Astoria, where the wide
mouth of the Columbia River results in sea level elevations
downwind of the town.

Although the overestimates east of the Cascade crest appear
significant, the total error involved ranges from .23" to .55",
which averages out to .01"-.02" errors for each model run.

Errors at other stations are more difficult to generalize.
The model overforecast precipitation in the Mt Hood area, but this
is not reliably the case. When errors are analyzed for specific
wind directions, the largest and most inconsistent variations in
model versus observed precipitation occur during southwest upper
level winds. However, close examination of the model terrain does
not indicate why this should be the case.

The model underforecasts precipitation for Mt. Baker Ski Area.
This may result because the ski area is located on Ptarmigan Ridge,
which extends northeast from the mountain and is at a higher
elevation than any of the terrain directly north, east or south of
it. As a result, the vertical velocity calculation produces
negative values for all of the most common precipitation producing
large scale wind directions, ie, south through northwest. Model
precipitation for Glacier, a low elevation station in the Ncoksack
River valley west of Mt Baker, often better reproduces the ski
areas observed precipitation. Although Glacier is not included in
this climatology summary, model output for Glacier is being printed
out at the NWAC.

The model did least well for Crystal Mountain Ski Area. It
tended to produce insufficient precipitation for southeast through
southwest wind directions. The ski area is located at relatively
high elevation at the southern end of a steep sided north-south
oriented valley. As a result, terrain induced vertical velocities

are negative for southerly winds and only weakly positive for southeast or southwest winds. The problems with forecasting precipitation quantities for Crystal Mountain are more complex than a simple terrain analysis can answer. Forecasters at the NWAC have struggled with understanding Crystal Mountain's precipitation for over 10 years. It often receives very light amounts of precipitation compared to other Cascade sites, presumably as a result of rain shadowing by Mt Rainier, 20 km to its southwest. However, Crystal may receive substantially more precipitation than most Cascade sites, including Paradise on Mt Rainier, as was the case on both March 13th and March 22nd. It has been suggested that under certain atmospheric conditions, Crystal may be located under a convergence zone that forms downwind of Mt Rainier. For these two cases, the Quillayute sounding 700 mb level winds were both 220 at 15 and 21 kts. Many more cases need to be evaluated before any generalizations can be made.

4. CONCLUSIONS

An orographic precipitation model, currently being used operationally at the Northwest Avalanche Center in Seattle, Washington, was presented. The precipitation model assumes that precipitation is directly proportional to the vertical velocity generated by the interaction of a wind field and topography. Surface wind data from the Mass and Dempsey (1) wind model is used to calculate a slope induced vertical velocity and convergence induced vertical velocity. Because momentum from upper levels in the atmosphere is felt at higher elevations, a separate wind field representing the large scale flow is imposed on the model terrain. The imposed wind field's direction is held constant over the model's domain while the wind speed varies with height. The wind speed profile and wind direction are taken either from the Quillayute sounding or from the Nested Grid Model (NGM) gridded data nearest Quillayute. A simple precipitation parameterization scheme is employed where the amount of condensation is proportional to vertical velocity. The moisture available for condensation is varied linearly north to south depending on the saturated mixing ratios from soundings or NGM gridded data along the west coast. The airmass is lifted dry adiabatically until it reaches saturation, at which point condensation progresses. For south through north-northwest wind directions, where the Cascades act as an efficient moisture barrier, the saturated mixing ratio is decreased by 67% from the western Cascade foothills to eastern Washington. A constant condensation to precipitation efficiency is assumed with the remaining condensate carried to the next grid point downstream.

Two case studies were presented. The first case was characterized by a north-northwesterly large scale flow and showery precipitation with observed precipitation quantities for March 7 varying from .95" at Paradise on Mt Rainier to less than .1" at most other stations. The model duplicated the precipitation at 19 sites fairly well; however, the model underpredicted precipitation in the Mt Hood area. The model's southeast winds did not match the observed southwest winds, which may account for the precipitation discrepancy. The wind model tends to produce southeast surface winds along the length of the Cascade crest during a southwesterly flow aloft. East or southeast winds are realistic for most of the low elevation passes; however, the observed wind direction

generally resembles the large scale wind direction 400-700 vertical meters above pass level. Mount Hood's proximity to the Columbia River Gorge may account for the model's consistent tendency toward southeast winds.

The second case had a moist southwesterly large scale flow. The model reproduced observed precipitation for many of the stations including Paradise, Snoqualmie Pass, Mt Baker Ski Area and Olympia. The model underpredicted precipitation along the Pacific Coast. Several factors may account for the underprediction, which is a consistent problem with model output. Low elevation coastal stations, which experience negligible vertical velocity from the imposed large-scale wind field, rely primarily on convergence induced vertical velocity to generate condensation. Although the Mass-Dempsey wind model does produce frictional convergence along the coast as air flows from the ocean onto land, the magnitude is generally insufficient to account for the relatively heavy precipitation that often falls at coastal stations.

The model was run at 12 hour intervals from March 7 through March 24, 1991. Total model precipitation for the period was compared to observed totals to test the models ability to reproduce climatology. The model did very well at Paradise, White Pass and Olympia. The model underpredicted precipitation along the Pacific coast; as explained in the preceding paragraph. East of the Cascade crest, the model overpredicted precipitation; however, the average error for each model run was only .01" to .02".

In conclusion, the precipitation model does very well considering the simple precipitation parameterizations that are employed. Most of the significant deviations from observations can either be attributed to errors in the wind model or can be anticipated by a forecaster familiar with the model's consistent errors. The precipitation model should provide forecasters with useful guidance during flow patterns that exhibit relatively two-dimensional characteristics. Although it is not expected to do well for situations with significant three-dimensional structure, the model may still be a useful predictive tool for sites like Paradise on Mt Rainier, which are high enough to be influenced largely by the upper level flow, as was the situation in case 2.

REFERENCES

Mass, C.F., and D.P. Dempsey, (1985). A one-level, mesoscale model for diagnosing surface winds in mountainous and coastal regions. Mon. Wea. Rev., 113, 1211-1227.

Danard, M.B., (1976). On frictional and orographic effects on precipitation in coastal areas. Boundary -layer Met., 10, 409-422.

Hill, F.F., Browning, K.A., and M.J. Bader, (1981). Radar and raingage observations of orographic rain over south Wales. Quart. J. R. Met. Soc., 107, 643-670.

An Analysis of the Record-Breaking Northern Plains Snowstorm of October 27-29 1991

By

William A. Abeling
Meteorologist, National Weather Service
Bismarck, North Dakota

Virginia Raps
Meteorologist Intern, National Weather Service
Bismarck, North Dakota

1. STORM DESCRIPTION

The first major winter storm of the 1991-1992 season moved across the northern plains in late October, 1991. The storm produced a variety of weather phenomena including episodes of light rain, thunderstorms, freezing rain, sleet, heavy snow, and finally, blowing snow. This wintry mix caused blizzard conditions across western and northern South Dakota, while near blizzard conditions existed over central and southwest North Dakota.

Over the three-day period of October 27-29, 1991, there were areas across central North Dakota that received 18 inches of new snow with ice deposits beneath the snow one and a half inches thick. (Fig. 1.)

During the evening of October 28th through the moring hours of October 29th, travel across North Dakota and western South Dakota was difficult, if not impossible. The combination of ice-covered roads, snow, and wind caused numerous traffic accidents. Motorists were stranded up to 16 hours, one passenger bus overturned in North Dakota injuring nine people, and ice accumulations trapped many persons inside their homes when their doors were sealed shut.

2. SURFACE ANALYSIS

Low pressure migrated from the Oregon coast east over the Rocky Mountains on October 26 and 27, while two arctic high pressure systems in Canada intensified. East of the associated frontal zone, warm air provided deceptively mild weather. The surface low actually filled as it moved into the plains states, however the strengthening of the arctic highs increased the pressure difference and the circulation around the low. Southerly winds pulled warm

and moist air into the central and northern plains, while cold air associated with the arctic high pressure systems poured into eastern Montana and northwestern North Dakota. (Fig. 2)

The cold frontal passage over southwest North Dakota generated thunderstorms with much of the precipitation falling as freezing rain, eventually changing to ice pellets, and finally falling as snow (Table 1). By 1200 UTC 27 October, snow was falling over a large portion of the central United States. The storm center tracked southeast, reaching its southernmost point at 1400 UTC 28 October over southeast Colorado, then curved sharply north and began moving toward Minnesota. By 1800 UTC 28 October up to 13 cm of snow had fallen over southwest through north central North Dakota, southwest South Dakota, Montana, and northeast Wyoming. Surface winds over western South Dakota were northwest at 10-15 m s-1.

As the storm continued north, there were periods of heavy snow over parts of Wyoming and central North Dakota. Between 1800 UTC 28 October and 0000 UTC 29 October Bismarck, North Dakota received 10 cm of new snow. A second band of heavy snow moved over northeast Wyoming and south central North Dakota between 0600 UTC and 1200 UTC 29 October depositing an additional 8 to 13 cm of snow (Table 2). The storm moved over northern Minnesota and curved east over southern Ontario, Canada. Snowfall tapered to flurries that continued over the Dakotas until 0000 UTC 30 October.

3. UPPER AIR ANALYSIS

Moist air from the Gulf of Mexico was transported northward by 850 and 700 mb winds of 20-35 m/s. Northwest of the state, cold air at 850 mb in the -10 to -15 C range opposed the moist flow and created strong moisture flux convergence values over the region. (Fig 3a-d) The patterns show a center of converging moisture and wind at the 700 mb level over southwestern North Dakota at 1200 UTC 28 October, with dryer, diverging air at 850 mb. The computed warm/cold advection fields are similar with warm air at 700 mb being pulled into western North Dakota and cold air slipping underneath. During this period of strong low level moisture flux convergence, the low level temperature gradient was increasing rapidly. Between 0000 UTC 28 October and 1200 UTC 29 October, the 850 mb temperature gradient between St. Cloud Minnesota (STC) and Glasgow Montana (GGW) increased from 21 C to 27 C, with similar increases in temperature gradient noted at 700 mb.

The mid level flow (500 mb) indicated a deepening trough moving inland over the western US as a ridge built into the eastern Pacific. (Fig 4) A broad area of mid level PIVA (Positive Isothermal Vorticity Advection) and quasi-geostrophic forcing (Q-vector convergence) implied verical motion over the region from 0000 UTC 28 October through 1200 UTC 29 October.

The upper flow (300 mb) underwent considerable change as rapid jet formation on the east side of the upper trough took place. (Fig. 5)

Initially, at 0000 UTC 28 October two main jets can be seen, the first oriented NW-SE was digging southeast over the western US toward the base of the 300 mb trough with maximum winds of 55 m/s resolved by the rawisonde network. A broad area of wind with speeds of 25 to 30 m/s continued through the base of the trough to a small jetlet, which is discernable over Oklahoma. The second main jet can be seen centered over central Montana with a max windspeed max of 55 m/s. Over the next 24 hours, rapid and dramatic changes took place over the central plains as the speed max on the eastern side of the 300 mb trough increased to 45 m/s. This was accompanied by 300 mb height falls of 280 gpm over Nebraska and 120 gpm height rises over Ohio. By 0000 UTC 29 October the entrance region of the Montana Jet moved to northeastern Montana while the exit region of the developing central plains jet moved to central Minnesota.

4. COMPARISON OF VERTICAL MOTIONS - KINEMATIC VERSES NGM INITIAL

In this study, the vertical motion was computed Kinematically utilyzing the continuity equation. The divergence is integrated from the surface to the top of the atmosphere, here assumed to be 100 mb. The vertical motion was assumed to be zero at 100 mb using the approach of O'Brien (1970). Then the vertical motion was adjusted throughout the column with the adjustment being a linear function of height.

A comparison of the kinematic vertical motions from the study with the model vertical motions appear reasonable, capturing the essential features represented by the model, even though the comparisons are at different levels. (Fig 6a-b). A broad area of upward motion was depicted over the entire region encompassing North and South Dakota as well as eastern Montana. The subtler features are also well represented with two discrete areas of maximum upward motion indicated, the first over western North Dakota and another through the Eastern Dakotas. These areas of upward motion will be examined more closely using cross section analysis.

5. JET STREAK INTERACTION

The idea of jet streak interaction, that is two separate jet systems interacting to enhance the vertical velocity field between them has received some attention recently. (Fig 7) Uccellini and Kocin (1987) have studied snowstorms over the east coast and found upward vertical motion was enhanced between the two systems. Additionally, the northward advection of warm moist air within the lower branch of the indirect circulation cell ascends over the low level cold air brought into proximity by the lower branch of the thermally direct circulation cell associated with the entrance region of the northern jet system. This configuration appears to be highly frontogenetic, increasing the thermal gradient and low level convergence as well as moisture transport.

a. Development of the Southern Jet Streak

A key feature of the snowstorm was the upper level jet systems and their proximity to North Dakota. This section examines the formation of the southern jet streak which was an important factor in maintaining an inertial advective ageostrophic component aloft and the associated lower branch ageostrophic accelleration.

Isentropic trajectories (12 hour) were constructed at the jet stream level (332 Kelvin) for three time periods 1200 utc/28 October through 1200 UTC 29 October. Changes in Montgomery streamfunction (Psi= Cp*T + g*z) and kinetic energy along the trajectory reveal the state of geostrophic balance the parcels encountered. Midpoint trajectory changes of Psi and Kinetic energy were plotted and analyzed for eight trajectories covering an area from the midwest to the northern plains. A check of the geostrophic balance along the trajectories revealed sub-geostrophic wind speeds from the base of the 300 mb trough through the north central US. The area over central Iowa experienced negative Psi changes (parcels crossing from higher to lower Psi values) and positive kinetic energy changes. (Fig 8a-b) This suggests the parcels encountered a pressure gradient force greater than the coriolis force along the trajectory resulting in a crossing toward lower Psi values and accelleration. Height changes computed from the 300 mb data between 1200 UTC 28 October and 1200 UTC 29 October revealed 280 gpm height falls centered over South Dakota and 120 pgm height rises over Ohio. The net result is a height-fall change of 400 gpm between northern Ohio and South Dakota, indicating an increasing height gradient. During this period, the 300 mb wind speeds increased from 80 to 120 kts over Dodge City (DDC) and from 70 to 110 Kts over Huron (HON) between 0000 UTC/29 October and 1200 UTC/29 October. Parcels in the exit region of the southern Jet at the base of the 300 mb trough experienced an acceleration towards lower PSI values along their trajectories as a result of the increased PSI gradient (assumed from the 300 mb height changes) resulting in increased kinetic energy due to cross contour flow.

b. Evidence of Jet Streak Circulations

If a response to the upper level jets propagation into the northern plains is occurring, it should be detectable in the lower level ageostrophic winds. Strong low level (850 MB) winds developed over the northern plains by 0000 UTC 29 October at several stations in Minnesota. International Falls (INL) reported a southeast wind of 50 kts, with Saint Cloud (STC) reporting 70 Kts. This southeast wind component provided a good source of warm moist air and momentum to the storm system. The ageostrophic winds at 850 mb are shown in Fig 9 and the 300 mb isotachs are overlain for convenience. The lower level branch of the ageostrophic circulation cell beneath the exit region of the 300 mb jet streak appears to have contributed to the strong southeast windflow and the associated moisture convergence over North Dakota.

c. Cross Section Analysis

The two upper level jet systems were positioned to interact during the 24 hour period between 1200 UTC 28 Oct and 1200 UTC 29 Oct. This was the period of heaviest snowfall over central North Dakota. This section will examine the degree of jet streak circulation and their interaction through cross section analysis.

Omega-Ageostrophic wind cross sections were constructed along a line cutting across the entrance region of the northern jet system and the exit region of the southern jet (Fig 10). The horizontal component of the vectors represent that portion of the ageostrophic wind component parallel to the cross section, and the vertical component represents the value of the kinematic vertical velocity interpolated to the cross section. The relative value of the vectors are shown on the diagram for comparison.

Two centers of circulation are apparent during the three time periods of interest and each one is associated with upward motion over the state. (Fig 11a-c) The first, centered about lat 49.3 and lon 111.3 at 1200 UTC 28 October appears at approximately 300 mb and is associated with an area of upward motion over western North Dakota. This feature remains consistent in space and time over the cross section period, developing a strong downward branch of the circulation cell over the western section of the cross section by 1200 UTC 29 October and a well defined upward branch over central North Dakota. The southern Jet exit region initially displayed upward motion associated with the circulation cell about 46.0 Lat 99.3 Lon just southeast of Bismarck, although the downward branch is weaker. This feature became less defined 12 hours later, although the strongest vertical motions shift to the lower layers, probably associated with the very strong low level convergence seen at the 850 and 700 mb levels. Then by 1200 UTC 29 Oct the jet circulations are well defined with the upward branches of the circulation cells merging over central North Dakota. Surface observations during this time period at Bismarck indicated the snowfall was occurring at the rate of two inches per hour (Table 2) with 5 inches of snowfall the previos six hours. What is also interesting is the low level undercutting observed over western North Dakota, near Lat 47.8 and Lon 105.1. This feature is present throughout the time periods and is accompanied by "overrunning" above it from the southern circulation cell. This is especially evident at 1200 UTC 29 October.

6. **EVALUATION OF HEAVY SNOW FORECASTING TECHNIQUES**

a. The Magic Chart

The "magic chart" is a combination of a 12-hour net vertical displacement (NVD) prog and a 12-hour prog of the 850-mb temperature field. In a recent study, the magic chart was reported to have given a good first guess of where the heaviest snowfall would occur and the predicted 12-hour snowfall amounts, given sufficient expected moisture (Chaston, 1991).

The heaviest snowfall in a developing or mature synoptic-scale low pressure system will occur in the area where the highest available moisture amounts are occurring in a deep layer coincident with the greatest synoptic-scale lifting. Additionally, these parameters must coincide with an area where the temperatures are cold enough for snow.

Where the greatest net vertical displacement (NVD) overlies the temperature region between -3 C and -5 C is where the heaviest snowfall is likely to occur using the following guidance for the time-period 12 to 24 hours after the initial time:

NET 12-HOUR VERTICAL DISPLACEMENT	12-HOUR SNOWFALL
20 mb to 40 mb	5 cm to 10 cm (2" to 4")
40 mb	10 cm (4")
60 mb	15 cm (6")
80 mb	20 cm (8")
100 mb	25 cm (10")
120 mb	30 cm (12")
140 mb	36 cm (14")
>140 mb	>36 cm (14")

The chosen parameters as studied by Chaston (1991) were the 850-mb temperature zone of -3 degrees C to -5 degrees C, where the temperature-dew point temperature spread was only a few degrees at the 850 and 700-mb levels.

A layer of moist air was forecast to exist over the northern plains by 1200 UTC 28 October (FIG showing 1200 UTC 28 OCT moisture outline). The magic chart forcast valid at 0000 UTC 29 October showed the possibility of a band of 25 cm to 30 cm of snow through central North Dakota (Fig 12).

Actual snowfall amounts over the area supported the validity of the magic chart as a reasonable "first guess" of where and when the greatest snowfall would occur.

b. Cook Technique

This method of heavy snow forecasting is simple and quick. An initial estimate is made from a calculation of the amount of warm advection using the 200 mb chart. Adjustments are made based on warm or cold advection at 700 mb and according to the following guidlines:

1. Heavy snow tends to occur between the 164 and 176 height lines on the 200 mb chart. Higher surface pressures (> 1015 mb) or

elevation > 3000 ft may necessitate choosing the 188 height line as the warm side limit. (This is a very general guide)

2. The difference between the cold pocket in the 200 mb ridge and warm pocket in the 200 mb trough represents the total potential warm advection. The maximum indicated warm advection is limited to 15 degrees latitude (840 nm) downstream from the warm pocket.

3. When warm advection is occurring at 700 mb in the area of interest, the potential advection is divided by 2 to yield the forecast snowfall for the following 24 hours. If cold advection is occurring, then the advection is divided by 4.

Using the 850 mb temperature field as a guide for snow, the area between the 176 and 188 heights were chosen as the potential heavy snow region. Warm advection was occurring at 700 mb so the following 24 hour forecasts were obtained:

Initial Time	Warm Advection	Forecasted Snow Amount.
00z/28 Oct	16 C	8 Inches through 00z/29 Oct.
12z/28 Oct	18 C	9 Inches through 12z/29 Oct.
00z/29 Oct	12 C	6 Inches through 00z/30 Oct.

Considering its simplicity, the Cook technique did remarkably well as a first guess. During the period between 00 UTC 28 October and 00 UTC 29 October, Bismarck received 6.3 inches of snow, with a portion falling as rain and freezing rain. This compares to an 8 inch forecast. From 12 UTC 28 October through 12 UTC 29 October 12.1 inches of snow fell, compared with a 9 inch forecast. The main problem with the technique in this case was the placement of the heavy snow area. The southwestern limit of the snow area should be located near the area of maximum warm advection, with the northeastern extent near the coldest pocket of air douwnstream. This would place the area north of North Dakota.

7. SUMMARY

This winter storm was unusual in both its heavy snowfall and early occurrance, breaking records for single day snowfall, storm total and monthly snowfall for Bismarck, ND. A key element of this storm was the development of a jet streak southeast of the state, bringing the region into the proximity of the entrance and exit regions of two upper level jet systems. Cross section analysis reveals the direct and indirect circulation cells associated with the entrance and exit regions of the jet streaks contributed to a widespread region of ascent over the state. The advection of Canadian air southward in the lower branch of the direct circulation cell provided the cold temperatures needed for snow, while the northward advection of warm moist air in the lower branch of the indirect circulation cell ascended over the cold air, increasing the moisture flux convergence. The juxtaposition of the circulation cells was also found to be highly frontogenetic, increasing the 850 mb temperature gradient between St. Cloud (STC) MN and Glasgow (GGW) Montana.

Two heavy snow forecasting techniques were evaluated. The "Magic Chart" placed the snowfall within the area of occurrance, with estimates of the maximum snowfall rather close to those reported. It appears this method provided an excellent estimate. Despite its simplicity, the Cook technique did remarkably well, although its main fault in this case was the placement of the heavy snow north of the state. It appears to be a very good first guess, especially since it does not rely on the availability of model data.

8. REFERENCES

Chaston, P., 1991: Graphical Guidance. 6th ed. Washington: GPO.

Cook, B. J., 1980: A snow index using 200 mb warm advection. National Weather Digest 5, 29-40.

O'Brein, J. J., 1970: Alternative solutions to the classic vertical velocity problem. J. Appl. Meteor., 9, 197-203.

Uccellini, L. W. and Paul J. Kocin, 1987: The interaction of jet streak circulations during heavy snow events along the east coast of the United States. Weather and Forecasting, 2, 289-308.
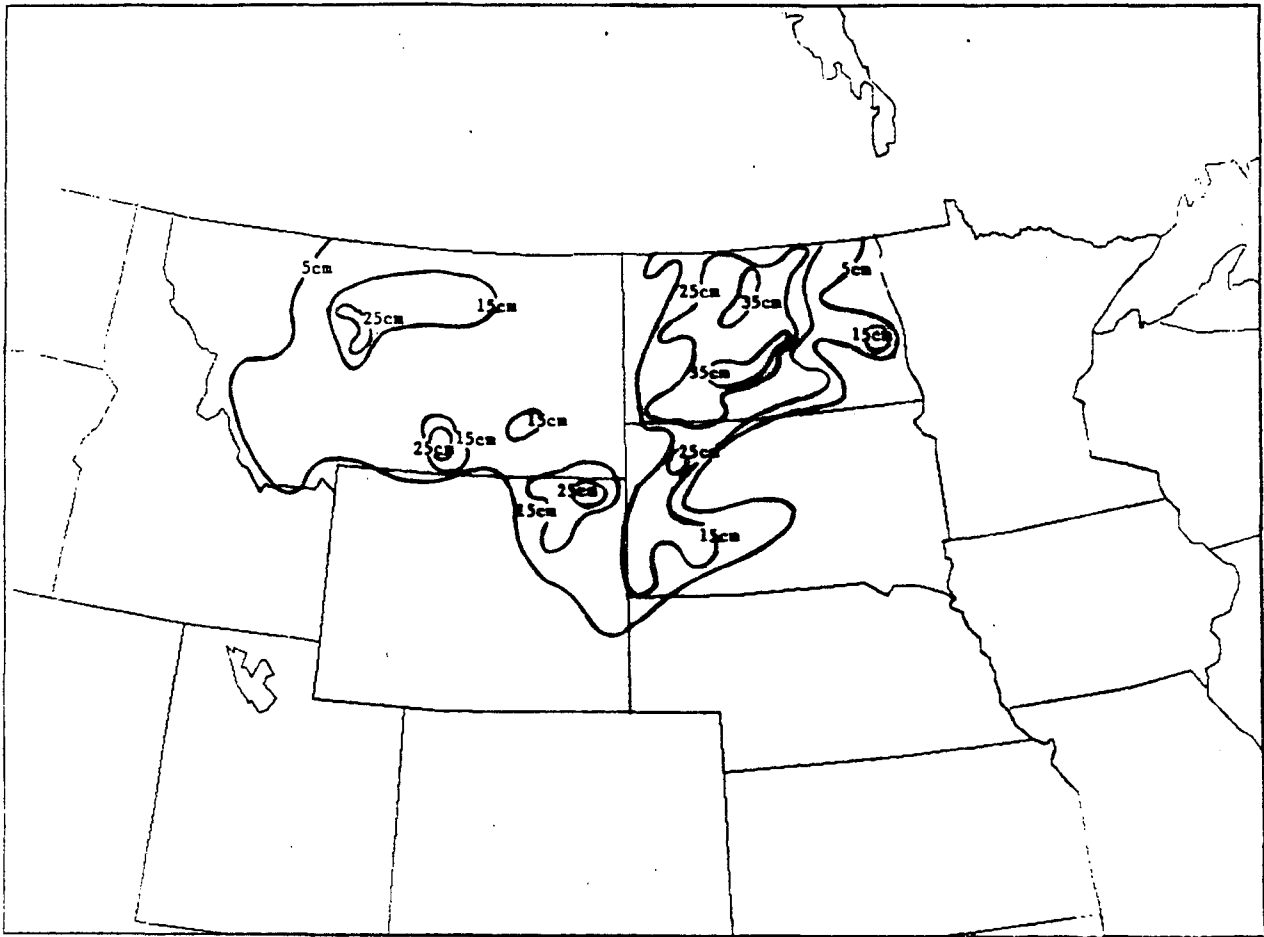
Figure 1. Storm Snowfall Totals. October 27-29, 1991

Date/Time UTC	Sky & Ceiling	Visibility & Weather	Temp	Wind	Remarks
27/1200	E250 OVC	10	43	1213	
27/1800	M10 OVC	6 L-F	50	1617G25	LB42
27/2220	M4 BKN 27 OVC	1 R-F	42	2818	WSHFT 37 LERB40
27/2300	-X M6 BKN 17 OVC	2 L-F	39	3014	F1 RELB33
28/0000	-X M7 BKN 18 OVC	2 L-F	39	3011	
28/0100	M5 OVC	3 R-F	38	3011	LERB35
28/0600	5 SCT M9 BKN 13 OVC	9 ZR-	31	3115	LB21REZRB28
28/0724	M9 BKN 15 BKN 30 OVC	7 ZR-IP-	30	3214	IPB23
28/0900	7 SCT M9 BKN 15 OVC	4 IP	30	3112	ZRE40
28/0950	M8 BKN 17 OVC	5 S-	27	3214	SB02IPE05
28/1018	M9 BKN 21 OVC	7 S-	25	3112	IPB0953E41
28/1200	E9 BKN 18 OVC	5 IPS-	24	3310	IPB25
28/1700	-X M15 OVC	2 IPS-F	20	3312	IP3 IPB20
28/1800	-X M16 BKN 23 OVC	1 1/2 IPS-F	19	3313	IP4 TWR VSBY 2 PRES UNSTDY
28/1900	-X M15 BKN 35 OVC	1 IPS-F	18	3415	IPS PRESFR
28/2003	-X M15 OVC	5/8 IP-S-F		3316	S8 DRFTG SNW
28/2100	W4 X	1 1/4 SBSF	18	3414	TWR VSBY 5/8 IPE14 SNOINCR 2/3/3
29/0000	W5 X	3/8 SBSF	17	E3226	
29/0600	-X 15 SCT E22 BKN 55 OVC	2 S-BS	15	E3325	
29/0700	-X M25 OVC	4 S-BS	15	E3120	S1
29/0800	-X M25 OVC	1 1/2 S-BS	14	E3220	S2
29/0900	-X 15 SCT M24 OVC	3/4 S-BS	14	E3222	S3
29/1000	-X M24 BKN 40 OVC	1 S-BS	13	E3022	S3
29/1100	-X M10 OVC	5/8 S-BS	13	E3125	S4 SNOINCR 1/3/8
29/1200	W4 X	3/8 SBS	12	E3120	SNOINCR 2/5/10
29/1300	W8 X	3/8 SBS	11	E3020	SNOINCR 1/1/11
29/1400	-X M20 BKN 36 OVC	1/2 SBS	12	E3218	S3 TWR VSBY 3/4
29/1500	-X M16 BKN 35 OVC	1/2 S-BS	13	E3122	S6 TWR VSBY 3/4
29/1600	-X M16 OVC	1/2V S-BS	13	E3123	S5 TWR BSBY 3/4 SFC VSBY 1/4V3/4
29/1800	-X M19 BKN 37 OVC	1V S-BS	15	E3222	S2 TWR VSBY 1 3/4 SFC VSBY 3/4V1 1/4
29/1827	-X M15 BKN 32 OVC	3 S-Bs		E3122	BS2
29/1943	-X M20 OVC	1 1/2 S-Bs		E2819	TWR VSBY 2
30/0000	16 SCT M30 BKN	12		E2914	DRFTG SNW

NOTES:

SNOINCR 2/3/3 - Snow depth increase in the past hour of 2"/snow depth increase of 3" since the last 6-hourly observation/. total snow depth of 3" on the ground at the time of observation

E - Wind Speed Estimated

Table 1 Selected surface observations at NWSFO Bismarck, North Dakota. 1200 UTC October through 0000 UTC October, 1991

Synoptic observations for Bismarck, ND

Date/time	Precip	Snowfall	Snow Depth	Max Temp	Min Temp
27/0000	0	0	1	44	41
27/1800	T	0	0	50	43
28/0000	.04	0	0	51	39
28/0600	.06	0	0	39	31
28/1200	.29	.4	T	31	24
28/1800	.34	1.0	1	24	19
29/0000	E.45	E4.9	4	19	17
29/0600	E.05	E1.0	5	17	15
29/1200	E.35	E5.2	10	15	12
29/1800	E.21	E3.2	11	15	11
30/0000	E.01	E0.2	10	16	13
30/0600	T	T	10	15	11
	1.80	15.9			

Table 2.
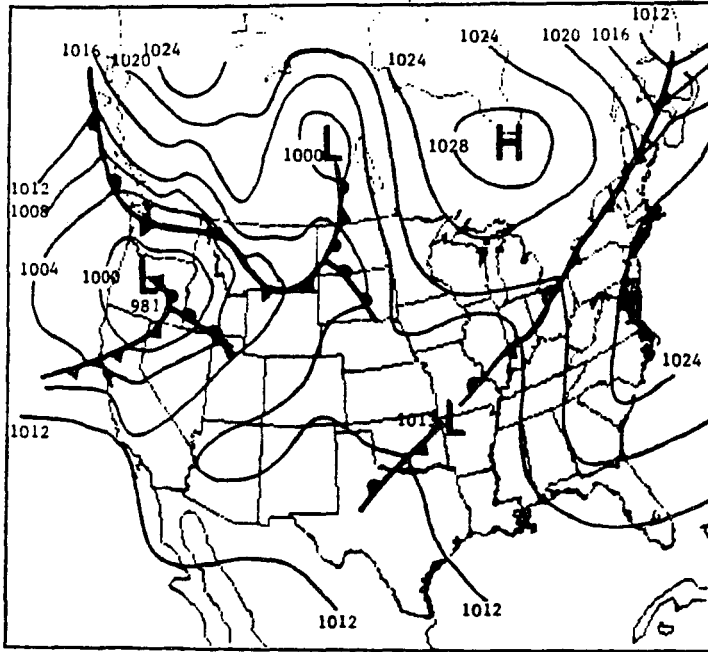
Surface Analysis 1200 UTC 26 October 1991
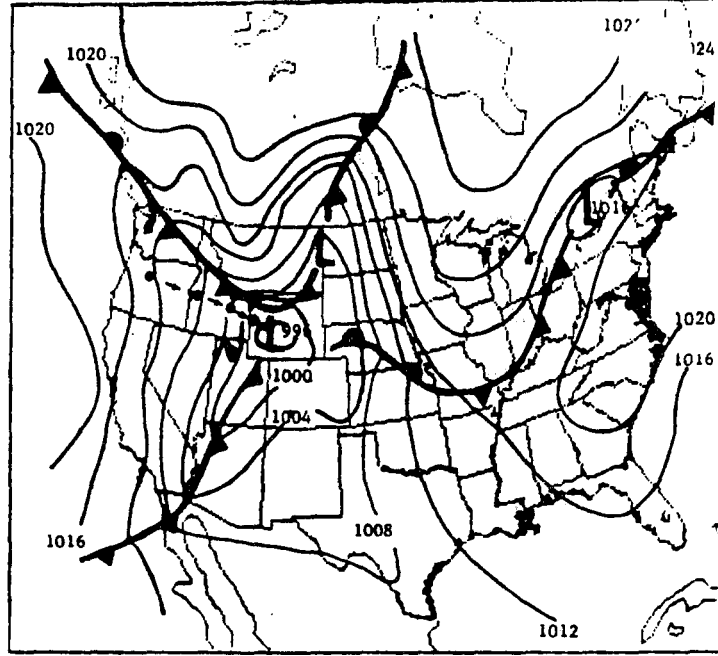
Surface Analysis 1200 UTC 27 October 1991
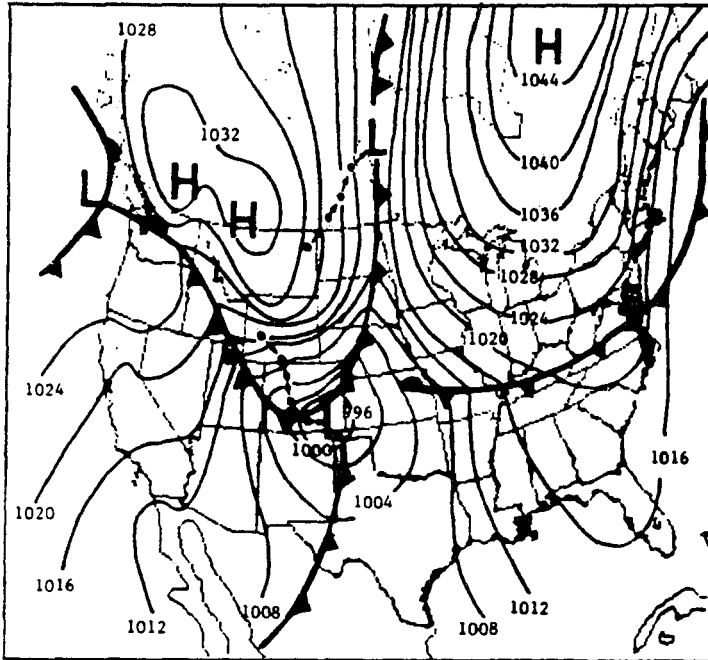
Surface Analysis 1200 UTC 28 October 1991
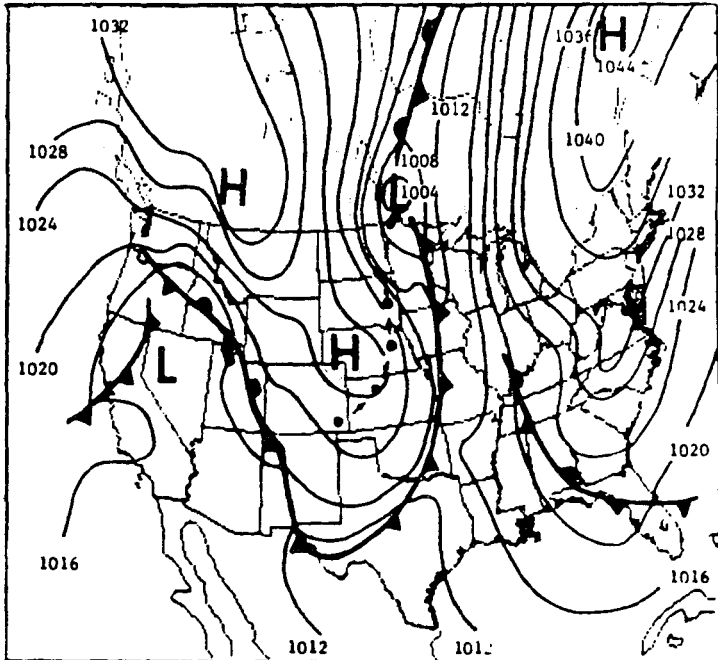
Surface Analysis 1200 UTC 29 October 1991

Figure 2.   Surface Analysis
          1200 UTC 26 October through 1200 UTC 29 October, 1991
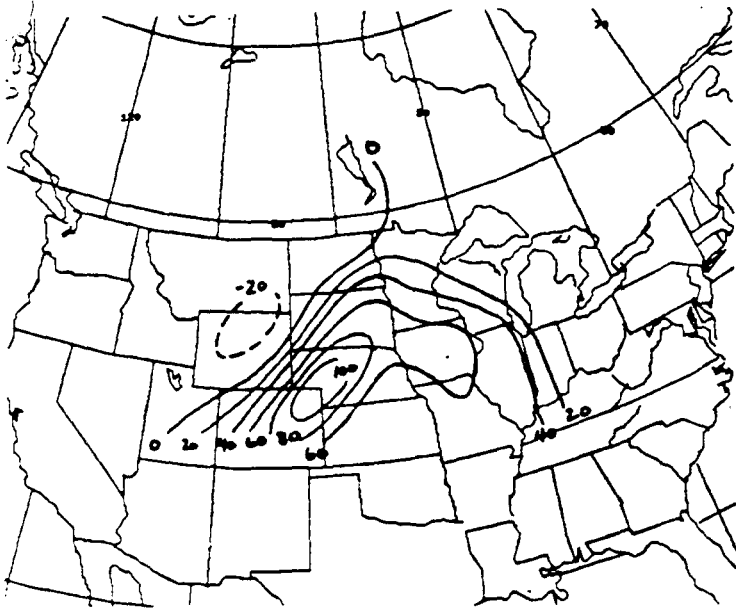
a) 850 mb moisture flux convergence. (g/kg/hr)*10
   1200 UTC 28 October 1991
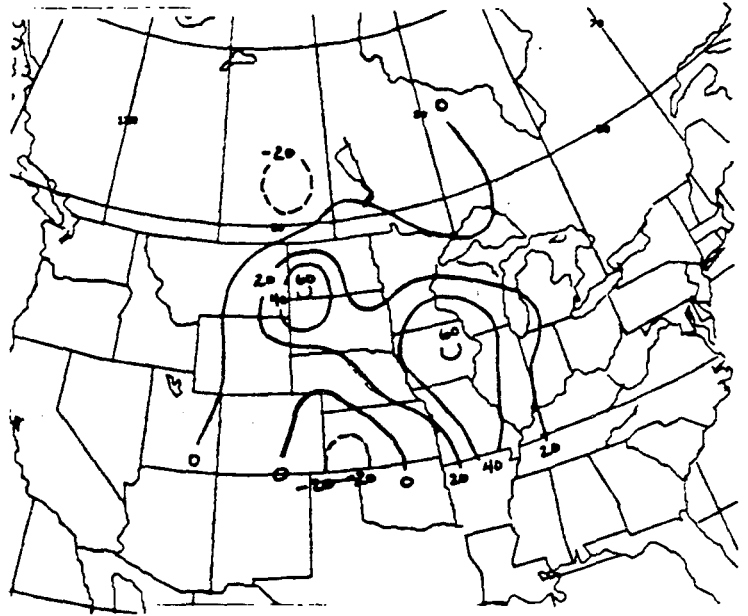
b) Same as a) for 700 mb
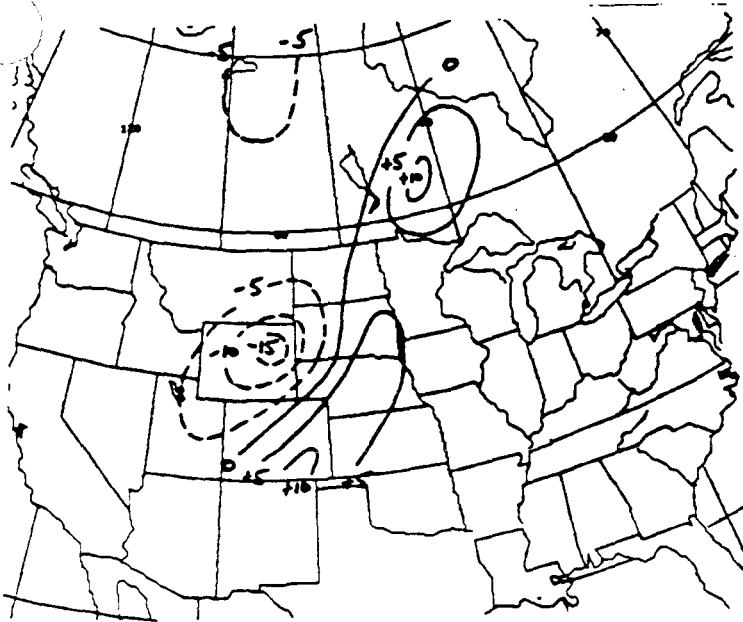
c) 850 mb temperature advection (instantaneous). (deg c/12 hr)
   1200 UTC 28 October 1991
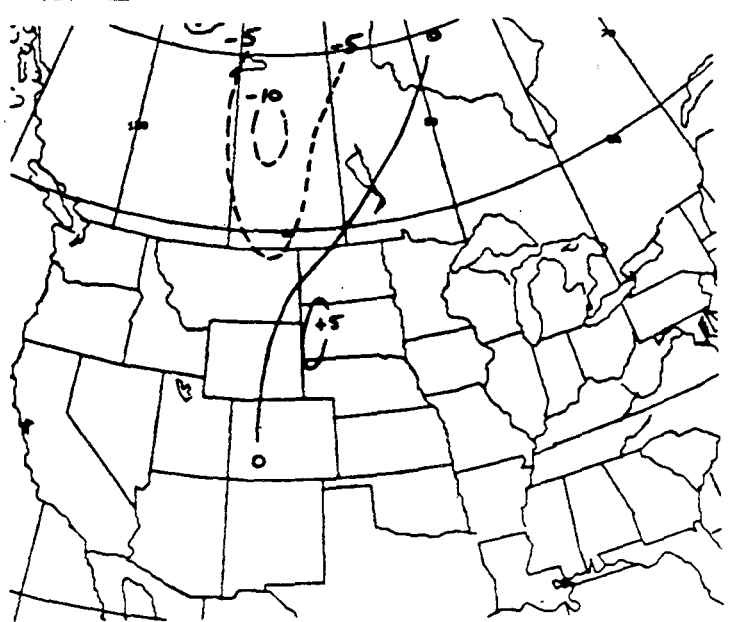
d) Same as c) for 700 mb

Fig. 3
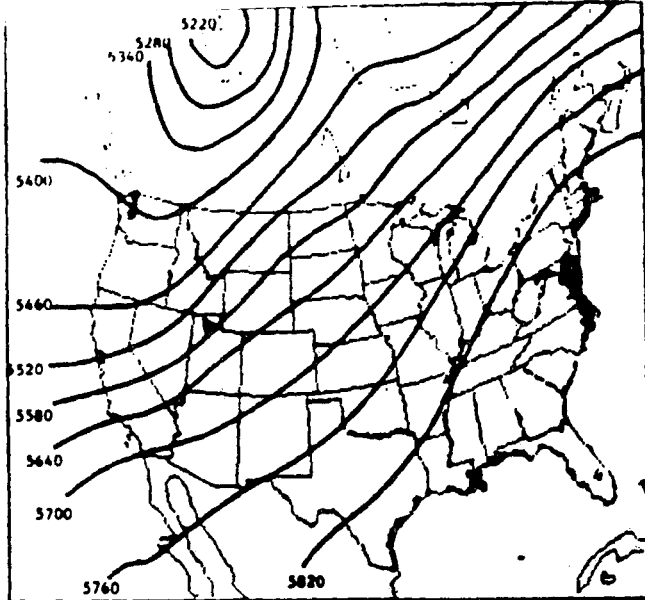
500 MB Height Analysis. 0000 UTC 27 October 1991
(meters)
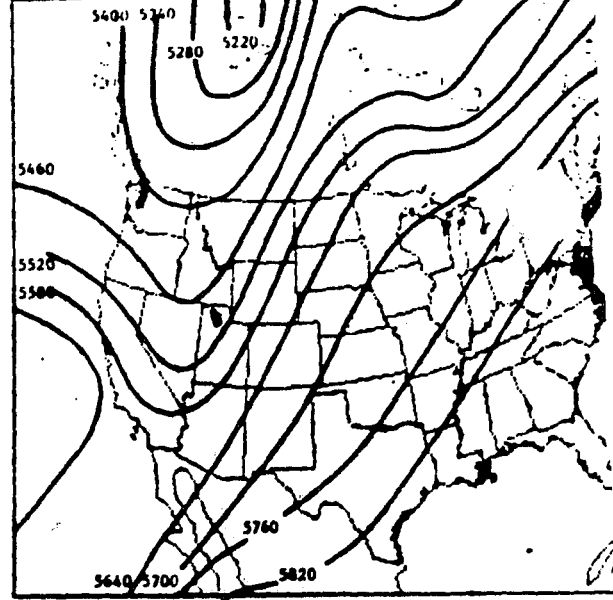
500 MB Height Analysis. 1200 UTC 27 October 1991
(meters)
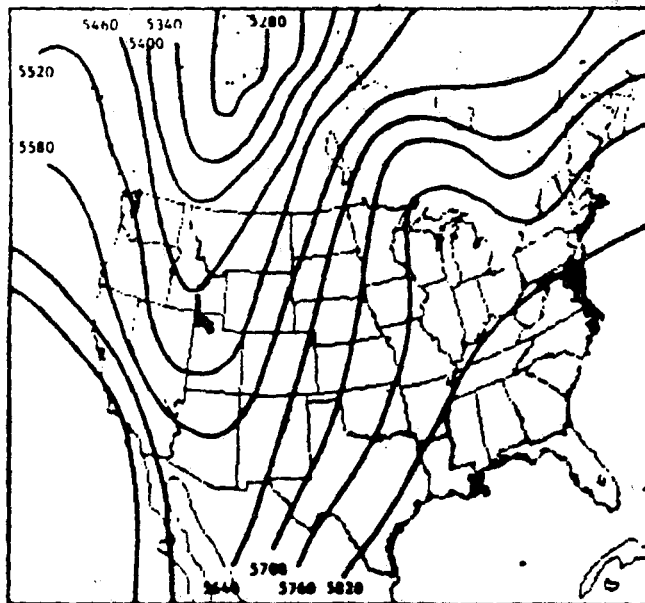
500 MB Height Analysis. 0000 UTC 28 October 1991
(meters)
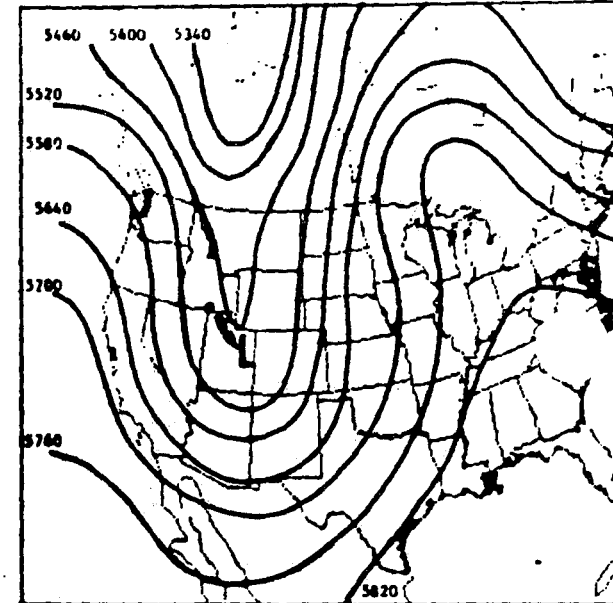
500 MB Height Analysis. 1200 UTC 28 October 1991
(meters)
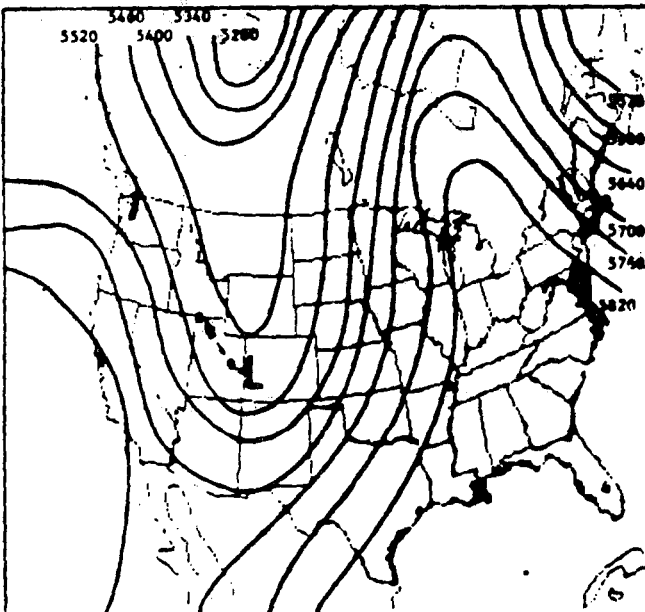
500 MB Height Analysis. 0000 UTC 29 October 1991
(meters)
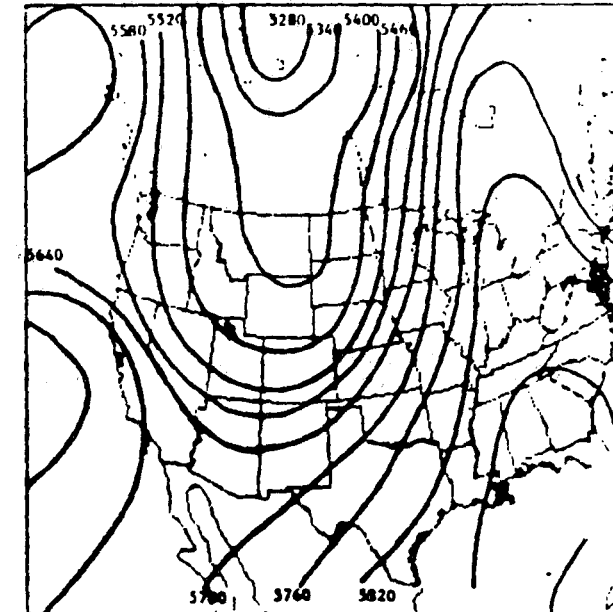
500 MB Height Analysis. 1200 UTC 29 October 1991
(meters)

Figure 4. 500 MB Height Analysis
0000 UTC 27 October through 1200 UTC 29 October 1991
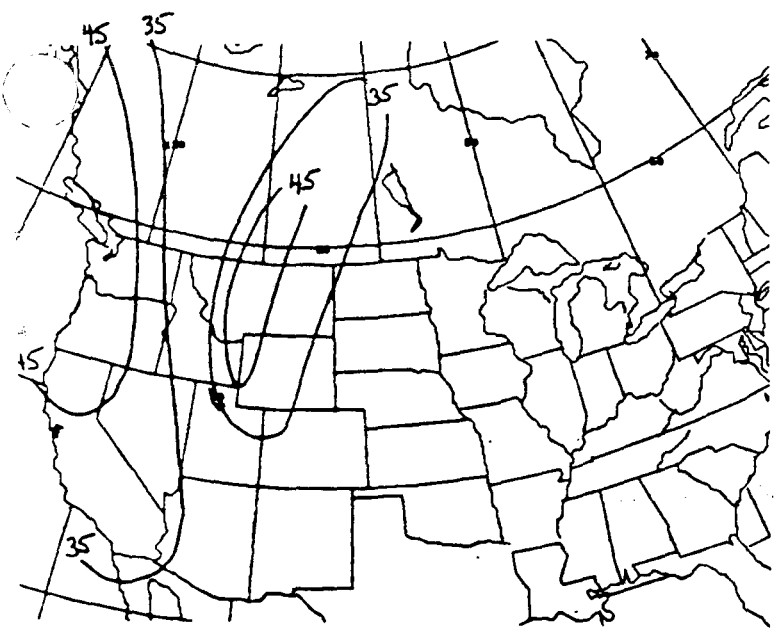
a) 0000 UTC 28 October.
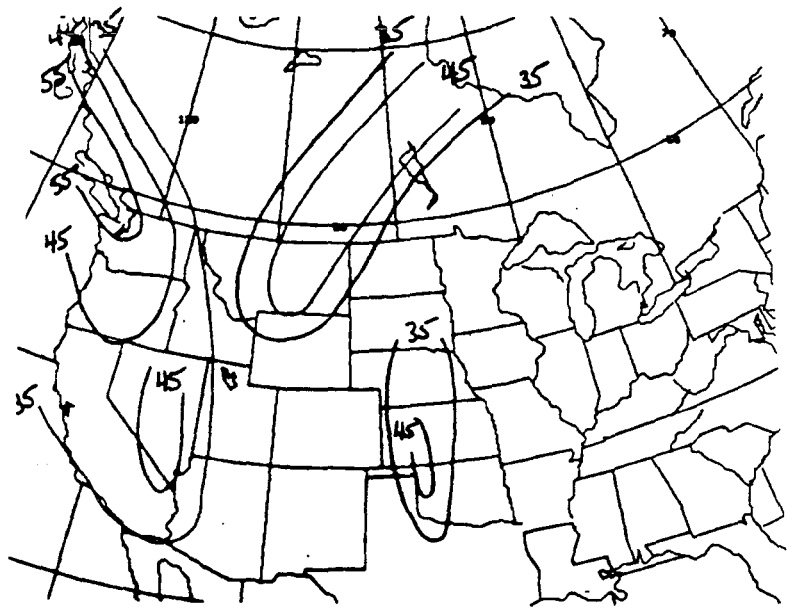
b) 1200 UTC 28 October.
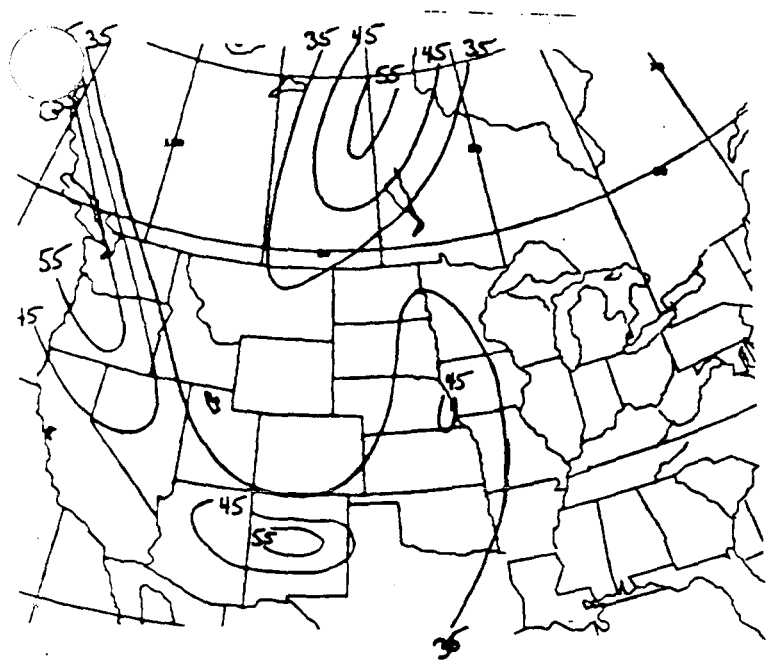
c) 0000 UTC 29 October.
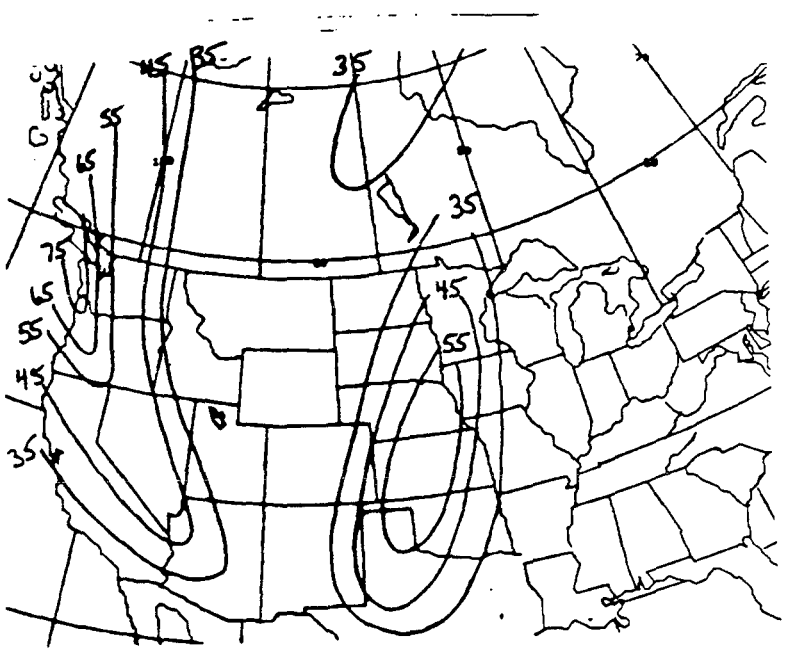
d) 1200 UTC 29 October.

Fig. 5 300 mb isotachs (m/s).
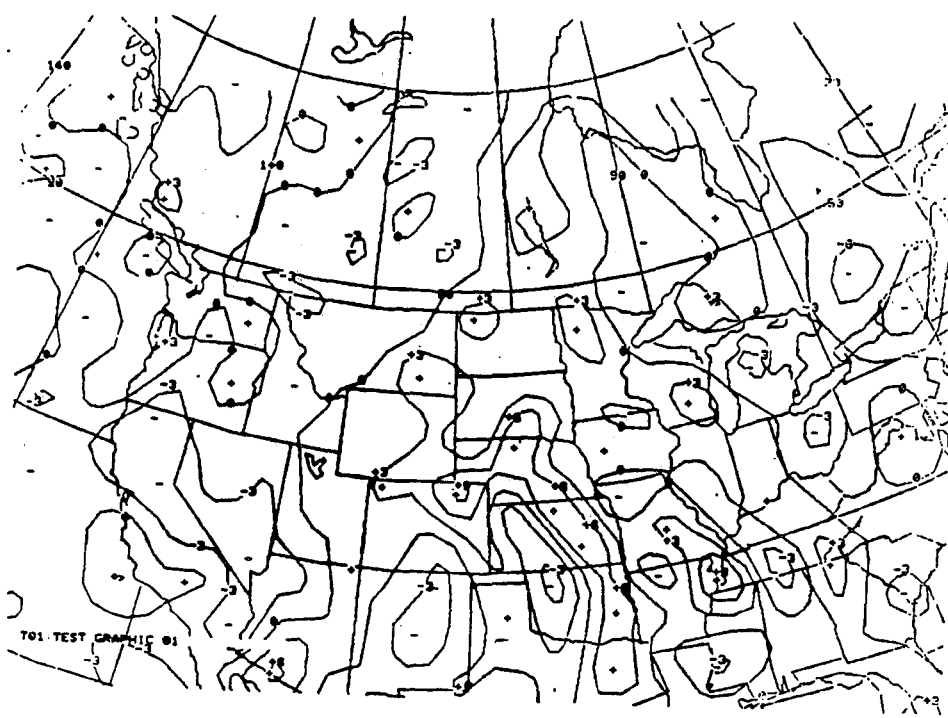
a) NGM 700 mb Vertical motion (00 Hour) (+ = Rising)
1200 UTC 28 October 1991
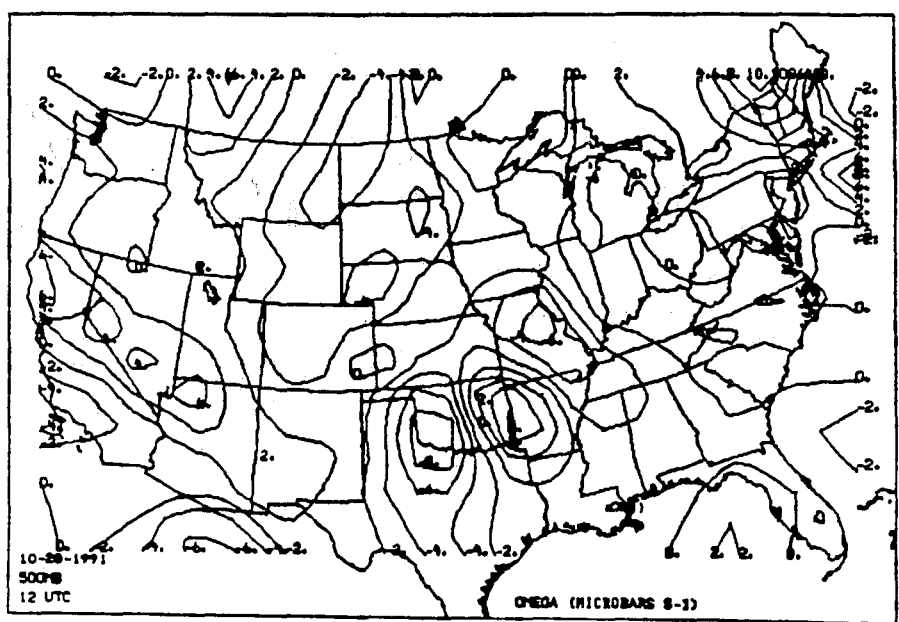
b) 500 mb Kinematic vertical motion (- = Rising)
1200 UTC 28 October 1991

Fig. 6 Vertical motion

Fig. 7 From Uccellini

Fig. 8   332 K   Mid point isentropic trajectory changes
0000 UTC - 1200 UTC 29 October
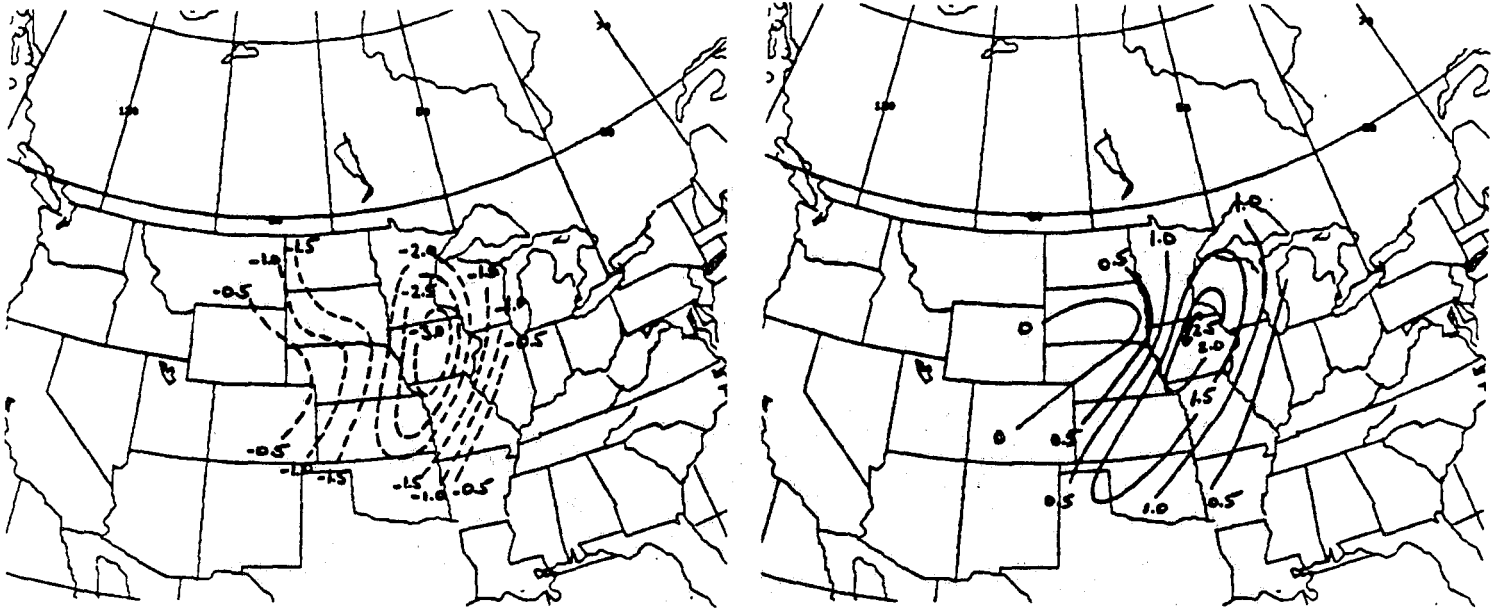
a) Change in Montgomery streamfunction

b) Change in kinetic energy change
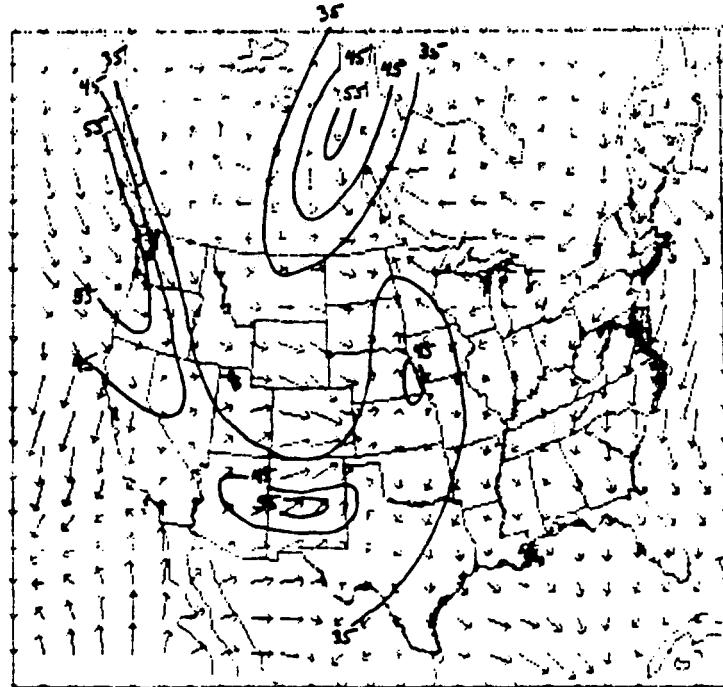
Fig. 9   850 mb Ageostrophic wind   0000 UTC 29 October
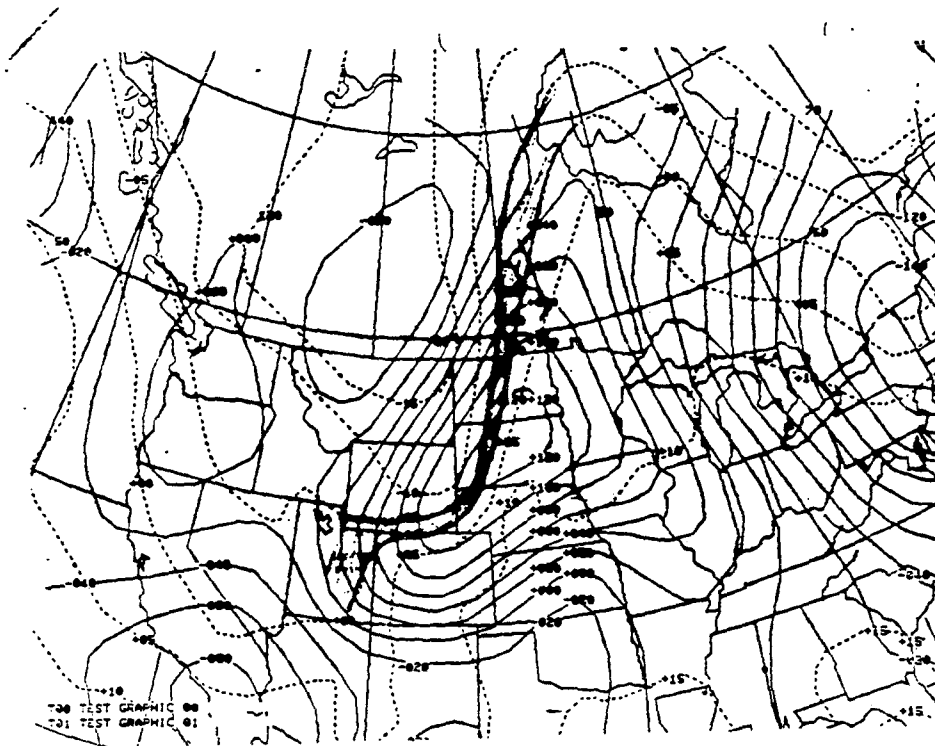300 mb isotach   0000 UTC 29 October
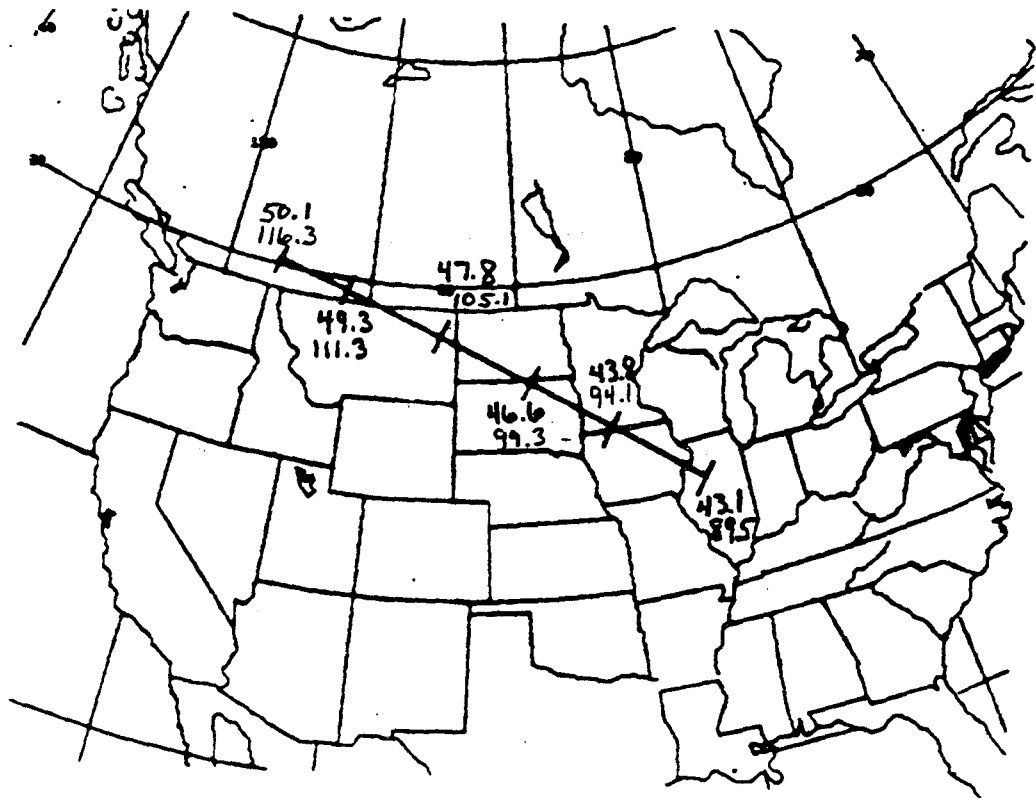
Fig. 10 Location of cross section.

Fig. 11 Omega-ageostrophic cross sections

a) 0000 UTC 28 October

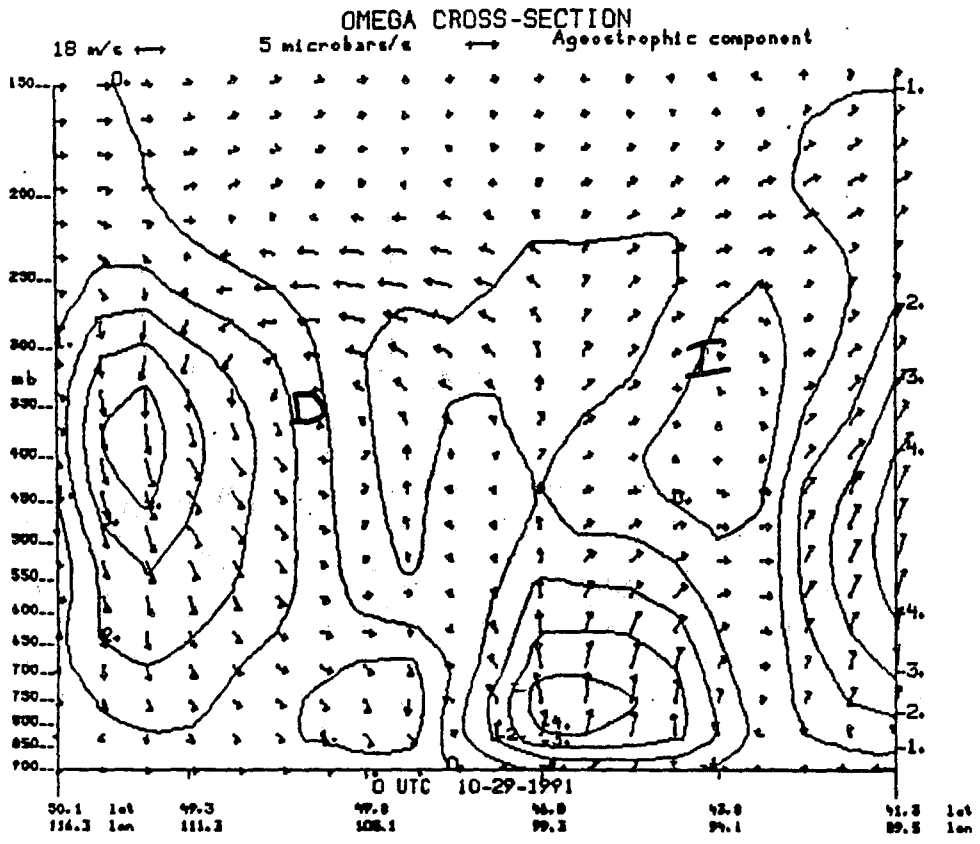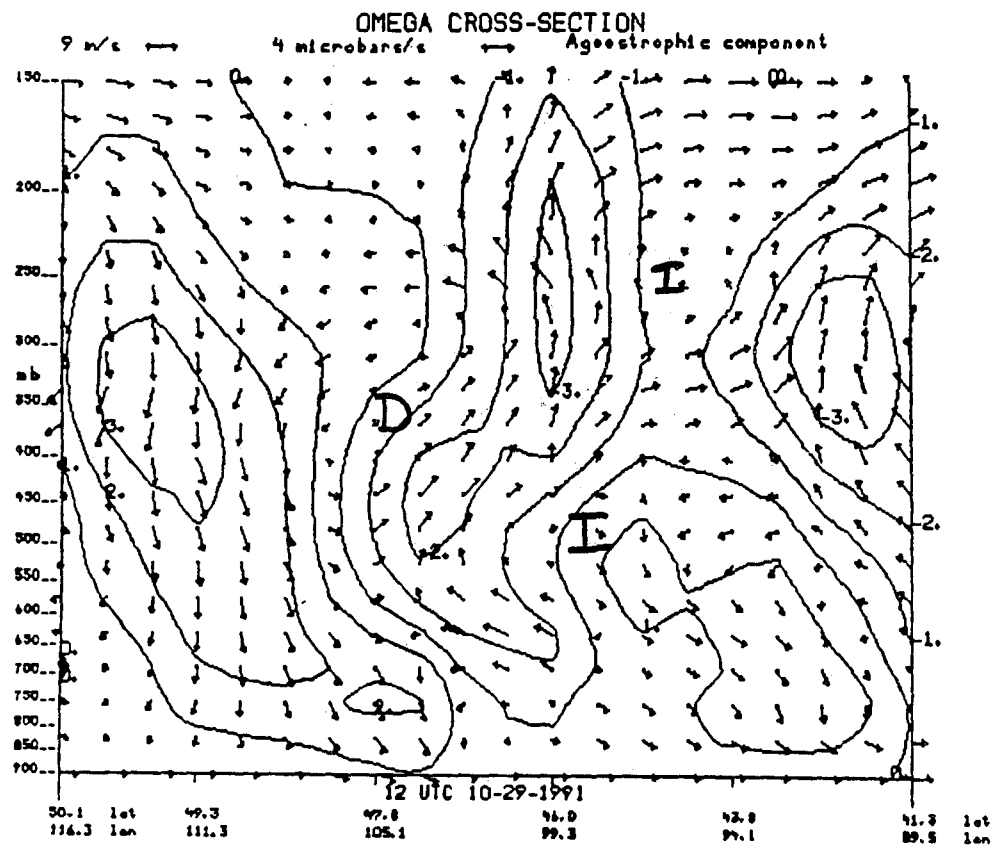b) 1200 UTC 28 October
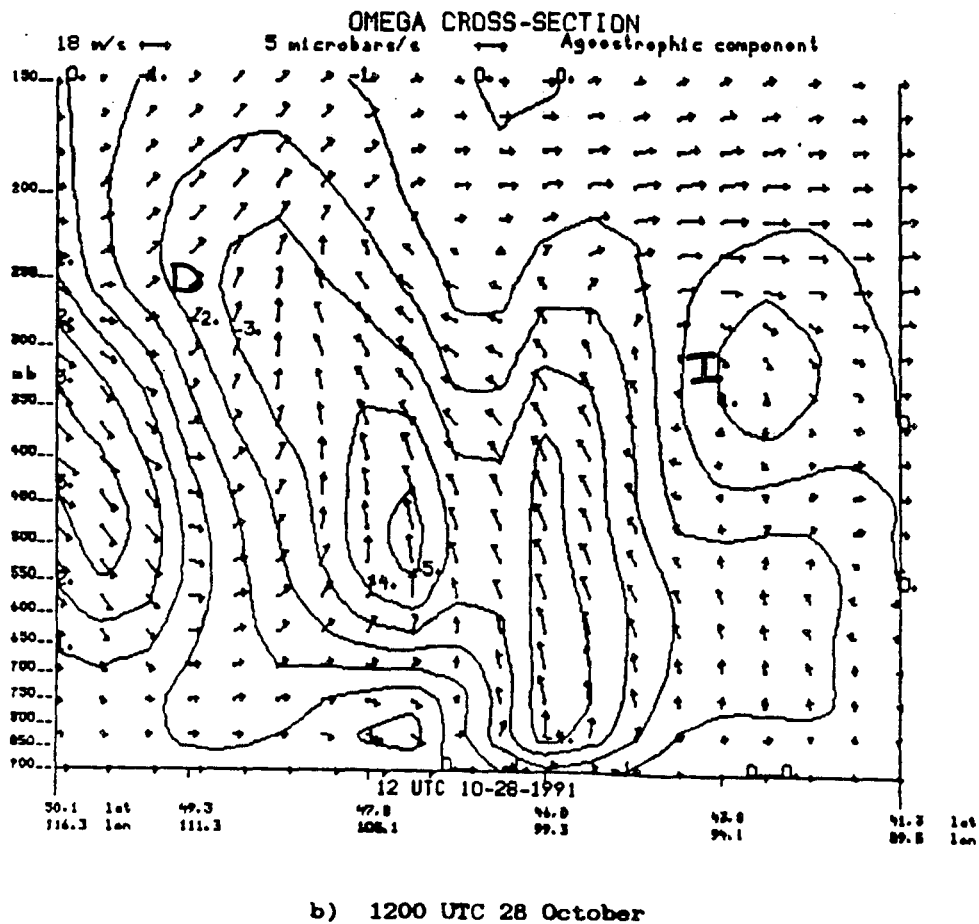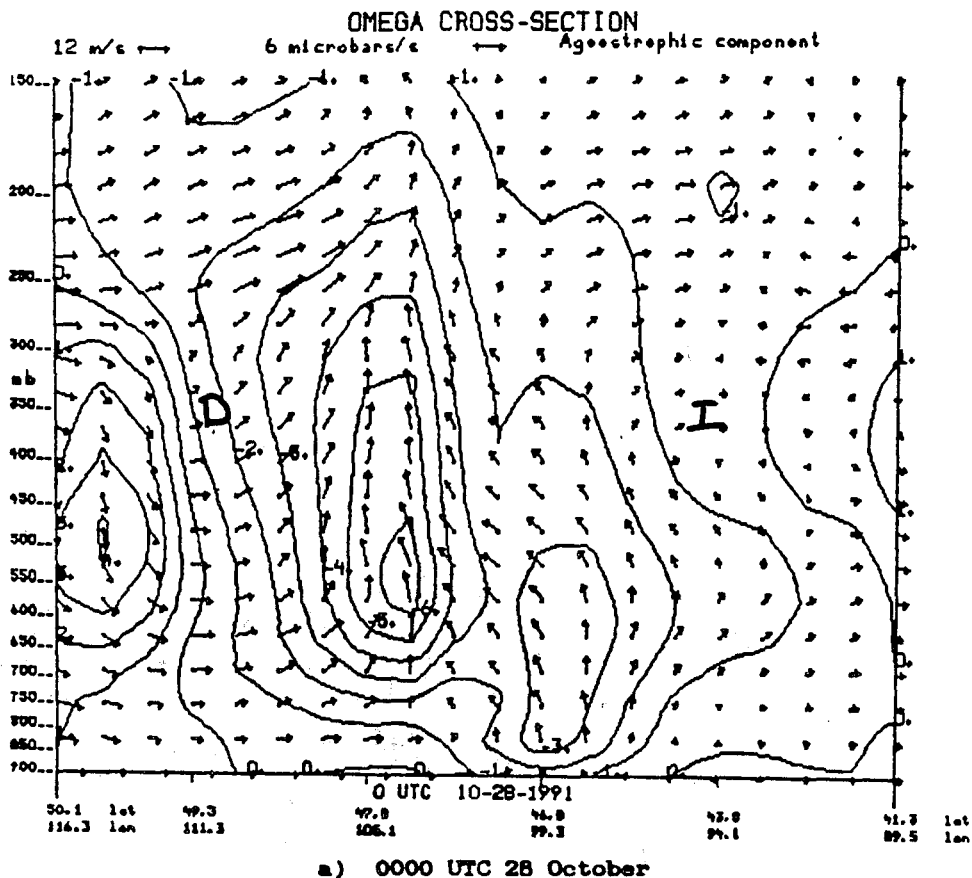
a) 12 hour net vertical dispalcement (mb) VT 0000 UTC 29 October
    12 hour 850 mb temperature (c) VT 1200 UTC 28 October
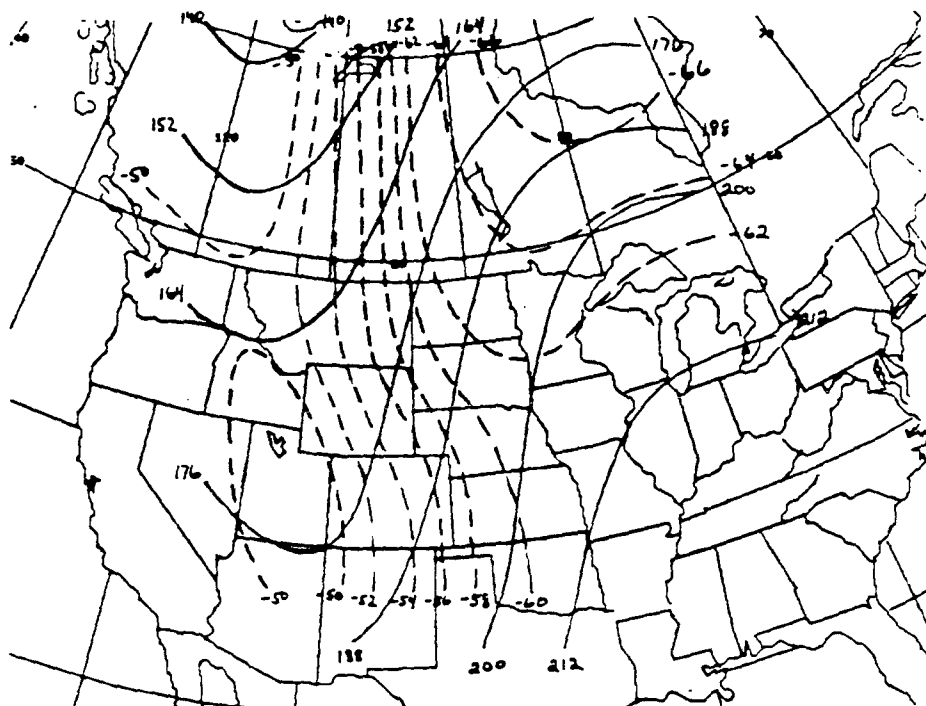
b) 200 mb height and temperature 1200 UTC 28 October.

Fig. 12

OMEGA CROSS-SECTION

18 m/s ⟶   5 microbars/s ⟷   Ageostrophic component

c) 0000 UTC 29 October

OMEGA CROSS-SECTION

9 m/s ⟶   4 microbars/s ⟷   Ageostrophic component

d) 1200 UTC 29 October

Snowstorms over the Western Washington Lowlands

Garth K. Ferber

National Weather Service, Seattle, Washington

Abstract

The relatively infrequent occurence of heavy snowfall in the
western Washington lowlands has severe impacts on regional
transportation and commerce. This post-print presents the
highlights of a study of heavy snowfall events over western
Washington State. First, a composite of 13 snowstorms
illustrates the synoptic scale evolution accompanying heavy snow
in the region. The 13 storms routinely possessed one or more of
the following regional components: coastal cyclogenesis, Arctic
frontal passage, synoptic overrunning of cold surface air masses
by a moist, warm airflow aloft, and mesoscale topographic
effects. A recent example of the latter is presented. Lastly,
there is a close connection between ENSO and snowfall in the
western Washington lowlands, with lesser snow amounts during El
Nino years.

1. Introduction

Predicting heavy snowfall over the western Washington lowlands is one of the most important and challenging tasks facing local forecasters. Because of the region's hilly terrain and the relative rarity of snow, even modest snowstorms result in numerous traffic accidents. Such storms can also cause widespread power outages and long delays at Seattle-Tacoma airport, a major hub for national and international flights.

Because of the climatological dominance of relatively warm, maritime air from the Pacific Ocean, heavy snow is an infrequent visitor to the Puget Sound lowlands. At Seattle-Tacoma Airport the average (1961-1990) winter snowfall only amounts to 12.3 inches. But as shown in Fig. 1, annual snowfall is quite variable, ranging from 64 inches to only a trace.

Skill in forecasting heavy snow in the region has been slow to develop for a number of reasons. One problem is the relative infrequency of heavy snowfall events, which has precluded the development of operational experience. But a more fundamental difficulty is the inherent complexity of snow events in this area of intricate terrain and land/water contrasts. Operational prediction models such as the NGM do not have sufficient spatial resolution for accurate depiction of local terrain features, which often play a crucial role in determining the distribution of snowfall. Improperly analyzed wind and moisture fields over the vast oceanic areas to the west of the Puget Sound region often prevent proper initialization and subsequent simulation of important synoptic features. Furthermore, it is difficult for humans to predict the many interacting mesoscale circulations even when good synoptic guidance is available. Snowfall prediction is further complicated by the often marginal nature of regional temperatures; small temperature variations can dramatically affect snowfall amounts or whether snow occurs at all. Finally, useful snow forecasting demands accurate quantitative estimates of precipitation amounts, a demand that meteorologists frequently avoid in lieu of precipitation probabilities.

Familiarity with the topography of the Pacific Northwest is essential for understanding the snow events that influence the region. Important features (Fig. 2) include the Olympic Mountains on the Olympic peninsula and the Cascade Range which run roughly north-south from British Columbia to California. The latter barrier and the Rocky Mountains to the east impede the westward movement of cold air that is often resident within the interior of the continent. Within the Cascade Range there are several important river drainages that, under proper synoptic conditions, allow cold Arctic air to reach the western Washington lowlands. Most important among them is the Fraser River Valley, with a source deep within the interior of British Columbia and a terminus near Bellingham, just north of the western Washington lowlands. The Olympic Mountains also have a dramatic influence on local weather, including leeward troughing, low-level convergence, and significant rainshadow effects (Mass 1981,

Ferber and Mass 1990).

Relatively little work has been undertaken regarding snow events along the northwest coast of the United States. Dickey and Wing (1963) discusses outbreaks of Arctic air into the region. In contrast, snowstorms along the northeast coast of the United States have received considerable attention. Such investigations have examined the contributions of upper level dynamics (Kocin and Uccellini 1990), symmetric instability (Sanders and Bosart 1985), low-level frontogenesis (Bosart et al. 1972, Bosart 1975, Ballentine 1980), and topographic damming east of the Appalachian Mountains (Lapenta and Seaman, 1992). Considerable attention has been given the President's Day Snowstorm of 1981 (Bosart 1981, Bosart and Linn, 1984). Finally, Kocin and Uccellini (1990) provides a detailed description of 20 major East Coast snow events and reviews the basic dynamical elements contributing to the storms.

This post-print presents the highlights of a study of heavy snowfall events affecting the western Washington lowlands, particularly the Puget Sound basin. First, a composite of thirteen snowstorms at Seattle-Tacoma Airport (SEA) is presented to illustrate the average synoptic scale evolution leading up to such events. Among these 13 storms, four recurring components were noted: coastal cyclogenesis, Arctic Front passage, synoptic overrunning of cold surface air masses by moist, westerly airflow aloft, and mesoscale topographic effects. In order to keep the post-print brief, a recent example of the only the latter is presented. Lastly, the relationship between ENSO (El Niño/Southern Oscillation) events and snowfall in the western Washington lowlands is examined. For the interested reader, the complete study will soon be submitted to the journal Weather and Forecasting.

2. Synoptic scale composite

We composited 13 snowstorms occurring after 1962 that met local National Weather Service (NWS) Winter Storm Warning criteria for snowfall (4 inch accumulation in 12 hours) at Seattle-Tacoma Airport. The fields used for the composite were taken from the National Meteorological Center (NMC) Grid Point Data Set on a compact disc. This dataset has a horizontal resolution of 380 km and provides grids twice a day (0000 UTC and 1200 UTC). The closest of these times to the start of the snowfall at Seattle-Tacoma Airport was used as the initiation time (00 hour) in the composite (Table 1). Statistical significance of the composited fields was computed using a two-tailed Students-T Test. It should be stressed that because of the limited resolution of the gridded data, the following composites only provide information on the synoptic evolution of these events.

Composite fields of 500 mb geopotential heights, deviation of the 500 mb heights from climatology, and statistical significance of the 500 mb height deviations are shown in Figure 3. Forty-eight hours prior to the start of heavy snow (-48 h), long wave ridging over the northeast Pacific Ocean and troughing

over southwest Canada is evident (Figs. 3a,b). Both features are significant at the 99% level (Fig. 3c). By -24 h the long-wave ridge strengthens considerably and builds northeastward, while a short wave trough sharpens over southeast Alaska and British Columbia (Fig. 3d, e). The areas of 99% significance over western Canada increase in size (Fig. 3f). At the onset of heavy snow (00 h), the ridge continues to amplify and the short wave trough deepens considerably southwest of Vancouver Island (Fig. 3g,h). The jet core passes offshore and to the south of Washington. Broad areas of the ridge and trough remain significant at the 99% level (Fig. 3i).

Composite 850 mb geopotential height and temperature fields are shown in Figure 4. At -48 hours a weak ridge extends northward over western Alaska, with weak troughing offshore of British Columbia and the Pacific Northwest (Fig. 4a). Temperatures at 850 mb range from -5°C over western Washington to -20°C in Yukon Territory (Fig. 4b). By -24 hours, the 850 mb ridge builds considerably into Alaska and the trough sharpens over southern British Columbia (Fig. 4c). Temperatures cool slightly over western Washington (ranging from -5 to -10°C) and the coldest air moves south into north British Columbia and north Alberta (Fig. 4d). At the initiation of heavy snow (00 h), the 850 mb ridge continues to build over the northeast Pacific and the trough over Vancouver Island deepens into a closed low centered over Vancouver Island and northwest Washington (Fig. 4e). Temperatures over the Pacific Northwest are only slightly cooler at this time, with the coldest air shifting southeast into south central Canada (Fig. 4f).

Composite fields of surface pressure, deviation of the surface pressure from climatology, and statistical significance of the surface pressure deviations are shown in Fig. 5. At -48 h, anomalously high pressure over the eastern Pacific extends into Alaska and the Yukon Territory, with relative troughing along the British Columbia and southeast Alaska coasts (Figs. 5a,b). At this time only the high pressure anomaly over the eastern Pacific and Alaska is significant at the 99% level (Fig. 5c). One day later (-24h), the high pressure over the Yukon Territory strengthens with the coastal trough still evident (Figs. 5d,e,f). At the time of snowstorm initiation (00 h) the coastal trough intensifies into a closed low off the Washington Coast and the inland high pressure center continues to shift to the southeast (Fig. 5g,h). Between these two features an intense low-level pressure gradient develops. Both the coastal trough and the high pressure anomaly are highly significant at this time (Fig. 5i).

Although the majority of snowstorms in the region possess a synoptic evolution broadly similar to that of the composite, there may be considerable variability in the details of the mesoscale developments. In the next section an example of such developments will be reviewed in more detail.

3. An example of mesoscale topographic effects

The complex topography of the Pacific Northwest profoundly

influences low-level atmospheric flow and thus greatly affects the evolution of regional snow events. Local topographic effects, such a terrain-induced convergence or upslope flows, can produce mesoscale regions of upward motion that can initiate or enhance snowfall. In western Washington State, the most important feature of this kind is the Puget Sound Convergence Zone (PSCZ), described in Mass (1981). The PSCZ occurs when the low-level coastal winds are from the west to northwest, producing a low-level trough and convergence zone in the lee of the Olympic Mountains. This zone of low-level convergence and attendant upward motion often produces a band of enhanced cloudiness and precipitation that extends from the Olympics, across Puget Sound, to the western slopes of the Cascade Mountains. The most frequent location for the PSCZ precipitation enhancement is the zone from downtown Seattle northward to the southern portion of the City of Everett (approximately 30 km to the north).

The PSCZ can produce or enhance low-elevation snowfall over Puget Sound in several ways. For example, during situations in which temperatures aloft are cold enough for snow, but insufficient synoptic upward motion is present, the PSCZ can supply the requisite vertical motion. The effects of the PSCZ can be greatly amplified under low-stability conditions such as when cold air spreads over the region aloft. Also, higher precipitation rates and greater diabatic cooling (due to melting) found in the PSCZ can produce a zone of snow, surrounded by rain.

Snowstorms with strong mesoscale topographic components are generally very difficult to forecast. Since current operational models do not resolve such scales, prediction is based on a forecaster's ability to subjectively predict the mesoscale evolution based on synoptic scale guidance. To illustrate the complexities of such cases, consider the snowstorm of 18 December 1990 in which a PSCZ, coupled with cold air advection aloft, produced heavy snow along a narrow swath north of downtown Seattle. Late in this event an Arctic Front passed through the region, bringing additional snow, rapidly dropping temperatures, and strong northerly winds.

At 00 UTC 19 December 1990 (about the mid point of the storm), a high-amplitude 500 mb ridge extended into Alaska and a short-wave trough, embedded in northerly flow, was digging southeast over the Pacific Northwest (Fig. 6a). At 850 mb a sharp trough was also moving south over Washington; north of this feature the temperature dropped rapidly to a minimum of less than -25 °C over most of western Canada (Fig. 6b). A similar pattern appeared at the surface, with a cold Arctic front resident within the surface trough near the international border (Fig. 6c). An intense surface pressure gradient was north of the front, with a strong anticyclone centered over eastern Alaska.

Surface mesoscale analyses for the storm are shown in Figure 7. Troughing and mesoscale convergence were over Puget Sound at 12 UTC 18 December (Fig. 7a) indicating the formation of the PSCZ. As noted above, such convergence is a frequent occurrence in the area and is associated with low-level westerly or northwesterly winds on the coast.

By 21 UTC, moderate snow was falling over central Puget

Sound. A visible GOES satellite image during this time (1931 UTC) shows clear evidence of a PSCZ, with the characteristic band of enhanced cloudiness over the Puget Sound, flanked by clear areas to the north and south (Fig. 8). Cloud streets of shallow cumulus are observed over the coastal waters; these cloud lines are produced as cold air form the interior of British Columbia moves westward over the relatively warm waters of the Pacific and is destablized and moistened at low levels. The cloud streets curve cyclonically in response to the low-level flow and terminate over the Oregon and Washington coasts. A mesoscale surface chart for 21 UTC, shows a closed low, associated the PSCZ, over central Puget Sound (Fig. 9b). Moderate southwesterly flow enters the convergence zone from the south, while in the northern Sound the winds are light and from a variety of directions. The Arctic Front entered western Washington by this time, with strong northeasterly flow observed at Bellingham, WA. near the Canadian border.

At 00 UTC 19 December moderate to heavy snow was falling from approximately downtown Seattle into the northern and eastern suburbs. The surface mesoscale analysis shows the continued existence of the low associated with the PSCZ as well as the rapid southwest movement of the Arctic Front (Fig. 7c). Behind the Arctic Front northeasterly flow and rapidly rising sea-level pressure was observed.

During the next six hours the Arctic Front pushed through the Puget Sound region. In the hours immediately prior to and during Arctic Front passage, several stations reported thunder-an indication of the convective nature of the convergence zone precipitation. The Arctic Front was accompanied by moderate snowfall, a switch to strong northerly winds, and rapidly falling temperatures. Passage of the Arctic Front passage ended the PSCZ, and snowfall associated with the Arctic Front ended within 1-3h after frontal passage. Figure 7d shows the surface mesoscale analysis at 06 UTC. An intense pressure gradient over western Washington behind the Arctic Front produced strong northerly flow at most locations, with wind speeds at some sites exceeding 40 kts. The total snowfall produced during this event is shown in Fig. 9. Snow was limited to a narrow band, approximately 30 km in width, that stretched from south of downtown Seattle into the northern suburbs of the city. Snowfall amounts exceeding 10 in. extended from North Seattle to the east, with some locations receiving as much as 15 in. This precipitation pattern is typical of PSCZ events. With heavy snow amounts falling prior to and during evening rush hour, traffic in this hilly region ground to a halt with gridlock and accidents being widespread.

An examination of the evolution of the vertical soundings provides additional insight into this event. At 12 UTC 18 December, the sounding on the Washington Coast at Quilliyute was conditionally unstable from the surface to 750 mb and was nearly saturated from 850 to 750 mb, with rapid drying aloft (Fig. 10a). Westerly winds near the surface strengthened and veered to the northwest aloft. It is reasonable to expect that the sounding over Puget Sound would be similar, considering the proximity and

near equality of the observed surface temperatures at the two locations. By 00 UTC 19 December the Forks sounding had cooled considerably at all levels, with the greatest temperatures falls above 700 mb (Fig. 10b). The relatively moist, conditionally unstable layer now reached 650 mb. It would be expected that the airmass over Puget Sound would be less stable since the surface temperatures in the region (e.g., SEA at 37°F) were considerably warmer than Forks (32°F) at the time the sounding was launched (23 UTC 18 December). The 12 UTC 19 December sounding indicated that the Arctic air along the coast was dry adiabatic and extended up to about 850 mb (Fig. 10c). Offshore flow is seen at all levels.

Thus, the following scenario is likely to have taken place. The synoptic flow, interacting with the Olympic Mountains, established a convergence zone over central Puget Sound on 18 December. With an unsaturated surface layer, the convergence zone was not able to release the conditional instability resident in the lower troposphere. Stability decreased during the next 6 to 12 h, as the low level air became moistened and advection cooled temperatures aloft. Instability was then released by the low-level convergence associated with the PSCZ. Also contributing to the release of convection was the synoptic scale vertical motion produced by the upper level trough that was approaching the Pacific Northwest.

4. The relationship between ENSO and snowstorms over the western Washington lowlands

As shown in Fig. 1, there is considerable year-to-year variability in snowfall at Seattle-Tacoma Airport. A significant proportion of this variability can be shown to be related to the El Niño/Southern Oscillation (ENSO). There is considerable evidence that ENSO events are reflected in global tropospheric circulation anomalies. For example, Horel and Wallace (1983) showed that warm equatorial SST anomalies (El Niño episodes) are associated with below-normal 700 mb heights in the North Pacific and above-normal 700 mb heights over western Canada. Ropelewski and Halpert (1986) investigated North American precipitation and temperature patterns associated with ENSO. For the Northwest U.S. they found significant warming during the second year of El Niño events. The ENSO-related precipitation signal for the region is far weaker, with a tendency for drier than normal conditions during the first year of an El Niño episode. The association of El Niño with enhanced ridging over western North America and warmer temperatures and a weak suppression of precipitation over the Pacific Northwest suggests that such episodes might be characterized by less than normal snowfall in the region.

Composites of deviations from climatology of 500 mb height, sea level pressure and 1000-500 mb thickness for El Niño and La Niña events (see Table 2 for a list of the events used in the composites) are presented in Figure 11. The composites, averaged for December through February, were constructed in the same way as those presented in Section 1 of this paper. At 500 mb, El

NiÑo years are characterized by below-normal heights over the eastern North Pacific and above-normal heights over North America (Fig. 11a). Thus one would expect enhanced southwesterly flow aloft. At the surface, these years are associated with below-normal pressure over the Pacific, which extends into Alaska and western Canada (Fig. 11c). The corresponding thickness field (Fig. 11e) shows higher than normal thickness (or 1000-500 mb mean temperature) over western Canada and the Pacific Northwest. Clearly, the El NiÑo flow anomalies are associated with warmer than normal lower-tropospheric temperatures over the Pacific Northwest; thus, one would expect less snowfall over the area, especially at lower elevations. In contrast, the La NiÑa composite anomalies (Fig. 11 b,d,f) are consistent with an enhanced probability of snowfall. At 500 mb, the combination of above-normal heights offshore and below-normal heights over western North America would produce enhanced northwesterly flow over the eastern Pacific (Fig. 11b). With only a minor shift, this anomaly pattern would closely resemble the snow composite presented in Section 2. At the surface (Fig 11d), an offshore center of above-normal sea-level pressure anomaly extends into Alaska and northern Canada. The resulting coastal trough is reminiscent of a similar trough found in the snow event composite in Section 2. The La NiÑa thickness composite evinces below-normal thickness (1000-500 mb mean temperature) over northwestern North America, with the largest thickness anomaly over Alaska (Fig. 11f). In summary, previous studies by other investigators and the composite results shown above suggest that the synoptic flow is more consistent with enhanced snowfall during La NiÑa than El NiÑo years.

Table 2 presents the snowfall at Seattle-Tacoma Airport for a collection of well-defined El NiÑo and La NiÑa years. The selection of the El NiÑo events through 1977 was based on the list of strong and moderate episodes in Quinn et al. (1978). More recent El NiÑos were selected based on large and persistent positive SST anomalies in the western tropical Pacific. La NiÑa events were selected by finding large and persistent negative SST anomalies over the same region. The most striking finding in Table 2 is that, on average, El NiÑo years are associated with far less snowfall at this location than La NiÑa years (5.0 versus 16.9 in.). Based on a Student's-T Test, it was found that both of these samples are significantly different (at the 99% level) from the station mean (12.3 inches). However, this relationship is not perfect; although six of the seven El NiÑo years had snowfall below normal, one of them (1965-1966) was nearly double the climatological amount. The La NiÑa years were all above normal except for 1975-1976, during which only 4.9 in. fell.

The relationship between Pacific SST and snowfall at Sea-Tac Airport was also explored using the Comprehensive Ocean Atmosphere Dataset compiled at the National Center for Atmospheric Research. Linear correlation coefficients between Sea-Tac snowfall and annual SST deviations from climotology in the equatorial eastern Pacific were calculated for 1946 through 1991. The correlation between SST anomaly and Sea-Tac snowfall was -.356. However, by considering only those years with

relatively strong SST anomalies (greater than or equal to .4 deg C), the correlation jumps to -.609. These results indicate that warm (cold) equatorial SST anomalies are associated with lesser (greater) than normal snowfall at Sea-Tac.

The close connection between Puget Sound snowfall and equatorial Pacific SST provides the potential for forecasting the general level of wintertime snowfall several months in advance. First, ENSO events are generally slow to evolve and thus the conditions observed during autumn provide substantial insight into the nature of the wintertime state of ENSO and thus the flow over the Northwest. For example, if the warm sea surface temperatures of an El Niño were rapidly fading during the summer and were becoming cooler than normal during the fall, one could reasonably predict normal or above normal snowfall over the Northwest during the subsequent winter. Second, new methods of ENSO prediction (Barnett et al., 1988, Cane et al. 1987) have shown considerable promise. These methods, coupled with the above relationships between ENSO and regional snowfall, offer the promise of increased skill in predicting the wintertime snowfall for this area as far as a year in advance.

5. Summary

Snow is a relative rarity over the Pacific Northwest because the Cascade and Rocky Mountains usually shield the coastal lowlands from the cold air of the interior. Composites of more than a dozen heavy snowfalls over the Puget Sound Basin reveals that at 500 mb the typical synoptic set-up for snow consists of high-amplitude ridging over the eastern Pacific and troughing over the northwest U.S. and southwest Canada. Near the surface there is an intense anticyclone and Arctic air over the interior of British Columbia and a mesoscale trough in the coastal zone.

Based on a collection of case studies, it was found that western Washington snowstorms involve complex interactions between the synoptic scale flow and the mesoscale topography of the region. Most regional snowstorms appear to possess one or more of the following components: coastal cyclogenesis, during which a mesoscale cyclone intensifies over the coastal wasters of British Columbia and Washington; Arctic Front passage, in which the climatological marine air mass is replaced by an dry, Arctic flow; overrunning, during which an approaching cyclone lifts warm, moist air over the Arctic flow below; and mesoscale topographic effects, in which air flows over and around terrain barriers can enhance or attenuate snowfall. An example of the latter situation was shown. A substantial proportion of the annual variability of western Washington snowfall appears to be related to the El Niño/Southern Oscillation phenomenon. Specifically, El Niño (La Niña) events, associated with above (below) normal sea surface temperatures in the tropical Pacific, are related to below (above) normal snowfall over the region.

6. References

Ballentine, R. J., 1980: A numerical investigation of New England coastal frontogenesis. Mon. Wea. Rev., 108, 1479-1497.

Barnett, T., 1988: Prediction of ENSO events. Science, 241, 192-196

Bosart, L. F.; C.J. Vaudo and J. H. Helsdon, Jr., 1972: Coastal frontogenesis. J. Appl. Met., 11, 1236-1258.

_____, 1975: New England coastal frontogenesis. Quart. J. Roy. Meteor. Soc., 101, 957-978.

_____, 1981: The President's Day snowstorm of 18-19 February 1979: A subsynoptic-Scale event. Mon. Wea. Rev., 109, 1542-1566.

_____, and S. C. Lin, 1984: A diagnostic analysis of the President's Day storm of February 1979. Mon. Wea. Rev., 112, 2148-2177

Cane, M. A., S. E. Zebiak, and S. C. Dolan, 1986. Experimental forecasts of El Niño. Nature, 321, 827-832

Dickey, W. W., and R. N. Wing, 1963: The unusual: Arctic air into the Pacific Northwest. Weatherwise, 306, 259-263.

Ferber, G. K., and C. F. Mass, 1990: Surface pressure perturbations produced by an isolated mesoscale topographic barrier, Part II: Influence on regional circulations. Mon. Wea. Rev., 118, 2597-2606.

Horel, J. D., and J. M. Wallace, 1981: Planetary scale atmospheric phenomena associated with the Southern Oscillation. Mon. Wea. Rev., 109, 813-829

Kocin, P. J., and L. W. Uccellini, 1990: Snowstorms along the northern coast of the United States: 1955 to 1985. Amer. Meteor. Soc., Boston, 280 pp.

Lapenta, W. M. and N. L. Seaman, 1992: A numerical investigation of East Coast cyclogenesis during the cold-air damming event of 27-28 February 1982. Part II: importance of physical mechanisms. Mon. Wea. Rev., 120, 52-76

Mass, C. F., 1981: Topographically forced convergence in western Washington State. Mon. Wea. Rev., 109, 1335-1347.

Quinn, W. H., D. O. Zopf, K. S. Short and R. T. W. Kuo Yang, 1978: Historical trends and statistics of the Southern Oscillation, El Niño, and Indonesian droughts. Fishery Bulletin, 76, 663-678

Ropelewski, C. F. and M. S. Halpert, 1986: North American
precipitation and temperature patterns associated with the El
Niño/Southern Oscillation (ENSO). Mon. Wea. Rev., 114, 2352-2362

Sanders, F., and L. F. Bosart, 1985: Mesoscale structure in the
megalopolitan snowstorm of 11-12 February 1983. Part I:
Frontogenetical forcing and symmetric instability. J. Atmos.
Sci., 42, 1050-1061.

Table 1. Initiation of snowfall for events used in the composite.

12 UTC 28 Feb 1962	00 UTC 27 Dec 1965	00 UTC 05 Jan 1967
00 UTC 19 Dec 1968	12 UTC 31 Dec 1968	12 UTC 27 Jan 1969
00 UTC 25 Jan 1972	00 UTC 12 Dec 1972	00 UTC 27 Dec 1974
00 UTC 08 Jan 1980	00 UTC 22 Nov 1985	12 UTC 27 Nov 1985
12 UTC 01 Feb 1989		

Table 2. Snowfall (in.) at Seattle-Tacoma Airport for El Nino and La Nina seasons.

El NiÑo Years

1991-1992	0.0
1986-1987*	1.4
1982-1983*	Trace
1976-1977*	1.9
1972-1973*	9.1
1965-1966*	22.9
1957-1958*	T

Average   5.0

La NiÑa Years

1988-1989*	14.2
1975-1976*	4.9
1970-1971*	16.1
1964-1965*	18.2
1955-1956*	24.2
1954-1955*	13.4
1950-1951*	27.4

Average   16.9

* Used in the El NiÑo/La NiÑa Composites

SEA-TAC SNOWFALL
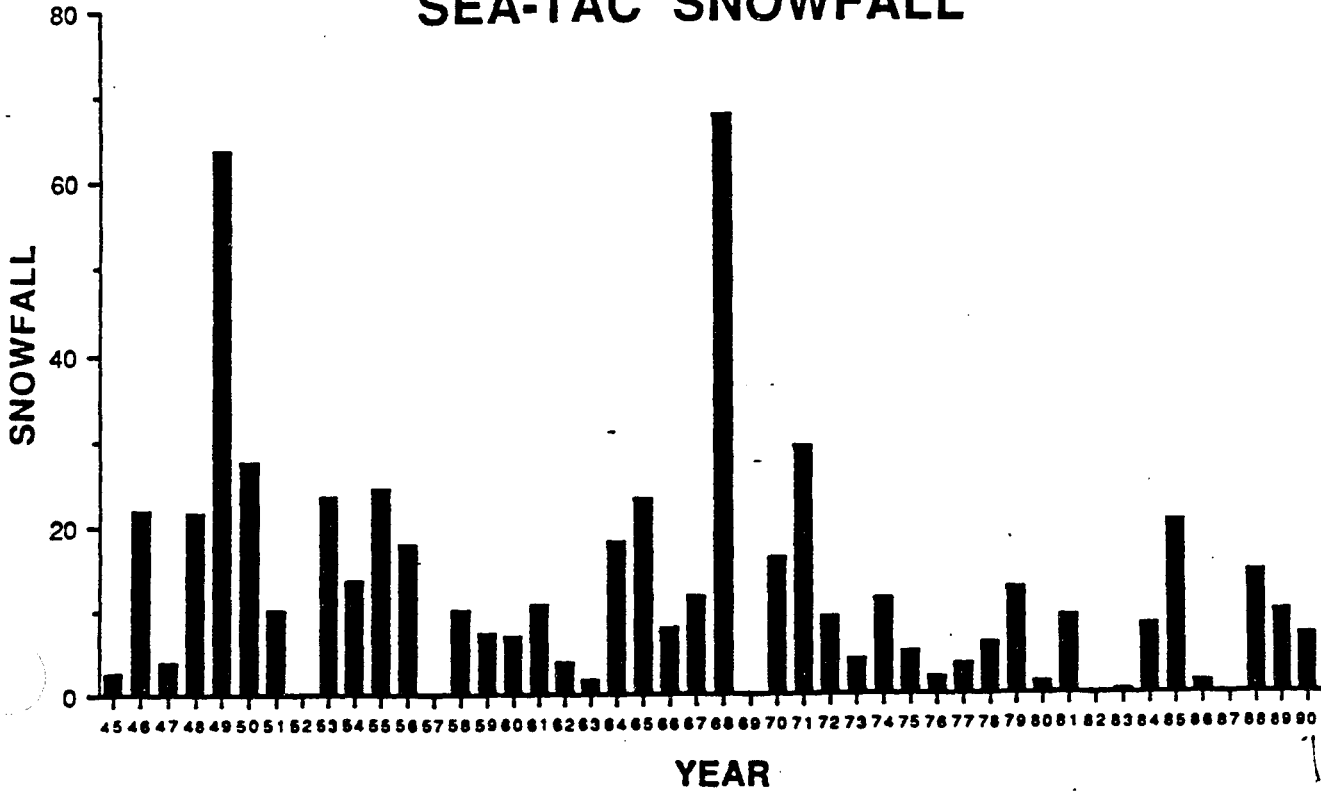
Figure 1. Annual snowfall (in.) at Seattle-Tacoma Airport from 1945 through 1991. Snowfall for the year X is for the winter X/X+1.
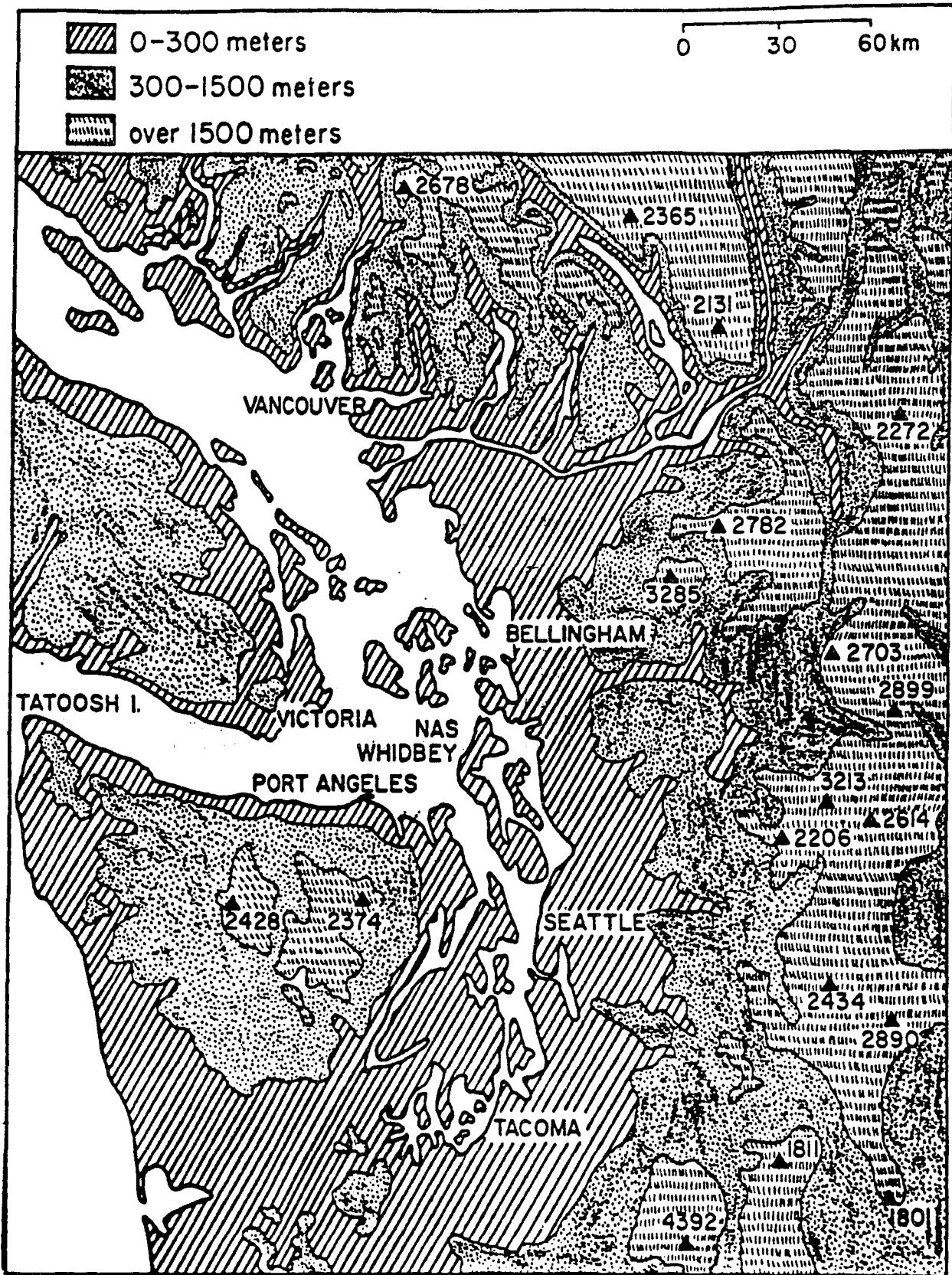
Figure 2. Geography of northwest Washington and southwest
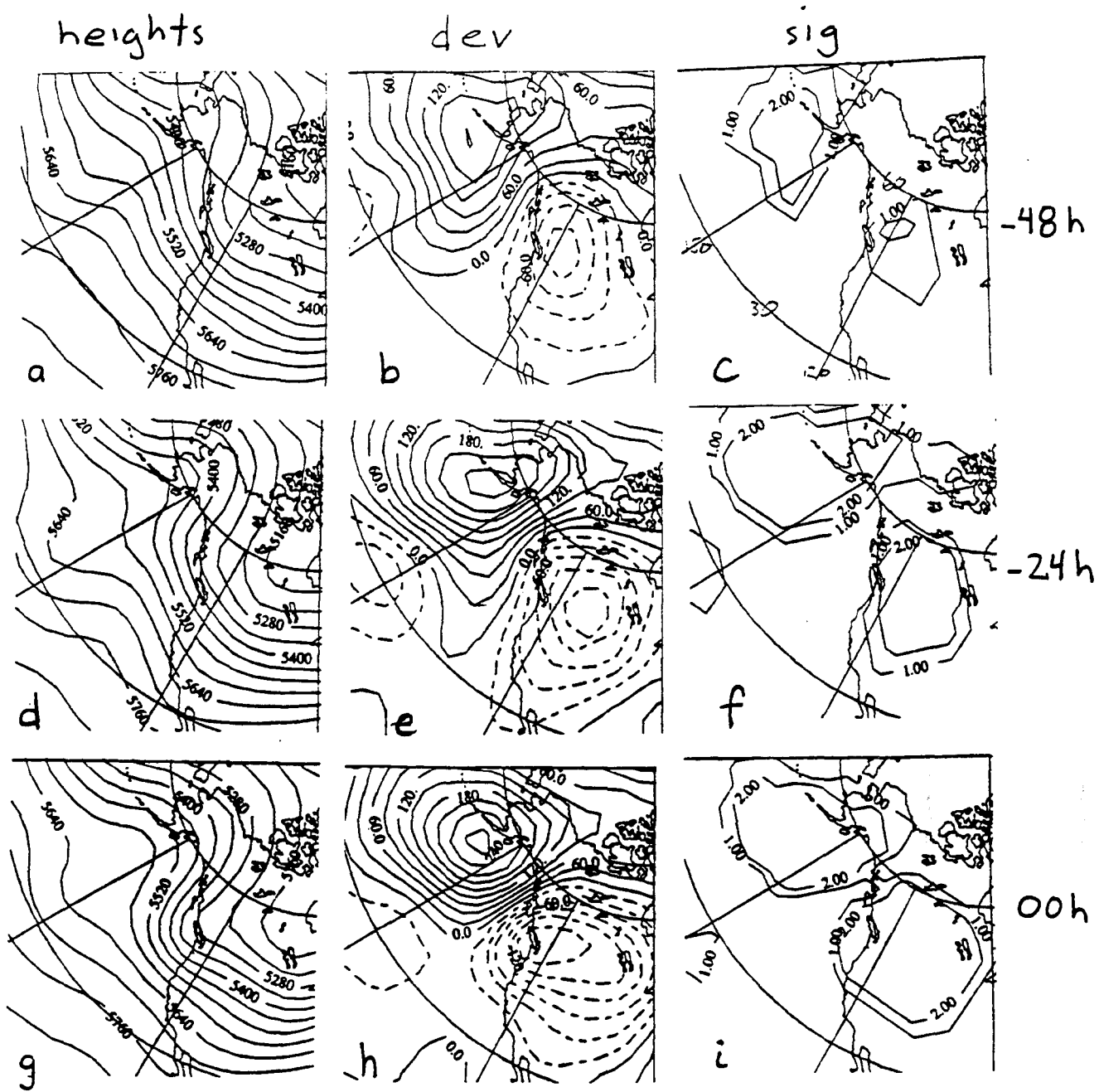British Columbia.

Figure 3. Composites of 500 mb geopotential heights (m), deviations of 500 mb height composites from climatology (m) and statistical significance of the deviations from climatology at the 95% (contour 1.00) and 99% (contour 2.00) levels for -48 h through 00 h (time is relative to the initiation of the composite event). The contour intervals for geopotential height and height deviations are 60 m and 30 m, respectively.
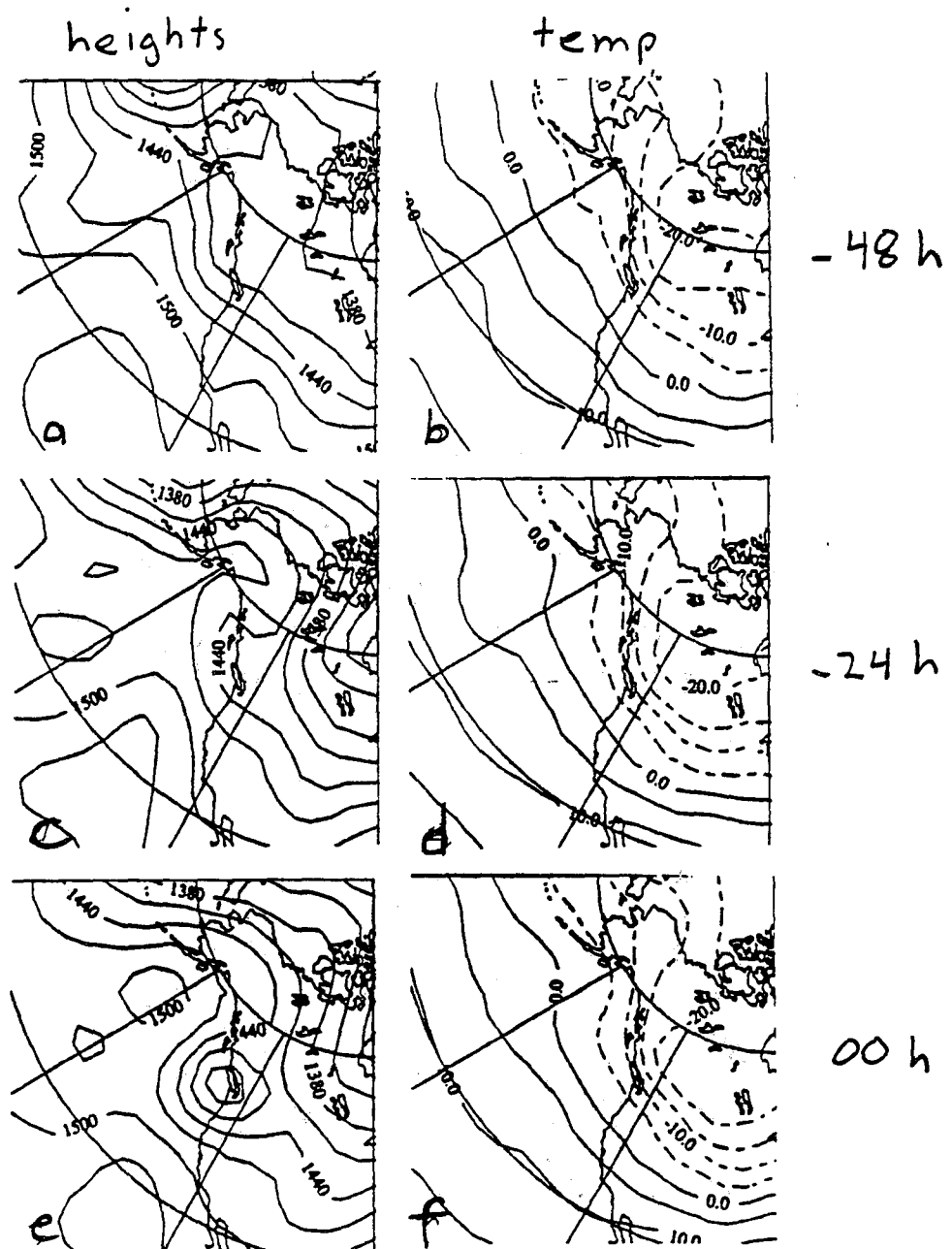
Figure 4. Composites of 850 mb geopotential height (m) and
temperature (°C) for -48h through 00 h.
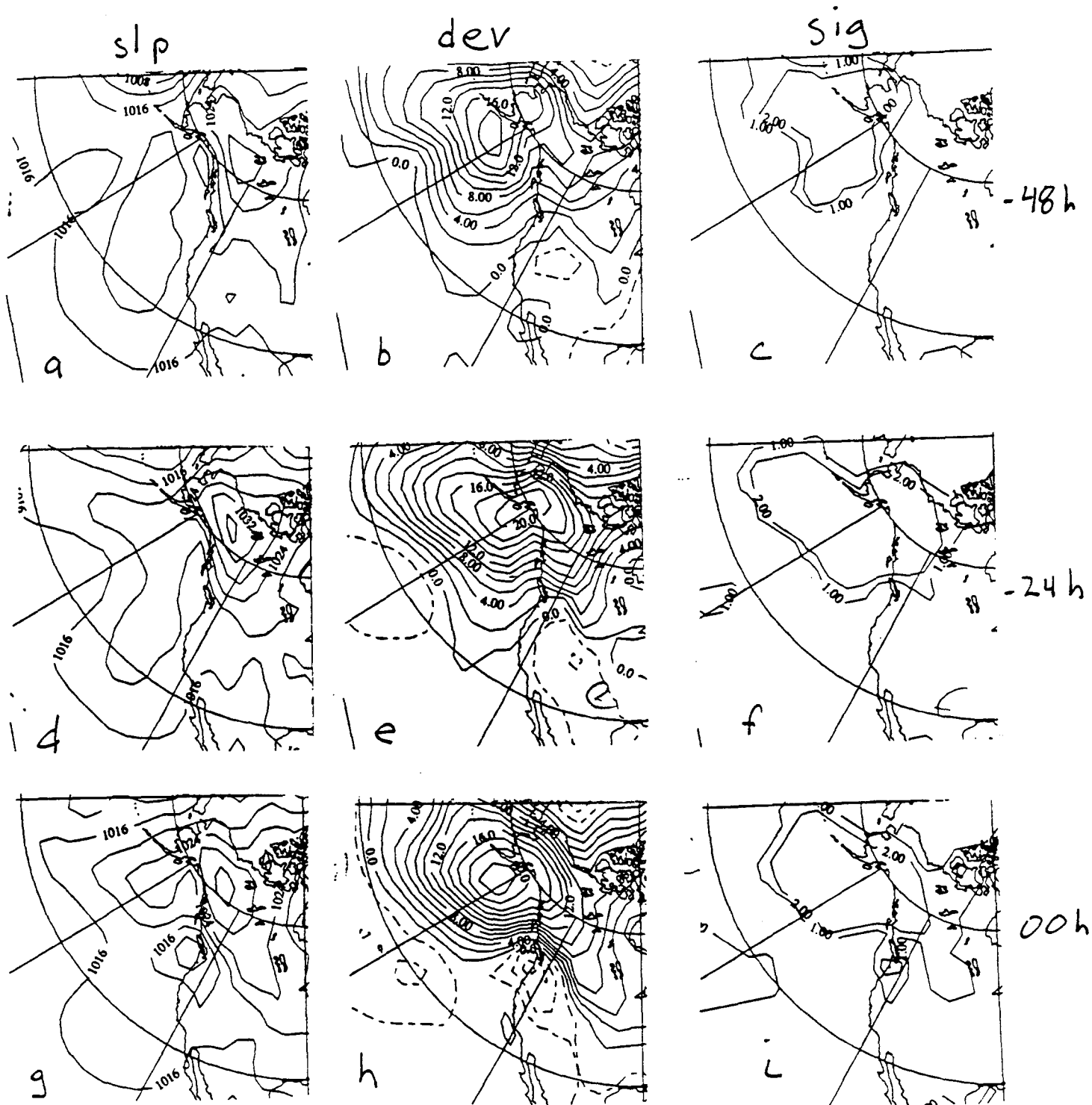
Figure 5. Composite fields of sea level pressure (mb), deviation of the surface pressure composite from climatology (mb), and the statistical significance of the surface pressure deviations for -48 h through 00 h. The contour intervals for sea level pressure and its deviations from climatology are 4 and 2 mb, respectively. The statistical significance is presented as in Fig. 3.
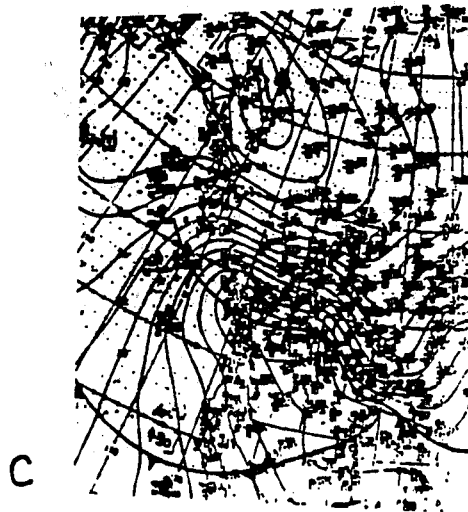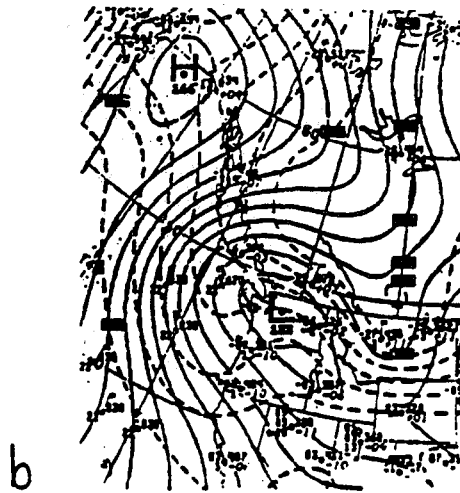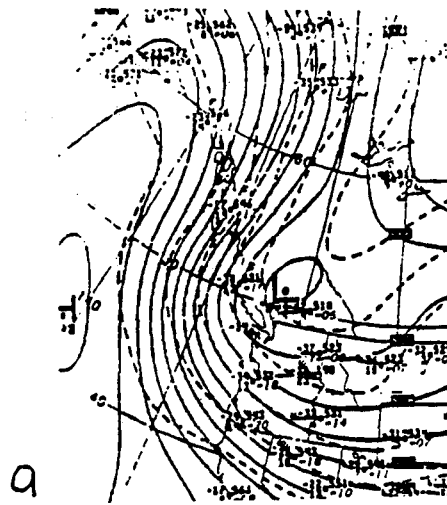
Figure 6. National Meteorological Center analyses at 00 UTC 19 December 1990. a). 500 mb heights (m) and temperatures (°C). b). 850 mb heights and temperatures. c.) Sea-level pressure (10XX mb).
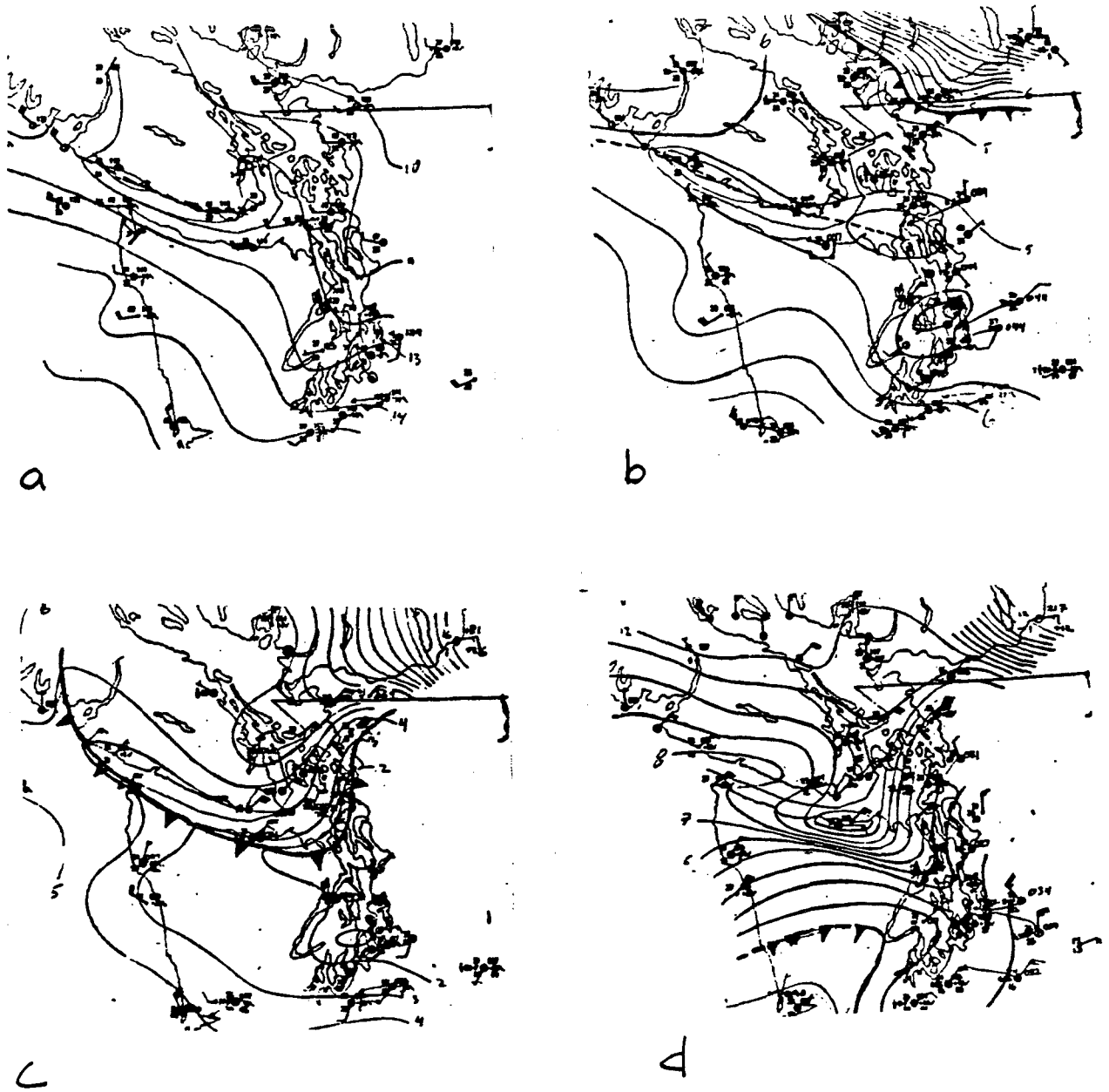
Figure 7. Mesoscale analyses for December 1990 case. Contour interval is 1 mb. a.) 12 UTC 18 December. b.) 21 UTC 18 December. c.) 00 UTC 19 December. d.) 06 UTC 19 December.

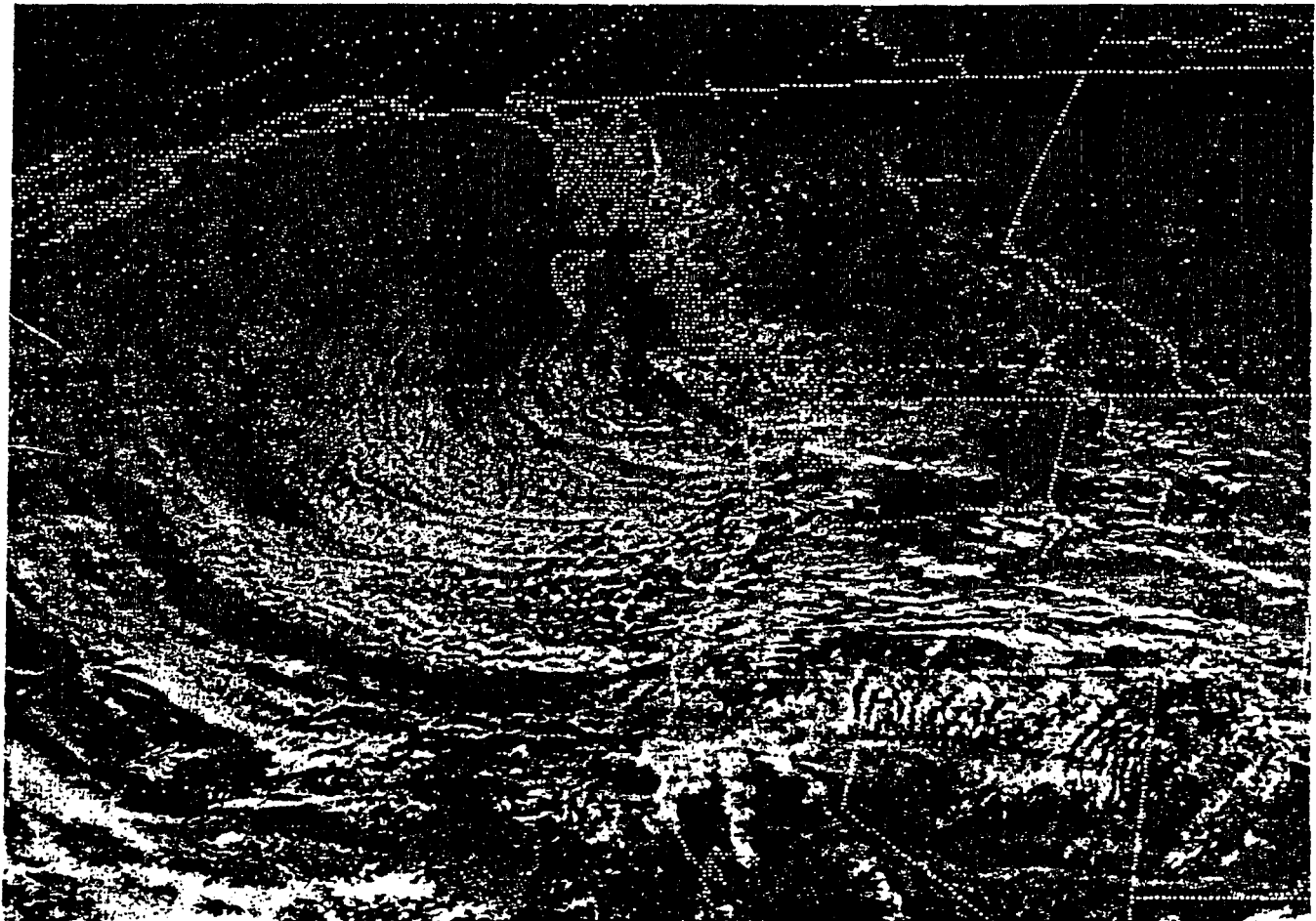1931 18DE90 19A-2   00892 15892 CB3

Figure 8.   Visible satellite imagery at 1931 UTC 18 December 1990.
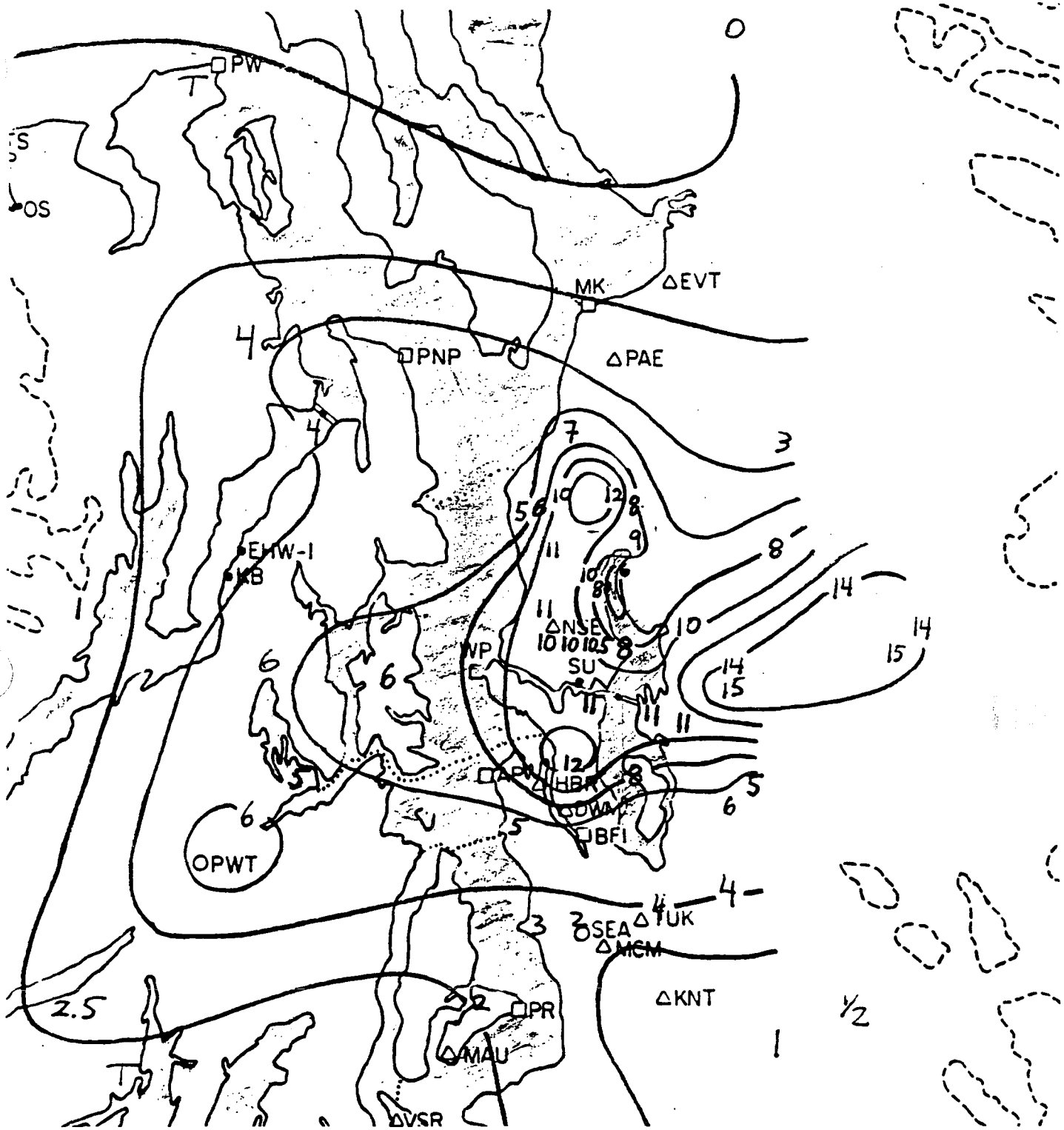
Figure 9. Snowfall map for the December 1990 case.
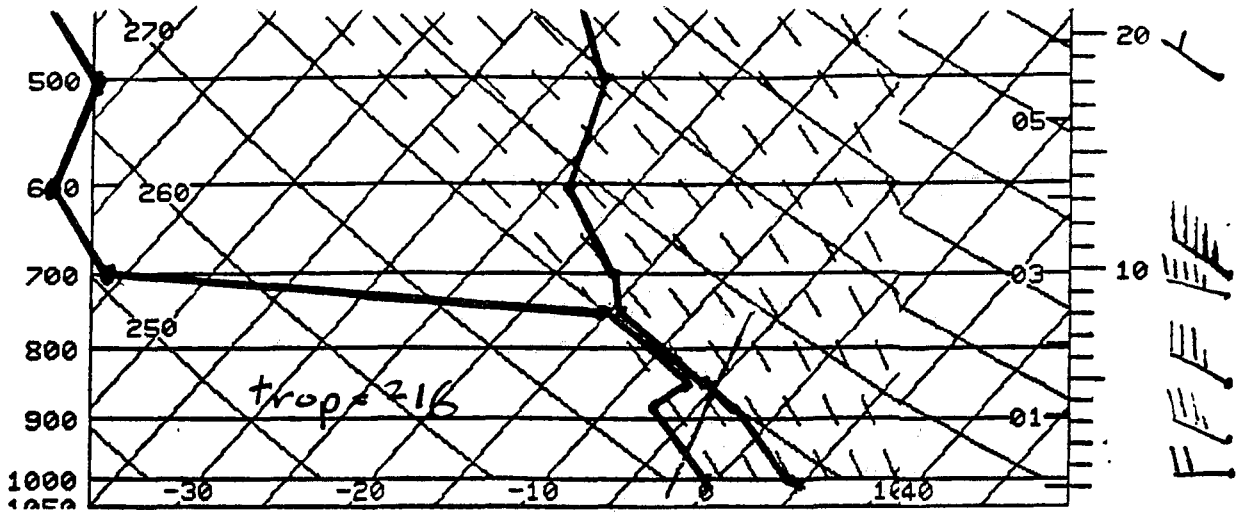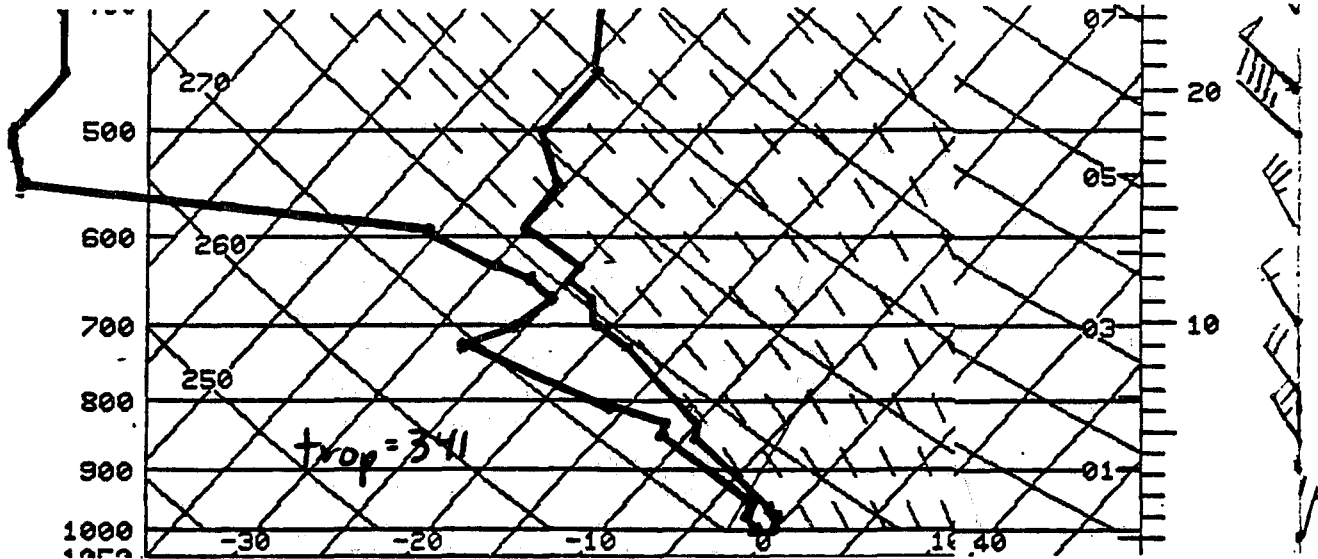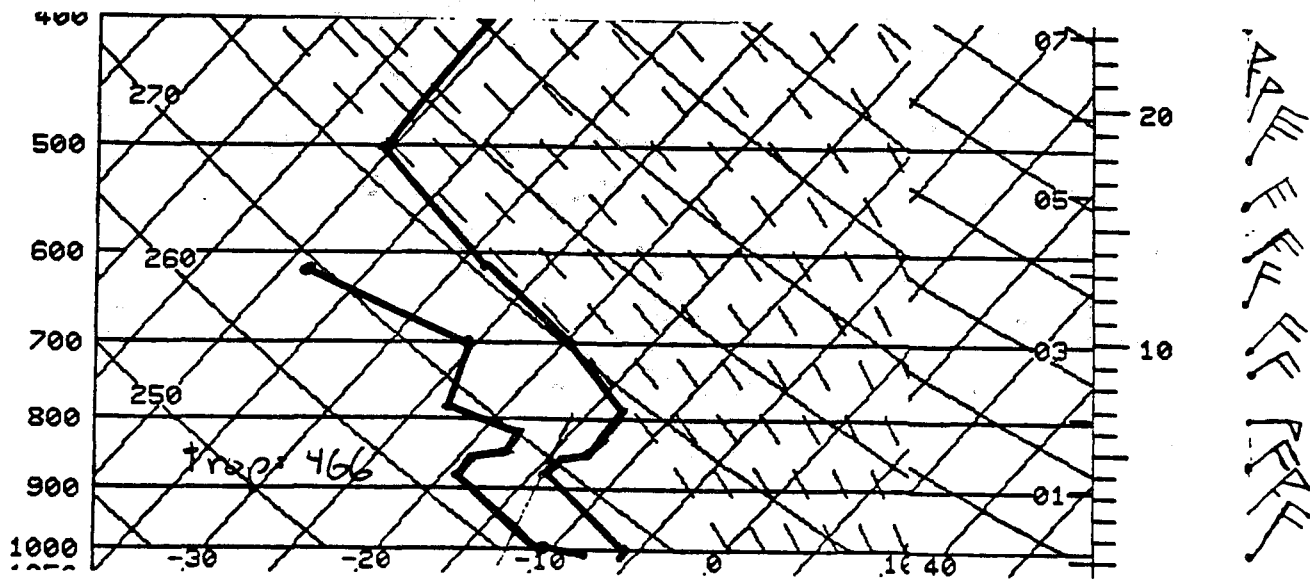
Figure 10. Vertical soundings of temperature, dewpoint and wind at Quilliyute, WA. for (a) 12 UTC 18 December, (b) 00 UTC 19 December 1990, and (c) 12 UTC 19 December 1990.
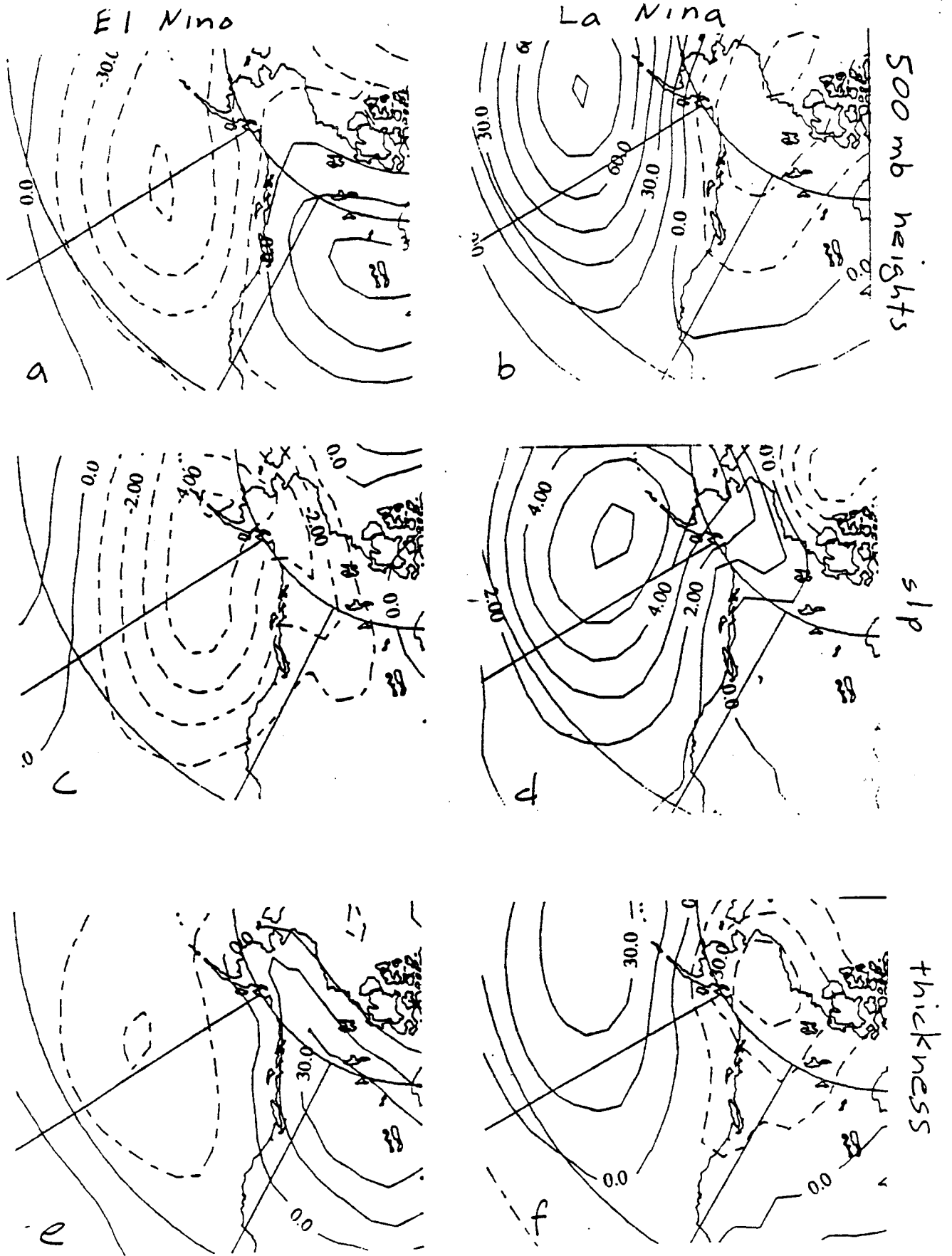
Figure 11. Mean December through February deviations from climatology of 500 mb height (m), sea-level pressure (mb), and 1000-500 mb thickness for El Niño and La Niña years. The contour intervals for 500 mb height, sea level pressure and 1000-500 mb thickness are 15 m, 1 mb, and 15 m, respectively.

THE USE OF HIGH RESOLUTION DATA FROM THE NESTED GRID MODEL FOR THE PREDICTION OF LAKE-EFFECT SNOWS

by Thomas A. Niziol and Steve McLaughlin
NWS Buffalo, NY

ABSTRACT

High resolution model output from the National Meteorological Center's Nested Grid Model was made available on an experimental basis to the National Weather Service Office in Buffalo, NY during the winter of 1991 for research and evaluation. Increased vertical and temporal resolution of the model data compared to the standard data available at NWS Buffalo allowed forecasters a more detailed look at parameters in the lowest layers of the atmosphere. This was especially important for the prediction of lake-effect snow, which is generally confined to the lowest 3km of the atmosphere.

Hourly wind direction forecasts were used to refine the timing on movement and location of lake-effect snowbands off Lakes Erie and Ontario. In addition, forecast hourly soundings were evaluated to determine the existence and height of the subsidence inversion that limits convective cloud growth in lake-effect snow. Case studies of single band storms that occurred during the winter of 1991-92 are presented here to show how the new model output can be used more efficiently as a forecast tool.

INTRODUCTION

Lake-effect snowstorms are notorious weather makers for the people that live downwind of Lakes Erie and Ontario during the late fall and winter months. This region is considered the snowiest populated area to the east of the Rocky Mountains, with annual snowfall amounts of greater than 500
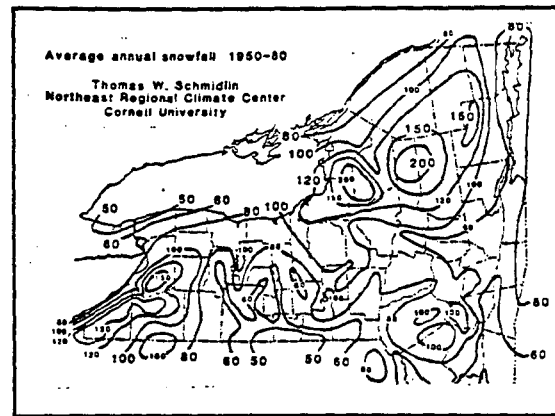
Fig 1. Average annual snowfall (inches) over New York State 1950-80. Note the snowfall maxima to the lee of Lakes Erie and Ontario. (Northeast Regional Climate Center)

cm (200 in) recorded at some locations (Fig 1).

These intense (yet very localized) snowstorms can severely impact an area, bringing a virtual halt to commerce and industry at times. For the forecast to be of more value to the public, the operational forecaster must be able to predict these events on very small scales in both time and space.

The NWS office at Buffalo, NY has been involved in an ongoing research effort to improve operational forecasts of these events to the lee of the eastern Great Lakes. During the fall and winter of 1991-92 the staff evaluated an experimental subset of the gridded data files from the NGM. These high resolution data files allowed the forecasters a much more detailed look at

parameters such as temperature, wind, and humidity, in the lowest layers of the atmosphere.

This paper will evaluate the high-resolution prognostic data for case studies that occurred during the winter of 1991-92, to determine whether improvements can be expected in short term forecasts for lake snows.

LAKE EFFECT SNOW ENVIRONMENT

Lake-effect snows are meso-alpha scale events as defined by Orlanski (1975). These storms are generally confined to the lowest 3 km of the atmosphere over a very localized area, with typical snowbands on the order of 5 to 20 km wide and less than 200 km in length (Hill 1971). Subtle changes in the large scale flow can cause snowbands to oscillate across a forecast region. These subtle changes may also occur over very short time scales, producing a wide range of weather conditions across the forecast area. Some of these storms have been known to produce extreme snowfalls with as much as 175 cm over a cross section less than 50 km wide (Sykes 1966, Niziol 1988).

Current numerical models, such as NMC's Nested Grid Model (NGM) are limited in their ability to simulate the mesoscale effects which the Great Lakes and local topography have on surrounding weather. In addition, prognostic model output made available to the forecaster usually is too limited in temporal and spatial resolution to accurately predict the evolution of lake-effect snow.

However, forecasters have developed a number of prediction schemes for lake-effect snow based on the synoptic scale data that is available from dynamic models (Niziol 1987). Using select forecast parameters, meteorologists are able to predict the general location and timing of these often intense snowstorms.

LAKE EFFECT FORECAST PARAMETERS

Forecasters generally follow the "Forecast Funnel" approach for the prediction of these mesoscale events (Snellman 1992). Synoptic scale pattern recognition categorizes the large scale weather features which will influence snowband development. Once a lake-effect favorable situation

is recognized, select meteorological parameters are analyzed to determine how they might influence the mesoscale event. These include:

a. temperature difference between the lake and 850 mb level, as well as the 700 mb level.
b. height and strength of the capping (subsidence) inversion.
c. wind direction at the 850 mb level.
d. alignment of winds from the boundary layer through 700 mb.
e. synoptic scale vorticity advection

The temperature difference between the lake and the 850 mb level is used as an index of boundary layer stability. In general, a difference of 13 degrees Centigrade is considered necessary for lake snow to develop (Rothrock 1960, Hill 1971), though with synoptic scale enhancement, the temperature difference may be a bit less (Dockus 1985).

The temperature difference between 850 mb and 700 mb implies boundary layer depth, and the possible existence of the subsidence inversion that often accompanies the arctic airmass (Petterssen 1956). The capping inversion limits convective growth of snow producing clouds, and can be used as a predictor of snowband strength or termination.

In general, snow producing clouds align themselves with the average wind direction within the cloud layer. Over the Eastern Great Lakes, McVehil (1966) showed that snowbands aligned themselves best with winds at about the 850 mb level. Based on the research, forecasters developed a series of locator charts for Lakes Erie and Ontario to predict potential snowband location (Fig 2).

The change in wind direction with height within the cloud layer not only signals warm or cold air advection within the airmass (synoptic scale), but can indicate the mesoscale organization of the band. Less than 30 degree change in wind direction with height contributes to well organized snowbands, whereas greater than 60 degree directional shear may spread the snowbands out or break them up altogether (Niziol 1987).

Synoptic scale forcing, analyzed operationally through positive vorticity advection, has been shown to elevate the capping inversion in the lake-effect snow environment (Jiusto et al 1970). As a result, the 500mb vorticity pattern is considered as a prime forcing function in lake-effect snow.
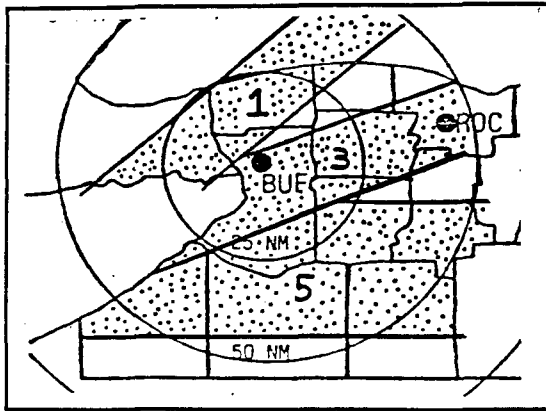
Fig 2. Locator chart for Lake Erie indicates to forecasters where the heaviest lake-effect snow will occur based on the 850 mb wind direction. Areas 1, 3, and 5 are shown here: (1) 230-239° (3) 250-259° and (5) 270-289°.

Current and past forecast procedures most often use information from the surface, 850 mb, 700 mb, and 500 mb levels to predict lake-effect snows. These levels were chosen because this was the only prognostic data available to the forecaster on a daily basis. Even though higher resolution data is computed by the NGM model, it is only available to forecasters at a minimum of 6 to 12 hour intervals. This does not adequately account for the types of changes that occur within the space and time scale of lake-effect snows. Consequently, the forecast can only generalize the potential scenario of a lake-effect snow event.

COMPARISON OF AVAILABLE MODEL DATA

The standard model output available in forecast offices includes both synoptic scale graphics, and alphanumeric listings of various forecast parameters for specific points (NGM FOUS Fig 3).

When the NGM FOUS data became available to forecast offices in the mid 1980's, it provided additional model output which was not previously available from the Limited-AREA Fine Mesh (LFM) model. The NGM FOUS includes temperature forecasts for 3 sigma levels below 700 mb, which allows forecasters to estimate the potential height and strength of the subsidence inversion (Reinking 1991). However, a major deficiency in the NGM FOUS data continues even today; that is the lack of wind forecasts below 700 mb, where most of the lake-effect snow events are confined.

The introduction of NGM high resolution prognostic data into the operational forecast setting fills many of the voids left by the original NGM FOUS, as shown in Fig 4.

Fig 3. NGM FOUS forecast for Buffalo, NY at 1200 UTC November 24, 1992 (Hauser 1986). The file provides a 48 hour forecast in 6 hour increments.

```
STATION = 42.93N   78.73W BUF BUFFALO
91112412 72528
*************************************

BUF  911112412 FORECAST PROJECTION= 0
LYR  TEMP DEPR   KTS  DIR  PRES   RH
 16 -56.7 36.0  21.0 203.   22.   1.
 15 -59.7 23.3  46.0 225.   80.   4.
 14 -56.8 17.9 103.0 223.  142.   9.
 13 -49.5 18.8 125.2 212.  208.  10.
 12 -47.8 21.5 144.8 211.  278.   7.
 11 -36.5 14.6 145.6 204.  349.  21.
 10 -26.3 24.1 132.9 202.  421.   9.
  9 -22.1 13.5 110.6 198.  494.  28.
  8 -17.4  5.0  81.4 202.  565.  65.
  7 -12.7  0.7  63.8 204.  634.  95.
  6  -7.8  6.7  55.5 209.  700.  58.
  5  -7.2  5.8  49.3 217.  762.  63.
  4  -5.9  1.6  35.5 231.  819.  88.
  3  -2.6  3.0  31.5 242.  870.  80.
  2   0.2  2.5  27.3 249.  915.  83.
  1   2.4  3.0  20.6 253.  953.  80.
PRCP(HR)=.000   PRCP(TOT)= 0.000
***********************************
```

Fig 4. NGM high resolution model output at t=0 hrs. for Buffalo, NY at 1200 UTC November 24, 1992. Forty eight hourly "soundings" are available to the forecaster for all 16 levels of the model.

The data is sometimes referred to as a forecast sounding and includes hourly forecasts of specific parameters for all 16 levels of the model, including 5 levels below 700 mb out to 48 hours. The forecast data includes temperature, dewpoint depression, wind speed and direction, relative humidity and precipitation for select locations, interpolated from the NGM grid. The NGM high resolution prognostic data provides a much more complete set of guidance for the forecast process.

MODEL SENSITIVITY

In order to evaluate the high-resolution model data as a forecast tool, a preliminary step was taken to compare the interpolated data to actual observations. Initialized model data was compared to observed upper air data taken twice a day at Buffalo, NY for the period January-March 1992. In addition, 12-48 hour NGM forecasts were compared to initialized NGM model data to determine the consistency of model runs. Parameters included wind direction and temperature observed at the 850 mb with model forecast data for sigma layer three (roughly 878 mb). Keeping in mind that only a limited data set was analyzed, a few observations can be made about the correlation of observed and forecast data.

Wind direction forecasts were filtered to remove data when wind speed was less than 10 mph, due to the wide variability of wind direction with weak winds. A comparison of NGM high resolution data and corresponding 0-24 hour forecast runs generally showed a standard deviation of less than

10 degrees difference. Thus, as a forecast tool, model wind direction may be a good indicator of snowband location orientation; however, as little as a 10 degree wind shift can relocate a snowband to a different part of the forecast area (Niziol 1987).

Similarly, a comparison of sigma level 3 data and observed temperature at 850 mb indicated that a standard deviation difference of approximately 1.5°C can be expected for 0-24 hour forecast runs. This would suggest that the model, in most cases, realistically forecasts temperatures in the lower layers of the atmosphere.

VERIFICATION

The major forecast parameter verified during the case studies was wind direction vs. snowband location. In addition the existence of the subsidence inversion was also evaluated for a specific event.

The wind direction forecasts were verified by comparing the location of precipitation echoes off the WSR-57 radar with model forecast wind direction. A line was drawn through the axis of the strongest radar echoes within the snowband to determine in which forecast area the heaviest snowfall was occurring. For the same time period, forecast wind directions for the bottom three sigma layers were analyzed to predict which of the six forecast Areas (Fig 2) should be receiving heavy snow. Sigma levels one and two were tested in addition to sigma level three to determine whether they would correlate better with snowband location. The observed forecast areas were compared to the predicted areas with contingency tables (Fig 5).

(a) sigma 1 (878 mb)

OBSRVD	1	2	3	4	5	6	TOT
1	\	1					2
2	1	\	1				3
3			\3				3
4				\	1		2
5				1	\6		7
6					1	\3	4
TOT	2	2	4	2	9	3	22

(b) sigma 2 (925 mb)

OBSRVD	1	2	3	4	5	6	TOT
1	\	1					2
2	1	\2					3
3		3	\				3
4		1		\	2		3
5			1	1	\5		7
6					3	\	4
TOT	2	7	1	1	10	1	22

(c) sigma 3 (965 mb)

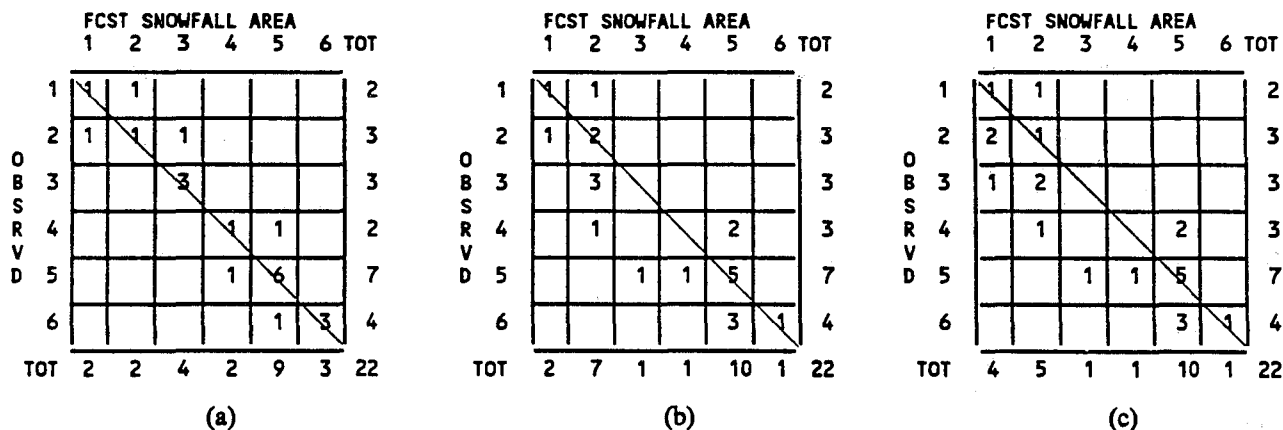| OBSRVD	1	2	3	4	5	6	TOT
1	\	1					2
2	2	\					3
3	1	2	\				3
4		1		\	2		3
5			1	1	\5		7
6					3	\	4
TOT	4	5	1	1	10	1	22

Fig 5. Contingency tables for forecast vs. observed snowband location for the six forecast Areas off Lake Erie at select times from the NGM forecast valid 1200 UTC 24 Nov 1991. Each table is based on wind direction at various sigma levels including: (a) sigma 1 (878 mb) (b) sigma 2 (925 mb) (c) sigma 3 (965 mb).

In addition, a standard forecast technique was evaluated with the new data set. Hourly wind forecasts from sigma level three were plotted against time. In this way the forecaster has an overall picture of the trend in wind direction throughout the forecast period. Then along with the locator charts in Fig 2, a general forecast of snowband movement and location with time can be provided to the public. This "real world" forecast approach provided the public with an expected scenario of the lake-effect storm (i.e. whether or not the storm would move into the northern suburbs that evening, or will it come back this way once it passes through...)

Soundings taken at Buffalo, NY were compared to forecast model data to determine if the NGM model could accurately predict the subsidence (or capping) inversion that often develops over the Great Lakes in association with the arctic or polar-continental airmass (Petterssen 1956). During intense lake-effect snow episodes however, the temperature inversion may be eroded away altogether, and the dry layer elevated somewhat due to convection within, and close to a snowband. In the case studies that were analyzed it was observed that when no subsidence temperature inversion existed, precipitation echo tops from the Buffalo radar were limited to within a few hundred meters of the base of the dry subsidence layer on the sounding. So, it was decided to compare the height of the base of the deep, dry subsidence layer between the forecast model data and the actual Buffalo sounding.

CASE STUDIES

The main case study was a single band snowstorm that occurred off Lake Erie over metropolitan Buffalo during 24-25 November 1991. About 37 cm (15 in) of snow was recorded near Buffalo during the event. In addition to the main case study, two other events are reviewed briefly to demonstrate the potential benefits of the hourly forecast wind direction plot as a forecast tool. The second event occurred during 18-19 January 1992 and produced two brief bouts of heavy snow over metropolitan Buffalo. The third event was a prolonged stationary single band storm off Lake Ontario that dumped about 225 cm (90 in) of heavy snow over portions of southern Oswego county in central New York State!

November 24-25 1991

The event of 24-25 November 1991 was a single band snowstorm that occurred at the east end of Lake Erie. This storm was significant, because it affected a population of over a million people in the Buffalo area. Storm totals of 37 cm (15 in) of snow fell over the suburbs just south of the Buffalo airport, with another maximum of 30 cm (12 in) over the southern tier of New York (Fig 6). During 26 November additional snowfall occurred over western new York from lake-effect streamers off Lake Huron.
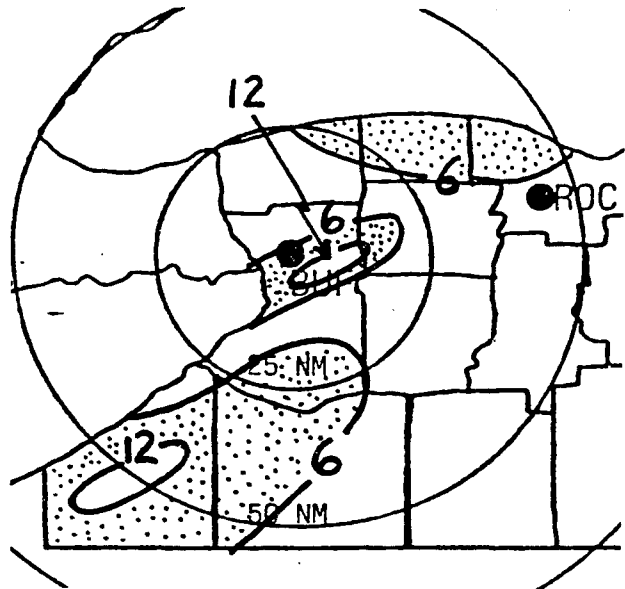
Fig 6. Total snowfall (inches) from the Lake Erie snowstorm during 24-25 Nov 1991. Note two snowfall maxima over a localized stretch.

Synoptic scale pattern recognition flagged this event to begin as an intense single band storm, which would eventually evolve into a multiple band event. A 500 mb closed low was forecast to move east from the upper Great Lakes to just south of James Bay Canada during the period (Fig 7a). At the surface, the nearly vertically stacked low was forecast to push a strong cold front through western New York on the morning of the 24th, followed by a secondary cold front associated with the upper trough, early on the 25th (Fig 7b).

Using the sigma level three wind output the operational forecaster predicted snowband location bordering across Areas 1-2 from 1200-2000 UTC on the 24th (Fig 8). A snowband did develop over Areas 1-2 during that morning (Fig. 9a). Wind direction was forecast to veer slightly during late
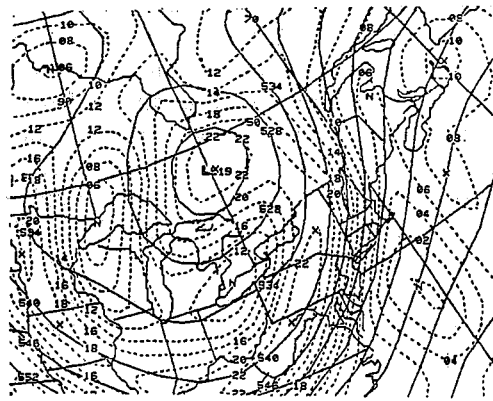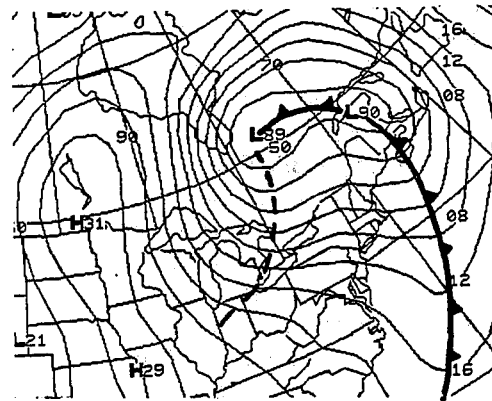
(a)   (b)

Fig 7. (a) NMC 500 mb analysis of height (dam) and vorticity (10⁶) at 0000 UTC 25 Nov 1991.
(b) NMC surface analysis (4mb contour) at 0600 UTC 25 Nov 1991.

afternoon and become steady again by evening. As predicted, by that evening the snowband had intensified and drifted south over the city of Buffalo and the airport (Fig 9b), where it remained for about a 4-5 hour period, producing snow at a rate of greater than 2 inches an hour in a very narrow band. Between 0000-0600 UTC nearly 33 cm (13 in) of snow was recorded across the southern suburbs. By 0600 UTC the band continued a slow drift south across the southern suburbs (Fig 9c). After 0700 UTC the band widened, weakened, and drifted well south of Buffalo over Area 5 (Fig 9d). The wind plot predicted the band to move to Area 5 and remain there for about an eighteen hour period. Although the fetch was reduced somewhat over Lake Erie, the snowband produced as much as 30 cm (12 in) of snow over the higher elevations of Area 5. Toward the end of the forecast period multiple snowbands were observed on radar off Lake Ontario and Lake Erie. Satellite imagery confirmed that these snowbands originated well upstream of western New York, off Lake Huron. The wind plot and locator tables also predicted this scenario.

A special weather statement issued early on the morning of the 24th posted snow squall warnings for portions of western New York off Lake Erie. The statement notified the public that "...squalls would most likely begin later in the morning off Lake Erie over parts of Niagara, Orleans, and extreme northern Erie counties, then shift southward into the Buffalo area later in the day". That night the squalls were forecast to "...most likely remain over parts of Erie and Genesee

counties for several hours before gradually moving toward northern Chautauqua and Cattaraugus counties...".

The comparison of wind direction forecasts for the first three sigma levels showed that sigma level 3 (878 mb) correlated best with observed snowband location (Fig 5a). In fact, all time periods were within one forecast sector of observed location. The predicted wind directions in both lower sigma levels generally were aligned a bit more south of west of the major snowband axis. Consequently forecast Areas for both levels were often one to two sectors away from observed snowband location. This reinforces the earlier research on the eastern Great Lakes in which McVehil (1966) found that snowbands generally align themselves with the winds near the 850 mb level.

For this case study the plot of forecast wind direction provided a fairly accurate depiction of the evolution of the storm, including the location, amount of time spent over each forecast area, and approximate timing of the movement of the snowband.

The forecast height of the dry layer associated with subsidence compared well to the observed height. Although lake snow did not cease altogether, most of the lake snow activity decreased to only a few flurries during the late afternoon of the 26th, when the predicted base of the dry layer dropped below the 800 mb level (Fig 10).

January 18-19 1992

This event was also a single band storm that

FORECAST WIND DIRECTION 878mb

Fig 8. NGM sigma level 3 (870mb) wind direction forecast vs. time for Buffalo, NY at 1200 UTC Nov 24, 1991. Corresponding forecast areas are numbered 1-6 at the right of the graph.
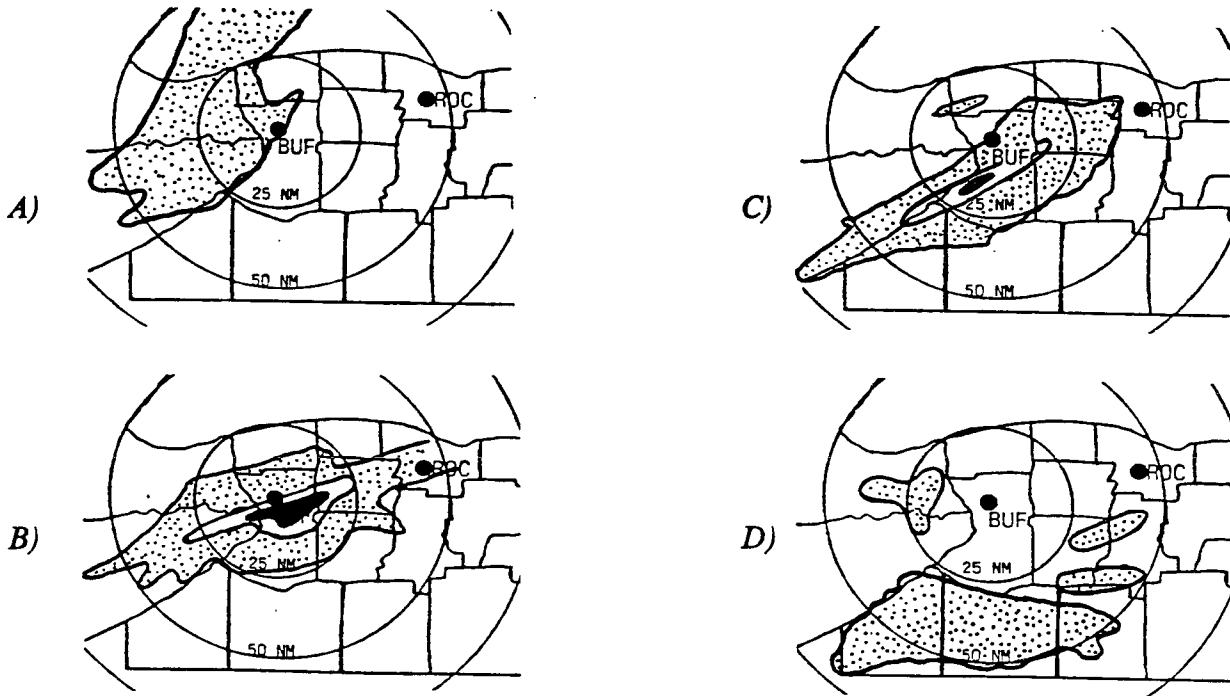
Fig 9. Radar overlays off the WSR-57 DVIP radar at Buffalo, NY. To highlight the intensity of low density lake-effect snow, the linear signal is outlined. level 1 = full gain, level 2 = 12dBz attenuation, level 3 = 21 dBz attenuation. (a) 1400 UTC 24 Nov 1991 (b) 0200 UTC 25 Nov 1991 (c) 0600 UTC 25 Nov 1991 (d) 1800 UTC 25 Nov 1991.

Pressure (mb)

500

600

700

800

900

1000

```
00z          12z          00z          12z          00z
25 Nov                    26 Nov                    27 Nov
```

Time (hours) Initialized 11/25/00z ==>

Fig 10. Approximate height of the subsidence level observed at Buffalo, NY (X), and the corresponding NGM forecast subsidence level (squares) for the NGM model run at 0000 UTC Nov 25 1991. The subsidence level is defined here as the base of a deep layer of dry air that exceeds a dewpoint depression of 5°C.

affected parts of western New York just east of Lake Erie including Buffalo. Total snowfall from this storm did not exceed 22 cm (9 in), however the event could have been quite a headache for forecasters because the migratory snowband produced two separate bouts of heavy snow over the metropolitan area around Buffalo.

The snowband developed during the morning of the 19th and continued through the morning of the 20th, before significant warm air advection stabilized the airmass across Lake Erie, ending the snow event.

The hourly wind direction forecast is plotted in Fig 11. As correctly predicted by the model winds, the snowband moved across metro Buffalo (Area 3) during the evening of the 19th, then crossed back south through the same area before sunrise on the 20th. The zone forecast correctly predicted this scenario; however the snowband crossed through Buffalo about 2 hours earlier than expected, and retraced its path through Buffalo a couple of hours later than the model winds predicted.

March 12-13 1992

This storm produced one of the most significant snowfalls in recent history off Lake Ontario. The combination of synoptic scale snowfall, and heavy lake effect snow produced about 225 cm (90 in) of total snowfall, in the town of Palermo, about 20 miles northwest of Syracuse, NY.

The NGM wind direction forecast, issued at 1200 UTC 12 Mar 1992 for Syracuse is shown in Fig 12. After a major synoptic scale snowfall covered the region, heavy localized lake effect snow squalls developed during the night of March 12th. The wind direction plot clearly shows a nearly constant wind direction for close to a 20 hour period, when Palermo was receiving snowfall rates of 8 to 10 cm (3 to 4 in) per hour. In addition, the model winds suggest a slight veering of the wind between 0000-0400 UTC on March 13th. During this time the snowband actually drifted south across metro Syracuse and reduced visibilities to less than 1/2 mile in moderate snow and blowing snow.

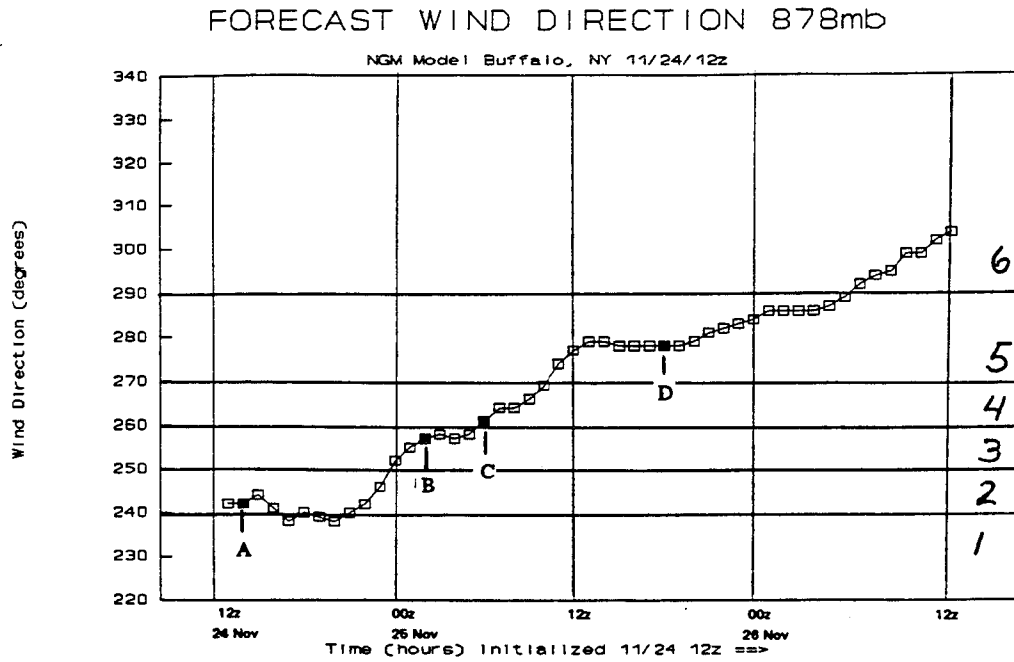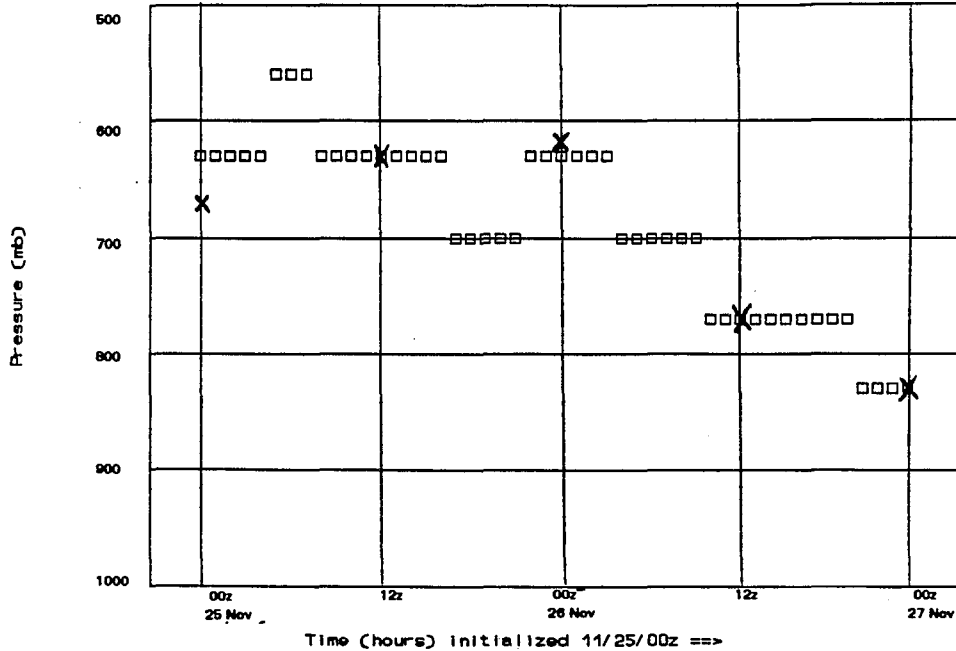## FORECAST WIND DIRECTION 878mb

NGM Model Buffalo, NY 01/19/12z

Fig 11. NGM sigma level 3 (870mb) wind direction forecast vs. time at Buffalo, NY for 1200 UTC Jan 19, 1992. Corresponding forecast areas for Lake Erie induced snowbands are numbered 1-6 at the right of the graph.

FORECAST WIND DIRECTION 878mb

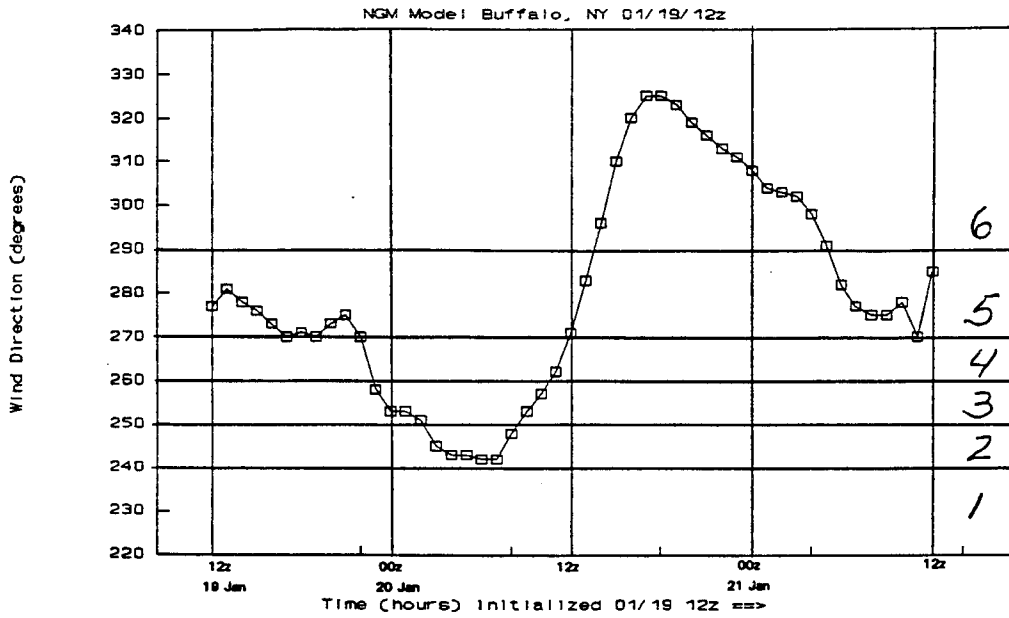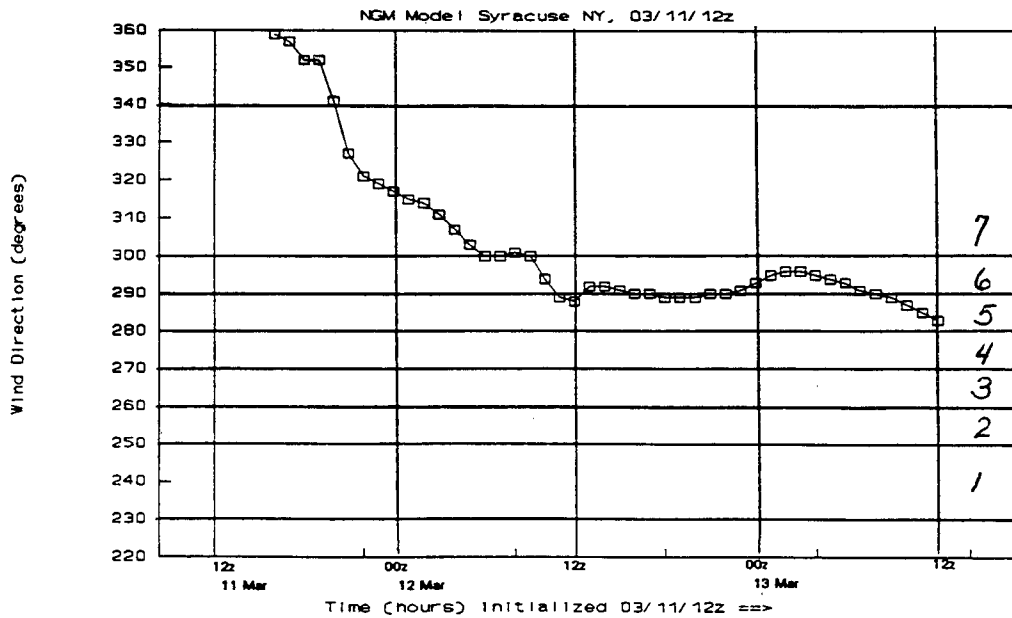NGM Model Syracuse NY, 03/11/12z

Fig 12. NGM sigma level 3 (870mb) wind direction forecast vs. time at Syracuse, NY for 1200 UTC Mar 11, 1992. Corresponding forecast areas for Lake Ontario (which has a different orientation to the prevailing wind compared to Lake Erie) induced snowbands are numbered 1-7 at the right of the graph.

As the three cases show, the plot of hourly forecast winds from sigma layer 3 produces a reasonable scenario of the expected location and movement of the snowband. Of course the model is not able to fully simulate the mesoscale affects of the lakes. In fact, in the 18-19 January 1992 case, there was a couple hour lag in the movement of the snowband as suggested by the wind forecast, at a time when the snowband was aligned along the longest axis of the lake. The lag time is important to note, because forecasters have seen this happen before. There is some suggestion that there is a persistence of the snowband and its mesoscale convergence zone to maintain its orientation along the long axis of the lake, until the synoptic scale weather pattern overpowers the mesoscale forcing. At the present time this cannot be predicted by such a large scale model as the NGM.

OPERATIONAL FORECAST LIMITS

Forecasts of snowfall amounts were not studied in this paper. Total snowfall is still a very difficult problem for the operational forecaster. Typically, total storm accumulations for any given area are a combination of snowfall rate, and the amount of time the snowband remains over an area. In addition, snow to water ratios vary greatly depending on the airmass temperature, and such local effects as orographic enhancement (Hjelmfelt 1992). However, the wind direction forecasts at least suggest the amount of time that the snowband might remain over a given area, and general categorical snowfall forecasts are possible in these cases.

Operational forecasters regard this information subjectively and issue snowfall forecasts that provide the most important information, without causing undue panic for the public. Currently, snowfall amounts are included in the first 12 to 24 hours of the forecast, and are categorized.

CONCLUSIONS

The availability of high resolution NGM data in the forecasting office has been received with great enthusiasm by forecasters. The high resolution model data was used to predict snowband evolution during the winter of 1991-92 at Buffalo, NY, based on past research at NWS Buffalo, relating low level wind forecast to snowband location. To simplify the time-consuming task of analyzing huge data files, a

computer generated forecast aid that plotted wind direction vs. time was developed. Although this was a very limited data set, the one case study suggested that sigma level three (878 mb) was found to correlate well with snowband location and movement, a statement that confirms previous research results. In general, the hourly wind forecasts could predict the location and movement of single banded storms with much better temporal and spatial resolution than previously available model data. Wind direction forecasts were not perfect, but they were shown to have provided valuable additional information to the forecaster for the prediction of the lake-effect snow event.

FUTURE WORK

The availability of high resolution data from dynamic models at the forecast office has opened up the possibility of mesoscale modelling for local forecast problems right in the operational forecast setting. Currently, the forecast office at Buffalo,NY is participating with the State University of New York (SUNY) Colleges at Brockport and Oswego in a COMET (Cooperative Program for Operational Meteorology, Education and Training) Partners Project which will evaluate the use of such new data sets with various mesoscale models. The ability to tap such a valuable information resource and use the data in the operational setting, should heed in the understanding of these events, and bring a great benefit in the form of better local forecasts to the end users.

REFERENCES

Dockus, Dale 1985: Lake effect snow forecasting in the computer age. Nat. Wea. Dig. , Vol 10, No. 4, pp. 5-19.

Hill, J. D., 1971: Snow Squalls in the lee of Lake Erie and Ontario. NOAA Tech. Memo. NWS ER-43.

Hjelmfelt, M. R., 1992: Orographic effects in simulated lake effect snowstorms over Lake Michigan. Mon. Wea. Rev., 120, 373-377.

Jiusto, J.E., Paine, D.A., Kaplan, M.L.,1970: Great Lakes snowstorms Part 2: Synoptic and Climatological Aspects. ESSA Grant

E22-13-060 (G) ASRC, SUNY Albany.

McVehil, G.E., and Peace, R. L., Jr., 1966:
    Project lake effect. A study of lake effect
    snowstorms. Final contract report. CWB
    1231, 52pp. available from CALSPAN,
    Buffalo, NY.

Niziol, T. A., 1987: Operational forecasting of lake
    effect snowfall in western and central New
    York. Wea. Forecasting, 2, 310-321.

Niziol, T. A., 1988: Some synoptic and mesoscale
    interactions in a lake effect snowstorm.
    Postprints, Winter Weather Workshop,
    Raleigh NC, NOAA Tech. Memo. NWS
    ER-82.

Orlanski, I., 1975: A Rational Subdivision of
    Scales for Atmospheric Processes. Bull,
    AMS, 56, 527-530.

Petterssen, S., 1956: Weather Analysis and
    Forecasting, Volume II. Weather and
    Weather Systems. McGraw-Hill. 266pp.

Reinking, R.F., 1991: Lake Ontario Winter Storms
    Project Final technical report. 213 pp.,
    Niagara Mohawk Power Corp, Syracuse
    NY.

Rothrock, H.J., 1960: An aid in forecasting
    significant lake snows, NOAA Tech.
    Memo. WBTM CR-30, Dept. of
    Commerce.

Snellman, L.W., 1992: An old forecaster looks at
    modernization - pros and cons. Nat Wea.
    Dig., Vol 16, No. 4, pp 2-5.

Sykes, R.J. Jr. 1966: The Blizzard of '66 in central
    New York: Legend in its time.
    Weatherwise 19, 241-247.

Lake Effect Snow Events in Eastern New York.

Warren R. Snyder

NOAA/NWS/WSFO Albany,New York

ABSTRACT.

Lake Effect snow events occur in much of upstate New York. Beyond the immediate lake shore regions, the conditions for developing and sustaining these events differ from those associated with "pure" lake effect snows. Subtle meteorological features produce snowfall events in a "channel" downwind of Lake Ontario, but not outside this channel. Channels can extend up to 300 km from the Great Lakes. These lake effect events range from widespread frequent flurries to localized snowfalls of 15 cm in a few hours. Events occur in the channel in responce to surface boundries, when preexisting instability is enhanced by the higher boundry layer moisture, and with passage of a 700 mb or 500 mb short wave trofs. An approach used to identify these events and an example of each are given.

1. Approach at WSFO Albany

At 0300 UTC and 1500 UTC during the winter season a 24 hour guidance package for lake effect snow is run at WSFO Albany. The guidance is produced using a modified and enhanced version of the technique of Niziol(1987), for eastern New York. The guidance evaluates lake surface to 700 mb temperature differential, directional wind shear from the surface to 700 mb, assigns instability class, and identifies most favored areas for lake effect. Its evalutation is presented to the forecaster as a brief narrative for each 6 hour period through 24 hours, and a table of input values and NGM veritcal velocities.

Using the guidance as a starting point, the forecaster analyses soundings and upper air data, from the surface to 500 mb, much the same way as is routinely done for summer season severe weather. This is done to identify factors that may enhance or suppress lake effect activity. From soundings, the presence of unstable layers below 500 mb, and capping inversions is evalutated. From upper air and surface data the presence of synoptic enhancement mechanisms is evaluated.

Ideally one is looking for a large scale environment that produces a "moisture channel", downwind of the the lake with minimal shear in cyclonic low level flow, with a long fetch across the lake. The channel allows maximum moisture, heat flux and destabilization of the trajectory across the lake. The channel can sometimes be identified from satelite imagery by enhanced celluar cumulus or stratocumulus, or in the surface dew point field. The presence of a moisture channel does not alway produce precipitation, other factors must be present.

2. Three Types of Lake effect events

   A. Lake Moisture Enhancement of Existing Instability-
      October 7,1989

This event produced a band of lake effect rain across southern Adirondacks from 1200 to 1400 UTC. The guidance output for 1200 UTC (Fig. 1) shows no shear through 700 mb, instability as conditional and a lake event possible only with forcing. 850 mb temperature was -3 C, with lake water temperature of 14C. There little cyclonic vorticity advection across the region. The su data at 1200 UTC (Fig. 2) show the dew point axis in and ju of the Mohawk Valley. The Albany 1200 UTC (Fig. 3) soundi unstable layer from 880 mb to 690 mb

Radar at 1330 UTC shows only part of the band due to depth (Fig 4.). In this case additional moisture pr lowest 100 to 200 mb of the atmosphere destabiliz produce a band of light rain, but only in the e moisture.

LAKE EFFECT IS LIKELY
LOCATION OUTPUT SHOULD BE USED TO PINPOINT LOCATIONS.

AT 12 HOURS INSTABILITY CONDITIONAL. SHEAR IS 0 DEGREES
FETCH > 80% . LAKE EFFECT RAIN SHOWERS LIKELY ONLY
WITH STRONG SYNOPTIC FORCING. EXAMPLES (STRONG PVA...
OR VORT MAX OF 16 UNITS (NGM) OR GREATER CROSSING AREA..
VERY CYCLONIC SURFACE/850 MB FLOW...SLOW MOVING E-W
COLD FRONTS). WITH SUFFICIENT SYNOPTIC FORCING SNOWFALL
RATES 1/2-1 INCH PER HOUR POSSIBLE. WITHOUT STRONG
FORCEING ONLY FLURRIES OR SPRINKLES POSSIBLE

CENTRAL ONEIDA COUNTY..HERKIMER COUNTY BETWEEN
ADIRONDACK PARK AND NYS THRUWAY. INCLUDES NORTH ZONE 9
AND MAY REACH DOWN NORTH SIDE OF MOHAWK VALLEY TO
GLOVERSVILLE AND OCCASIONALY TO SARATOGA COUNTY.
IN A SINGLE BAND

Figure 1. Albany Lake Effect Guidance Valid 1200 UTC October 7, 1989

ALB   12Z/OC/ 07/ 89
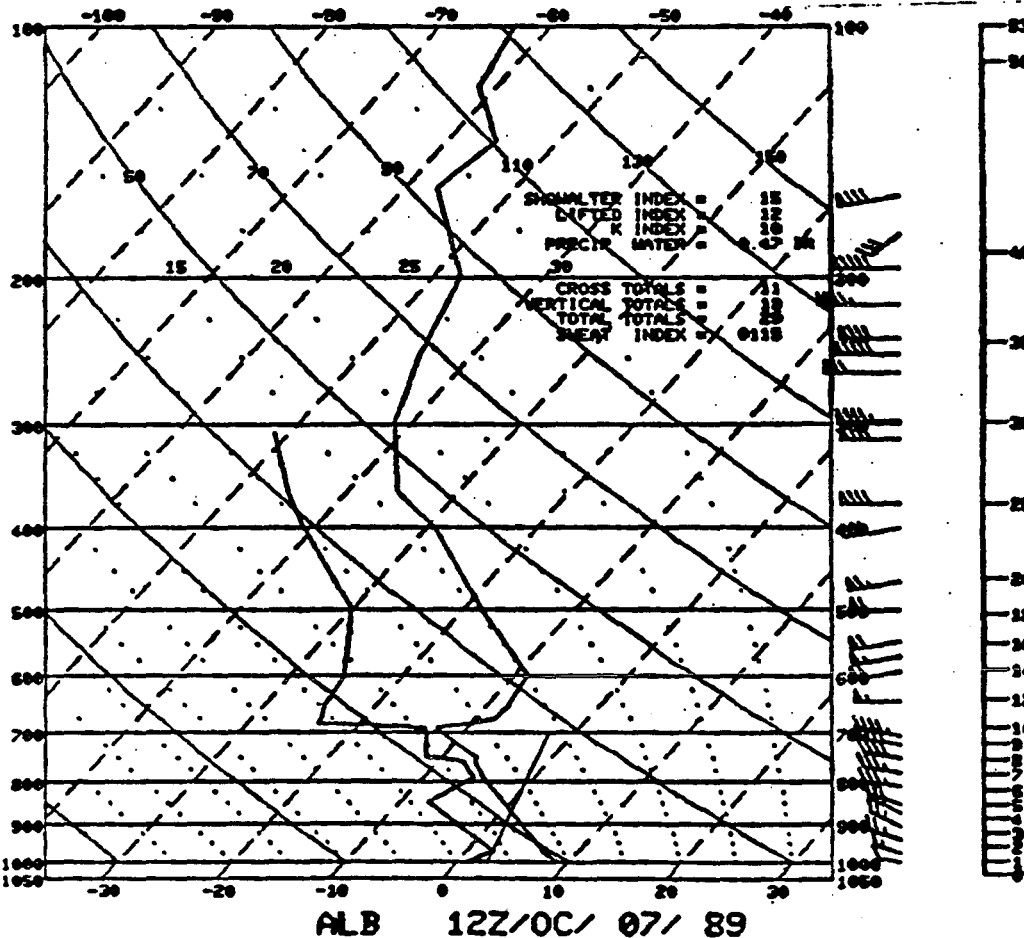
Figure 2. Albany 1200 UTC Octoer 7, 1989 Sounding, showing unstable
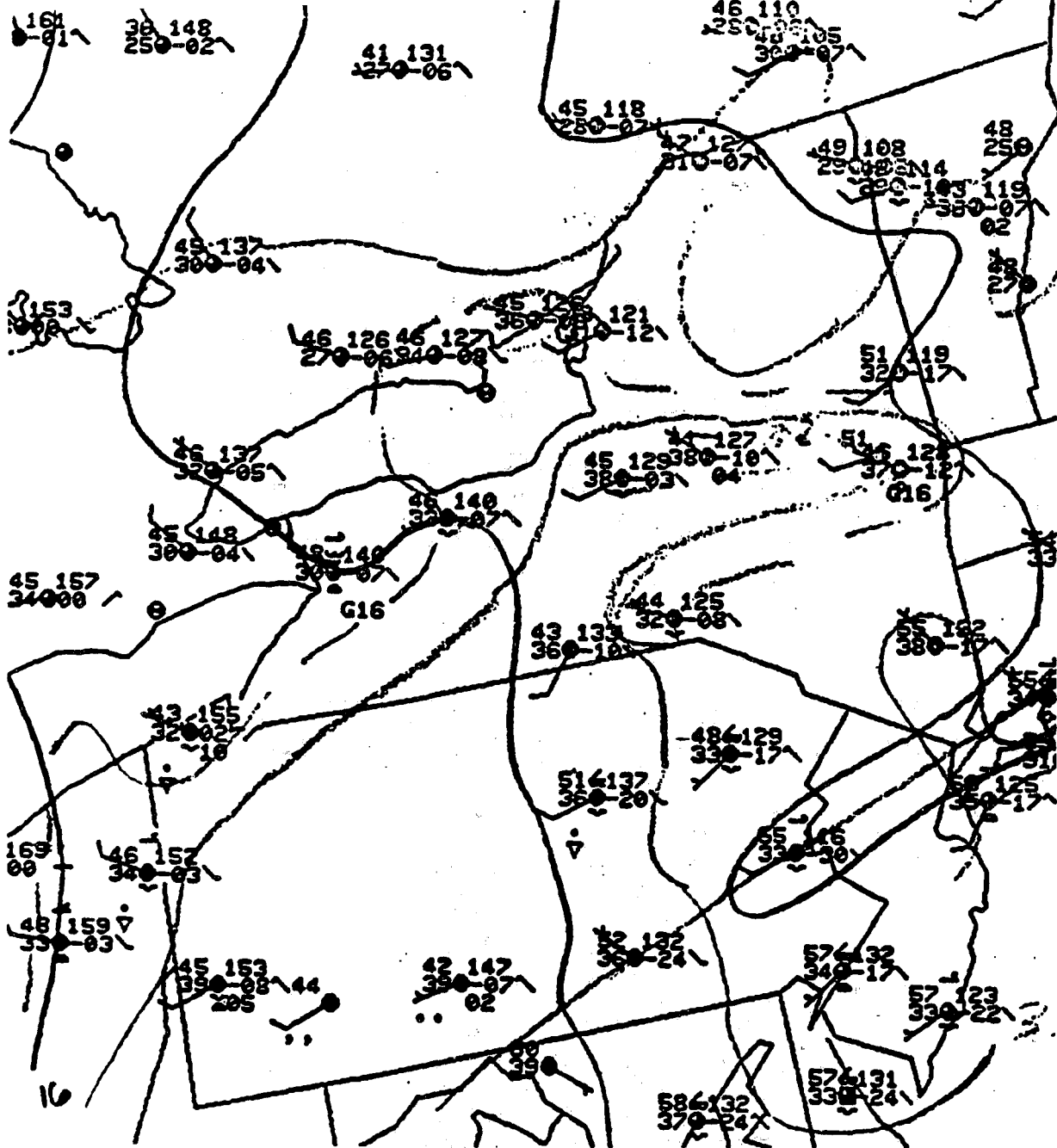layer from about 880 to 690 mb.

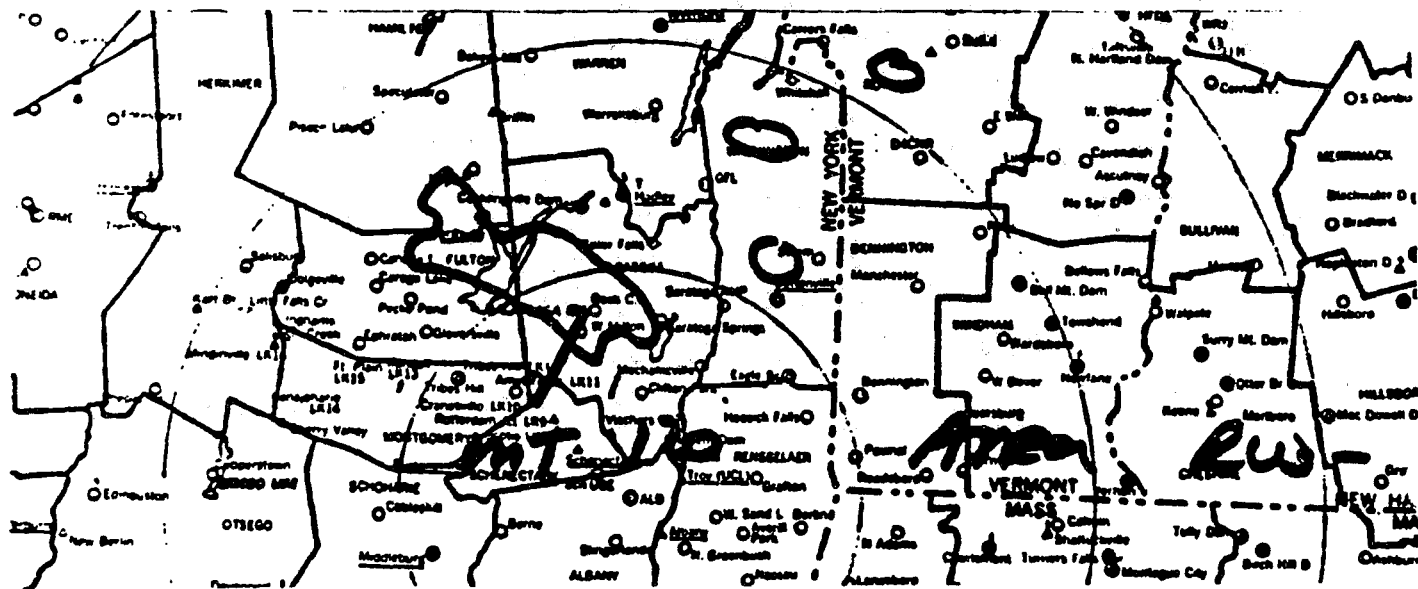Figure 3. Suface analysis 1200 UTC October 7, 1989

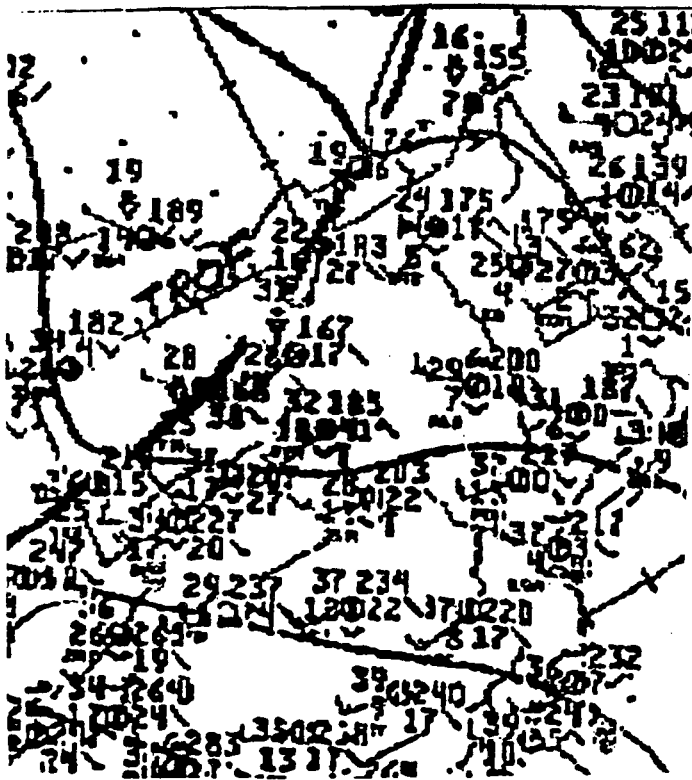Figure 4. Albany WSR-74C overlay from 1330 UTC October 7, 1989

Figure 5a. Surface Analysis- from
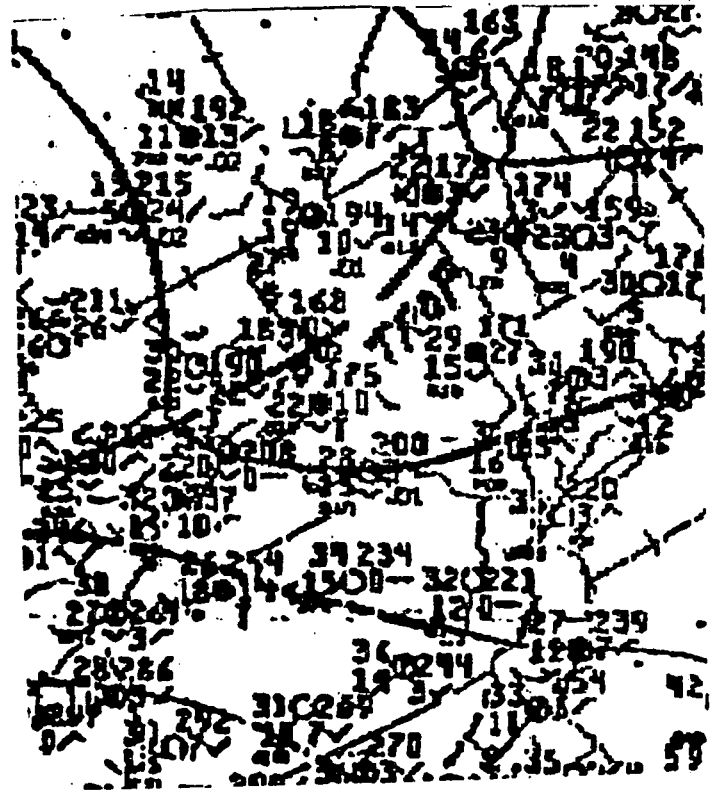2100 UTC December 4, 1988
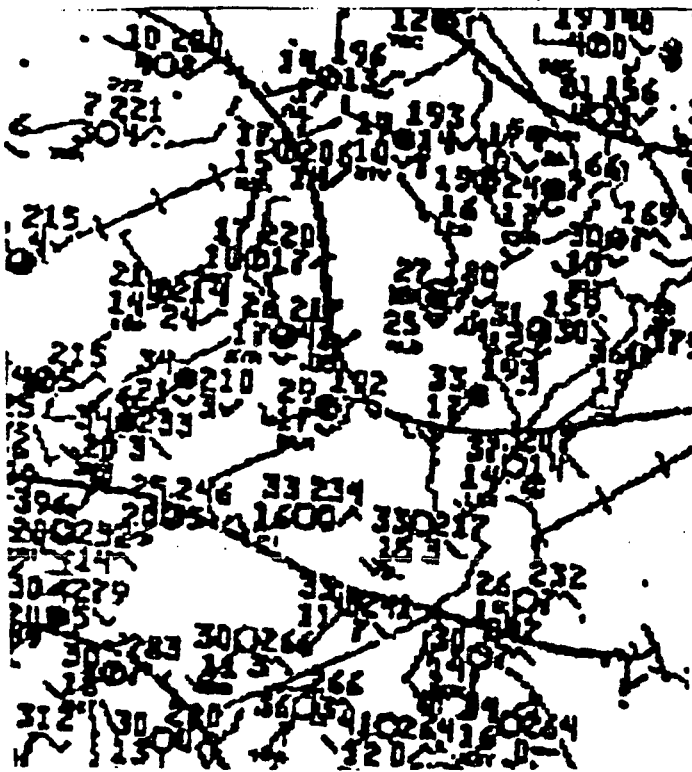

Figure 5b. same at 0000 UTC
December 5, 1988

Figure 5c same-0300 UTC
December 5, 1988

IN THE EASTERN MOHAWK VALLEY...OCCASIONAL SQUALLS
AS FAR EAST AS GREATER CAPITAL DISTRICT.

****

LAKE EFFECT IS LIKELY
LOCATION OUTPUT SHOULD BE USED TO PINPOINT LOCATIONS.

AT 12 HOURS INSTABILITY MODERATE. SHEAR IS 20 DEGREES. FETCH > 50%.
LAKE EFFECT SNOW SHOWERS LIKELY.
SNOWFALL RATES 1"/HOUR LIKELY IN SQUALLS.
FROM TABORG-BLOSSVALE AREA TO ROME...UTICA AND
LITTLE FALLS. DOWN MOHAWK VALLEY. AXIS ALONG AND SOUTH
OF NYS THRUWAY EAST OF UTICA IN A SINGLE BAND .

WIDESPREAD LIGHT SNOW SHOWERS
IN THE EASTERN MOHAWK VALLEY...OCCASIONAL SQUALLS
AS FAR EAST AS GREATER CAPITAL DISTRICT.

****

LAKE EFFECT IS LIKELY
LOCATION OUTPUT SHOULD BE USED TO PINPOINT LOCATIONS.

AT 18 HOURS INSTABILITY MODERATE. SHEAR IS 10 DEGREES. FETCH > 50%.
LAKE EFFECT SNOW SHOWERS LIKELY.
SNOWFALL RATES 1"/HOUR LIKELY IN SQUALLS.
FROM TABORG-BLOSSVALE AREA TO ROME...UTICA AND
LITTLE FALLS. DOWN MOHAWK VALLEY. AXIS ALONG AND SOUTH
OF NYS THRUWAY EAST OF UTICA IN A SINGLE BAND .

WIDESPREAD LIGHT SNOW SHOWERS
IN THE EASTERN MOHAWK VALLEY...OCCASIONAL SQUALLS
AS FAR EAST AS GREATER CAPITAL DISTRICT.

****

LAKE EFFECT IS LIKELY
LOCATION OUTPUT SHOULD BE USED TO PINPOINT LOCATIONS.

AT 24 HOURS INSTABILITY MODERATE. SHEAR IS 10 DEGREES. FETCH > 50%.
LAKE EFFECT SNOW SHOWERS LIKELY.
SNOWFALL RATES 1"/HOUR LIKELY IN SQUALLS.
MADISON AND EXTREME SOUTHERN ONEIDA COUNTIES IN A SINGLE BAND .

****

LAKE TEMPERATURE INPUTTED WAS 42.0 DEGREES

SUMMARY OF INPUT VALUES

TIME	WINDS				TEMPERATURES		
	BNDRY LYR	850 MB	700MB	VV	BNDRY	850 MB	700 MB
0 HOURS	31	32	33	-5.5	-5.5	-15.5	-20.5
6 HOURS	29	29	31	-2.8	-4.5	-12.8	-21.5
12 HOURS	29	29	31	-.6	-4.0	-11.5	-21.5
18 HOURS	30	29	31	-.6	-6.0	-11.5	-20.5
24 HOURS	30	30	31	-.6	-8.0	-11.5	-19.5
30 HOURS	29			-1.8	-5.0	-10.8	
36 HOURS	28			-2.3	-4.0	-7.8	
42 HOURS	24			-.3	-3.5	-3.5	
48 HOURS	24			-.5	-3.0	.8	

Figure 6

B. Synoptic Scale Boundrys- December 4-5, 1988

A surface trough moved south across New York from 2100 December 4
to 0500 UTC December 5, 1988. (Fig. 5a-c). The 850 mb flow was 290
degrees by 0000 UTC and remained so until through the event.
Directional wind shear was 10 to 20 degrees below 700 mb during this
event and lake surface to 850 temp difference was 17 degrees C. A
weak 500 mb trough crossed New York from 1800 to 0000 UTC but during
the event New York was west of the trough axis. The surface troughs
southward movement was accompanied by little snowfall except brief
flurries as it moved south through the Adirondacks. The lake
guidance (Fig 6.) identified the Mohawk Valley though the Capital
District as the most likely area for lake effect during this period.
The Mohawk Valley corridor was therefore the "channel" or favored
area of greater thermodynamic instability and moisture, than areas
north or south of it.

Instability was in the moderate catagory. Average NGM vertical
velocities across New York, were strongly negative through
1800 UTC December 4, and then became neutral by 00 UTC December 5,
and remained so during the event. This suppressed lake effect snow
until 2300 UTC, and the surface trough was probly the feature that
caused the vertical velicity to change. Between 2300 UTC and 0400
UTC the surface trof was orientated east-west, and moved through the
channel. A band of snow formed from the north side of the Mohawk
valley to extreme southern Vermont about 2300 UTC. The surface
trough moved south of the Mohawk Valley by 0300 UTC, and the snow
band disipated by 0400 UTC. The trough itself produced little
significant snow north of the "lake effect channel", or south of
it. The snowfall maxima axis was orientated east-west from the north
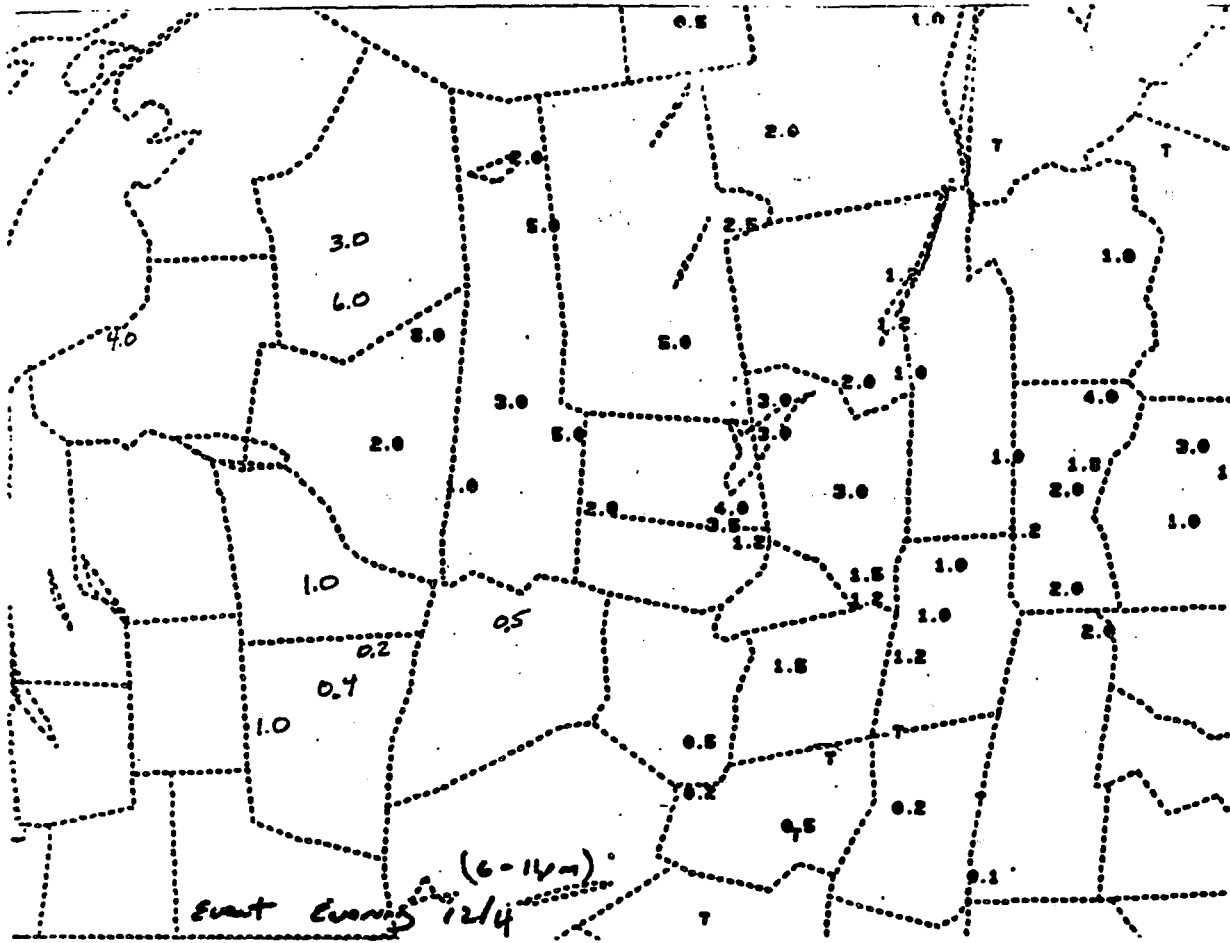side of the Mohawk Valley to southern Vermont. (fig 7).

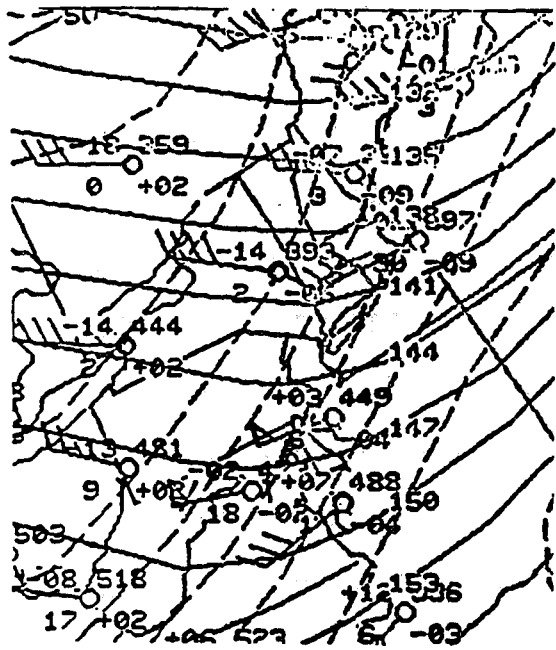Figure 7. Total Snowfall 2100 to 0400 UTC December 4-5, 1988.

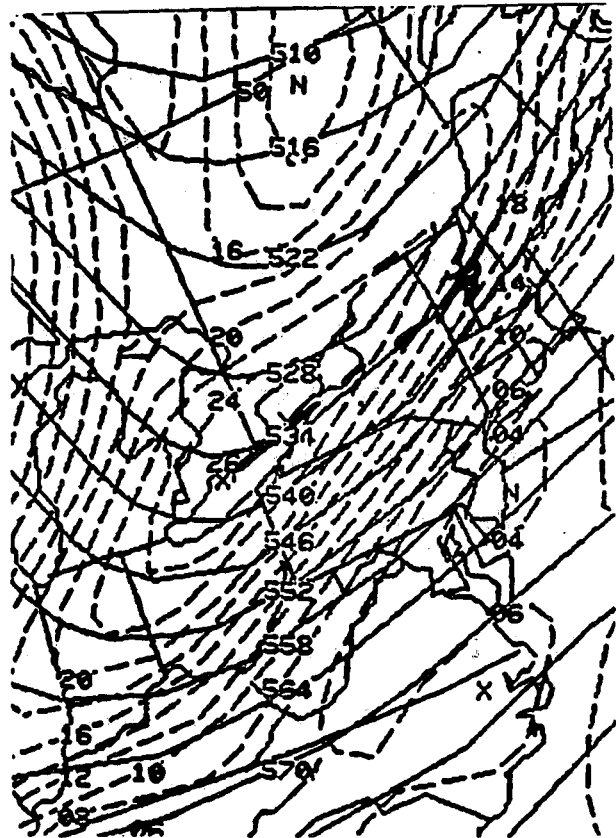Figure 8. 850 mb 1200 UTC
January 13, 1989

Figure 10. Initial NGM 500 mb
Hieghts and Vorticity

         January 13,1989-The Utica Blizzard.

   Prior to this event strong cold advection occurred over upstate New
York from 0000 UTC through 1200 UTC, establishing a deep cold layer of
air across New York. (Fig 8.) The lake guidance indentifies only a
narrow window for a potential event (Fig 9), and even so conditions
are marginal. The lake surface temperature was 2 deg. C. At 0600 UTC
the lake to 850 temperature difference was 7 deg C., by 1000 UTC it
was 13 deg C, and was 14 to 15 deg during the event. Instability was
conditional.

Between 1000 and 1800 UTC January 13, the lake effect channel was
aligned in the Mohawk Valley. Normally these conditions would only
produce frequent flurries at Utica, but the difference between
normal and this case was a 26 x 10-5/sec vorticity maximum (fig 10)
at 500 mb centered over lake Erie at 1200 UTC, which was producing
considerable cyclonic vorticity advection across the Mohawk Valley.
Shortly after 0900 UTC a lake snow band developed from the Lake into
the Mohawk Valley to Utica to Albany. The band remained stationary
until 1500 UTC, then migrated slowly south as the 850 mb wind
direction became more northwesterly. By 2100 UTC the band was from
south Onieda County to Columbia county. After the passage of the 500
mb short wave trof, the synoptic scale vertical velocities became
strongly negative, and the snow became light.

The city of Utica is 120 km from Lake Ontario, yet in this event
17.5 to 20 cm of snow fell in the city of Utica, with 12.5 cm at
Oriniskiny Airport (UCA) from 1200 UTC to 1700 UTC where visabilities
were below 1/2 mile in snow and heavy snow. 12.5 cm fell in Herkimer
(155 km from the Lake), and 12.5 to 15 cm of snow fell in the
Helderburg mountain towns, about 18 km southwest of Albany and 245 km
from the lake. Orograhpic enhancement was probly not much of a factor
in these towns, because the trajectory taken by the snow band brought
it over higher terrain well before reaching the Helderburg area.

NIZIOL ASSESMENT OF LAKE EFFECT FOR LAKE ONTARIO
pc software developed by warren r. snyder wsfo albany c.1989

OUTPUT FROM NGM 00Z JAN 13 89

NOT ENOUGH DIFFERENTIAL FOR LAKE EFFECT AT 0 HOURS.

****

NOT ENOUGH DIFFERENTIAL FOR LAKE EFFECT AT 6 HOURS.

****

            LAKE EFFECT IS POSSIBLE
LOCATION OUTPUT SHOULD BE USED TO PINPOINT LOCATIONS.

AT 12 HOURS INSTABILITY CONDITIONAL. SHEAR IS 10 DEGREES. FETCH > 80%.
LAKE EFFECT SNOW SHOWERS ONLY WITH STRONG SYNOPTIC FORCING.
WITH SYNOPTIC FORCING SNOWFALL RATES 1/2-1"/HR POSSIBLE.
WITHOUT IT ONLY   SNOW FLURRIES· POSSIBLE

EXAMPLES OF SYNOPTIC FORCING INCLUDE
1. STRONG PVA OR VORT MAX OF 16 UNITS OR MORE.
2. VERY CYCLONIC SURFACE/850/700 MB FLOW.
3. PVA WITH TROFS OR WEAK E-W COLD FRONTS.

FROM TABORG-BLOSSVALE AREA TO ROME...UTICA AND
LITTLE FALLS. DOWN MOHAWK VALLEY. AXIS ALONG AND SOUTH
OF NYS THRUWAY EAST OF UTICA IN A SINGLE BAND .

****

AT 18 HOURS INSTABILITY CONDITIONAL. SHEAR IS 10 DEGREES. FETCH < 80%.
LAKE EFFECT UNLIKELY- LAKE INDUCED CLOUDINESS MAY OCCUR.
****

NOT ENOUGH DIFFERENTIAL FOR LAKE EFFECT AT 24 HOURS.

****

LAKE TEMPERATURE INPUTTED WAS 37.0 DEGREES

            SUMMARY OF INPUT VALUES

TIME		WINDS				TEMPERATURES		
		BNDRY LYR	850 MB	700MB	VV	BNDRY	850 MB	700 MB
0 HOURS		24	26	25	-1.0	3.5	1.5	-4.0
6 HOURS		29	28	25	1.5	-1.5	-5.3	-10.5
12 HOURS		29	29	20	-2.0	-6.0	-12.0	-19.5
18 HOURS		29	30	30	-4.1	-6.5	-13.0	-15.5
24 HOURS		29	32	33	-4.2	-6.0	-8.3	-11.5
30 HOURS		26			-.8	-6.5	-4.3	
36 HOURS		26			-1.0	-6.0	.0	

A CASE STUDY OF A MESOSCALE SNOW EVENT IN NEW YORK'S CAPITAL DISTRICT

Michael E. Wooldridge
Warren R. Snyder
National Weather Service Forecast Office
Albany, New York

1. INTRODUCTION

Surface low pressure moved from near Cleveland, Ohio at 1200 UTC, February 24, 1990, to about 270 km southeast of Cape Cod, Massachusetts by 1200 UTC, February 25, 1990. The passage of this synoptic scale system produced snowfall amounts of 1 to 7 inches across upstate New York (Figure 1) from the southern Adirondack mountains to the central Catskill mountains, including the Hudson and Mohawk valleys. Snow associated with the passage of the surface low pressure system became light after 1400 UTC, and was mainly associated with the effects of Lake Ontario. Between 1800 and 2100 UTC, a north-south convergence line formed in the Hudson Valley from near Albany south to Poughkeepsie. At the same time, a band of light lake effect snow was oriented east-west through the Mohawk valley. In the vicinity of Albany, these two bands intersected, while cyclonic vorticity was increasing above 700 mb, resulting in a mesoscale snowburst from 1800 to 2100 UTC. Localized snowfalls of 4 inches fell in New York's Capital District.

2. SYNOPTIC ENVIRONMENT

At 1200 UTC, February 25th, a cyclone was over the western Atlantic Ocean, centered approximately at 39°N, 68°W, or roughly 270 km southeast of Cape Cod. Strong surface cold advection was occurring from Boston, Massachusetts to Duluth, Minnesota.

At 850 mb, a low was over southeast New York (Figure 2). This supplied a departing 500 mb short wave with Atlantic moisture, and strong low level warm air advection. Southeast moving short waves are usually sparsely supplied with moisture. This short wave acquired more moisture than usual, for a "clipper type" system, and its associated surface cyclone produced 1 to 3 inches of snow across New York's Capital District with up to 7 inches in the Catskills and Lower Hudson Valley prior to 1200 UTC (Figure 3).

At 700 mb, a trough was over central New York. Weak warm or neutral thermal advection was occurring east of the trough axis, with cold advection west of it (Figure 4). At 500 mb (Figure 5), a sharp, negatively tilted trough was between Buffalo and Syracuse. This 500 mb trough, like the one at the lower levels, was propagating to the east.

Warm air advection was over Albany at 500 mb, in advance of the trough. At 500 mb, divergence was quite large across west New York and Pennsylvania (Figure 6).

By 1800 UTC on February 25th, the surface low was well out to sea, with cold air advection occurring from 500 mb to the

surface. Between 1800 at 2100 UTC, moderate to heavy snow fell at Albany County Airport. Surface observations (Figure 7), and streamline analysis of the surface wind field (Figure 8), indicated a northeast flow at Albany and adjacent areas of New England. A strong northwest flow covered much of New York state west of the Hudson valley. A line of surface convergence was evident through the Hudson Valley from Saratoga County to Dutchess County. During this time, the area of divergence at 500 mb, along with cyclonic vorticity advection, continued to move east across New York.

2. INFLUENCE OF LAKE ONTARIO

Lake effect snow guidance for New York is available via a local computer applications program (Snyder 1989), based on an adaptation and enhancement of the Niziol (1987) approach for forecasting lake effect snows. This program utilizes FD wind and NGM layer temperature forecasts. For 1800 UTC, the lake effect guidance output showed 850 mb temperatures were progged to be below -20°C, with the 700 mb temperatures near -30°C. The surface water temperature of Lake Ontario was 3°C near Rochester, New York. The lake water to 850 mb temperature difference was 23°C, well in excess of the 13°C typically associated with the onset of "pure" lake effect effect snow (Holyrod, 1971).

The guidance provided the following assessment for lake effect at 1800 UTC, February 25, 1990:

1. Instability class was extreme (Niziol 1987) by 1800 UTC across New York. Instability class for lake effect events is determined by lake surface to 850 mb and lake surface to 700 mb temperature. There are 3 instability classes: conditional, moderate and extreme. Lake effect precipitation is often a result of various combinations of instability, fetch across the lake and synoptic forcing mechanisms.

2. Winds were 20 to 30 kt from 310 to 330° for the boundary layer to 700 mb. Directional wind shear was therefore less than 30°, which is favorable for lake effect snow.

3. Due to short fetch of this trajectory across Lake Ontario, lake effect snow would likely be multibanded and considerably lessened in intensity.

4. The most likely areas to be effected would be from the Finger Lakes and Binghamton areas westward. Light snow or flurries would be widespread across central New York. (Actual surface observations confirmed this, as light snow was widespread from the western Catskills to the Finger Lakes.)

Visibility at Binghamton (BGM) dropped below 1/2 mile in a snow squall at 1800 UTC, and was below 1 1/2 miles in snow from 1800 to 2000 UTC. Visibility at other central New York locations remained above 3 miles, and at times snow did not occur at these locations.

5. Below 700 mb flow was cyclonic. Based on quasi-geostrophic theory and the Ekman spiral, cyclonic flow increases low level convergence.

Analysis of 1200 UTC data with the Southern Region Upper Air Analysis Program (Foster 1988) detailed the following features:

1. Cyclonic vorticity advection decreased with height from 850 mb to 700 mb (Figures 9 and 10), and cold advection was occurring (Figures 2 and 4) from western New York to eastern Michigan. Cyclonic vorticity advection increased significantly from 700 to 500 mb (Figure 11), where thermal advection was neutral. Thus, quasi-geostrophic upward vertical motion was implied above 700 mb, with sinking motion below 700 mb.

2

2. At 1200 UTC, a geostrophic vorticity maxima was located over upper Lake Michigan (Figure 12). This maxima rotated rapidly east, and by 1800 UTC, was producing cyclonic vorticity advection across eastern New York. Satellite imagery indicated a cloud band through the Mohawk Valley. This band was outside the area previously described as the most favorable area for lake effect band formation. Its existence appears to have been a result of the influence of the local terrain forcing.

Elevations rise from 125 m mean sea level in the Mohawk valley to 800 m on both sides of it. Surface winds were northwest 10 to 20 knots from 1700 to 2000 UTC across central New York. Streamline analysis and surface observations at Utica (UCA) and Rome (RME), New York at 1700 and 1800 UTC (not shown), indicated that air was being funneled into the Mohawk Valley. Since the pressure gradient was directed east, the air was channeled down the valley.

3. DETAILED CHRONOLOGY

3.1. Prior to 1531 UTC, February 25, 1990

Cold air advection was occurring over the relatively warmer Lake Ontario. The surface wind, though primarily between 320 and 340° was funneled into the Mohawk Valley. Funneling added more westerly component to the wind, with the prevailing wind down the valley from 290 to 310°. A bright cellular area (usually associated with snow squalls) originated in the western Mohawk Valley, between Pulaski and Rome at 1400 UTC. This pulse was initiated by surface wind convergence and orographic uplift along the lakeshore.

As the squall propagated east it weakened. When it approached Little Falls, in the Mohawk valley, it was enhanced by terrain.

3.2. 1531 UTC, February 25, 1990

Cyclonic quasi-geostrophic vorticity advection, associated with a strong 500 mb short wave was beginning to move over central New York, destabilizing the atmosphere above 700 mb. Enhanced upward vertical velocity above 700 mb strengthened once the air was lifted to 700 mb. The squall started propagating with the upper level cyclonic vorticity max. At this point, the event's dynamics appeared to shift from primarily lake effect, to those associated with the approaching 500 mb trough.

3.2. 1631 UTC, February 25, 1990

The pulse continued to propagate east, down the Mohawk Valley. It weakened between Little Falls and west Schenectady county. In western Schenectady county, the pulse moved into the area of maximum surface wind convergence, and dramatically strengthened. Surface winds (Figure 8) were 290° in the Mohawk Valley, 340° from the Adirondacks, and 40° in the Hudson Valley.

A plume of enhanced clouds (implying some vertical extent) on satellite images (not shown) streamed from an origin in west Schenectady county into the Hudson Valley, the Berkshires, and extreme northwest Connecticut. Surface observations showed the pulse produced moderate to heavy snow in this narrow swath.

3.4. 1831 UTC, February 25, 1990

The enhanced areas were now less defined, but snow continued moderate to heavy in the Greater Capital District. The area associated with heavier snow expanded south, down the Hudson Valley, in response to boundary layer convergence. The cyclonic vorticity maximum had passed the origin point and moved over New York's Capital District.

3.5. 1931 UTC, February 25, 1990

By this time, the initial Mohawk valley pulse lost most of its definition and dissipated. The differential cold air advection and surface wind convergence decreased over Lake Ontario. The convergence point moved east, and the snow band persisted. Heavy snow was falling from Schenectady to Colonie with moderate snow from Amsterdam to Glens Falls.

3

4. THE MESOSCALE SNOWBURST

At Albany, light snow began at 0550 UTC. The snow was associated with a surface low just south of Long Island. Snow became light after 1200 UTC, and remained so at Albany until after 1700 UTC. Surface pressure rose rapidly after 1150 UTC, with north surface winds. By 1650 UTC, the surface winds displayed a more easterly component (20°). Meanwhile, at Poughkeepsie (POU), surface winds were 320 to 340° degrees, and 270 to 300° degrees at UCA and RME.

At 1800 UTC, the leading edge of the snow pulse reached the Albany County Airport (ALB). Surface winds were 20° at 13 kt. At the same time, at Stewart Field in Newburgh (SWF), surface winds were 320° at 15 kt, and POU was 340° at 10 kt. Figure 13 shows surface observations in the Hudson valley at Glens Falls (GFL), ALB, SWF, and POU during the event. The area of maximum surface wind convergence passed through Albany, between 1800 and 1900 UTC.

Ceiling and visibility were reduced as the light snow became moderate snow. The center of the initial pulse passed through ALB, between 1855 and 2016 UTC. Heavy snow fell between 1911 UTC, and 1942 UTC (Table 1). Winds shifted to 320° at 8 kts around 1950 UTC. Moderate snow became light by 2016 UTC. The snow ended at 2134 UTC at Albany. Total snowfall is shown in Figure 14.

5. CONCLUSIONS

Surface wind convergence is an excellent mechanism for inducing an upward vertical motion, especially in the lowest levels of the atmosphere. In this case upward vertical motion associated an approaching 500 mb short wave trough was superimposed over a region of strong lower tropospheric cold advection and decreasing cyclonic vorticity advection from the surface to 700 mb.

This type of situation contributes to quasi-geostrophic downward vertical motion below 700 mb.

Hour Ending (UTC)	Liquid Equivalent (inches)	Snowfall (inches)
1600	0.01	0.2
1700	0.01	0.2
1800	0.01	0.2
1900	0.03	0.6
2000	0.05	1.0
2100	0.03	0.6
2200	0.02	0.4
2300	0.00	0.0

Table 1. Hourly observed precipitation at Albany, New York, 1500-2300 UTC, February 25, 1990.

Lake effect snow events are noted for limited vertical development, with most occurring below 500 mb and often below 700 mb. From the continuity equation, convergence in a shallow layer (100-200 mb) will lead to upward vertical motions throughout the layer. The orographically forced surface convergence (by the Mohawk and Hudson valleys), diabatic heating from Lake Ontario, and cyclonic vorticity advection at 500 mb acted to overcome the quasi-geostrophic subsidence expected below 700 mb. The convergence at the surface and divergence at 500 mb, resulted in a layer of upward vertical motion.

The only way to see such an events operationally is to study SWIS loops and to draw hourly stream line analysis. Hourly mesoscale computations of divergence throughout the lower 500 mb would identify favorable locations for these types of events, but such data will have to await the deployment of Doppler radars and wind profilers. When these technologies are operational, such an event will have a

4

greater likelihood of being detected, thus prediction and nowcasting of such an event should be improved.

6. ACKNOWLEDGMENTS

REFERENCES

Foster, M. P., 1988: Upper air analyses and quasi-geostrophic diagnostics for personal computers. NWS Southern Region Scientific Services, Fort Worth, Texas. 29 pp.

Holyrod, E. W., III, 1971: Lake effect cloud bands as seen from weather satellites. J. Atmos. Sci., 28, 1165-1170.

Niziol, T. A., 1987: Operational forecasting of lake effect snowfall in western and central New York. Wea. and Forecasting, 2, 310-321

Snyder, W. R. 1989: Lake Effect Guidance Software for Eastern New York. WSFO Albany software (unpublished).
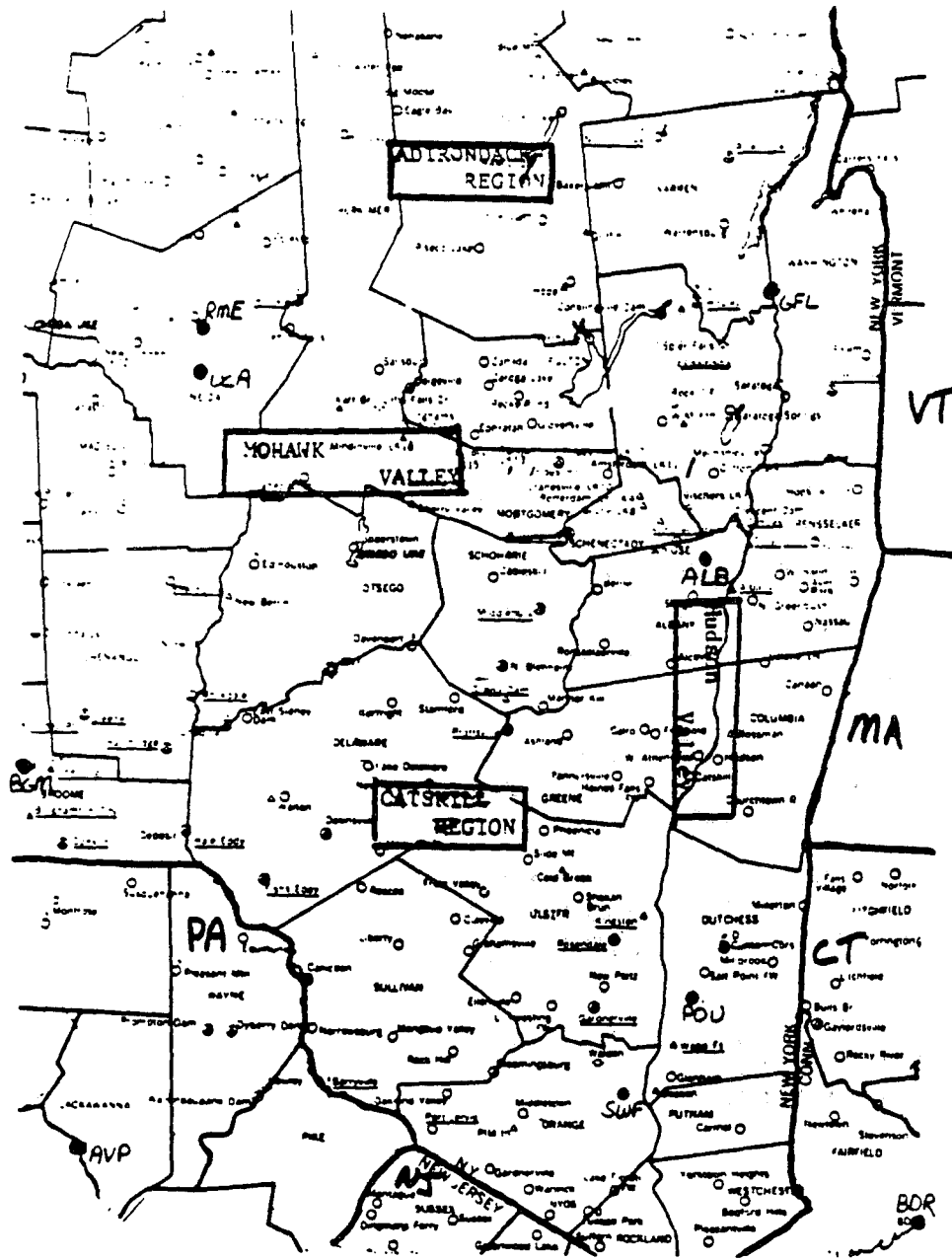
Figure 1. Map of Eastern New York. County names are in capital letters, and topographic regions are indicated.

Figure 2. 850 mb analysis for 1200 UTC, February 25, 1990. Solid lines are height contours (30 m interval), dashed lines are isotherms (2°C interval).

Figure 3. Observed 24 hour snowfall (inches) ending 1200 UTC, February, 25 1990.
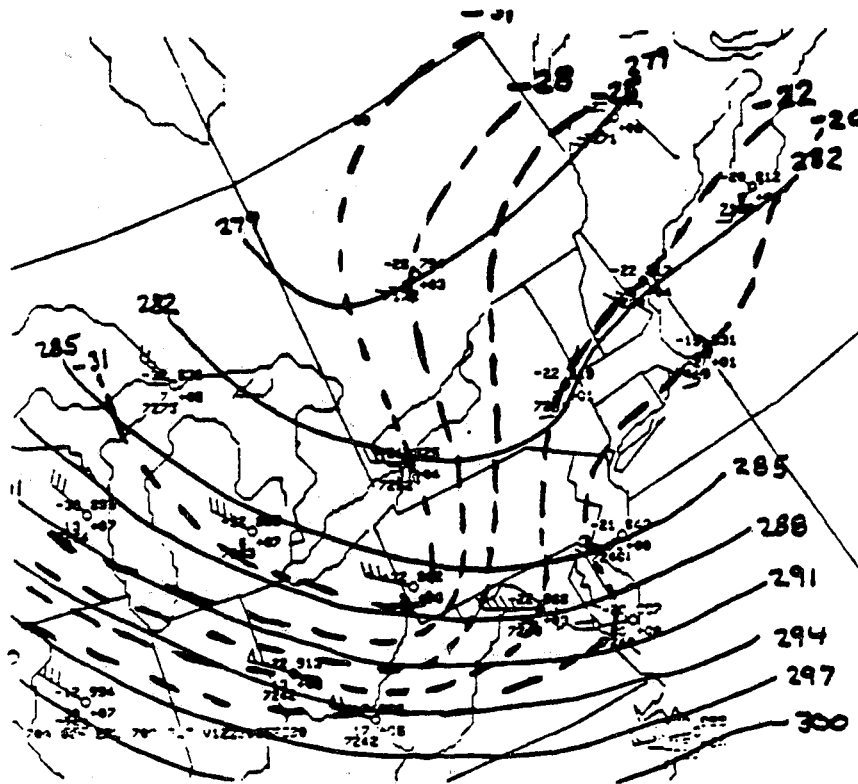
Figure 4. 700 mb analysis for 1200 UTC, February 25, 1990. Solid lines are height contours (30 m interval), dashed lines are isotherms (3°C interval).
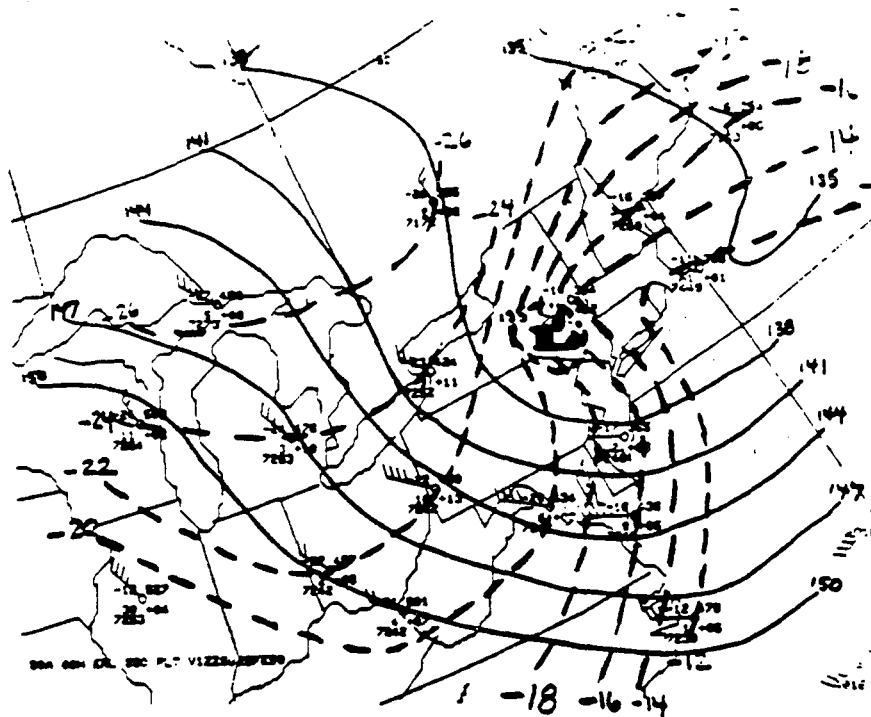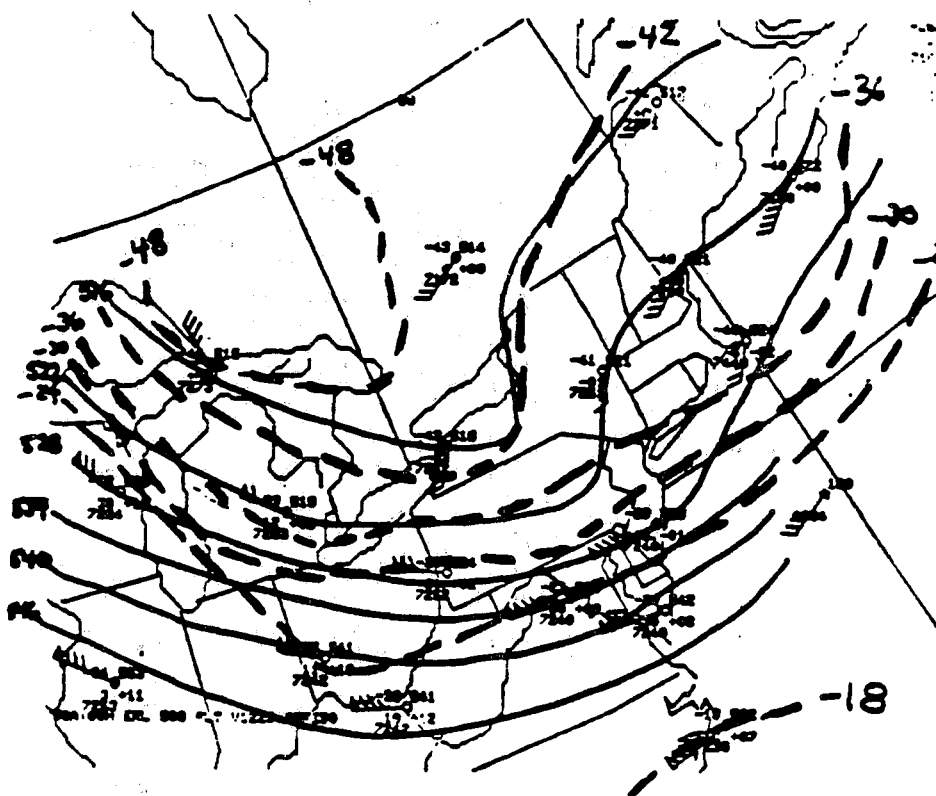

Figure 5. 500 mb analysis for 1200 UTC, February 25, 1990. Solid lines are height contours (60 m interval), dashed lines are isotherms (6°C interval).
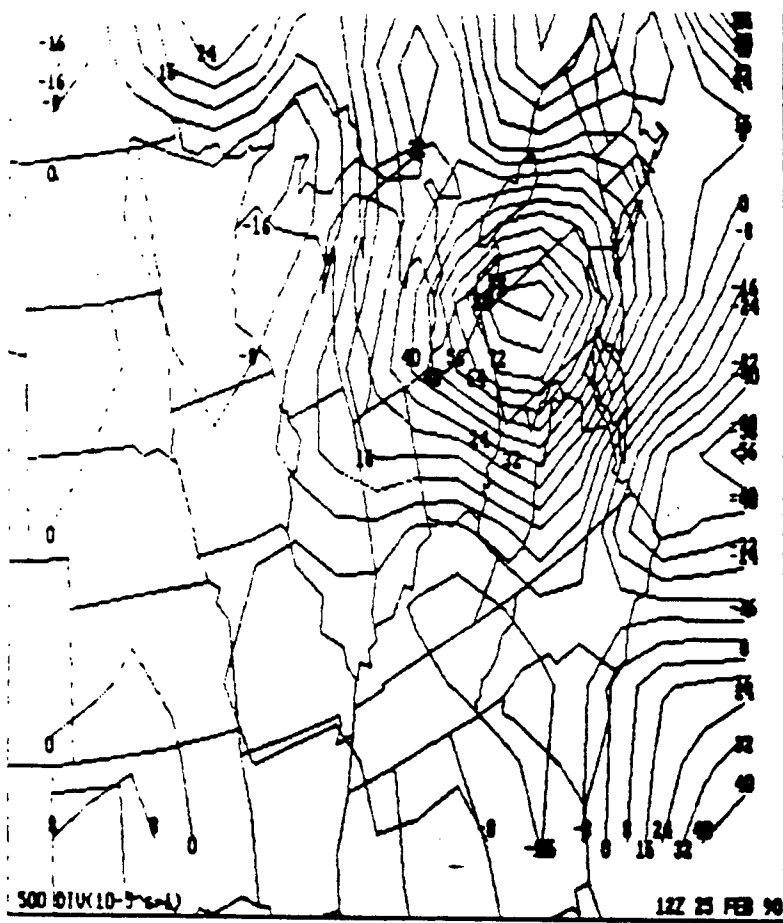
Figure 6. 500 mb divergence (10^{-5} sec^{-1}) for 1200 UTC, February 25, 1990.
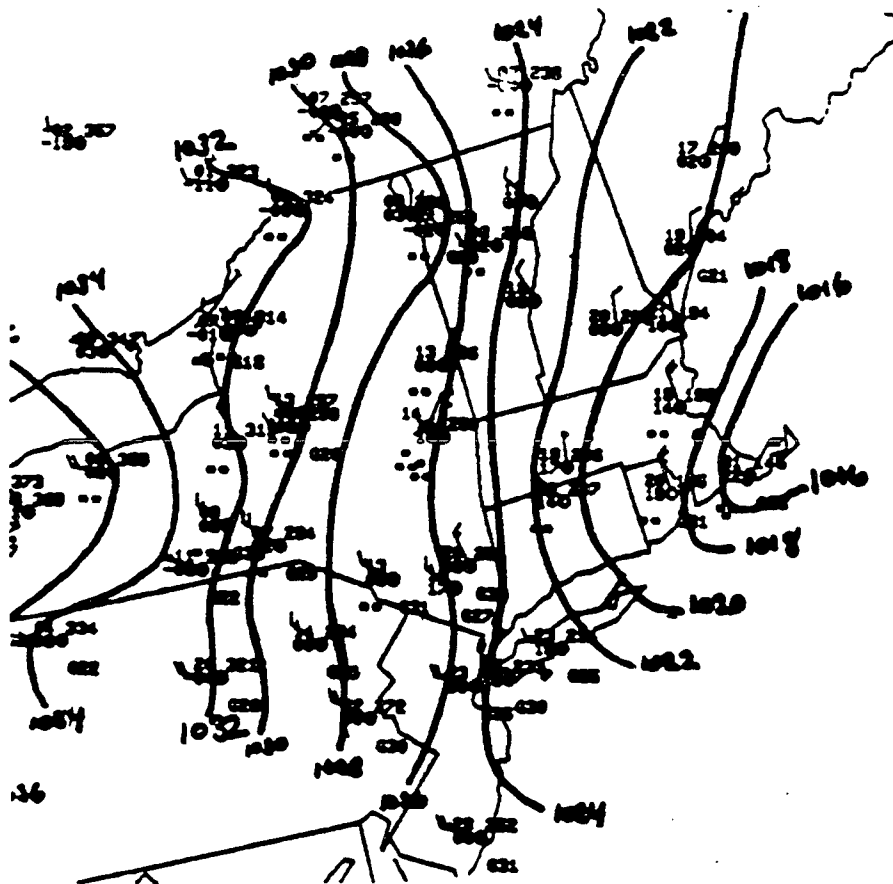
Figure 7. Surface Analysis (2 mb interval) for 1900 UTC, February 25, 1990.
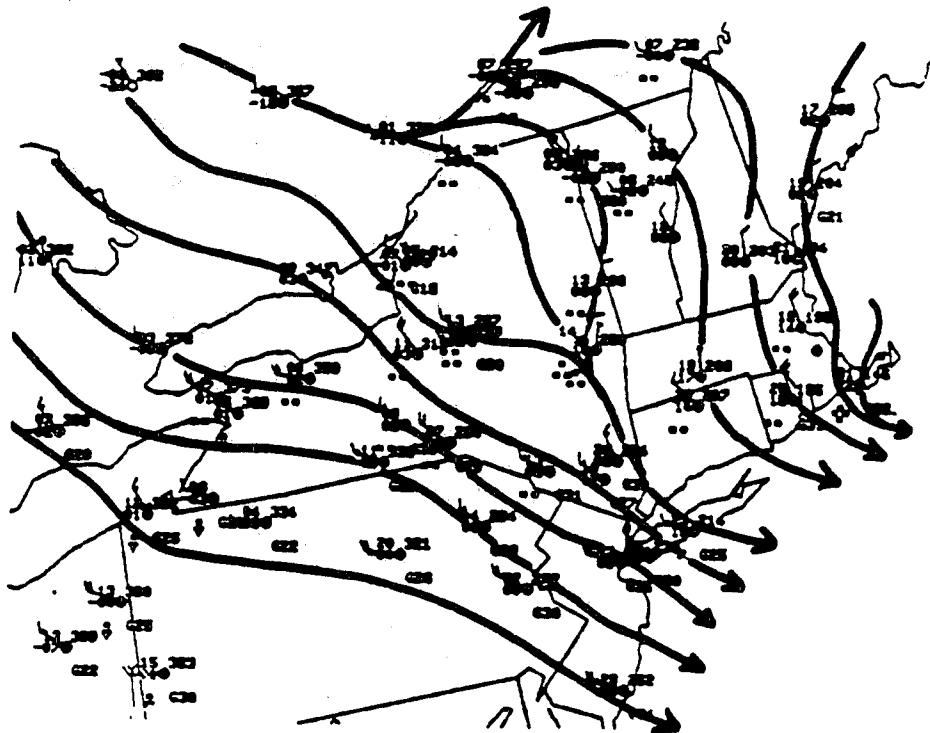
Figure 8. Surface streamline analysis for 1900 UTC, February 25, 1990.
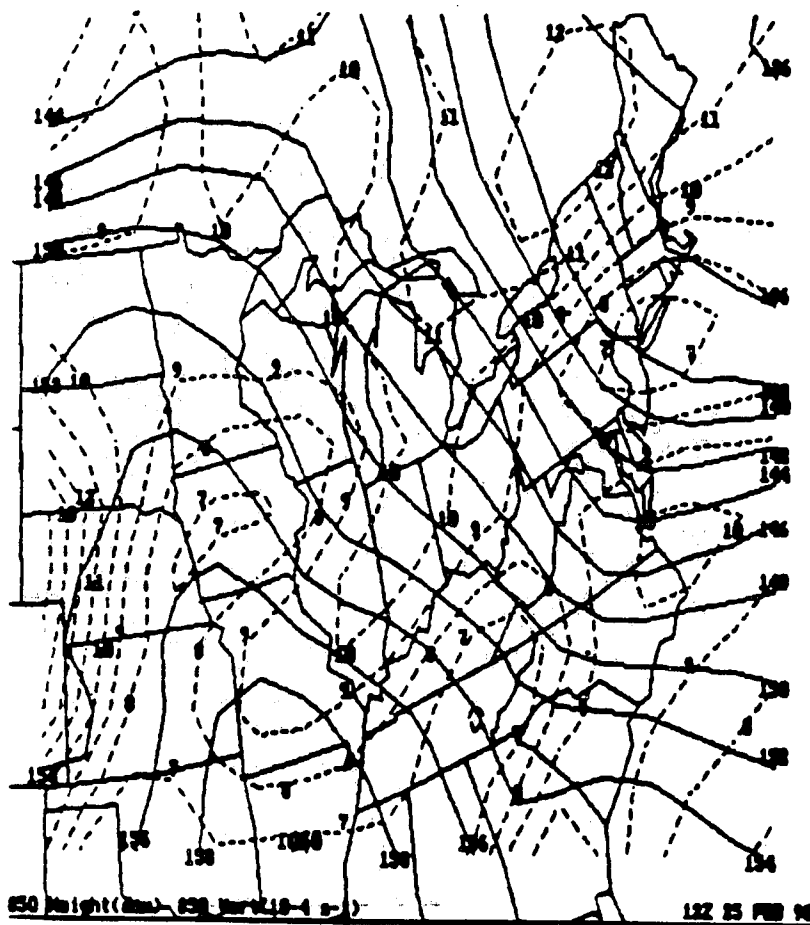
Figure 9. 850 mb heights (solid) and vorticity (dashed) for 1200 UTC, February 25, 1990.
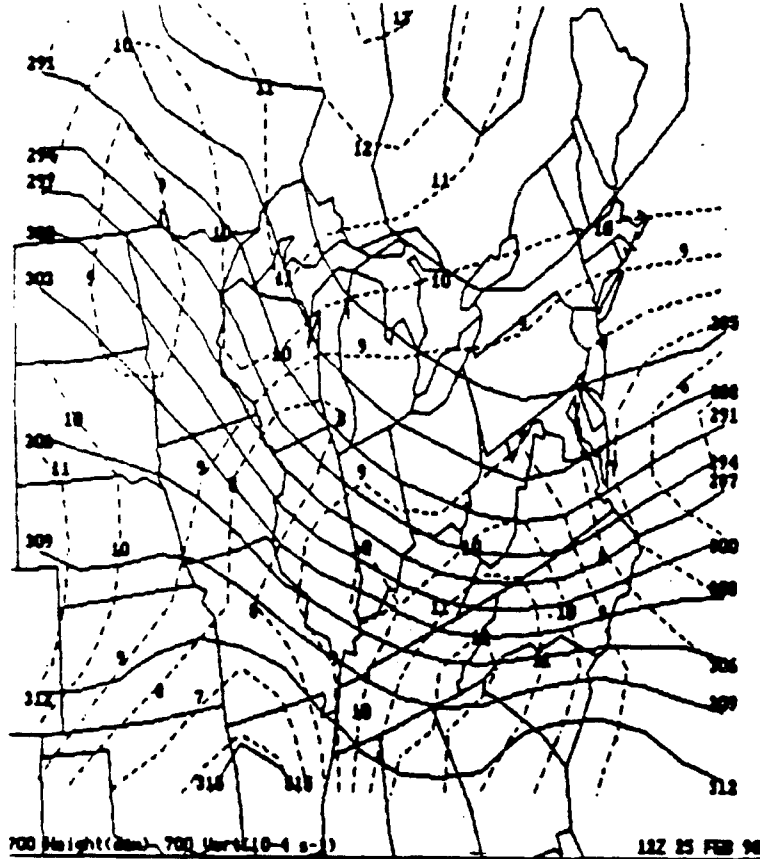
Figure 10. 700 mb heights (solid) and vorticity (dashed) for 1200 UTC, February 25, 1990.
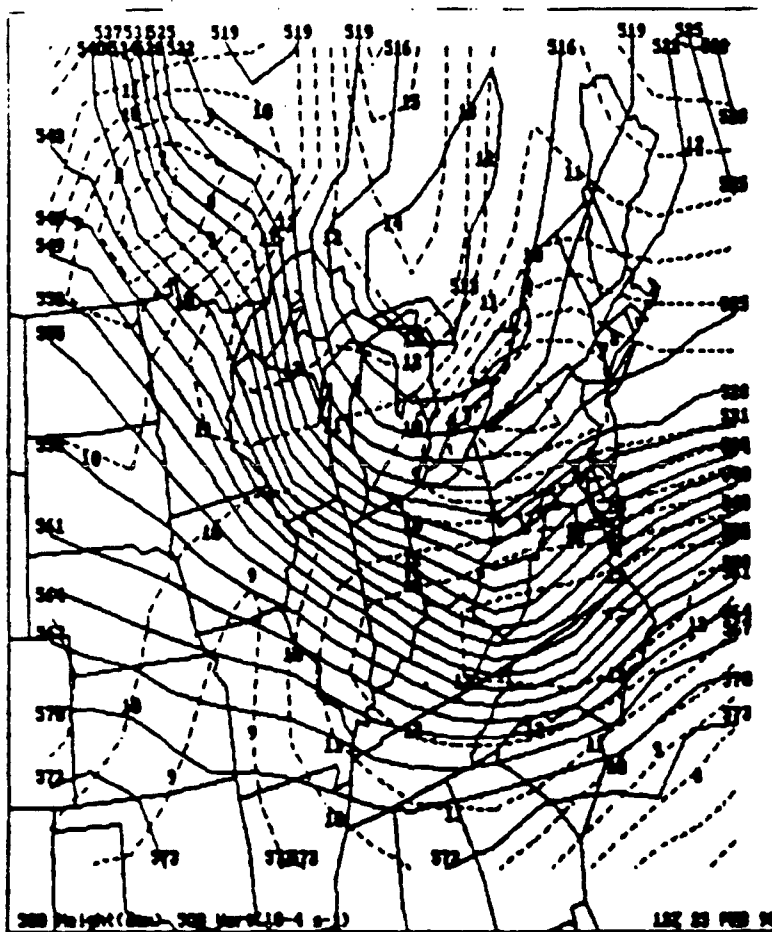
Figure 11. 500 mb heights (solid) and vorticity (dashed) for 1200 UTC, February 25, 1990.
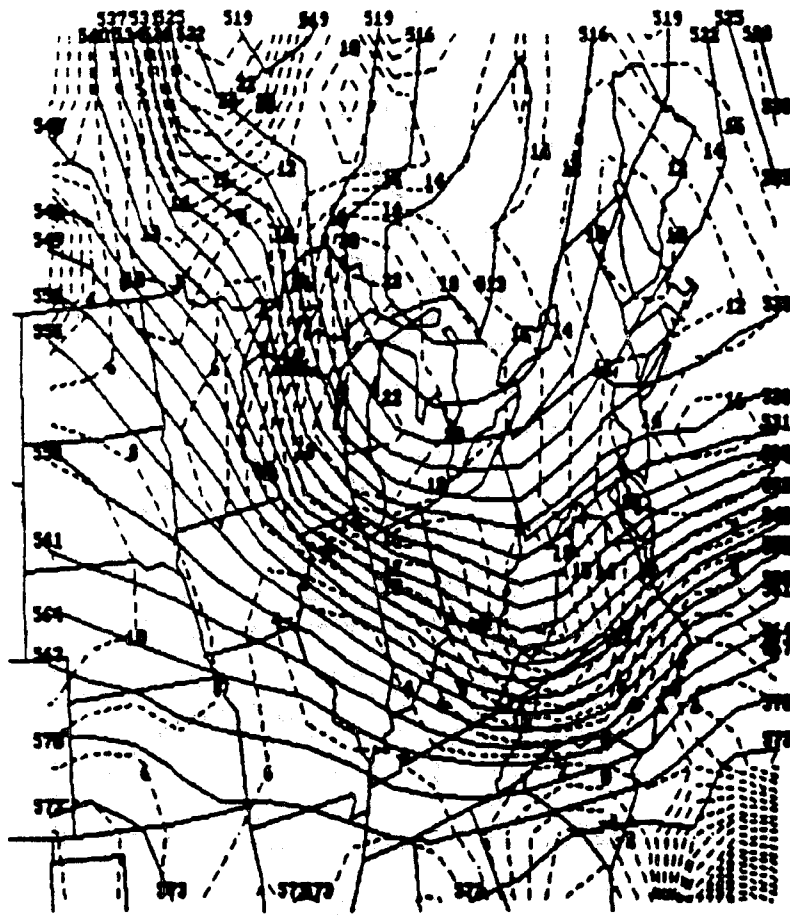
Figure 12. 500 mb heights (solid) and vorticity of geostrophic wind (dashed) for 1200 UTC, February 25, 1990.
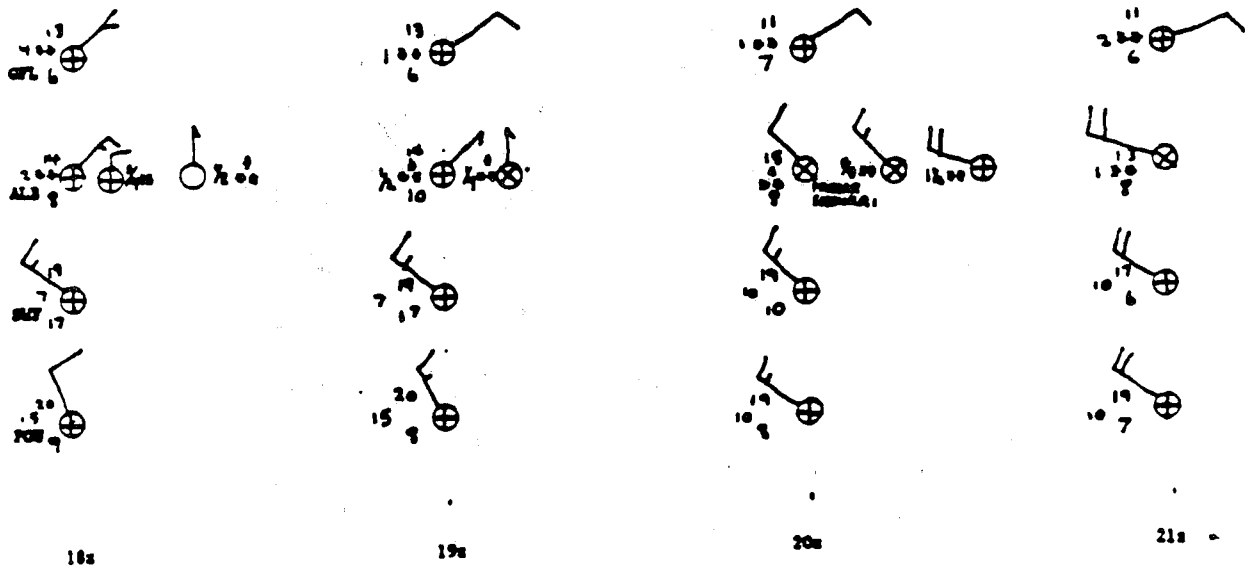
Figure 13. Surface observations from GFL, ALB, SWF, and POU (top to bottom, respectively) for 1800 to 2100 UTC (left to right), February 25, 1990.

Figure 14. Mesoscale snowburst event total snowfall (inches), for 1200 UTC, February 25, 1990 thru 0000 UTC, February 26, 1990.

Characteristic of Surface Cyclone Forecasts in the Aviation Run of the Global Spectral Model

Richard H. Grumm, NMC/MOD/TDG

An examination of the performance of the Aviation run (AVN) of the Global Spectral Model (GSM) was presented. The AVN is run twice daily at 00 and 12 UTC. Currently, the T126 GSM is used to produce the AVN and MRF forecasts. The T126 GSM replaced the T80 GSM in March of 1991. A new Spectral Statistical Interpolation (SSI) scheme was introduced in June, 1991. The results presented here show the impact of the recent model changes. The performance of the AVN is also compared to the operational Nested Grid Model (NGM) output from the Regional Data Analysis System (RAFS). The AVN cyclone errors are available from 12 to 72 h and the results are stratified by month and season.

Seasonal results are shown in Tables 1-4. The data are for the Autumn (Sep-Nov, AU90 and AU91) and Winter (Dec - Feb, WI91 and WI92). The significant thing to note is the tendency for the AVN to produce deeper cyclones (errors are taken as Forecast - Observed) during AU91 and WI92 compared to AU90 and WI91. This is believed to be the result of the implementation of the finer resolution T126 GSM in the Spring of 1991.

The geographical distribution of surface cyclones during WI91 and WI92 is shown in Fig. 1. The lack of surface cyclones over the southeastern US and western North America was due to a persistent upper level ridge during WI92. The large scale circulation pattern resulted in a northward shift of the cyclone activity over most of North America and the adjacent oceans.

The ability of the AVN to forecast the sign of the 12 h pressure change valid at the 24 h forecast period is shown in Fig. 2. The upper right and lower left quadrants represent the correct forecast of the sign of the observed 12 h pressure changes. The AVN correctly forecasts the sign of the 12 h pressure change at 24 h more than 80% of the time. There appears to be no significant differences between the tendencies observed during AU90 and AU91.

Figs 3 and 4 show a comparison of the AVN and NGM in forecasting the central pressure and position of surface cyclones. Generally, the AVN has smaller errors at 24 and 48 h than the NGM. The Root Mean Square Errors (RMS) are also smaller in the AVN than in the NGM. Examination of the pressure errors reveals that the overall character of the pressure errors (the bias or mean error) in the AVN have become similar to those found in the NGM since the implementation of the T126 GSM (March, 1991).

The results suggest that the T126 GSM produces deeper cyclones than the T80 GSM. The results also suggest that the AVN is better able to forecast the central pressure and the position of surface cyclones than the NGM.

Month	Fcst	Number	Pressure (mb)		Temp 850 (K)		Thickness (m)		Distance (km)	
			mean	RMS	mean	RMS	mean	RMS	mean	RMS
AU90	12	712	0.56	2.08	0.03	1.80	−4.63	29.05	115	148
AU90	24	662	0.63	3.02	0.30	2.04	−2.59	32.80	170	216
AU90	36	608	0.48	3.73	0.49	2.63	−0.63	42.54	227	290
AU90	48	553	0.43	4.55	0.74	2.93	2.19	49.48	290	371
AU90	60	483	0.48	5.51	1.05	3.25	6.81	54.95	344	431
AU90	72	430	0.25	5.98	1.03	3.50	7.22	59.31	409	515

Table 1. The mean pressure, 850 mb temperature, thickness and distance errors
by forecast hour (Fcst) in AVN cyclones for the winter of 1992. Data
include season, the number of cases, the mean pressure error (mb), 850 mb
temperature (K), thickness (m) and distance (km) errors, and the root
mean square errors (RMS).

Month	Fcst	Number	Pressure (mb)		Temp 850 (K)		Thickness (m)		Distance (km)	
			mean	RMS	mean	RMS	mean	RMS	mean	RMS
AU91	12	598	0.03	1.98	−0.14	1.90	−3.51	27.76	104	130
AU91	24	575	−0.03	2.93	−0.15	2.25	−4.37	35.09	165	214
AU91	36	529	−0.18	3.65	−0.22	2.49	−5.64	39.50	222	283
AU91	48	498	−0.31	4.56	−0.05	2.59	−3.33	41.95	285	367
AU91	60	453	−0.25	5.72	0.15	2.98	−0.76	49.50	361	473
AU91	72	410	−0.27	6.80	0.20	3.35	−0.05	54.63	416	523

Table 2. As in Table 1 except for Autumn, 1991 (SEP – NOV, 1991).

Month	Fcst	Number	Pressure (mb)		Temp 850 (K)		Thickness (m)		Distance (km)	
			mean	RMS	mean	RMS	mean	RMS	mean	RMS
WI91	12	634	0.65	2.55	−0.23	1.93	−7.67	32.41	116	148
WI91	24	558	1.05	3.73	−0.05	2.43	−8.81	42.14	164	204
WI91	36	523	1.18	4.58	0.24	3.03	−4.96	51.08	229	289
WI91	48	479	1.10	5.53	0.26	3.28	−5.99	57.61	292	365
WI91	60	449	1.47	6.64	0.57	4.19	−1.70	73.46	385	503
WI91	72	397	1.40	7.53	0.51	4.45	−1.80	78.82	472	606

Table 3. As in Table 1 except for Winter, 1991 (Dec, 1990 – Feb, 1991).

Month	Fcst	Number	Pressure (mb)		Temp 850 (K)		Thickness (m)		Distance (km)	
			mean	RMS	mean	RMS	mean	RMS	mean	RMS
WI92	12	673	0.01	2.19	−0.29	1.94	−5.21	29.45	106	143
WI92	24	644	−0.26	3.28	−0.37	2.39	−6.65	37.17	162	212
WI92	36	604	−0.69	4.61	−0.50	3.15	−7.57	49.66	229	300
WI92	48	552	−0.89	5.36	−0.47	3.52	−5.71	56.41	286	360
WI92	60	494	−1.09	6.27	−0.42	4.17	−7.38	65.01	383	484
WI92	72	435	−1.00	6.57	−0.47	4.12	−9.18	68.51	446	557

Table 4. As in Table 1 except for Winter, 1992 (Dec, 1991 – Feb, 1992).

a. AVN Cyclones MT91
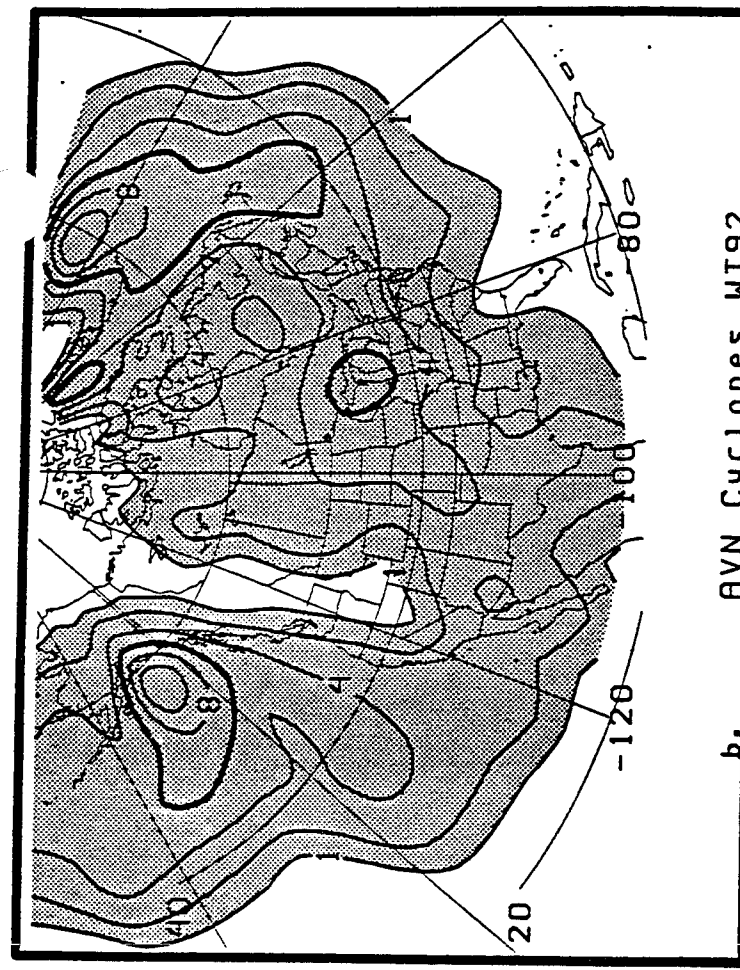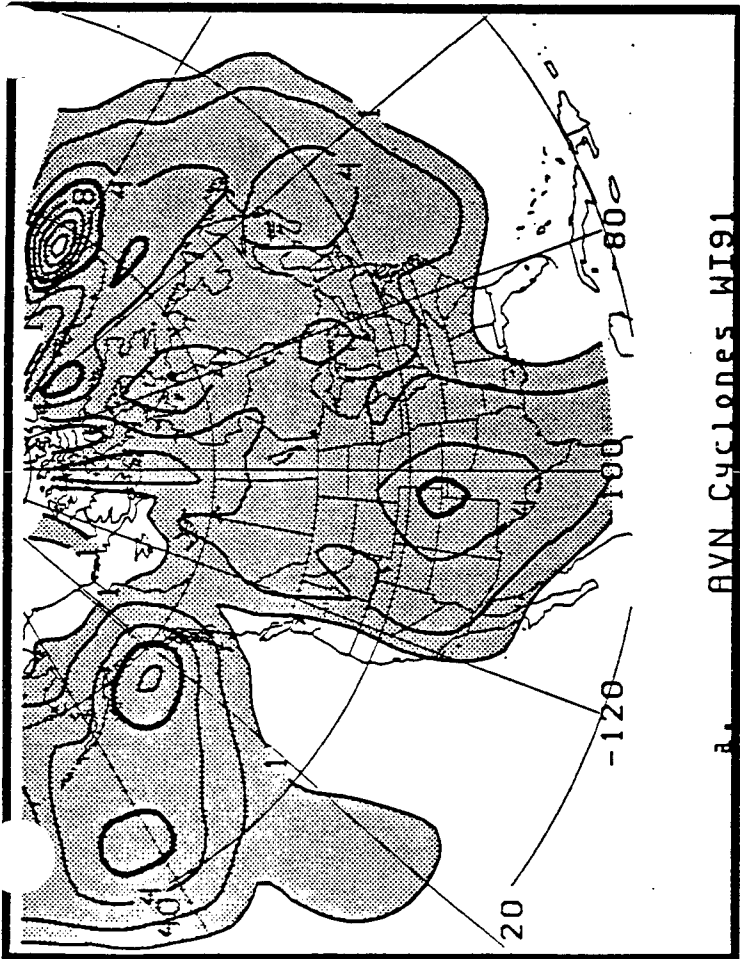
b. AVN Cyclones MT92

Forecast vs Observed Pressure Change

24 h forecasts — AU90 r=0.84

Observed Pressure Change (mb)

+   24 dp   —

Forecast vs Observed Pressure Change

24 h forecasts — AU91 r=0.86

Observed Pressure Change (mb)

+   24 dp

e

f
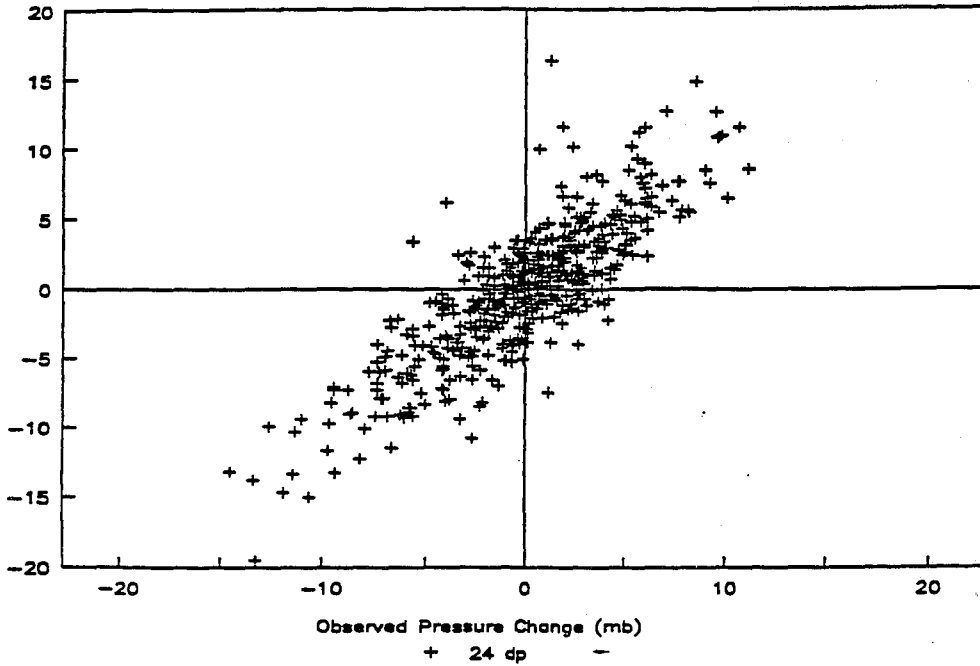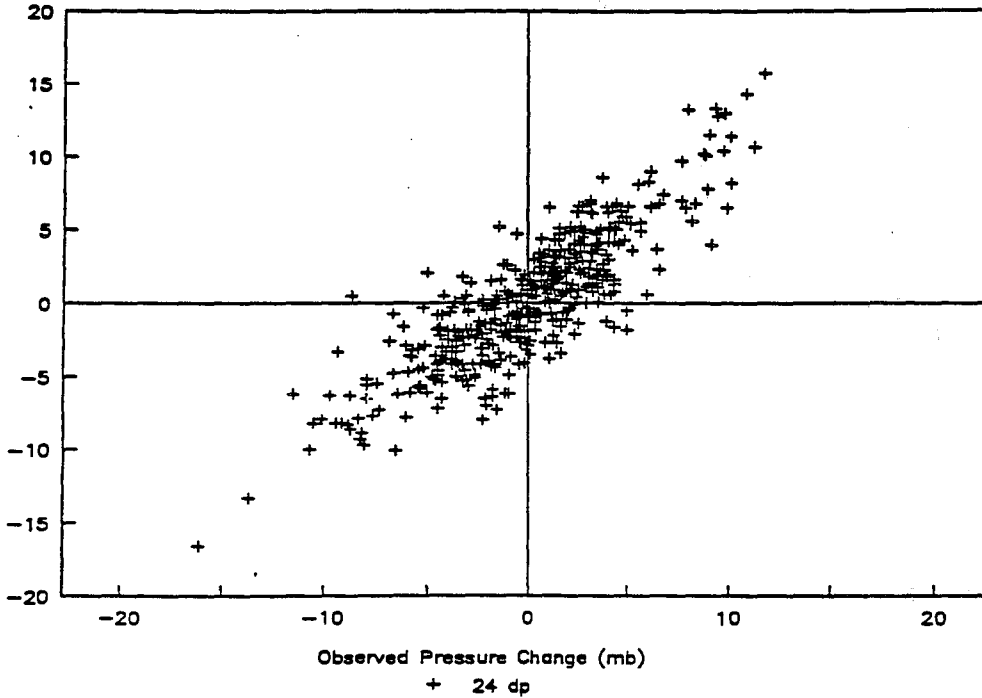
fig = 2 Cont

AVN vs NGM
24 h Cyclone Pressure Errors

Pressure Error (mb)

RMS (mb)

SepOctNovDecJanFebMarAprMayJun Jul AugSepOctNovDecJanFeb
Month

- ─*─ 24 h AVN dp
- ─*─ 24 h NGM dp
- ▦ 24 h AVN RMS
- ▦ 24 h NGM RMS
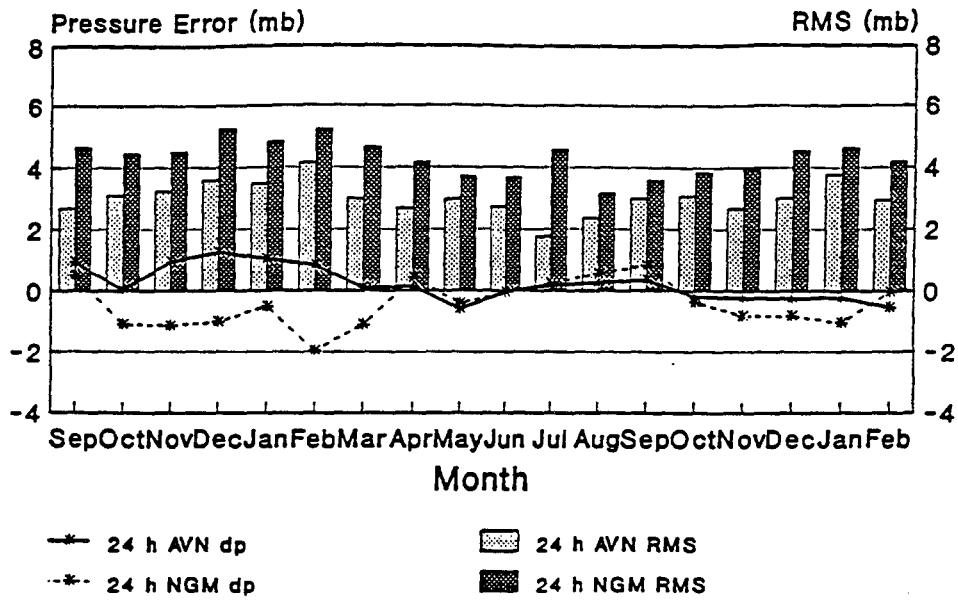
Sep 1990 - Feb 1992

AVN vs NGM
48 h Cyclone Pressure Errors

Pressure Error (mb)

RMS (mb)

SepOctNovDecJanFebMarAprMayJun Jul AugSepOctNovDecJanFeb
Month

- ─*─ 48 h AVN dp
- ─*─ 48 h NGM dp
- ☐ 48 h AVN RMS
- ▦ 48 h NGM RMS
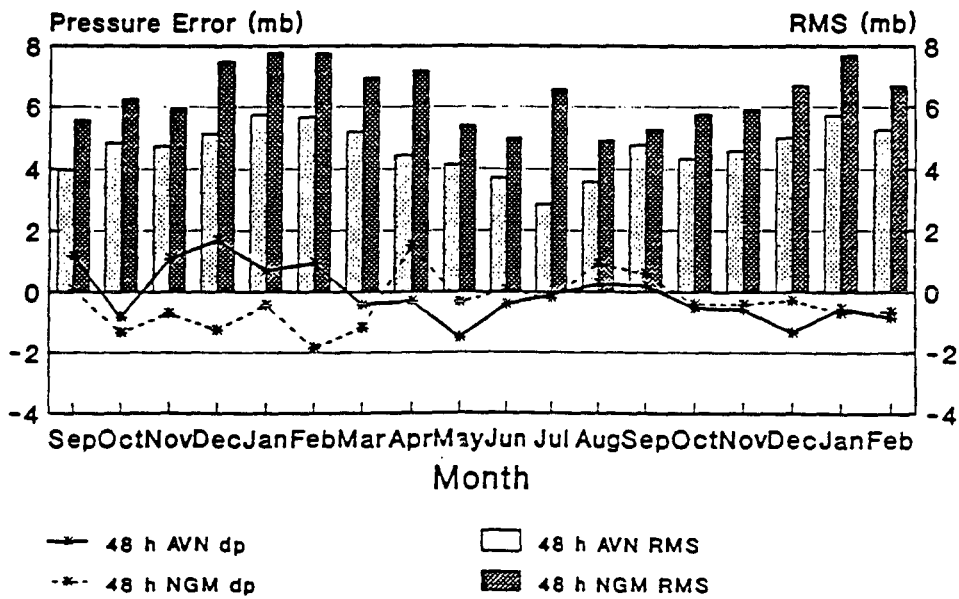
Sep 1990 - Feb 1992

Fis 3

AVN vs NGM
24 h Cyclone Distance Errors

Sep 1990 - Feb 1992

AVN vs NGM
48 h Cyclone Distance Errors
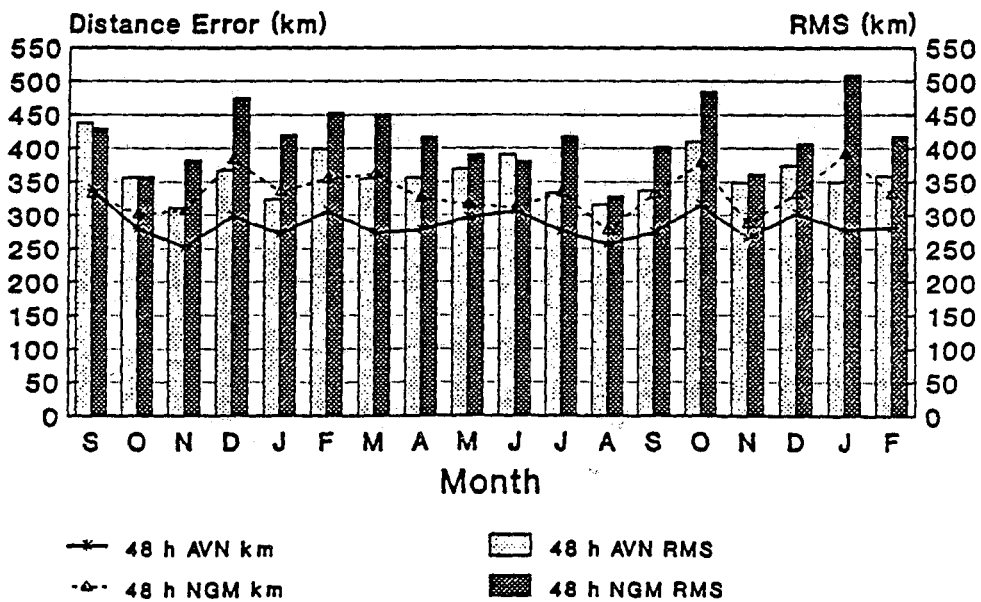
Sep 1990 - Feb 1992

fig 4
r.. 22

MODEL AND FORECASTER TEMPERATURE BIASES IN A
STAGNANT PATTERN OF LOW CLOUDS AND FOG

TIMOTHY W. MCCLUNG
WSFO SLC

POST-PRINT

-

MODEL AND FORECASTER TEMPERATURE BIASES IN A
STAGNANT PATTERN OF LOW CLOUDS AND FOG

TIMOTHY W. MCCLUNG
WSFO SLC

I. INTRODUCTION

SALT LAKE CITY, UTAH IS LOCATED IN A NORTHERN UTAH VALLEY. THE
WASATCH MOUNTAINS TO THE EAST RISE OVER 7000 FEET ABOVE THE VALLEY
FLOOR WHILE THE OQUIRRH MOUNTAINS TO THE WEST STAND 5000 FEET ABOVE
THE VALLEY. THE GREAT SALT LAKE LIES TO THE NORTHWEST OF THE CITY.
THE LOCAL TOPOGRAPHY FORCES THE DEVELOPMENT OF INVERSIONS IN THE
VALLEY DURING THE WINTER SEASON, ESPECIALLY DURING LATE DECEMBER
AND EARLY JANUARY, WHEN NIGHTS ARE LONGEST. THE DENSE FOG AND
ASSOCIATED STRATUS MAY REMAIN TRAPPED FOR WEEKS AT A TIME UNTIL
EITHER THE INVERSION ERODES DOWN TO THE SURFACE OR WINDS FROM AN
APPROACHING SHORT WAVE SCOUR THE INVERSION AND FOG OUT OF THE
VALLEY.

II. MODEL AND FORECASTER TEMPERATURE BIASES

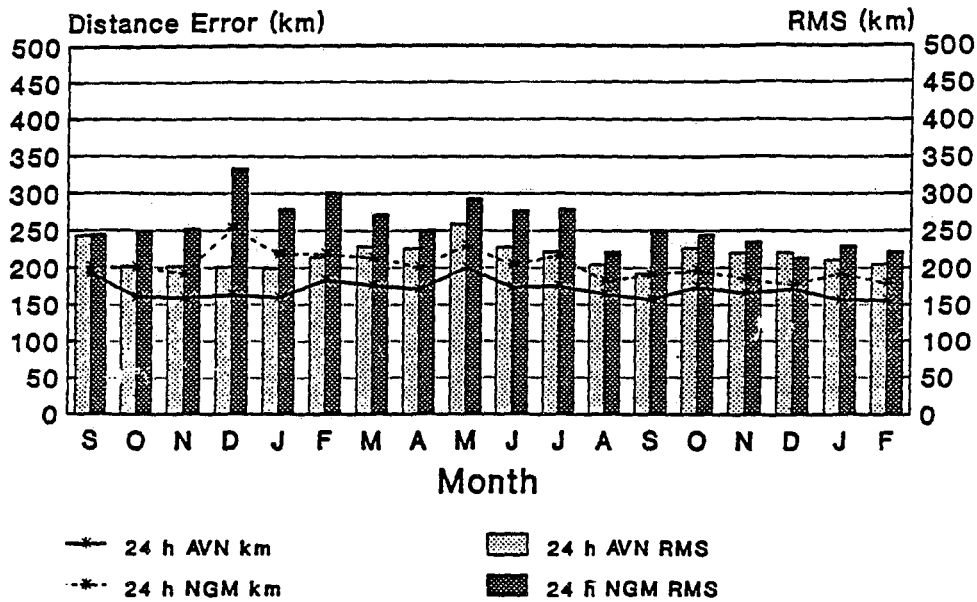DURING THE WINTER OF 1991-1992, SEVERAL INVERSIONS AND ASSOCIATED
DENSE FOG DEVELOPED OVER THE SALT LAKE VALLEY. THE MEAN ABSOLUTE
ERROR FOR BOTH MOS DURING THE VARIOUS INVERSIONS RANGED FROM 4°F TO
10°F. THE LFM AND NGM MOS EXHIBITED A PERSISTENT WARM BIAS IN THE
DAYTIME PERIODS AND COLD BIAS IN THE NIGHTTIME PERIODS WHEN THESE
INVERSIONS EXISTED AT THE TIME OF THE MODEL RUN.

EXAMINATION OF THE LFM/NGM MOS EQUATIONS POSSIBLY EXPLAINS WHY THE
MODELS HAD DIFFICULTY FORECASTING TEMPERATURES DURING THE
INVERSIONS. BOTH MOS, AND ESPECIALLY THE NGM, USED PREDICTANDS
THAT WERE EXTRAPOLATED FROM LEVELS BELOW THE SURFACE. FOR
LOCATIONS, SUCH AS SALT LAKE CITY, WHERE THE SURFACE ELEVATION IS
ABOVE THE 1000 MB LEVEL, THE MODELS EXTEND THE ACTUAL SOUNDING
BELOW THE SURFACE TO 1000 MB IN A WAY THE MODELS BELIEVE IS
REASONABLE AND MEANINGFUL. IN THESE WINTER EVENTS AT SALT LAKE
CITY, WITH SHALLOW BUT STEEP INVERSIONS NEAR THE SURFACE, THE MODEL
MAY CREATE A POOR DEPICTION OF THE SOUNDING BELOW THE SURFACE THUS
PUTTING UNREPRESENTATIVE DATA INTO THE EQUATIONS.

THE NGM MOS FORECASTED A LARGER DIURNAL RANGE OVER THE WINTER OF
1991-1992 THAN THE LFM MOS. THE NGM MOS EQUATIONS ARE BASED ON A
TWO YEAR DATA SET WHERE THE LFM EQUATIONS WERE DERIVED USING FOUR
YEARS OF DATA. THE NGM-BASED PERFECT PROG EQUATIONS ARE DEVELOPED
FOR TWO SEASONS FOR ALL FORECAST ELEMENTS; WARM (APRIL THROUGH
SEPTEMBER) AND COOL (OCTOBER THROUGH MARCH). AT SALT LAKE CITY,
THE LFM MOS EQUATIONS HAVE BEEN DEVELOPED FOR FOUR SEASONS. THE
LFM MOS EQUATIONS WOULD LIKELY FORECAST MORE ACCURATE TEMPERATURES
FOR SALT LAKE CITY THAN THE NGM-BASED PERFECT PROG EQUATIONS DURING
THIS UNIQUE WINTER SEASON PHENOMENON.

THE FORECASTERS AT SALT LAKE CITY IMPROVED ON BOTH MOS DURING THE WINTER OF 1991-1992 BUT BY ONLY A SMALL MARGIN. IN MANY CASES, THE FORECASTER'S MEAN ABSOLUTE ERROR WAS GREATER THAN 5°F. CONSIDERING THE DIURNAL RANGE ON MANY DAYS WITH INVERSIONS AND FOG PRESENT WAS AS SMALL AS 5°F TO 7°F, THE FORECASTERS MEAN ABSOLUTE ERROR APPEARS IMPROVABLE.

III. CONCLUSIONS

THE LFM MOS IS SCHEDULED TO BE UNAVAILABLE AFTER THE WINTER OF 1992-93. THE NGM MOS EQUATIONS ARE SCHEDULED TO INCORPORATE FOUR YEARS OF DATA IN THE FALL OF 1992, HOPEFULLY LOWERING THE MODEL'S MEAN ABSOLUTE TEMPERATURE ERROR. STILL, THE NEW NGM EQUATIONS ARE UNLIKELY TO ACCURATELY PREDICT MAXIMUM AND MINIMUM TEMPERATURES WHEN INVERSIONS ARE IN PLACE OVER SALT LAKE CITY IN FUTURE WINTER SEASONS.

THEREFORE, A TYPE OF MOS EQUATION IS BEING DEVELOPED FOR FORECASTING HIGHS AND LOWS AT SALT LAKE CITY WHEN AN INVERSION AND/OR STRATUS LAYER IS EXPECTED TO EXIST THROUGHOUT THE FORECAST CYCLE. THE "MINI-MOS" EQUATION IS A STATISTICAL RELATIONSHIP BASED ON ACTUAL SALT LAKE CITY SOUNDINGS AND TEMPERATURE VERIFICATIONS FROM THE WINTERS OF 1989-90, 1990-91, AND 1991-92.

THE EQUATION HAS YET TO BE FINALIZED BUT IS EXPECTED TO USE UP TO EIGHT PREDICTANDS INCLUDING PERSISTENCE, SURFACE TEMPERATURE AND DEW POINT, 850MB TEMPERATURE AND DEW POINT, AND DEPTH OF THE INVERSION AND/OR STRATUS LAYER. THE EQUATION WILL BE TESTED THIS WINTER AT THE SALT LAKE CITY FORECAST OFFICE.

FORECASTER APPLICATION AND IMAGERY SYSTEM
VERSION 4.0

Glen W. Sampson, Dennis Gettman and Timothy Barker

National Weather Service
Western Region Headquarters
Salt Lake City, Utah

1.   INTRODUCTION

The Forecaster Application and Imagery System (FAIS - pronounced as "face") provides a simple, inexpensive platform for integrating and manipulating data sets unique to operational meteorology. Two primary objectives behind the FAIS development effort are to extend the meteorological capabilities of existing National Weather Service (NWS) systems, and to begin the integration of new data sets into an operational forecast setting.

To reduce implementation costs, the system runs on personal computer hardware under OS/2 Version 2.0. A minimum configuration consists of:

- 80386DX-based personal computer
  8 MB of memory
  100 MB hard disk
  5.25" or 3.5" diskette drive
  keyboard
- color VGA monitor
- mouse
- OS/2 Version 2.0

The FAIS has a modular design, so a user can pick and choose which pieces to implement. Many modules are totally independent of other modules to provide the greatest possible flexibility in system configuration and implementation.

2.   FAIS DESIGN OVERVIEW

Two modules comprise the heart of the FAIS software: the user menu interface, and the Meteorological DataBase (MDB). The MDB module provides a generic data management system from which applications can easily obtain and distribute products. The database software is optimized for fast product retrieval and is compatible with Novell's Netware/386. The user interface provides a standardized method for retrieving and displaying products which reside in MDB.

Once MDB is implemented on a system, other software modules can be added as needed. These modules provide for:
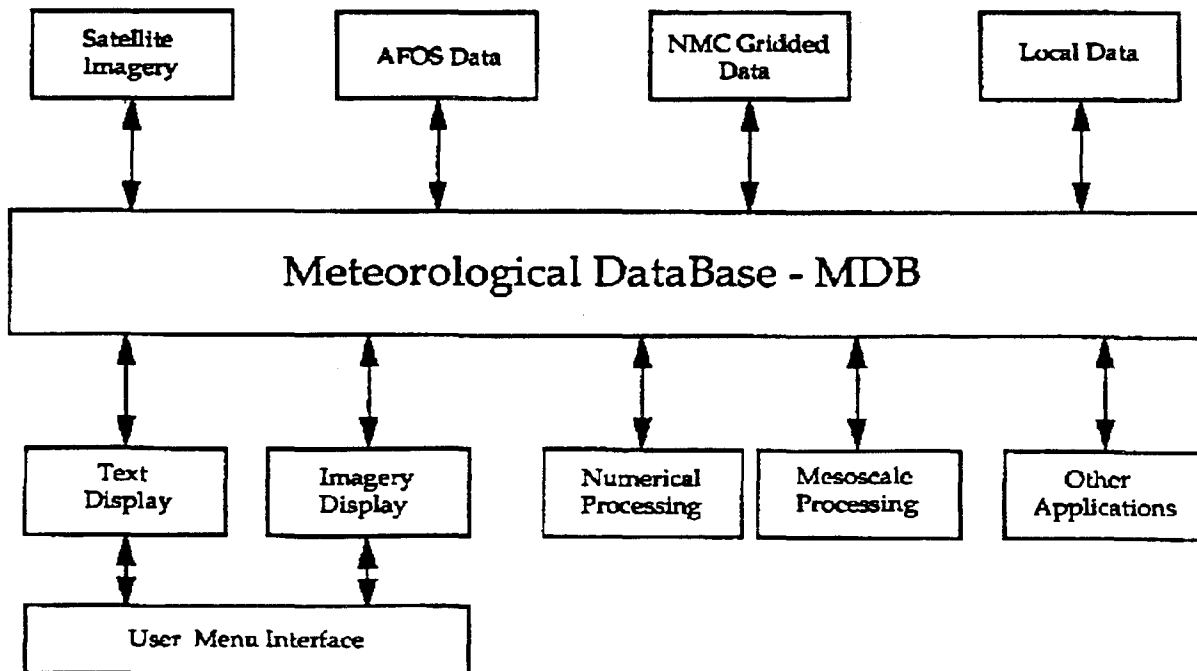

Figure 1 - The general data flow between FAIS software modules.

a. the ingest and storage of Automation of Field Operations and Services (AFOS) products;
b. the ingest and display of GOESTAP satellite imagery;
c. the ingest, processing and display of NMC model gridded data sets, and;
d. the ingest and processing of surface data sets associated with mesoscale forecasting.

Figure 1 depicts the software modules available in FAIS and the general data flow between the modules.

3. DATABASE AND PRODUCT RETRIEVAL CAPABILITIES

The Meteorological DataBase (MDB) was designed for implementation in an operational forecasting environment. The speed of product retrieval and the ability to provide distributed access in a network setting were the two highest priority design characteristics. The capability to retrieve an image product within 1.5 seconds over a network, and within 1 second in a stand-alone version, was deemed essential for operational use.

MDB provides the flexibility to allow easy implementation on existing systems which support OS/2 Version 2.0. The database can range in size from 1000 bytes to several gigabytes. The number of products can range from 1 to over 15,000. Each product can have three different data types, for example, vector graphic and bitmap, and each data type can have 256 versions. Thus, the maximum number of products which can be stored with the MDB module is over 11 million. These numbers translate to about 3 times the data capabilities of an operational AFOS system.

One hundred map background categories are available for use in the database. Fifty of these backgrounds are classified as graphic backgrounds and fifty are image backgrounds. Three graphics products can be overlaid on a graphic background, and two graphic products can be overlaid on an image background.

The user menu interface provides a consistent method for user's to retrieve all products which reside in the database. Programs exist with the user interface to automatically analyze the database and customize the menus shown to the user. Thus, every FAIS implementation has a unique set of menus.

Both text and graphics products are easily displayed by the users. Text products are placed in windows which can be scrolled, resized and printed. Graphic and imagery products are displayed full screen to utilize the full VGA resolution. Animation, zoom capability and user-defined color enhancement curves are some of the features available to the user during graphics and imagery display.

4. AFOS DATA COMMUNICATIONS

Modules exist for a complete AFOS asynchronous communication interface. The ability to automatically receive and send products to AFOS is important for maintaining an operationally integrated data set. Many meteorological PC programs within the NWS require data to be in an AFOS-type of format; thus, access to AFOS data maintains current PC data requirements.

5. GOES IMAGERY

Real-time GOES imagery is delivered to NWS offices through the GOESTAP telecommunication network. A GOESTAP connection provides an amplitude modulated facsimile signal which can contain up to four satellite images an hour (Clark, 1983). Hence, additional hardware is required to ingest a satellite image into a personal computer. Specifically, a receiver demodulator unit and an analog-to-digital board.

The receiver demodulator unit used in FAIS was developed by the NWS and is not an off-the-shelf piece of hardware. Conceptually, the receiver demodulator unit removes the carrier and telephone line noise from the analog signal. Once demodulated, the imagery data remains as a base band analog signal and is digitized by the analog-to-digital board (Sampson, 1990). The total cost for both pieces of hardware is about $600.

Imagery is ingested and stored into the MDB automatically. This task requires a substantial amount of CPU resources. Implementation of GOES imagery along with several other FAIS modules is not recommended on a minimally configured system. (Much of the software used for satellite imagery was developed in FAIS Version 3.0 and was implemented in many NWS offices as MicroSWIS.)

6. GRIDDED DATA PROCESSING

Gridded data processing programs are a module of the FAIS. Gridded data from any numerical model can be store in the MDB on either latitude/longitude grids, or equally spaced grids on a polar stereographic projection. A different storage grid is allowed for each model.

A decoding program for GRIB Version 1 exists to unpack and translate data, transform the data to a particular storage grid and store it into the database. A second program retrieves the gridded data from MDB, performs the calculations for various meteorological quantities, draw contours or wind barbs and store bitmap graphics back into the database for the user to display. Once the bitmap graphics are in the database, the user interface program can access them for viewing.

Numerous meteorological fields are available, and are listed below:

- height (dm)
- temperature (°C)
- relative humidity (%)
- vertical motion (cm/sec)
- wind barbs (knots)
- isotachs (knots)
- total precipitation (inches)
- convective precipitation (inches)
- mean sea level pressure (mb)
- temperature advection (x 10^{-4} °C/sec)
- geostrophic wind barbs (knots)
- ageostrophic wind barbs (knots)
- absolute vorticity (x 10^{-5}/sec)
- absolute vorticity advection (x 10^{-9}/sec^2)
- divergence (x 10^{-6}/sec^2)
- dew-point depression (°C)
- Q-vector barbs (x 10^{-11} K/sec m^2)
- Q-vector divergence (x 10^{-15} K/sec m^2)
- lapse rate (°C)
- potential temperature (°K)
- equivalent potential temperature (°K)
- thickness (dm)

A wide variety of contouring and wind barb drawing options are implemented to give users sufficient control over the visual aspects of the bitmap graphic products.

7. MESOSCALE DATA EFFORTS

The mesoscale portion of the FAIS consists of two areas: (1) the generation of map backgrounds and (2) the plotting and analysis of surface data. The capability to generate map backgrounds exists at all sites. Data sets exist to include any combination of the following in a map background:

- state and county boundaries
- latitude and longitude lines
- rivers and waterways
- major roads
- major cities and landmarks
- topographical data
- user-defined data

Plans are to develop the ability to automatically decode and plot all surface observations which exist in the standard SAO format. Several station plot models are required for fire weather data, marine data, general aviation data and hydrological data types.

Much of the effort required for establishing a quality mesoscale data set is unique to a local site. Thus, the data collection programs are site specific. The MDB module provides a well-defined application programming interface (API) to allow for easier development of these local data collection programs.

Secondary to the establishment of a quality data set is to perform an objective analysis and generate the common analyses, such as pressure, pressure

tendency, dew-point temperature, ambient temperature, fuel moisture, fuel temperature, precipitation, streamlines and surface convergence.

8. CAPABILITY SUMMARY

The Forecaster Application and Imagery System (FAIS) is a multi-faceted project capable of processing AFOS data, GOES imagery data, GRIB formatted gridded data and mesoscale surface observations. Many of these areas are currently in active development with approximately 95% of the software completed, except for mesoscale data processing which is 30% completed.

9. REFERENCES

Clark, J.D., 1983: The GOES User's Guide, United States Department of Commerce, 6-29 and 6-30.

Sampson, G.W., and Clark, G.N., 1990: The Forecaster Application and Imagery System, Preprint Sixth International Conference on Interactive Information and Processing Systems, 237-240.

An Overview of ARO-NET

The Alaska Region Operations Network

by Paul Shannon, Meteorologist
WSFO Juneau, Alaska

The Alaska Region of the National Weather Service has evolved a unique means of collecting, processing, and distributing meteorological information in the absence of AFOS (Automation of Field Operations and Services). Dubbed ARCCS (Alaska Region Computer and Communications System), the program centers around PRIME 6150 and 4150 mini-computers. The computers ingest the standard meteorological data sets, and decode and store the resulting information in a data-base developed by regional programmers.

The meteorological data is then distributed, through a series of application programs, to operational personnel for display and analysis. Prior to 1990, each forecast position consisted of two IBM PS/2's and a single ASCII terminal to display the information. The region still relied on the facsimile machine as the primary method of distributing graphical forecast products from NMC to the field.

Then, during December of 1989, Mt Redoubt (90 nautical miles southwest of Anchorage) emerged from its dormant phase and began to erupt periodically over a period of months. Each eruption emitted a series of ash-laden clouds across the state. The ash clouds played havoc with air traffic across the region during the eruptive phase. The most serious incident involved a large commercial passenger jet that experienced flameout on all engines after traversing an ash cloud.

It was clear the NWS in Alaska required both higher resolution observational and forecast data sets in order to more accurately predict the movement and dispersal of future eruption clouds. It was also clear that ARCCS was incapable of either distributing, or displaying these new meteorological data sets. ARO-NET was developed to handle the increased workload.

The goal of ARO-NET was to blend the new data sources with the alpha-numeric database to form a consistent, integrated meteorological visualization tool. These data sources include: GRIB (gridded binary) data from various synoptic-scale, numerical weather prediction models (to eventually replace the current facsimile products); NGM sounding data for over 50 locations around the region in BUFR (Binary Universal Form for Representation) format; real-time lightning information provided by the Bureau of Land Management; and digital polar-orbiting imagery, acquired from the regional ground station located in Anchorage. The system has the capability to ingest and process digital GOES data as well.

The NMC models currently available on ARO-NET include the NGM, the GSM and the MRF. Plans are in the works to begin receiving the ECMWF and the UKMET along with ETA model from NMC. The MAPS (Mesoscale Analysis and Prediction System) for FSL is also slated to be available soon. Also available on the network are all the soundings from upper air stations in Alaska along with surface data, and a climatological database for all the WSO's and forecast offices.

An additional complexity to the equation was supporting the forecast operations at the Fairbanks and Juneau offices in addition to the Anchorage office (See Figure 1). The solution to this dilemma was a distributed, decentralized computing environment linked by high-speed communications circuits (See Figure 2). Standards such as UNIX, X-Windows, Motif and IEEE 802.3 Ethernet with the TCP/IP network protocol suite were selected to minimize the difficulties inherent in a heterogeneous computer environment. An advanced network routing scheme coupled with a sophisticated network management strategy was selected for fault-tolerance and error recovery in the Local and Wide Area Networks (LAN/WAN).

At each of the forecaster workstations the region has integrated the ARCCS PS/2 Model 70s and 80s as both graphic and alpha-numeric workstations. New IBM RS6000-320 workstations are employed as application and file servers with Hewlett-Packard 9000-720 series workstations functioning as the network satellite imagery servers (See Figure 3).

Through X-Windows/Motif and the Network File System (NFS), a forecaster is able to integrate meteorological data from any combination of sources across ARO-NET, including model data, satellite images and observed data both at the surface and aloft. The PRIME mini-computers continue to ingest and process data as before, however, the data sets are distributed through ARO-NET.

The ARO-NET system is still very much in an evolutionary stage with new products coming on-line all the time. Having access to the gridded model data is something very new to most forecasters and requires new ways of looking at and interpreting the available data. This holds both a promise and a challenge for each forecaster to discover how best to use the new wealth of data. With almost all of the programming being done by personnel in the Alaska region, each forecaster has an opportunity to have his or her input on what techniques and displays are useful (or just potentially useful) and should be incorporated into ARO-NET. This is helping the Alaska Region computer network become simple to use, fast and flexible with many new and exciting developments to come.

Alaska Region Operations Network

ANCHORAGE CWSU

To Fairbanks Forecast Office

ANCHORAGE Headquarters

To Juneau Forecast Office

ANCHORAGE River Forecast Office

ANCHORAGE Forecast Office

FAIRBANKS Forecast Office

ANCHORAGE Headquarters

JUNEAU Forecast Office
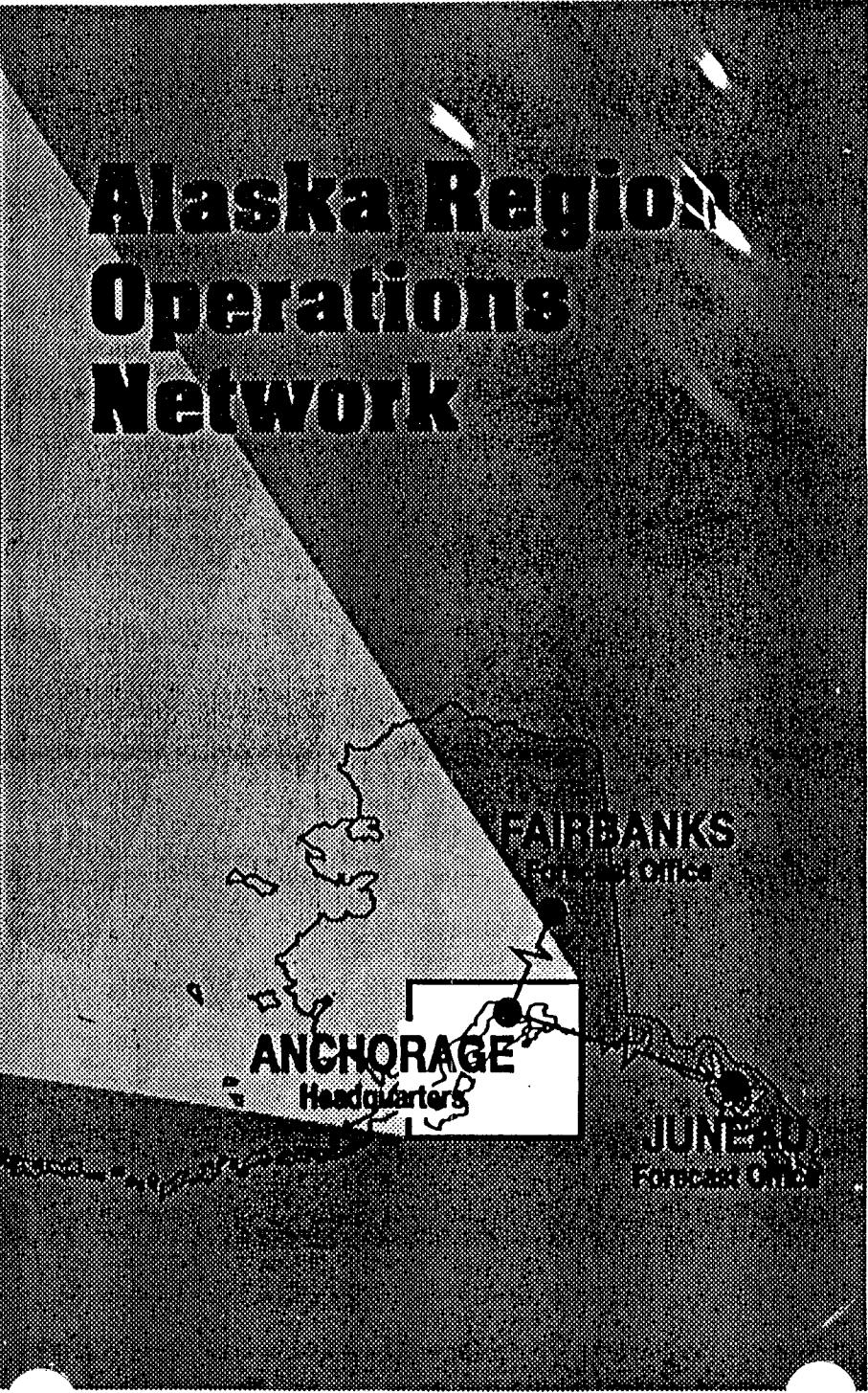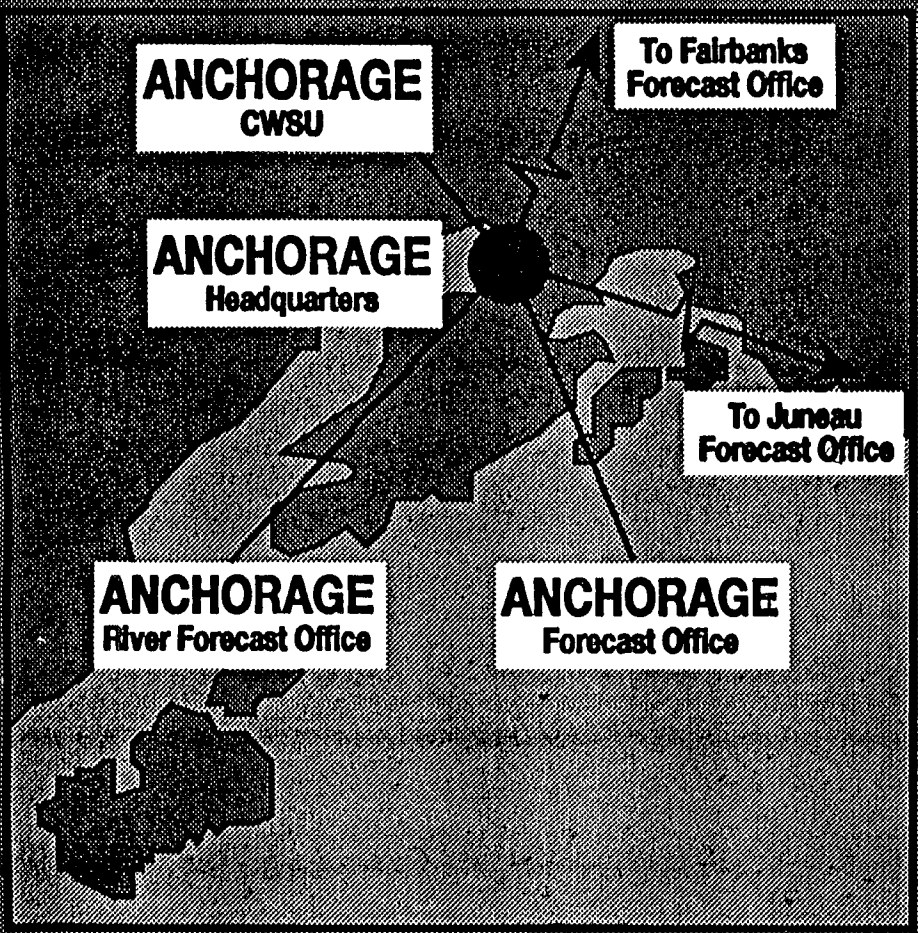
Figure 1

DATA FLOW ON THE ALASKAN REGION
WIDE AREA NETWORK
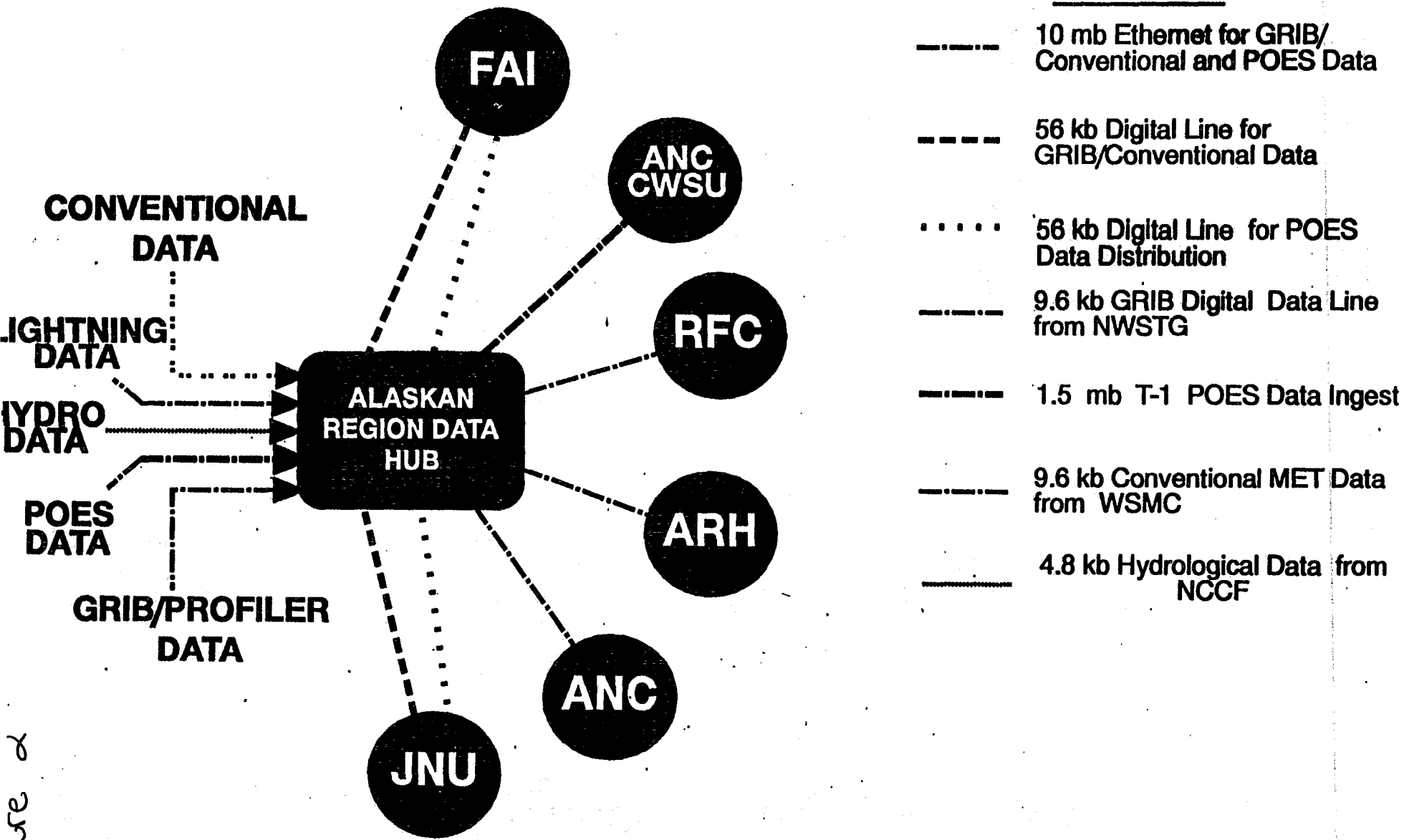
Figure α

ALASKA REGION OPERATIONS NETWORK ARCHITECTURE
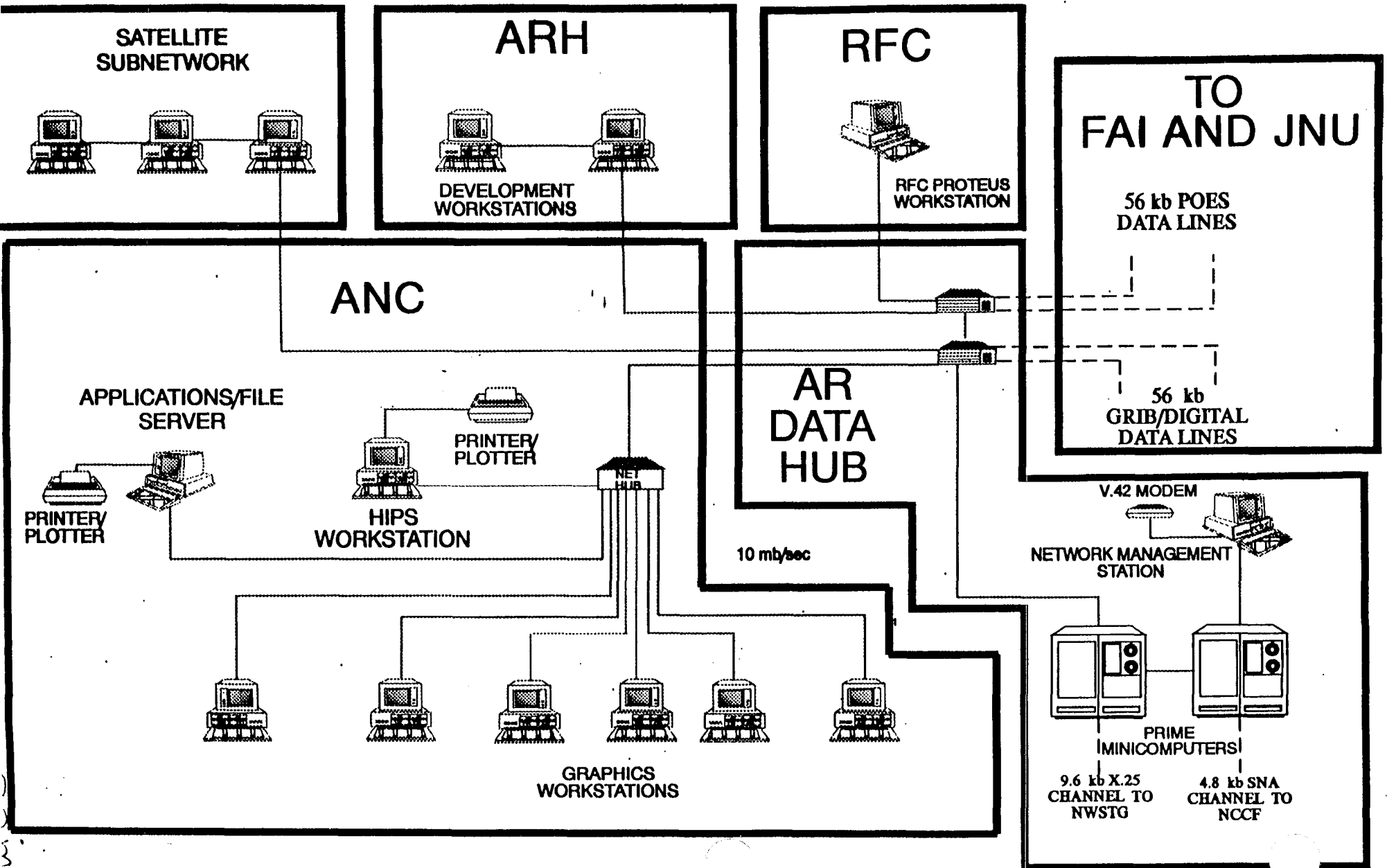
SATELLITE SUBNETWORK

ARH

RFC

TO FAI AND JNU

56 kb POES DATA LINES

DEVELOPMENT WORKSTATIONS

RFC PROTEUS WORKSTATION

ANC

AR DATA HUB

56 kb GRIB/DIGITAL DATA LINES

APPLICATIONS/FILE SERVER

PRINTER/ PLOTTER

NET HUB

V.42 MODEM

NETWORK MANAGEMENT STATION

PRINTER/ PLOTTER

HIPS WORKSTATION

10 mb/sec

GRAPHICS WORKSTATIONS

PRIME MINICOMPUTERS

9.6 kb X.25 CHANNEL TO NWSTG

4.8 kb SNA CHANNEL TO NCCF

NGM Model Output Error and the Effect on Forecasting
A Great Basin Cyclogenic Event: A Case Study

Michael C. Conger

National Weather Service Forecast Office
Salt Lake City, Utah

September 24, 1992

ABSTRACT

A late October 1989 storm that produced widespread heavy amounts of rain and snow across northwest Utah was associated with a rapidly intensifying 700 mb low over western Utah. A "conventional" examination of vertical motion forcing using 500 mb positive vorticity advection (PVA) placed the strongest upward vertical motions well south of the area of cyclogenesis. Subjective analysis of rawinsonde data prior to and during the development of the storm indicates the greatest upward motions were further north and more closely related to the precipitation maximum. In addition, a quasi-geostrophic examination of vertical motion forcing using the advection of vorticity by the thermal wind and the divergence of Q both supported cyclogenesis where it was observed. This evidence suggest that some kind of error exists in the initialized gridded data fields of the Nested Grid Model (NGM).

In order to verify this possibility, gridded data fields generated from the NGM were examined. These fields consisted of the initialized and 12 hour forecasts prior to and the initialized fields during the development of the storm. Three approaches were used to identify the weaknesses in the model output. The first approach was a comparison of model output against the corresponding subjective analyses of 250 mb isotachs and 700 mb geopotential heights, winds and temperatures. The second approach was to generate difference fields (initialized minus the previous 12 hour forecast) for the 250 mb observed and ageostrophic winds, for the divergence of the observed and ageostrophic winds, and for cross sections of omega overlaid with the ageostrophic wind transverse to the exit region of the jet streak. The final approach involved a quasi-geostrophic examination of the vertical motion forcing using the divergence of Q and the Trenberth Approximation. Gridded analysis from rawinsonde data generated by a Barnes analysis were compared against analysis generated by an Optimum Interpolation (OI) to determine which better identified the area of heavy precipitation.

Results of this study show 1) a "conventional" examination of vertical motion forcing using 500 mb PVA from the NGM model failed to explain heavy precipitation over northwest Utah; 2) the model's inability to properly initialize the jet streaks at 1200 UTC, 25 October, led to a 12 hour forecast where the ageostrophic forcing of vertical motion and the attending secondary (indirect) circulation were much less than initialized at 0000 UTC, 26 October; 3) small differences between the initialized and 12 hour forecast fields of the total wind both valid at 0000 UTC produced large errors in the total ageostrophic wind field; 4) the model's misrepresentation of the 700 mb wind field and the failure to generate a closed circulation center over eastern Nevada; 5) the divergence of Q at 500 mb, as computed from the gridded analysis generated by a Barnes analysis, did a better job of identifying the area of strongest upward vertical motion (heavy precipitation) than did the gridded NGM analysis generated through Optimum Interpolation.

1. Introduction

Between 1800 UTC, 25 October 1989, and 1800 UTC, 26 October 1989, widespread heavy precipitation amounts were recorded across northwest Utah. A cold core 700 mb low moving southeast across Nevada on the afternoon of the 25th experienced rapid intensification as it entered western Utah during the afternoon hours. Thunderstorms developed over western Utah along the strong baroclinic zone associated with the 700 mb low and continued until around 0300 UTC. After 0600 UTC on the 26th, the 700 mb low accelerated northeastward through central Utah. The main area of precipitation shifted to northern Utah with the heaviest amounts confined to the northwest quarter of the state. By 1500 UTC on the 26th, the storm center had moved into southwest Wyoming with precipitation ending over all but northeast Utah around 1800 UTC.

Climatologically, heavy precipitation events (amounts $\geq$ 25 mm/24 hours) in Utah are rare. When they occur, they are commonly associated with strong convection or orographic enhancement. In either event, heavy precipitation is generally confined to a limited geographic area. The 25-26 October storm was exceptional in that heavy precipitation was not localized, but spread over a relatively large area of the northwest valleys and mountains (Fig. 1).

Typically, a moist cold core 700 mb low moving through the Great Basin will produce widespread light precipitation without any significant intensification of the low. In this storm, however, the 700 mb low intensified over the Great Basin during the afternoon of the 25th. The resultant enhanced upward vertical motion supported strong convective activity and heavy precipitation over western Utah. As the 700 mb low moved northeast through Utah early on the 26th, the flow over northwest Utah gradually backed to a northwesterly direction. The resultant cold air advection across Great Salt Lake triggered "lake effect" precipitation in the lee of the lake and amplified orographically induced snowfalls in the mountains.
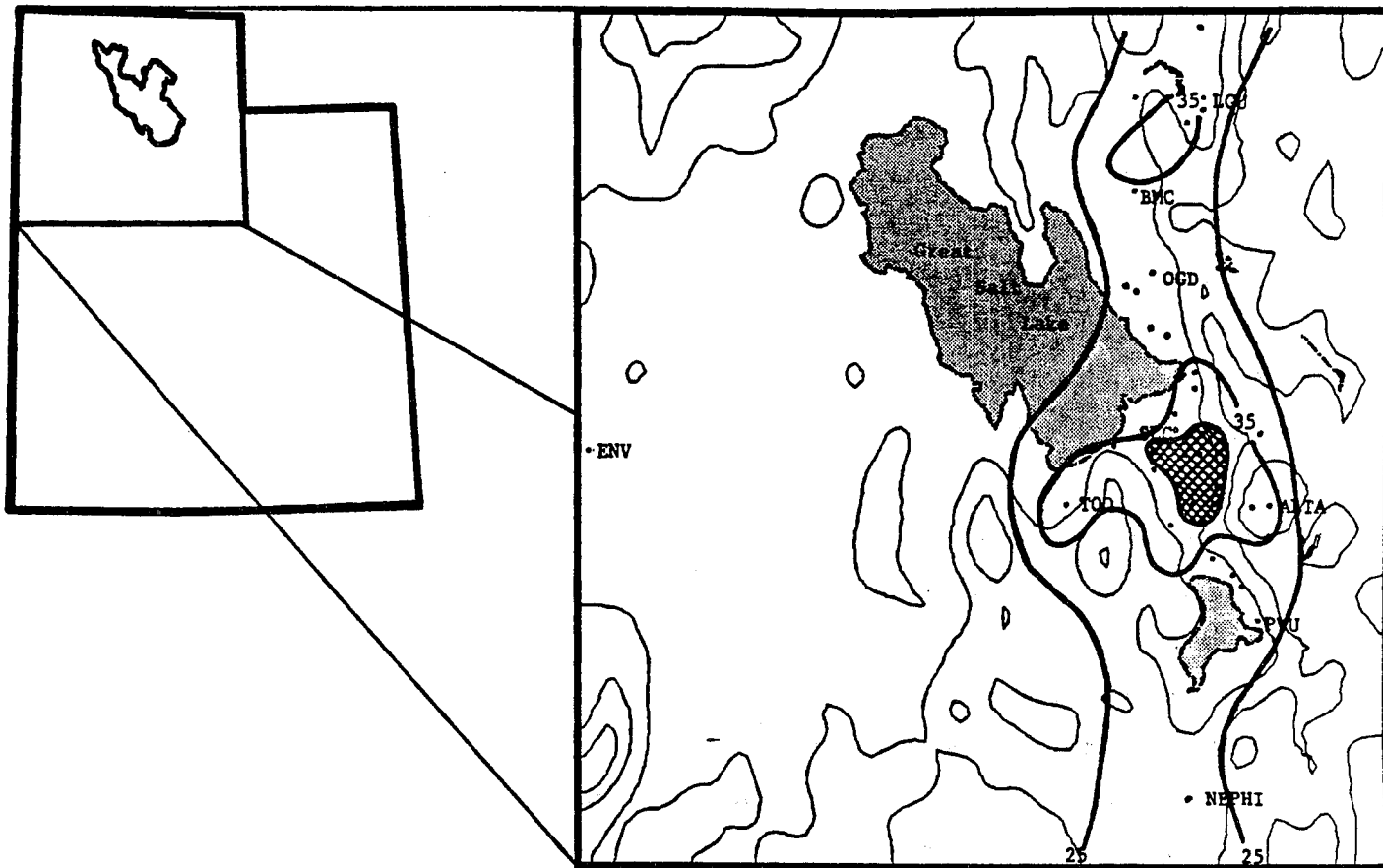
Figure 1. Distribution of heavy 24-hour precipitation over northern
          Utah from 1800 UTC, 25 October, to 1800 UTC, 26 October,
          1989. Precipitation contours in mm with intervals of
          10mm above 25mm. Gridded region $\geq$ 45mm. Elevation
          isopleths (solid, thin) in 500m intervals above 1500m.
          Elevation increases radially from Great Salt Lake.

From a forecaster's perspective, it was not readily apparent from the Nested Grid Model (NGM) output that the greatest vertical motion would be over western Utah on the afternoon of the 25th. A "conventional" estimation of vertical motion using 500 mb positive vorticity advection (PVA) from the 1200 UTC, 25 October, NGM (initial and 12 hour forecast) placed the greatest upward vertical motions over western Arizona/extreme southern Utah (Figs. 2a&b). Vertical motion (omega) at 700 mb from the same NGM cycle did support stronger upward vertical motions over western Utah in the 12 hour forecast (Fig. 3a). However, omega from the 0000 UTC, 26 October, NGM initialized data set placed the strongest upward vertical motions over northwest Arizona (Fig. 3b) even though 700 mb cyclogenesis and heavy convective precipitation were taking place over western Utah.

In this study, the failure of the model to properly locate vertical motion forcing associated with 700 mb cyclogenesis will be examined primarily from an ageostrophic perspective. Subjective analysis of rawinsonde and aircraft data will be compared against corresponding NGM gridded output (both initialized and 12 hour forecasts). Normally, the Salt Lake City Forecast Office uses the 250 mb and 700 mb levels to represent the jet level and lower level of the atmosphere respectively. This convention will be followed in this paper. Discrepancies found between observed/initialized forecast fields will be identified and if relevant, used to explain why the model failed in this storm. In order to document the model's failure to properly forecast the position of the jet, difference fields at 250 mb (0000 UTC, 26 October, initialized fields minus 1200 UTC, 25 October, 12 hour forecasts) for wind (total and ageostrophic) and divergence of the ageostrophic wind were computed along with a difference cross-section of the ageostrophic wind and vertical motion (omega) through the exit region of the jet streak. These computed fields will serve to quantify the model's error in handling the jet streak and the subsequent failure to handle the attending secondary circulation.
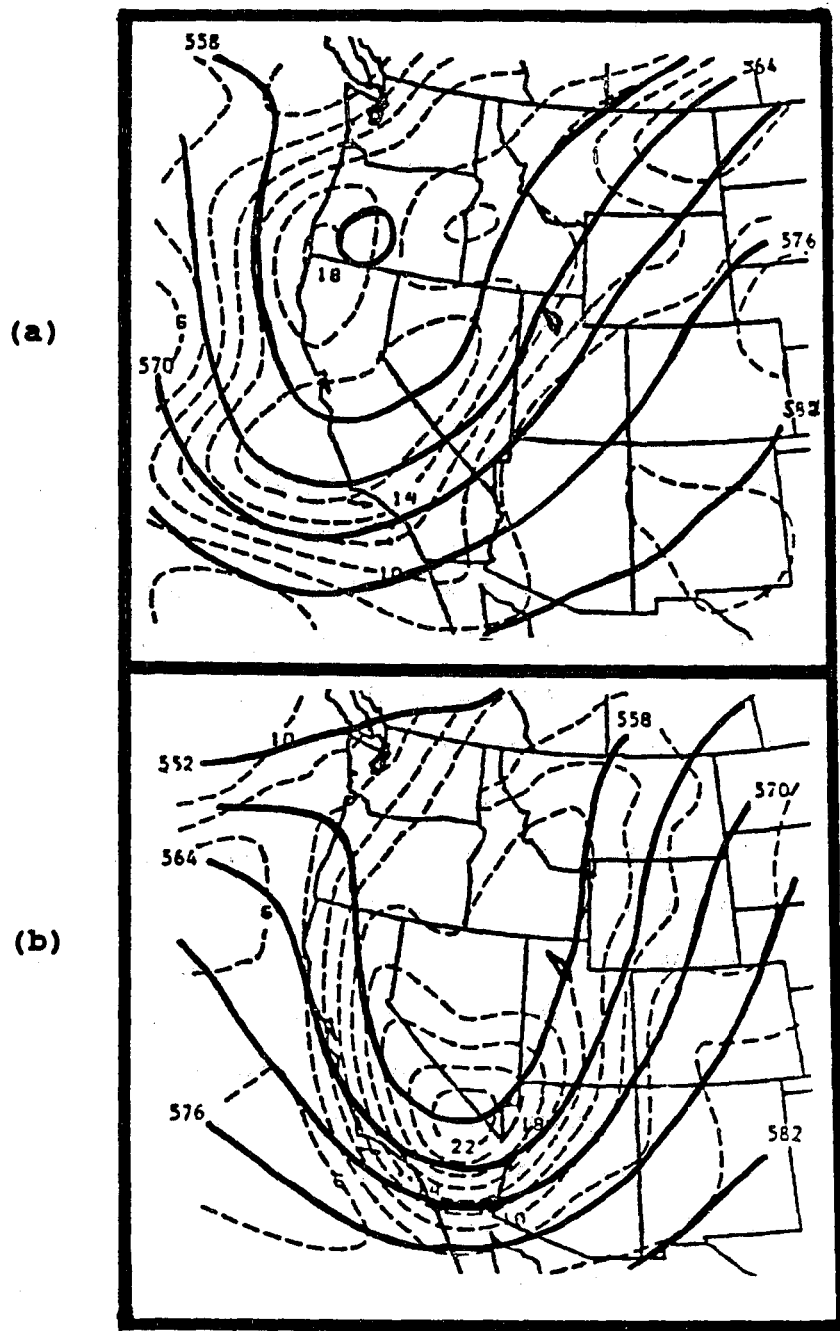
Figure 2. Nested Grid Model (NGM) 500 mb geopotential height
(solid, intervals 6dam) and vorticity (dashed, intervals
2*10**-5/s) for (a) 1200 UTC, 25 October, (initialized),
and (b) 0000 UTC, 26 October, (12 hour forecast valid
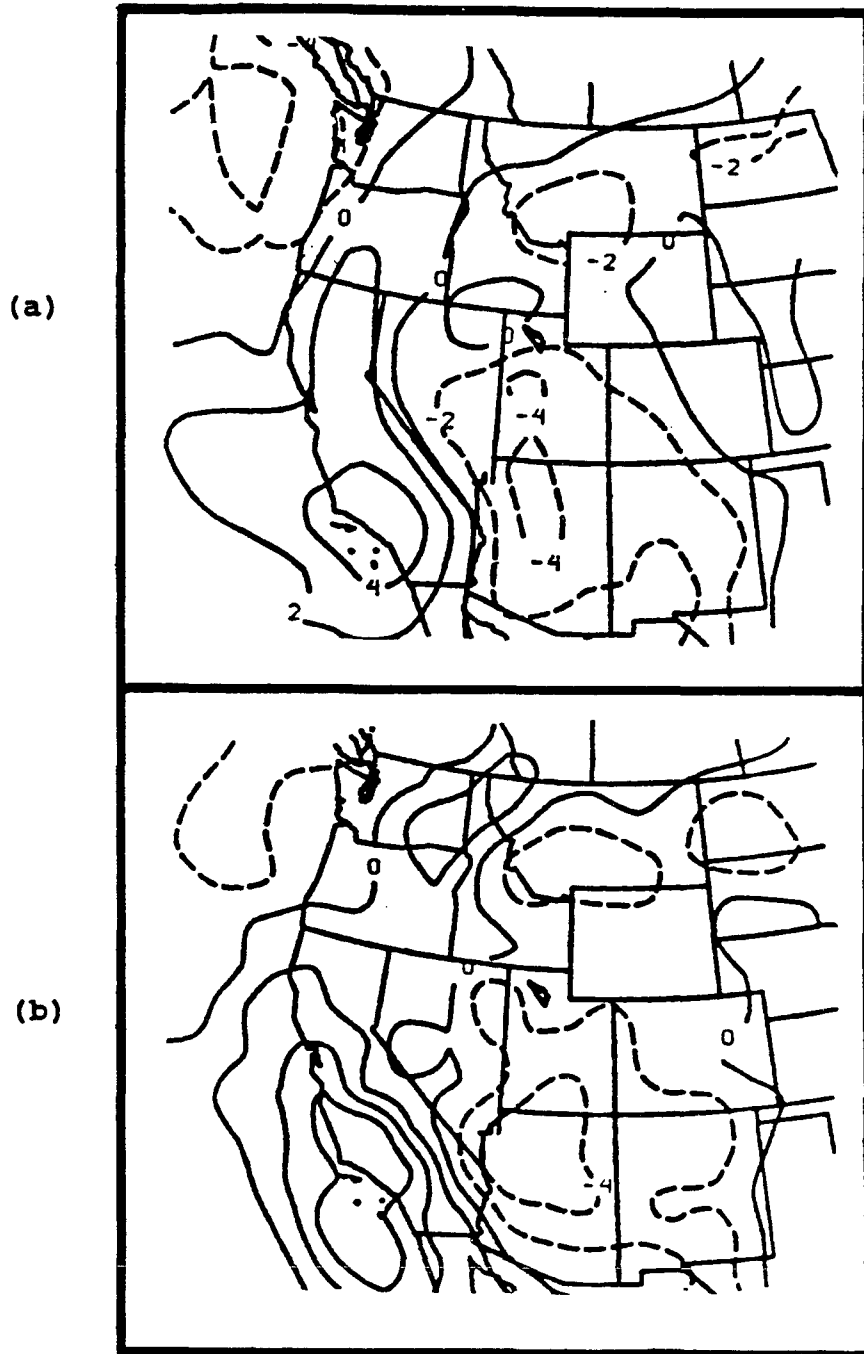0000 UTC).

(a)

(b)

Figure 3. Nested Grid Model (NGM) omega at 700 mb for (a) 1200 UTC, 25 October, (12 hour forecast valid 0000 UTC, 26 October) and (b) 0000 UTC, 26 October, (initialized). Intervals are 2 microbars/s.

Finally, a brief examination of quasi-geostrophic forcing of vertical motion will be performed using two methods; the advection of vorticity by the thermal wind and the Divergence of Q. Here gridded analysis from rawinsonde data generated by a Barnes analysis (Barnes 1964) will be compared against NGM gridded data generated by an Optimum Interpolation (OI) to show which method best relates the area of greatest vertical motion forcing to the area of heaviest precipitation.

2. Comparisons of Subjective Analysis Against Corresponding NGM Gridded Output

In an operational forecast environment, the first step in determining the reliability of the model output is to compare the initialized fields against observed data (rawinsonde, surface observations, satellite imagery, etc..). Here discrepancies in model output can be identified and their impact on the model's forecast assessed.

At 1200 UTC, 25 October, 250 mb isotachs produced through a subjective analysis of rawinsonde/airep data were compared against NGM model output prior to rapid cyclogenesis over western Utah. Both methods showed the jet stream off the southern California coast then arcing northeast into the Great Basin and continuing into southern Canada (Figs. 4a&b). Within the jet stream, two 55+m/s jet streaks were identified in the subjective analysis; one over southern California and the other over northeast Nevada/northwest Utah. In the NGM output, there is a suggestion of these features with core speeds slightly less than those observed.

At 0000 UTC, 26 October, the subjective analysis and NGM model analysis both placed the jet stream from southern California northward into southern Canada (Figs. 5a&b). Two separate jet streaks were analyzed with the one affecting Utah extending from southwest Arizona into northeast Utah/northwest Colorado. As was the case at 1200 UTC, the 0000 UTC NGM initialized wind field (Fig. 5b) failed to capture the maximum observed wind speed from the rawinsonde data (Fig. 5a).
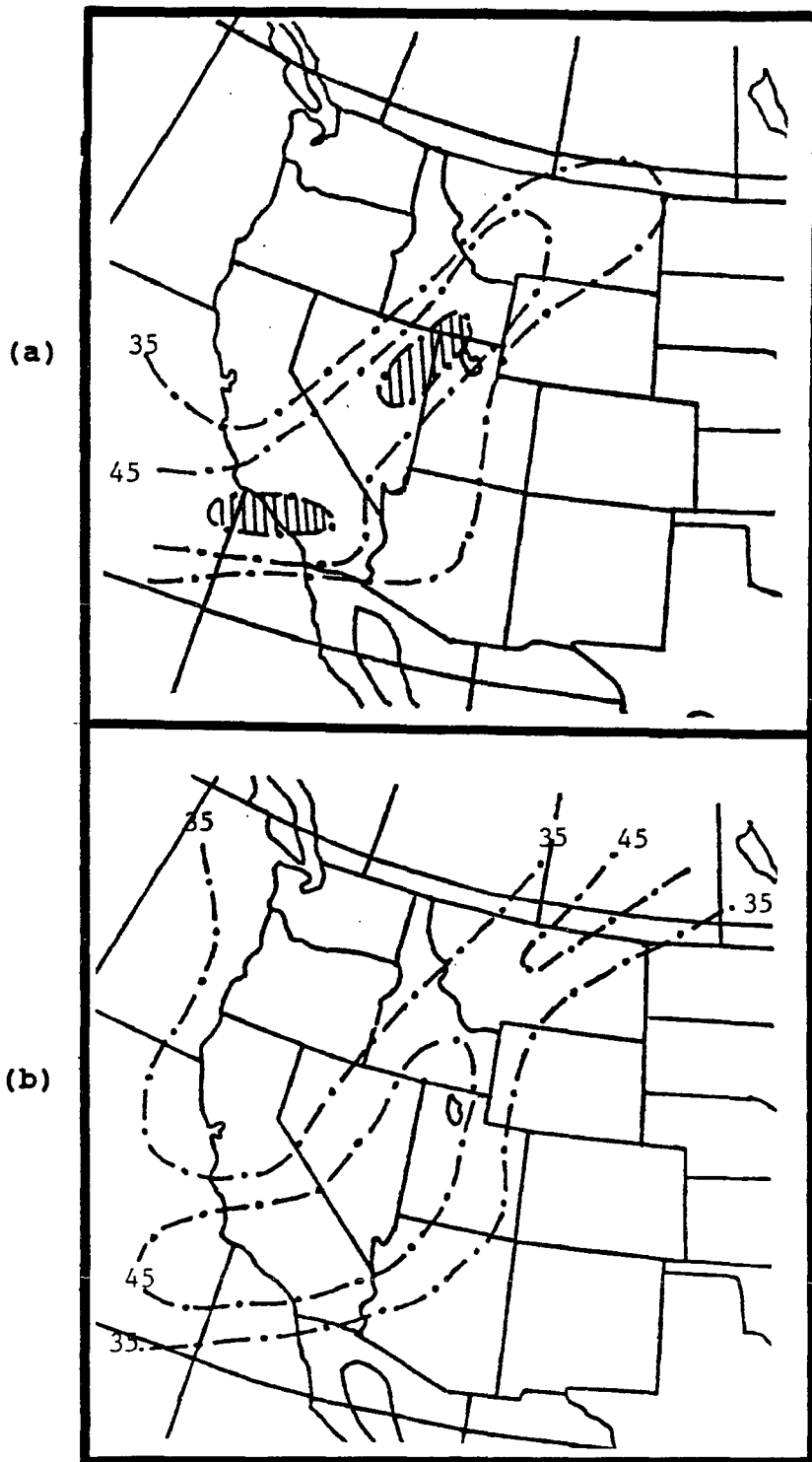
Figure 4. 1200 UTC, 25 October, 250 mb isotachs produced from
(a) subjective analysis of rawinsonde/airep data and
(b) NGM initialized data field. Units are in m/s with
intervals of 10m/s above 35m/s. Dashed areas > 55m/s.

Interestingly, the 12 hour forecast valid at 0000 UTC (Fig. 5c) did forecast winds of 50m/s or greater through eastern Utah, though the core of strongest winds extends much further southwest than the observed wind field indicates.

Though the emphasis of this study is on the jet streak-induced vertical motions, errors found in the 700 mb NGM initialized and 12 hour forecast fields of temperature, geopotential height and wind warrant discussion. Prior to rapid cyclogenesis, temperature errors in the model were only 1-2°C too warm across Nevada (Figs. 6a&b). By 0000 UTC, these errors had increased to as much as 3°C across western Utah/eastern Nevada (Figs. 6c&d). As expected, this problem was not resolved in the 12 hour forecast valid 0000 UTC as temperatures errors approached 4°C too warm over eastern Nevada (Figs. 6e&f).

Subtle, yet important differences were detected in comparisons of the 700 mb geopotential height and wind fields. At 1200 UTC, 25 October, both the subjective analysis and the NGM model output of the geopotential height field show a trough through Nevada (Figs. 7a&c) with a weak circulation center evident in both the rawinsonde and NGM data over extreme northern Nevada (Figs. 7a&b). By 0000 UTC, the subjective analysis placed a closed circulation center over western Utah (Fig. 8). This location was supported by satellite imagery (not shown). Neither the NGM initialized or 12 hour forecast geopotential height fields valid at 0000 UTC could identify this feature over western Utah (Figs. 9a&c). Instead, circulation centers were defined in the wind field much further north over southwest Montana and central Idaho respectively (Figs. 9b&d).

Evidence presented has shown that certain elements of observed wind, temperature and geopotential height differ from those represented in the NGM gridded data fields (both initialized and 12 hour forecast valid the same time). In the next section arguments presented will show from an ageostrophic perspective that though the 12 hour forecast and initialized wind fields valid the same time appear similar, the minor variations between them result in large differences in the amount of ageostrophic forcing each indicates.
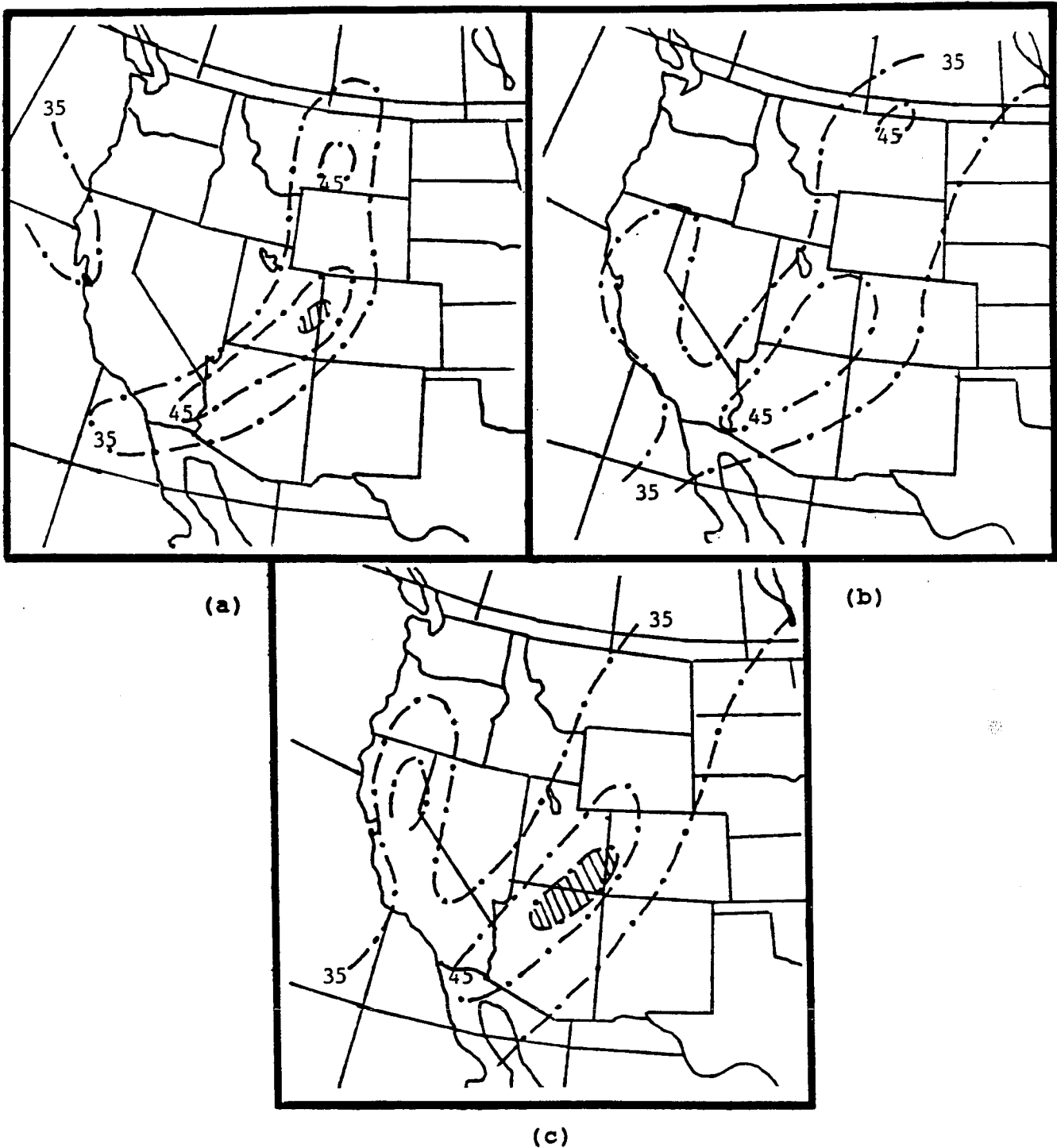
Figure 5. 0000 UTC, 26 October, 250 mb isotachs produced from
(a) subjective analysis of rawinsonde/airep data,
(b) NGM initialized data field, and (c) NGM 12 hour
forecast data field valid 0000 UTC. Intervals are 10m/s
above 35m/s. Dashed areas ($\geq$ 50m/s).
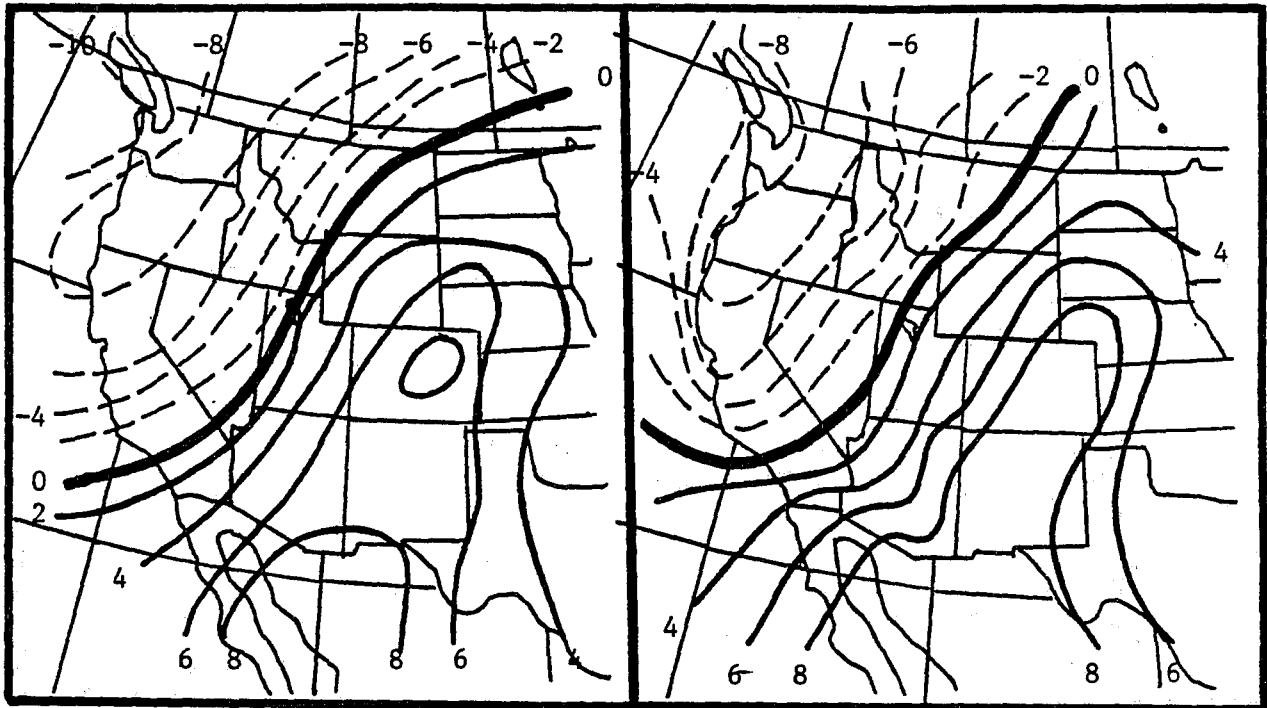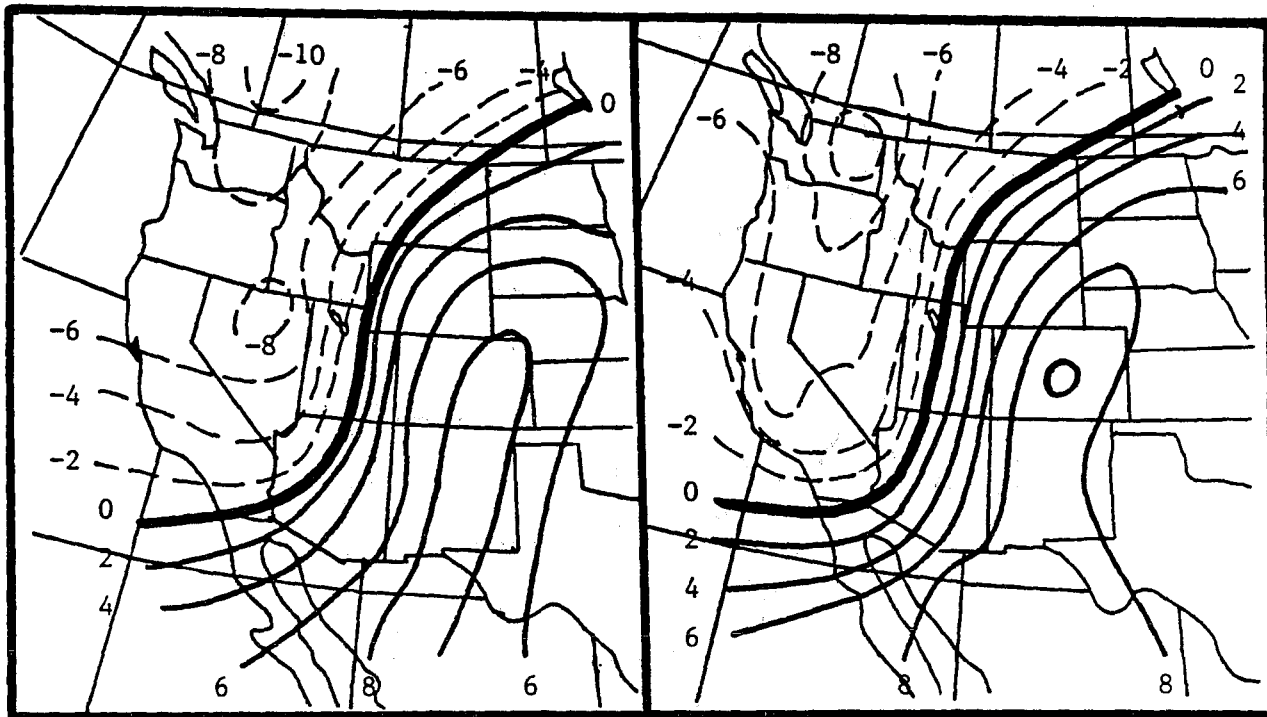
Figure 6. Isotherms (°C) at 700 mb for 1200 UTC, 25 October, from
(a) subjective analysis of rawinsonde data, (b) NGM
initialized data field. Figures (c) & (d) same as (a)
& (b) respectively for 0000 UTC, 26 October.

(e)　　　　　　　　　　　　　　　　(f)
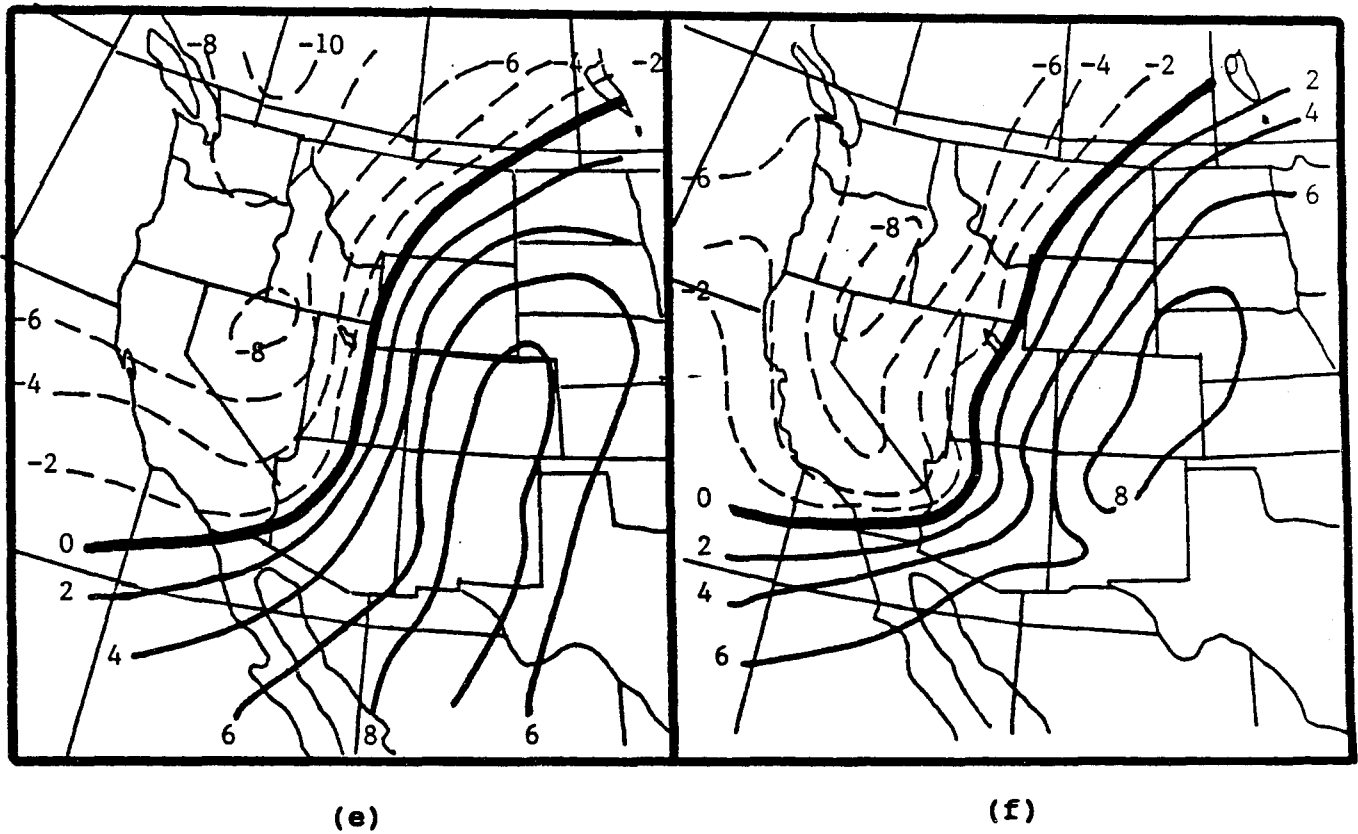
**Figure 6. Isotherms (°C) at 700 mb for 0000 UTC, 26 October, from
(e) subjective analysis of rawinsonde data, (f) NGM
12 hour forecast valid 0000 UTC.**
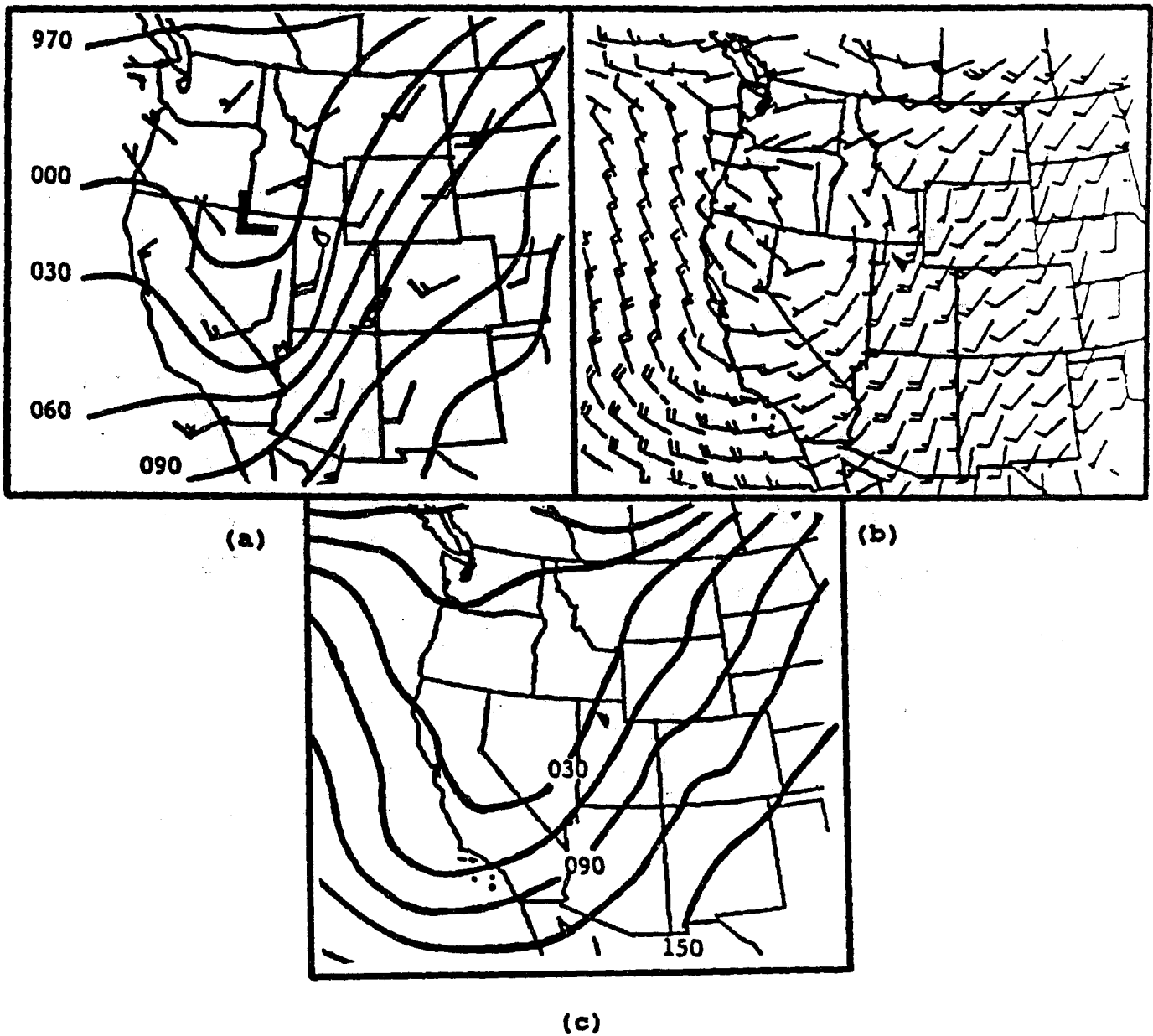
Figure 7. 1200 UTC, 25 October, 700 mb geopotential heights and winds from (a) subjective analysis of rawinsonde data, (b) the NGM initialized wind field and (c) the NGM initialized height field. Height intervals 30m centered on 3000m.
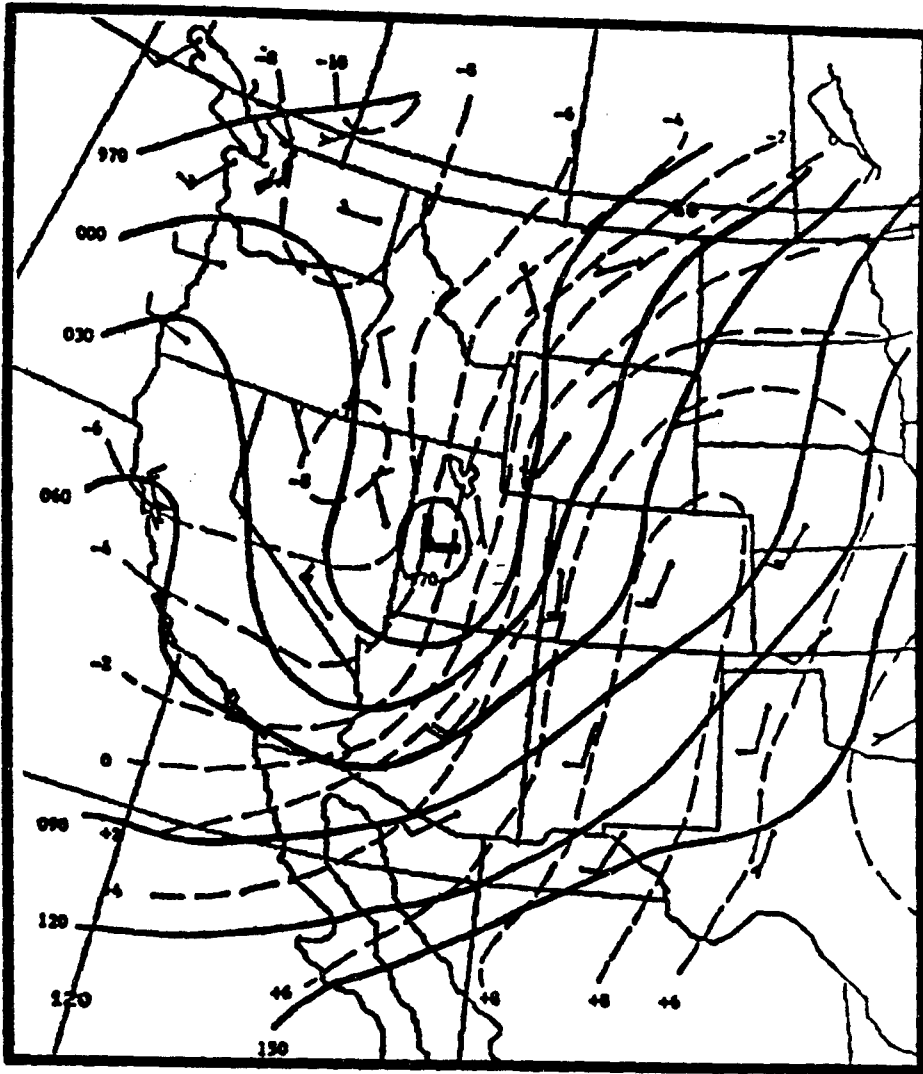
Figure 8. 0000 UTC, October 26, 700 mb subjective analysis of geopotential height (solid), temperature (dashed, °C), and wind (barbs). Height intervals 30m centered on 3000m.
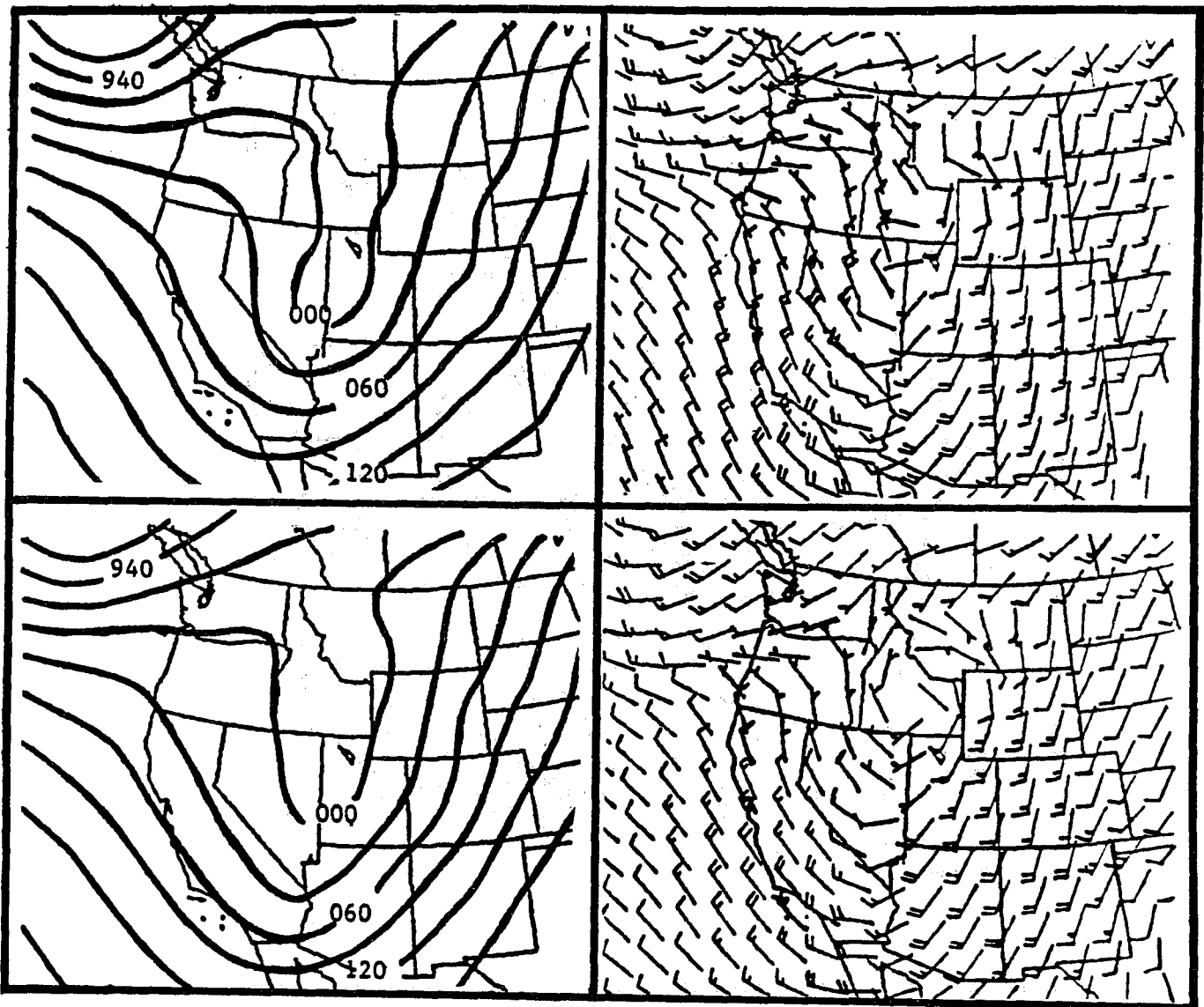
(a)/(c)   (b)/(d)

Figure 9. 700 mb NGM data fields valid 0000 UTC, 26 October, for
(a) geopotential height, (b) corresponding wind field,
and 1200 UTC, 25 October, 12 hour forecast valid 0000 UTC
for (c) geopotential height, (d) corresponding wind
field. Height intervals 30m centered on 3000m.

3. NGM Model Forecast Error in Handling the Jet Streak: An Ageostrophic Perspective

According to **Bjerkes** (1951), **Uccellini** and **Johnson** (1979), and others, a jet streak with little or no curvature at the entrance region has a transverse ageostrophic component directed toward the cyclonic-shear (left-rear) side of the jet. Conversely, at the exit region the ageostrophic component is directed toward the anticyclonic-shear (right-front) side of the jet (Fig. 10). At the entrance region, this ageostrophic component represents the upper branch of the direct circulation. This circulation is marked by rising (sinking) motion on the anticyclonic or warm (cyclonic or cold) side of the jet. At the exit region this component represents the upper branch of the indirect circulation with the rising (sinking) motion on the cyclonic or cold (anticyclonic or warm) side of the jet.

With the 250 mb trough just upstream from the jet streak, strong curvature exists at the entrance region of the jet streak. A study by **Cammas** and **Ramond** (1989) demonstrated that the effects of curvature can be predominant to the point that the direct circulation is masked in the upper tropospheric divergence field. In this storm, the greatest development occurred in the exit region of the jet where curvature effects were minimal. It will be shown later that an indirect circulation does exist at the exit region of the jet streak in this case similar to what is defined in the straight-line jet streak model.

To quantify the NGM model's failure to identify the jet streak, difference fields at 250 mb (0000 UTC initialized field minus the 12 hour forecast field valid at 0000 UTC) for the total and ageostrophic winds were computed. The isotachs of the total wind for the initialized and 12 hour forecast fields (Figs. 11a&b respectively) valid 0000 UTC appear quite similar. The only notable differences are slightly higher jet core wind speeds and more elongation of the jet core in the 12 hour forecast. The magnitude of the difference (Fig. 11c) was quite small with the initialized values ranging from 1-4m/s slower than the 12 hour forecast across northern Arizona, Utah and western Colorado. Though the magnitude of the differences were small, they did produce significant
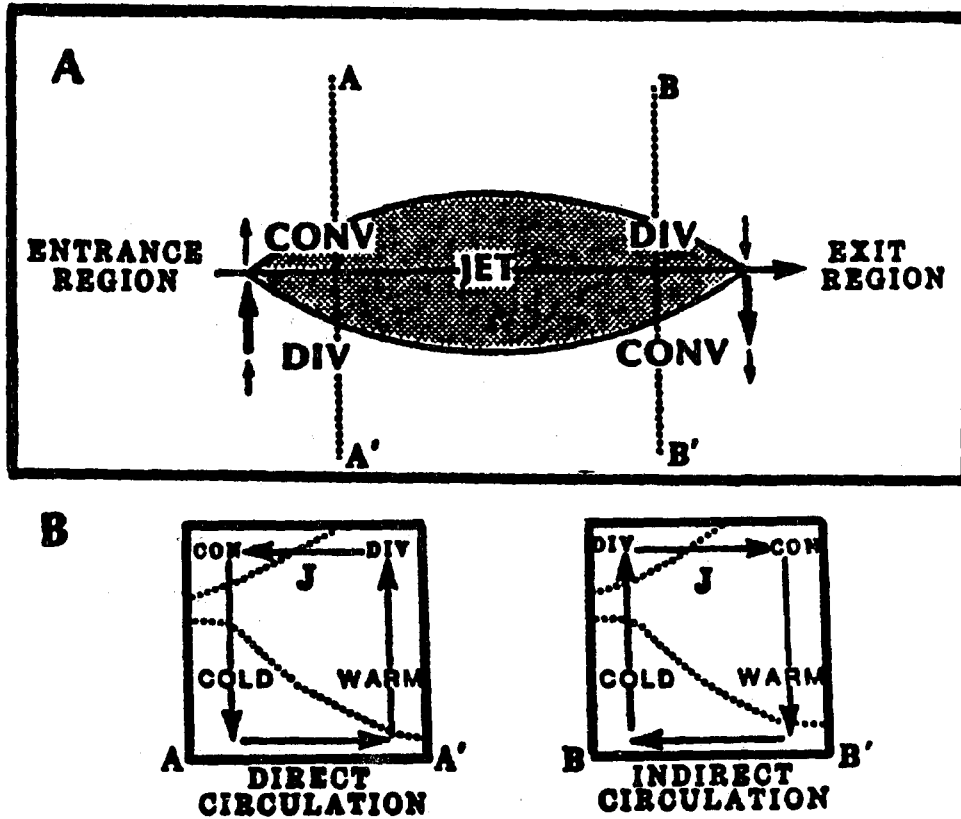
Figure 10. (a) Schematic of transverse ageostrophic wind
components and patterns of divergence associated with
the entrance and exit regions of a straight jet streak
(after Bjerknes (1951)). (b) Vertical cross sections
illustrating direct and indirect circulations in the
entrance region (along line A-A') and exit region
(along line B-B') of a jet streak.

Figure 11. NGM 250 mb isotachs for (a) 0000 UTC, 26 October, initialized field, (b) 12 hour forecast field from 1200 UTC, 25 October, valid 0000 UTC. (c) Difference field of the total wind (0000 UTC initialized field minus 12 hour forecast valid at 0000 UTC). Units are m/s with intervals in a&b 5m/s beginning at 35m/s. Dashed region $\geq$ 50m/s.

differences in the ageostrophic wind field. Comparisons of the initialized and 12 hour forecast fields of the ageostrophic wind (Figs. 12a&b respectively) both show the strongest ageostrophic winds through the base of the trough at the entrance region of the jet. The core of the strongest ageostrophic winds extends further north and east in the initialized field. Also, within the exit region of the jet, the magnitudes are stronger than in the 12 hour forecast.

Examination of the difference field for the ageostrophic wind illustrates these differences quite well. Underforecasting of the magnitude approaches 7m/s near the entrance region of the jet, while at the exit region it approaches 10m/s (Fig. 12c). When the ageostrophic wind is broken down into it's longitudinal and transverse components (Figs. 13a&b), the difference in the total ageostrophic wind at the entrance region of the jet appears to result from a stronger longitudinal component in the initial analysis. At the exit region of the jet, the transverse component in the initial analysis appears stronger than in the 12 hour forecast through western Colorado.

The seemingly minor differences in the total wind speed within the jet stream were demonstrated to have a serious impact on the total (longitudinal and transverse) ageostrophic motion which in turn affects the convergence/divergence pattern associated with jet dynamics. Further evidence of this impact can be gathered by examining the divergence of the ageostrophic wind. On a constant pressure surface, the ageostrophic divergence is expressed as:

$$\nabla_p \cdot V_a = \nabla_p \cdot V - \nabla_p \cdot V_g$$

Through scaling arguments, both the ageostrophic divergence and total divergence maximum are approximately an order of magnitude higher than the geostrophic divergence maximum. Therefore, the divergence of the ageostrophic wind can be used to interpret the divergence/convergence maximum of the total wind field by neglecting the lesser ordered first approximation of the

(a)

(b)

(c)
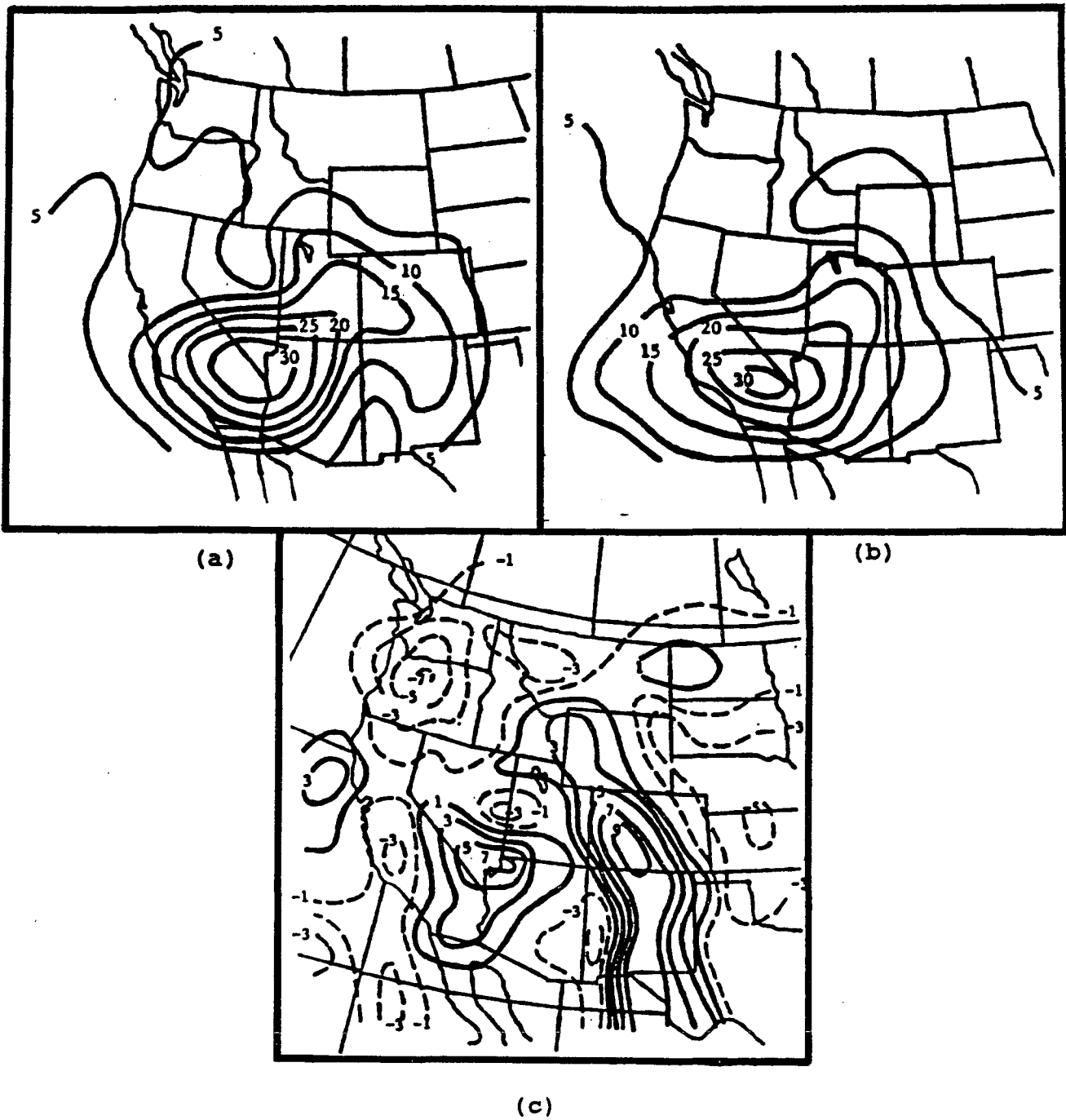
Figure 12. NGM 250 mb ageostrophic wind fields for   (a) 0000 UTC,
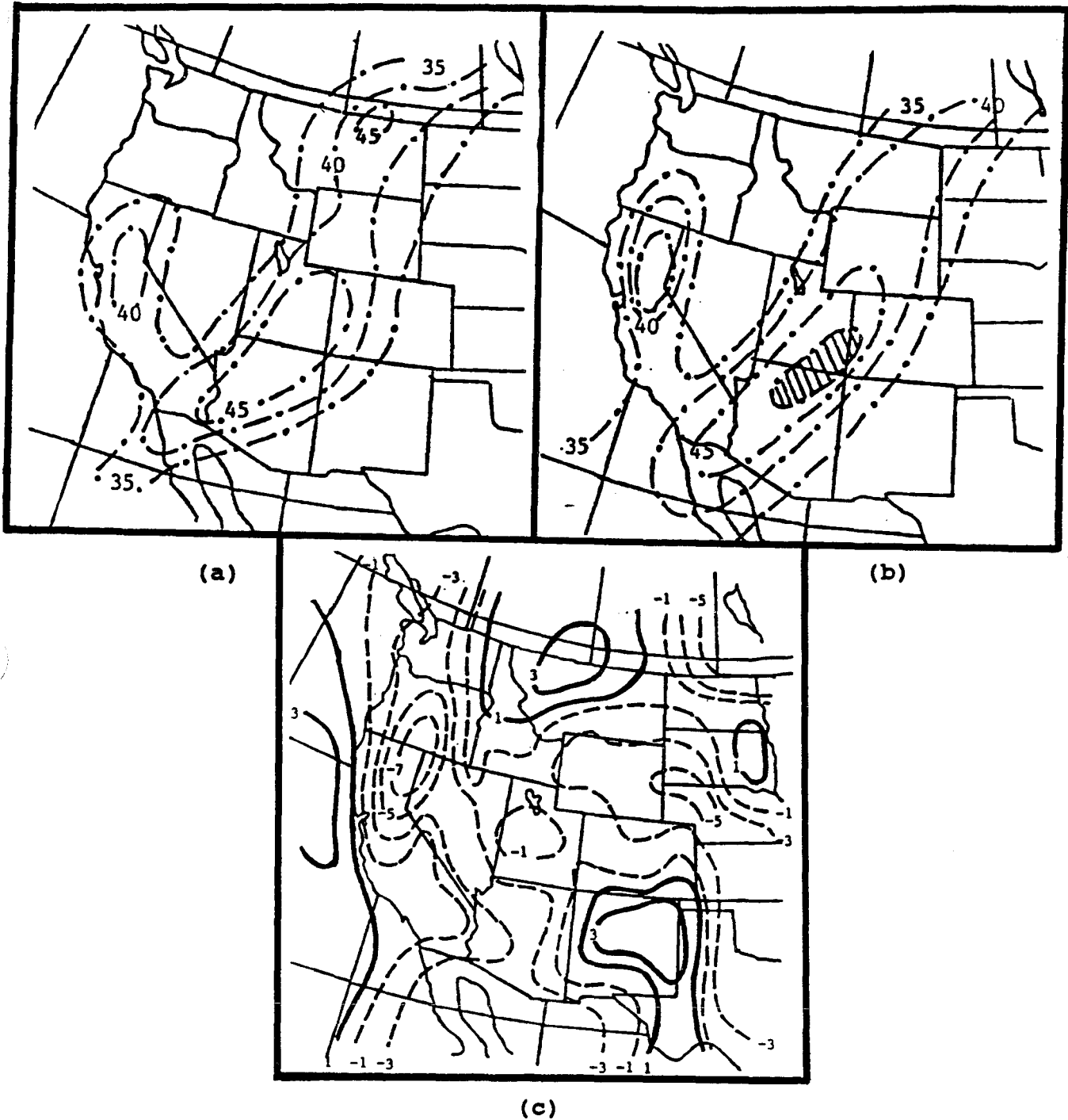26 October, initialized field,   (b) 12 hour forecast
field from 1200 UTC, 25 October, valid 0000 UTC.
(c) Difference field of the ageostrophic wind (0000 UTC
initialized field minus 12 hour forecast valid at 0000
UTC).   Units are m/s with intervals in a&b 5m/s.

(a)   **(b)**
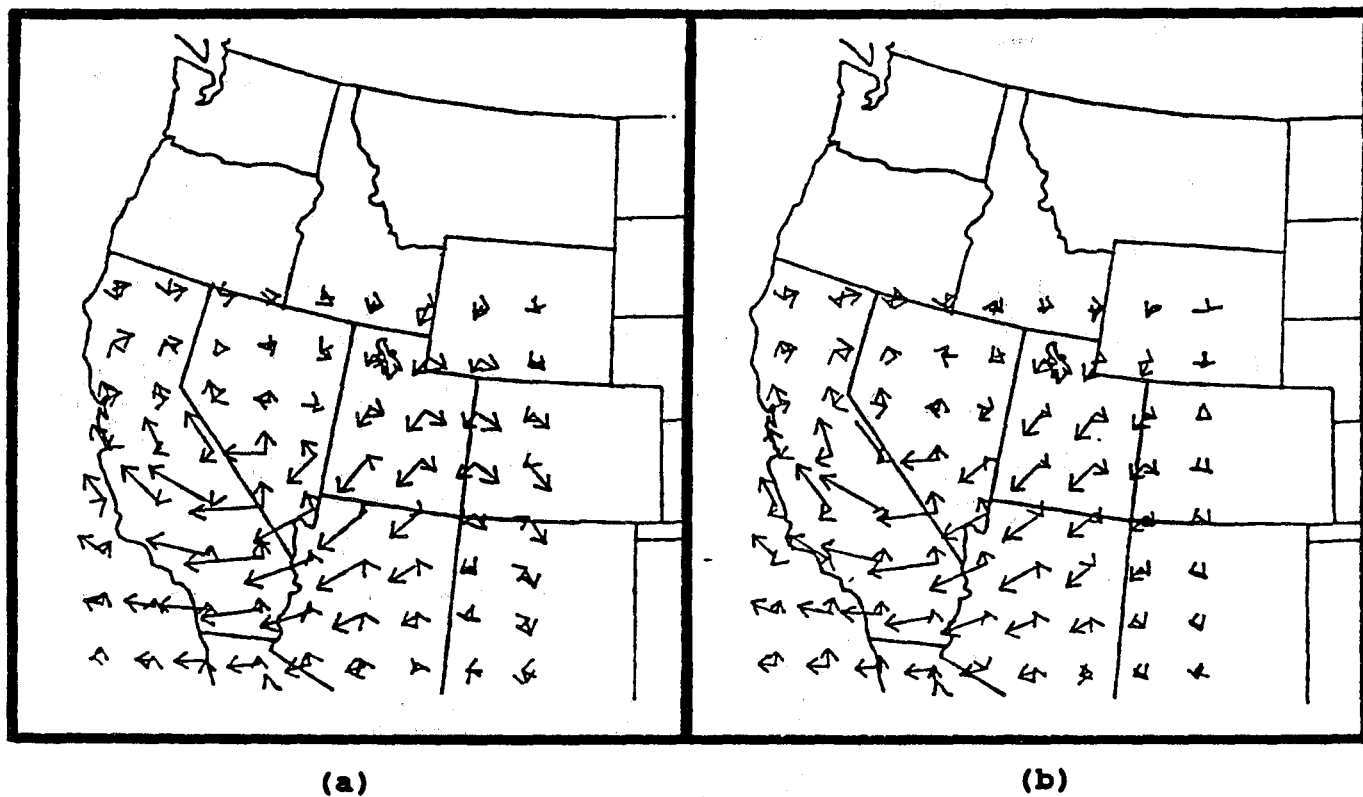
Figure 13. Longitudinal and transverse components of the total
ageostrophic wind from   (a)   0000 UTC, 26 October,
initialized data,   (b)   1200 UTC, 25 October, 12 hour
forecast valid 0000 UTC, 26 October.

geostrophic divergence. In this case, the maximum divergence of the ageostrophic wind from the initialized data was centered over southern Utah (Fig. 14a) while in the 12 hour forecast (Fig. 14b) a weaker divergence maximum was placed over northwest Arizona. The resultant difference field has a stronger than forecast divergence maximum on the order of 1-2x10**-5/s located near the exit region of the jet (Fig. 14c).

Evidence presented so far has shown in a two-dimensional sense how the transverse circulations were affected by errors in the model forecast of the total wind. However, indirect (and direct) circulations are a consequence of three-dimensional variations in the ageostrophic wind and upper-level divergence that a two-dimensional straight-line jet streak does not adequately explain (Uccellini et. al., 1984, Keyser and Shapiro, 1986, and others).

To illustrate this point and to show how the model failed to handle the indirect circulation, cross-sections of the ageostrophic wind and omega were computed through the exit region of the jet streak. In both the initialized and 12 hour forecast valid at 0000 UTC (Figs. 15a&b respectively), the indirect transverse circulation is definable. A subjective comparison of the two circulations shows that the upward branch of the circulation in the initial analysis appears stronger and further east than in the 12 hour forecast. A difference cross-section (Fig. 15c) confirms that the initial analysis does in fact have the stronger circulation.

The NGM model's failure to properly identify the jet streak has led to considerable underdevelopment of the three-dimensional vertical circulation associated with the exit region of the jet streak. The extent that this underforecasting affected precipitation over northern Utah is not quantitatively definable in this case. However, when viewed from a strictly upper tropospheric dynamics perspective, the vertical motion indicated in the 12 hour forecast was probably not strong enough to support the deep convection observed early in the

(a)

(b)

(c)
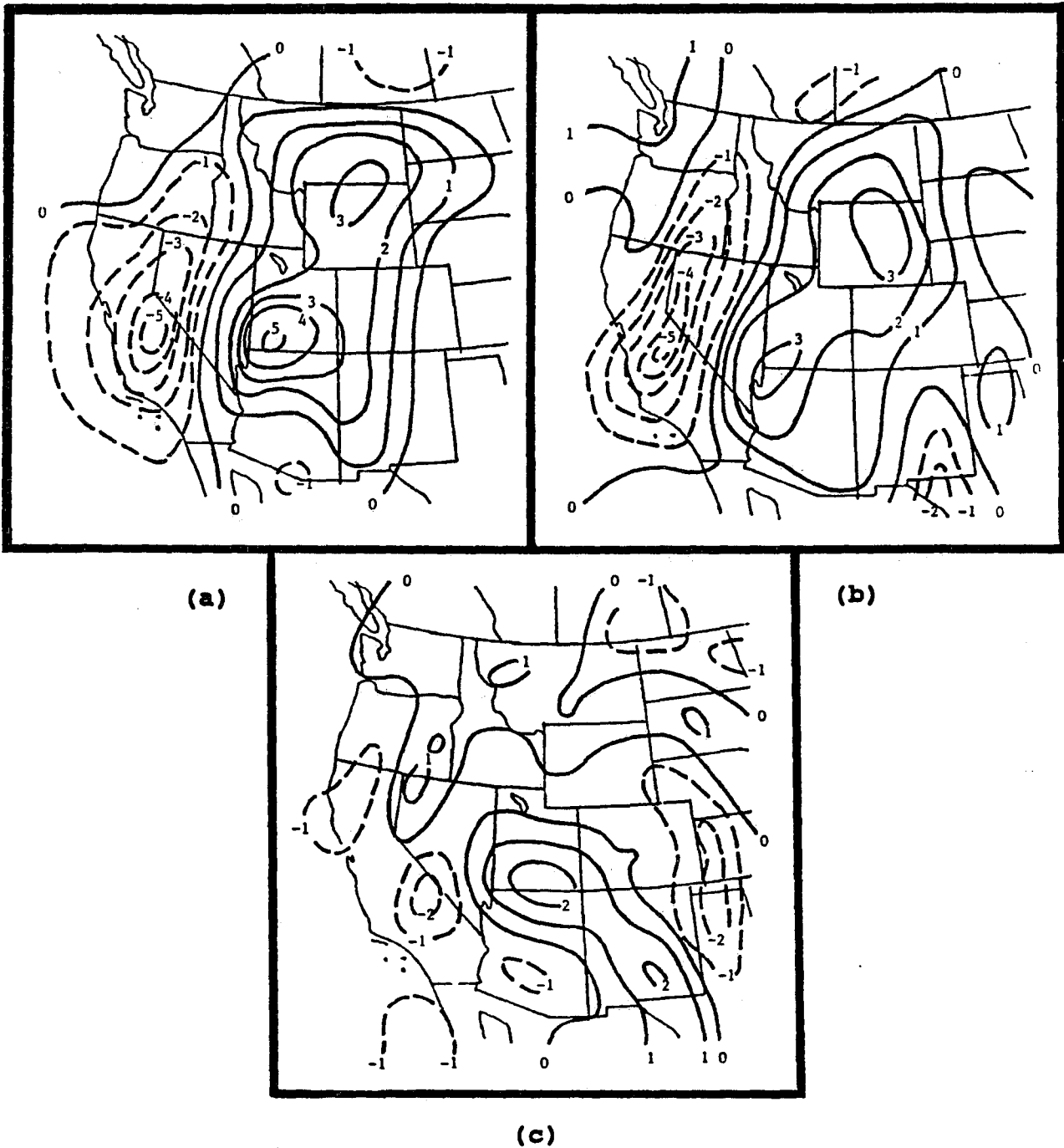
Figure 14. Divergence of the ageostrophic wind for the (a) 0000
UTC, 26 October, initialized data, (b) 1200 UTC, 25
October, 12 hour forecast data valid 0000 UTC. (c)
Divergence of the difference of the ageostrophic wind
(divergence of the 0000 UTC initialized ageostrophic
wind minus the 12 hour forecast valid at 0000 UTC).
Intervals are 10**-5/s.
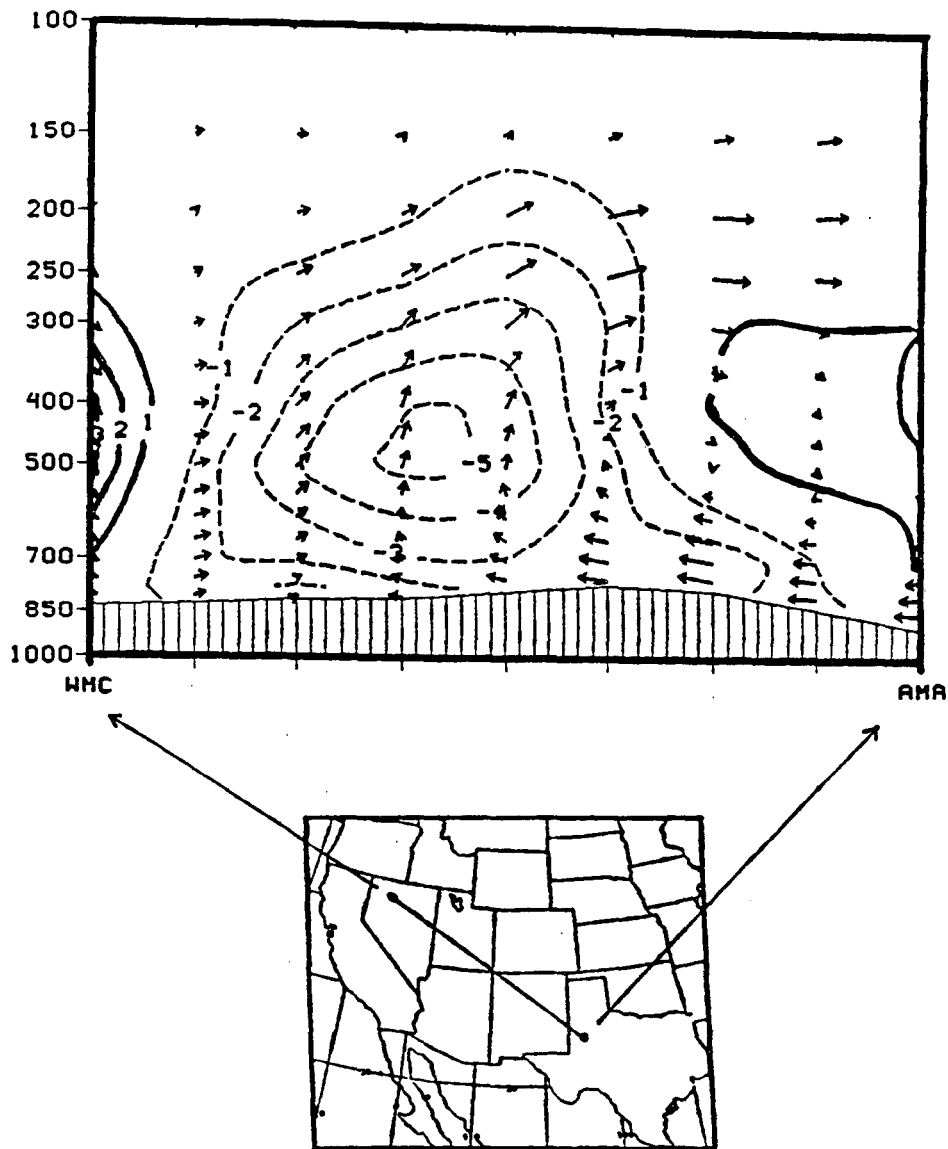
(a)

Figure 15. Ageostrophic wind (arrows) and omega (dashed/solid)
parallel to the plane of the cross-section at 0000 UTC,
26 October, for (a) the initialized field, (b) the 12
hour forecast field valid at 0000 UTC. (c) Difference
field of the ageostrophic wind and omega (initialized
minus previous 12 hour forecast valid 0000 UTC).
Intervals of omega are microbars/s.
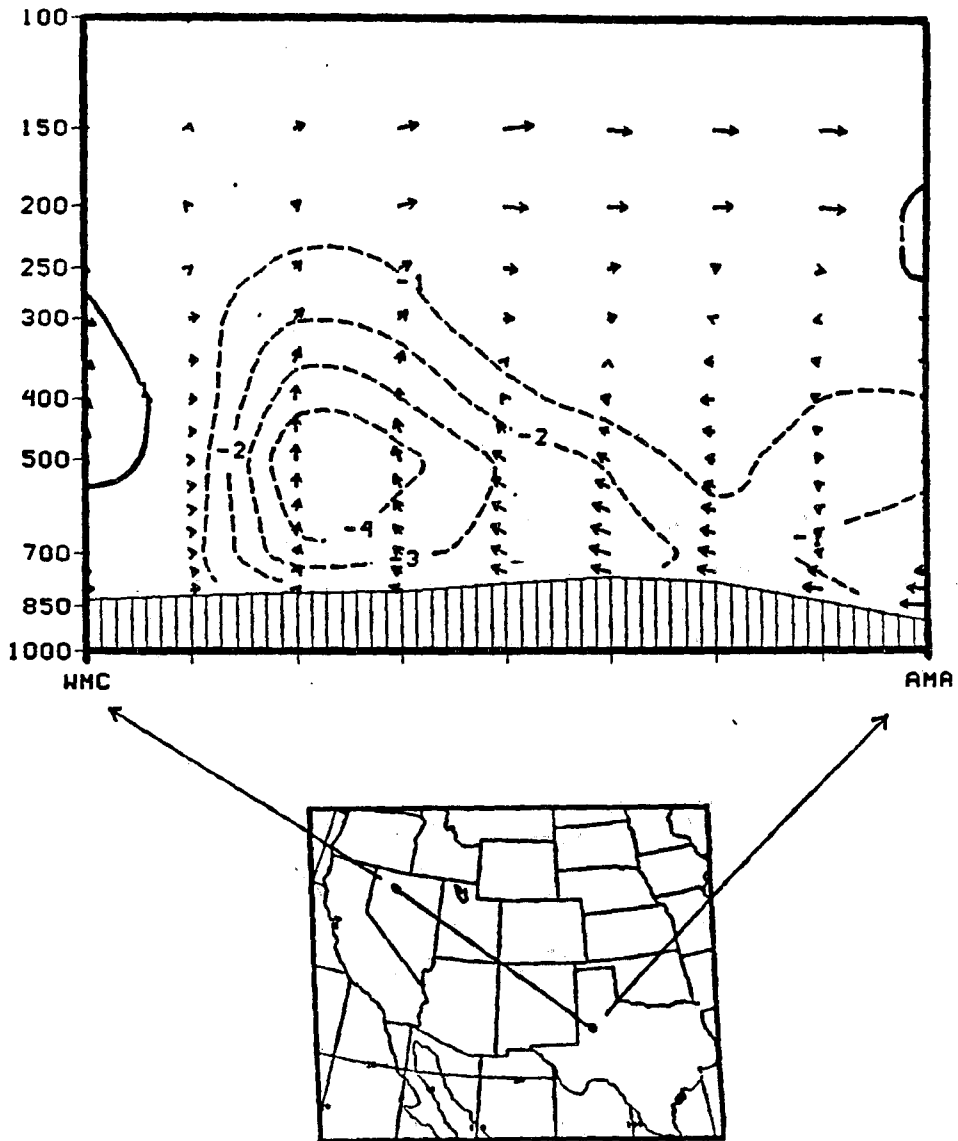
Figure 15b
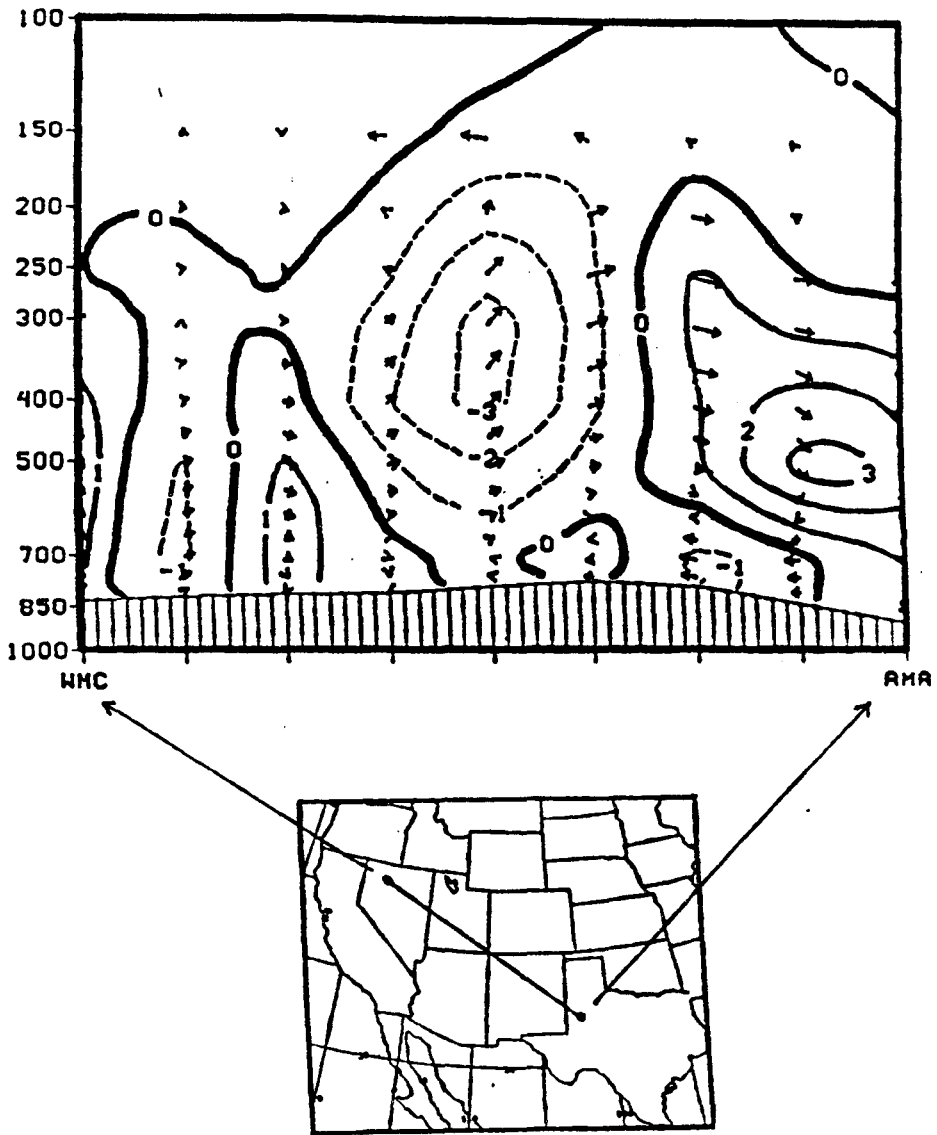
Figure 15c

storm across western Utah (this neglecting the diabatic effects that may have played heavily at this point to enhance vertical motions induced by the jet-streak).

4. Quasi-geostrophic Vertical Motion Forcing

Vertical motion forcing from a quasi-geostrophic (QG) perspective can be estimated through many different means. Two different methods; vorticity advection by the thermal wind (**Trenberth** 1978) and Q-vectors (**Barnes** 1985,1986) were used in this study. Both methods are derived from the right hand side of the quasi-geostrophic omega equation (differential vertical vorticity advection (DVVA) plus the two-dimensional Laplacian of temperature advection. As demonstrated by **Trenberth**, the right hand-side of the omega equation is dominated by the advection of vorticity by the thermal wind. Thus, synoptic-scale ascent should occur in the area where there is advection of cyclonic vorticity by the thermal wind. This is not a complete representation of QG omega equation, but is still a good estimate of vertical motion forcing within the middle layers (600-400 mb) of the atmosphere. The Q-vector as suggested by **Hoskin et al** (1978) is defined as being equal to the rate of change of the horizontal potential temperature gradient when following a parcel. In the Q-vector formulation of the diagnostic omega equation, the divergence of Q is proportional to omega and will be examined in this study.

The gridded analysis from rawinsonde data generated by a Barnes analysis will be compared against the NGM gridded analysis generated by an Optimum Interpolation (OI) to determine subjectively which method best defined the area of heaviest precipitation. Comparisons will be made around the time of heaviest convective activity (0000 UTC).

Beginning with the **Trenberth** method, a thickness layer between 700-300 mb with vorticity at 500 mb was used to represent the middle layers of the atmosphere. Both analysis indicated strong vertical motion forcing over southern

Nevada extending northeastward into western Utah (Figs. 16a&b). The divergence of Q beginning at 700 mb shows both analysis placing the strongest vertical motion over northwest Utah (Figs. 17a&b). This placement appears proper when viewed in terms of 700 mb cyclogenesis and distribution of heavy precipitation. When viewed at 500 mb, the areas of strongest vertical motion differ noticeably between the two gridded data sets. From the gridded data generated from rawinsonde data (Fig 18a), the strongest vertical motion is over western Utah in close proximity to the heavy precipitation. From the NGM gridded data, the strongest vertical motion is placed well south over western Arizona (Fig 18b).

The reason for this discrepancy cannot be determined with any certainty, as output for DVVA is not produced for the rawinsonde gridded data set. Output of the two-dimensional Laplacian of temperature advection was available from both gridded data sets. Warm advection patterns computed from both data sets were found to closely align with their respective maximum upward vertical motions as indicated from the divergence of Q (Figs. 19a&b). This could suggest a much stronger contribution from this term than from the DVVA term in explaining upward vertical motion and would explain to some extent the difference in the two outputs. Again however, any explanation of the differences in the two outputs would be speculative as the relative contribution of the DVVA term in the computation of the divergence of Q is not known.

5. Summary

The rapid intensification of this late October storm implies that stronger vertical motion forcing existed than was indicated by the NGM model output. A conventional examination of vertical motion forcing using 500 mb pattern recognition placed the strongest vertical motions well south of where it was observed over western Utah.

An examination of vertical motion forcing from a strictly ageostrophic perspective was done using both observed data and NGM gridded data fields as
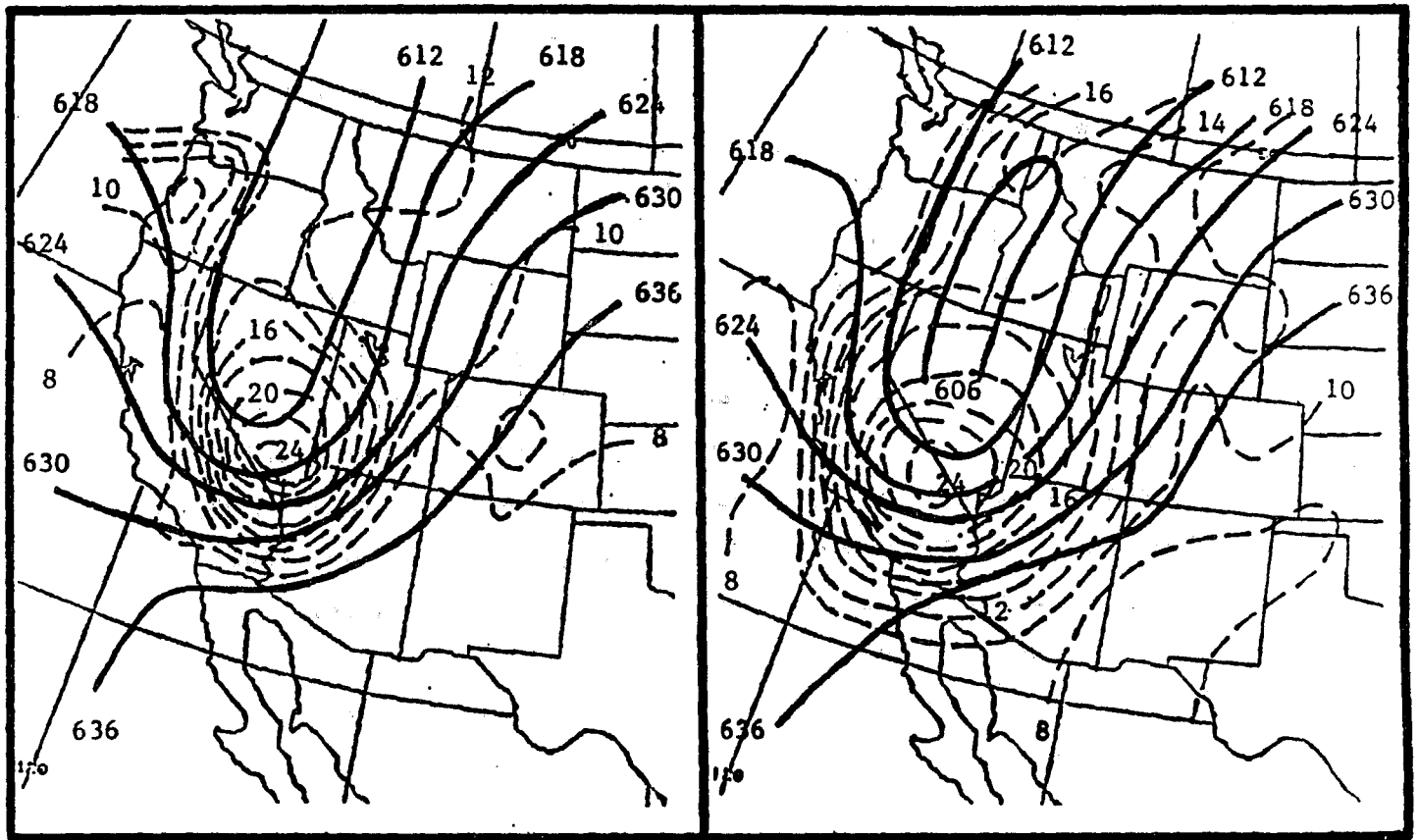
(a)   (b)

Figure 16. Advection of 500 mb vorticity by the thermal wind
           between 700-300 mb at 0000 UTC using (a) a Barnes
           analysis to generate gridded data fields from rawinsonde
           data, and (b) an Optimum Interpolation (OI) to generate
           gridded NGM data fields. Solid lines are 700-300 mb
           thickness (intervals 6 dam) and dashed lines vorticity
           (intervals 2*10**-5/s).
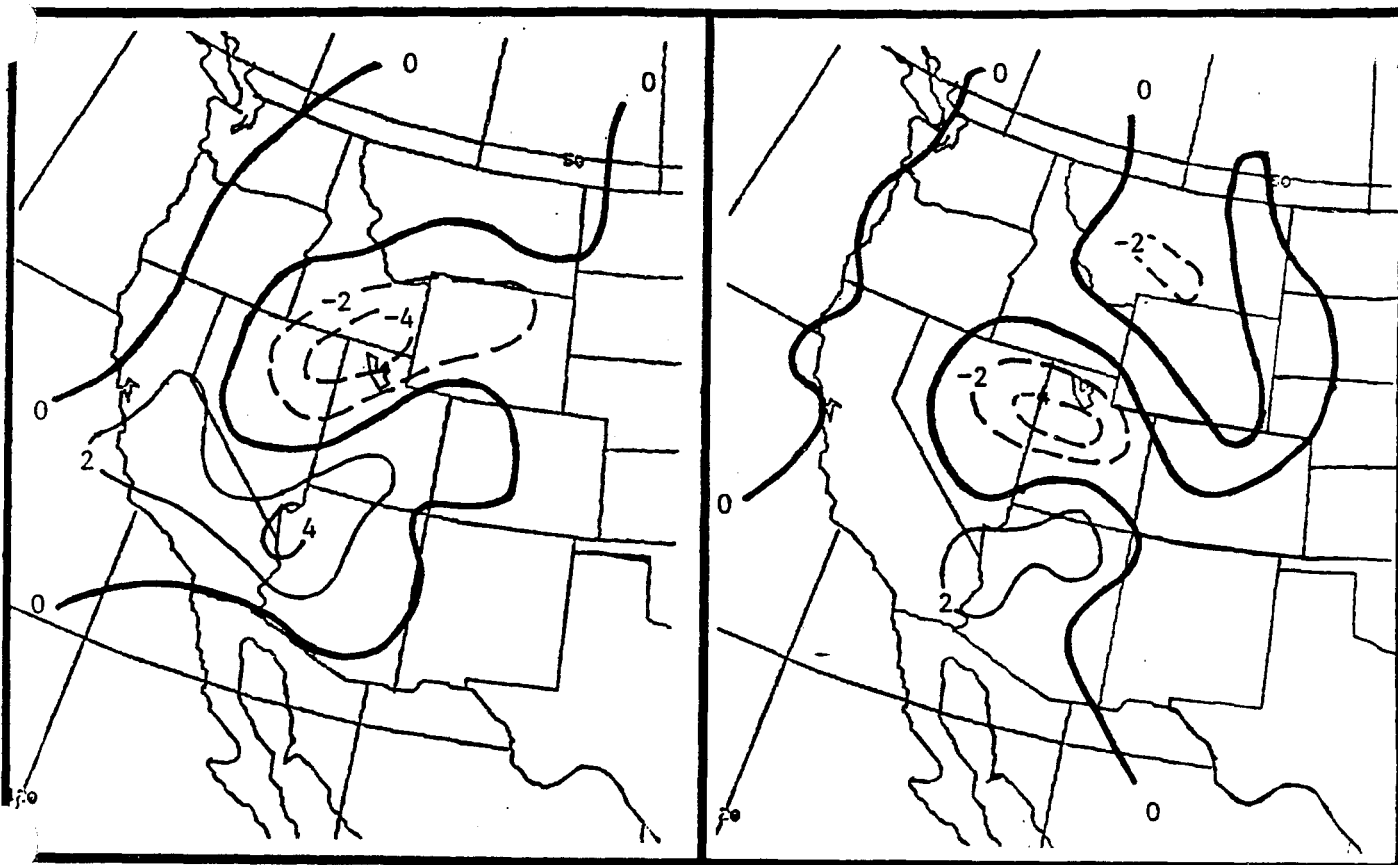
(a)   **(b)**

Figure 17. Divergence of Q at 0000 UTC, 26 October, for 700 mb
using (a) a Barnes analysis to generate gridded data
fields from rawinsonde data, (b) Optimum Interpolation
(OI) to generate gridded NGM data fields. Negative
values represent areas of upward vertical motion.
Intervals are 2*10**-17/s**3 mb.
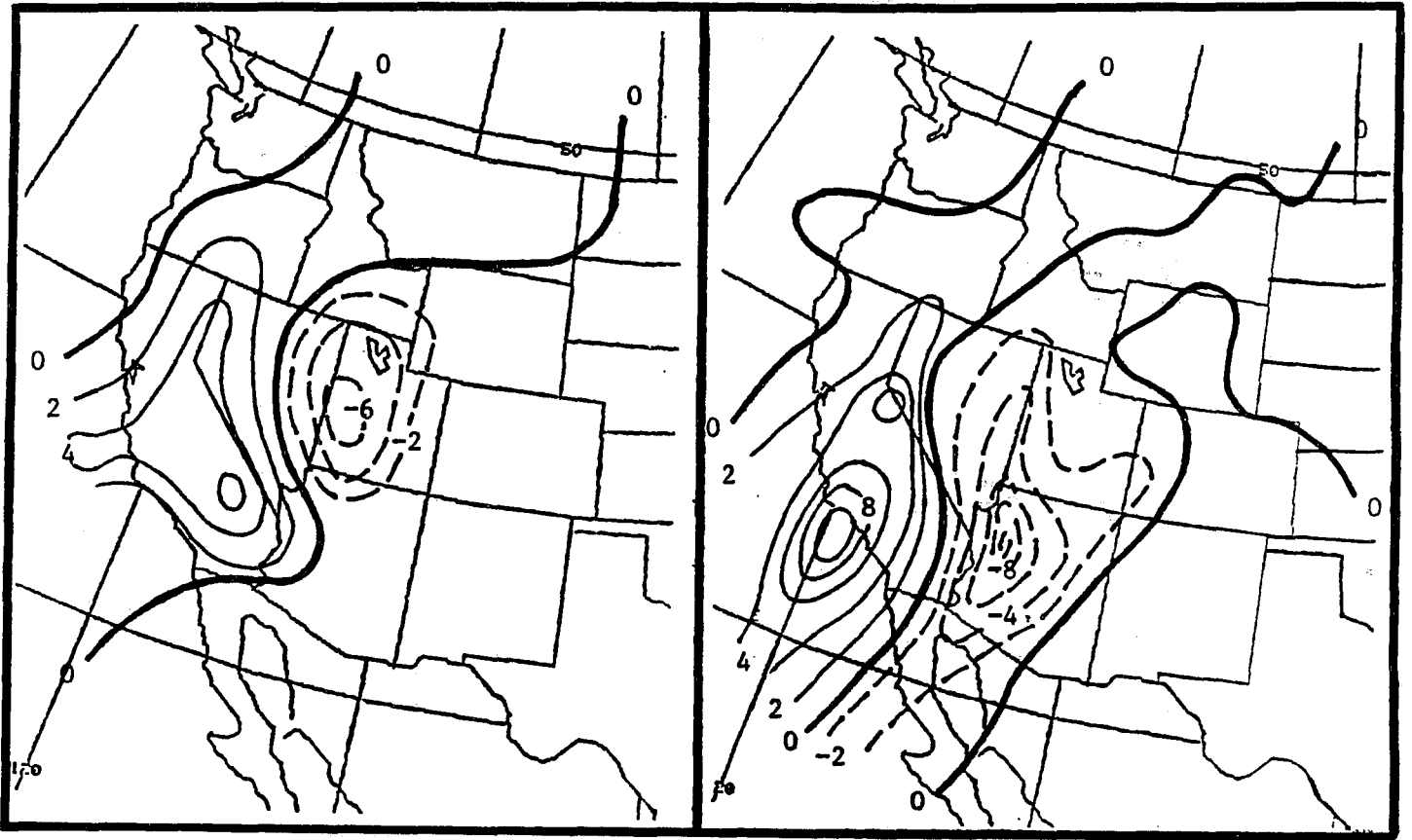
(a)   (b)

Figure 18. Divergence of Q at 0000 UTC, 26 October, for 500 mb
            using (a) a Barnes analysis to generate gridded data
            fields from rawinsonde data, (b) Optimum Interpolation
            (OI) to generate gridded NGM data fields. Negative
            values represent areas of upward vertical motion.
            Intervals are 2*10**-17/s**3 mb.

(a)

(b)

Figure 19. Two-dimensional Laplacian of temperature advection for 0000 UTC, 26 October, computed from (a) gridded data generated from rawinsonde data using a Barnes analysis, (b) gridded NGM data generated from an Optimum Interpolation (OI). Positive values (solid) represent areas of warm advection.

comparisons. Subjective analysis of the observed data prior to the development of the storm defined a jet streak configuration that the initialized NGM data field smoothed and weakened slightly. This would imply that jet streak-induced vertical motions, as viewed in terms of a straight line jet streak, in the left-front quadrant of the observed jet streak were stronger than those in the model jet streak. This supports the rapid intensification observed as the low entered western Utah and may explain why the model failed to detect this event. The failure of the model to properly place the jet further east in the 12 hour forecast was also illustrated in the difference fields of total and ageostrophic winds. The model's 12 hour forecast of the total wind, while slightly stronger than the initialized total wind valid the same time, failed to identify a well defined jet streak. This resulted in a weaker ageostrophic flow which would indicate that less vertical motion forcing existed in the exit region of the jet. The affect on the attendant secondary (indirect) circulation was that a much weaker vertical circulation was forecast than was actually analyzed.

Interestingly, in this case the difference in magnitude between the model's forecasted and analysis wind speeds only varied by a few meters/second through the jet streak. However, the magnitude of the ageostrophic winds was considerably larger in the analysis even though the wind speeds were greater in the 12 hour forecast. This illustrates that it's not the magnitude of the wind velocity within the jet streak, but variations in the along and transverse components of the total wind that influences vertical motion.

Discrepancies found in comparisons of NGM gridded data (initialized/12 hour forecast) against observed data (temperature, wind, and geopotential height) at 700 mb further illustrates the model's inability to forecast this storm. Considerable errors were found in the NGM wind output. Both the initial analysis and the 12 hour forecast wind fields valid at 0000 UTC placed a circulation center well north of where it was actually located in the observed data. Model output of the geopotential heights also performed poorly in identifying the

700 mb low center. Though the actual geopotential height values from the model were close to the observed values (consistently 10-20 meters higher than the observed values), they failed to indicate a closed circulation apparent in the observed winds data and supported by satellite imagery. Differences in the temperature fields from the model output ranged from 1-4°C warmer than observed through western Utah/eastern Nevada during peak cyclogenesis. The influence these differences had on diabatic effects (especially latent heat release), while not discussed in this study, have been shown in other studies to increase jet-streak induced vertical circulations. Considering the explosive nature of this storms development and the deep convection observed, it's conceivable that diabatic effects did play heavily in this particular storm.

A quasi-geostrophic (QG) examination of vertical motion forcing was performed to compare the gridded analysis from rawinsonde data generated by a Barnes analysis against the NGM gridded analysis generated by an Optimum Interpolation (OI). The advection of vorticity by the thermal wind (Trenberth method) and Divergence of Q were used to evaluate each 0000 UTC analysis. Results showed that both the Trenberth method and the Divergence of Q at 700 mb properly identified the region of strongest upward vertical motion (heaviest precipitation). A noticeable difference was found in the Divergence of Q at 500 mb. Values computed from the gridded data generated by the Barnes analysis properly located the stronger upward vertical motions over western Utah. Values computed from the NGM gridded data were much further south over western Arizona in the area where the model showed strong 500 mb positive vorticity advection.

6. Conclusions

Within the operational forecasting environment, two important points can be gained from this study. One, subjective analysis of observed data provides a means of identifying areas of vertical motion forcing and verifying the accuracy of initialized/forecast model output. Two, vertical motion is a result of three-

dimensional processes and is not simply confined to conventional 500 mb parameters. With the coming of gridded data, the meteorologist (forecaster) will have to become familiar with the theory behind vertical motion forcing in order to effectively use the new data that will become available in the forecast offices of the future.

REFERENCES

Barnes, S. L., 1964: A technique for maximizing detail in numerical weather map analysis. J. Appl. Meteor., 3, 396-409.

——, 1985: Omega diagnostics as a supplement to LFM/MOS guidance in weakly forced convective situations. Mon. Wea. Rev., 113, 2122-2141.

——, 1986: The limited-area fine mesh model and the quasi-geostrophic theory: A disturbing case. Wea. Forecasting, 1, 89-96.

Bjerknes, J., 1951: Extratropical cyclones. Compendium of Meteorology, T.F. Malone, Ed., Amer. Meteor. Soc., 577-598.

Cammas, J-P, and D. Ramond, 1989: Analysis and Diagnosis of the Composition of Ageostrophic Circulations in Jet-Front Systems, Mon. Wea. Rev., 117, 2447-2461.

Dunn, L. B., 1988: Vertical motion evaluation of a Colorado snowstorm from a synoptician's perspective. Wea. Forecasting, 3, 261-272.

Durran, D. R., and L. W. Snellman, 1987: The diagnosis of synoptic-scale vertical motion in an operational environment. Wea. Forecasting, 1, 17-31.

Holton, J. R., 1979: An Introduction to Dynamic Meteorology. 2nd ed., Int. Geophys. Ser., 23, Academic Press, 391 pp.

Hoskins, B. J., and M. S. Pedder, 1980: The diagnosis of middle latitude synoptic development. Quart. J. Roy. Meteor. Soc., 106, 707-719.

Keyser, D. A., and D. R. Johnson, 1984: Effects of diabatic heating on the ageostrophic circulation of an upper tropospheric jet streak. Mon. Wea. Rev., 112, 1709-1724.

Murray, R., and S. M. Daniels, 1953: Transverse flow at entrance and exit region to jet streams. Quart J. Roy. Meteor. Soc., 79, 236-241.

Namias, J., and P. F. Clapp, 1949: Confluence theory of high tropospheric jet stream. L. Meteor., 6, 330-336.

National Weather Service, 1978: Optimum interpolation in final cycle. NWS Tech. Proc. Bull. 249.

Sutcliffe, R. C., 1947: A contribution to the problem of development. Quart. J. Roy. Meteor. Soc., 73, 370-383.

Trenberth, K. E., 1978: On the interpretation of the diagnostic quasi-geostrophic omega equation. Mon. Wea. Rev., 106, 131-137.

Uccellini, L. W., and P. J. Kocin, 1987: The interaction of jet streak circulations during heavy snow events along the East Coast of the United States. Wea. Forecasting, 2, 289-308.

———, and D. R. Johnson, 1979: The coupling of upper- and lower-tropospheric jet streaks and implications for the development of severe convective storms. Mon. Wea. Rev., 107, 682-703.

A Winter Severity Index For Pittsburgh Pennsylvania

By Victor J. Nouhan

May 11, 1992

A Winter Severity Index For Pittsburgh Pennsylvania

Introduction

Winter weather has a great impact upon many facets of every day life. The extent of this impact is a function of location and resources sensitive to winter weather. Severe winter weather may be a detriment to transportation, agriculture, and industry. On the other hand, reservoir capacity, tourism, and winter sports may actually benefit from elements of severe winter weather.

Given a location and a list of critical resources dependent on winter weather, winter severity has historically been measured by departures from 1) winter mean temperatures, 2) mean seasonal snowfall, and 3) other locally defined parameters (such as days with minimum temperatures below zero or maximums below 32 degrees).

This study will combine several traditional winter parameters to produce an integrated winter severity index for Pittsburgh, Pennsylvania for 105 winter seasons from the 107 year Pittsburgh Local Climatological Data (LCD) record; 1884/85 to 1990/91. This study is based upon a similar index produced for New Brunswick, NJ (Rubinfeld 1976).

In deriving a total index value for each winter season, Rubinfeld used linear regression equations for each parameter to produce sub-index values. These parameter sub-index values were then scaled on a 100 point system. The mildest occurrence of a parameter was given a near zero value and the most severe a near 100 value. All scaled sub-index values were then combined with their respective weighting factors to produce a total index value for a given winter season. Lastly, a quadratic smoothing function and an overall linear correction factor was applied to each winter's total index value to correct for skewness and to center the mean for all total winter indecies at 50.

A similar approach was used in this project, however with several modifications. The four parameters chosen along with their weighting factors are:

1) seasonal snowfall (S)   45%
2) winter (Dec,Jan,and Feb combined) mean temperatures (W) 30%
3) extreme cold temperature index (EC)   15%
4) combined Nov/Mar mean temperatures for each season (NM) 10%

Seasonal snowfall (S) was chosen because of the impact it has on community snow removal budgets, school cancellations, skiing and etc. Winter mean temperature (W) was chosen mainly due to the impact on the heating season and fuel costs.

The extreme cold temperature (EC) index is a new parameter

devised for this study. It incorporates both the number of days
with maximum temperature below 32 deg F and days with minimums
below 0 deg F and other temperature threshold values which are
important for Pittsburgh. The index is computed by assigning
points to each day based on threshold values of temperature.
Points for each day were then tallied on a monthly basis and
combined to produce a seasonal total. Threshold temperatures and
point values per day are as follows:

Temperature Threshold (deg F)	POINTS
A) max g.t. 32 <u>and</u> min g.t. 10	0
B)	
1. max l.t. or eq. to 32	1
2. max l.t. 40 <u>and</u> min l.t. 10	1
3. max g.t. 40 <u>and</u> min l.t. or eq. to 0	1
C)	
1. max l.t. or eq. to 20	2
2. max l.t. or eq. to 32 <u>and</u> min l.t. 10	2
3. max l.t. 40 <u>and</u> min l.t. or eq. to 0	2
D)	
1. max l.t. 10	3
2. max l.t. or eq. 20 <u>and</u> min l.t. or eq. to 0	3
3. max l.t. or eq. 32 <u>and</u> min l.t. or eq. to -10	3
E)	
1. max l.t. or eq. to 0	4
2. max l.t. 10 <u>and</u> min l.t. or eq. to -10	4

l.t.=less than   g.t.=greater than   eq.=equal

There are two advantages with this system. First, a threshold
scheme more accurately accounts for cold weather events by
weighting successive thresholds of cold temperatures. This can
be illustrated with an example. If a high temperature of 35
occurred after a low of 2, there would be no record of a cold day
in either the max temperatures l.t. or eq. to 32 or min
temperatures l.t. or eq. to 0 deg F categories despite being
within a couple of degrees of each category. This new threshold
scheme would allow one point for this example where none would be
allowed under Rubinfelds scheme. The second advantage is the
greater weighting of severe Arctic outbreaks. During an
extremely cold day at Pittsburgh the temperature may not rise
above 0 deg F and the low may be less than -10 deg F. This type
of event should be weighted more than simply assigning it to the
days with min temperatures at or below zero category because 1) a
very low high temperature greatly increases heating degree days
and home heating costs, 2) outbreaks of this type are usually
accompanied by strong winds which produce very low wind chill
temperatures and further increases heating demands, and 3) to
place greater emphasis on rare events.

The last parameter devised for this study is the combined
November and March mean temperature (NM), for each season. NM

was only weighted 10 percent as a result of November and March contributing only a small portion of the total winter weather at Pittsburgh compared to December, January, and February. However, on occasion, substantial cold spells occur in these months that may lengthen the winter season. An example of this is the winter of 1959/60 where the most severe March this century turned an average winter at Pittsburgh into a severe one. It should be noted that extreme cold in November and March will also be accounted in the EC index. This linkage thereby increases the 10 percent weighting factor for the NM index alone.

The assigned weighting factors of each parameter was based on its relative contribution to a winter season at Pittsburgh. As a result, S, W, and EC were given the greatest weights. The weighting factors for W and EC combined are equal to S (45 percent), which is roughly similar to the Rubinfeld study.

Procedure

Unlike the approach used by Rubinfeld, the four parameters were individually normalized to produce sub-indexes for each parameter in this study. This was done in order to simplify the procedure for WSFO PIT and to easily use it for future calculations. The four sub-indexes were then linearly combined with their respective weighting factors to produce the final index (I). The step by step procedure used to generate the final index is as follows:

1) Determine the mean for each parameter.

2) Determine the standard deviation (s) for each parameter.

3) Ensure each parameter is normally distributed. W and NM are normally distributed, however, S and EC failed the test for a normal distribution because both were skewed to the left (i.e., means were significantly less than the medians). Normally, the best way to analyze highly skewed distributions is to assume non-normality and create independent incomplete gamma distributions for each parameter. Unfortunately, this is a complicated procedure requiring significant manual calculations.

Therefore, an alternate approach was taken to solve this problem. Normal distributions for each parameter were assumed and the extreme endpoint values of both S and EC were assigned as +3s and -3s. Then by dividing the difference of each endpoint from each respective parameter mean by 3, two approximate s values were generated for each parameter; one for above and the

other for below the mean (see table 1).[1]

4) Determine a statistical "Z" for all data values using the appropriate mean and s for each parameter. The equation used was:

(1) $Z = \dfrac{x - mean}{s}$

where x represents a value from any of the four parameters.

Signs of Z for each parameter were determined by how each contributes toward higher I values. Positive departures of S and EC are associated with severe winters, so the sign of Z for these parameters correctly reflect their contribution. Conversely, negative departures of W and NM from their means contribute to greater winter severity. Therefore, the opposite sign of Z for these parameters must be taken to properly account for a positive contribution toward I.

5) Find the fraction (Zp) of the area under the normal curve right (+Z) or left (-Z) of the mean for each data point. This can be done by taking the fractional value listed for each Z from a normal curve statistics table. Zp values derived from a negative Z must be preceded by a negative sign to reflect the proper contribution toward I.

6) Compute individual sub-indexes (i) for each parameter using the following equation, where x represents any of the four parameters:

(2) $ix = \dfrac{2(50 + 16.5Z) + (50 + 100Zp)}{3}$

If Z exceeds 3s but is less than or equal to 4s, then equation 3 must be used:

(3) $ix = \dfrac{2[99.5 + .5(Z-3)] + (50 + 100Zp)}{3}$

Equation 2 was used for all but two points. The other two values exceeded 3s, requiring equation 3. Note that both equations linearly smooth the total area under the normal curve right of each individual Z value. Individual indexes could have been computed by multiplying the result of .50 + or - Zp by 100. However, the resulting index values obtained would have varied

---

[1]The mean for EC was adjusted slightly toward the median from 49.2 to 50.0 and the value of 116 was chosen to represent 3s. This was done only on this highly skewed parameter to facilitate step 3 of the procedure.

too greatly between -1s and + 1s, because index values near 1s would be too high and those near -1s values too low (see table 3). To expand the index scale over a greater range of Z, a linear smoothing term was included in both equations 2 and 3 (first term of numerator). This smoothing term provided a linear index value based on an input Z value. The smoothing term was always less than the raw value term (second term of numerator in equations 2 and 3) for +Z values and more for -Z values. Inclusion of the smoothing term expanded the range where ix rapidly changed from -1s to +1s to -2s to +2s and further delineated ix values below and above -2.5s and +2.5s over the raw ZP values. A close examinination of table 3 shows that the smoothed ix values differ the most from the raw values between -1.0s and -1.5s and between 1.0s and 1.5s (i.e., greatest smoothing intervals). Both values are the same at Z=0 and begin to approach each other again beyond -2.5s and +2.5s.

7) Apply appropriate weighting factors to each of the individual indexes and compute the total index (T) for each winter season. The two equations used for this step are:

$$(4) \quad T = .45iS + .45iW + .10iNM \quad \text{(from 1884/85-1903/04)}$$

$$(5) \quad T = .45iS + .30iW + .15iEC + .10iNM \quad \text{(1904/05 to present)}$$

Equation 4 was used because EC could not be computed for seasons prior to 1904/05 due to missing monthly LCDs.

8) Compute the final index (I) by applying a linear correction of +3.2 to center the mean of all 105 total indexes at 50.0.

$$(6) \quad I = T + 3.2$$

The reason for this correction is due to the estimation done in step 3. The split standard deviation approach employed in this step did not completely center the mean on the median values of S and especially EC.

Results

Individual parameter values (including overall means and s values), final index values, and five year running mean index values (5RM) are given in Table 1. Decade means are listed in table 2. Table 3 gives raw Zp values along with smoothed sub-index values (ix) for whole values of Z. The qualitative winter rating threshold scheme is shown in table 4, including the distribution of all 105 seasons within this scheme. Severe and very mild winters were defined based on the average of all parameters equaling or exceeding + or - 1s respectively. This is numerically equivalent to a seasonal final index value of 72.5 for a severe winter and 27.5 for a very mild winter. Table 5 lists the 10 severest and mildest winters by final index, the

10 coldest and warmest winters, and the 10 snowiest and least snowiest winters. For reference, table 6 gives significant winter events at Pittsburgh that occurred during the 107 year period. Lastly, figure 1 shows the graphs of the final index vs. the five year running means, and figure 2, the final index vs. the decade means.

The five year running mean data in Figure 1 indicates that winter severity in Pittsburgh gradually increased from the late 1880s through the mid 1910s. Winter severity then declined sharply through the 1920s and reached its mildest point as reflected by the running mean of 27.5 during the 1930/31 winter season. Winter severity returned to the "average" category by the late 1930s and remained so through the mid 1940s. After a slight decline in the late 1940s and early 1950s, winter severity greatly increased through the late 1950s with the running mean index reaching a record maximum of 77.8 during the 1961/62 season. In other words, the 5-winter-span centered on the 1961/62 season actually averaged severe. The running mean index continued above 70 for most of the 1960s, then briefly declined back into the average category in the early 1970s. Another increase in winter severity occurred in the late 1970s as reflected by the 73.1 value of the running mean index during the 1978/79 season. Since then, however, winter severity has gradually decreased with the 1988/89 running mean value of 36.9 the mildest since 1947/48.

Discussion

The derived index data for Pittsburgh during the periods 1957/58 to 1971/72 and 1976/77 to 1981/82 indicated a much greater frequency of severe winters than the rest of the record. This is supported by Rubinfeld's data which also showed a marked increase in winter severity for central NJ from 1957/58 to 1971/72 and again during the late 1970s.

LCD Data for other locations from southern New England southward to about North Carolina and westward to the Ohio and Tennessee Valleys also indicated colder and snowier winters during the late 1950s through the 1960s. Interestingly, for the same time period, northern New England locations had colder than normal winters but less than the normal snowfall, while central and northern Plains locations also had below normal snowfall but with near normal temperatures. Although the late 1970s and early 1980s featured several very cold winters for western Pennsylvania and much of the eastern US, they generally were not as snowy as the first period.

This distribution of temperature and snowfall across much of the eastern US, indicates a long wave trough with greater than normal amplitude, resided near the Ohio-Tennessee River Valley longitude with higher than normal frequency during the 1957/58-

1971/72 winters. Frequent strong transient short waves during this anomalous flow pattern resulted in a higher frequency of cyclogenesis in the deep south and along the east coast. With plenty of cold air available, these systems often generated large snow canopies as they moved northeastward, bringing deep snow cover to areas that normally didn't receive it, including the Pittsburgh area (Kocin and Uccellini 1990). Once an anomalously large snow cover became established, subsequent arctic air masses did not modify greatly as they moved southward over the eastern US, and this helped to maintain the cold regime during many of these winters. The winters of the late 1970s and early 1980s featured a similar long wave pattern across the eastern US, except a lesser frequency of vigorous short waves and less resultant snowfall occurred. A notable exception was 1977/78, a winter similar to those of the snowier 1960s variety.

Variations of winter severity over different portions of the US are initiated and maintained by different phases of mid-tropospheric teleconnection patterns (Namias 1978). The most important of these in western Pennsylvania are the Pacific-North American (PNA) and the North Atlantic Oscillation (WA, i.e., the Western Atlantic). Yarnal proposed that 60 percent of the total variation in Pennsylvania winter mean temperatures may be controlled by these two patterns (Yarnal 1987). The rest of the variation is controlled by other teleconnections (such as Southern Oscillation), large scale snow cover, and local parameters (topography, influence from the great lakes, and etc.).

Most of the Pittsburgh winters during the 1957/58-1971/72 and 1976/77-1981/82 periods were accompanied by the positive phase of the PNA and/or the negative phase of the NAO teleconnection patterns. The frequent re-occurrence of these patterns during this period may be linked to a steady-state or a re-emergence of similar sea surface temperature anomalies during successive winters in both the mid-latitude Pacific and perhaps, Atlantic Oceans (Namias 1980). It's interesting to note that both periods of severer winters began and terminated with notable El-Ninos (1957/58, 1972/73 and 1976/77, 1982/83). This suggests a winter bi-modal circulation regime in which a noteworthy El-Nino may activate a cold/snowy circulation regime for several successive winters until another noteworthy El-Nino activates the mild/less snowy regime. Other El-Ninos also occurred, especially during the longer first period, but without much of an affect on subsequent winter severity within this period. Why certain El-Ninos greatly increase/decrease winter severity at Pittsburgh and adjacent areas of the northeast US for several successive winters while others do not, is not known but may be linked to concomitant sea surface temperature anomallies in the mid-latitude north Pacific and Atlantic basins at the onset of an El-nino event. Further speculation is beyond the scope of this study.

Although no other analogs to the 1957/58-1971/72 and 1976/77-1981/82 periods were found in the remainder of the Pittsburgh record, longer records from other northeast US locations dating back to the late 18th century indicate at least two other periods of similar winter severity. Both periods were lengthy compared to the two found in this study. The first extended from 1776/77 to 1819/20 and the second from 1834/35 to 1859/60. Both of these periods came in the final 100 years of what climatologists refer to as the "Little Ice Age", a period known for longer winters, backward springs, and alpine glacial advance in both the US and Europe (Ludlam 1966/68).

Summary

Several common winter parameters for Pittsburgh, Pennsylvania were selected, normalized and linearly combined to produce an overall winter severity index. The parameters used in this study included seasonal snowfall, mean winter temperatures, and occurrences of extreme cold. The derived index is believed to be more conservative and useful in judging overall winter severity than using one parameter alone. The weighting for each parameter can be altered to reflect its relative importance at a particular location.

In deriving this index on the 107 year record at Pittsburgh, two periods of greater incidence of severe winters were found, 1957/58-1971/72 and 1976/77-1981/82. Examination of another winter severity index for central New Jersey as well as seasonal snowfall and mean winter temperature for other locations in the eastern U.S. indicate a similar incidence of severe winters, especially during the 1960s. The frequency of "severe" and "hard" winters during these periods compared to the rest of the time series is much higher than random chance would suggest. This indicates a different mode of mid-tropospheric circulation during most of these seasons. There may be a link to persistence of, or a reoccurrence of favorable sea surface temperature anomaly distributions during these periods over the mid-latitude portions of both the north Pacific and Atlantic Oceans and the anomalous atmospheric circulation regimes that accompanied both periods. Both periods were initiated and terminated during notable El-Nino years.

Longer records for other locations in the northeast US dating back to the late 18th century indicate two lengthy periods only separated by 15 years where overall winter severity was much greater. However, since 1860, their have been few consecutive or near consecutive severe winters at Pittsburgh with the execeptions of the 1957/58-1971/72 and 1976/77-1981/82 periods.

Table 1

	YR	S (in)	W (deg F)	EC	NM (deg F)	I	5RM
1.	1884/85	43.6	28.9	--	37.8	66.5	----
2.	85/86	39.5	31.5	--	42.5	52.6	----
3.	86/87	32.2	33.2	--	39.9	40.2	45.4
4.	87/88	21.0	32.9	--	40.5	32.9	34.3
5.	88/89	28.6	33.4	--	44.3	34.9	34.0
6.	89/90	11.4	43.0	--	39.7	11.1	32.4*
7.	90/91	51.4	35.4	--	41.5	50.8	40.6*
*	91/92	----	35.4	--	38.6	----	----
8.	92/93	42.3	28.2	--	40.9	65.4	49.6*
9.	93/94	30.0	34.8	--	44.5	32.6	45.2*
*	94/95	----	28.8	--	38.4	----	----
10.	95/96	28.3	33.7	--	39.2	37.7	31.0*
11.	96/97	19.9	32.5	--	46.6	29.1	39.0*
12.	97/98	22.2	34.8	--	46.4	24.8	38.4
13.	98/99	48.7	29.9	--	41.5	64.4	42.4
14.	99/1900	22.7	32.3	--	40.3	36.0	50.2
15.	1900/01	43.8	30.6	--	43.5	57.6	51.9
16.	01/02	56.2	30.0	--	41.7	68.1	49.4
17.	02/03	26.0	32.1	--	50.7	33.4	53.0
18.	03/04	22.3	26.2	--	40.4	51.8	49.0
19.	04/05	34.1	27.3	57	47.2	54.2	45.1
20.	05/06	30.5	34.2	29	37.1	37.7	46.0
21.	06/07	36.5	31.4	46	44.7	48.2	41.3
22.	07/08	27.9	31.2	37	42.8	38.2	42.4
23.	08/09	26.2	35.7	22	40.4	28.0	45.6
24.	09/10	48.0	28.7	53	49.6	60.1	50.5
25.	10/11	44.3	32.5	30	37.1	53.3	48.4
26.	11/12	41.2	28.1	77	37.3	72.7	57.6
27.	12/13	25.9	34.9	27	43.8	28.0	56.2
28.	13/14	78.5	31.5	53	41.0	74.0	56.3
29.	14/15	41.6	32.4	39	38.1	52.9	51.1
30.	15/16	38.3	32.0	52	39.7	53.8	60.0
31.	16/17	32.0	30.5	55	42.6	46.6	48.0
32.	17/18	45.4	25.3	85	42.2	72.9	48.6
33.	18/19	8.8	26.3	21	43.0	14.0	41.2
34.	19/20	31.4	26.9	56	42.6	55.8	39.5
35.	20/21	15.4	35.3	21	46.5	16.8	31.6
36.	21/22	33.4	32.7	25	43.8	38.0	37.3
37.	22/23	24.4	32.1	35	42.0	33.6	34.5
38.	23/24	35.1	33.7	31	40.0	42.1	43.4
39.	24/25	34.5	33.5	42	42.6	42.1	43.8
40.	25/26	44.4	31.0	50	37.2	61.4	44.0
41.	26/27	31.8	33.3	34	43.1	40.0	42.7
42.	27/28	22.1	32.3	49	42.9	34.6	41.6
43.	28/29	25.0	30.8	38	45.2	35.2	35.0
44.	29/30	28.3	35.1	47	39.4	36.9	29.4
45.	30/31	19.0	33.1	29	40.2	28.3	27.5
46.	31/32	14.7	40.5	14	42.6	12.0	31.9

Table 1 (con't)

	YR	S (in)	W (deg F)	EC	NM (deg F)	I	5RM
47.	32/33	15.7	35.9	32	39.6	25.3	30.0
48.	33/34	33.5	29.6	68	38.1	57.1	41.4
49.	34/35	23.9	32.7	26	47.2	27.3	45.8
50.	35/36	63.6	23.4	97	42.6	85.5	47.0
51.	36/37	27.8	34.7	23	36.3	33.8	43.9
52.	37/38	18.7	31.8	40	42.4	31.1	53.3
53.	38/39	35.1	33.3	34	42.0	41.8	47.7
54.	39/40	47.3	27.2	76	37.0	74.3	50.6
55.	40/41	38.8	30.9	48	36.3	57.5	57.1
56.	41/42	34.2	30.6	46	42.9	48.3	56.8
57.	42/43	46.4	30.1	58	40.1	63.8	55.0
58.	43/44	24.7	31.5	43	37.8	40.1	51.0
59.	44/45	50.3	27.2	49	46.9	65.4	52.0
60.	45/46	28.6	30.5	36	47.3	37.5	49.5
61.	46/47	36.5	31.5	50	39.7	53.0	45.3
62.	47/48	30.9	29.0	58	41.6	51.4	37.3
63.	48/49	21.1	37.0	21	44.3	19.3	45.0
64.	49/50	22.3	36.4	23	38.5	25.5	44.3
65.	50/51	82.0	31.3	43	39.0	75.6	39.5
66.	51/52	45.7	34.8	31	38.2	49.8	41.9
67.	52/53	27.0	35.3	19	42.6	27.1	45.5
68.	53/54	23.9	33.8	32	40.5	31.4	41.2
69.	54/55	26.5	29.6	45	41.0	43.4	40.6
70.	55/56	37.4	30.2	39	38.1	54.4	46.6
71.	56/57	37.7	33.0	38	40.8	46.8	54.2
72.	57/58	37.9	28.5	49	39.4	56.9	60.7
73.	58/59	45.6	26.7	61	40.5	69.5	66.9
74.	59/60	62.2	31.4	74	32.5	76.0	70.6
75.	60/61	76.0	26.0	77	42.2	85.5	76.1
76.	61/62	43.1	28.6	60	39.7	65.2	77.8
77.	62/63	53.4	21.5	104	40.9	84.4	74.7
78.	63/64	62.6	26.9	64	41.9	77.7	69.6
79.	64/65	42.2	30.2	58	40.4	60.6	70.5
80.	65/66	48.0	30.3	56	41.1	60.3	68.8
81.	66/67	59.6	29.8	52	41.5	69.7	64.4
82.	67/68	50.5	26.8	73	38.6	75.6	69.9
83.	68/69	30.4	27.9	59	37.8	55.8	73.0
84.	69/70	70.7	25.0	76	37.4	88.3	71.9
85.	70/71	59.9	28.7	60	38.3	75.7	63.9
86.	71/72	51.9	31.6	51	38.4	64.3	58.1
87.	72/73	26.3	31.9	40	43.8	35.4	52.5
88.	73/74	16.6	32.4	34	42.7	26.7	46.6
89.	74/75	58.7	32.4	33	40.1	60.4	50.9
90.	75/76	35.6	31.2	44	45.8	46.3	60.6
91.	76/77	49.6	20.7	130	38.4	85.9	69.6
92.	77/78	62.2	24.9	91	41.3	83.8	67.2
93.	78/79	40.8	24.0	97	43.1	71.6	73.1
94.	79/80	24.1	28.6	66	40.2	48.3	70.0

Table 1 (con't)

	YR	S (in)	W (deg F)	EC	NM (deg F)	I	5RM
95.	80/81	48.0	26.8	81	37.2	75.8	59.9
96.	81/82	45.1	26.2	60	39.4	70.5	59.9
97.	82/83	30.1	34.2	28	42.7	33.2	61.4
98.	83/84	49.2	28.3	70	38.5	71.9	58.7
99.	84/85	36.4	29.7	62	42.8	55.8	52.5
100.	85/86	46.3	29.0	52	44.1	61.9	56.4
101.	86/87	30.0	31.2	28	41.2	39.6	48.3
102.	87/88	35.1	30.2	58	42.8	52.7	45.8
103.	88/89	21.7	31.7	32	42.7	31.3	37.5
104.	89/90	28.4	31.0	53	42.3	43.7	----
105.	90/91	17.2	34.4	20	44.2	20.4	----
Averages		37.0	31.0	50	41.3		
Standard deviations		14.8	3.6	21.6	3.0		
Split s values	s−	9.4		12.0			
	s+	15.0		22.0			

s− is applied for values below and s+ for values above the mean.

*Running mean values are not as reliable since these seasons were computed with less than five I values.

Table 2
Decade Means for I

1890/91–1899/1900	42.5	1940/41–1949/50	45.7
1900/01–1909/10	48.3	1950/51–1959/60	52.2
1911/20–1919/20	51.7	1960/61–1969/70	73.3
1920/21–1929/30	37.4	1970/71–1979/80	60.1
1930/31–1939/40	40.6	1980/81–1989/90	53.6

Table 3
Zp Fractions vs Smoothed Values

Z	ZP	ix
−3	0.1	0.4
−2	2.3	12.1
−1	15.9	27.6
0	50.0	50.0
1	84.1	72.4
2	97.7	87.9
3	99.9	99.6

Table 4
Qualitative Threshold Rating Scheme

	I Value	Winter Rating	Data Distribution
1.	less than 27.5	"Very Mild"	11
2.	27.5-39.9	"Mild"	26
3.	40.0-59.9	"Average"	33
4.	60.0-72.4	"Hard"	19
5.	72.5 or greater	"Severe"	16
			105 Seasons

Table 5
Top Ten Winter Rankings

A. By Severity Index:

	Severest				Mildest	
	Season	Index Value			Season	Index Value
1.	1969/70	88.3		1.	1889/90	11.1
2.	1976/77	85.9		2.	1931/32	12.0
3.	1960/61	85.5		3.	1918/19	14.0
4.	1935/36	85.5		4.	1920/21	16.8
5.	1962/63	84.4		5.	1948/49	19.3
5.	1977/78	83.8		6.	1990/91	20.4
7.	1963/64	77.7		7.	1897/98	24.8
8.	1959/60	76.0		8.	1932/33	25.3
9.	1980/81	75.8		9.	1949/50	25.3
10.	1970/71	75.7		10.	1973/74	26.7

Underlined seasons in part B. and C. of this table are those found in part A.

B. By Temperature:

	Coldest				Warmest	
	Season	(deg F)			Season	(deg F)
1.	1976/77	20.7		1.	1889/90	43.0
2.	1962/63	21.5		2.	1931/32	40.5
3.	1935/36	23.4		3.	1879/80*	40.3
4.	1978/79	24.0		4.	1881/82*	37.7
5.	1977/78	24.9		5.	1948/49	37.0
6.	1969/70	25.0		5.	1877/78*	37.0
7.	1917/18	25.3		7.	1949/50	36.4
8.	1960/61	26.0		8.	1918/19	36.3
8.	1874/75*	26.0		9.	1932/33	35.9
10.	1903/04	26.2		10.	1908/09	35.7

*Monthly temperature averages for Pittsburgh have been tabulated from 1871/72 to 1883/84, but without any corresponding snowfall data.

Table 5 (con't)
C. By Snowfall:

	Heaviest Season	(in)		Lightest Season	(in)
1.	1950/51	82.0	1.	1918/19	8.8
2.	1913/14	78.5	2.	1889/90	11.4
3.	1960/61	76.0	3.	1931/32	14.7
4.	1969/70	70.7	4.	1920/21	15.4
5.	1935/36	63.6	5.	1932/33	15.7
6.	1963/64	62.6	6.	1973/74	16.6
7.	1977/78	62.2	7.	1990/91	17.2
7.	1959/60	62.2	8.	1937/38	18.7
9.	1970/71	59.9	9.	1930/31	19.0
10.	1966/67	59.6	10.	1896/97	19.9

Table 6
Significant Winter Events at Pittsburgh

	Season	Event
1.	1889/90	The "winter" without a winter; Pittsburgh's mildest winter with many days above 60 deg F.
2.	1890/91	Big December snow of 23.9 inches on the 16th and 17th, of which, 22.0 inches fell on the 16th establishing the record for most snow in 24 hours at Pittsburgh.
3.	1898/99	Pittsburgh recorded its all time lowest temperature of -20 deg F on February 10th.
4.	1913/14	Pittsburgh's second snowiest winter with the total of 78.5 inches unmatched until 1950/51.
5.	1918/19	Pittsburgh least snowiest winter (8.8 inches).
6.	1931/32	Pittsburgh second mildest winter.
7.	1933/34	Severely cold February (monthly mean of 19.7 deg F); coldest until 1963.
8.	1935/36	Severely cold and snowy winter during a period of mild winters. Rated 3rd most severe by index.
9.	1939/40	Hard winter which featured Pittsburgh 2nd coldest January (mean of 17.2 deg F).
10.	1950/51	Pittsburgh's snowiest winter on record (82.0 inches) inaugurated by Thanksgiving day blizzard that produced Pittsburgh's greatest snowfall of 27.4 inches over a 3 day period.
11.	1960/61	This winter tied 1935/36 in severity and featured the 3rd heaviest total snowfall with much below normal temperatures.
12.	1962/63	Another in series of severe winters which featured heavy snows and Pittsburgh coldest February on record (mean of 19.3 deg F).
13.	1969/70	Rated most severe by index, this winter featured the greatest combination of cold and snow in one winter, although neither parameter alone was of record proportions.
14.	1976/77	Coldest winter of record at Pittsburgh and rated second by index with January the coldest

Table 6 (con't)

calendar month of record (mean of 11.4 deg F).

15. 1977/78   Second consecutive severe winter teamed heavy
               snow with much below normal temperatures.

16. 1989/90   An otherwise mild winter which featured the
               coldest December of record (mean of 19.2 deg F).

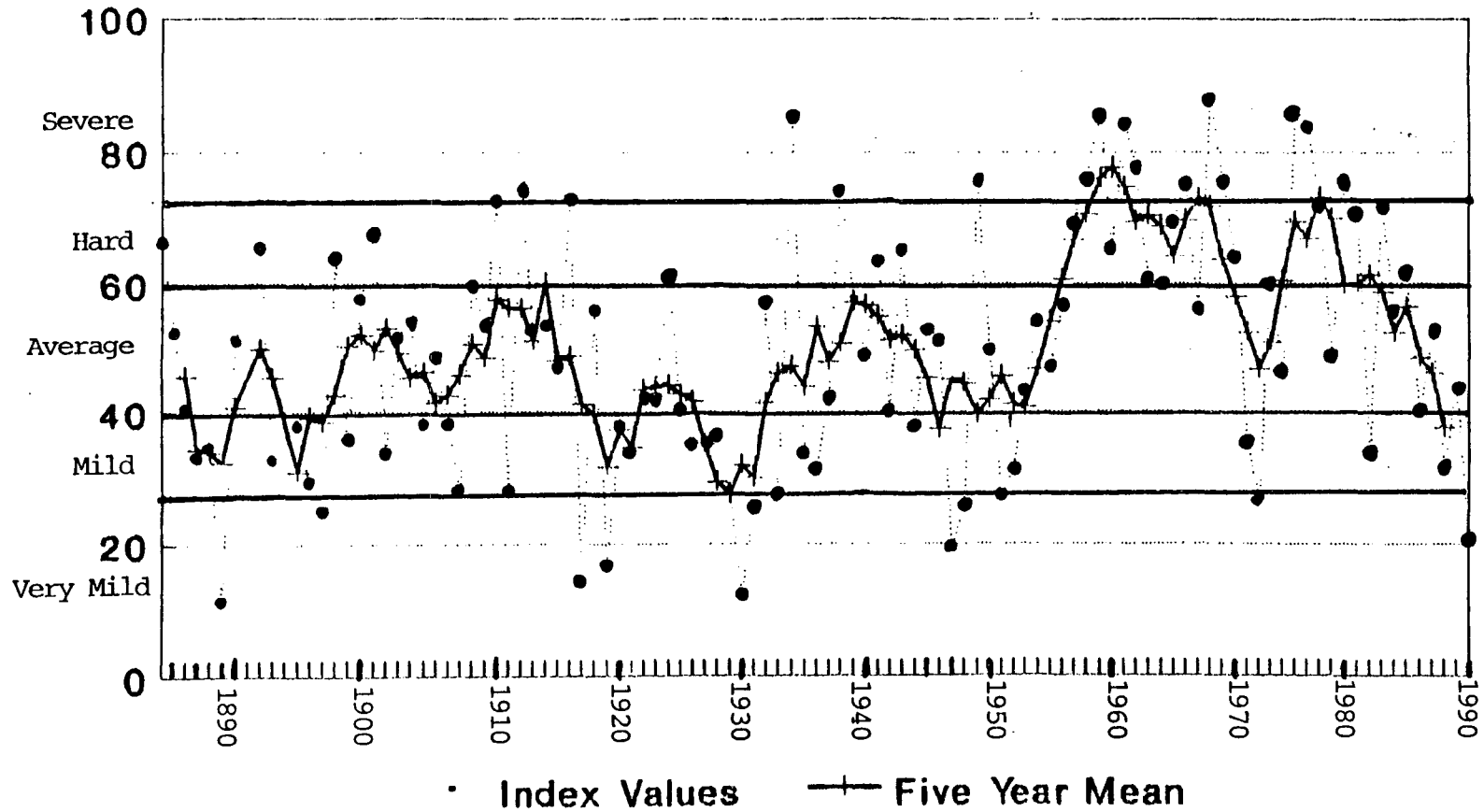Figure

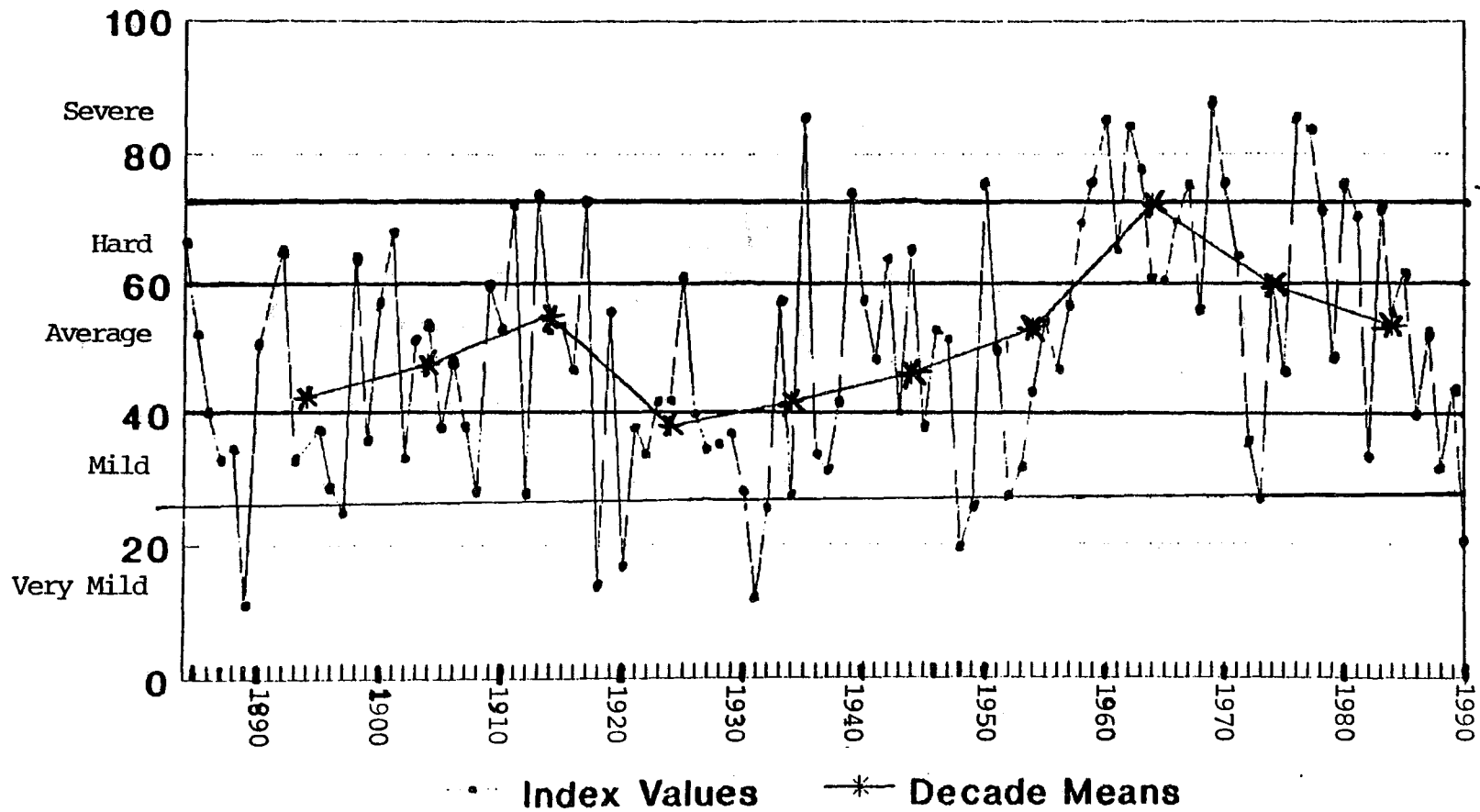# SEASONAL INDEX VALUES
AND FIVE YEAR RUNNING MEANS

• Index Values   —+— Five Year Mean

Figure 2

SEASONAL INDEX VALUES
AND DECADE MEANS

• Index Values   ─*─ Decade Means

Kocin, P., L. Uccellini, 1990: Snow Storms Along the Northeastern Coast of the United States, American Meteorological Society, 96-220.

Ludlum, D., 1966: Early American Winters 1, American Meteoroligical Society, 85-199.

Ludlam, D., 1968: Early American Winters 2, American Meterological Society, 18-64.

Namias, J., 1978: Multiple Causes of the North America Abnormal Winter of 1976/77. Monthly Weather Review, 106, 279-295.

Namias, J., 1980: Causes of Extreme Northern Hemisphere Climatic Anomalies from Summer 1978 Through the Subsequent Winter. Monthly Weather Review, 108, 1333-1346.

Rubinfeld, M., 1976: A Winter Severity Index For Central New Jersey. Bulletin of New Jersey Academy of Science, 21, 1-5.

Yarnal, B., 1987: Teleconnections and Pennsylvania Winter Temperatures. Earth and Mineral Sciences, 56, 17-21.

142 The Usefulness of Data from Mountaintop Fire Lookout Stations in Determining Atmospheric Stability. Jonathan W. Corey, April 1979. (PB298899/AS)

143 The Depth of the Marine Layer at San Diego as Related to Subsequent Cool Season Precipitation Episodes in Arizona. Ira S. Brenner, May 1979. (PB298817/AS)

144 Arizona Cool Season Climatological Surface Wind and Pressure Gradient Study. Ira S. Brenner, May 1979. (PB298900/AS)

146 The BART Experiment. Morris S. Webb, October 1979. (PB80 155112)

147 Occurrence and Distribution of Flash Floods in the Western Region. Thomas L. Dietrich, December 1979. (PB80 160344)

149 Misinterpretations of Precipitation Probability Forecasts. Allan H. Murphy, Sarah Lichtenstein, Baruch Fischhoff, and Robert L. Winkler, February 1980. (PB80 174576)

150 Annual Data and Verification Tabulation - Eastern and Central North Pacific Tropical Storms and Hurricanes 1979. Emil B. Gunther and Staff, EPHC, April 1980. (PB80 220486)

151 NMC Model Performance in the Northeast Pacific. James E. Overland, PMEL-ERL, April 1980. (PB80 196033)

152 Climate of Salt Lake City, Utah. Wilbur E. Figgins (Retired) and Alexander R. Smith. Fifth Revision, July 1992. (PB92 220177)

153 An Automatic Lightning Detection System in Northern California. James E. Rea and Chris E. Fontana, June 1980. (PB80 225592)

154 Regression Equation for the Peak Wind Gust 6 to 12 Hours in Advance at Great Falls During Strong Downslope Wind Storms. Michael J. Oard, July 1980. (PB91 108367)

155 A Raininess Index for the Arizona Monsoon. John H. Ten Harkel, July 1980. (PB81 106494)

156 The Effects of Terrain Distribution on Summer Thunderstorm Activity at Reno, Nevada. Christopher Dean Hill, July 1980. (PB81 102501)

157 An Operational Evaluation of the Scofield/Oliver Technique for Estimating Precipitation Rates from Satellite Imagery. Richard Ochoa, August 1980. (PB81 108227)

158 Hydrology Practicum. Thomas Dietrich, September 1980. (PB81 134033)

159 Tropical Cyclone Effects on California. Arnold Court, October 1980. (PB81 133779)

160 Eastern North Pacific Tropical Cyclone Occurrences During Intraseasonal Periods. Preston W. Leftwich and Gail M. Brown, February 1981. (PB81 205494)

161 Solar Radiation as a Sole Source of Energy for Photovoltaics in Las Vegas, Nevada, for July and December. Darryl Randerson, April 1981. (PB81 224503)

162 A Systems Approach to Real-Time Runoff Analysis with a Deterministic Rainfall-Runoff Model. Robert J.C. Burnash and R. Larry Ferral, April 1981. (PB81 224495)

163 A Comparison of Two Methods for Forecasting Thunderstorms at Luke Air Force Base, Arizona. LTC Keith R. Cooley, April 1981. (PB81 225393)

164 An Objective Aid for Forecasting Afternoon Relative Humidity Along the Washington Cascade East Slopes. Robert S. Robinson, April 1981. (PB81 23078)

165 Annual Data and Verification Tabulation, Eastern North Pacific Tropical Storms and Hurricanes 1980. Emil B. Gunther and Staff, May 1981. (PB82 230336)

166 Preliminary Estimates of Wind Power Potential at the Nevada Test Site. Howard G. Booth, June 1981. (PB82 127036)

167 ARAP User's Guide. Mark Mathewson, July 1981, Revised September 1981. (PB82 196783)

168 Forecasting the Onset of Coastal Gales Off Washington-Oregon. John R. Zimmerman and William D. Burton, August 1981. (PB82 127051)

169 A Statistical-Dynamical Model for Prediction of Tropical Cyclone Motion in the Eastern North Pacific Ocean. Preston W. Leftwich, Jr., October 1981. (PB82195298)

170 An Enhanced Plotter for Surface Airways Observations. Andrew J. Spry and Jeffrey L. Anderson, October 1981. (PB82 153883)

171 Verification of 72-Hour 500-MB Map-Type Predictions. R.F. Quiring, November 1981. (PB82 158098)

172 Forecasting Heavy Snow at Wenatchee, Washington. James W. Holcomb, December 1981. (PB82 177783)

173 Central San Joaquin Valley Type Maps. Thomas R. Crossan, December 1981. (PB82 196064)

174 ARAP Test Results. Mark A. Mathewson, December 1981. (PB82 198103)

176 Approximations to the Peak Surface Wind Gusts from Desert Thunderstorms. Darryl Randerson, June 1982. (PB82 253089)

177 Climate of Phoenix, Arizona. Robert J. Schmidli, April 1969 (Revised December 1986). (PB87 142063/AS)

178 Annual Data and Verification Tabulation, Eastern North Pacific Tropical Storms and Hurricanes 1982. E.B. Gunther, June 1983. (PB85 106078)

179 Stratified Maximum Temperature Relationships Between Sixteen Zone Stations in Arizona and Respective Key Stations. Ira S. Brenner, June 1983. (PB83 249904)

180 Standard Hydrologic Exchange Format (SHEF) Version I. Phillip A. Pasteris, Vernon C. Bissel, David G. Bennett, August 1983. (PB85 106052)

181 Quantitative and Spacial Distribution of Winter Precipitation along Utah's Wasatch Front. Lawrence B. Dunn, August 1983. (PB85 106912)

182 500 Millibar Sign Frequency Teleconnection Charts - Winter. Lawrence B. Dunn, December 1983. (PB85 106276)

183 500 Millibar Sign Frequency Teleconnection Charts - Spring. Lawrence B. Dunn, January 1984. (PB85 111367)

184 Collection and Use of Lightning Strike Data in the Western U.S. During Summer 1983. Glenn Rasch and Mark Mathewson, February 1984. (PB85 110534)

185 500 Millibar Sign Frequency Teleconnection Charts - Summer. Lawrence B. Dunn, March 1984. (PB85 111359)

186 Annual Data and Verification Tabulation eastern North Pacific Tropical Storms and Hurricanes 1983. E.B. Gunther, March 1984. (PB85 109635)

187 500 Millibar Sign Frequency Teleconnection Charts - Fall. Lawrence B. Dunn, May 1984. (PB85 110930)

188 The Use and Interpretation of Isentropic Analyses. Jeffrey L. Anderson, October 1984. (PB85 132694)

189 Annual Data & Verification Tabulation Eastern North Pacific Tropical Storms and Hurricanes 1984. E.B. Gunther and R.L. Cross, April 1985. (PB85 1878887AS)

190 Great Salt Lake Effect Snowfall: Some Notes and An Example. David M. Carpenter, October 1985. (PB86 119153/AS)

191 Large Scale Patterns Associated with Major Freeze Episodes in the Agricultural Southwest. Ronald S. Hamilton and Glenn R. Lussky, December 1985. (PB86 144474AS)

192 NWR Voice Synthesis Project: Phase I. Glen W. Sampson, January 1986. (PB86 145604/AS)

193 The MCC - An Overview and Case Study on Its Impact in the Western United States. Glenn R. Lussky, March 1986. (PB86 170651/AS)

194 Annual Data and Verification Tabulation Eastern North Pacific Tropical Storms and Hurricanes 1985. E.B. Gunther and R.L. Cross, March 1986. (PB86 170941/AS)

195 Radid Interpretation Guidelines. Roger G. Pappas, March 1986. (PB86 177680/AS)

196 A Mesoscale Convective Complex Type Storm over the Desert Southwest. Darryl Randerson, April 1986. (PB86 190998/AS)

197 The Effects of Eastern North Pacific Tropical Cyclones on the Southwestern United States. Walter Smith, August 1986. (PB87 106258AS)

198 Preliminary Lightning Climatology Studies for Idaho. Christopher D. Hill, Carl J. Gorski, and Michael C. Conger, April 1987. (PB87 180196/AS)

199 Heavy Rains and Flooding in Montana: A Case for Slantwise Convection. Glenn R. Lussky, April 1987. (PB87 185229/AS)

200 Annual Data and Verification Tabulation Eastern North Pacific Tropical Storms and Hurricanes 1986. Roger L. Cross and Kenneth B. Mielke, September 1987. (PB88 110895/AS)

201 An Inexpensive Solution for the Mass Distribution of Satellite Images. Glen W. Sampson and George Clark, September 1987. (PB88 114038/AS)

202 Annual Data and Verification Tabulation Eastern North Pacific Tropical Storms and Hurricanes 1987. Roger L. Cross and Kenneth B. Mielke, September 1988. (PB88 101935/AS)

203 An Investigation of the 24 September 1986 "Cold Sector" Tornado Outbreak in Northern California. John P. Monteverdi and Scott A. Braun, October 1988. (PB89 121297/AS)

204 Preliminary Analysis of Cloud-To-Ground Lightning in the Vicinity of the Nevada Test Site. Carven Scott, November 1988. (PB89 128649/AS)

205 Forecast Guidelines For Fire Weather and Forecasters -- How Nighttime Humidity Affects Wildland Fuels. David W. Goens, February 1989. (PB89 162549/AS)

206 A Collection of Papers Related to Heavy Precipitation Forecasting. Western Region Headquarters, Scientific Services Division, August 1989. (PB89 230833/AS)

207 The Las Vegas McCarran International Airport Microburst of August 8, 1989. Carven A. Scott, June 1990. (PB90-240268)

208 Meteorological Factors Contributing to the Canyon Creek Fire Blowup, September 6 and 7, 1988. David W. Goens, June 1990. (PB90-245085)

209 Stratus Surge Prediction Along the Central California Coast. Peter Felsch and Woodrow Whitlatch, December 1990. (PB91-129239)

210 Hydrotools. Tom Egger. January 1991. (PB91-151787/AS)

211 A Northern Utah Soaker. Mark E. Struthwolf, February 1991. (PB91-168716)

212 Preliminary Analysis of the San Francisco Rainfall Record: 1849-1990. Jan Null, May 1991. (PB91-208439)

213 Idaho Zone Preformat, Temperature Guidance, and Verification. Mark A. Mollner, July 1991. (PB91-227405/AS)

214 Emergency Operational Meteorological Considerations During an Accidental Release of Hazardous Chemicals. Peter Mueller and Jerry Galt, August 1991. (PB91-235424)

215 WeatherTools. Tom Egger, October 1991.

216 Creating MOS Equations for RAWS Stations Using Digital Model Data. Dennis D. Gettman, December 1991. (PB92-131473/AS)

217 Forecasting Heavy Snow Events in Missoula, Montana. Mike Richmond, May 1992.

NOAA SCIENTIFIC AND TECHNICAL PUBLICATIONS

The National Oceanic and Atmospheric Administration was established as part of the Department of Commerce on October 3, 1970. The mission responsibilities of NOAA are to assess the socioeconomic impact of natural and technological changes in the environment and to monitor and predict the state of the solid Earth, the oceans and their living resources, the atmosphere, and the space environment of the Earth.

The major components of NOAA regularly produce various types of scientific and technical information in the following kinds of publications.

PROFESSIONAL PAPERS--Important definitive research results, major techniques, and special investigations.

CONTRACT AND GRANT REPORTS--- Reports prepared by contractors or grantees under NOAA sponsorship.

ATLAS--Presentation of analyzed data generally in the form of maps showing distribution of rainfall, chemical and physical conditions of oceans and atmosphere, distribution of fishes and marine mammals, ionospheric conditions, etc.

TECHNICAL SERVICE PUBLICATIONS--Reports containing data, observations, instructions, etc. A partial listing includes data serials; prediction and outlook periodicals; technical manuals, training papers, planning reports, and information serials; and miscellaneous technical publications.

TECHNICAL REPORTS--Journal quality with extensive details, mathematical developments, or data listings.

TECHNICAL MEMORANDUMS--Reports of preliminary, partial, or negative research or technology results, interim instructions, and the like.

Information on availability of NOAA publications can be obtained from:

NATIONAL TECHNICAL INFORMATION SERVICE

U. S. DEPARTMENT OF COMMERCE

5285 PORT ROYAL ROAD

SPRINGFIELD, VA 22161